LOW TEMPERATURE PHYSICS VOLUME 31, NUMBERS 8–9 AUGUST–SEPTEMBER 2005

On seven decades of antiferromagnetism

[DOI: 10.1063/1.2008126]

In tracing the history of the discovery of the cooperative ordering of electron spins in an antiparallel orientation of their moments in the solid substances and the use of the term ''antiferromagnetism'' to denote this new magnetic state of matter in physical discourse, one would invariably start from the experiments that raised the necessity of altering the molecular field concept introduced by Weiss in 1906 for the description of ferromagnetism. These were experiments investigating the temperature dependence of the magnetic susceptibilities of the metals Mn, Cr, the alloys Co–Fe, Fe–Mn, Fe–Cr, and the chlorides $FeCl_2$, $CrCl_3$, and $NiCl_2$. As it would turn out, these substances are by no means the simplest of antiferromagnets, and it is possibly for that reason that the path to antiferromagnetism was not the easiest one. For some time this new magnetic state was called anomalous ferromagnetism.

In 1932 L. Néel, striking off from Heisenberg's notions of the exchange interaction, deepened Weiss's concept of the molecular field by introducing the concept of a ''local molecular field.'' He allowed for the possibility of this field being oriented in the opposite direction to that of the magnetic moment created by the neighboring ion. That made it possible to explain the temperature behavior of the magnetic susceptibility of PtCo alloys [L. Néel, Ann. Phys. (Paris) **17**, 5 (1932)] and the anomalously large temperature-independent susceptibility of chromium [L. Néel, J. Phys. et Radium (Paris) **3**, 160 (1932)]. Subsequently Néel introduced the concept of interpenetrating magnetic sublattices into the theory of the ''generalized ferromagnet'' (later called ''antiferromagnet''). The thermodynamic theory developed by Néel made it possible to perceive the cooperative character of the antiferromagnetic ordering and to predict a peak on the temperature dependence of the susceptibility upon the spontaneous onset of antiferromagnetic order [L. Néel, Ann. Phys. (Paris) **5**, 232 (1936)]. This peak was soon observed, and the temperature of the transition to the new magnetic state has come to be called the Néel temperature.

During this same period of years, L. V. Shubnikov and L. D. Landau in Kharkov were intrigued by the seemingly contradictory magnetic properties of layered anhydrous crystals of the chlorides of iron, cobalt, nickel, and chromium. In the paramagnetic temperature region the magnetic susceptibility of these salts increased with decreasing temperature as in ordinary ferromagnets—faster than required by the Curie-Weiss law—but no ferromagnetism arose on further cooling below the paramagnetic Curie temperature, and the susceptibility itself became dependent on the magnetic field strength [H. R. Woltjer, Leiden Comm. N173b (1926); H. R. Woltjer and Kamerlingh Onnes, Leiden Comm. N173c (1926); H. R. Woltjer and E. C. Wiersma, Leiden Comm. N201a (1930)].

In 1933 Landau developed a phenomenological model of a layered magnet wherein he took into account the possibility of a strong dependence of the exchange interaction on the distance between magnetic ions and assumed that the interaction between magnetic ions belonging to the same layer is positive (ferromagnetic) while that between ions of different layers is negative, i.e., promoting an antiparallel orientation of the magnetic moments. He introduced two magnetic subsystems formed by the ions of neighboring layers with oppositely directed magnetic moments, and the vectors now known as the ferromagnetic and antiferromagnetic vectors. Landau also took into account the interaction of the magnetic moments of the ions with the lattice, which causes magnetic anisotropy. The minimum of the energy in the model corresponds to an antiparallel orientation of the magnetic moments of the layers. The model explained the magnetic anomalies observed and predicted spontaneous cooperative magnetic ordering with zero resultant magnetic moment of the whole crystal but with nonzero magnetic moments of its subsystems; such ordering should be accompanied by characteristic features on the depend dependence of the heat capacity and magnetic susceptibility. Landau obtained expressions for the temperature dependence of the magnetic susceptibility in all crystallographic directions [L. Landau, Phys. Zs. Sowjet. **4**, 675 (1933)].

In a parallel effort an experiment designed by L. Shubnikov was carried out to detect the anomalies of the temperature dependence of the heat capacity that should accompany cooperative magnetic ordering in $FeCl_3$ at low temperatures. The experiment was brilliantly completed in 1934. The observed peak [O. N. Trapeznikowa and L. W. Shubnikov, Nature **134**, 378 (1934)] attested to the cooperative character of the spontaneous antiparallel ordering of the magnetic moments and confirmed the conclusions of the theory that had been developed at that time. Subsequently these same anomalies of the heat capacity were found in all of the chlorides displaying anomalous magnetic behavior [O. N. Trapeznikova, L. V. Shubnikov, G. A. Milyutin, Zh. Éksp. Teor. Fiz. **6**, 421 (1936)]. Soon after, the expected features on the temperature dependence of their magnetic susceptibilities were also observed [L. W. Schubnikow and S. S. Schalyt, Phys. Z. Sowjet. **11**, 566 (1937); Zh. Éksp. Teor. Fiz. **8**, 518 (1938)].

The years 1932–1936 can be considered to be the date of birth of antiferromagnetism. That is the period in which the observation of the magnetic and thermal properties expected to accompany the formation of a magnetic state of matter with an antiparallel orientation of the magnetic moments was achieved. This state did not yet have a name. This was conferred later, in 1937. In his Nobel Lecture, Néel would credit F. Bitter with the introduction of the term ''antiferromagnetism'' [F. Bitter, Phys. Rep. **54**, 79–86 (1938)]. However, the term can also be found in an earlier paper [J. H. van Vleck, Phys. Rev. **52**, 1178–1198 (1937)].

Attempts at a quantum description of the phenomenon of antiferromagnetism had not been so successful, since a strict

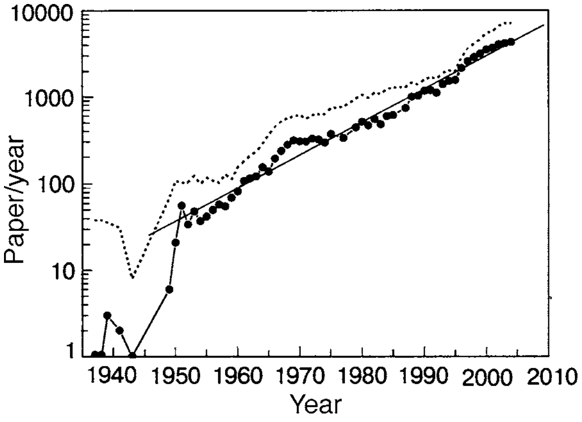

FIG. 1. Number of papers per year containing the term "antiferromagnetic" in the title or abstract. The search was done using the search engine Google Scholar. The dotted line shows the analogous result for the term "ferromagnetic." The time interval over which the number of papers increases by a factor of *e* (the straight line) is 11.2 yr for "antiferromagnetic" and 12.5 yr for "ferromagnetic."

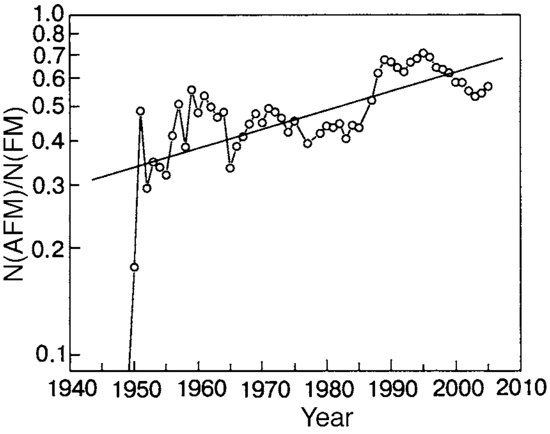

FIG. 2. Time dependence of the ratio of the number of papers per year containing the term "antiferromagnetic" to the number of those containing the term "ferromagnetic."

antiparallel orientation of the spins of magnetic sublattices did not correspond to the ground state of the quantum systems studied. This situation led to some skepticism as to whether that picture was correct. Only the neutron-diffraction experiments in 1949 [C. G. Shull and J. S. Smart, Phys. Rev. **76**, 1256 (1949)], in which additional diffraction peaks were observed to appear upon the transition of the MnO crystal to the magnetically ordered state, made it possible to assert that the antiferromagnetic ordering of the spin moments on the macroscopic scale actually occurs. The magnetic structure of MnO was described beautifully by the model of two interpenetrating magnetic sublattices. The stability of such structures in time was later confirmed indirectly and then directly, by the observation of stable 180-degree (time-reversed) antiferromagnetic domains.

Subsequent experimental and theoretical research on antiferromagnets revealed many new structures and properties. It soon became clear that collinear antiferromagnets with completely compensated magnetic moments represent only one of many groups of antiferromagnets. The great diversity of states united by the property of nearly complete compensation of all their elementary magnetic moments is evident merely from a list of the terms that have been introduced to identify the different classes of antiferromagnetic substances: collinear or noncollinear antiferromagnets, many-lattice noncollinear antiferromagnets, metamagnets, antiferromagnets with weak ferromagnetism, the set of modulated antiferromagnetic structures commensurate and incommensurate with the period of the unit cell of the crystal, antiferromagnetic glasses, dimeric spin structures, antiferromagnetic chains and ladders, gap antiferromagnets, antiferromagnetic vortex structures, frustrated antiferromagnetic structures, molecular cluster antiferromagnets, nuclear antiferromagnets, and, finally, artificial heteromagnetic nanostructures. We hope that the papers published in this issue will give an idea of the different fields of antiferromagnetics research being pursued at various research centers of Europe, Asia, and America.

The pace of research on antiferromagnetism since the time of its discovery is demonstrated in Figs. 1 and 2. Although the data presented are far from complete, they do reflect more accurately the evolutionary trends of such research. One might think that this temperature dependence could be altered noticeably by recent developments such as the wide application of artificial antiferro/ferromagnetic structures for data storage and readout devices in information technology and the growing interest in the role of antiferromagnetism in high-temperature superconductivity, but in reality the exponent characterizing the growth of interest varies in direct proportion to time and fluctuates little. It is also curious that over the entire history of antiferromagnetism the ratio of the number of papers on antiferromagnets to the number of papers on ferromagnets is steadily growing.

In closing, we note that many famous names in physics are linked with research on antiferromagnets, but the discovery of antiferromagnetism as a physical phenomenon is associated with the names of those who were first: L. Néel, L. D. Landau, and L. V. Shubnikov. There is no doubt that the physical concepts introduced by them, which have since come to be called antiferromagnetism, Néel temperature, magnetic sublattice, and the antiferromagnetic vector, will endure for a long time to come.

N. F. Kharchenko

LOW TEMPERATURE PHYSICS VOLUME 31, NUMBERS 8–9 AUGUST–SEPTEMBER 2005

Mesoscopic antiferromagnets: statics, dynamics, and quantum tunneling (Review)

B. A. Ivanov*

Institute of Magnetism of the National Academy of Sciences of Ukraine, pr. Vernadskogo 36b, Kiev 03142, Ukraine; Taras Shevchenko National University, pr. Glushkova 2, Kiev 03127, Ukraine

(Submitted March 4, 2005)
Fiz. Nizk. Temp. **31**, 841–884 (August–September 2005)

The static and dynamic, quantum and classical properties of antiferromagnets (AFMs) are discussed from a unified point of view. Attention is directed mainly toward mesoscopic magnets, i.e., materials with characteristic scales of nonuniformities of the order of atomic dimensions. The creation of such materials and their study and application have largely shaped the face of the physics of our day. This class includes small magnetic particles and their arrays, magnetic superlattices and clusters, and high-spin molecules. The traditional problems of the physics of antiferromagnetism are also discussed (symmetry analysis of AFMs, reorientation transitions, equations of spin dynamics), but they are represented only to the extent that it is useful to do so for subsequent consideration of the quantum and classical properties of mesoscopic AFMs. For description of the spin dynamics of AFMs, a magnetic Lagrangian of a form matched with the quantum-mechanical Hamiltonian is constructed. The lowering of the symmetry of the AFMs, both that due to conventional causes such as an external magnetic field and that due to the partial decompensation of the sublattice spins, is taken into account. The latter effect is especially important for mesoscopic particles of AFMs of the ferrite type. The influence of defects and of the surface on the reorientation transitions in AFMs is discussed in detail. These effects, which are of fundamental importance for the description of small particles of AFMs, are observed for magnetic superlattices with an antiferromagnetic interaction of the elements of the superlattices. The description of macroscopic quantum effects in mesoscopic AFMs plays a prominent role. The spin Lagrangian obtained describes new tunneling effects such as an oscillatory dependence of the tunneling probability on magnetic field. Quantum effects in magnetic systems with a nonuniform ground state are investigated. These effects can be described as the change due to processes of tunneling of the topological charges of various natures that characterize these states. [DOI: 10.1063/1.2008127]

I. INTRODUCTION

The study and practical application of mesoscopic materials with characteristic length scales of the nonuniformities from micron to atomic dimensions started at the boundary of the twentieth and twenty-first centuries. The class of mesoscopic magnets includes materials with different spatial scales, such as small magnetic particles of micron and submicron dimensions and ordered arrays of such particles, magnetic superlattices, magnetic clusters, and, finally, high-spin molecules, including tens of spins with a strong exchange interaction.[1,2] Mesoscopic magnets can be divided, in terms of the character of their ordering (we are talking about the focus of the spins both in an individual small particle and the ordering of the magnetic moments of individual elements of a superlattice), into the same classes as bulk materials (ferromagnets, AFMs, ferrimagnets). These materials often manifest unique physical properties that are absent in bulk samples. It suffices to mention the macroscopic quantum effects manifested in the coherent quantum behavior of tens, hundreds, and even thousands of spins.

The physics of mesoscopic magnets owes its progress to the achievements of the traditional physics of magnetically ordered crystals. Undoubtedly the significant results from the study of ‘‘ordinary’’ AFMs, elaborated and explained in the many monographs devoted wholly or largely to this field of physics,[3–9] have played a large role in the study of the subject of this review: the manifestations of antiferromagnetism in the properties of mesoscopic magnets.

In the past seven decades the study of antiferromagnetism has comprised a significant part of the fundamental physics of magnetism.[10,11] This is due not only to the features of ‘‘purely magnetic’’ properties of these materials, among which one might mention the broad spectrum of spontaneous and field-induced order-disorder phase transitions (see monographs[5,12]) and interesting resonance properties of AFMs, primarily the ‘‘exchange enhancement’’ of the resonance frequencies.[7] No less important are the manifestations of antiferromagnetism in such ‘‘nonmagnetic’’ properties of materials such as optical,[8,13] galvanomagnetic,[13] and acoustic.[13,14] We know of no examples of the application of conventional crystalline AFMs as functional materials for solid-state electronics, although their many unique parameters, e.g., the presence of magnetic resonance frequencies in the submillimeter region[7] and the enormous domain-wall velocities (tens of kilometers per second),[6,15] look very promising for applications in modern functional electronics. In the past decade, however, novel objects that might be classified as ‘‘artificial AFMs’’ have arrived in the physics of magnetism. Among these are one-dimensional (1D) superstructures of the multilayer film type and two-dimensional (2D) superstructures comprising lattices of magnetic elements of submicron scale on a nonmagnetic substrate. Such materials are promising for the development of new devices for high-density magnetic recording,[16–18] magnetic field sensors and magnetic heads,[19,20] and logic elements for computers.[21] The interaction of the structural elements can be antiferromagnetic in both 1D[19,22] and 2D[23] superlattices.[23] Antiferromagnetic order of the structural elements of a superlattice and the change of this order under the influence of magnetic field (analogous to spin-flop or spin-flip transitions in crystalline AFMs;[24–26] see Sec. 4) determine its giant magnetoresistance,[19,20] a property of practical importance.

The main feature specific to the physics of mesoscopic magnets is the presence in them of macroscopic coherent quantum tunneling effects, which were observed more than 10 years ago.[1,27–30] These effects are of interest because of the importance, from a general physical standpoint, of manifestations of quantum effects in the macro world. Mesoscopic objects, which have quantum-mechanical properties, are of interest for their potential application as elements of quantum computers.[31] Furthermore, a number of subtle and beautiful effects, e.g., the suppression of tunneling transitions on account of interference of the instanton trajectories.[32,33] The possibility of controlling tunneling effects (turning the tunneling on or off) is important for the use of mesoscopic magnets as elements of quantum computers.[31]

Analysis of macroscopic quantum tunneling effects requires the use of a number of complicated methods of modern quantum physics of magnets and quantum field theory. However, the exposition becomes much more compact and simple if results from the classical physics of magnets are used. Comparison of the classical and quantum pictures of magnets is made in Sec. 3. On the basis of that discussion, in Sec. 4 we investigate reorientation transitions in magnets, both in the framework of the conventional approach, which is adequate for describing bulk AFMs, and for mesoscopic magnets. In Sec. 5 we turn to an analysis of the semiclassical dynamics of AFMs in a formulation that is closest to the conventional theory of the dynamical properties of magnets but which permits a consistent analysis of purely quantum effects. A detailed discussion of the problems of tunneling in small particles of AFMs on this basis is presented in Sec. 6. Finally, in Sec. 7 we discuss the question of the topological spin nonuniformities in mesoscopic AFMs and, on the basis of non-one-dimensional instantons, describe the tunneling effects for such nonuniform states of AFMs.

For reasons of space an author must always select those areas that are of greatest interest at the given time. Naturally, even though one tries to be objective, such a selection cannot avoid subjectivity. Here we do not touch upon questions of the dynamics of nonlinear excitations (solitons) in low-dimensional crystalline AFMs (see reviews[34–38]). In this paper attention is devoted mainly to the properties specific to mesoscopic AFMs, both quantum (macroscopic quantum tunneling, destructive interference effects) and purely classical, deriving from the special role of the surface and of defects, and also to those physical phenomena in which the aforementioned features of mesoscopic AFMs are manifested jointly. The traditional problems, e.g., the character of reorientation transitions and the form of the dynamical equations for the order parameter, our understanding of which has been furthered substantially in recent years, are represented to the extent that it is useful to do so for the subsequent discussion of mesoscopic AFMs. This review does not claim to give a complete description of all the phenomena mentioned above. However, the author hopes that the discussion of the static and dynamic (including nonlinear) quantum and classical properties of AFMs, though brief, will be useful to the reader.

II. ANTIFERROMAGNETICS AT THE TURN OF THE CENTURY

At the present time many different types of spin ordering of condensed media are known, both crystalline and amorphous.[10,11] From time immemorial man has made practical use of magnets having nonzero mean values of the spin density $\langle \mathbf{S} \rangle$ or magnetization $\mathbf{M}$; in the simplest case $\mathbf{M} = -g\mu_B \langle \mathbf{S} \rangle$, where g is the Lande factor ($g \approx 2$ for ions in the s state), and μ_B is the *modulus* of the *Bohr magneton*. In the language of the theory of symmetry this means that such materials (including not only pure ferromagnets but also a large class of ferrimagnets, some spiral magnets, etc.) are characterized by spontaneous breaking of the symmetry with respect to time inversion $t \to -t$, whereupon both the mean value of the spin of an individual ion and also the value of the magnetization changes sign. Antiferromagnets are a fundamentally different class of materials. In them the symmetry with respect to time inversion is spontaneously broken, but the spontaneous magnetization is equal to zero. The phenomenon of antiferromagnetism was discovered over 70 years ago, and a theoretical explanation for it was given at that time in the papers by Néel[39,40] and Landau.[41]

The situation with complete compensation of the magnetization is presented most simply by assuming that the crystal lattice of the AFMs contains a finite number n of magnetic sublattices, each of which has a nonzero magnetization $\mathbf{M}_\alpha$, but these magnetizations compensate each other so that the total magnetization of the AFMs in the ground state is equal to zero, $\mathbf{M} = \Sigma_{\alpha=1}^{n} \mathbf{M}_\alpha = 0$. The simplest example, to which we shall limit discussion, is that of a two-sublattice AFM in the ground state of which the magnetizations $\mathbf{M}_1$ and $\mathbf{M}_2$ are equal in magnitude and antiparallel. In such a definition it is understood that the sublattices must necessarily be crystallographically equivalent, i.e., there exists an element of the crystal symmetry group (the symmetry group of the paraphase) that takes one sublattice into the other. One of the most important contains reached after many years of study of the phenomenon of antiferromagnetism and the ‘‘nonmagnetic’’ effects associated with it lies in the extreme importance of symmetry analysis of AFMs. It is because of symmetry restrictions that there can be a *strictly zero* value of the magnetization $\mathbf{M} = 0$ in the face of a nonzero mean value of the spins, i.e., exact compensation of the magnetizations of the individual spins in a finite region of a medium. A symmetry description of magnets is based on the use of either magnetic[4,9,42] or exchange[43] symmetry groups. A symmetry operation that does not permute the magnetic sublattices will be called *even*, following Turov,[4] while one that does permute will be called *odd*, and their signs will be denoted as $(+)$ or $(-)$, respectively. A criterion of antiferromagnetism is the presence of at least one odd symmetry element of the paraphase. This condition distinguishes AFMs from *ferrimagnets*, the sublattices of which are inequivalent, although their total magnetization can go to zero at a compensation point. This definition of antiferromagnetism (and not the condition that the spontaneous magnetization equals zero) is now standard.

The magnetization of AFMs can be nonzero in the presence of an external field $\mathbf{H} \neq 0$ without eliminating the spontaneous symmetry breaking. Here it is appropriate to compare the behavior of the different *Heisenberg* magnets, the Hamiltonian of which contains only a purely isotropic exchange interaction of the form

$$\hat{H}^{(\mathrm{Heis})} = J\hat{\mathbf{S}}_1 \cdot \hat{\mathbf{S}}_2, \tag{1}$$

where J is the exchange integral, $J > 0$ for AFMs, and $\hat{\mathbf{S}}_{1,2}$ are spin operators. In a Heisenberg ferromagnet (FM), if one disregards the anisotropic interactions of a relativistic nature, the magnetization $\mathbf{M}$ is parallel to the field $\mathbf{H}$, i.e., there is no spontaneous symmetry breaking for $\mathbf{H} \neq 0$. For an isotropic AFM the magnetization caused by the field is also nonzero, $\mathbf{M} = \chi \mathbf{H}$, where χ is the susceptibility of the AFM. However, contrary to the FM case, a difference of the sublattice magnetizations and, hence, antiferromagnetic order exists over a wide region of values of the field $|\mathbf{H}| < H_{\mathrm{ex}}$, where H_{ex} is the exchange field. These same relationships on the whole remain valid when the relativistic interactions are taken into account (if they are not too strong): magnetic order exists in a ferromagnet only when the field $\mathbf{H}$ is oriented along certain selected symmetry axes, while in an AFM the ordering in the presence of anisotropy remains unbroken as before at fields $H < H_{\mathrm{ex}}$.

The criterion $\mathbf{M} = 0$ for defining antiferromagnetism is not exhaustive, because in certain crystalline AFMs with the relativistic interactions taken into account the compensation of the magnetizations is not complete, even in the absence of external magnetic field, and a weak spontaneous moment appears. For a two-sublattice AFMs the incomplete compensation of the magnetizations (the physics of weak ferromagnetism) can be described as a manifestation of noncollinearity, or canting, of the magnetizations $\mathbf{M}_1$ and $\mathbf{M}_2$. Such AFMs are called *weak ferromagnets* or canted AFMs. The theory of weak ferromagnetism was constructed by Dzyaloshinskii[44] on the basis of a phenomenological approach (see the recent monograph by Turov *et al.*[9] for details), and a microscopic mechanism was proposed by Moriya.[45]

Application of the usual concepts of the physics of crystalline AFMs for the description of mesoscopic AFMs can require a certain modification. For atomic clusters containing hundreds or thousands of spins with an antiferromagnetic interaction, the role of the surface becomes extremely important. Even for an atomically smooth surface the number of particles in the sublattices can differ. As a consequence, an uncompensated total spin of the AFM particle arises. As an example, let us consider ferritin particles, which play an important role in the vital activity of warm-blooded animals. These particles are used as a model object for experimental study of the properties of AFM particles.[27] The magnetic part of a ferritin particle consists of approximately 4500 iron ions Fe^{3+} with spin $S = 5/2$, coupled by an antiferromagnetic interaction and ordered in an almost ideal magnetic structure of a typical crystalline AFM—hematite α-$\mathrm{Fe}_2\mathrm{O}_3$. However, the uncompensated magnetic moment of the ferritin particle is not small: it has a value of around $200\mu_B$, i.e., of the order of 1% of the maximum possible value. Thus, from the standpoint of analysis of the magnetization, ferritin is a ferrimagnet close to the compensation point, and that fundamentally alters its dynamic properties, both classical and (especially) quantum; see Secs. 5 and 6. On the other hand, for the majority of the magnetic atoms, lying in the central part of such a particle, the standard description in the language of crystal magnetic groups is applicable.

In recent years, new objects that can be classified as mesoscopic magnets have appeared. Their characteristic scales are still smaller than for the ferritin particles mentioned above but are larger than atomic scales. These are the so-called high-spin molecules, containing tens of spins with an interaction close to the isotropic Heisenberg interaction (1) and rather strong (the exchange integral J has a value up to 100 K); see reviews.[1,46] Such molecules are also known to exhibit manifestations of the Dzyaloshinskii-Moriya interaction. High-spin molecules typically have a regular distribution of magnetic ions, forming a quite definite magnetic structure. Essentially, the synthesis and study of high-spin molecules, and especially the creation of high-quality single crystals of such molecules with good orientation of the magnetic axes of the molecules in the crystal, have opened up a new era in the study of the macroscopic quantum effects in magnets. An important class of such molecules (and a fundamentally new object in the physics of antiferromagnetism) is that of the so-called *spin rings* (the term *ferric wheels* is also used). In such molecules an odd number of magnetic ions (the best-studied are molecules with 6, 8, and 10 iron ions Fe^{3+} with spin $S = 5/2$) form a closed ring with an antiferromagnetic interaction of the nearest neighbors ($J \sim 15-30$ K) and a completely compensated total spin.[48–52] In high-spin molecules proper (molecular magnets) the interaction is mainly ferromagnetic, and their total magnetic moment can reach a value of $26\mu_B$.[53] Some high-spin molecules should be classified as molecular ferrimagnets. They consist of two inequivalent groups of spins with a ferromagnetic interaction within a group and an antiparallel orientation of the spins of the two groups (analogous to sublattices). This class of objects includes the best-studied molecular magnet Mn_{12}-ac, in which 8 manganese ions Mn^{3+} with $S = 3/2$ give a total spin $S_{\mathrm{tot}} = 10$.[48] High-spin molecules with half-integer spin are also known; among them are Mn_4 complexes with spin 9/2.[54,55] For Mn_{12}-ac the decompensation is not small, but for the V_{16} molecule with 15 vanadium atoms with spin $S = 1/2$ the total spin is equal to 1/2.[56] From the point of view of classical symmetry analysis the high-spin molecules should be described by finite classes of magnetic symmetry, but, unlike the known crystalline magnetic classes, here such symmetry elements as C_n, D_n, S_n axes with $n = 5$ or $n > 6$ can also be present. An example is the $\mathrm{Mn}_{72}\mathrm{Fe}_{30}$ molecule, in which the 30 iron ions Fe^{3+}, coupled by an antiferromagnetic exchange interaction, form an icosadodecahedral structure with 5- and 3-fold axes.[57]

Finally, let mention the "antiferromagnetic" aspects of the physics of purely man-made magnetic materials (magnetic superstructures) created with the use of modern nanotechnologies. This class includes multilayer systems consisting of layers of ferromagnetic metals a few atoms thick, separated by spacer layers of nonmagnetic or antiferromagnetic metals.[19] For such 1D superstructures the interaction of the magnetic elements (the individual layers) is determined by the exchange across the spacers and can be ferromagnetic or antiferromagnetic; for these structures biquadratic exchange effects are also known.[19,22]

In recent years, 2D superstructures composed of lattices of submicron magnetic particles on a nonmagnetic substrate have also been widely studied. Depending on their shape, these particles are called magnetic dots, strips, rings, or wires. Most often they are made of magnetically soft materials such as Co, Fe, and Permalloy.[17] The interaction of individual particles in such a system is determined by the magnetic dipole interaction of their magnetic moments, i.e., they are a pure implementation of dipolar AFMs.[58] Thus the orientation of the magnetic moments of the elements of the superstructures (macroscopic spins) is often antiferromagnetic,[23] and such systems can be regarded as "artificial AFMs." They exhibit effects inherent to ordinary crystalline AFMs, such as spin-flop or spin-flip transitions,[24–26] with the feature that the boundary elements (surface) play a significant role. These and other novel effects, such as a transition to a specific incommensurate phase, are discussed in detail in subsection 4.3.

We do not know of any effects in which the scatter in the values of the magnetic moments of individual structural elements leads to "decompensation of the macroscopic spins" of artificial AFMs. However, another important effect of nonideality of the structure on the atomic level is well known for them: topological defects of the atomic structure of AFMs or FM-AFM interfaces give rise to mesoscopic nonuniformities on account of frustration effects. The properties of such nonuniform states, including the problem of quantum tunneling for them, will be considered in Sec. 7.

III. CLASSICAL AND QUANTUM DESCRIPTION OF MAGNETS

For magnetic insulators and for a number of materials with metallic conductivity[59] an adequate description can be given on the basis of a Hamiltonian written in terms of spin operators $\mathbf{S}_\alpha$ localized at crystal lattice sites α. As an example, let us consider a Hamiltonian $\hat{H}$ containing an interaction bilinear in the operators, of the form $J_{ij}S_1^{(i)}S_2^{(j)}$. Here the tensor J_{ij} specifies both the isotropic (exchange) and the anisotropic pair interaction of the spins, and it can also contain an antisymmetric part due to the Dzyaloshinskii–Moriya interaction.[45] The discussion below will be based on a Hamiltonian with only a nearest-neighbor interaction. We shall use a simple version of it with purely uniaxial symmetry (the selected axis z is a C_∞ axis):

$$\hat{H}=\sum_{\langle\alpha\beta\rangle}\{J\mathbf{S}_\alpha\cdot\mathbf{S}_\beta+(\mathbf{d}\cdot[\mathbf{S}_\alpha\times\mathbf{S}_\beta])+\kappa S_\alpha^z S_\beta^z\}$$

$$-\mathrm{d}-K\sum_\alpha (S_\alpha^z)^2-g\mu_B\sum_\alpha \mathbf{H}\cdot\mathbf{S}_\alpha. \qquad (2)$$

Here the first three terms, in which the summation is over nearest-neighbor pairs $\langle\alpha\beta\rangle$ and each pair is counted once, describe bilinear interactions of the spins. They determine three types of interactions: the standard isotropic exchange [the Heisenberg exchange of Eq. (1)] with an exchange integral J; the antisymmetric Dzyaloshinskii–Moriya interaction,[44,45] which is written in terms of the dual vector $\mathbf{d}$ associated to the antisymmetric part of J_{ij}; and, the symmetric anisotropic interaction. This last is often called the *interion anisotropy*. The Hamiltonian $\hat{H}$ also includes the *single-ion anisotropy* with the constant K, which can exist only for site spins $S\geqslant 1$. The last term describes the Zeeman interaction of the spins with the external magnetic field. Here and below it is assumed for convenience and transparency that the spin vector operator $\mathbf{S}_\alpha$ is parallel to the magnetization. We shall mainly consider the case of weakly anisotropic magnets, for which $\kappa, K \ll J$, and the value of the exchange-relativistic constant $d\sim\sqrt{(\kappa,K)J}\ll J$.

Let us discuss the transition from a quantum spin Hamiltonian of the type (2) to the customary phenomenological description of magnets. Although in reality the macroscopic description is often used as a starting point, it is of interest to analyze this transition, primarily for investigating macroscopic quantum effects. No less important is the fact that a consistent microscopic analysis can shed light on the adequacy of the macroscopic approach for description of a given experiment.

For transition from the spin operators to the corresponding field variables one usually uses the spin coherent states (SCS) $|\boldsymbol{\sigma}\rangle$, which were introduced by Radcliffe[60] (see also the review[61]) are parametrized by a unit vector $\boldsymbol{\sigma}$, $\boldsymbol{\sigma}^2=1$, or the angular variables θ, φ:

$$\sigma_x=\sin\theta\cos\varphi,\quad \sigma_y=\sin\theta\sin\varphi,\quad \sigma_z=\cos\theta. \qquad (3)$$

The spin coherent states can be constructed by acting with the rotation operator $\hat{\mathbf{O}}$ on the spin state $\hat{\mathbf{S}}$ with a specified maximum projection $S_z=S$ on a certain direction $\mathbf{n}$. These states are eigenstates of the operator $\boldsymbol{\sigma}\cdot\hat{\mathbf{S}}$, $\boldsymbol{\sigma}\cdot\hat{\mathbf{S}}|\boldsymbol{\sigma}\rangle=\mathbf{S}|\boldsymbol{\sigma}\rangle$, and for them the mean value of the spin operator corresponds to its classical value

$$\langle\boldsymbol{\sigma}|\hat{S}|\boldsymbol{\sigma}\rangle=S\boldsymbol{\sigma}. \qquad (4)$$

This property is handy for making the transition from the quantum physics of spins to a phenomenological theory of magnetism. The SCS are a complete (more precisely, overcomplete) set of quantum states of the spin operator Ŝ, a property reflected in the existence of the "decomposition of unity" relations

$$\int \mathcal{D}\boldsymbol{\sigma}|\boldsymbol{\sigma}\rangle\langle\boldsymbol{\sigma}|=\hat{\mathbf{1}},\quad \int\mathcal{D}\boldsymbol{\sigma}=\frac{(2S+1)}{4\pi}\int\sin\theta d\theta d\varphi, \qquad (5)$$

where $\hat{\mathbf{1}}$ is the unit operator and $\mathcal{D}\boldsymbol{\sigma}$ is the measure, which is defined in terms of an area element on the sphere $\boldsymbol{\sigma}^2=1$.

For applications to the theory of Heisenberg magnets it is important that all the mean values of powers of the spin components can be expressed in terms of the corresponding powers of the means of the spin components, e.g.,[62,63]

$$\langle \boldsymbol{\sigma}|(\hat{\mathbf{S}}\cdot\mathbf{e})^2|\boldsymbol{\sigma}\rangle=\left(1-\frac{1}{2S}\right)\langle \boldsymbol{\sigma}|\hat{\mathbf{S}}\cdot\mathbf{e}|\boldsymbol{\sigma}\rangle^2+\frac{S}{2}. \tag{6}$$

This relation is valid for any value of the spin; for spin $S=1/2$ this corresponds to a well-known property of the Pauli matrices[64] and rules out the existence of single-ion anisotropy. Here it is important to note that the SCS are constructed without the use of any approximations of the large-spin type. However, there do exist a number of properties of the SCS that permit their constructive use only in that semiclassical limit.

An important distinction of the SCS (as for other coherent states) from the states usually adopted in quantum mechanics is the lack of orthogonality:

$$|\langle \boldsymbol{\sigma}_1|\boldsymbol{\sigma}_2\rangle|=\left[\frac{1}{2}(\mathbf{1}+\boldsymbol{\sigma}_1\cdot\boldsymbol{\sigma}_2)\right]^S.$$

In the limit $S\to\infty$ the value of $\langle \boldsymbol{\sigma}_1|\boldsymbol{\sigma}_2\rangle$ is exponentially small; in certain calculations this formally permits one to assume that these states are orthogonal in the large spin limit.

Spin coherent states, like the "ordinary" coherent states $|\alpha\rangle$ for bosons, where α is a complex number (introduced by Glauber,[65] these states are defined as eigenfunctions of the boson annihilation operator $\hat{a}$, $\hat{a}|\alpha\rangle=\alpha|\alpha\rangle$), are particular examples of the *generalized coherent states* (GCS) introduced by Perelomov.[66] They can be constructed for any Lie group $\hat{G}$. For spin coherent states, $\hat{G}$ coincides with the rotation group of three-dimensional space SO(3), and for boson states this is the so-called Heisenberg–Weyl group.[61] All GCS share the fundamental property that they minimize the indeterminacy of the values of the variables determined by the quantum uncertainty relation. This means that the GCS (in particular, the SCS) are the quantum states whose properties are most nearly classical. The use of coherent states is most efficient when the Hamiltonian of the system is linear with respect to the generators of the Lie group $\hat{G}$. Then if an initial state is coherent and described by a certain GCS, its quantum evolution will reduce to a variation of the parameters of the GCS, which are described by classical equations of motion.[61] This permits a simple and elegant construction of exact solutions of a number of problems of the quantum evolution of an arbitrary spin in an external variable magnetic field.[61] Exact solution of more-complex problems of the interaction of several spins, with a Hamiltonian bilinear in the operators of the spin components, is also possible.

For our problem it is very important that the use of the GCS permits one to obtain in a consistent manner the semiclassical Lagrangian of the system, which *in principle* cannot be recovered solely from the classical equations of motion. Lagrangians describing the same classical equations of motion of the system can differ by terms that are total derivatives with respect to time. Such a term cannot influence the classical dynamics of the system but is responsible for interference of the instanton trajectories[67,68] (see Sec. 6); it is also important for the definition of the soliton momentum.[69]

The most elegant way of obtaining the Lagrangian for any coherent states is based on the possibility of representing the quantum *propagator* P_{12} (the probability amplitude of a transition from one quantum state to another) in terms of a path integral over trajectories:[67]

$$P_{12}\equiv\langle\psi_1|\exp\{i\hat{H}t/\hbar\}|\psi_2=\int_{\psi_1}^{\psi_2}\mathcal{D}\psi\exp\{i\mathcal{A}[\psi]/\hbar\}, \tag{7}$$

where $\mathcal{A}[\psi]$ is the action functional known from classical physics, $\mathcal{A}[\psi]=\int dt\mathscr{L}[\psi]$, $\mathscr{L}$ is the Lagrangian of the system, and the integration is over all values of the variable ψ describing the GCS. We shall not discuss here the problem of consistent definition of the measure $\mathcal{D}\psi$. This approach is in essence based on the idea of the Feynman path integrals. It has the advantage that it can be applied to quantum field problems when one is speaking about space-time configurations $\psi\equiv\psi(\mathbf{x},t)$ of the field.[67,68]

Using the properties of the GCS $|\psi\rangle$, we can write the Lagrangian $\mathscr{L}[\psi]$ in the form

$$\mathscr{L}=-\hbar\langle\psi|\partial/\partial t|\psi\rangle-W(\psi),\quad W(\psi)\equiv\langle\psi|\hat{H}|\psi\rangle. \tag{8}$$

The Lagrangian has the standard form $T-W$, where the form of the kinetic term T can easily be found for coherent states of any Lie group. The "potential energy" W in this formula is simply the quantum Hamiltonian of the system averaged over the coherent state $\langle\psi|\hat{H}|\psi\rangle$.

Let us return to the description of magnets in terms of the SCS $|\boldsymbol{\sigma}\rangle$. The Lagrangian of an individual spin S in the angular variables (3) is usually written in the form[34–38,67]

$$\mathscr{L}=\hbar S(\partial\varphi/\partial t)(1-\cos\theta)-W(\varphi,\theta), \tag{9}$$

where $W(\pi,\theta)$ has the meaning of the classical energy $W(\boldsymbol{\sigma})=\langle\boldsymbol{\sigma}|\hat{H}|\boldsymbol{\sigma}\rangle$, expressed in terms of the angular variables for the vector $\boldsymbol{\sigma}$. Variation of this Lagrangian gives the well-known Landau–Lifshitz equation[70] in angular variables (see the monograph and review[34–37,71]).

The kinetic term can be represented in a more general form than (9) directly for the vector dynamical variable $\boldsymbol{\sigma}$:

$$\mathscr{L}=\hbar S\mathbf{A}(\sigma)\cdot\frac{\partial\boldsymbol{\sigma}}{\partial t}-W(\boldsymbol{\sigma}),\quad \mathbf{A}(\boldsymbol{\sigma})=\frac{\boldsymbol{\sigma}\times\mathbf{n}}{\sigma(\sigma+\boldsymbol{\sigma}\mathbf{n})}, \tag{10}$$

where $\mathbf{n}$ is the quantization axis of the coherent state. For transparency of interpretation it is convenient to assume that the variable $\boldsymbol{\sigma}$ is not restricted by the condition $\sigma^2=1$ but has a length $|\boldsymbol{\sigma}|=\sigma\neq 1$. Then this Lagrangian corresponds formally to the dynamics of a charged particle with a radius vector $\boldsymbol{\sigma}$, moving in a magnetic field with vector potential $\mathbf{A}$. The vector potential $\mathbf{A}$ in formula (10) is the field of a magnetic monopole, having a singularity at $\boldsymbol{\sigma}\cdot\mathbf{n}=-\sigma$, i.e., on a semi-infinite line segment in the space $\boldsymbol{\sigma}$. One usually chooses $\mathbf{n}=\mathbf{e}_z$, and here the quantity $\mathbf{A}(\boldsymbol{\sigma})\cdot(\partial\boldsymbol{\sigma}/\partial t)$ takes the well-known form (9). For constructing the Lagrangian of an AFM it is more convenient to use the general form (10).

Let us discuss the question of the description of the static characteristics of an AFM — its energy first and foremost. The coherent state for a spin Hamiltonian of the type (2) is chosen in the form a direct product of SCS, $|\boldsymbol{\sigma}\rangle=\Pi_\alpha|\boldsymbol{\sigma}_\alpha\rangle$, where $|\boldsymbol{\sigma}_\alpha\rangle$ are the SCS for the spin operator $\hat{\mathbf{S}}_\alpha$ located at site α. In this case the transition from the spin Hamiltonian, which does not contain products of operators of the spin components at a given site, to the classical energy is done by replacing the operators $\hat{\mathbf{S}}_\alpha$ by classical vectors $S\boldsymbol{\sigma}_\alpha$ of length S.

This way of writing the energy corresponds in the highest degree with our intuitive ideas about how to make the transition from the quantum spin Hamiltonian to the classical energy of a magnet. We note that the possibility of such a transition (rather than writing, say, the spin $\mathbf{S}_\alpha$ in the form $\boldsymbol{\sigma}_\alpha\sqrt{S(S+1)}$, naively employing the condition $\hat{\mathbf{S}}^2=S(S+1)$, which is incorrect), does not rely on the approximation $S\gg 1$.

Let us now discuss the specifics of magnets whose Hamiltonian contains products of the spin component operators at a single site. Such terms are present for magnets with single-ion anisotropy (2) or a biquadratic exchange interaction of the form $J'(\mathbf{S}_\alpha\cdot\mathbf{S}_\beta)^2$. Magnets with non-small interaction of this type are often called *non-Heisenberg*.[72] For them the "classical" limit corresponds to the substitution $\langle\boldsymbol{\sigma}_\alpha|(\hat{\mathbf{S}}_\alpha\cdot\mathbf{e})^2|\boldsymbol{\sigma}_\alpha\rangle\rightarrow(1-1/2S)(\mathbf{e}\cdot\boldsymbol{\sigma}_\alpha)^2+\text{const}$; see formula (6). Actually, however, the description of Heisenberg magnets on the basis of the SCS $|\boldsymbol{\sigma}\rangle_\alpha$ encounters more-serious problems than the renormalization of the single-ion anisotropy constants $K\rightarrow K(1-1/2S)$.

Let us discuss the specifics of Heisenberg magnets for the example of a magnet with strong easy-plane single-ion anisotropy of the form KS_z^2, $K>0$.[72] The ground state of such an ion is a quantum state with fixed projection $S_z=0$, for which $\langle\hat{S}_x\rangle=0$, $\langle\hat{S}_y\rangle=0$, but $\langle\hat{S}_x^2\rangle=\langle\hat{S}_y^2\rangle=S(S+1)/2$. The properties of this state are far from those of the corresponding SCS with projection $\sigma_z=0$, in which the vector $\boldsymbol{\sigma}$ has a definite direction in the (x,y) plane. Therefore it can hardly be expected that the ground state of such a Hamiltonian, even in the presence of the exchange interaction, will be well described in terms of SCS. Of course, this state can be described in the form of a superposition of spin coherent states (completeness of the set of SCS!), but this approach is extremely awkward.

For description of non-Heisenberg magnets Ostrovskiĭ and Loktev[73,74] proposed to use the GCS for Lie group SU$(2S+1)$, which for spin $S>1/2$ is more general than the SCS. [Recall that the SCS are constructed with the use of the rotation group SO(3), which is equivalent to the group SU(2).] This approach permits one to construct a consistent field theory of the unusual states of such magnets, including not only the magnetically ordered phases but also the so-called *nematic* or *quadrupolar* phases, in which magnetic ordering is absent. These phases are invariant with respect to time inversion but can be characterized by spontaneous symmetry breaking due to anisotropy of the quadrupole variables of the type $\langle\hat{S}_x^2\rangle,\langle\hat{S}_y^2\rangle$. The geometric image of the spin state of the nematic phase is an ellipsoid. In the nematic phase of spin systems with an isotropic Hamiltonian the low-frequency dynamics is described in terms of the sigma-model for the vector director $\mathbf{n}$ that specifies the orientation of this ellipsoid.[75] Even in the quadrupolar-ferromagnetic phase with $\mathbf{M}\neq 0$ for such magnets the dynamics of the magnetization $\mathbf{M}$ includes the variation of $\mathbf{M}$ in length and differs substantially from that which is obtained with the use of the Landau–Lifshitz equation.[76] The static state of this type has long been studied; as an example we cite the analysis of a domain wall in which $|\mathbf{M}|$ goes to zero at the center of the wall.[77] In the last few years the problem of the nematic phases and other nontrivial types of nonmagnetic order of spins systems has drawn increasing interest in connection with the study of Bose–Einstein condensations of neutral atoms with nonzero spin.[78–80]

For many magnets the non-Heisenberg interactions are rather weak, and the SCS are the most convenient formalism for their semiclassical description. Let us return to an analysis of almost-Heisenberg AFMs in the framework of the SCS. We consider a system of localized spins in which the nearest neighbors are coupled by an antiferromagnetic interaction of the type in Eq. (1). We shall assume that the sites at which the spins are located can be divided into two groups in such a way that all the spins belonging to nearest-neighbor pairs are in different groups. (This condition is violated, e.g., for a frustrated triangular lattice.) For an ideal AFM these two groups correspond to two magnetic sublattices. The introduction of sublattices can also be thought of as a division of the lattice into pairs of spins (dimers). The Lagrangian of an AFM can be written in terms of two unit vectors $\boldsymbol{\sigma}_1$ and $\boldsymbol{\sigma}_2$ for each such dimer. In the case of an extended magnet one can also introduce a more general description of slightly nonuniform states on the basis of the spin densities $\boldsymbol{\sigma}_1(\mathbf{x},t)$ and $\boldsymbol{\sigma}_2(\mathbf{x},t)$ [or their irreducible combinations $\mathbf{l}(\mathbf{x},t)$ and $\mathbf{m}(\mathbf{x},t)$; see Eq. (14); $\mathbf{x}$ is the coordinate of the dimer] as continuous functions of the coordinates. The energy of the nonuniformity into account is taken into account by expanding in the gradients; see formula (40) below.

In many problems, e.g., the quantum tunneling in AFM molecules, the nonuniformities can be neglected, and all the vectors $\boldsymbol{\sigma}_{1,2}$ assumed parallel. Then it is convenient to introduce the sublattice spins $\mathbf{S}_1=\Sigma\mathbf{S}_{\alpha_1}$ and $\mathbf{S}_2=\Sigma\mathbf{S}_{\alpha_2}$ and the coherent states for the spins of each sublattice, $\mathbf{S}_1=sN_1\boldsymbol{\sigma}_1$ and $\mathbf{S}_2=sN_2\boldsymbol{\sigma}_2$. Here and below, s denotes the value of the spin at the site, $N_{1,2}$ is the number of sites in each sublattice, and we shall use the notation

$$N=N_1+N_2,\quad N_{\text{ex}}=N=N_1-N_2, \tag{11}$$

where N_{ex} gives the excess (uncompensated) spin $S_{\text{ex}}=sN_{\text{ex}}$, and N is the total number of sites in the AFM. Thus we arrive at a description of the uniform dynamics of the AFM sample in terms of two vectors of unit length, $\boldsymbol{\sigma}_1$ and $\boldsymbol{\sigma}_2$:

$$\mathscr{L}=\hbar sN_1\mathbf{A}_1(\boldsymbol{\sigma}_1)\frac{\partial\boldsymbol{\sigma}_1}{\partial t}+\hbar sN_2\mathbf{A}_2(\boldsymbol{\sigma}_2)\frac{\partial\boldsymbol{\sigma}_2}{\partial t}-W(\boldsymbol{\sigma}_1,\boldsymbol{\sigma}_2). \tag{12}$$

The kinetic terms are represented in terms of the vector potential (10) of the field of a magnetic monopole, and $W(\boldsymbol{\sigma}_1,\boldsymbol{\sigma}_2)$ is the classical energy of the AFM, which corresponds to the Hamiltonian (2). As we are interested in the case of small decompensation, $N_{\text{ex}}\ll N$, in the expression for this energy we keep the term with $N_{\text{ex}}\neq 0$ only in the Zeeman term and set $N_1=N_2=N/2$ everywhere else; we then get

$$W(\boldsymbol{\sigma}_1,\boldsymbol{\sigma}_2)=\frac{1}{2}s^2ZN[J\boldsymbol{\sigma}_1\cdot\boldsymbol{\sigma}_2+(\mathbf{d}\cdot[\boldsymbol{\sigma}_1\times\boldsymbol{\sigma}_2])]$$
$$+\frac{1}{2}s^2N[\kappa Z\sigma_{z,1}\sigma_{z,2}-K(\sigma_{z,1}^2+\sigma_{z,2}^2)]$$
$$-\frac{1}{2}g\mu_B s\mathbf{H}\cdot[N(\boldsymbol{\sigma}_1+\boldsymbol{\sigma}_2)+N_{\mathrm{ex}}(\boldsymbol{\sigma}_1-\boldsymbol{\sigma}_2)],\tag{13}$$

where Z is the coordination number, the second group of terms describes the anisotropy energy, and the third the Zeeman energy. In addition to the unit vectors $\boldsymbol{\sigma}_1$ and $\boldsymbol{\sigma}_2$, it is convenient to introduce their irreducible combinations

$$\mathbf{l}=(\boldsymbol{\sigma}_1-\boldsymbol{\sigma}_2)/2,\quad \mathbf{m}=(\boldsymbol{\sigma}_1+\boldsymbol{\sigma}_2)/2,\tag{14}$$

which are related by

$$\mathbf{l}^2+\mathbf{m}^2=1\quad\text{and}\quad \mathbf{m}\cdot\mathbf{l}=0.\tag{15}$$

These new variables describe the characteristic symmetry of AFMs with respect to permutation of the sublattices and are convenient for writing the phenomenological energy of an AFM. We write the energy (13) in terms of the vectors **l** and **m**:

$$W(\mathbf{l},\mathbf{m})=Js^2zN\mathbf{m}^2+s^2zN(\mathbf{d}\cdot[\mathbf{m}\times\mathbf{l}])$$
$$+\frac{1}{2}s^2N[\kappa Z(m_z^2-l_z^2)-K(l_z^2+m_z^2)]$$
$$-g\mu_B sN\mathbf{m}\cdot\mathbf{H}-g\mu_B sN_{\mathrm{ex}}\mathbf{l}\cdot\mathbf{H}.\tag{16}$$

We note an important relationship that holds for any AFM: the anisotropy energy always contains only even powers of the components of the vector **l** or **m**, and the Dzyaloshinskii interaction is linear in **m**. In the general case instead of $(\mathbf{d}\cdot[\mathbf{m}\times\mathbf{l}])$ the expression $D_{ik}(\mathbf{l})m_il_k$ appears, where the tensor $D_{ik}(\mathbf{l})$ contains even power of the components of **l** and is determined by the symmetry of the AFM.

IV. FIELD-INDUCED PHASE TRANSITIONS IN ANTIFERROMAGNETS

The ground state of an AFM is determined by the minimum of the energy (16) with respect to the vectors **l** and **m**. Néel himself called attention to the fact that this state can change in a jump upon a continuous change of magnetic field.[40] In other words, phase transitions induced by a strong magnetic field can occur in AFMs. An example is the spin-flop transition (SFT),[40] the experimental observation of which was a long time in coming because of the necessity of using high fields.[81] The SFT has been studied for over 50 years and is still attracting great research interest (see the monograph and reviews[5,9,12,82]). As we have said, in recent years the study of "novel" AFMs (spin pairs and clusters, magnetic superlattices) has revealed a number of phenomena similar to the SFT.

A. Classical bulk transitions

In a boundaryless magnet the SFT occurs simultaneously throughout the volume of the material; we shall call this a bulk SFT. The origin of such a transition is easily explained by analysis of a purely uniaxial AFM model (16). For simplicity we shall assume that $\mathbf{d}=0$ and the magnetic field is parallel to the easy axis of the AFM (a more general case will be considered below). Analyzing the energy of the AFM (16), one can show that in this case the vectors $\boldsymbol{\sigma}_1$ and $\boldsymbol{\sigma}_2$ lie in a single plane (say, the (x,z) plane) at all values of the field. Then the irreducible vectors **m** and **l** are determined solely by the two variables θ, m:

$$l_z=l\cos\theta,\quad l_x=l\sin\theta,\quad l=\sqrt{1-m^2},$$
$$m_z=m\sin\theta,\quad m_x=-m\cos\theta.\tag{17}$$

Minimization of the energy with respect to the variable m leads to the simple relation

$$m=\frac{g\mu_B H\sin\theta}{s(2JZ+2K\cos 2\theta+Z\kappa)}.\tag{18}$$

Formula (18) reflects the anisotropy of the susceptibility of the AFM with respect to the mutual orientation of the magnetic field **H** and the vector **l**. In particular, for $\mathbf{l}\|\mathbf{H}$ $(\theta=0)$ the magnetization **m** is equal to zero even for $H\neq 0$. It will be convenient in what follows to eliminate the total spin **m** and to write the energy of the AFM in terms of the angular variable θ alone:

$$W=-\frac{(g\mu_B H)^2N\sin^2\theta}{2(2ZJ+Z\kappa+2K\cos 2\theta)}+\left(K+\frac{Z\kappa}{2}\right)s^2N\sin^2\theta.\tag{19}$$

In the absence of magnetic field we get the standard result: both the exchange and the single-ion anisotropy give an additive contribution to the effective magnetic anisotropy:

$$W_a(\theta)=\frac{1}{2}s^2K_{\mathrm{eff}}N\sin^2\theta,\quad K_{\mathrm{eff}}=2K+\kappa Z,\tag{20}$$

which is of the easy-axis type for $2K+Z\kappa>0$. For this model the stable phase at $H<H_1$ is the collinear phase $\Phi_\|$, in which $\theta=0$ or π, and for $H>H_2$ the stable phase is the spin-flop phase $\Phi_\perp$, in which $\theta=\pi/2$. For model (19) the characteristic fields for loss of stability of the collinear $\Phi_\|$ and spin-flop $\Phi_\perp$ phases, H_1 and H_2, are given by the formulae

$$H_1=\frac{s}{g\mu_B}\sqrt{(2K+\kappa Z)(2ZJ+\kappa Z+2K)},\quad H_2=\frac{H_1^2}{H_{sf}},$$
$$H_{sf}=\frac{s}{g\mu_B}\sqrt{(2K+\kappa Z)(2ZJ+\kappa Z-2k)}.\tag{21}$$

In the spin-flop phase m_z increases linearly with increasing field as

$$m_z=\frac{H}{H_{\mathrm{ex}}},\quad H_{\mathrm{ex}}=\frac{s(2JZ+\kappa Z-2K)}{g\mu_B},\quad H\leqslant H_{\mathrm{ex}},\tag{22}$$

where H_{ex} is the exchange field of the AFM in model (19), and $H_1,H_2\ll H_{\mathrm{ex}}$. If the value of the field H exceeds H_{ex}, then $\mathbf{l}=0$ for $m=1$, and the system reaches saturation. The transition to the saturated state Φ_{PM} with $\mathbf{l}=0$ is accompanied by the destruction of the antiferromagnetic order and is called a *spin-flip* transition. It is a typical second-order transition of the order-disorder type, but it is brought on not by an increase in temperature but by an increase of the external field.

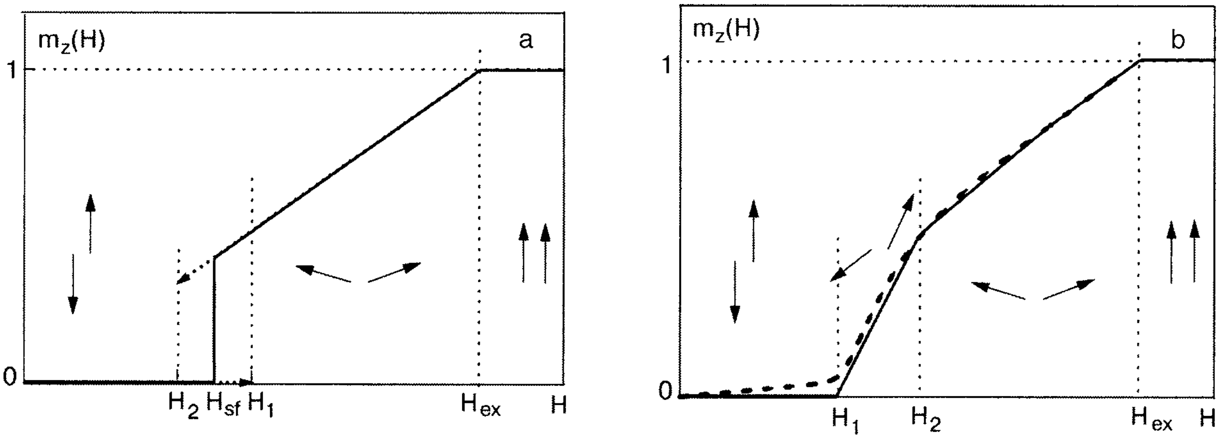

FIG. 1. The ground state of a classical AFM with energy (19) for different K and different values of the field (schematic). The arrows indicate the directions of the sublattice spins in different states of the AFM; see text. (a) $K>0$; first-order transition, the continuations of the curves into the region of metastability of the phases are indicated by dotted lines, which terminate at the arrowheads at the instability points. (b) $K<0$, second-order transition, the dashed curve corresponds to the variation of the magnetization in a canted field.

It is important to take both types of anisotropy into account simultaneously for the description of all possible phases of an AFM and transitions between them. If the anisotropy is of a purely exchange character, i.e., $K=0$, then a degenerate SFT, for which critical fields H_1 and H_2 coincide, occurs. If $K>0$, then the SFT occurs as a first-order transition at the field H_{sf} introduced above in Eq. (21), with a jump ΔS_z of the total spin S_z of the system:

$$\Delta S_z = 2sN\sqrt{\frac{\kappa Z+2K}{2JZ+\kappa Z-2K}}. \tag{23}$$

There is another possible case, when $H_1<H_2$, and the stability regions of the phases $\Phi_\parallel$ and $\Phi_\perp$ do not overlap. Then in the field interval $H_1<H<H_2$ a canted phase $\Phi_<$ with $0<\theta<\pi/2$ exists, and the value of S_z changes from zero to ΔS_z by a linear law but with a larger slope than in the region of the spin-flop phase (see Fig. 1). In this case the transition $\Phi_\parallel \leftrightarrow \Phi_\perp$ occurs via two second-order transitions through the canted phase. In model (19) this requires the presence of competing anisotropies—single-ion anisotropy with $K<0$ (which for $\kappa=0$ corresponds to easy-plane anisotropy) and a rather large exchange anisotropy, with $\kappa Z>2|K|$, so that the effective magnetic anisotropy is easy-axis.

B. Lowering of the symmetry of the problem

We have discussed phase transitions (the spin-flop and spin-flip transitions) in the simplest and most symmetric case of the model (2), assuming in addition that $\mathbf{d}=0$ and that the magnetic field is strictly parallel to the easy axis of the AFM. For possible applications of the theory developed it is important to know whether these transitions are preserved when one goes beyond the framework of such a model. As we have said, in the case of a ferromagnet the Curie point vanishes in the presence of magnetic field. For an AFM the situation is more favorable, and both the first-order spin-flop and the spin-flip transition at which the antiferromagnetic order is destroyed "survive" in a quite general case.

We start with an analysis of the question of what happens when the magnetic field $\mathbf{H}$ deviates from the easy axis of the AFM by some small angle ψ in the framework of the model in Eq. (16). For $\psi\neq 0$ the vector $\mathbf{l}$ is not directed along symmetry directions, $\theta\neq 0,\pi/2$. The phases that are transformed into $\Phi_\parallel$ and $\Phi_\perp$ at $\psi=0$ will be called Φ_1 and Φ_2, respectively. The stability fields H_1 and H_2 of these phases behave differently with increase of the angle ψ, H_1 decreasing and H_2 increasing according to the laws[83]

$$H_1(\psi)=H_1[1-a\psi^{2/3}], \quad H_2(\psi)=H_2[1+a\psi^{2/3}], \tag{24}$$

where $a=(3/2)(K/JZ)^{1/3}$ is small, with a degree of smallness K/J. It follows that at a certain value $\psi=\psi_c$ all the characteristic values of the field coincide, $H_1(\psi_c)=H_2(\psi_c)=H_c\approx H_{sf}$, and the phase transition $\Phi_1\leftrightarrow\Phi_2$ exists only at a sufficiently small value of the angle $\psi\leqslant\psi_c$,

$$\psi_c=\frac{2}{3}\left(\frac{K}{JZ}\right)^{2/3}. \tag{25}$$

Thus in the model (16) on the (H,ψ) plane the line of first-order phase transitions terminates in a critical point (ψ_c,H_c), at which $\theta_1(\psi_c,H_c)=\theta_2(\psi_c,H_c)=\pi/4$.[83]

For $K<0$, when two second-order transitions are realized in the symmetric case $\psi=0$, the tilt of the field is of fundamental importance: for $\psi\neq 0$ the second-order phase transitions $\Phi_{1,2}\leftrightarrow\Phi_<$ vanish. Indeed, for $\psi\neq 0$ the vector $\mathbf{l}$ deviates from the symmetric directions $\theta=0,\pi/2$ at any value of the field, and therefore the symmetry differences of the phases Φ_1,Φ_2 from the canted phase $\Phi_<$ vanish. At very small $\psi\neq 0$ the angle θ varies rather sharply with field at values near where the second-order transitions would occur for $\psi=0$, and the field dependence approximately reiterates $\theta(H)$ for $\psi=0$ (see Fig. 1) but is analytic and has no kinks.

In the analysis of phase transitions in a concrete model, e.g., the model of Eq. (2), the question of whether the results might change when some other invariants are taken into account. An example of such a situation was presented above: the second-order transitions $\Phi_{1,2}\leftrightarrow\Phi_<$ are very sensitive to the symmetry of the problem and vanish at an arbitrarily small deviation of the field from the axis, while the first-order transition "survives" a rather strong perturbation of the problem. A general (model-free) analysis of the existence of the spin-flip transition can be given on the basis of symmetry arguments.[84] In the saturated phase Φ_{PM} the magnetic moments of the sublattices are parallel to each other and to the magnetic field, i.e., all the components of **l** are equal to zero. The phase Φ_{PM} has a higher symmetry than any antiferromagnetic phase, in which $\mathbf{l}\neq 0$. Its symmetry group coincides the symmetry group of the paramagnetic phase in the presence of an external magnetic field, G_{PM}^{H}. The order parameter describing the transition to the paramagnetic phase Φ_{PM} is the vector **l**. This transition will be realized only in the case when none of the components of the vector **l** is an invariant with respect to elements of the symmetry group G_{PM}^{H}. It turns out that if the symmetry elements of the paramagnetic phase include odd translations or inversion, then the spin-flip transition will occur at arbitrary orientation of the magnetic field **H**.[84] If such elements are not present, then the spin flip transition will either be absent altogether or will occur only for an orientation of the field **H** along preferred directions. This conclusion agrees with the results of an analysis of the effective energy of an AFM with the Dzyaloshinskii interaction; see formula (38) below.

Odd symmetry elements of the translation or inversion type are characteristic for a number of crystalline AFMs, and their presence forbids the existence of any type of Dzyaloshinskii interaction. Such discrete symmetry elements as odd inversion can be important not only for crystalline AFMs (AFMs with such an element have unique properties; see the monograph by Turov *et al.*[9]) but also for finite spin clusters with an antiferromagnetic interaction.

The foregoing discussion pertains only to the case of a completely compensated AFM. It is of interest to determine whether reorientation transitions are possible for small AFM particles, in which the spins of the sublattices are not equal, $S_1\neq S_2$, and in the exchange approximation a nonzero magnetic moment is present in the system. Assuming for definiteness that $S_1>S_2$, we find that this moment will tend to orient along the field in such a way that the spin $\mathbf{S}_1$ is parallel to the field and $\mathbf{S}_2$ is antiparallel. However, besides the "ferromagnetic" spin-orientation effect, which is linear in the field, there also exists another orientation effect which is quadratic in the field, which also arises for $S_1=S_2$ and leads to a spin-flop transition. The combined effect of these two factors in the case of sufficiently small decompensation gives a certain analog of the spin-flop transition, which for simplicity we shall discuss in the exchange approximation.

Suppose that the magnetizations of the sublattices make angles θ_1 and θ_2 with the magnetic field. The collinear state described above, with antiparallel spins $\theta_1=0$, $\theta_2=\pi$, is realized only at sufficiently low fields, $H\leqslant H_c$, where

$$H_c=H_{\text{ex}}(S_1-S_2)/(S_1+S_2). \tag{26}$$

For $H\geqslant H_{\text{ex}}$ the spins are parallel, $\theta_1=\theta_2=0$. It is clear that in terms of symmetry these states are equivalent to the paramagnetic state Φ_{PM} and are not degenerate. However, in an intermediate field region $H_c<H<H_{\text{ex}}$ the sublattice spins $\mathbf{S}_1$ and $\mathbf{S}_2$ are noncollinear, $\theta_1,\theta_2\neq 0,\pi$.[85] Here the total spin is parallel to **H**, and the value of its transverse (perpendicular to **H**) projection $S_1 \sin\theta_1+S_2\sin\theta_2=0$, but the state of the system is degenerate with respect to direction of the vector **l** (see Fig. 2). For the case of interest, that of small decompensation $N_1-N_2\ll N$, the value of H_c is small, $H_c\ll H_{\text{ex}}$, and therefore the ground state of the AFM is degenerate over a wide range of fields.

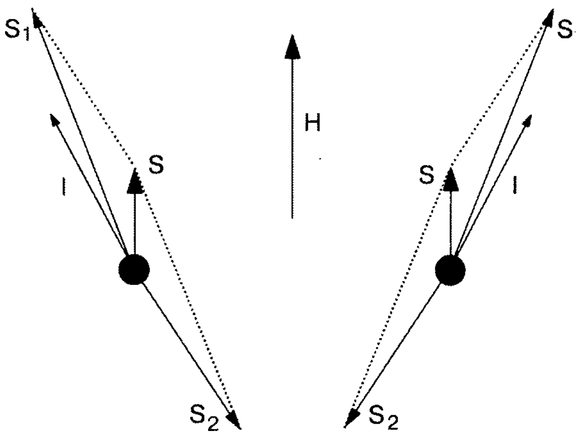

FIG. 2. Two possibilities for the arrangement of the vectors of the magnetic field **H**, total spin **S**, sublattice spins $\mathbf{S}_1$ and $\mathbf{S}_2$, and also the antiferromagnetic vector **l** in the noncollinear state of a particle of an uncompensated AFM in an external magnetic field.

The calculation presented above was done in neglect of the magnetic anisotropy. Taking anisotropy into account is somewhat awkward, and the result depends on the ratio of the characteristic fields H_c (26) and the field H_{sf} introduced above. Importantly, even when certain forms of anisotropy are taken into account the degeneracy (discrete) of the ground state is preserved upon decompensation of the AFM in a strong magnetic field. Between these states, coherent quantum tunneling effects are possible.

C. Spin-flop transition and incommensurate phases near the surface and defects

For large enough samples the demagnetizing effect of the surface of the a magnet will lead to the existence of a thermodynamic-equilibrium domain structure. For an AFM such a structure (intermediate state of the AFM) consists of domains of the phases $\Phi_{\parallel}$ and $\Phi_{\perp}$ (Ref. 86; see also the reviews[12,87]). For mesoscopic AFMs it becomes important that the spins at the boundary have a coordination number $\tilde{Z}<Z$. Quite some time ago Mills[88] and also Keffer and Chow[89] noted that in such a case the value of the spin-flop transition field (21) is lower at the boundary than in the bulk. The calculation in those papers concerned the SFT in semi-infinite systems, in which the boundary of the crystal contains spins of only one sublattice. This model is essentially equivalent to a spin chain, $\tilde{Z}=Z/2$ (see Fig. 3), for which the field of the surface SFT is $H_c\cong H_{sf}/\sqrt{2}$.[88–90] A surface SFT is accompanied by the appearance of a soft mode of surface magnons.[90] Granted, the possibility of realizing this interesting phenomenon is largely determined by the quality of the surface, and for a real (non atomically smooth) surface of a crystal its observation is difficult. That is possibly why attempts at experimental observation of a surface SFT have not met with success.[91]

It turns out that the surface SFT is realized for one-dimensional magnetic superstructures of the type represented by Fe/Cr multilayer films with an antiferromagnetic interac-

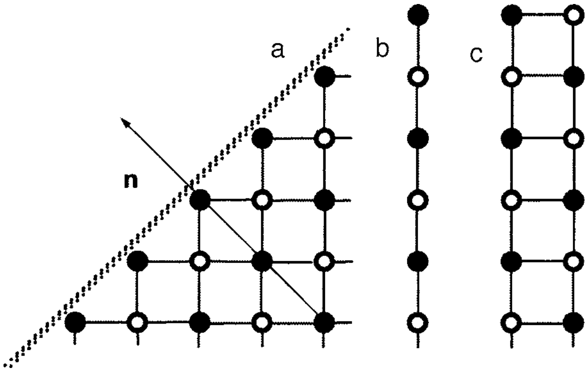

FIG. 3. Collinear antiferromagnetic state for several systems discussed in the text. Here and in the subsequent diagrams of spin structures in this Section the easy axis of the AFM is perpendicular to the plane of the figure, the magnetic field is assumed to be directed upward, the light and dark circles denote the spin-up and spin-down states, respectively, and the solid line represent exchange bonds. Part (a) shows the uncompensated AFM surface considered in Refs. 88–90, and the arrow indicates the direction of the normal to the surface, **n**. The other parts show model low-dimensional systems: the spin chain (b) and spin ladder (c).

tion of the layers, grown on an anisotropic MgO(110) substrate. These materials have growth anisotropy with an easy axis in the plane of the layer.[92] The lower value of the exchange field in the boundary layer can cause surface nonuniformity.[93] The localized surface SFT in such materials has been observed and investigated by various methods.[24–26] Initially, in the spirit of Refs. 88–90, it was interpreted[94] as the nucleation of the spin-flop phase near the surface, i.e., as a rotation of the magnetic moments of the surface layers by an angle close to 90°. Later, on the basis of calculations in the model of a semi-infinite spin chain and analysis of the experimental data, it was shown that the situation is more complicated.[26,95,96] It turns out that the boundary spin antiparallel to the field in the initial state reverses direction under the influence of the field. Because of this, the state arising near the surface is not the spin-flop but an antiferromagnetic state with zero magnetization, but with opposite directions of the magnetic moments in comparison with the bulk. In other words, the antiferromagnetic state near the surface differs from the bulk state by the direction of the vector **l**, and they are separated by a 180° domain wall. Such a state is appropriately called an incommensurate phase.[95]

References 24, 26 and 95 aroused interest not only in the problem of the SFT near the surface and the incommensurate phases in AFMs. Keffer and Chow[89] had noted the possibility of existence of localized transitions of a similar type in bulk AFMs containing defects of the dislocation and grain-boundary types. For dislocations the situation is not so simple (see Sec. 7 below), but it quite likely that analogs of the surface SFT should be observed near defects of "ordinary" crystalline AFMs.

Let us consider the simple case when magnetic ions in low-dimensional magnets are replaced by nonmagnetic ions, and the corresponding exchange bonds are broken. The result is simplest for spin chains, in which the substitution of a magnetic ion by a nonmagnetic impurity within the chain leads simply to the breaking of the chain and the formation of two "surfaces" of the type considered in the early papers.[88,89] In this case each chain "breaks" independently, and a finite density of nonmagnetic impurities of substitution creates an ensemble of identical "surfaces" on which observation of the localized SFT effect is possible.

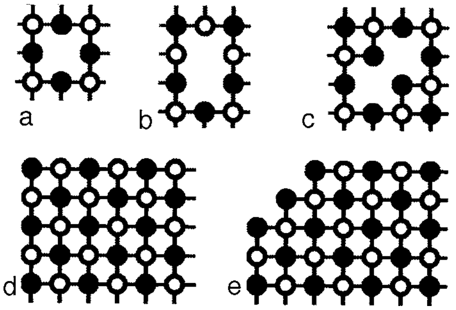

FIG. 4. Collinear (Néel) state of a two-dimensional AFM for several defects, bulk and surface: a—a single-atom defect formed by a nonmagnetic impurity; b and c—two-atom defects, compensated and uncompensated, respectively; d—a corner of the sample; e—two types of boundaries (see text). The easy axis is perpendicular to the plane of the figure, and the magnetic field is directed upward. The light and dark circles denote the spin-up and spin-down states, respectively, and the solid lines represent exchange bonds.

Let us discuss the nature of the surface states and transitions to these states for more complex systems. For all AFMs, excluding the simple chain, two types of surfaces can be distinguished from the standpoint of spin states. The surface can be *compensated*, containing an equal number of spins of the different sublattices and having zero surface magnetization in the Néel state, or *uncompensated*, with nonzero surface magnetization, as in Fig. 3a. It is intuitively clear that in these cases the nonuniform states that arise are very different. As an example let us consider the layered (2D) AFMs of the manganese halide type, which have been studied for many years.[97] Substitution of the Mn^{2+} ions with spin $S=5/2$ by nonmagnetic impurities such as Zn or Cd ions[98,99] isolated or combined into clusters gives rich possibilities for realization of various magnetic defects (bulk and surface, compensated and uncompensated) with a locally weakened exchange interaction (see Fig. 4).

The basic regularities of these phenomena can be understood from an analysis of a model object—the so-called *spin ladder* (SL).[100,101] A spin ladder contains two spin chains coupled by an AFM interaction (see Fig. 3). Such spin systems occur as structural elements in many low-dimensional magnets and have interesting quantum properties.[102,103] A spin ladder can be represented as a chain of spin dimers with AFM coupling of the spins both within each dimer and between neighboring dimers. It is natural to introduce vectors $\mathbf{m}_n$ and $\mathbf{l}_n$ for the structural dimers of a SL, where n is the number of the dimer. Importantly, a finite SL can contain an analog of the compensated boundary illustrated in Fig. 3c and an uncompensated boundary with an incomplete dimer (uncompensated spin) at the end (see Fig. 7 below) and also various bulk defects that do not reduce to breaking of the SL.

Let us give the results of an analysis for SLs with these types of boundaries. For an SL with an uncompensated spin the value of the critical field H_c for the transition to a nonuniform state differs significantly more strongly from the bulk field $H_1 \simeq H_{sf}$ than for an SL with a regular dimer at the end.[100,101] Numerical minimization of the discrete Hamiltonian (2) has shown that the structures of the phases are also different, e.g., the form of the distribution of m_z and l_z as

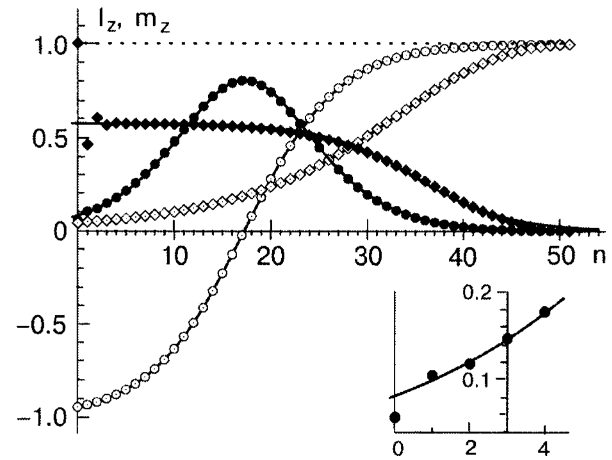

FIG. 5. Distributions of l_z (light symbols) and m_z (dark symbols) as functions of the number of the site for a semi-infinite spin ladder with single-ion anisotropy and different boundaries for values of the field above the critical.[101] The circles are for a spin ladder with a regular end, and the diamonds are for a spin ladder with an uncompensated spin at the end. For clarity the values of m_z have been multiplied by 4 for the SL with the uncompensated spin at the end and by 20 for the SL with the regular end. The irregular behavior of $m_z(n)$ is clearly seen for the SL with the uncompensated spin; for the regular SL the details of its behavior near the boundary are shown in the inset.

functions of the distance n from the end of the ladder (see Fig. 5).[101] For a regular SL, which can be regarded as a model AFM with a compensated surface, the data on the distribution of l_z show the existence of a surface SFT. In such systems the vector **l** rotates by approximately 90° in going from the surface to the bulk; here the magnetization is nonzero in the entire spin-flop region near the surface and falls to zero in the bulk. For an uncompensated SL, as can be seen in Fig. 5, an incommensurate state arises in which the magnetization is close to zero both on the surface and in the bulk, while the nonuniformity of the spins is characterized by the presence of a 180° domain wall. In both cases the dependence of the vector **l** on the number of the dimer n is rather smooth and well described by formulae obtained for the components of **l** in antiferromagnetic domain walls: $\tan\theta_n=\exp[-(n-n_0)/\Delta_{\pi/2}]$ for a 90° wall, or $\tan(\theta_n/2)=\exp[-(n-n_0)/\Delta_\pi]$ for a 180° wall. However, the numerical data show that, unlike that of **l**, the behavior of m_z near the boundary is substantially irregular.

To explain these features, let us consider the problem of stability of a collinear phase having the values $\theta_n=0$ and $m_n=0$.[101] The stability of this state can be investigated using the Hamiltonian (2) written in the quadratic approximation in the small variables θ_n and m_n; for the end dimer the index $n=0$. The states of dimers with $n>0$ are described by the same equations as for a boundryless spin ladder:

$$J(2\theta_n-\theta_{n+1}-\theta_{n-1})+K_{\text{eff}}\theta_n-hm_n=0,$$

$$(4J+K_{\text{eff}})m_n+J(m_{n+1}+m_{n-1})-h\theta_n=0, \tag{27}$$

where $K_{\text{eff}}=2K+3\kappa$, and $h=g\mu_BH/s$ is a dimensionless field. The solutions of these equations are a complex analog of the Bloch state in an ideal lattice, $\theta_n, m_n\propto\exp(-Qn)$. The corresponding "dispersion relation" has two solutions for the "quasi-momentum" Q, and therefore two exponentials arise in the solution:

$$\theta_n=\theta_p e^{-np}+(-1)^n\theta_q e^{-nq},$$

$$m_n=m_p e^{-np}+(-1)^n m_q e^{-nq}, \tag{28}$$

where

$$2\cosh p=3\tilde{J}/J-1;\quad 2\cosh q=3\tilde{J}/J+1,$$

$$3\tilde{J}=\sqrt{9J^2+(h_1^2-h^2)}\simeq 3J.$$

The relations between the amplitudes $\theta_{p,q}$ and $m_{p,q}$ can be written in the form $\theta_p=Am_p$, $\theta_q=m_q/A$, where $A\approx h/6J\ll 1$. Therefore for a slowly damped exponential with $p\ll 1$ it is found that $m_p\ll\theta_p$, and for an oscillatory exponential with fast damping $(q\sim 1)$ the situation is the opposite.

The structure of the equations for the boundary dimer is different from (27). A stability analysis can be carried out using the equations for variables describing the spins that do not belong to regular dimers with $n>0$. These include the variables θ_0, m_0 describing the last dimer, and the angular variables θ, φ for the "additional" spins present in an uncompensated SL. The solvability conditions of the linear homogeneous equations for all these variables are satisfied only for a certain value of the magnetic field, which is what determines the stability field H_c and also the relation between the variables θ_p and θ_q. Analysis of SL models with the use of this example has led to the following results.[101]

For a regular SL the critical field, to a first approximation in the small parameters $(\kappa,K)/J$, has the form

$$H_c^2=H_1^2-2(s/g\mu_B)^2(K+\kappa\sqrt{3})^2. \tag{29}$$

This value is smaller than the bulk critical field H_1, but the difference between H_c and H_1 is proportional to the small parameter $(\kappa,K)/J$. A calculation showed that $\theta_q\ll\theta_p$, and the behavior of the vector **l** is regular, while the values of m_p and m_q are comparable, $m_q\approx 2m_p/(1+\sqrt{3})\simeq 0.73m_p$. This explains the presence of irregular behavior of the magnetization in the immediate vicinity of the boundary of the SL (see Fig. 5).

In the analysis of an uncompensated SL the result for the critical field turns out to be qualitatively different, $H_c=\sqrt{2/5}H_1\approx 0.63H_1$. As in the case of the spin chain,[88,89] the value of H_c is substantially lower than H_1; the difference between H_c and H_1 is of the order of H_c and does not contain small factors. In this case $\theta_q\ll\theta_p$, but again irregular behavior of the magnetization appears, and the ratio of m_q and m_p has a different sign than for a spin ladder with a regular boundary: $m_q\approx -m_p/(1+\sqrt{3})\simeq -0.37m_p$. This property also corresponds well to the numerical data (see the inset in Fig. 5). For a wide class of quasi-one-dimensional systems with an uncompensated boundary or bulk defect, the critical field H_c is expressed by the simple formula

$$H_c^2=\frac{2\tilde{Z}^2}{2\tilde{Z}^2+Z}H_1^2, \tag{30}$$

where $\tilde{Z}$ and Z are the coordination numbers for the boundary spin and the regular part of the AFM, respectively. For a spin chain ($\tilde{Z}=1$ and $Z=2$) this gives the known result $H_c^2=H_1^2/2$.[88,89] For a single nonmagnetic defect inside the

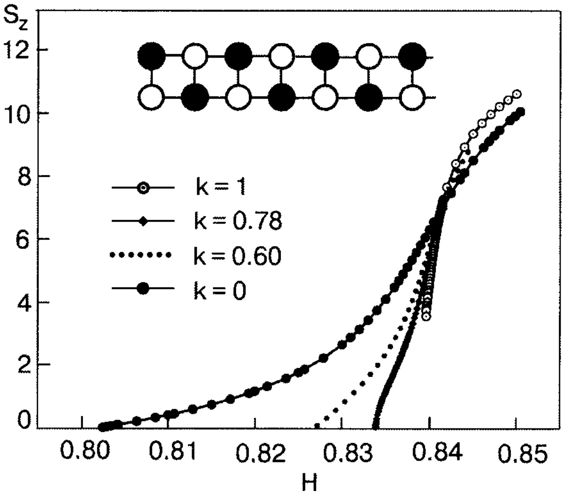

FIG. 6. Dependence of the z projection of the total spin S_z on magnetic field for a spin ladder with a regular dimer at the end and an effective anisotropy constant $K_{\mathrm{eff}}=0.06J$.[101] The data shown are for pure exchange and single-ion anisotropy and also for two types of combined anisotropy with different ratios of the contributions of the constants K and κ ($k=K/K_{\mathrm{eff}}$).

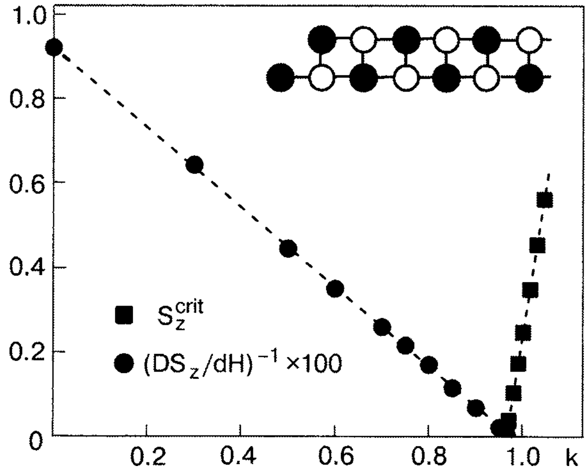

FIG. 7. Dependence of the quantities characteristic for analysis of the order of a phase transition, $S_z^{(\mathrm{crit})}$ and $(dS_z/dH)^{-1}$, on the parameter $k=2K/K_{\mathrm{eff}}$, found numerically at the transition point $H=H_c$ for a spin ladder with uncompensated spin at the boundary at a value of the effective anisotropy constant $K_{\mathrm{eff}}=0.02J$.[101] The structure of the SL in the collinear state is illustrated in the inset.

SL, which breaks one of the spin chains making up the spin ladder, $\tilde{Z}=2$ and $Z=3$, one obtains the answer $H_c=\sqrt{8/11}H_1\approx 0.853H_1$, which is in good agreement with the numerical results.

The majority of studies of the surface SFT have considered only modes with single-ion anisotropy and discussed only first-order transitions. A numerical analysis shows that two types of behavior of the magnetic-field dependence of the z component of the total spin S_z are present. For a system with single-ion anisotropy for the nonuniform phase there is a finite value of S_z at the transition point, where the energies of the collinear and nonuniform phases coincide. However, for the case of exchange anisotropy the value of S_z tends toward zero at the transition point, as is shown in Fig. 6. Such behavior can be interpreted as signs of a first-order and second-order transition, respectively. As in the case of the bulk SFT, the kind of localized SFT depends largely on the microscopic origins of the anisotropy. For all of the defect models in a SL with pure single-ion anisotropy there is a first-order transition. For the case of exchange anisotropy the transition to the nonuniform phase is a second-order transition, and the amplitude of the nonuniform distribution goes to zero at the transition point. In the vicinity of this point the state cannot be classified as a surface spin-flop phase or an incommensurate phase; it is more aptly characterized as a slightly distorted Néel state with a distortion amplitude that falls off in an oscillatory manner with distance from the surface into the interior of the crystal.

The presence of first- and second-order transitions for a given system indicates the presence of a tricritical point. The square-root dependence characteristic of a tricritical point is clearly seen in Fig. 6 for $k=K/K_{\mathrm{eff}}\approx 0.78$. Numerical minimization of the energy of the system near second-order transitions and especially near a tricritical point is greatly complicated, but the analysis can be simplified by using Landau's phenomenological theory of phase transitions. Taking into account that the z projection of the dimer spin $m_{z,n}=\theta_n m_n$ is quadratic in the variables of the linear problem, θ_n, m_n, and that $S_z=0$ in the Néel state, we arrive at the conclusion that S_z should be considered to be the square of the order parameter. For description of the phase diagram with a tricritical point one must expand the energy of the system to sixth order in the order parameter:

$$F=-(H-H_c)S_z+\frac{1}{2}\beta S_z^2+\frac{1}{3}\gamma S_z^3. \tag{31}$$

The form of the first term in formula (31) is obtained analytically from the expression for the energy of the SL and the equations of the linear approximation. Determination of the coefficients β and γ requires solution of a nonlinear problem, but in the analysis they can be treated as phenomenological parameters and their values determined from the numerical data.[101] If the coefficients are known, then the further analysis is simple: for $\beta>0$ the transition is second-order with a linear dependence of $S_z(H)$: $S_z=(H-H_c)/\beta$. For $\beta<0$ and $\gamma>0$ the transition will be first-order with a nonzero value of the total spin total spin $S_z^{(\mathrm{crit})}$ at the transition point: $S_z^{(\mathrm{crit})}=3|\beta|/4\gamma$. Thus both quantities, $(dS_z/dH)^{-1}=\beta$ for $\beta>0$ and $S_z^{(\mathrm{crit})}$ for $\beta<0$, are proportional to the value of $|\beta|$. Near the tricritical point $\beta\rightarrow 0$, and extrapolation of the curves of these two quantities as functions of $2K/K_{\mathrm{eff}}$ to zero at a constant value of the effective uniaxial anisotropy $K_{\mathrm{eff}}=2K+3\kappa$ gives the value of the parameters of the tricritical point. Such a graphical analysis of the SL model with an uncompensated spin at the end is presented in Fig. 7. It gives the position of the tricritical point for an anisotropy ratio $2K/K_{\mathrm{eff}}\approx 0.97$. For a simple spin chain the tricritical point corresponds to the value $2K/K_{\mathrm{eff}}\approx 0.67$. For a regular SL the tricritical point is found at $2K/K_{\mathrm{eff}}\approx 0.78$. Recall that the bulk SFT occurs as a first-order transition for all values $K>0$. One can therefore state that for localized transitions the case of a second-order phase transition is more typical than for a bulk transition.

For a 2D AFM the situation remains qualitatively the same as for the SL: single-ion anisotropy gives a first-order transition, and anisotropy of the interaction gives a second-order transition. For all the uncompensated surface or bulk defects the value of the critical field (30) is substantially lower than the instability field H_1, and the difference $H_c^2 - H_1^2 \sim H_1^2$ does not contain any small parameters of the type $(K,\kappa)/J$. In a 2D AFM, as for the SL, for all the compensated defects $H_c^2 - H_1^2 \sim (K,\kappa) H_1^2/J \ll H_1^2$. There is only one difference of a quantitative character, viz., the localization of the states in the 2D case is weaker, while the difference of the fields of the bulk and localized SFTs is less than for the SL. Since the SL is in essence a one-dimensional object, this regularity corresponds to the known tendency for localization effects to weaken as the dimensionality of the system increases.[34,35] However, for such defects as an uncompensated surface and especially a corner of the sample (see Fig. 4d, e), the effects of localization of the SFT in a 2D AFM are manifested more strongly than for a spin ladder.

The possibility of realization of 2D localized transitions is due to some novel objects—arrays of magnetic dots of different shapes, made from magnetically soft ferromagnets, which can be arranged in square, rectangular, or staircase structures. The interaction between dots is of a magnetostatic nature, and in a weak field it leads to antiferromagnetic order of the magnetic moments of the dots.[23] An important circumstance derives from the character of the anisotropy in these artificial systems. The effective anisotropy inherent to a single dot is determined by its shape, while the anisotropy of the interaction energy of the dots is related to the shape of the lattice. This makes it possible the control independently the parameters analogous to the single-ion or exchange anisotropy constants by modifying the geometry of the dot and lattice, respectively.

D. Quantum analog of the spin-flop transition

We have actually been discussing the spin-flop transition in a model of two large spins. In recent years many experiments have been done that can be described directly in terms of this model. We are talking about processes of magnetization of spin pairs with an antiferromagnetic interaction,[104] including pairs of the high-spin Mn_4 molecules with a maximum value of the total spin $2S=9$.[54,55] For an ensemble of such pairs (and also more complex clusters like spin triplets, quartets, etc.) a stepped magnetization is observed, i.e., a macroscopic manifestation of the spin quantization effect.[104]

The process of magnetization of spin pairs when only isotropic exchange and the external field are taken into account can be described on the basis of the exact solution of the quantum problem (2) with $K=0$, $\kappa=0$. Taking into account the identity $2\hat{\mathbf{S}}_1\cdot\hat{\mathbf{S}}_2=\hat{\mathbf{S}}_{\mathrm{tot}}^2-2S(S+1)$, we can write this Hamiltonian solely in terms of the total spin operator of the system, $\hat{\mathbf{S}}_{\mathrm{tot}}=\hat{\mathbf{S}}_1+\hat{\mathbf{S}}_2$, and its projection in the field direction $\hat{S}_z$. Corresponding to the eigenstates are fixed values of the total spin S_{tot}, $\mathbf{S}_{\mathrm{tot}}^2=S_{\mathrm{tot}}(S_{\mathrm{tot}}+1)$, and S_z, and their energy is determined by the expression $E(S,S_z)=JS_{\mathrm{tot}}(S_{\mathrm{tot}}+1)/2 - g\mu_B H S_z$. Comparing these values of the energy, it is easy to find that the value of S_z jumps from $S_z=n-1$ to $S_z=n$ at a field $H_n=Jn/(g\mu_B)$. Saturation $S_{\mathrm{tot}}=2S$ is reached at $H_{\mathrm{ex}}^{\mathrm{Heis}}=2JS/(g\mu_B)$, and the value of the field H_{ex} coincides with that given by the classical formula (22) for $K=0$, $\kappa=0$, and $Z=1$. Thus the process of magnetizing a spin pair is reminiscent of the magnetizing of macroscopic isotropic AFMs, with the difference that for pairs of quantum spins the linear dependence $S_z(H)$ for $H<H_{\mathrm{ex}}$ becomes steplike, with a change in spin by unity.

The exact solution of the quantum problems of finite spin clusters with an antiferromagnetic interaction for arbitrary value of the spin S is known only for certain simple models.[105] An interesting model is that of a closed spin chain with four spins,

$$\hat{H}=J\sum_{i=1}^{3}\hat{\mathbf{S}}_i\cdot\hat{\mathbf{S}}_{i+1}+J\hat{\mathbf{S}}_4\cdot\hat{\mathbf{S}}_1.$$

The Hamiltonian of this model is easily rewritten in terms of the "sublattice spin" operators $\hat{\mathbf{S}}_1^{sl}=\hat{\mathbf{S}}_1+\hat{\mathbf{S}}_3$, $\hat{\mathbf{S}}_2^{sl}=\hat{\mathbf{S}}_2+\hat{\mathbf{S}}_4$, and the total spin operator $\hat{\mathbf{S}}_{\mathrm{tot}}=\hat{\mathbf{S}}_1^{sl}+\hat{\mathbf{S}}_2^{sl}$; with accuracy up to an additive constant, it takes the form

$$\hat{H}=\frac{J}{2}[\hat{\mathbf{S}}_{\mathrm{tot}}^2-(\hat{\mathbf{S}}_1^{sl})^2-(\hat{\mathbf{S}}_2^{sl})^2].$$

The eigenvalues of the Hamiltonian are expressed in terms of the value of the total spin S_{tot} of the system and the values of the sublattice spins, $(\hat{\mathbf{S}}_{1,2}^{sl})^2=S_{1,2}^{sl}(S_{1,2}^{sl}+1)$. As in the classical Néel state, in the ground state of this system the sublattice spins have the maximum possible value $S_{1,2}^{sl}=2S$. For systems with a large number of spins such a simple treatment cannot be done, and the conclusion that the sublattices are "saturated" is apparently invalid. When the anisotropy is taken into account the exact solution is known only for the Ising model, which corresponds to $J,K=0$ in (2). In this case, in essence classical, we have $S_z=0$ at $H<H_{\mathrm{ex}}$ and saturation of the state, $S_z=2S$, at $H>H_{\mathrm{ex}}$. At a value of the exchange field $H_{\mathrm{ex}}=\kappa S/(g\mu_B)$ the state of an Ising system is degenerate, and S_z can take any value from 0 to $2S$.

In the classical theory even weak anisotropy can alter the purely linear trend of $S_z(H)$, giving rise to a spin-flop transition of either first or second order (see Fig. 3). Suppose the classical SFT field $H_{sf}\cong S\sqrt{2JK}/(g\mu_B)$ exceeds the field of the first quantum jump, H_n for $n=1$, $H_{(n=1)}=J/(g\mu_B)$, as can occur for moderate anisotropy $K>J/S^2$. Then in the behavior of the spin pair one expects the appearance of the quantum analog of a spin-flop transition.[106] The problem for a spin pair in the presence of magnetic anisotropy of a general form does not have an exact solution even in the most symmetric case (2). A numerical analysis by Kireev and the author for a pair of spins in the simple model (2) with allowance for general types of anisotropy showed that even for not very large spins such as $S=3-5$ one observes fair agreement of the quantum and classical results. The behavior of the quantum jumplike magnetization curve is determined, as for classical AFMs, by the microscopic character of the magnetic anisotropy. In particular, the value $S_z=0$ is maintained up to field values $H\gg H_{(n=1)}$. Further, for single-ion anisotropy there exists a microscopic analog of the first-order spin-flop transition, viz., the jump of S_z from zero to values $\Delta S_z>1$. For the case when in the macroscopic problem has second-order transitions, for a quantum system the jumps

$\Delta S_z = 1$ are concentrated in a narrow region of field values that correspond approximately to the characteristic fields H_1, H_2 of the classical theory.

V. LAGRANGIAN FOR THE DESCRIPTION OF THE DYNAMICS OF REAL AFMs

Kaganov and Tsukernik[107] and Turov and Irkhin[108] first proposed to describe the dynamics of AFMs on the basis of a system of two Landau–Lifshitz equations for the sublattice magnetizations, which can be written in terms of the unit vectors $\boldsymbol{\sigma}_1$ and $\boldsymbol{\sigma}_2$ (10), as the field variables. An equivalent but more convenient description is based on a system of equations for the irreducible vectors **l**, **m** (see the detailed analysis of this approach and further generalizations of the such equations in the monograph by Turov *et al.*9). It later became clear that by using the natural small parameters of the AFM theory, $g\mu_B H/S \sim \sqrt{K_{\text{eff}}J} \ll J$ [see Eq. (2)], one can satisfactorily describe the behavior of an AFM using only the equation for the antiferromagnetic vector **l** alone. In this case the vector **m** is small, $|\mathbf{m}| \ll 1$, it is a slave variable and is determined by the vector **l** and its time derivative $\partial \mathbf{l}/\partial t$. In this approximation the vector **l**, which for $\mathbf{m} \neq 0$ is three-component with a variable length [see Eq. (15)], can be treated as a unit vector.

The dynamical equations for the antiferromagnetic unit vector **l** can be constructed on the basis of symmetry arguments[43] and can be obtained directly from the Landau–Lifshitz equations for the sublattice magnetizations[109–112] (see reviews[12,34,36,38]). In both approaches one obtains the same classical equations of motion for the unit vector **l**, which are called the σ-model equations. The simplest version of the σ-model has high dynamical symmetry, and the time derivatives of **l** appear in the Lagrangian in the trivial form $(\partial \mathbf{l}/\partial t)^2$. The use of such equations as these have made it possible to describe the Lorentz-invariant domain-wall dynamics observed experimentally for a number of AFMs, where it was found that the domain walls move with a characteristic velocity c equal to the magnon velocity in the AFM.[6,15,37,38] Both the magnetic field and certain forms of the Dzyaloshinskii–Moriya interaction lower the dynamical symmetry of the classical σ-model, and its Lagrangian acquires terms linear in $\partial \mathbf{l}/\partial t$.

A key development in the use of the equations of the σ-model in the quantum physics of AFMs was to obtain the Lagrangian of the σ-model on the basis of the spin coherent states.[67,113–116] We begin by considering the σ-model for the uniform dynamics of the vector $\mathbf{l} = \mathbf{l}(t)$ with the magnetic field and the Dzyaloshinskii interaction taken into account, with the possibility of a small decompensation of the sublattice spins. The nonuniform dynamics will be briefly discussed at the end of this Section. In Secs. 6 and 7 we shall present this Lagrangian for investigating tunneling effects.

The derivation of the σ-model is done under the assumption that the magnetic moment is small, $|\mathbf{m}| \ll |\mathbf{l}|$. Using the smallness of **m**, one can write the Lagrangian (10) in the form an expansion in powers of that vector. The kinetic term in the Lagrangian for the sublattice spins (12) can be described in the approximation linear in **m** as

$$
\begin{aligned}
& sN_1\hbar \mathbf{A}_1(\sigma_1)\cdot \dot{\boldsymbol{\sigma}}_1 + sN_2\hbar \mathbf{A}_2(\boldsymbol{\sigma}_2)\cdot \dot{\boldsymbol{\sigma}}_2 \\
& \quad = s\hbar \frac{\partial \mathbf{l}}{\partial t}\cdot [N_1\mathbf{A}_1(\mathbf{l}) - N_2\mathbf{A}_2(-\mathbf{l})] \\
& \qquad + s\hbar \frac{\partial \mathbf{m}}{\partial t}\cdot [N_1\mathbf{A}_1(\mathbf{l}) + N_2\mathbf{A}_2(-\mathbf{l})] \\
& \qquad + s\hbar m_i \frac{\partial \mathbf{l}}{\partial t}\cdot \left[N_1 \frac{\partial \mathbf{A}_1(\mathbf{l})}{\partial l_i} + N_2 \frac{\partial \mathbf{A}_2(-\mathbf{l})}{\partial l_i} \right].
\end{aligned}
\tag{32}
$$

Up to this point we have not specified a concrete choice of axes of the singularities $\mathbf{n}_1$ and $\mathbf{n}_2$ for the potentials $\mathbf{A}_1$, $\mathbf{A}_2$. We choose them so as to eliminate the singular term, at least in the case of a compensated AFM.[117,118] The corresponding condition is $\mathbf{A}_1(\mathbf{l}) = \mathbf{A}_2(-\mathbf{l})$, which is possible when $\mathbf{n}_1 = -\mathbf{n}_2$. For $N_{\text{ex}} \neq 0$ one cannot get rid of the singular term, but it is proportional to the small quantity $N_{\text{ex}} \ll N$.

The dynamic term in (32) for the case of a "pure" AFM begins with the term linear in **m**, which can be represented in the form[118]

$$
\hbar \mathbf{m}\cdot \left[\mathbf{B}\times \frac{\partial \mathbf{l}}{\partial t} \right], \quad B_i = \varepsilon_{ijk}\left(\frac{\partial A_j}{\partial l_k} - \frac{\partial A_k}{\partial l_j} \right). \tag{33}
$$

Thus, in contrast to the FM case, the Lagrangian of a compensated AFM contains only the gauge-invariant quantity $\mathbf{B} = \mathbf{A}$, which has the meaning of a magnetic monopole field, $\mathbf{B} = \mathbf{l}/|\mathbf{l}|^3$. Applying the condition $\mathbf{m}\cdot\mathbf{l} = 0$, we easily obtain for the slave variable **m**

$$
\mathbf{m} = \frac{\hbar}{2sJZ}\left\{ \gamma(\mathbf{H}^{(\text{eff})} - \mathbf{l}(\mathbf{H}^{(\text{eff})}\cdot \mathbf{l})) + \left[\frac{\partial \mathbf{l}}{\partial t}\times \mathbf{l} \right] \right\}, \tag{34}
$$

where $\gamma = g\mu_B/\hbar$ is the gyromagnetic ratio, and $\mathbf{H}^{(\text{eff})}$ is the sum of the external field **H** and the Dzyaloshinskii field $\mathbf{H}^{(D)}$. For the model (10), in which the Dzyaloshinskii–Moriya interaction has the purely antisymmetric form $\mathbf{d}\cdot(\boldsymbol{\sigma}_1 \times \boldsymbol{\sigma}_2)$, the Dzyaloshinskii field $\mathbf{H}^{(D)} = sZ(\mathbf{d}\times\mathbf{l})/g\mu_B$. For the usual form of this interaction, proportional to $D_{ik}(\mathbf{l})m_i l_k$ [see the discussion following formula (16)], and the Dzyaloshinskii field $H_i^{(D)} = D_{ik}(\mathbf{k})l_k$. Thus for a general AFM model the expression for the effective field becomes

$$
H_i^{\text{eff}} = H_i + D_{ik}(\mathbf{l})l_k. \tag{35}
$$

We note that the vector **m** determines the value of the total spin $\mathbf{S}_{\text{tot}}$ of the system only in the case of a compensated sample, when $N_{\text{ex}} = 0$. If $N_{\text{ex}} \neq 0$, the total spin vector will contain both a "transverse" term, proportional to the components of **m**, and a "longitudinal" term, which is due to the excess spin and is parallel to **l**:

$$
\mathbf{S}_{\text{tot}} = sN_{\text{ex}}\mathbf{l} + sN\mathbf{m}. \tag{36}
$$

The derivation of the σ-model equations can be carried further without specifying a concrete form of $D_{ik}(\mathbf{l})$. Substituting **m** into formula (10), we obtain an effective Lagrangian for the vector **l** of an AFM sample containing N spins:

$$
\begin{aligned}
\mathscr{L} = & \frac{\hbar^2 N}{2JZ}\left[\frac{1}{2}\left(\frac{\partial \mathbf{l}}{\partial t} \right)^2 - \gamma\left(\mathbf{H}^{(\text{eff})}\cdot \left[\mathbf{l}\times \frac{\partial \mathbf{l}}{\partial t} \right] \right) \right] \\
& + s\hbar N_{\text{ex}}\mathbf{A}(\mathbf{l})\cdot \left(\frac{\partial \mathbf{l}}{\partial t} \right) - \widetilde{W}(\mathbf{l}).
\end{aligned}
\tag{37}
$$

Here the first term governs the characteristic dynamics for a "pure" AFM, the second term is "ferromagnetic" in form and is due to decompensation of the spins, and the last term $\widetilde{W}(\mathbf{l})$ has the meaning of an effective "potential energy" of the system:

$$\widetilde{W}(\mathbf{l}) = W_a(\mathbf{l}) - g\mu_B s N_{\text{ex}}(\mathbf{H}\cdot\mathbf{l}) + \frac{(g\mu_B)^2 N}{4JZ}[(\mathbf{H}\cdot\mathbf{l})^2 - \mathbf{H}^2] + \frac{(g\mu_B)^2 N}{2JZ}(\mathbf{H}\times[\mathbf{l}(\mathbf{H}^{(D)}\cdot\mathbf{l}) - \mathbf{H}^{(D)}]). \qquad (38)$$

In writing $\widetilde{W}$ here we have written out separately all the terms that depend on the magnetic field. The expression for $W(\mathbf{l})$ has the meaning of the effective anisotropy energy of the AFM. This energy is made up of the "bare" anisotropy energy mentioned above (the second group of terms in formulae (13) and (16), which are taken for $\boldsymbol{\sigma}_1 = -\boldsymbol{\sigma}_2 = \mathbf{l}$ or $\mathbf{m} = 0$, respectively), and also the additional term $(\mathbf{H}^{(D)}\cdot\mathbf{l})^2 - (\mathbf{H}^{(D)})^2$, which is acquired in the elimination of $\mathbf{m}$. It is clear that there is no sense in separating out these contributions, and $W(\mathbf{l})$ is the real anisotropy energy determined from static measurements. In essence, in writing $W(\mathbf{l})$ one must simply use the phenomenological expression whose form is determined by the crystal symmetry of the magnet and, as a rule, is well known. Below we shall often consider a model AFM of rhombic symmetry and use the expression

$$W(\theta,\varphi) = s^2 N[K_u(l_x^2 + l_y^2) + K_p l_y^2], \qquad (39)$$

where the constants K_u and K_p describe the uniaxial anisotropy and the anisotropy in the basal plane (x,y), respectively.

The energy $\widetilde{W}(\mathbf{l})$ of the system also contains terms linear and quadratic in the magnetic field. The meaning of the first term in (38) is simple: it describes the Zeeman energy of the excess spin in a magnetic field. A second term, quadratic in the field components, is present for any AFM. The meaning of this contribution is very clear: it is due to the anisotropy of the susceptibility of the AFM. The role of this term can be represented as the appearance of a field-induced uniaxial anisotropy with a hard axis along the magnetic field. The competition of this induced anisotropy with the initial easy-axis crystalline anisotropy is responsible for the existence of the spin-flop transition (see Sec. 4). Finally, the last term, which is bilinear in the components of the external field $\mathbf{H}$ and the Dzyaloshinskii field $\mathbf{H}^{(D)}$, describes the energy of the weak ferromagnetic moment caused by the Dzyaloshinskii interaction with the external magnetic field.[12] It contains terms linear in the components of the vector $\mathbf{l}$, making it possible to explain easily the conclusion of a symmetry analysis that the spin-flip transition exists for any orientation of the external magnetic field only in the absence of the Dzyaloshinskii interaction. Analyzing this term, one can easily indicate those selected orientations of the field for which the spin-flip transition can occur for nonzero $\mathbf{H}^{(D)}$. Indeed, the terms linear in $\mathbf{l}$, which destroy that transition, go to zero under the condition $D_{ik}H_i = 0$, which determines the desired direction of $\mathbf{H}$.

Thus the Lagrangian for the vector $\mathbf{l}$, with the external magnetic field and the general form of the Dzyaloshinskii interaction taken into account, differs from the Lagrangian of the σ-model of an ideal AFM[67] by the presence of a number of additional gyroscopic terms linear in $\partial\mathbf{l}/\partial t$. They describe a lowering of the real dynamical symmetry on an AFM on account of the magnetic field and/or the Dzyaloshinskii interaction. We note that in the original papers[43,112,119] these terms of different origin were written in the correct form of total derivatives. This pertains to terms resulting from the magnetic field (cf. Refs. 43 and 51), the Dzyaloshinskii interaction (Refs. 119 and 118), and also from the form of the Lagrangian for an AFM with incomplete compensation of the spin (cf. Refs. 112 and 120). Therefore, in particular, the soliton momentum P, which is not invariant with respect to the addition of total derivatives, and the dispersion relation $E = E(P)$ for a soliton of the kink type were found correctly in Refs. 119, 121, and 122.

Let us discuss the form of the Lagrangian (37) in various limiting cases. The standard σ-model of a pure AFM corresponds to $S_1 = S_2$, or $N_{\text{ex}} = 0$. For the transition to the Lagrangian of a "pure" ferromagnet the term proportional to $(\partial\mathbf{l}/\partial t)^2$ must be set to zero. Taking this term into account goes beyond the accuracy of the calculation for sufficiently small $N_{\text{ex}}/N > \sqrt{K/J}$.[111,120] However, in doing so we alter the Hamiltonian structure of the system; specifically, the number of degrees of freedom (the dimension of the phase space) decreases by half, which is of fundamental importance for the analysis of instantons.

In the derivation of the Lagrangian (37) the possibility of nonuniform states was neglected for simplicity. They can be taken into account without difficulty by allowing for the dependence of the vector $\mathbf{l}$ on the spatial coordinates. For the model of an AFM with a D-dimensional Heisenberg lattice with lattice constant a, this dependence is put in by changing from the dynamical variable $\mathbf{l}(t)$ to the field variable $\mathbf{l}(\mathbf{x},t)$ and making the substitution

$$N(\mathscr{L}/N) \to \int \frac{dx^D}{a^D}\left[(\mathscr{L}/N) - \frac{1}{2}Ja^2s^2(\boldsymbol{\nabla}\cdot\mathbf{l})^2\right]. \qquad (40)$$

The value of $\mathscr{L}/N$ has the meaning of the value of the Lagrangian per spin for the uniform case (37), and the second term in the integrand is taken with the opposite sign to the energy of nonuniformity of the spins (see, e.g., Ref. 71). We note that for $\mathbf{H}^{\text{eff}} = 0$ the derivatives with respect to the coordinate and time appear in the Lagrangian in the Lorentz-invariant combination

$$\nabla^2 - c^2(\partial^2/\partial t^2), \quad c = saJ\sqrt{2Z}/\hbar, \qquad (41)$$

where c has the meaning of the magnon phase velocity in the AFM.

A special case is the one-dimensional AFM, e.g., a spin chain, when the vector $\mathbf{l}$ depends on one spatial coordinate, $\mathbf{l} = \mathbf{l}(x,t)$. In the case of a simple chain the action acquires an additional topological term[67,116]

$$\mathcal{A}^{\text{topol}} = 2\pi\hbar SQ, \quad Q = \frac{1}{4\pi}\int dx\,dt\left(\mathbf{l}\cdot\left[\frac{\partial\mathbf{l}}{\partial x}\times\frac{\partial\mathbf{l}}{\partial t}\right]\right). \qquad (42)$$

The quantity Q is a topological invariant of the mapping of the (x,t) plane onto the sphere $\mathbf{l}^2 = 1$. For a continuous function $\mathbf{l} = \mathbf{l}(x,t)$ having a unique value for $x,t \to \infty$, this quantity takes on only integer values, $Q = 0, \pm 1, \pm 2, \ldots$. It is clear that the variation of this quantity is equal to zero, and its presence is not manifested in the equations of motion for the vector **l**. However, the topological term does influence the behavior of the non-small quantum fluctuations; in particular, it leads to differences in the character of the ground state of the AFM chain with integer and half-integer spin.[67,116] The topological term also determines interference effects for non-one-dimensional instantons for the problem of tunneling in disclinations and domain walls[123,124] (see Sec. 7 below). The presence of the topological term depends fundamentally on the magnetic symmetry of the AFM; in particular, it is present for a simple spin chain but absent for a spin ladder (which we discussed in Sec. 4 in connection with the problem of the spin-flop transition); this circumstance leads to fundamentally different behavior of quantum fluctuations in these systems.[102] The question of whether topological invariants exist in AFMs of higher dimension, e.g., the Hopf invariant, which describes the mapping of the three-dimensional manifold (x,y,t) onto the sphere $\mathbf{l}^2=1$, remains open to discussion.

VI. TUNNELING IN SMALL AFM PARTICLES AND ANTIFERROMAGNETIC MOLECULES

In the study of the macroscopic quantum effects, the phenomenon of *coherent* macroscopic quantum tunneling between energetically equivalent but physically different states in systems with discrete degeneracy of the ground state is of particular interest.[1,28,29] A typical effect of this type is the mixing of two equivalent classical states and the tunneling splitting of the energy levels corresponding to them, which are degenerate in the classical case. The original papers on the theory of quantum tunneling were done for small particles of ferromagnets under the assumption that all the spins in the particle are parallel to each other (the large-spin model).[125–128] Then it turned out that from an experimental standpoint AFMs are a more convenient class of objects for investigation of quantum tunneling. According to calculations,[129,130] in AFMs the level splitting is stronger than in ferromagnets, and the effects can be observed at higher temperature. It is not surprising that the first observation of quantum tunneling effects was done for ferritin particles of biological origin, which have an antiferromagnetic structure[27] (see Sec. 2).

Tunneling in magnets entails subtle and beautiful effects of interference of instanton trajectories. For ferromagnetic particles in the absence of magnetic field these effects lead to suppression of tunneling for half-integer total spin of the system,[32,33] and this can be considered an example of the working of Kramers' theorem on the ground-state degeneracy. In the presence of magnetic field **H**, Kramers' theorem is inapplicable, and the result cannot be predicted beforehand. For ferromagnets, tunneling in the case $H\neq 0$ was studied theoretically by Garg with the use of the instanton method.[131] The analysis led to an extremely nontrivial result that a partial (non-Kramers) interference can arise. If the field is parallel to the hard axis of a particle with rhombic anisotropy, then the tunneling level-splitting will have an oscillatory dependence on the magnetic field. In pure AFMs, i.e., for complete compensation of the sublattice spins, interference effects can appear in an applied magnetic field[51,132] and in the presence of certain types of Dzyaloshinskii–Moriya interaction.[118]

Without fear of contradiction it can be said the synthesis and study of high-quality single crystals of high-spin molecules with precise orientation of the molecular axes (their properties were discussed in Sec. 2) have opened up a new era of research on macroscopic quantum effects.[1] Both effects of tunneling between excited levels, for which the splitting is larger,[133,134] and tunneling in the ground state[135–139] have been observed for such systems. Parallel orientation of the anisotropy axes of the molecules in single crystals has made it possible to really address the question of observing the oscillations predicted by Garg[131] in the tunneling splitting as a function of the external magnetic field, and only for a field parallel to the hard axis of the magnetic particle. Such oscillations have been observed by the method of relaxation time measurements at low temperatures[139] for high-spin molecules both with integer spin $S=10$ (Refs. 137 and 138) and for systems with half-integer spin $S=9/2$; for these cases the phase of the oscillations is shifted by $\pi/2$. Recently the direct observation of the tunneling level-splitting for antiferromagnetic Fe_8 molecules by the method of inelastic neutron scattering was reported.[140] This led to new theoretical studies of the tunneling problem for an ensemble of oriented particles.[141,142]

A. Instanton approach to the description of tunneling

The probability amplitude of a transition from state $|2\rangle$ to a different state $|1\rangle$ (the propagator P_{12}) can be written in terms of a path integral (7). If one is talking about tunneling, i.e., motion in the classically forbidden region, then the value of the mechanical action in the ordinary mechanics of the particles is purely imaginary. Then the Feynman exponent $\exp(i\mathcal{A}/\hbar)$ will be a purely real expression $\exp(-\mathcal{A}_{\mathrm{Eu}}/\hbar)$, where $\mathcal{A}_{\mathrm{Eu}}=-i\mathcal{A}$ is the *Euclidean action*. For magnets whose Lagrangian contains terms linear in the derivatives, the Euclidean action can have both real and imaginary parts. In the classically forbidden region the real Feynman exponent appears automatically, but the transition from $i\mathcal{A}$ to $\mathcal{A}_{\mathrm{Eu}}$ is conveniently done with the aid of a transition to imaginary time, $t\rightarrow i\tau$. Then for estimation of effects of macroscopic quantum tunneling we immediately employ the Euclidean action functional, which can be written in the form

$$\mathcal{A}_{\mathrm{Eu}}[\mathbf{l}]\equiv\int_{-\infty}^{\infty}\mathscr{L}_{\mathrm{Eu}}d\tau=\int_{-\infty}^{\infty}d\tau\left\{\frac{\hbar^2N}{2JZ}\left[\frac{1}{2}\left(\frac{\partial\mathbf{l}}{\partial\tau}\right)^2+i\gamma\left(\mathbf{H}^{(\mathrm{eff})}\cdot\left[\mathbf{l}\times\frac{\partial\mathbf{l}}{\partial\tau}\right]\right)\right]+is\hbar N_{\mathrm{ex}}\mathbf{A}(\mathbf{l})\cdot\left(\frac{\partial\mathbf{l}}{\partial\tau}\right)+\widetilde{W}(\mathbf{l})\right\},\qquad(43)$$

where the energy $\widetilde{W}(\mathbf{l})$, the effective field $\mathbf{H}^{(\mathrm{eff})}$, and the vector potential $\mathbf{A}(\mathbf{l})$ are determined by the same formulae as in the "ordinary" action (37).

To analyze the tunneling in an AFM between different classical degenerate ground states having different values of the vector **l**, labeled $\mathbf{l}^{(+)}$ and $\mathbf{l}^{(-)}$, and to find the value of the tunneling splitting Δ of the energy of these states, one must estimate the tunneling exponent $\mathrm{Re}\,\mathcal{A}_{\mathrm{Eu}}/\hbar$. The main object in that formalism consists in the so-called *instantons*,[28–30,68,143] which are solutions of the Euler–

Lagrange equations for the Euclidean version of the AFM Lagrangian $\mathbf{l}=\mathbf{l}(\tau)$. The instantons correspond to the minimum of $\mathrm{Re}\,\mathcal{A}_{\mathrm{Eu}}[\mathbf{l}]$ under the condition that for $\tau\to\pm\infty$ the vector $\mathbf{l}$ tends toward two different ground states, $\mathbf{l}(\tau)\to\mathbf{l}^{(\pm)}$. In the semiclassical approximation the value of $\mathrm{Re}(\mathcal{A}_{\mathrm{Eu}}/\hbar)$ is not small, and the contribution to the splitting is given only by Euclidian trajectories having the minimum value of the real part of the Euclidean action $\mathcal{A}_{\mathrm{Eu}}[\mathbf{l}]$. An important feature of magnets is the presence of several equivalent instanton paths. In the leading approximation in the parameter $\exp(-\mathcal{A}_{\mathrm{Eu}}/\hbar)$ for physically observable splitting Δ of the degenerate energy levels of the ground state, one can write[143]

$$\Delta=\hbar\omega_0\left|\sum_{\alpha} D_\alpha \exp(-\mathcal{A}_{\mathrm{Eu}}^{(\alpha)}/\hbar)\right|, \tag{44}$$

where for convenience we have immediately separated out the factor $\hbar\omega_0$, where ω_0 is the frequency of small oscillations of the vector $\mathbf{l}$, and the index α enumerates the equivalent instanton paths corresponding to the same (smallest) value of $\mathrm{Re}\,\mathcal{A}_{\mathrm{Eu}}^{(\alpha)}$. The coefficient D_α is the pre-exponential factor for a given instanton path, which in standard quantum mechanics is determined by the first correction to the classical solution.[64] In the instanton approach this factor (the fluctuation determinant) is due to small fluctuations around the instanton. Its calculation is a complex mathematical problem that will be discussed below.

Importantly, in magnets the corresponding partial contributions $D_\alpha \exp(-\mathcal{A}_{\mathrm{Eu}}^{(\alpha)}/\hbar)$ can be (and often are) complex, i.e., they contain a phase factor $\exp(i\Phi^{(\alpha)})$, which leads to *interference of the instanton paths*. Often such interference arises because of a difference of the values of the *imaginary* part of $\mathcal{A}_{\mathrm{Eu}}^{(\alpha)}$. For example, in a rhombic ferromagnet the quantities $\mathcal{A}_{\mathrm{Eu}}^{(\alpha)}$ for two instanton paths ($\alpha=1,2$) contain terms $i\pi S_{\mathrm{tot}}\hbar$ and $-i\pi S_{\mathrm{tot}}\hbar$. Therefore, the splitting $\Delta=D|\exp(-\mathcal{A}_{\mathrm{Eu}}^{(1)}/\hbar)+\exp(-\mathcal{A}_{\mathrm{Eu}}^{(2)}/\hbar)|$ acquires an interference factor $|\cos\pi S_{\mathrm{tot}}|$,[32,33] which describes a suppression of tunneling for half-integer spin. Chiolero and Loss[120] gave an example of a tunneling problem in an AFM for which the pre-exponential factor D_α is complex and gives a substantial contribution to the phase factor. To take interference effects into account explicitly for a system with several instantons (for a magnet with easy axis C_n there exist n instanton trajectories) it is convenient to write[118]

$$\Delta=2\hbar\omega_0 D\sqrt{K}\exp(-\mathrm{Re}\,\mathcal{A}_{\mathrm{Eu}}^{(\alpha)}/\hbar), \tag{45}$$

where D is now the modulus of the fluctuation determinant, and we have explicitly separated out the phase (combinatorial) factor K:

$$K=\left|\sum_{\alpha,\beta}\cos\left(\frac{\Delta\Phi^{(\alpha,\beta)}}{2}\right)\right|,\quad \Delta\Phi^{(\alpha,\beta)}=\Phi^{(\alpha)}-\Phi^{(\beta)}, \tag{46}$$

where the summation is over all pairs of instantons, and $\Delta\Phi^{(\alpha,\beta)}$ is the difference of the phase factors for the α and β instantons.

In this formula $\exp(-\mathrm{Re}\,\mathcal{A}_{\mathrm{Eu}}/\hbar)$ coincides exactly with the exponential factor that appears in the coefficient of transparency of a barrier in the semiclassical approximation of ordinary quantum mechanics. For the simplest version of the σ-model the Lagrangian is real, all the $\Phi^{(\alpha)}$ are equal to zero, and therefore the combinatorial factor is trivial, $\sqrt{K}=n$, i.e., for n equivalent paths the value of the level splitting is equal to the contribution of one instanton, multiplied by the number of paths.

B. Instantons as solutions of the dynamical problem

For analysis of the instanton solutions one can exploit the extremely useful analogy with the problem of finding the separatrix solutions of finite-dimensional dynamical systems. The vector $\mathbf{l}$ is conveniently parametrized by the usual angular variables:

$$l_1=\sin\theta\cos\varphi,\quad l_2=\sin\theta\sin\varphi,\quad l_3=\cos\theta. \tag{47}$$

In the case of the general form of the Lagrangian (43) the structure of the instanton is determined by a general system of two second-order Euler–Lagrange equations for the variables $\theta(\tau),\varphi(\tau)$, which are in general complex. Let us discuss the possibility in principle of constructing the instanton solutions of such a system. The boundary conditions for the given problem have the form $\mathbf{l}\to\mathbf{l}_{\pm}^{(0)}$, $\partial\mathbf{l}/\partial\tau\to 0$ for $\tau\to\pm\infty$. This problem is similar to the problem of finding a moving domain wall, which is described by solutions of the form $\mathbf{l}=\mathbf{l}(\xi)$, where $\xi=x-vt$, v being the velocity of the wall, with the same boundary conditions for $\xi\to\pm\infty$. Consequently, the instanton (like a soliton of the wall type) corresponds to a heteroclinic separatrix trajectory of the dynamical system (43), which joins the pair of equivalent minima $\mathbf{l}_{\pm}^{(0)}$ of the potential $\tilde{W}(\mathbf{l})$. For the problem with more than one degree of freedom it is by no means always possible to construct such a solution. The situation in the case of instantons is still worse than for solitons, since the solutions, generally speaking, are not real and, in essence, the number of degrees of freedom is doubled.

An arbitrary solution of the equations of motion of a given dynamical system can be constructed if the system is integrable. If even the vector $\mathbf{l}$ is real, we will have a system with two degrees of freedom. For it to be integrable there must exist two independent integrals of motion. One of them is easily written: it is the Euclidean analog of the total energy:

$$\mathcal{E}_{\mathrm{Eu}}=\frac{\hbar^2 N}{4JZ}\left[\left(\frac{\partial\theta}{\partial\tau}\right)^2+\sin^2\theta\left(\frac{\partial\varphi}{\partial\tau}\right)^2\right]-W(\theta,\varphi), \tag{48}$$

but the second integral of motion by no means always exists. It can be constructed trivially for the case when the anisotropy is purely uniaxial, i.e., when $\mathscr{L}_{\mathrm{Eu}}$ does not depend on φ. Below we shall use this integral of motion (68) to construct instanton solutions for a purely uniaxial AFM in magnetic field. However, in the case of any nonzero decompensation of the sublattices for a purely uniaxial model the moving domain wall[12,34,35] and instanton[144] are absent; their existence is contingent on anisotropy in the basal plane.

Analysis of dynamical systems with more than one degree of freedom, in particular, the construction of integrable systems, has remained one of the most important problems of analytical dynamics for over a hundred years and is still under intensive study.[145] Among the integrable systems known are models of the dynamics of a unit vector, e.g., the classical Neumann problem[146] of the motion of a material point along a sphere in the field of a potential that is a quadratic function of the Cartesian coordinates, and its generalization for a number of other polynomial potentials.[147] We note especially the integrable model with $W=K_{ik}l_il_k$ for $\mathbf{H}=0$, $D_{ij}=0$ and with a gyrotropic term of the monopole field type.[147,148] Integrability of such a model also follows from the exact integrability of the Landau–Lifshitz equations for the magnetization of a two-dimensional ferromagnet, which was established by Sklyanin.[149] Diagonalizing the matrix K_{ik} and taking into account the condition $\mathbf{l}^2=1$, we arrive at the anisotropy energy (39) for a rhombic AFM. This model describes the exact instanton solutions for the AFM model (77) at arbitrary decompensation.[144]

On going from an AFM to the Lagrangian of a ferromagnet, which is a nontrivial operation, the problem simplifies substantially. Formally, one can obtain the Lagrangian of a ferromagnet from (43) if the term quadratic in the derivative, $(\partial\mathbf{l}/\partial\tau)^2$, is set to zero. However, in so doing one would alter the Hamiltonian structure of the system, and the dimension of the phase space would decrease by half. While for an AFM the angles θ and φ that parametrize $\mathbf{l}$ can be treated as canonical coordinates, and the momenta corresponding to them contain $\dot{\theta}$ and $\dot{\varphi}$, for a ferromagnet the Hamiltonian variables are expressed only in terms of $\mathbf{l}$. As the canonical pair one can choose the momentum $P=\cos\theta$ and the coordinate $Q=\varphi$. A ferromagnet corresponds to an integrable Hamiltonian system with one degree of freedom, and the role of Hamilton's function is played by the energy $W(\theta,\varphi)$ of the ferromagnet. For instantons the corresponding Hamiltonian is complex,

$$i\frac{\partial P}{\partial\tau}=-\frac{\partial W}{\partial Q},\quad i\frac{\partial Q}{\partial\tau}=\frac{\partial W}{\partial P},\tag{49}$$

and the solution in a ferromagnet cannot be real, and therefore the number of degrees of freedom is actually equal to two. However, in a recent paper by Kulagin and the author it was shown that for any ferromagnet model, integrability is present even in this case.[150] We write $W=H_1+iH_2$, where H_1 and H_2 are real-valued functions. Assuming P and Q are complex, $P=P'+iP''$, $Q=Q'+iQ''$, we separate the real and imaginary parts of equations (49). As a result, we obtain a system of four real equations, the right-hand sides of which will contain the derivatives of H_1 and H_2 with respect to the variables P',P'',Q',Q''. However, if it is required that W be an analytic function of the complex variables P and Q and satisfy the Cauchy–Riemann conditions independently, then the right-hand sides can be rewritten in terms of the derivatives of H_1 only or of H_2 only. As a result, the system of equations for the real variables becomes a Hamiltonian system. In particular, by choosing pairs of canonical variables in the following way:

$$p_1=P',\quad q_1=Q'';\quad p_2=P'',\quad q_2=Q',\tag{50}$$

the system can be written in the form of the standard (real) Hamiltonian system with two degrees of freedom, $\dot{p}_i=-\partial H_1/\partial q_i$, $\dot{q}_i=\partial H_1/\partial p_i$, $i=1,2$, with the Hamiltonian function $H_1=H_1(p_1,q_1,p_2,q_2)$ and the additional integral of motion H_2. Using only the Cauchy–Riemann condition for W, one can show that the Poisson bracket of the functions H_1 and H_2, calculated in terms of the canonical variables p_i,q_i, is equal to zero. Consequently, any ferromagnet model whose energy $W(\cos\theta,\varphi)$ is analytic with respect to $\cos\theta$ and φ in the sense indicated above reduces to an exactly integrable dynamical system. The efficiency of this way of constructing the instanton trajectories for a number of ferromagnet models was demonstrated in Ref. 150. The same arguments can be applied to the instantons in an AFM, which in the case of complex variables θ, φ are described by a dynamical system with four degrees of freedom, but the construction of one additional first integral does not solve the problem of integrability of the problem in general form.

For the often-used model of strong easy-plane anisotropy the equations of motion give the approximate relation $\cos\theta\simeq\text{const}\cdot(\partial\varphi/\partial t)$, and $\cos\theta$ is a dependent variable.[36] In this approximation the Lagrangian takes on the standard form for mechanics, $M_{\text{eff}}(\varphi)(\partial\varphi/\partial t)^2/2-W(\varphi)$, where $M_{\text{eff}}(\varphi)$ and $W(\varphi)$ are the effective mass and the potential, which are determined by the parameters of the system. In this case the problem reduces to a mechanical system with one degree of freedom. However, such a reduction of the phase space of a Hamiltonian system with two degrees of freedom can lead to a loss of important physical effects in tunneling.[150]

C. Fluctuation determinant

Let us discuss the evaluation of the pre-exponential factor D in formula (45) for the tunneling level-splitting. In the instanton approach this factor is due to the contribution of small deviations of the trajectory in the total Feynman integral from the classical paths θ_0,φ_0 corresponding to the instanton. This contribution can be estimated in the Gaussian approximation (the semiclassical approach!) with the aid of an expansion of the Euclidean action to second order in the small deviations:

$$\theta(\tau)=\theta_0(\tau)+\vartheta(\tau),\quad \varphi(\tau)=\varphi_0(\tau)+\delta\varphi(\tau).\tag{51}$$

For instantons of the form $\theta_0=\theta_0(\tau)$, $\varphi_0=\text{const}$, which often arise in tunneling problems in AFMs, the variables ϑ and $\delta\varphi$ describe the longitudinal and transverse deviations from the instanton trajectory. Introducing the variable $\mu=\delta\varphi\sin\theta_0$, we obtain the factor D in the form

$$D=\int\mathcal{D}[\vartheta]\mathcal{D}[\mu]\exp\left(-\frac{1}{2}\int dx(\Psi,\hat{\mathbf{A}}\Psi)\right),\tag{52}$$

where $\Psi=(\vartheta,\mu)$ is a two-component vector, and $\hat{\mathbf{A}}$ is a 2×2 matrix differential operator, with operators of the Schrödinger type with respect to the dimensionless variable $\xi=\omega_0\tau$ along the diagonal. An example of such an operator that arises in a particular problem is given below; see formula (71). The off-diagonal structure of $\hat{\mathbf{A}}$ corresponds to two interacting field degrees of freedom, which substantially complicates the calculation of D as compared to the standard case of instantons in a system with one degree of freedom. Sometimes—for example, for instantons in the simple model of an uncompensated AFM—this factor can be calculated.[144] However, in a number of cases the operator $\hat{\mathbf{A}}$ is diagonal, in which case the fluctuation determinant decomposes into a product of two independent factors, longitudinal $D_\parallel$ and transverse $D_\perp$. We shall limit discussion to this simpler example.

Calculation of the longitudinal determinant $D_\parallel$ is a rather nontrivial mathematical problem that has nonetheless become a standard element of the theory of instantons.[68,143] Its value can be formally written in terms of an infinite product of *nonzero* eigenvalues of the corresponding Schrödinger operator λ_k, $D_\parallel \sim [\Pi_k(1/\lambda_k)]^{1/2}$. Besides them, the Schrödinger operator for the longitudinal deviations always contains a zero mode with $\lambda=0$. The presence of the zero mode is due to the invariance of the Euclidean action with respect to the substitution $\mathbf{l}_0(\tau)\rightarrow\mathbf{l}_0(\tau-\tau_0)$, where τ_0 is an arbitrary parameter. The contribution of this mode cannot be described in the Gaussian approximation; its inclusion causes a large factor $(\mathrm{Re}\,\mathcal{A}_{\mathrm{Eu}}/\hbar)^{1/2}$ to appear in $D_\parallel$ (see details in the reviews[68,143]). As a result, the longitudinal fluctuation determinant can be written in the form

$$D_\parallel = C\left(\frac{\mathrm{Re}\,\mathcal{A}_{\mathrm{Eu}}}{2\pi\hbar}\right)^{1/2}, \tag{53}$$

where C is a numerical factor of the order of unity.

The structure of the transverse fluctuation determinant $D_\perp$ is not so universal. For a purely uniaxial AFM model with a symmetry axis C_∞ its form is exactly the same as for $D_\parallel$. Then the *square* of the standard large parameter $(\mathrm{Re}\,\mathcal{A}_{\mathrm{Eu}}/\hbar)^{1/2}$ appears in the splitting[151] [see formula (72) below]. This result is an example of the implementation of the general rule of working with instantons in systems with more than one zero mode, according to which *each* zero mode gives such a factor in the level splitting.[143] If there is a small but finite anisotropy $K_p \ll K_u$ in the basal plane x,y, then instead of this large parameter one will have $\sqrt{K_u/K_p}$.

D. Instantons in uniaxial AFMs

The structure of the instanton is determined by a general system of second-order Euler-Lagrange equations for the angular variables; this system can be written schematically in the form

$$-\ddot{\theta}+\dot{\varphi}^2\sin\theta\cos\theta+\omega_0^2\frac{\partial w_a(\theta,\varphi)}{2\partial\theta}+i\dot{\varphi}\Gamma(\theta,\varphi)=0,$$

$$-(\dot{\varphi}\sin^2\theta)+\omega_0^2\frac{\partial w_a(\theta,\varphi)}{2\partial\varphi}-i\dot{\theta}\Gamma(\theta,\varphi)=0, \tag{54}$$

where a dot denotes a derivative with respect to τ, and the terms with $\Gamma(\theta,\varphi)$ are determined by variation of the gyroscopic terms in the Lagrangian (43). The dimensionless function $w_a(\theta,\varphi)$ is proportional to the anisotropy energy $W(\theta,\varphi)$. The coefficient of proportionality is chosen so as to make ω_0 coincide with the frequency of small oscillations of the vector $\mathbf{l}$, which corresponds to $\omega_0^2 w_a=(4JZ/\hbar^2N)W$. The form of $w_a(\theta,\psi)$ and the function $\Gamma(\theta,\varphi)$, which is generated by the Dzyaloshinskii interaction or a magnetic field, is discussed below for specific examples. In the case of an AFM with a decompensation of the sublattice spins one has $\Gamma=\gamma H_{\mathrm{ex}}(N_{\mathrm{ex}}/N)\sin\theta$, i.e., its form is the same as for the Landau–Lifshitz equation.

The general equations (54) contain a large number of independent parameters of various natures that are due to the external field, the Dzyaloshinskii interaction, and possible decompensation. As we shall see, the role of these interactions is extremely diverse, and even if one could write down a general formula for the Euclidean action with all these factors included, it would be difficult to analyze. We therefore consider the role of individual interactions that lower the dynamical symmetry of an AFM, moving from the simple to the complex. The presence of uncompensated spins complicates the analysis significantly, and we shall therefore begin with the case of a completely compensated AFM, for which $N_{\mathrm{ex}}=0$. It is convenient to begin discussion with the tunneling in the simplest case of a model with the highest dynamical symmetry, which corresponds to $\Gamma=0$. The point is that for certain AFM models with the Dzyaloshinskii–Moriya interaction and nonzero $\Gamma(\theta,\psi)\neq 0$ the results turn out to be exactly the same as for $\Gamma(\theta,\psi)=0$ (this will not happen in the case of magnetic field).

If $\Gamma(\theta,\varphi)=0$ the problem can be analyzed without difficulty. We limit discussion to the case of a particle of an easy-axis AFM with an n-fold axis, in the ground state of which the vector $\mathbf{l}$ is parallel to the principal axis C_n. For such a magnet $\omega_0=\gamma H_{sf}$, and the anisotropy energy w_a can be written in the form

$$\omega_0^2 w_a(\theta,\varphi)=\omega_0^2\sin^2\theta+\omega_p^2\sin^n\theta\sin^2(n\varphi/2), \tag{55}$$

where the second term corresponds to the simplest expression for the anisotropy in the basal plane, and usually for $n>2$ one has $\omega_p \ll \omega_0$. For such a choice of energy the z and x axes are always the easy and medium axes of the AFM, respectively. It is easy to see that the instanton solution corresponds to a solution of the form $\varphi=\varphi_0=\mathrm{const}$, $\theta=\theta(\tau)$. The admissible values of φ_0 are determined by the relation

$$\left.\frac{\partial w_a(\theta,\varphi)}{\partial\varphi}\right|_{\varphi=\varphi_0}\propto\sin n\varphi_0=0. \tag{56}$$

There exist $2n$ solutions of this equation, $\varphi_k^{(0)}=\pi k/n$, $k=0,1,\dots,2n-1$, of which n solutions with even k, $\varphi_{k,\min}^{(0)}$ give a minimum of $w_a(\theta,\varphi)$, and the remaining n with $\varphi_{k,\max}^{(0)}$ give a maximum of this function for all $\theta\neq 0,\pi$. Instantons with $\varphi_{k,\min}^{(0)}$ correspond to lower values of the Euclidean action. The function $\theta(\tau)$ can be found from the second-order equations, for which the first integral (48) is known. Taking into account the boundary conditions $\theta\rightarrow 0,\pi$ for $\tau\rightarrow\pm\infty$, we obtain

$$\left(\frac{d\theta}{d\tau}\right)^2=\omega_0^2 w_a(\theta,\varphi_k^{(0)}). \tag{57}$$

The Euclidean action is real-valued on the trajectories for all values of φ and is given by the formula

$$\mathcal{A}_{\mathrm{Eu}}=\frac{\hbar^2\omega_0 N}{2JZ}\int_0^\pi d\theta\sqrt{w_a(\theta,\varphi)}\simeq 2\hbar sN\sqrt{\frac{K_u}{JZ}}. \tag{58}$$

Of course, if $\Gamma(\theta,\varphi)\neq 0$ but does vanish at a certain value of $\varphi_{k,\min}^{(0)}$, corresponding to a minimum of the anisotropy energy, then the "planar" real solution $\theta=\theta(\tau)$, $\varphi=\varphi_k^{(0)}=\mathrm{const}$ is possible. For these planar solutions the contribution of the gyroscopic term to the Euclidean action $\mathcal{A}_{\mathrm{Eu}}$ can be purely imaginary (examples will be given below). As it turns out, however, if the function $\Gamma(\theta,\varphi)$ goes to zero for *all* of the same values of φ for which $\partial w_a(\theta,\varphi)/\partial\varphi$ does, viz., the *minima* $\varphi^{(0)}_{k,\min}$ and the *maxima* $\varphi^{(0)}_{k,\max}$, i.e., $\Gamma(\theta,\varphi)\propto\sin n\varphi$, then the contribution of the gyroscopic term to $\mathcal{A}_{\rm Eu}$ is identically zero. In such a case both the instanton solution and the Euclidean action are exactly the same as when one is considering only the simplest model, with $\Gamma(\theta,\varphi)=0$. The situation described is not realized for an AFM in a field, but for those AFMs for which the gyroscopic terms are determined solely by the Dzyaloshinskii interaction it is in no way exotic. It occurs for all AFMs with an even (according to Turov) principal axis, as is confirmed by a symmetry analysis.[118]

Analysis of the various AFM models with an external magnetic field along the symmetry axis of the crystal or with a Dzyaloshinskii interaction in an easy-axis AFM leads to the conclusion that besides the trivial case described above, two more situations can be realized.[118,151] Thus for an AFM with sufficiently high symmetry, three types of behavior of the instanton solutions have been established. The trivial case is realized in an AFM with $\mathbf{H}=0$ and an even principal axis. For the other two nontrivial cases the behavior is substantially different.

1. One nontrivial type of behavior corresponds to the case when $\Gamma(\theta\varphi^{(0)}_{k,\min})=0$ and a planar real instanton is realized but $\Gamma(\theta,\varphi^{(0)}_{k,\max})\neq 0$. For this case the value of the real part of the Euclidean action $\mathcal{A}_{\rm Eu}$ does not depend on the gyrotropy parameter $|\mathbf{H}^{(\rm eff)}|$, but a nonzero imaginary part of $\mathcal{A}_{\rm Eu}$ appears which is proportional to $|\mathbf{H}^{(\rm eff)}|$.

2. In the second nontrivial case, when $\Gamma(\theta,\varphi^{(0)}_{k,\min})\neq 0$, the planar solution $\varphi=\text{const}$ is absent. Then one must find a general solution of system (54) in the form $\theta=\theta(\tau)$, $\varphi=\varphi(\tau)$. This solution is complex and cannot always be constructed exactly. It can be shown, however, that for such complex instantons the imaginary part of the Euclidean action does not appear, $\mathrm{Im}\,\mathcal{A}_{\rm Eu}=0$, and the real part $\mathrm{Re}\,\mathcal{A}_{\rm Eu}$ contains only contributions quadratic in $(\mathbf{H}^{(\rm eff)})^2$.

The latter case will be discussed in detail below for the example of an AFM in magnetic field. Now let us discuss the first case, when the instanton trajectories are planar and real. In the case of real trajectories for calculation of the imaginary part of the Euclidean action one can use the following simple method.[117,118] We introduce a vector $\mathbf{r}=r\mathbf{l}$ that is not restricted by the condition $\mathbf{r}^2=1$, and we write the term with the first derivative from (43) in the form

$$-i\gamma\tilde{\mathbf{A}}\cdot\frac{\partial\mathbf{r}}{\partial\tau},\quad\text{where }\tilde{\mathbf{A}}=\frac{\mathbf{r}\times\mathbf{H}^{(\rm eff)}}{r^2}.\tag{59}$$

This expression has the same structure as the term in the nonrelativistic Euclidean Lagrangian describing the interaction of a charged particle having coordinate $\mathbf{r}$ and velocity $\mathbf{v}=d\mathbf{r}/d\tau$ with the formal magnetic field $\tilde{\mathbf{B}}=\mathrm{curl}\tilde{\mathbf{A}}$. The magnetic field enters the Lagrangian of a charged particle through the vector potential $\tilde{\mathbf{A}}$ (we have introduced the notation $\tilde{\mathbf{A}}$ to prevent confusion of this quantity with the monopole-field vector potential $\mathbf{A}$ introduced above) at the point $\mathbf{r}$, which is determined only to within a certain gauge, while at the same time the field $\tilde{\mathbf{B}}$ is gauge invariant. In the Lagrangian of an AFM for any $\mathbf{H}^{(\rm eff)}$ this formal magnetic field $\tilde{\mathbf{B}}$ is directed radially and can be written as

$$\tilde{\mathbf{B}}=\frac{\mathbf{r}}{r^2}\mathcal{B}(\theta,\varphi),\quad \mathcal{B}=2(\mathbf{H}^{(\rm eff)}\cdot\mathbf{l})-\frac{\partial H^{(\rm eff)}_k}{dl_k}+\frac{\partial H^{(\rm eff)}_i}{dl_j}l_il_j.\tag{60}$$

For $\mathbf{H}=0$ the formula for $\mathcal{B}$ is conveniently written directly in terms of the Dzyaloshinskii tensor D_{ij}:

$$\mathcal{B}=3D_{ij}l_il_j-D_{ii}+\frac{\partial D_{ij}}{\partial l_k}l_jl_k-\frac{\partial D_{ij}}{\partial l_i}l_j.\tag{61}$$

The values of $\mathcal{B}(\theta,\varphi)$ for different AFMs with the Dzyaloshinskii interaction are given in Ref. 118. The imaginary part of the Euclidean action $\mathrm{Im}\,\mathcal{A}_{\rm Eu}$ for the αth instanton is written in the form of a contour integral $\int\tilde{\mathbf{A}}d\mathbf{r}$. To calculate the value of the tunneling splitting one needs to know only the phase difference $\Delta\Phi^{(\alpha,\beta)}=\Phi^{(\alpha)}-\Phi^{(\beta)}$ for all instanton pairs (46). The $\Delta\Phi^{(\alpha,\beta)}$ are expressed in terms of the integral $\oint\tilde{\mathbf{A}}\cdot d\mathbf{r}$ over a closed contour consisting of these two trajectories. Using Stokes' theorem, one can write this quantity as the flux of the formal magnetic field $\tilde{\mathbf{B}}$ introduced above, through the part of the unit sphere bounded by that contour. This leads to the simple expression

$$\Delta\Phi^{(\alpha,\beta)}=\int_0^\pi\sin\theta d\theta\int_{\varphi_\alpha}^{\varphi_\beta}d\varphi\mathcal{B}(\theta,\varphi),\tag{62}$$

where φ_α and φ_β are the values of the angle φ for the given instantons. Importantly, for all possible forms of the Dzyaloshinskii interaction and for all orientations of the external magnetic field $\mathbf{H}$, the total flux of the formal field $\tilde{\mathbf{B}}$ through the sphere is equal to zero. We note that here the situation is fundamentally different from the case of an uncompensated total spin $S_{\rm ex}$, when $\mathbf{A}$ describes the field of a magnetic monopole and the flux through some region of the sphere is proportional to its area, and the total flux $\Phi_{\rm tot}=4\pi S$. Of course, in the case of an uncompensated magnet, too, the individual phases are determined by $\mathbf{A}$, i.e., they depend on the gauge, but the phase difference $\Delta\Phi^{(\alpha,\beta)}$ is gauge invariant. However, this phase difference is not equal to zero for any trajectories. In particular, for two diametrically opposed trajectories $\Delta\Phi=2\pi S$, so that in the spin tunneling problem one obtains the phase factor $\cos(\pi S)$ discussed above, and the tunneling is suppressed for a half-integer uncompensated spin. We note that, in accordance with Dirac's discussion of the single-valuedness of the wave function of an electron in a monopole field,[67,152] this condition yields $\cos(\Phi_{\rm tot}/2)=0$, which leads to a half-integer quantization of the spin.

Returning to the case of a compensated AFM, we note that formula (62) permits easy calculation of the phase factor K (46) in formula (45) for the level splitting. The overall form of $\mathcal{B}(\theta,\varphi)$ for an AFM with an n-fold axis is determined by its symmetry.[118] For an AFM with an even principle axis $C_n^{(+)}$, i.e., one that does not permute the permutation of the sublattices, the function $\mathcal{B}(\theta,\varphi)\propto\sin^n\theta\sin n\varphi$, all the phase factors are equal to zero and there is no interference.

If the principle axis is odd, $C_n^{(-)}$, however, the situation is different for different n. If $n=4k$, i.e., $n=4,8,\ldots$ (for crystalline AFMs only $n=4$ is meaningful, but for magnetic clusters and high-spin molecules values greater than $n=6$ are also possible) the function $\mathcal{B}(\theta,\psi)$ is proportional to $\sin^{n/2}\theta\sin(n\varphi/2)$ or to $\sin^{n/2}\theta\cos(n\varphi/2)$, depending on the details of the position of the twofold axes in the basal plane.

In this case the integral (62) can be nonzero, and destructive interference is possible.[118] In the case of an odd axis with $n=2(2k+1)$, i.e., for $n=2,6,10,\ldots$, in particular for rhombic and hexagonal AFMs, the function $\mathcal{B}(\theta,\varphi)$ is also proportional to $\sin(n\varphi/2)$ or $\cos(n\varphi/2)$. However, it contains a factor $\sin^{n/2}\theta\cos\theta$, by virtue of which the phase difference (62) is identically equal to zero on account of the integral over θ, and destructive interference is absent.

Thus the Dzyaloshinskii interaction leads to destructive interference in tunneling only for AFMs with an odd principal axis $C_n^{(-)}$ for $n=4k$, i.e., $n=4,8,\ldots$. A more important role in this phenomenon is played by the external magnetic field. At low field one can assume that the trajectory is planar and real, and the phase factor can then be written as

$$\cos\Phi=\cos\left(\frac{\pi s g\mu_B HN}{2JZ}\cos\psi\right), \tag{63}$$

where ψ is the angle between the plane in which the instanton trajectories lie and the external magnetic field $\mathbf{H}$. The more interest case of a non-small field is discussed in the next subsection.

E. Tunneling for an AFM in magnetic field

Let us consider the important case of an AFM in the presence of a strong magnetic field.[51,151,153] For concrete calculations we shall consider an AFM with rhombic anisotropy of the form (39), where the constants $K_u>0$ and $K_p>0$ describe uniaxial anisotropy and anisotropy in the basal plane, and the z and y axes are the easy and hard axes, respectively. For subsequent applications it is convenient to rewrite this energy in the form used in Eqs. (54), in terms of the characteristic values of the frequency:

$$\omega_0^2 w_a(\theta,\varphi)=\omega_u^2\sin^2\theta+\omega_p^2\sin^2\theta\sin^2\varphi, \tag{64}$$

where $\omega_u=\gamma H_{sf}$, H_{sf} is the field of the spin-flop transition, $\omega_p=\gamma H_p$, and the characteristic field $H_p=2s\sqrt{JZK_p}/g\mu_B$ describes the influence of the field on the anisotropy in the basal plane (see below). For this energy in the absence of field the instantons corresponding to the condition $\theta(+\infty)=0$, $\theta(-\infty)=\pi$ correspond to solutions with a planar rotation of $\mathbf{l}(\tau)$ in the symmetry planes of the system for which $\varphi=(\pi/2)k$, with k an integer,

$$\cos\theta=\tanh\bar{\omega}\tau,\quad \sin\theta=1/\cosh\bar{\omega}\tau, \tag{65}$$

where $\bar{\omega}$ is defined by the expression $\bar{\omega}=\omega_u$ for $\varphi=0,\pi$ and $\bar{\omega}=\sqrt{\omega_u^2+\omega_p^2}$ for $\varphi=(\pi/2)(2k+1)$. The values of the Euclidean action for all these instantons can be written in a unified way:

$$\mathcal{A}_{\mathrm{Eu}}=\hbar N(\hbar\bar{\omega}/ZJ)\quad\text{for}\quad H=0, \tag{66}$$

and for zero field the minimum of the Euclidean action corresponds to only one pair of instantons, with $\varphi=0,\pi$, i.e., with a rotation of the vector $\mathbf{l}$ in the easier plane (z,x).

When taking the magnetic field into account, we restrict discussion to the case when it is directed along one of the symmetry axes: z, x, or y. The function $\Gamma(\theta,\varphi)$ appearing in Eq. (54) for θ, φ can be written in the compact form[118]

$$\Gamma(\theta,\varphi)=2\gamma(\mathbf{H}\cdot\mathbf{l})\sin\theta, \tag{67}$$

and it does not equal zero for any orientation of the field.

We recall that if the magnetic field is directed along the easy axis z of the AFM and $H>H_{sf}$, then a spin-flop transition occurs from the state with $\mathbf{l}\|\mathbf{e}_z$ to a state with $\mathbf{l}\|\mathbf{e}_y$ (see Sec. 4). In this case the influence of the field on the static properties of the AFM can be described by renormalization of the constant K_u: $K_u(H)=K_u(1-H^2/H_{sf}^2)$. For the case of $\mathbf{H}$ parallel to the medium axis $\mathbf{e}_x$, the constant K_u increases with increasing field, $K_u(H)=K_u+(g\mu_BH)^2/(4s^2JZ)$, while K_p decreases, $K_p(H)=K_p-(g\mu_BH)^2/(4s^2JZ)$. At the characteristic field H_p introduced in (64) the quantity $K_p(H)$ changes sign, and for $\mathbf{H}\|\mathbf{e}_x$, $H>H_p$ there is a change of character of the axes in the basal plane: the y axis become the medium axis and the x axis the hard axis. Finally, if the magnetic field is directed along the hard axis $\mathbf{e}_y$, then it effectively increases both K_u and K_p: $K_{u,p}(H)=K_{u,p}+(g\mu_BH)^2/(4s^2JZ)$, and the field does not influence the character of the anisotropy axes at all.

If one naively uses the renormalized anisotropy constants to describe the instantons in the framework of Eqs. (65) (which leads to incorrect results!), one finds that for the orientation of the field along the easy axis the quantity $\mathcal{A}_{\mathrm{Eu}}$ goes to zero for $H\to H_{sf}$, and for the field direction along the medium axis the value of $\mathcal{A}_{\mathrm{Eu}}$ on two classes of paths, $\varphi=(\pi/2)(2k+1)$ and $\varphi=\pi k$, become equal at $H=H_p$. However, as we shall show below, such a description is absolutely incorrect. Besides the aforementioned renormalization of the anisotropy, the field alters the character of the dynamics of the vector $\mathbf{l}$, and that also influences the structure of the instantons and the value of the Euclidean action for them.

We begin by considering the case of the field parallel to the easy axis z, which does not break the symmetry in the (x,y) plane. As a consequence, the gyroscopic term in Eqs. (54) is independent of the angle φ: $\Gamma\propto\sin\theta\cos\theta$. In this case, under the condition $K_p=0$ a purely uniaxial AFM model is realized. Analysis of such a model leads to instructive physical results,[151] and we shall therefore discuss this analysis. In the purely uniaxial case the Lagrangian (43) is independent of φ and is the Noetherian integral of motion $\Omega=\partial\mathscr{L}_{\mathrm{Eu}}/\partial\dot{\varphi}$, the expression for which can be written in the form

$$\Omega=(\dot{\varphi}-i\gamma H)\sin^2\theta=\text{const}, \tag{68}$$

and the problem is integrable. The instanton solutions of the type $\theta\to0,\pi$ for $\tau\to\pm\infty$ correspond to $\Omega=0$, i.e., $\varphi=i\gamma H(\tau-\tau_1)$, where τ_1 is an arbitrary constant. When this formula is taken into account, the equation for $\theta(\tau)$ assumes the form $\theta^2=\omega_u^2\sin^2\theta$. Hence it is easy to obtain a solution of the form (65) with $\bar{\omega}=\omega_u$. For the components of the vector $\mathbf{l}$ in the instanton the following formulae are obtained:

$$l_z=\tanh[\omega_u(\tau-\tau_0)],$$

$$l_x=\frac{\cosh[\gamma H(\tau-\tau_1)]}{\cosh[\omega_u(\tau-\tau_0)]},\quad l_y=i\frac{\sinh[\gamma H(\tau-\tau_1)]}{\cosh[\omega_u(\tau-\tau_0)]}. \tag{69}$$

This solution has the correct asymptotic behavior ($l_{x,y}\to$ for $\tau\to\pm\infty$) for $\gamma H<\omega_u$, i.e., at all values of the field smaller than the SFT field H_{sf}. Consequently, the instanton solution found is valid in the entire stability region of the state with $\mathbf{l}=\pm\hat{\mathbf{z}}$. Despite the fact that in this region the effective anisotropy constant $K_u(H)$ varies from K_u to zero for H

$\to H_{sf}$, the Euclidean action for solution (69) is independent of H. Its imaginary part is equal to zero, and the real part is the same as for $H=0$:

$$\mathcal{A}_{\text{Eu}}^{(0)}=2s\hbar N\sqrt{K_u/JZ} \qquad \text{for} \quad K_p=0, \quad H<H_{sf}. \tag{70}$$

This simple example has shown that the gyroscopic term can substantially suppress the static renormalization of the anisotropy energy.

For this simple example is is possible to do an exact calculation of the pre-exponential factor D in the form (52).[151] The contribution of the two types of deviations, longitudinal and transverse, are determined in this case by identical operators $\hat{M}$. These operators arise for many tunneling problems in magnets, and we shall therefore give their form and the complete set of their eigenfunctions:

$$\hat{M}=-\frac{d^2}{d\xi^2}-\frac{2}{\cosh^2\xi}; \quad Mf_0=0, \quad f_0=\frac{1}{\sqrt{2}\cosh\xi};$$

$$\hat{M}f_k=(1+k^2)f_k, \quad f_k=\frac{(\tanh\xi-ik)e^{-ik\xi}}{\sqrt{L(1+k^2)}}. \tag{71}$$

The total fluctuation factor in this problem is the square of the longitudinal fluctuation determinant $D_\parallel$ [see Eq. (53)], and as a result, the level splitting due to tunneling has the form

$$\Delta=C\hbar\omega_u\left(\frac{\mathcal{A}_{\text{Eu}}^{(0)}}{2\pi\hbar}\right)\exp(-\mathcal{A}_{\text{Eu}}^{(0)}/\hbar), \tag{72}$$

where C is a numerical factor of the order of unity. The additional large parameter $\sqrt{\mathcal{A}_{\text{Eu}}/\hbar}$ appears in the problem in connection with the fact that the instanton solution (69) in the model with $\omega_p=0$ contains two continuous parameters, τ_1 and τ_0 (see Sec. 6.3). We note also that the level splitting Δ is independent of magnetic field, even when the fluctuation determinant is taken into account. This fact can be justified on the basis of an exact quantum treatment. Indeed, for $\omega_p=0$ the Hamiltonian of the system commutes with the z projection of the total spin, S_z^{tot}. Consequently, the states of the system are characterized by a definite value $S_z^{\text{tot}}=0,\pm 1, \pm 2,\ldots$. The tunneling splitting of the doublet corresponds to $S_z^{\text{tot}}=0$, and the magnetic field cannot influence the energies of these states. We note that in these terms the spin-flop transition is due to the circumstance that for $H>H_{sf}$ a level with $S_z^{\text{tot}}>0$ becomes the lowest level. This in essence brings about the quantum analog of the spin-flop transition, which was discussed in Sec. 4.

Let us consider another simple case, when the magnetic field is directed along the hard axis of the AFM (the y axis). In this case $\Gamma(\theta,\varphi)=2\gamma H\sin^2\theta\sin\varphi$, and for instanton pairs with $\varphi=0,\pi$ it has the value $\Gamma=0$. Consequently, in this case there are two planar instanton solutions of the form $\varphi=0,\pi$, $\theta=\theta(\tau)$. These solutions determine the instantons with a rotation of the vector in the easier plane (z,x) and at the same time have the minimum value of the real part of $\mathcal{A}_{\text{Er}}$. The Euclidean action for them is independent of field and is given by formula (66):

$$\mathcal{A}_{\text{Eu}}^{(\text{HA})}(H)=2s\hbar N\sqrt{\frac{K_u}{JZ}}\pm i\frac{\pi\hbar g\mu_B HN}{2JZ}. \tag{73}$$

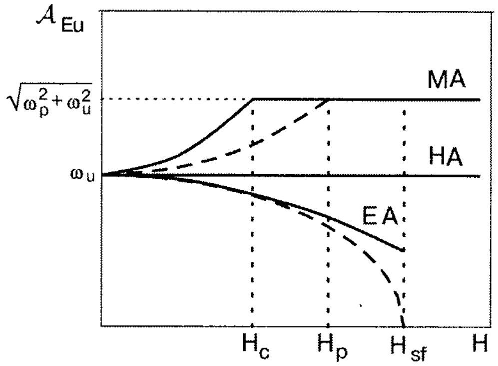

FIG. 8. Real part of the Euclidean action in units of $\hbar^2N/2JZ$ as a function of magnetic field (schematic). The curves for the field along the easy, medium, and hard axes are labeled EA, MA, and HA, respectively. The solid lines represent a consistent calculation[151] of the value of $\mathcal{A}_{\text{Eu}}$, and the dotted line is the result obtained by a "naive" approach taking into account only the static renormalization of the anisotropy constants; see text.

Thus for magnetic field directed along the hard axis of the AFM the real part of the Euclidean action $\mathcal{A}_{\text{Eu}}^{(\text{HA})}(H)$ is independent of the field strength (see Fig. 8), and the signs of its imaginary part for the two instantons differ.[51,132] In this case, however, the interference effects and the oscillatory dependence of the splitting on field are due not only to the imaginary part of the Euclidean action. In this geometry the most interesting effects appear on account of the fluctuation determinant. In this case the equations for small deviations of ϑ and μ from the instanton solution are uncoupled, and $D=D_\parallel D_\perp$. The transverse determinant contains the Schrödinger operator with a complex potential. The value of $D_\perp$ is complex, with different phases for the two different equivalent instantons, and that modifies the phase shift. Even for moderate values of the field the presence of $D_\perp$ leads to a phase shift of the oscillatory function $\Delta(H)$ by $\pi/2$ in comparison with that caused by the imaginary part of the Euclidean action itself.[51,153]

In the presence of field the planar solution corresponds to rotation of the vector **l** in the plane perpendicular to the direction of the field **H**. When **H** is oriented along the hard axis the planar instanton clearly has the lowest value of the Euclidean action for all values of the field. A planar rotation in other symmetry planes (and the more so for a rotation in a plane that is not a symmetry plane of the AFM) would correspond to a nonzero function $\Gamma(\theta,\varphi)$ and is therefore impossible. Investigation of the distribution of **l** requires analysis of a system with two degrees of freedom; although it cannot be done exactly, it can be done using various approximate methods.[151] Analysis showed a large diversity in the behavior of nonplanar instantons for different orientations of the field. Let us briefly discuss the results.

As was shown above on the basis of an exact solution, for a field along the easy axis at $K_p=0$ the level splitting due to tunneling is independent of field up to the field of the spin-flop transition. In the presence of anisotropy in the basal plane, $K_p\neq 0$, the value of $\mathcal{A}_{\text{Eu}}(H)$ falls off with increasing field:

$$\mathcal{A}_{\text{Eu}}^{(\text{EA})}(H)=2s\hbar N\sqrt{\frac{K_u}{JZ}}\sqrt{1-\eta\frac{H^2}{H_{sf}^2}}, \tag{74}$$

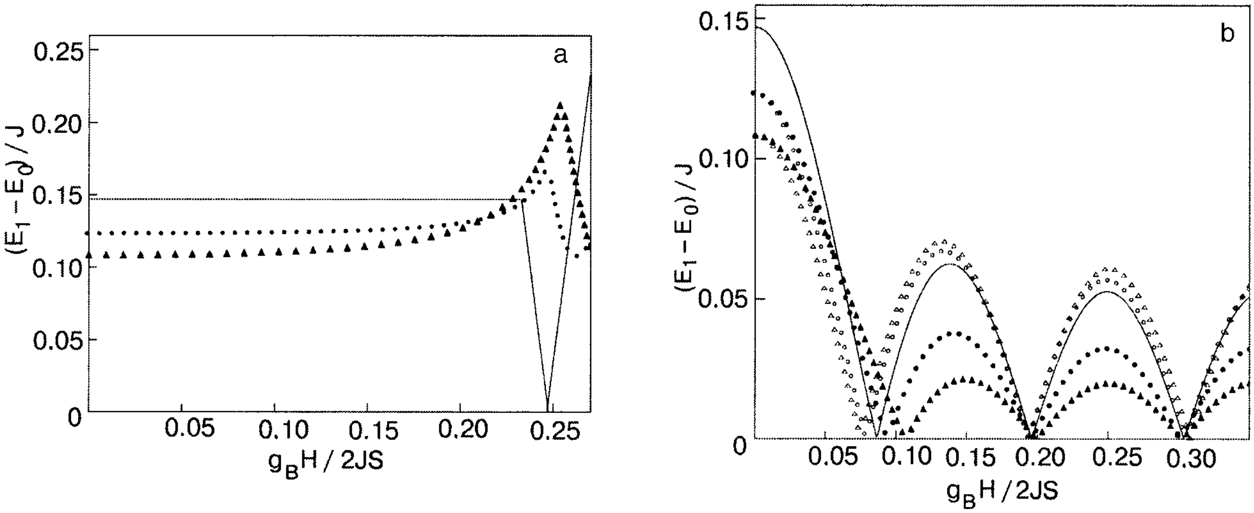

FIG. 9. Tunneling splitting of the lower level of an AFM described by the Hamiltonian (39) with spin $S=5$ and uniaxial anisotropy $K_u/J=0.1$, for three different values of the planar anisotropy: $K_p/K_u=0$ (–), 0.2 (●, ○), and 0.4 (▲,△). a—Field parallel to the easy axis; the kinks correspond to the spin-flop transition. b – Field parallel to the hard axis (○, △) and medium axis (●, ▲).

where the coefficient η is small at small K_p/K_u, $\eta \approx \pi(K_p/K_u)$; the value $\eta=1$ that is characteristic for the case when the influence of the field is taken into account in a "naive" manner is reached only in the limit $K_p/K_u \to \infty$ (see Fig. 8). Thus in a rhombic AFM for field parallel to the easy axis the tunneling level-splitting $\Delta(H)$ increases with increasing field, and this effect is more pronounced for larger values of K_p.

For field direction along the medium axis the situation is somewhat more complicated: there can be competition between different instantons. Here there exists a planar solution with a rotation of **l** in the (z,y) plane, containing the hard axis y. For this solution the value of the real part of $\mathcal{A}_{\rm Eu}$ is larger than in the case of the field along the hard axis (73), where **l** rotates in the easier plane (z,x), containing the medium axis x:

$$\mathcal{A}_{\rm Eu}^{(\rm MA,phanar)}(H)=2s\hbar N\sqrt{\frac{K_u+K_p}{JZ}}\pm i\,\frac{\pi\hbar g\mu_B HN}{2JZ}. \tag{75}$$

This value is also larger than for a planar instanton in the case $H=0$. The plane solution with rotation of **l** in the (z,x) plane for a field $H\neq 0$ parallel to the medium axis does not exist, and at nonzero field it is transformed to a nonplanar solution. For this nonplanar solution the Euclidean action is real, and its value $\mathcal{A}_{\rm Eu}^{(\rm MA,nonplanar)}(H)$ grows with increasing field, and the growth is substantially faster than for the "naive" way of taking the field into account (see Fig. 8). As a result, for a certain critical value H_c the value of the action for the nonplanar solution becomes equal to the value of the real part of the action for the planar solution (75), which is independent of field. At low anisotropy in the basal plane the value of H_c is substantially lower than the value of H_p (64):

$$H_c=H_p(2/\pi)^2(K_p/K_u)\ll H_p. \tag{76}$$

The value of H_c remains lower than H_p even in the limiting case $K_p/K_u\to\infty$, at which $H_c\to 0.616H_p$. Thus the nonplanar instantons govern the tunneling only at sufficiently low field $H<H_c$. For $H>H_c$ the tunneling is due to planar instantons and goes according to the scenario that is characteristic for the above-described case of the field parallel to the hard axis, with an oscillatory dependence of the level splitting on the field at an almost constant oscillation amplitude.

Calculations in the framework of the instanton approach are in good agreement with the results of a numerical analysis done by direct diagonalization of the Hamiltonian of a spin pair (see Fig. 9).[151] For field along the easy axis in the purely uniaxial case $K_p=0$ the energy difference $\Delta=E_1-E_0$ of the two lowest levels is independent of field up to the field of the spin-flop transition. For $K_p\neq 0$ the splitting increases with increasing field, and this effect is more pronounced for larger values of K_p/K_u. In the case of magnetic field parallel to the hard axis and also for a sufficiently large field $H>H_c$ directed along the medium axis, oscillations of the splitting with variation of the field are observed, with an amplitude that depends weakly on K_p.[51,153] If the field is parallel to the medium axis, then at low fields one observes decay of the splitting, which then gives way to oscillatory behavior, the characteristic value of the transition field increasing and the amplitude of the oscillations decreasing with increase of K_p/K_u. Granted, there is some quantitative disagreement. For example, a numerical analysis demonstrates that a characteristic field that can be interpreted as the field of the spin-flop transition exhibits dependence on the value of K_p/K_u. A slight falloff of the oscillation amplitude with increasing field is also observed for tunneling through planar instantons at a non-small value of the field H, when the pre-exponential factor should be independent of field.[51,153] These effects are absent in the semiclassical description and can be attributed to quantum fluctuations in a system with finite spin. A more detailed comparison of the numerical data for different values of the spin $S\leqslant 20$ with the calculations based on the instanton approach can be found in Ref. 151.

6.6. Influence of sublattice decompensation on the tunneling

Let us turn to the case of an uncompensated AFM, assuming the absence of external field and Dzyaloshinskii interaction. In the general case this problem is much more complicated for analysis than the exactly integrable case of a pure ferromagnet or the symmetric models of compensated AFMs discussed above when an external field or Dzyaloshinskii interaction is taken into account. However, there is a case in which the system is integrable; for anisotropy of the form (39), quadratic in the components of the vector **l**. The Euclidean version of the Lagrangian for this model is conveniently written in the form

$$\mathscr{L}_{\mathrm{Eu}}=\frac{\hbar^2 N}{2JZ}\left[\frac{1}{2}(\dot{\theta}^2+\dot{\varphi}^2\sin^2\theta)-i\omega_n\dot{\varphi}(1-\cos\theta)+\frac{1}{2}\sin^2\theta(\omega_u^2+\omega_p^2\sin^2\varphi)\right], \tag{77}$$

by introducing three parameters with dimensions of frequency. The parameter $\omega_n=\gamma H_{\mathrm{ex}}(S_{\mathrm{ex}}/S_{\mathrm{tot}})$, $S_{\mathrm{ex}}=|S_1-S_2|$ is the excess spin, and the quantities ω_p,ω_u determine the form of the energy of magnetic anisotropy with easy axis z and hard axis y [see Eq. (64)]. For constructing the instanton solution it is helpful to recall the form of the Walker solution in real time, which describes a moving domain wall (see, e.g., Refs. 12, 34, and 35). In this solution the magnetization is rotated in the plane $\varphi=\varphi_0=\mathrm{const}$, passing through the easy axis, and the value of φ_0 does not correspond to a plane of symmetry and is determined by the velocity of the wall. The instantons of Lagrangian (77) also have this property.[144] In that case the angle φ_0 is complex, $\varphi_0=\pi k/2+2i\alpha$, where k is an integer,

$$\cosh\alpha=\frac{\sqrt{4\omega_n^2\bar{\omega}^2+\omega_n^4+\omega_p^4}-\omega_n^2}{\omega_p^2},\quad \bar{\omega}^2=\omega_u^2+\frac{\omega_p^2}{2}. \tag{78}$$

For $\theta(\tau)$ one has the standard formula of the type (65), $\cos\theta=\tanh[\bar{\omega}(\varphi_0)\tau]$, with a real parameter $\bar{\omega}^2(\varphi_0)=\omega_u^2+\omega_p^2\sin^2\varphi_0$. Here one needs to consider only one pair of equivalent instantons, which have even $k=0,2$ and a lower value of the real part of the Euclidean action $\mathcal{A}_{\mathrm{Eu}}$. The imaginary parts of $\mathcal{A}_{\mathrm{Eu}}$ for instantons of this pair have different signs, and that gives an interference effect with the usual phase factor for ferromagnets, $|\cos\pi S_{\mathrm{ex}}|$.

A fundamental feature of uncompensated AFMs is the presence of nonanalyticity with respect to the parameter $\omega_n\sim S_{\mathrm{ex}}$. For a compensated AFM with $\omega_n=0$, equation (78) gives the real value $\varphi_0=\pi k/2$, and tunneling is possible even in a purely uniaxial model [see the exact solution (65)]. For $\omega_n\neq 0$ and $\omega_p=0$, solutions with finite $\mathcal{A}_{\mathrm{Eu}}$ do not exist, and for arbitrarily small decompensation it is necessary that there be anisotropy in the basal plane. This circumstance is clearly manifested in the nonanalytic dependence of the Euclidean action on the parameter ω_n/ω_p. In the most characteristic case $\omega_p,\omega_n\ll\bar{\omega}$ this dependence has the form

$$\mathrm{Re}\,\mathcal{A}_{\mathrm{Eu}}=\frac{\hbar^2 N}{2JZ}\left(2\bar{\omega}+\omega_n\ln\frac{\omega_n}{\omega_p}\right). \tag{79}$$

For $\omega_n\to 0$ this gives a finite value (70), and for $\omega_p/\omega_n\to 0$ a divergence of $\mathrm{Re}\,\mathcal{A}_{\mathrm{Eu}}$ appears, and tunneling is suppressed.

Analysis of the pre-exponential factor D in this problem reduces to a coupled system of equations for ϑ and $\delta\varphi$, i.e., the differential operator $\hat{\mathbf{A}}$ in (52) is not diagonal. The calculation showed that the fluctuation determinant is real and does not influence the interference, and its dependence on ω_n is nonanalytic: $D\propto 1/\sqrt{\omega_n}$.[144]

The question of the influence of external magnetic field on the coherent tunneling has been discussed repeatedly in connection with the problem of tunneling in ferritin particles.[154] For an AFM with decompensated spins a weak field completely lifts the degeneracy of the system, and these effects are thereby ruled out. In Sec. 4.2 however, in a discussion of the states of an AFM with uncompensated spins, it was noted that for sufficiently high fields it is possible to have ground-state degeneracy due to the noncollinearity of the sublattices. This leads to a new type of macroscopic tunneling effects when a freely oriented AFM particle with incomplete compensation of the spins is found in a strong external field.[85] In this case the height of the tunnel barrier and the phase factor depend substantially on the field strength, making it possible to control the tunneling probability by varying the field.

VII. NONUNIFORM STATES IN AFMs: STRUCTURE, TOPOLOGICAL ANALYSIS, AND QUANTUM TUNNELING EFFECTS

It is a common belief that mesoscopic magnets should be typical single-domain particles. However, it has recently been shown that even for extremely small particles of ferromagnets the distribution of the spins in the ground state can be nonuniform. For submicron particles of nonellipsoidal shape and sizes smaller than the critical, $R<R_c$ (for Permalloy $R_c\lesssim 100$ nm), certain specific weakly nonuniform magnetic states are realized: the so-called of "flower" or "leaf" states.[155] For $R>R_c$, topologically nontrivial[156,157] states with a magnetic vortex[158] appear which have recently been studied experimentally.[159] There is now a peak of interest in vortex states in magnetic dots[1,2] and magnetic rings[160] (see the recent papers[161–164] devoted to analysis of the dynamics of vortices in such systems).

The dipole interaction is important for FMs and negligible for AFMs, but it is not the only source of nonuniformities. Dimitrov and Wysin showed[165] that the surface single-ion anisotropy with local easy axis perpendicular to the surface of the sample at each point of the surface also leads to a nonuniform nontopological "flower" or "leaf" states. The origin of this nonuniformity is clear: in this case the conditions of minimum energy in the bulk (uniform state) and at the surface (the spin must be perpendicular to the surface) are contrary, i.e., frustration occurs. The strong surface anisotropy limit gives a geometric problem for the distribution of a unit vector perpendicular to the surface of the object at each point of the surface. The solution of this problem for any simply connected object has a singularity; such singularities actually arise for liquid crystals[166] and the A phase of superfluid ^{3}He.[167] Therefore the strong surface an-

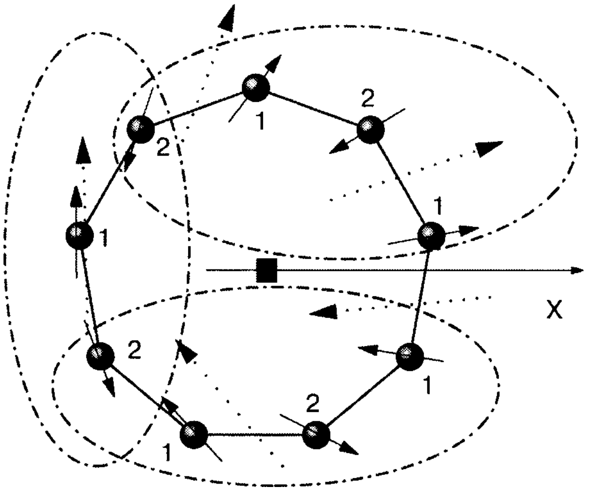

FIG. 10. Spin chain with 9 spins; the thin solid lines are exchange bonds. The solid arrows show the direction of the spins for the solution (80) with $m=1$; the dotted arrows show the direction of the vector **l** for the dimers. The regions of consistent numbering of the sublattices (the numbers 1 and 2 next to the spins) are enclosed by the dotted-and-dashed lines; on the polar (x) axis the consistency is disrupted, and the vector **l** has a jump.

isotropy can give rise to vortices of the magnetization in both FMs and AFMs.[168]

For AFMs specific nonuniform states can be caused by frustration of the exchange interaction. The concept of frustration is usually associated with spin glasses, but it is encountered for crystalline AFMs if the division of the lattice into a finite number of magnetic sublattices cannot satisfy the condition of antiparallel orientation of neighboring spins; an example is an AFM with the triangular lattice.[169] The division of the AFM into magnetic sublattices is sensitive to the presence of atomic dislocations of the crystal lattice, which disrupt the topology of the atoms planes. As was shown by Dzyaloshinskii[170] and also by Kovalev and Kosevich,[171] this gives rise to macroscopic magnetic defects—domain walls and disclinations; such defects have been observed in thin films of chromium.[172] For magnetic layered systems, atomic steps on the FM/AFM interface are also a source of formation of such defects.[173,174]

The appearance of disclinations in a crystal with dislocations can be explained by the circumstance that any contour drawn along the exchange bonds and encompassing the axis of the dislocation contains an odd number of sites. Therefore the problems of the ground state of an AFM with dislocations and of a closed spin chain with antiferromagnetic interaction and an odd number of sites have a number of traits in common. The latter model in the exchange approximation has an exact solution,[175] and it is helpful to discuss it before considering the disclination. For such an odd chain, all the spins lie in one plane, $\theta_k=\pi/2$, in which the direction of the kth spin $\boldsymbol{\sigma}_k$ is determined by the angle φ_k:

$$\varphi_k=\frac{\pi}{2}[1-(-1)^k]+m\frac{\pi k}{N}, \tag{80}$$

where $m=\pm 1,\pm 3,\ldots$ is an odd integer, and the minimum of the energy corresponds to $m=\pm 1$ (see Fig. 10). For an odd chain, as for a crystal with a dislocation, there is no possible division into sublattices that is consistent for the whole system. However, one can introduce sublattices and define the vector **l** locally in any region that does not contain the center of the dislocation. This is reminiscent of the procedure used in the theory of elasticity when introducing a strain field for describing a crystal with a dislocation.[176,177] The character of the behavior around the singular line can be illustrated by the example of a screw dislocation in a layered AFM of the $CoCl_2$ type, in which the exchange interaction of the spins in the planes is ferromagnetic and stronger than the antiferromagnetic interaction of neighboring planes.[178] The smallness of the latter makes it possible to describe a disclination consistently for vectors **m**, **l** in the framework of continuum theory.[179] Near the dislocation line the σ-model approximation breaks down, and $|\mathbf{m}|\sim|\mathbf{l}|$, and at the very center of the disclination $\mathbf{m}=1$ and $\mathbf{l}=0$. Recently a general macroscopic approach was proposed for the description of topological defects in layered AFMs.[180,181]

Thus a disclination in an AFM with a dislocation can be treated in the framework of the σ-model as a singular line of the field of the vector **l** (the direction of **l** is not defined on the line) with a jump of **l** at the surface, which rests on the dislocation line and extends to the boundary of the crystal. The distribution of the vector **l** in a rectilinear disclination sufficiently far from its central part (core), for $r\gg a$, is described by the formula

$$\theta\simeq\pi/2,\quad \varphi=(m/2)\chi+\varphi_0, \tag{81}$$

where r,χ are polar coordinates on the plane perpendicular to the disclination line. This formula, like that for the spin chain (80), contains the *odd* integer $m=\pm 1,\pm 3,\ldots$. The distribution (81) is also characteristic for the director vector **n** of a nematic liquid crystal with a disclination,[166] and the number m is called the Frank index. The same distribution arises for a disclination in the state of a spin nematic, which is realized for magnets with a strong biquadratic exchange interaction.[75] The simple distribution (81) is characteristic both for a purely isotropic medium and in the presence of planar anisotropy, say, for an AFM with an isotropic easy plane (x,y). In the latter case the polar axis for the vector **l** must be chosen along the hard axis z of the AFM. Formula (81) for large $r\gg r_0$ [see Eq. (83) below] is also valid for an antiferromagnetic vortex, but the value of the Frank index for it is *even*, $m=\pm 2,\pm 4\ldots$.[6,34,157]

For the description of the nonuniform states in an AFM and tunneling effects for them it is convenient to use the method of homotopic topology.[156] The possibility that singular lines of the disclination type, with nonuniformity far from the line, is due to the continuous degeneracy of the energy of the system with respect to a change of the order parameter in the *degeneracy space* $\mathcal{M}_D$ of the system. Let us consider the behavior of the order parameter (the vector **l** for an AFM or **n** for a nematic) in traversing a closed contour γ around the singular line in coordinate space. Here the order parameter describes a closed contour Γ in the degeneracy space $\mathcal{M}_D$. This contour is a map of the singular line from the standpoint of the behavior of the order parameter far from the line. Two contours Γ_1 and Γ_2 are called *homotopic* if they can be transformed into each other by a continuous deformation. The classes of all homotopic contours for a given space $\mathcal{M}_D$ form a group called the *fundamental homotopy group* of this space and is denoted $\pi_1(\mathcal{M}_D)$. The product of Γ_2 and Γ_1

corresponds to a contour $\Gamma_2\cdot\Gamma_1$ obtained in traversing first Γ_1 and then Γ_2. A contour that can be continuously deformed into an infinitely small one (or, as we say, "contracted to a point") corresponds to the unit element of the group. The element of $\pi_1(\mathcal{M}_D)$ that is the inverse of Γ corresponds to a contour Γ^{-1} with the opposite direction of traversal.

Thus from the standpoint of the behavior at infinity, the singular lines of the order parameter are classified by group elements of the fundamental homotopy group of the degeneracy space $\mathcal{M}_D$ of the system, $\pi_1(\mathcal{M}_D)$, which are called *topological charges*. Removable singularities correspond to the unit element of the group. When singular lines merge, a kind of conservation law for topological charge is obeyed. When lines corresponding to the contours Γ and Γ^{-1} merge, they give a removable singularity. The mergine of singular lines with charges Γ_1 and Γ_2 give a line with a charge equal to the product of the elements $\Gamma_1\cdot\Gamma_2$. We note that the fundamental homotopy group can be non-Abelian, but we shall not consider examples of that kind.

It is important to note that the classification of singular lines according to elements of the group $\pi_1(\mathcal{M}_D)$ can be incomplete; singular lines that are equivalent in the sense of $\pi_1(\mathcal{M}_D)$ cannot *always* be transformed into each other by a continuous deformation of the field of a vector $\mathbf{l}^2=1$. For a complete description of the singular lines in magnets one must also take other topological charges into account. We discuss this question below; right now let us turn to the classification of vortices or disclinations according the topological charges of the group $\pi_1(\mathcal{M}_D)$.

In the description of spin disclinations in an AFM their similarity to disclinations in nematics is usually emphasized. This similarity is undoubtedly productive for the topological classification of disclinations. However, there are essential differences in the properties of disclinations for these ordered media. The point is that for the same nematic sample the Frank index m in the distribution (81) takes on any, even or odd, integer values, $m=0,\pm 1,\pm 2...$; $m=0$ corresponds to a uniform distribution. For an AFM the parity of the Frank index m is wholly determined by the atomic structure of the sample, which may be assumed to remain unchanged in the course of any changes in the spin structure. For AFMs with a dislocation only odd values of m are admissible in formula (81), while for an AFM with an ideal topology of the atomic planes either a uniform distribution with $m=0$ or a vortex with even $m=2q$ is possible.

In a purely isotropic magnet or a nematic, the state is degenerate with respect to changes of the unit vector on the sphere $\mathbb{S}^2\{\mathbf{l}^2=1\}$. Any geometrically closed contour on the sphere can be contracted to a point, and the fundamental homotopy group of the sphere $\pi_1(\mathbb{S}^2)$ consists of only the unit element. Therefore no topologically nontrivial singular lines for an order parameter of the spin $\boldsymbol{\sigma}$ type exist in a ferromagnet.

However, for the description of a nematic it is important that the states with $\mathbf{n}$ and $-\mathbf{n}$ are physically indistinguishable; $\mathbf{n}$ is not a physical unit vector of the spin $\boldsymbol{\sigma}$ type but a director vector with an indeterminate sign, as is emphasized by its name. Therefore, for a nematic the degeneracy space is additionally factorized by the sign of $\mathbf{n}$, and that is indicated in writing as $\mathcal{M}_D=\mathbb{S}^2/\mathbb{Z}_2$. Here $\mathbb{Z}_2$ is a group of two elements, 0 and 1, $1\oplus 1=0$. This condition means that any contour on the sphere which connects points $\mathbf{n}$ and $-\mathbf{n}$ can be assumed closed physically. All such contours can be deformed into one another, but cannot be contracted to a point; they correspond to a nontrivial element of the group π_1, while all the geometrically closed contours correspond to the unit element of this group. Consequently, the homotopy group $\pi_1(\mathbb{S}^2/\mathbb{Z}_2)$ consists of two elements and is equivalent to that group $\mathbb{Z}_2$ described above. For an isotropic nematic all the disclinations with odd Frank indices m can be transformed into energetically more favorable ones with $m=\pm 1$, and the latter are topologically equivalent, while all the disclinations with even Frank indices are topologically removable. In an isotropic nematic, disclinations with $m=2k$ can be brought to the ground state (formally the state with $m=0$) by a nonplanar deformation, which is descriptively called "escaping into the third dimension."[156]

The state of a planar nematic in which $\mathbf{n}$ lies in the plane of the sample is degenerate with respect to a change of $\mathbf{n}$ along a circle, or the one-dimensional sphere $\mathbb{S}^1\{l_x^2+l_y^2=1, l_z=0\}$, with allowance for the factorization of the degeneracy space $\mathcal{M}_D=\mathbb{S}^1/\mathbb{Z}_2$. In this case all of the different values of m correspond to topologically different states of the disclination of the nematic, and m plays the role of a π_1-topological charge belonging to the group of integers with respect to summation $\mathbb{Z}$.

It is now understood what will happen in the case of an AFM. For an AFM with a dislocation only those singular lines such that the vector $\mathbf{l}$ changes sign on going around them are allowed. This means that in that case there are only disclinations with odd values of m. The minimum of the energy of an isotropic AFM corresponds two disclinations with $m=+1$ and $m=-1$, illustrated in Fig. 11a. They can be transformed into each other by a rotation in spin space about the x axis, which corresponds to a departure of $\mathbf{l}$ from the plane and is a typical example of "escaping into the third dimension." Thus for an isotropic AFM with a dislocation there is a nonuniform ground state, which cannot be characterized by any sort of discrete degeneracy. For an isotropic AFM without a dislocation only even m are allowed, and the ground state corresponds to a uniform distribution of $\mathbf{l}$ with $m=0$.

For an easy-plane AFM with an isotropic easy plane (x,y) in the presence of a dislocation the minimum of energy also corresponds to two disclinations with $m=\pm 1$, which, unlike the isotropic case, are topologically different. In this case the ground state is twofold degenerate, and macroscopic quantum tunneling effects are possible (see below). In the easy-plane AFM without a dislocation the only admissible distributions are of the form (81) with *even* value of the Frank index $m=2q$; these correspond to an antiferromagnetic vortex. The integer $q=m/2$, $q=\pm 1,\pm 2,\ldots$ is called the *vorticity*. In other words, the vorticity is the π_1-topological charge of the vortex, which belongs to the group of integers $\mathbb{Z}$. One can write an expression for it in terms of an integral over a closed contour γ:

$$q=\frac{1}{2\pi}\oint_\gamma(\mathbf{e}_z\cdot[\mathbf{l}\times\nabla_\alpha\mathbf{l}])dx_\alpha=\frac{1}{2\pi}\int_0^{2\pi}\frac{\partial\varphi}{\partial\chi}d\chi. \qquad (82)$$

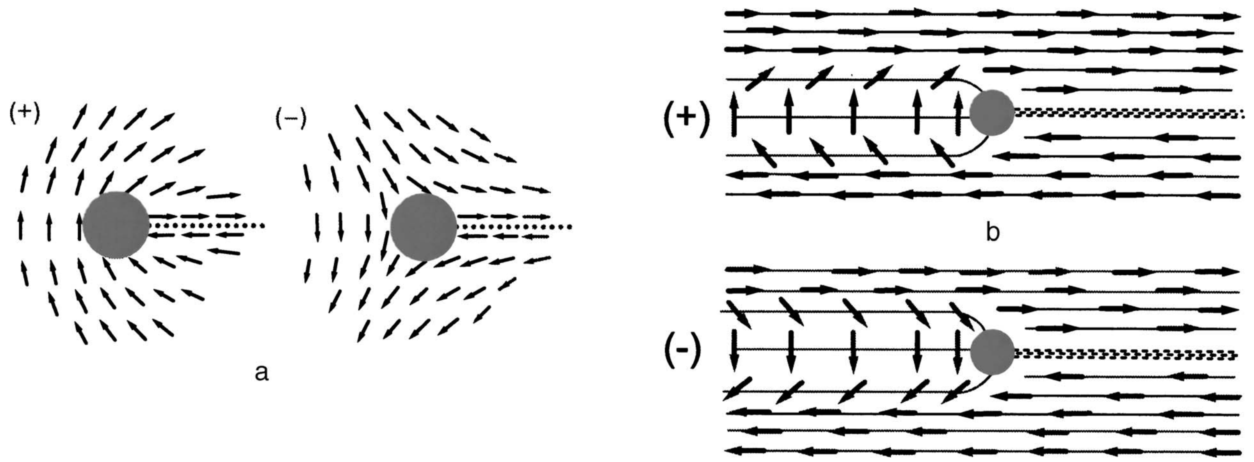

FIG. 11. Distribution of the vector **l** in an antiferromagnetic disclination associated with an atomic dislocation and the domain wall generated by the disclination; disclinations with values of the Frank index $m=1$ and -1 and the associated DWs with different chiralities are labeled by $(+)$ and $(-)$ in parts a and b. a—exchange approximation; short distances. The line of dots shows a line of formal discontinuity of the vector **l**; the shaded area shows the central part, of the order of atomic size, in which the vector **l** cannot be uniquely introduced. b—The influence of anisotropy at distances greater than the width of the wall; the shaded region shows a central part corresponding approximately to the "exchange" region, where the distribution of **l** is as shown in part a.

Far from the vortex one has $\theta=\pi/2$, but at the center of the vortex, unlike a disclination, there is no singularity. This is possible when **l** is collinear with the unit vector along the hard axis, $\mathbf{e}_z$, i.e., $\theta=0,\pi$. Thus at a given vorticity q we have two different states of the vortex, the structures of which are described by the solutions

$$\varphi=q\chi+\varphi_0,\quad \theta=\theta_0^{(\pm)}(r),\quad \cos\theta_0^{\pm}(0)=p=\pm 1. \tag{83}$$

The functions $\theta^{(\pm)}(r)$ differ from $\pi/2$ in a vortex-core region of diameter r_0, which, for a slightly anisotropic AFM, has the value $r_0=a(J/K_u)^{1/2}\gg a$. The two distributions of **l** with the same values of the π_1 topological charge q can differ by the values of the other topological invariant, the so-called π_2 topological charge, which corresponds to mapping not to contours but to two-dimensional manifolds. In the case of a 2D magnet we are talking about a mapping of the (x,y) plane onto the sphere $\mathbb{S}^2\{\mathbf{l}^2=1\}$. This charge is determined by the integral topological invariant Q introduced above [Eq. (42)] with the substitution $t\rightarrow y$. For a vortex the value of Q is half-integer, $Q=-qp/2$, where $p=\pm 1$ determines the sign of l_z in the core of the vortex (83). Vortex states with $Q=\pm 1/2$ differ topologically and cannot be transformed into each other by a continuous deformation. Consequently, the vortex is characterized by two topological charges: the π_1 charge—the vorticity q—and the p_2 charge, the *polarization* $p=\pm 1$. This is manifested in the analysis of the merging of two vortices with vorticities q and $-q$: if the polarizations of the vortices are different, one obtains a localized (trivial from the standpoint of π_1) soliton with an integer value of the π_2 topological charge $Q=\pm q$, while if the polarizations are of the same sign p, one obtains a topologically trivial state.

Let us study the transformation of the structure of vortices and disclinations in the presence of weak anisotropy in the easy plane (x,y). Let us consider a rhombic AFM with anisotropy energy of the form (39), assuming that $K_u<0$ and $K_p>0$, i.e., z is the hard axis and x is the easy axis in the easy plane. When the anisotropy in the basal plane is taken into account, the distribution of the vector **l** will no longer have the simple form (81) or (83). For regions found far enough away from the core of the disclination, a domain wall (DW) is formed; see Fig. 11b. The static two-dimensional DW corresponds to the solution $\mathbf{l}=\mathbf{l}_0(x)$ with a rotation of the vector **l** in the easy plane (x,y):

$$l_x=\varsigma_0\tanh(x/x_0),\quad l_y=\frac{\varsigma}{\cosh(x/x_0)},\quad l_z=0, \tag{84}$$

where $x_0\simeq(J/K_p)^{1/2}a\gg a$ is the DW thickness, and the numbers $\varsigma_0,\varsigma=\pm 1$. The value of ς_0 determines the values of l_x at two points far from the center of the DW. These two points can be called a zero-dimensional sphere, by virtue of which the value of σ_0 has the meaning of the π_0 topological charge of the DW. The change of ς_0 is due to the overcoming of a potential barrier proportional to the size of the system (formally, an infinite barrier), and tunneling cannot occur. The second topological charge of the type π_1 is due to the mapping of the line perpendicular to the DW onto the circle $\{l_x^2+l_y^2=1,\ l_z=0\}$. This charge q is defined by the integral (82) in which $\oint_\gamma dx_\alpha$ is replaced by $\int_{-\infty}^{\infty}dx$; for a DW it has the value $q=-\varsigma_0\varsigma/2$. Consequently, the DW *chirality* $\zeta=\pm 1$, which at fixed ζ_0 determines the direction of rotation of **l** in going along the chain, is the π_1 topological charge of the DW. On different sides of a vortex with $q=\pm 1$, two such walls, with different signs of the chirality, appear. Such DWs with a vortex are observed in thin films of ferromagnets and are called walls with a vertical Bloch line.[6,182]

Tunneling effects presuppose the presence of several different but energetically equivalent states of the system separated by a finite potential barrier. For topological nonuniformities the question arises of tunneling-induced change of the signs of the topological charges. A change of the "main" charge such as the vorticity q for a vortex in an infinite system involves the overcoming of an infinite barrier. In that case tunneling-induced change of "auxiliary" topological charges—the chirality for a DW or the polarization for a vortex—is possible. In small particles tunneling of a "main" charge such as the Frank index for a disclination is also possible. The problems of the tunneling-induced change of the chirality of a DW and tunneling of the topological charge

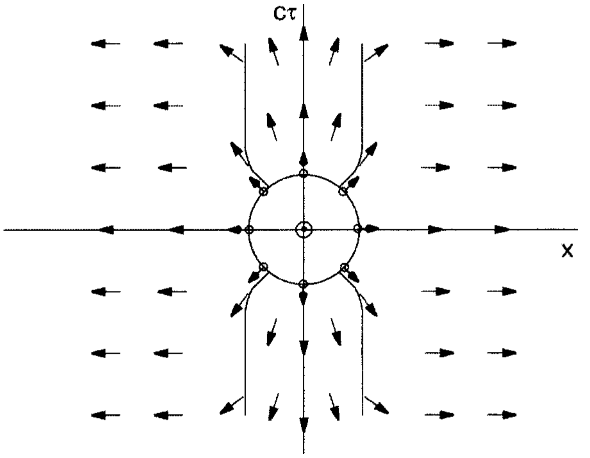

FIG. 12. Structure of the instanton describing the tunneling transition between states of the DW with opposite chiralities (the top and bottom in the figure). The thick arrows denote the projection of the vector **l** on the easy plane; the solid lines denote the curves on which **l** makes a 45° angle to the hard axis (it is perpendicular to the plane of the figure). These lines show the DW boundaries and also the core region at the center of the vortex, which is characteristic for an out-of-plane magnetic vortex. The vortex shown has polarization $p=1$, i.e., the direction of $\mathbf{l}(0,0)$ is upward.

of a disclination in an easy-plane AFM are extremely similar, and it is convenient to discuss them together.

We begin with an analysis of the tunneling of chirality for a DW of the form (84) in quasi-one-dimensional AFMs of the spin-chain type or systems of coupled spin chains forming a mesoscopic wire or ribbon.[124] For the description of the tunneling dynamics we use the Lagrangian (40) for a nonuniform distribution of the vector **l** [more precisely, its Euclidean version for $\mathbf{l}=\mathbf{l}(x,\tau)$] with the topological term (42) and anisotropy (39) included. The state of the wall (84) is degenerate with respect to the value of the DW chirality, and a tunneling transition between the two DW states with $\zeta=\pm 1$ can occur. For its description we must construct the two-dimensional instanton solution of the equations for $\mathbf{l}=\mathbf{l}(x,\tau)$. Its solution should give $\mathbf{l}\rightarrow\pm\mathbf{e}_x$ for $x\rightarrow\pm\infty$, and go over to two DWs with different chiralities for $\tau\rightarrow\pm\infty$. These conditions lead to the situation that in going along the boundary of a sufficiently large large part of the Euclidean plane (x,τ) (see Fig. 12), the vector **l** rotates by an angle $2\pi q=\pm 2\pi$ in the easier plane (x,y) of the AFM. In this case, for continuity of the solution it is necessary that at some point the vector **l** be perpendicular to the easy plane. That point is naturally called the center of the instanton and placed at the origin of coordinates in the Euclidean plane, $x=0$, $\tau=0$, and at it $l_z(0,0)=\pm 1$. Thus the instanton configuration has the properties of an out-of-plane magnetic vortex for which the vorticity $q=1$ and the polarization $p=\pm 1$ (see Fig. 12). Thus for tunneling of the DW chirality there are two equivalent instanton paths having different signs of the polarization $l_z(0,0)\equiv\cos\theta(0,0)=p=\pm 1$.

The instanton corresponds to the separatrix solution of a partial differential equation with a finite value of the Euclidean action (43). It is by no means always possible to construct even one-dimensional instanton solutions. However, a sufficiently complete analysis of the problem can be carried out on the basis of the formal similarity between the two-dimensional instanton of interest to us, with $\mathbf{l}=\mathbf{l}(x,\tau)$, and a soliton of the vortex type, or, more precisely, its anisotropic analog—a vertical Bloch line in a two-dimensional DW, for which $\mathbf{l}=\mathbf{l}(x,y)$.[6,182] Often the similarity of instantons and the static nonuniformities is extremely constructive and permits one to predict the character of the behavior of **l** in non-one-dimensional instantons and to estimate the tunneling amplitude.

An example is the simple case of non-one-dimensional instantons in an AFM with $\mathbf{H}^{\mathrm{eff}}=0$. In this case the vector **l** in the solution will be real. For a $D+1$-dimensional instanton describing tunneling for a D-dimensional nonuniform distribution $\mathbf{l}(\mathbf{x})$ the problem of finding the real part of the Euclidean action $\mathrm{Re}\,\mathcal{A}_{\mathrm{Eu}}=\hbar\mathcal{W}[\mathbf{l}]$ reduces to minimization of the real dimensionless functional $\mathcal{W}[\mathbf{l}]$:

$$\mathcal{W}[\mathbf{l}]=\int\frac{dx^{D+1}}{a^D\hbar}\left[\frac{1}{2}Ja^2s^2(\nabla\mathbf{l})^2+W(\mathbf{l})\right], \tag{85}$$

where $dx^{D+1}=dx^D d\tau,\nabla$ denotes the gradient operator in the $D+1$-dimensional Euclidean space $(\mathbf{x},x_0)$, $x_0=c\tau$, and the function $\mathcal{W}(\mathbf{l})$ is given by the same expression as the usual static energy per spin for a magnet (37). The imaginary part of the Euclidean action for real **l** can only be due to the topological term and is manifested only for $D=1$.

It is important no note that in the FM case such a situation does not arise: instanton solutions are *never* real, and the analysis of non-one-dimensional instantons in a ferromagnet is much more complicated. The problem of tunneling of the DW chirality in a ferromagnet has been discussed by many authors.[63,183–187] It differs from the AFM case not only in that the corresponding instanton solution $\boldsymbol{\sigma}=\boldsymbol{\sigma}(x,\tau)$ is complex. It is also important that the DW chirality in a ferromagnet is directly related to the DW momentum. For example, nonmoving DWs with different values of the chirality have different values of the momentum (see the discussion of this unusual property in Ref. 69). Therefore, for a free (with no pinning) DW in a ferromagnet, the momentum of the DW is conserved, and tunneling of the chirality is altogether impossible.[186]

Now let us return to the AFM case. The construction of a two-dimensional vortex instanton solution describing the tunneling of chirality in a DW can be done by minimization of the functional (85), which upon the substitution $x\rightarrow x$, $c\tau\rightarrow y$ corresponds formally to the well-studied energy of a vertical Bloch line in a two-dimensional DW on the (x,y) plane for a ferromagnet with rhombic anisotropy.[6,182] The value of the instanton action can easily be found by analogy with the energy of this state. In the limiting cases of weak and strong basal-plane anisotropy of $\mathcal{W}[\mathbf{l}]$, an estimate for the instanton solution $\mathcal{W}[\mathbf{l}_0]\equiv\mathcal{W}_0$ is given by the formula[124,188]

$$\mathcal{W}_0=s\cdot\begin{cases}2\pi\ln(2.2\sqrt{\rho}), & \rho\gg 1,\\ 8\rho^{1/2}, & \rho\ll 1,\end{cases} \tag{86}$$

where we have introduced the rhombicity parameter $\rho=K_p/K_u$. The limiting case of small rhombicity $\rho\ll 1$ can be investigated in the effective one-dimensional instanton approximation.[188] We emphasize that, although the tunneling process involves a macroscopically large number of spins, $N_0=x_0/a\gg 1$, this number does not appear in the tunneling exponent. In the case $\rho\ll 1$ the value of the tunneling expo-

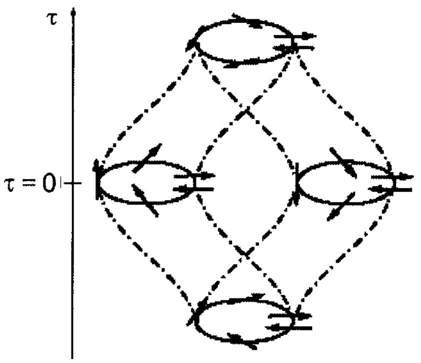

FIG. 13. Structure of two instanton paths determining the tunneling transition between states of a disclination with opposite values of the Frank index. These two paths have the opposite signs of the topological invariant Q and of the imaginary part of the Euclidean action.

nent for one spin chain $S\sim 1$ is small, and the dynamics of the internal degrees of freedom of the domain wall is not semiclassical but essentially quantum.[123,189] For $\rho\ll 1$, one can speak of macroscopic tunneling, which requires satisfaction of the condition $\mathcal{W}_0\gg 1$, only for a mesoscopic sample containing a large number of chains. In the case of strong rhombic anisotropy the tunneling of the chirality is semiclassical even for a DW in a quasi-one-dimensional AFM.[124]

For a two-dimensional instanton of the vortex type there is also an imaginary part of the Euclidean action, which is determined by the topological term (42) in the latter. For the two instanton paths $\operatorname{Im}\mathcal{A}_{\mathrm{Eu}}=2\pi sQ=s\pi qp$, which for $p=\pm 1$ gives $\operatorname{Im}\mathcal{A}_{\mathrm{Eu}}=\pm\pi s$. For half-integer spin of an atom of the chain the interference of these two instanton paths leads to suppression of tunneling. This can be explained by the fact that a DW in an antiferromagnetic spin chain has a spin equal to the value of the atomic spin s.[123,189,190] For a sample consisting of several coupled chains with half-integer spin, tunneling is forbidden for an odd number n of such chains.

The behavior of the imaginary part of the instanton action and the overall picture of the tunneling in an AFM is fundamentally altered in the presence of even a weak external magnetic field **H**. The magnetic field gives an additional contribution to the imaginary part of the Euclidean action, and the value of the tunneling splitting is an oscillatory function of magnetic field.[124]

Let us consider the change of the Frank index of a disclination as a result of tunneling in a small 2D AFM particle of radius R (an island of a quasi-monoatomic film).[30,191] For simplicity we shall assume that $\rho=K_p/K_u\sim 1$ and $x_0\sim r_0$. For a small parameter $R\ll x_0$ a DW does not form, and there is a smooth distribution of spins of the type $\varphi=\pm\chi/2$. In this case there are also two instanton paths, the structure of which is illustrated in Fig. 13. An estimate of the exponential factor gives

$$W_0^{(\mathrm{part})}=\pi s(R^2/ax_0). \tag{87}$$

This value is much smaller than the total number of spins in the particle, $N^{(\mathrm{part})}=\pi(R/a)^2$. For a disclination in a particle of size R the factor $W_0^{(\mathrm{part})}$ increases with increasing R up to the value $R\sim x_0\sim r_0$ at which a DW forms. For $R\gg x_0$ tunneling occurs within a DW, and the factor in the exponent, $\mathcal{W}^{(DW)}=(R/a)W_0$, where W_0 is given by formula (86), increases linearly as a function of the DW length R. For two different paths the imaginary part of the Euclidean action is determined by the topological term (42); it is equal to $\pm\pi sN^{(\mathrm{chain})}$, where $N^{(\mathrm{chain})}$ is the number of atomic chains that enclose the center of the disclination. For AFM displacements with half-integer spin s and an odd number of chains, tunneling is suppressed in the absence of magnetic field. This result can be explained by starting from Kramers' theorem and noticing that the total number of spins in a sample with an odd number of chains and an odd number of atoms in a chain is necessarily odd.

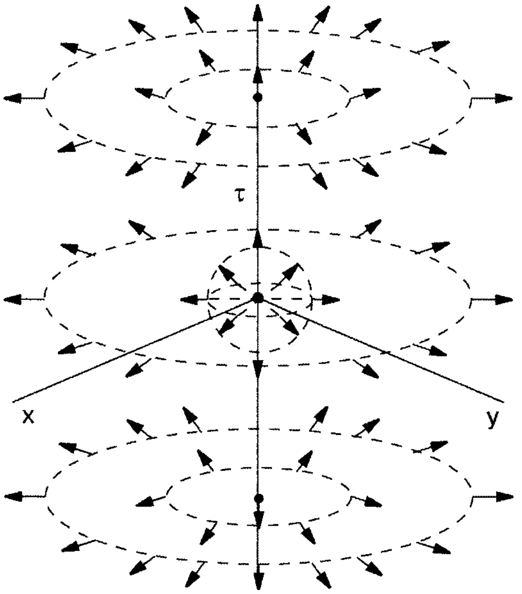

FIG. 14. Structure of the instanton determining the tunneling transition between states of a magnetic vortex with opposite polarizations. The sphere around the origin of coordinates, on which a singular structure of the "hedgehog" type is shown, represents the region where the description of the AFM in terms of a unit vector **l** is impossible.

For vortices in two-dimensional AFMs there arises the question of whether tunneling can affect the π_2 topological charge of the vortex: the polarization p.[192] The vortex core region of diameter $r_0\gg a$ (a is the interatomic distance) contains a large [of the order of $(r_0/a)^2\sim J/K_u$] number of spins, the direction of which changes in the quantum transition between vortex states with $p=+1$ and -1. The corresponding three-dimensional instanton solution $\mathbf{l}=\mathbf{l}(x,y,\tau)$ is real; it inevitably contains a singular point of the hedgehog type at the center of the instanton (see Fig. 14). Analysis of the behavior of the AFM near this singularity must go beyond the framework of the standard σ-model. It can be done qualitatively in the same way as for a Bloch point in a ferromagnet.[182] Estimates shown that the main contribution to the Euclidean action is given not by the singularity but by a peripheral region with size of the order of that of the vortex core, r_0. The value of the factor in the tunneling exponent is obtained[192] in the form $\mathcal{W}_0^{(\mathrm{vort})}\sim(r_0/a)$. As in the case of tunneling in a DW, this value is smaller than the number of spins taking part in the process, $N^{(\mathrm{vort})}\sim s(r_0/a)^2\sim J/K_u$, but it nevertheless contains the large factor $r_0/a\sim(J/K_u)^{1/2}$. Therefore, tunneling of the vortex polarization is possible in a quasi-two-dimensional AFM with sufficiently large anisotropy. It is important to emphasize that the vortex structure and, consequently, the value of $W_0^{(\mathrm{vort})}$ is determined solely by the parameters of the AFM, and for an ensemble of vortices (as for high-spin molecules) there is no spread of the parameters characterizing the tunneling.

VIII. CONCLUSION

When an article is finished, one can better see what questions, for objective or subjective reasons, have been discussed in less than adequate detail or left out completely.

Let us list the questions that have been left out of this review but which would benefit from a brief discussion in order to get a better idea of the range of problems that we have discussed. In this review we have discussed both purely classical aspects of AFM physics and problems of quantum tunneling for small particles or clusters of AFMs. In the latter case it turned out that quantum tunneling effects in essence violate the initial premise of the "classical" part of this review. Indeed, the classical description is based on the Neél picture of an AFM, which includes the concepts of magnetic sublattices and, consequently, the existence of an antiferromagnetic vector $\mathbf{l}$. On the other hand, tunneling in an AFM essentially amounts to a change in the sign of $\mathbf{l}$ as a result of tunneling, i.e., destruction of the Néel order. For small AFM particles the intensity of these effects is proportional to the number of spins in the system, while tunneling is possible only for extremely small samples.

One of the important results in AFM physics in the twentieth century is the establishment of the fact that non-small quantum fluctuations can break the Néel order even in infinite systems, in particular, in quasi-one-dimensional AFMs. An example is the spin chain and spin ladders with two or more legs. This striking and significant area of AFM physics is often called "quantum magnetism." The author certainly had not planned any detailed discussion of this topic in this review. However, it is useful to at least outline the range of topics and to cite references to the main publications. Furthermore, since we have used models of the spin-ladder type in this review, it is necessary to discuss at least briefly the degree to which the classical approach is applicable to the description of these materials, which are commonly associated with the quantum theory of AFMs.

Effects of non-small quantum fluctuations involving the destruction of Néel order were first revealed in the analysis of the exact solution of the quantum problem of the states of an isotropic spin chain with spin $S=1/2$, constructed by Bethe in 1931[193] and then generalized by Baxter for a chain with the same spin $S=1/2$ but with an anisotropic nearest-neighbor interaction.[194] For $S=1/2$ chains there is no Néel order even at zero temperature, and the correlators $\mathcal{F}(x) \equiv \langle \mathbf{l}(0)\mathbf{l}(x)\rangle$ fall off in a power-law manner with increasing distance x between spins. Such a state is customarily called a critical state or a state with quasi-long-range order. (It cannot be called purely disordered, since that would require that the correlators have exponential behavior, $\hat{F}(x) \propto \exp(-x/\lambda)$, where λ is the correlation length.) Quasi-long-range order is also characteristic for the Berezinskii phase, which exists in two-dimensional easy-plane magnets at nonzero temperature $T<T_{BKT}$, where T_{BKT} is the Berezinskii–Kosterlitz–Thouless transition temperature.[195,196] The Bethe method does not admit generalization to systems with large spin, and for a long time it remained unclear to what extent this result is applicable for AFMs with $S=1/2$. At first glance it can be shown that for large spins or systems of the spin-ladder type the quantum effects should be weaker, but reality turned out to be much more interesting. Haldane showed that for $S=1$ and all integer spins the long-range order is completely destroyed, the correlators fall off exponentially, and the spectrum of excitations contains a finite gap (the so-called Haldane gap $\Delta \sim \hbar c/\lambda$).[114,115] Zvyagin obtained a similar result for an exactly solvable model of coupled spins chains (in modern parlance, a spin ladder) with spin $S=1/2$: the long-range order is destroyed for an even number of chains.[197] In the case of half-integer spin, for a chain or an odd number of coupled chains with spin $S=1/2$ there is quasi-long-range order with a gapless dispersion relation. These results for spin ladders have been confirmed by other methods,[102,199–201] including direct numerical simulation.[198] For this review it is important that such results can be obtained on the basis of the σ-model both for a spin chain[113,202,203] and for a spin ladder.[200,201] The analysis scheme here is essentially the same as that used for describing quantum tunneling in AFM particles (see Sec. 6). The Néel state and the σ-model for a 1D AFM are taken as starting points of the analysis, and then the quantum fluctuations in this state are investigated. The consistent incorporation of fluctuations, including non-small ones, "rectifies" the problem that coherent states are not exact quantum states of the AFM Hamiltonian. The destruction of the long-range order in this approach can be described on the basis of the instanton formalism. The corresponding instantons are determined by two-dimensional solutions of the type discussed in Sec. 7 for the problem of nonuniform tunneling. A remarkable property of these effects is that the difference of integer and half-integer spins enters the problem through the phenomenon of interference of instanton paths, and the imaginary part of the Euclidean action is determined by the topological term (42) (see the review by Affleck[116] for more details).

This brief discussion shows that not only is the use of the classical σ-model consistent with the presence of non-small quantum fluctuations, it is actually the most universal and convenient formalism for investigating them. Simple intuitive arguments about the possible instanton paths and estimates of the Euclidean action for them make it possible to understand directly the role of the quantum destruction of the Néel long-range order. In particular, it is quite difficult to picture the three-dimensional $\mathbf{l}=\mathbf{l}(x,y,\tau)$ instanton of this type and the realization of similar effects in the 2D case. The instanton approach also lets one draw conclusions about the exponential suppression of tunneling effects for non-small spins, the Haldane gap $\Delta \propto \exp(-2\pi S)$. Recent numerical simulations have established that even for spin $S=2$, which is next to the minimum Haldane spin $S=1$, a disordered phase with a finite gap exists only for extremely small anisotropy and is suppressed by a weak magnetic field.[204] Therefore it can be expected that the application of the classical version of the σ-model to two-dimensional magnets of the manganese halide type ($S=5/2$) or even to spin ladders with ions of this type in connection with the spin-flop transition in Sec. 4 is entirely adequate.

The spin order in materials with an antiferromagnetic interaction is not limited to the simplest Neél structure. The author's only regret is that it was not possible to discuss the nematic phases of non-Heisenberg magnets, frustrated AFMs or AFMs with noncollinear spin order, especially since such spin structures are known not only for crystalline AFMs but also for the unique magnetic molecules $\{\mathrm{Mo}_{70}\mathrm{Fe}_{30}\}$.[57] However, the author hopes that this review, in which a wide class of problems, both static and dynamic, classical and quantum, are discussed from a unified point of view for the simplest two-sublattice AFMs will be useful to the reader.

This review could never have been written without the collaboration of many colleagues and discussions with them of the questions addressed in it. In closing I express deep gratitude to V. G. Bar'yakhtar, V. E. Kireev, A. K. Kolezhuk, A. M. Kosevich, A. S. Kovalev, N. E. Kulagin, and C. E. Zaspel for fruitful collaboration and helpful discussions. I am also indebted to E. G. Galkina for a long collaboration and invaluable assistance on this review article.

[*] E-mail: bivanov@i.com.ua

---

[1] W. Wernsdorfer, Adv. Chem. Phys. **118**, 99 (2001).
[2] R. Skomski, J. Phys.: Condens. Matter **15**, R841 (2003).
[3] A. S. Borovik-Romanov, *Antiferromagnetism* [in Russian], Vol. 4 of Itogi Nauki, Fiz.-Mat. Nauki, Ya. G. Dorfman, ed., Izd-vo AN SSSR, Moscow (1962).
[4] E. A. Turov, *Physical Properties of Magnetically Ordered Crystals*, Academic Press, New York (1965), Izd-vo AN SSSR, Moscow (1963).
[5] K. P. Belov, A. K. Zvezdin, A. M. Kadomtseva, and R. Z. Levitin, *Orientational Transitions in Rare-Earth Magnets* [in Russian], Nauka, Moscow (1979).
[6] V. G. Baryakhtar, M. V. Chetkin, B. A. Ivanov, and S. N. Gadetskii, *Dynamics of Topological Magnetic Solitons. Experiment and Theory*, Vol. 139 of Springer Tracts in Modern Physics, Springer-Verlag, Berlin (1994).
[7] A. G. Gurevich, *Magnetic Resonance in Ferrites and Antiferromagnets* [in Russian], Nauka, Moscow (1973); A. G. Gurevich and G. A. Melkov, *Magnetic Oscillations and Waves*, CRC Press, Boca Raton, Florida (1996), Nauka, Moscow (1994).
[8] V. V. Eremenko, N. F. Kharchenko, Yu. G. Litvinenko, and V. M. Naumenko, *Magneto-Optics and Spectroscopy of Antiferromagnets*, Springer-Verlag, New York (1992), Naukova Dumka, Kiev (1989).
[9] E. A. Turov, A. V. Kolchanov, V. V. Men'shenin, I. F. Mirsaev, and V. V. Nikolaev, *Symmetry and the Physical Properties of Antiferromagnets* [in Russian], Fizmatlit, Moscow (2001).
[10] S. V. Vonsovskiĭ, *Magnetism*, Vols. 1 and 2, Wiley, New York (1974), Nauka, Moscow (1971).
[11] G. Rado and H. Suhl (eds.), *Magnetism*, in four volumes, Academic Press, New York (1963).
[12] V. G. Bar'yakhtar and B. A. Ivanov, *Intermediate State and the Dynamic and Static Properties of Domain Walls in Two-Sublattice Magnets*, Vol. 6 of Sov. Sci. Rev. Sec. A–Phys., I. M. Khalatnikov (ed.), Harwood, Amsterdam (1985), p. 404.
[13] E. A. Turov, *Kinetic, Optical, and Acoustic Properties of Antiferromagnets* [in Russian], Izd-vo UrO RAN, Sverdlovsk (1990).
[14] E. A. Turov and V. G. Shavrov, Usp. Fiz. Nauk **140**, 429 (1983) [Sov. Phys. Usp. **26**, 593 (1983)].
[15] V. G. Bar'yakhtar, B. A. Ivanov, and M. V. Chetkin, Usp. Fiz. Nauk **146**, 417 (1985) [Sov. Phys. Usp. **28**, 563 (1985)].
[16] V. Novosad, Y. Otani, A. Ohsawa, S. G. Kim, K. Fukamichi, J. Koike, K. Maruyama, O. Kitakami, and Y. Shimada, J. Appl. Phys. **87**, 6400 (2000).
[17] S. O. Demokritov, B. Hillebrands, and A. N. Slavin, Phys. Rep. **348**, 441 (2001).
[18] S. O. Demokritov, J. Phys.: Condens. Matter **15**, 2575 (2003).
[19] M. N. Baibich, J. M. Broto, A. Fert, F. Nguyen Van Dau, F. Petroff, P. Eitenne, G. Greuzet, A. Friederich, and J. Chazeles, Phys. Rev. Lett. **61**, 2472 (1988).
[20] R. P. Cowburn, D. K. Koltsov, A. O. Adeyeye, and M. E. Welland, J. Appl. Phys. **87**, 7082 (2000).
[21] R. P. Cowburn and M. E. Welland, Science **287**, 1466 (2000).
[22] S. O. Demokritov, J. Phys. D **31**, 925 (1998).
[23] K. Yu. Guslienko, Appl. Phys. Lett. **75**, 394 (1999); K. Yu. Guslienko, S. Choe, and S. Shin, *ibid.* **76**, 3609 (2000).
[24] R. W. Wang, D. L. Mills, E. E. Fullerton, J. E. Mattson, and S. D. Bader, Phys. Rev. Lett. **72**, 920 (1994).
[25] R. W. Wang, D. L. Mills, E. E. Fullerton, S. Kumar, and M. Grimsditch, Phys. Rev. B **53**, 2627 (1996).
[26] S. Rakhmanova, D. L. Mills, and E. E. Fullerton, Phys. Rev. B **57**, 476 (1998).
[27] D. D. Awschalom, J. F. Smyth, G. Grinstein, D. P. DiVincenzo, and D. Loss, Phys. Rev. Lett. **68**, 3092 (1992).
[28] E. M. Chudnovsky and J. Tejada, *Macroscopic Quantum Tunneling of the Magnetic Moment*, Cambridge University Press (1998).
[29] L. Gunter and B. Barbara (eds.), *Quantum Tunneling of Magnetization*, Vol. 301 of NATO ASI Series E, Kluwer, Dordrecht (1995).
[30] B. A. Ivanov and A. K. Kolezhuk, in *Frontiers in Magnetism of Reduced Dimension Systems*, V. G. Bar'yakhtar, P. E. Wigen, and N. A. Lesnik (eds.), Vol. 49 of NATO ASI Series 3. High Technology, Kluwer, Dordrecht (1998).
[31] L. N. Leuenberger and D. Loss, Nature (London) **410**, 789 (2001); W. Wernsdorfer, N. Aliaga-Alcalde, D. N. Hendrickson, and G. Christou, *ibid.* **416**, 406 (2002).
[32] D. Loss, D. P. DiVincenzo, and G. Grinstein, Phys. Rev. Lett. **69**, 3232 (1992).
[33] J. von Delft and C. L. Henley, Phys. Rev. Lett. **69**, 3236 (1992).
[34] A. M. Kosevich, B. A. Ivanov, and A. S. Kovalev, *Nonlinear Waves of Magnetization. Dynamical and Topological Solitons* [in Russian], Naukova Dumka, Kiev (1983).
[35] A. M. Kosevich, B. A. Ivanov, and A. S. Kovalev, Phys. Rep. **194**, 117 (1990).
[36] H. J. Mikeska and M. Steiner, Adv. Phys. **40**, 191 (1991).
[37] V. G. Bar'yakhtar and B. A. Ivanov, "Solitons and Thermodynamics of Low-Dimensional Magnets," Soviet Scientific Reviews, Section A. Physics (I. M. Khalatnikov, ed.), Vol. 16 (1992).
[38] B. A. Ivanov and A. K. Kolezhuk, Fiz. Nizk. Temp. **21**, 355 (1995) [Low Temp. Phys. **21**, 275 (1995)].
[39] L. Néel, Ann. Phys. (Paris) **17**, 61 (1932).
[40] L. Néel, Ann. Phys. (Paris) **5**, 232 (1936).
[41] L. D. Landau, Phys. Zs. Sowjetunion **4**, 675 (1933).
[42] L. D. Landau and E. M. Lifshitz, *Electrodynamics of Continuous Media*, 1st ed., Pergamon Press, Oxford (1960), Gostekhizdat, Moscow (1957).
[43] A. F. Andreev and V. I. Marchenko, Usp. Fiz. Nauk **130**, 39 (1980) [Sov. Phys. Usp. **23**, 21 (1980)].
[44] I. E. Dzyaloshinskiĭ, Zh. Éksp. Teor. Fiz. **32**, 1547 (1957) [Sov. Phys. JETP **5**, 1259 (1957)].
[45] T. Moriya, Phys. Rev. **120**, 91 (1960).
[46] Jurgen Schnack, "Quantum theory of molecular magnetism," in *Quantum Magnetism*, Vol. 645 of Lecture Notes in Physics, Springer-Verlag, Heidelberg (2004).
[47] H. De Raedt, S. Miyashita, K. Michielsen, and M. Mashida, Phys. Rev. B **70**, 064401 (2004).
[48] D. Gatteschi, A. Caneschi, L. Pardi, and R. Sessoli, Science **265**, 1054 (1994).
[49] A. Cornia, A. G. M. Jansen, and M. Affronte, Phys. Rev. B **60**, 12177 (1999).
[50] O. Waldmann, R. Koch, S. Schromm, P. Müller, I. Bernt, and R. W. Saalfrank, Phys. Rev. Lett. **89**, 246401 (2002).
[51] A. Chiolero and D. Loss, Phys. Rev. Lett. **80**, 169 (1998).
[52] F. Meier and D. Loss, Phys. Rev. Lett. **86**, 5373 (2001); Phys. Rev. B **64**, 224411 (2001).
[53] G. Christou, D. Gatteschi, D. N. Hendrickson, and R. Sessoli, MRS Bull. **25**, 66 (2000).
[54] W. Wernsdorfer, S. Bhaduri, C. Boskovic, G. Christou, and D. N. Hendrickson, Phys. Rev. B **65**, 180403 (2002).
[55] R. S. Edvards, S. Hill, S. Bhaduri, N. Aliaga-Alcalde, E. Bolin, S. Maccagnano, G. Christou, and D. N. Hendrickson, Polyhedron **22**, 1911 (2003).
[56] D. Caneschi, L. Pardi, A. L. Barra, A. Müller, and J. Döring, Nature (London) **354**, 463 (1991).
[57] A. Müller, S. Sarkar, S. Q. N. Shah, H. Bögge, M. Schmidtmann, Sh. Sarkar, P. Kógerler, B. Hauptfleisch, A. X. Trautwein, and V. Schünemann, Angew. Chem., Int. Ed. Engl. **38**, 3238 (1999).
[58] J. M. Luttinger and L. Tisza, Phys. Rev. **70**, 954 (1946); P. I. Beloboro-

dov, R. C. Gekht, and V. A. Ignatchenko, Sov. Phys. JETP **57**, 636 (1983); J. G. Brankov and D. M. Danchev, Physica A **144**, 128 (1987); S. Prakash and C. L. Henley, Phys. Rev. B **42**, 6574 (1990).

[59] T. Moriya, *Spin Fluctuations in Itinerant Electron Magnetism*, Springer-Verlag, Berlin (1985), Mir, Moscow (1988).

[60] J. M. Radcliffe, J. Phys. A **4**, 313 (1971).

[61] A. M. Perelomov, Usp. Fiz. Nauk **123**, 23 (1977) [Sov. Phys. Usp. **20**, 703 (1977)]; A. Perelomov, *Generalized Coherent States and Their Applications*, Springer-Verlag, Berlin (1986).

[62] H. Kuratsuji and T. Suzuki, J. Math. Phys. **21**, 472 (1980).

[63] S. Takagi and G. Tatara, Phys. Rev. B **54**, 9920 (1996).

[64] L. D. Landau and E. M. Lifshitz (Lifshits), *Quantum Mechanics: Non-Relativistic Theory*, transl. of 3rd ed., Pergamon Press, Oxford (1977), Nauka, Moscow (1989).

[65] R. J. Glauber, Phys. Rev. **130**, 2529 (1963); **131**, 2766 (1963).

[66] A. M. Perelomov, Commun. Math. Phys. **26**, 222 (1972).

[67] E. Fradkin, *Field Theories of Condensed Matter Systems*, Vol. 82 of Frontiers in Physics, Addison-Wesley (1991).

[68] R. Rajaraman, *Solitons and Instantons: An Inroduction to Solitons and Instantons in Quantum Field Theory*, North-Holland, Amsterdam (1982).

[69] E. G. Galkina and B. A. Ivanov, JETP Lett. **71**, 259 (2000).

[70] L. D. Landau and E. M. Lifshitz, "On the theory of the magnetic permeability of ferromagnetic solids," see L. D. Landau, *Collected Works* [in Russian], Nauka, Moscow (1969), Vol. 1, p. 128.

[71] A. I. Akhiezer, V. G. Bar'yakhtar, and S. V. Peletminskii, *Spin Waves*, North-Holland, Amsterdam (1968), Nauka, Moscow (1967).

[72] É. L. Nagaev, *Magnets with Nonsimple Exchange Interactions* [in Russian], Nauka, Moscow (1988).

[73] V. S. Ostrovskiĭ, Zh. Éksp. Teor. Fiz. **91**, 1690 (1986) [Sov. Phys. JETP **64**, 999 (1986)].

[74] V. M. Loktev and V. S. Ostrovskiĭ, Fiz. Nizk. Temp. **20**, 983 (1994) [Low Temp. Phys. **20**, 775 (1994)].

[75] B. A. Ivanov and A. K. Kolezhuk, Phys. Rev. B **68**, 052401 (2003).

[76] B. A. Ivanov, A. N. Kichizhiev, and Yu. N. Mitsaĭ, Zh. Éksp. Teor. Fiz. **102**, 618 (1992) [JETP **75**, 329 (1992)].

[77] L. N. Bulaevskiĭ and V. L. Ginzburg, Zh. Éksp. Teor. Fiz. **45**, 772 (1963) [Sov. Phys. JETP **18**, 530 (1964)].

[78] M. R. Mathews, B. P. Anderson, P. C. Halljan *et al.*, Phys. Rev. Lett. **83**, 2498 (1999).

[79] K. W. Madison, F. Chevy, W. Wohlleben, and J. Dalibard, Phys. Rev. Lett. **84**, 806 (2000).

[80] Fei Zhou, "Quantum spin nematic states in Bose-Einstein condensates," Electronic preprint ArXiv:cond-mat/0108473 (2002).

[81] N. J. Poulis and G. E. G. Hardeman, Physica (Utrecht) **18**, 201 (1952); **18**, 315 (1952).

[82] S. Foner, in *Magnetism*, Vol. 1, G. Rado and H. Suhl (eds.), Academic Press, New York (1963).

[83] V. A. Popov and V. I. Skidanenko, "Condensed matter physics," Tr. FT-INT AN USSR, Kharkov, vyp. 7, 49 (1970); G. K. Chepurnykh, Fiz. Tverd. Tela (Leningrad) **10**, 1917 (1968) [Sov. Phys. Solid State **10**, 1517 (1968)].

[84] V. A. L'vov and D. A. Yablonskiĭ, Fiz. Nizk. Temp. **8**, 951 (1982) [Sov. J. Low Temp. Phys. **8**, 479 (1982)].

[85] B. A. Ivanov and V. E. Kireev, JETP Lett. **69**, 398 (1999).

[86] V. G. Bar'yakhtar, A. E. Borovik, and V. A. Popov, JETP Lett. **9**, 391 (1969)]; V. G. Bar'yakhtar, A. A. Galkin, S. M. Kovner, and V. A. Popov, Zh. Éksp. Teor. Fiz. **58**, 494 (1970) [Sov. Phys. JETP **31**, 264 (1970); K. L. Dudko, V. V. Eremenko, and V. I. Fridman, Zh. Éksp. Teor. Fiz. **61**, 1553 (1971) [*ibid.* **34**, 828 (1971); A. King and D. Paquete, Phys. Rev. Lett. **30**, 662 (1972).

[87] V. G. Bar'yakhtar, A. N. Bogdanov, and D. A. Yablonskiĭ, Usp. Fiz. Nauk **156**, 47 (1988) [Sov. Phys. Usp. **31**, 810 (1988)].

[88] D. L. Mills, Phys. Rev. Lett. **20**, 18 (1968).

[89] F. Keffer and H. Chow, Phys. Rev. Lett. **31**, 1061 (1973).

[90] D. L. Mills and W. Saslow, Phys. Rev. B **171**, 488 (1968).

[91] W. E. Tennant, R. B. Bailey, and P. L. Richards, in *Proceedings of the Conference on Magnetism and Magnetic Materials*, San Francisco, 1974, C. D. Graham, G. H. Lander, and J. J. Rhyne (eds.), AIP Conf. Proc. Number 24, American Institute of Physics, New York (1975).

[92] E. E. Fullerton, M. J. Conover, J. E. Matson, C. H. Sowers, and S. D. Bader, Phys. Rev. B **48**, 15755 (1993).

[93] F. C. Nortemann, R. L. Stamps, A. S. Carrico, and R. E. Camley, Phys. Rev. B **46**, 10847 (1992).

[94] L. Trallori, P. Politi, A. Rettoti, M. G. Pini, and J. Willain, Phys. Rev. Lett. **72**, 1925 (1994); J. Phys.: Condens. Matter **7**, L451 (1995).

[95] C. Micheletti, R. B. Griffiths, and J. M. Yeomans, J. Phys. A **30**, L233 (1997).

[96] N. Papanicolaou, J. Phys.: Condens. Matter **10**, L131 (1998).

[97] J. de Jongh and A. R. Miedema, Adv. Phys. **23**, 1 (1974).

[98] K. Subbaraman, C. E. Zaspel, and J. E. Drumheller, Phys. Rev. Lett. **80**, 2201 (1998).

[99] C. E. Zaspel and J. E. Drumheller, Int. J. Modern Phys. **10**, 3649 (1996).

[100] B. A. Ivanov, C. E. Zaspel, and A. Yu. Merkulov, J. Appl. Phys. **89**, 7198 (2001).

[101] B. A. Ivanov, C. E. Zaspel, and A. Yu. Merkulov, Phys. Rev. B **68**, 212403 (2003).

[102] A. K. Kolezhuk and H. J. Mikeska, Phys. Rev. B **53**, R8848 (1996).

[103] A. K. Kolezhuk and H. J. Mikeska, Int. J. Mod. Phys. B **12**, 2325 (1998).

[104] Y. Shapira and V. Bindilatti, J. Appl. Phys. **92**, 4155 (2002).

[105] O. Waldmann, Phys. Rev. B **61**, 6138 (2000).

[106] B. A. Ivanov and V. E. Kireev, JETP Lett. **81**, 321 (2005).

[107] M. I. Kaganov and V. M. Tsukernik, Zh. Éksp. Teor. Fiz. **34**, 106 (1958) [Sov. Phys. JETP **7**, 73 (1958)].

[108] E. A. Turov and Yu. P. Irkhin, Izv. AN SSSR Ser. Fiz. **22**, 1168 (1958).

[109] I. V. Bar'yakhtar and B. A. Ivanov, Fiz. Nizk. Temp. **5**, 759 (1979) [Sov. J. Low Temp. Phys. **5**, 361 (1979)].

[110] H.-J. Mikeska, J. Phys. C **13**, 2913 (1980).

[111] B. A. Ivanov and A. L. Sukstanskiĭ, Zh. Éksp. Teor. Fiz. **84**, 370 (1983) [Sov. Phys. JETP **57**, 214 (1983)].

[112] B. A. Ivanov and A. L. Sukstanskii, Solid State Commun. **50**, 523 (1984).

[113] I. Affleck and I. Affleck, Nucl. Phys. B **257**, 397 (1985); **265**, 409 (1986); Phys. Rev. Lett. **57**, 1048 (1986).

[114] F. D. M. Haldane, Phys. Lett. A **93**, 464 (1983).

[115] F. D. M. Haldane, Phys. Rev. Lett. **50**, 1153 (1983).

[116] I. Affleck, J. Phys.: Condens. Matter **1**, 3047 (1989); I. Affleck, in *Fields, Strings and Critical Phenomena*, E. Brézin and J. Zinn-Justin (eds.), North-Holland, Amsterdam (1990), p. 567.

[117] B. A. Ivanov, in *Path Integrals from peV to TeV: 50 Years after Feynman's Paper*, R. Casalbuoni, R. Giachetti, V. Tognetti, R. Vaia, and P. Verrucchi (eds.), World Scientific, Dordrecht (1999), p. 410.

[118] B. A. Ivanov and V. E. Kireev, Zh. Éksp. Teor. Fiz. **121**, 320 (2002) [JETP **94**, 270 (2002)].

[119] E. V. Gomonaĭ, B. A. Ivanov, V. A. L'vov, and G. K. Oksyuk, Zh. Éksp. Teor. Fiz. **97**, 307 (1990) [Sov. Phys. JETP **70**, 174 (1990)].

[120] A. Chiolero and D. Loss, Phys. Rev. B **56**, 738 (1997).

[121] B. A. Ivanov, A. K. Kolezhuk, and G. K. Oksyuk, Europhys. Lett. **14**, 151 (1991).

[122] I. V. Bar'yakhtar and B. A. Ivanov, Zh. Éksp. Teor. Fiz. **85**, 328 (1983) [Sov. Phys. JETP **58**, 190 (1983)].

[123] B. A. Ivanov and A. K. Kolezhuk, Fiz. Nizk. Temp. **21**, 986 (1995) [Low Temp. Phys. **21**, 760 (1995)].

[124] B. A. Ivanov, A. K. Kolezhuk, and V. E. Kireev, Phys. Rev. B **58**, 11514 (1998).

[125] E. M. Chudnovskiĭ, Zh. Éksp. Teor. Fiz. **77**, 2158 (1979) [Sov. Phys. JETP **50**, 1035 (1979)].

[126] E. M. Chudnovsky and L. Gunter, Phys. Rev. B **37**, 9455 (1988).

[127] M. Enz and R. Schilling, J. Phys. C **19**, L711 (1986).

[128] J. L. van Hemmen and A. Sütö, Physica B **141**, 37 (1986).

[129] B. Barbara and E. M. Chudnovsky, Phys. Lett. A **145**, 205 (1990).

[130] I. V. Krive and O. B. Zaslavskii, J. Phys.: Condens. Matter **2**, 9457 (1990).

[131] A. Garg, Europhys. Lett. **22**, 205 (1993).

[132] V. Y. Golyshev and A. F. Popkov, Europhys. Lett. **29**, 327 (1995); V. Yu. Galyshev and A. F. Popkov, Zh. Éksp. Teor. Fiz. **108**, 1755 (1995) [JETP **81**, 962 (1995)].

[133] J. R. Friedman, M. P. Sarachik, J. Tejada, and R. Ziolo, Phys. Rev. Lett. **76**, 3830 (1996).

[134] L. Thomas, F. Lionti, R. Ballou, D. Gatteschi, R. Sessoli, and B. Barbara, Nature (London) **383**, 145 (1996).

[135] C. Sangregorio, T. Ohm, C. Paulsen, R. Sessoli, and D. Gatteschi, Phys. Rev. Lett. **78**, 4645 (1997).

[136] S. M. J. Aubin, N. R. Dilley, M. W. Wemple, M. B. Maple, G. Christou, and D. N. Hendrickson, J. Am. Chem. Soc. **120**, 839 (1998).

[137] W. Wernsdorfer and R. Sessoli, Science **284**, 133 (1999).

[138] W. Wernsdorfer, M. Soler, G. Christou, and D. N. Hendrickson, J. Appl. Phys. **91**, 7164 (2002).

[139] W. Wernsdorfer, S. Bhaduri, C. Boskovic, G. Christou, and D. N. Hendrickson, Phys. Rev. B **65**, 180403R (2002).

[140] O. Waldmann, C. Dobe, H. Mutka, A. Furrer, and H. U. Güdel, "Mesoscopic quantum coherence in antiferromagnetic molecular clusters," Electronic Preprint cond-mat/0410447 (2004).

[141] E. Kececioglu and A. Garg, Phys. Rev. Lett. **88**, 237205 (2002); Phys. Rev. B **67**, 054406 (2003).
[142] E. M. Chudnovsky and X. M. Hidalgo, Europhys. Lett. **50**, 395 (2000).
[143] A. I. Vaĭnshteĭn, V. I. Zakharov, V. A. Novikov, and M. A. Shifman, Usp. Fiz. Nauk **136**, 553 (1982) [Sov. Phys. Usp. **25**, 195 (1982)].
[144] B. A. Ivanov and V. E. Kireev, Fiz. Nizk. Temp. **25**, 1287 (1999) [Low Temp. Phys. **25**, 966 (1999)].
[145] A. I. Perelomov, *Integrable systems of classical mechanics and Lie algebras*, Birkhäuser, Basel (1990), Nauka, Moscow (1990).
[146] C. Neumann, J. Reine Angew. Math. **56**, 46 (1859).
[147] V. M. Eleonskiĭ and N. E. Kulagin, Zh. Éksp. Teor. Fiz. **84**, 616 (1983) [Sov. Phys. JETP **57**, 356 (1983)].
[148] V. M. Eleonskiĭ, N. N. Kirova, and N. E. Kulagin, Zh. Éksp. Teor. Fiz. **77**, 409 (1979) [Sov. Phys. JETP **50**, 209 (1979)].
[149] E. K. Sklyanin, "On complete integrability of the Landau-Lifshitz equation," Preprint LOMI E-3-79 (1979).
[150] B. A. Ivanov and N. E. Kulagin, Zh. Éksp. Teor. Fiz. **126**, 1479 (2004) [JETP **99**, 1291 (2004)].
[151] B. A. Ivanov and V. E. Kireev, Phys. Rev. B **70**, 214430 (2004).
[152] R. Jackiw, Commun. Nucl. Part. Phys. **13**, 141 (1984); Usp. Fiz. Nauk **149**, 137 (1986).
[153] H. Hu, R. Lü, J.-L. Zhu, and J.-J. Xiong, Commun. Theor. Phys. **36**, 245 (2001); Electronic Preprint cond-mat/0006292 (2000).
[154] A. Garg, Phys. Rev. Lett. **71**, 4249 (1993); **74**, 1458 (1995).
[155] N. A. Usov and S. E. Peschany, J. Magn. Magn. Mater. **130**, 275 (1994); M. Grimsditch, Y. Jaccard, and I. K. Shuller, Phys. Rev. B **58**, 11539 (1998); R. P. Cowburn and M. E. Welland, *ibid.* **58**, 9217 (1998); R. P. Cowburn, A. O. Adeyeye, and M. E. Welland, Phys. Rev. Lett. **81**, 5415 (1998), E. V. Tartakovskaya, J. W. Tucker, and B. A. Ivanov, J. Appl. Phys. **89**, 8348 (2001); B. A. Ivanov and E. V. Tartakovskaya, Zh. Éksp. Teor. Fiz. **125**, 1159 (2004) [JETP **98**, 1015 (2004)].
[156] G. E. Volovik and V. P. Mineev, Zh. Éksp. Teor. Fiz. **72**, 2256 (1977) [Sov. Phys. JETP **45**, 1186 (1977)].
[157] B. A. Ivanov, H. J. Schnitzer, F. G. Mertens, and G. M. Wysin, Phys. Rev. B **58**, 8464 (1998).
[158] N. A. Usov and S. E. Peschany, J. Magn. Magn. Mater. **118**, L290 (1993).
[159] K. Runge, T. Nozaki, U. Okami *et al.*, J. Appl. Phys. **79**, 5075 (1996); R. P. Cowburn, D. K. Koltsov, A. O. Adeyeye *et al.*, Phys. Rev. Lett. **83**, 1042 (1999); A. Fernández and C. J. Cerjan, J. Appl. Phys. **87**, 1395 (2000); Jing Shi, S. Tehrani, and M. R. Scheinfein, Appl. Phys. Lett. **76**, 2588 (2000); T. Pokhil, D. Song, and J. Nowak, J. Appl. Phys. **87**, 6319 (2000).
[160] M. Kläui, C. A. F. Vaz, L. Lopez-Diaz, and J. A. C. Bland, J. Phys.: Condens. Matter **15**, R985 (2003).
[161] P. Park, P. Eames, D. M. Engebretson, J. Berezovsky, and P. A. Crowell, Phys. Rev. B **67**, 020403R (2003).
[162] M. Buess, R. Höllinger, T. Haug, K. Perzlmaier, U. Krey, D. Pescia, M. R. Scheinfein, D. Weiss, and C. H. Back, Phys. Rev. Lett. **93**, 077207 (2004).
[163] S. B. Choe, Y. Acremann, A. Scholl, A. Bauer, A. Doran, J. Stöhr, and H. A. Padmore, Science **304**, 420 (2004).
[164] B. A. Ivanov and C. E. Zaspel, Phys. Rev. Lett. **94**, 027205 (2005).
[165] D. A. Dimitrov and G. M. Wysin, Phys. Rev. B **50**, 3077 (1994); **51**, 11947 (1995).
[166] P.-G. de Gennes, *The Physics of Liquid Crystals*, Clarendon Press, Oxford (1974), Mir, Moscow (1974).
[167] N. D. Mermin, in *Quantum Fluids and Solids*, S. B. Trickey, E. D. Adams, and J. W. Duffey (eds.), Plenum Press, New York (1977), p. 3; P. W. Anderson and R. G. Palmer, *ibid.*, p. 23.
[168] V. E. Kireev and B. A. Ivanov, Phys. Rev. B **68**, 104428 (2003).
[169] R. S. Gekht, Usp. Fiz. Nauk **59**, 261 (1989).
[170] I. E. Dzyaloshinskiĭ, JETP Lett. **25**, 414 (1977).
[171] A. S. Kovalev and A. M. Kosevich, Fiz. Nizk. Temp. **3**, 259 (1977) [Sov. J. Low Temp. Phys. **3**, 125 (1977)].
[172] M. Kleiber, M. Bode, R. Ravlić, and R. Wiesendanger, Phys. Rev. Lett. **85**, 4606 (2000).
[173] R. L. Stamps and R. E. Camley, Phys. Rev. B **54**, 15200 (1996); R. L. Stamps, R. E. Camley, and R. J. Hicken, *ibid.* **54**, 4159 (1996).
[174] P. Bodeker, A. Hucht, J. Borchers, F. Guthoff, A. Schreyer, and H. Zabel, Phys. Rev. Lett. **81**, 914 (1998); H. Zabel, J. Phys.: Condens. Matter **11**, 9303 (1999).
[175] B. A. Ivanov, V. E. Kireev, and V. P. Voronov, Fiz. Nizk. Temp. **23**, 845 (1997) [Low Temp. Phys. **23**, 635 (1997)].
[176] L. D. Landau and E. M. Lifshitz, *Theory of Elasticity*, 2nd Eng. ed., Pergamon Press, Oxford (1970), Nauka, Moscow (1965).
[177] A. M. Kosevich, *Dislocations in the Theory of Elasticity*, Naukova Dumka, Kiev (1978).
[178] D. C. Wiesler, H. Zabel, and S. M. Shapiro, Z. Phys. B: Condens. Matter **93**, 277 (1994).
[179] B. A. Ivanov and V. E. Kireev, Pis'ma Zh. Éksp. Teor. Fiz. **73**, 210 (2001) [JETP **46**, 188 (2001)].
[180] A. S. Kovalev, Fiz. Nizk. Temp. **20**, 1034 (1994) [Low Temp. Phys. **20**, 815 (1994)].
[181] O. K. Dudko and A. S. Kovalev, Fiz. Nizk. Temp. **24**, 559 (1998) [Low Temp. Phys. **24**, 422 (1998)]; Fiz. Nizk. Temp. **25**, 25 (1999) [Low Temp. Phys. **25**, 18 (1999); Fiz. Nizk. Temp. **26**, 821 (2000) [Low Temp. Phys. **26**, 603 (2000)].
[182] A. P. Malozemoff and J. C. Slonczewski, *Magnetic Domain Walls in Bubble Materials*, Academic Press, New York (1979), Mir, Moscow (1982).
[183] H. B. Braun and D. Loss, Phys. Rev. B **53**, 3237 (1996).
[184] H. B. Braun and D. Loss, Int. J. Mod. Phys. B **10**, 219 (1996).
[185] H. B. Braun, J. Kyriakidis, and D. Loss, Phys. Rev. B **56**, 8129 (1997).
[186] J. Shibata and S. Takagi, Phys. Rev. B **62**, 9920 (2000).
[187] J. A. Freire, Phys. Rev. B **65**, 104436 (2002).
[188] B. A. Ivanov and A. K. Kolezhuk, JETP Lett. **60**, 805 (1994).
[189] B. A. Ivanov and A. K. Kolezhuk, Phys. Rev. Lett. **74**, 1859 (1995).
[190] N. Papanicolaou, Phys. Rev. B **51**, 15062 (1995).
[191] B. A. Ivanov, V. E. Kireev, and A. Yu. Merkulov, Mater. Sci. Forum **373–376**, 807 (2001).
[192] E. G. Galkina and B. A. Ivanov, JETP Lett. **61**, 511 (1995).
[193] H. J. Bethe, Z. Phys. **71**, 205 (1931).
[194] R. J. Baxter, Ann. Phys. **70**, 323 (1972).
[195] V. L. Berezinskii, Sov. Phys. JETP **34**, 610 (1972).
[196] J. M. Kosterlitz and D. J. Thouless, J. Phys. C **6**, 1181 (1973).
[197] A. A. Zvyagin, Sov. Phys. Solid State **32**, 181 (1990); Sov. J. Low Temp. Phys. **18**, 558 (1992).
[198] E. Dagotto, J. Riera, and D. J. Scalapino, Phys. Rev. B **45**, 5744 (1992).
[199] D. V. Khveshchenko, Phys. Rev. B **50**, 380 (1994).
[200] D. Senechal, Phys. Rev. B **52**, 15319 (1995).
[201] G. Sierra, J. Phys. A **29**, 3299 (1996).
[202] H. J. Schulz, Phys. Rev. B **34**, 6372 (1986).
[203] M. den Nijs and K. Rommelse, Phys. Rev. B **40**, 4709 (1989).
[204] U. Schollwock and Th. Jolicoeur, Europhys. Lett. **30**, 493 (1995); U. Schollwock, O. Golinelli, and T. Jolicoeur, Phys. Rev. B **54**, 4038 (1996).

Translated by Steve Torstveit

LOW TEMPERATURE PHYSICS VOLUME 31, NUMBERS 8–9 AUGUST–SEPTEMBER 2005

Quantum Heisenberg antiferromagnets: a survey of the activity in Florence (Review)

U. Balucani

Istituto dei Sistemi Complessi, Consiglio Nazionale delle Ricerche, via Madonna del Piano 10,
I-50019 Sesto Fiorentino (FI), Italy

L. Capriotti

Valuation Risk Group, Credit Suisse First Boston (Europe) Ltd., One Cabot Square, London, E14 4QJ,
United Kingdom and Kavli Institute for Theoretical Physics, University of California, Santa Barbara,
California 93106, USA

A. Cuccoli, A. Fubini, and V. Tognetti

Dipartimento di Fisica dell'Università di Firenze, via G. Sansone 1, I-50019 Sesto Fiorentino (FI), Italy
and Istituto Nazionale per la Fisica della Materia, Unità di Ricerca di Firenze, via G. Sansone 1,
I-50019 Sesto Fiorentino (FI), Italy

T. Roscilde

Department of Physics and Astronomy, University of Southern California, Los Angeles,
CA 90089-0484, USA

R. Vaia

Istituto dei Sistemi Complessi, Consiglio Nazionale delle Ricerche, via Madonna del Piano 10,
I-50019 Sesto Fiorentino (FI), Italy and Istituto Nazionale per la Fisica della Materia, Unità di Ricerca di
Firenze, via G. Sansone 1, I-50019 Sesto Fiorentino (FI), Italy

P. Verrucchi

Istituto Nazionale per la Fisica della Materia, Unità di Ricerca di Firenze, via G. Sansone 1, I-50019 Sesto
Fiorentino (FI), Italy and Istituto dei Sistemi Complessi, Consiglio Nazionale delle Ricerche, via
Madonna del Piano 10, I-50019 Sesto Fiorentino (FI), Italy

(Submitted January 20, 2005)
Fiz. Nizk. Temp. **31**, 885–906 (August–September 2005)

Over the years the research group in Florence (Firenze) has produced a number of theoretical results concerning the statistical mechanics of quantum antiferromagnetic models, which range from the theory of two-magnon Raman scattering to the characterization of the phase transitions in quantum low-dimensional antiferromagnetic models. Our research activity was steadily aimed to the understanding of experimental observations. © *2005 American Institute of Physics.* [DOI: 10.1063/1.2008128]

I. INTRODUCTION

The Heisenberg model may well be considered the cornerstone of the modern theory of magnetic systems; the reason for such an important role is the simple structure of the Hamiltonian, whose symmetries underlie its peculiar features. The basic forces which determine the alignment of the spins are represented by the exchange integrals J. At variance with the ferromagnet, where the parallel alignment is promoted, in the antiferromagnet a lot of peculiar arrangements of the spins can occur, with strong differences between classical and quantum systems. As a matter of fact, even for nearest-neighbor antiferromagnetic interactions only the ground state of the Hamiltonian is different from the Néel state with antialigned spins, and the (staggered) magnetization shows the so-called spin reduction with respect to the saturation value also at $T=0$. The linear excitations of an antiferromagnet can be roughly associated in two families, and pair excitations with vanishing total magnetization are possible: the fact that the total momentum of them can be close to zero allows for their investigation by light scattering.

While these peculiar features of antiferromagnetism already occur in three-dimensional (3D) compounds, they are more pronounced in the low-dimensional ones, where other effects caused by the enhanced role of classical and quantum fluctuations are present, and exotic spin configurations associated with field theory models can appear. Indeed, the last two decades have seen a renewed interest both in the case of the one-dimensional (1D) quantum Heisenberg antiferromagnet (QHAF), for which a peculiar behavior of the ground state versus spin value was predicted,[1] and of the two-dimensional (2D) QHAF, because of its theoretically challenging properties and of the fact that it models the magnetic behavior of the parent compounds of some high-T_c superconductors.[2,3] The experimental activity on 2D antiferromagnets stems from the existence of several real compounds whose crystal structure is such that the magnetic ions form parallel planes and interact strongly only if belonging to the same plane. As a consequence of such structure, their magnetic behavior is indeed 2D down to such low temperatures that the weak interplane interaction becomes relevant, driving the system towards a 3D ordered phase.

In addition, the 2D Heisenberg model can be enriched through symmetry-breaking terms—we considered easy-axis (EA) and easy-plane (EP) anisotropy, as well as an external uniform magnetic field—which are useful for reproducing the experimental behavior of many layered compounds. In the EA case one is left with a chain with discrete reflection symmetry, and the system undergoes an Ising-like phase transition. In the EP case or when a magnetic field is applied the residual O(2) symmetry prevents finite-temperature ordering,[4] but vortex excitations are possible and determine a Berezinskii-Kosterlitz-Thouless (BKT) transition between a paramagnetic and a quasi-ordered phase. In spite of the tiny anisotropies of real systems (usually $\lesssim 0.01J$), it can be shown that they dramatically change the behavior of the spin array already at temperatures of the order of J.

In this paper we report about the progresses in the theory of Heisenberg antiferromagnets that have been obtained by our group in Florence. The early work on the theory of two-magnon Raman scattering is summarized in Sec. 2, while the subsequent Sections report the recent activity on low-dimensional antiferromagnetism.

Section 3 is devoted to 1D models, and concerns the study of the effect of soliton-like excitations in the compound TMMC, as well as the anisotropic spin-1 model, for which a reduced description of the ground state allows one to investigate the quantum phase transition in a unitarily transformed representation and to obtain quantitative results for the phase diagram. Section 4 concerns the theory of the isotropic 2D QHAF, for which we reproduced the experimental correlation length by means of a semiclassical approach, also deriving the connection with (and the limitations of) famous quantum field theory results. In Sec. 5 we summarize several recent results concerning the anisotropic 2D QHAF, with emphasis onto the different phase diagrams and the experimentally measurable signatures of XY or Ising behavior. Eventually, in Sec. 6 results on the 2D frustrated J_1-J_2 isotropic model are described.

II. TWO-MAGNON RAMAN SCATTERING IN HEISENBERG ANTIFERROMAGNETS

The scattering of radiation is a very powerful tool for studying elementary excitations in condensed matter physics. Any complete experiment gives rise to a quasi-elastic component due to nonpropagating or diffusive modes and to symmetrically shifted spectra corresponding to the states of the system under investigation with an amplitude ratio governed by the detailed balance principle.

The most sensitive probes for this investigation are undoubtedly thermal neutrons, because the characteristic energies and wave vectors fit very well with those of the magnetic elementary excitations. However, light-scattering experiments can require a simpler apparatus and offer a better accuracy, although the transfer wave vector $\mathbf{k}$ is much smaller than the size of the Brillouin zone, so that usually only the center of this zone can be directly probed. In spite of this, two-spin Raman scattering involving the creation and destruction of a pair of elementary excitations can be performed, with the contribution of two magnons having equal frequencies and opposite wave vectors. This two-magnon scattering is expected to be spread over a band of frequencies in antiferromagnets. However, the density of states strongly enhances the contribution of zone-boundary (ZB) excitations,[5] i.e., at $\mathbf{k}\sim\mathbf{k}_{ZB}$.

While in ferromagnets the two-spin process is only due to a second-order mechanism, orders of magnitude smaller than the first order one, in antiferromagnets a different independent process is permitted, stronger than the corresponding one for single-spin spectra.[6] Specifically, an exchange mechanism does not change the total z component of the spins: exciting two magnons in the two different sublattices $(\Delta M=0)$[7] is the dominant scattering process.

The one-spin Raman scattering peak disappears at the Néel temperature because it probes the smallest wave vectors, related with the long-range correlations. In contrast, two-magnon Raman scattering essentially probes the highest wave vectors, related to short-range correlations. Therefore two-spin Raman scattering features persist also in the paramagnetic phase[7] where short-range order is still present. Let us consider the following antiferromagnetic Hamiltonian with exchange integral $J>0$, z nearest neighbors with displacements labeled by $\mathbf{d}$, and two (a,b) sublattices:[8]

$$\mathcal{H}=\frac{J}{2}\sum_{\mathbf{id}}\mathbf{S}_{\mathbf{i},a}\cdot\mathbf{S}_{i+\mathbf{d},b}\,. \tag{1}$$

The scattering cross section $S(\omega)$ turns out[9] to be proportional to the Fourier transform of $\langle M(0)M(t)\rangle$, where

$$M=\sum_{\mathbf{k}}\mathcal{M}_{\mathbf{k}}\mathbf{S}_{\mathbf{k}}\cdot\mathbf{S}_{-k}\,, \tag{2}$$

is the effective Raman scattering operator.

Many antiferromagnetic compounds can be mapped onto this model, even though a small next-nearest-neighbor exchange interaction without competitive effects, as well as anisotropy terms could be present. For instance, there are 3D perovskite and rutile structures (e.g., $\mathrm{KNiF_3}$, $\mathrm{NiF_2}$) and 2D layered structures (e.g., $\mathrm{K_2NiF_4}$, $\mathrm{LaCuO_2}$).

Let us remember that the exact ground state is not exactly known, except in 1D models with $S=1/2$ or $S=\infty$ (i.e., the classical case): in the latter case it coincides with the "Néel state" with antialigned sublattices.

In the ordered phase the theory can be developed in terms of two families of magnon operators $(\alpha_{\mathbf{k}},\beta_{\mathbf{k}})$, through the Dyson-Maleev spin-boson transformation and a Bogoliubov transformation:

$$\mathcal{H}=E_0+\mathcal{H}_0+V+\ldots, \tag{3}$$

where E_0 is the ground-state energy in the interacting spin-wave approximation, and

$$\mathcal{H}_0=\sum_{\mathbf{k}}\omega_{\mathbf{k}}(\alpha_{\mathbf{k}}^{\dagger}\alpha_{\mathbf{k}}+\beta_{\mathbf{k}}^{\dagger}\beta_{\mathbf{k}}) \tag{4}$$

is the quadratic part of the Hamiltonian of a magnon gas whose frequencies, renormalized by zero-T quantum fluctuations, are

$$\omega_{\mathbf{k}}=JSz\left(+\frac{C}{2S}\right)\sqrt{1-\gamma_{\mathbf{k}}^2};\qquad \gamma_{\mathbf{k}}=\frac{1}{z}\sum_{\mathbf{d}}\mathrm{e}^{-i\mathbf{k}\cdot\mathbf{d}}. \tag{5}$$

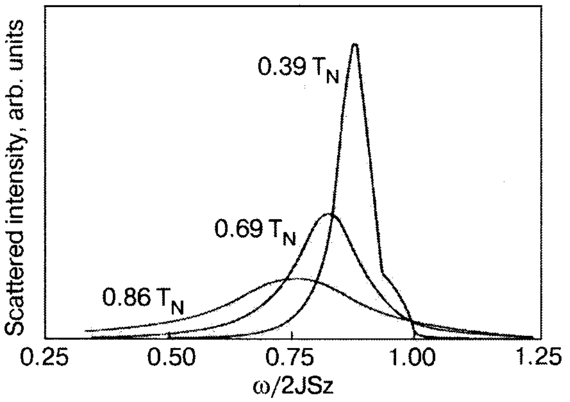

FIG. 1. Theoretical two-magnon spectra in $\mathrm{KNiF_3}$ at different temperatures.[10]

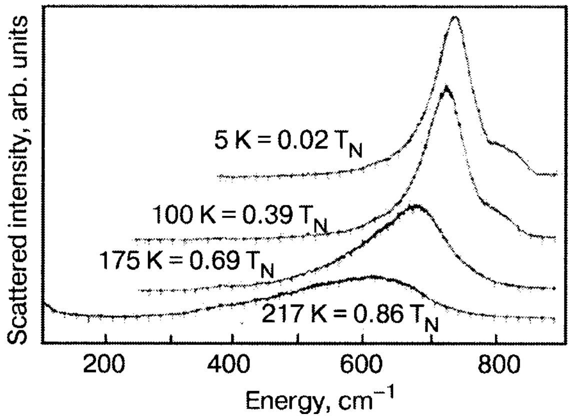

FIG. 2. Experimental two-magnon spectra in $\mathrm{KNiF_3}$ at different temperatures.[5]

The last term in the Hamiltonian, V, represents the four-magnon interaction, whose most significant term refers to two magnons of each family and turns out to be

$$V=\frac{2Jz}{N}\sum_{\mathbf{qq}'\mathbf{pp}'}\delta_{\mathbf{q}+\mathbf{p},\mathbf{q}'+\mathbf{p}'}I^{\alpha\beta}_{\mathbf{qq}',\mathbf{pp}'}\alpha^{\dagger}_{\mathbf{q}}\alpha_{\mathbf{q}'}\beta^{\dagger}_{\mathbf{p}}\beta_{\mathbf{p}'}, \tag{6}$$

where the coefficients $I^{\alpha\beta}_{\mathbf{qq}'\mathbf{pp}'}$ are known functions of $\gamma_{\mathbf{k}}$.

In the Hartree-Fock approximation[10] the temperature-dependent Raman scattering operator (2) can be written as

$$M=\alpha(T)S\sum_{\mathbf{k}}\Phi_{\mathbf{k}}(\alpha_{\mathbf{k}}\beta_{\mathbf{k}}+\alpha^{\dagger}_{\mathbf{k}}\beta^{\dagger}_{\mathbf{k}}) \tag{7}$$

with $\omega_{\mathbf{k}}(T)=\alpha(T)\omega_{\mathbf{k}}$. The two magnons created or destroyed by the operator (7) interact through V as given by (6), so that the peak of the cross section $S(\omega)$ appears at values smaller than $2\omega_{ZB}$ by an amount of the order of J. The explicit $S(\omega)$ at $T=0$ was calculated in the "ladder approximation" by Elliott and Thorpe and found in very good agreement with experiments.[9]

The finite-temperature calculation of the two-magnon Raman scattering cross section in the ordered region, up to $T\sim 0.95T_N$ was performed by Balucani and Tognetti,[10] who calculated the two-magnon propagator in the "ladder approximation," also taking into account the damping and the temperature renormalization of the magnons at the boundary of the Brillouin zone.[11] The calculated spectra $S(\omega)$, at increasing temperatures, were found in very good agreement with the experimental ones,[8] and their characteristic parameters (peak and linewidth) permitted determination of the temperature behavior of the frequency and damping of the ZB magnons.[12] In Figs. 1 and 2 we show the excellent agreement of our theoretical approach with the experiments in the ordered phase.[13] The validity of light scattering in probing the characteristic of ZB magnons has been confirmed both from the theoretical and the experimental point of view.[12] In Fig. 3 our theoretical ZB magnon damping calculations are compared with experimental data from different techniques.

In the paramagnetic phase all the experimental spectra show the persistence of a broad inelastic peak up to $T\sim 1.4T_N$. Only at $T\gg T_N$ do the spectra have a structureless shape centered around $\omega=0$. As matter of fact, the highest wave vectors sample only the behavior of clusters of neighboring spins, thus giving a measure of the short-range antiferromagnetic order that is present at all finite temperatures.

In the disordered phase conventional many-body methods are of little use for a quantitative interpretation of the observed, largely spread spectra. The concept of quasiparticle loses its meaning because of the overdamped character of the "excitations." The calculation of $S(\omega)$ can be instead approached by other more general theoretical methods devoted to the representation of the dynamical correlation functions based on the linear response theory.[11] Let us consider the "Kubo relaxation function" associated with our scattering process:

$$f_0(t)\equiv\frac{1}{\langle M(0)M(0)\rangle}\int_0^{\beta}d\lambda\langle e^{\lambda\mathcal{H}}M(0)e^{-\lambda\mathcal{H}}M(t)\rangle. \tag{8}$$

Its Laplace transform $f_0(z)$ is related to the scattering cross section:

$$S(\omega)\propto\frac{\omega}{1-e^{-\beta\omega}}\mathfrak{R}f_0(z=i\omega). \tag{9}$$

Mori[14] has given the following continued-fraction representation of the relaxation function:[11]

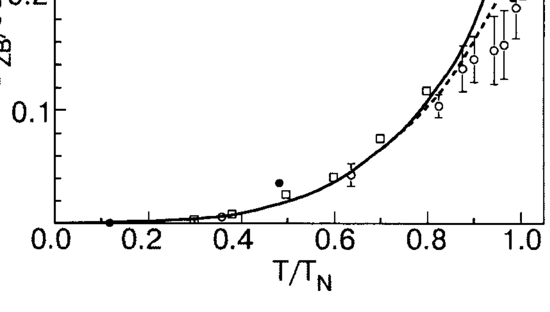

FIG. 3. Zone-boundary damping Γ_{ZB} versus temperature. The symbols refer to different experimental techniques: in particular, the unfilled circles are light scattering data.[12] The dashed line is an improvement[12] to a previous (solid) theoretical curve.[10]

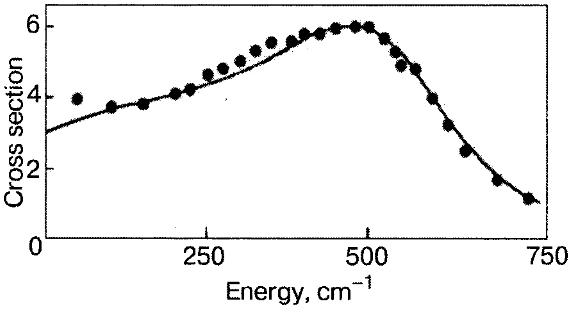

FIG. 4. Two-spin Stokes spectrum in KNiF$_3$ at $T \simeq = 1.02 T_N$. The line reports the theoretical shape,[15] compared with experimental data.

$$f_0(z) = \frac{1}{z + \Delta_1 f_1(z)}; \quad f_n(z) = \frac{1}{z + \Delta_{n-1} f_{n+1}(z)}, \tag{10}$$

which is formally exact, but allows one to perform some approximations in respect to the level of the termination $f_{n+1}(z)$. The quantities Δ_n can be expressed in terms of frequency moments:

$$\langle \omega^{2n} \rangle = \int_{-\infty}^{\infty} d\omega \omega^{2n} f_0(\omega). \tag{11}$$

In our calculations of $f_0(z)$ in the entire paramagnetic phase,[15,16] the coefficients Δ_1 and Δ_2 have been evaluated approximately by means of a decoupling procedure. Moreover, the third stage of the continued fraction (10) is evaluated assuming that

$$\Delta_3 f_3(z) \sim \Delta_3 [f_3(0) + z f_3'(0)]. \tag{12}$$

The parameters involved in (12) can be estimated from knowledge of the short-time behavior of $f_0(t)$ determined by the first moments, $\langle \omega^2 \rangle$ and $\langle \omega^4 \rangle$.

The results of our approach in the paramagnetic region are compared with the experiment in Fig. 4, showing the persistence of the peak of the ZB magnetic excitations above the critical temperature.

III. THE ONE-DIMENSIONAL ANTIFERROMAGNET

A. Solitons in the antiferromagnet TMMC

Interest in low-dimensional systems is motivated by the simpler calculations as compared with the 3D ones, accompanied by interesting peculiar behavior. The powerful mathematical approach based on the inverse-scattering and Bethe ansatz techniques permits one to solve exactly some 1D models, calculating thermodynamic and sometimes transport quantities both in the classical and quantum cases.[17] The most celebrated realizations of these models occur in 1D magnets. An original suggestion by Mikeska[18] was that the antiferromagnetic chain TMMC $[(CH_3)_4NMnCl_3]$ can be mapped onto a classical 1D sine-Gordon model. The elementary excitations of the sine-Gordon field are given in terms of linear small-amplitude spin waves and nonlinear breathers and kink-solitons. The nonlinear elementary excitations give a detectable contribution to the magnetic specific heat.

TMMC is composed of Heisenberg ($S = 5/2$) antiferromagnetic chains along the z axis:

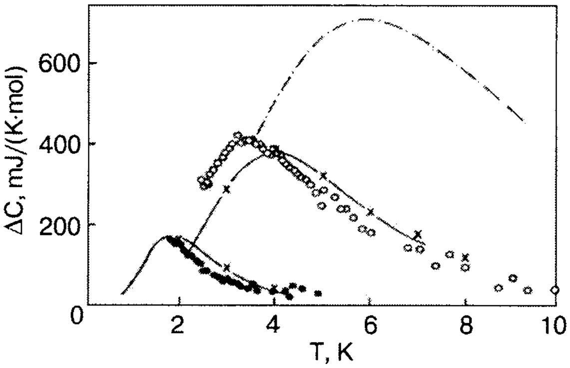

FIG. 5. Experimental contribution of nonlinear excitations to the specific heat of TMMC, $\Delta C = C(H) - C(0) - \Delta C_{SW}$. The field values are $H = 5.39$ T (●) and $H = 2.5$ T (○). The dotted-and-dashed line reports the result of the free soliton gas phenomenology. The planar model (interpolated crosses) appears to explain quantitatively the behavior of TMMC.

$$\mathcal{H} = J \sum_i (\mathbf{S}_i \cdot \mathbf{S}_{i+1} - \delta S_i^z S_{i-1}^z) \tag{13}$$

with a very small easy-plane anisotropy ($\delta = 0.0086$).

A magnetic field of the order of 1–10 T can be applied perpendicularly (y axis) or along the chain. In the first case, with approximations the more valid the lower the magnetic field ($H < 5$ T), in the continuum limit TMMC can be represented by the classical sine-Gordon Hamiltonian:

$$\mathcal{H} = \frac{A}{2} \int dx [\dot{\Phi}^2 + c_0^2 \Phi_x^2 2 \omega_0^2 (1 - \cos \Phi)], \tag{14}$$

whose parameters are related with the magnetic Hamiltonian (13), the reduced magnetic field $h = g \mu_B H$, and the lattice spacing a as follows:

$$A = \frac{1}{8Ja}, \quad c_0 = aJS \sqrt{1 - \frac{\delta}{2}}, \quad \omega_0 = h \sqrt{1 - \frac{\delta}{2}}. \tag{15}$$

The energy of a kink-soliton turns out to be

$$E_s = 8A \omega_0 c_0 \simeq hS, \tag{16}$$

and depends on the applied field. At variance with the ferromagnetic solitons, these solitons can be easily excited at lowest temperatures and can give a significant contribution to the thermodynamics.[19] When the field is applied longitudinally along the z axis only spin waves are present: therefore, the specific-heat measurements were performed in the two configurations. The contribution from the nonlinear excitations was obtained as the difference ΔC between the two experiments.

The thermodynamic quantities were calculated by the classical transfer-matrix method[20] for the sine-Gordon model (14). We then used a classical discrete planar model:[21]

$$\mathcal{H} = \sum_i [2JS^2 \cos(\Phi_i - \Phi_{i+1}) + hS(1 - \cos \Phi_i)], \tag{17}$$

verifying that it is qualitatively similar to the sine-Gordon. The comparison[21] is shown in Fig. 5, where the linear spin-wave specific heat was subtracted to emphasize the nonlinear contribution, together with the prediction of the "classical soliton gas phenomenology." [19]

This proved the presence of nonlinear excitations similar to sine-Gordon solitons, but the peak of the specific heat occurs at temperatures where solitons cannot be considered to be noninteracting and the "classical soliton-gas phenomenology" breaks down. When the magnetic field is increased to 9.98 T the model (17) is no longer able to describe the experiments. A quasi-uniaxial model[21] was proposed and found to be in good agreement. For general reference on the subject see Ref. 22.

B. The $S=1$ quantum antiferromagnet

We deal here with quantum antiferromagnetic spin chains, focusing our attention on the class of models defined by the Hamiltonian

$$\frac{\mathcal{H}}{J}=\sum_i \left[(S_i^x S_{i+1}^x+S_i^y S_{i+1}^y)+\lambda S_i^z S_{i+1}^z+d(S_i^z)^2\right] \qquad (18)$$

with exchange integral $J>0$ and single-ion anisotropy d.

One of the most surprising evidences of the difference between ferro- and antiferromagnetic systems is related with the so-called Haldane conjecture, i.e., with $T=0$ properties of integer-spin antiferromagnetic chains. In general, we expect three possible situations for the ground state of a magnetic system: either it is ordered (with finitely constant correlation functions), or quasi-ordered (with power-law decaying correlation functions), or completely disordered (with exponentially decaying correlation functions). One could intuitively expect the third option to be possibly dismissed, based on the idea that, when thermal fluctuations are completely suppressed, the system is in an ordered or at least quasi-ordered ground state. This idea is in fact proved correct for half-integer spin systems, thanks to the so-called Lieb-Schultz-Mattis theorem.[23] Despite the impossibility of generalizing such a theorem to integer-spin systems, its general validity has been taken for granted till 1983, when Haldane[1] suggested, for the integer-spin Heisenberg chain, an unexpected $T=0$ behavior: a unique and genuinely disordered ground state, meaning exponentially decaying correlation functions and a finite gap in the excitation spectrum. After more than two decades Haldane's idea that integer-spin systems can have a genuinely disordered ground state still stands as a conjecture. However, theoretical,[24–27] experimental,[28–32] and numerical[33–39] works have definitely confirmed its validity.

Let us consider Eq. (18) for integer spin: in the (d,λ) plane one may identify different quantum phases, corresponding to models whose ground states share common features. For $\lambda>0$ three phases are singled out: the Néel phase $(\lambda \gg d)$, where the ground state has a Néel-like structure, the so-called large-d phase $(d \gg \lambda)$, where the ground state is characterized by a large majority of sites where $S^z=0$, and the Haldane phase, which extends around the isotropic point $(d=0,\lambda=1)$, and is characterized by disordered ground states.

We first deal with the Ising limit,

$$\mathcal{H}/J=\lambda\sum_i S_i^z S_{i+1}^z .$$

Upon its ground state, the antiferromagnetically ordered Néel state, one may construct three types of excitations: a single deviation, a direct soliton, an indirect soliton, where *direct (indirect)* refers to the fact that the excitation be generated by flipping all the spins on the right of a given site while keeping the z component of the spin on such site unchanged (setting it to zero). All of the above configurations have energy $+2\lambda$ with respect to that of the ground state, and, when properly combined, generate all of the excited states; among them, we concentrate upon those containing a couple of adjacent indirect solitons and notice that their energy is $+3\lambda$, while excited states containing two separate indirect solitons have energy $+4\lambda$. Therefore, indirect solitons are characterized by a binding energy λ; moreover, one may easily see that isolated solitons may effectively introduce disorder in the global configuration of the system, while coupled solitons only reduce the magnetization of each of the two antiferromagnetic sublattices.[40] In fact, strings containing any odd (even) number of adjacent solitons act on the order of the global configuration as if they were isolated (coupled) solitons.

As we move from the Ising limit, the transverse interaction $\Sigma_i(S_i^x S_{i+1}^x+S_i^y S_{i+1}^y)$ comes into play, and it is seen[41] to lower the energy of the system more efficiently by delocalizing indirect solitons rather than single deviations or direct solitons, thus indicating that configurations which uniquely contain indirect solitons are crucial in understanding how the system evolves from the Ising limit (Néel phase) to the isotropic case (Haldane phase).

From the above ideas we may draw a simple but suggestive scheme for such evolution:

—in the Ising limit $(\lambda\to\infty)$ the ground state is the antiferromagnetically ordered Néel state;

—as λ decreases, indirect solitons appear along the chain in pairs, thus keeping the antiferromagnetic order;

—as λ is further lowered, indirect soliton pairs dissociate due to the transverse interaction which, by spreading solitons along the chain, can cause the ground state to be disordered.

Due to the privileged role of indirect solitons in the above scheme, we concentrate on configurations which contain only indirect solitons. Such configurations generate a subspace for the Hilbert space of the system, which is referred to in the literature as the reduced Hilbert space.[42] States belonging to the reduced Hilbert space are strongly characterized by the fact that if one eliminates all the sites with $S^z=0$, a perfectly antiferromagnetically ordered chain is left. Remarkably, this type of order, which is called *hidden order* in the literature, is not destroyed by dissociation of soliton pairs, and it actually characterizes the disordered ground state of a Haldane system, as discussed below.

In 1992 Kennedy and Tasaki (KT) defined a nonlocal unitary transformation[43] which makes the *hidden order* visible, meanwhile clarifying its meaning. The transformation is defined by

$$U=(-1)^{N_0+[N/2]}\prod_k U_k$$

with

$$U_k=\frac{1}{2}\left[\exp\left(i\pi\sum_{p=1}^{k-1}S_p^z\right)-1\right]\exp(i\pi S_k^x)$$
$$+\frac{1}{2}\left[\exp\left(i\pi\sum_{p=1}^{k-1}S_p^z\right)+1\right],$$

where N is the number of sites of the chain, $[N/2]$ is the integer part of $N/2$, and N_0 is the number of odd sites where $S^z=0$. If the pure state $|\Psi\rangle$ has *hidden* order, meaning that it only contains indirect solitons, then $U|\Psi\rangle$ has spins with $S^z\neq 0$ all parallel to each other. This point is made transparent by the introduction of the string order parameter[44]

$$O^{\alpha}_{\text{string}}(\mathcal{H})\equiv\lim_{|i-j|\to\infty}\left\langle S_i^{\alpha}\exp\left[i\pi\sum_{l=i}^{j-1}S_l^{\alpha}\right]S_j^{\alpha}\right\rangle_{\mathcal{H}}, \tag{19}$$

where $\alpha=x,\ y,\ z$, and $\langle\ldots\rangle_{\mathcal{H}}$ indicates the expectation value over the ground state of the Hamiltonian $\mathcal{H}$. It may be shown that $O^z_{\text{string}}\neq 0$ if and only if the ground state belongs to the *reduced* Hilbert space. In other terms, while ferromagnetic order is revealed by the ferromagnetic order parameter

$$O^{\alpha}_{\text{ferro}}=\lim_{|i-j|\to\infty}\langle S_i^{\alpha}S_j^{\alpha}\rangle_{\mathcal{H}},$$

the *hidden* order is revealed by the *string* order parameter Eq. (19). In fact, the nonlocal transformation U relates the above order parameters through the relation

$$O^{\eta}_{\text{string}}=O^{\eta}_{\text{ferro}}(U\mathcal{H}U^{-1}), \tag{20}$$

for $\eta=x,z$, meaning that the analysis of the *hidden* order in a system described by $\mathcal{H}$ may be developed by studying the ferromagnetic order in the system described by the transformed Hamiltonian $\tilde{\mathcal{H}}\equiv U\mathcal{H}U^{-1}$, which reads, for $\mathcal{H}$ defined by Eq. (18),

$$\frac{\tilde{\mathcal{H}}}{J}=\sum_i\left[-S_i^xS_{i+1}^x+S_i^y\mathrm{e}^{i\pi(S_i^z+S_{i-1}^x)}S_{i+1}^y-\lambda S_i^zS_{i+1}^z\right.$$
$$\left.+d(S_i^z)^2\right]. \tag{21}$$

Our work developed as follows: one first assumes that the relevant configurations, as far as the Néel-Haldane transition is concerned, belong to the *reduced* Hilbert space; this permits, by the KT transformation, to restrict the analysis to the subspace of states with either $S_i^z=1$ or $S_i^z=0$, $\forall i$. Then the expectation value of the transformed Hamiltonian $\tilde{\mathcal{H}}$ in Eq. (21) is minimized on a trial ground state whose structure takes into account at least short-range correlations between spins. By this procedure, we aim at following the effective dissociation of soliton pairs, in order to clarify the connection between the occurrence of isolated solitons in the ground state, and the transition towards the completely disordered Haldane phase.[39,41,42,45]

In the framework of a standard variational approach, we should minimize $\langle\Phi_0|\mathcal{H}|\Phi_0\rangle$ with respect to a certain number of variational parameters entering the expression of the normalized trial ground-state $|\Phi_0\rangle$. By applying the nonlocal unitary transformation $\mathcal{U}$ we instead minimize $\langle\Psi_0|\mathcal{U}\mathcal{H}\mathcal{U}^{-1}|\Psi_0\rangle$ with $|\Psi_0\rangle\equiv\mathcal{U}|\Phi_0\rangle$ and the transformed Hamiltonian $\tilde{\mathcal{H}}\equiv\mathcal{U}\mathcal{H}\mathcal{U}^{-1}$ defined by Eq. (21); if $|\Phi_0\rangle$ belongs to the reduced Hilbert space, it is

$$|\Psi_0\rangle\equiv\mathcal{U}|\Phi_0\rangle=\sum_{\{s\}}c_{\{s\}}|s_1s_2\ldots s_N\rangle \tag{22}$$

with $\{s\}\equiv(s_1,s_2,s_3,\ldots s_N)$ and $s_i\equiv\langle\Psi_0|S_i^z|\Psi_0\rangle=+1,0$.

The simplest trial ground state allowing the description of soliton pair dissociation is that defined by Eq. (22) with $c_{\{s\}}=t_{s_1s_2s_3}t_{s_2s_3s_4}\ldots t_{s_{N-2}s_{N-1}s_N}$. The variational parameters are the six amplitudes t_{+++}, $t_{+-0}=t_{0++}$, t_{+0-}, t_{0+0}, $t_{00+}=t_{+00}$, t_{000}, where $|t_{s_{i-1}s_is_{i-1}}|^2$ represents the probability for $(S_{i-1}^z,S_i^z,S_{i+1}^z)$ to be equal to (s_{i-1},s_i,s_{i+1}); a common arbitrary factor may be used for normalizing $|\Psi_0\rangle$. We notice that the chosen form for $c_{\{s\}}$ is such that the probability for $|\Psi_0\rangle$ to contain coupled solitons is finite independently of that relative to the occurrence of isolated solitons, whose presence is unambiguously marked by $t_{+0+}\neq 0$.

Without going into the details of the variational calculations, reported in Ref. 46, we discuss here our final results. Due to the normalization condition, the number of variational parameters is reduced from six to five; moreover, the energy $\langle\Psi_0|\mathcal{U}\tilde{\mathcal{H}}\mathcal{U}^{-1}|\Psi_0\rangle$ is found to depend just on four precise combinations of the original parameters,

$$\gamma\equiv|t_{++0}|^2|t_{00+}|^2\Rightarrow(\cdots++00++\cdots),$$
$$\pi\equiv|t_{++0}|^2|t_{+0}|\Rightarrow(\cdots++0++\cdots),$$
$$\chi\equiv|t_{00+}|^2|t_{0+0}|\Rightarrow(\cdots00+00\cdots),$$
$$\rho\equiv|t_{000}|\Rightarrow(\cdots000\cdots), \tag{23}$$

whose square moduli are related to the probabilities that the corresponding strings ($\Rightarrow$) be contained in $|\Psi_0\rangle$; in particular, γ^2 and π^2 refer to the probabilities for coupled and isolated solitons, respectively, to occur in the ground state.

Both the analytical expression for the energy and the numerical minimization show that a critical value $\lambda_c=\lambda_c(d)>d$ exists such that for $\lambda>\lambda_c$ the minimal energy is attained for $\pi=\rho=0$; the condition $\lambda=\lambda_c(d)$ can, hence, define a curve of phase separation. We therefore single out three different phases, characterized by

$$(a)\pi=\rho=0,(b)\text{all parameters}\neq 0,(c)\chi=t_{+++}=0 \tag{24}$$

in the ground state. The corresponding phase diagram is shown in Fig. 6, together with that obtained with a factorized trial ground state[43] and by numerical simulations.[33]

The $(a)-(b)$ transition is seen to quite precisely describe the Néel-Haldane one, and this leads us to define the condition (a), meaning the occurrence of exclusively coupled solitons, as typical of the Néel phase. As to the $(c)-(b)$ transition, one should note that the use of the reduced Hilbert space is not fully justified in the $\lambda<d$ region, where we in fact do not expect quantitatively precise results.

For a comparison between our results and the exact numerical data available, we have considered, along the $d=0$ axis, two specific quantities: the critical anisotropy $\lambda_c(d)$, where the Néel phase becomes unstable with respect to the Haldane phase, and the ground-state energy $E_0(d,\lambda)$ at the isotropic point $\lambda=1$. For the critical anisotropy we find $\lambda_c(0)=1.2044(5)$ as compared to the value obtained by exact diagonalization,[37] $\lambda_c(0)\approx 1.19$; for the energy we find $E_0(0,1)=-1.3663(5)$ as compared to $E_0(0,1)=$

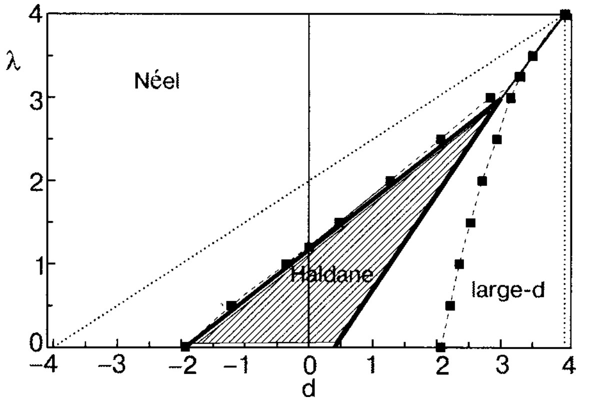

FIG. 6. Phase diagram in the $\lambda>0$ half-plane: our results (squares) are shown together with those of Ref. 43 (dotted lines); the Haldane phase should correspond to the shaded area, according to the best available numerical data[33] (solid lines).

$-1.4014(5)$, again from an exact diagonalization technique;[47] the value obtained with the factorized trial ground state is $E_0(0,1)=-4/3$.[43]

In Fig. 7 we show the variational parameters as λ is varied for $d=0$, i.e., along the y axis of the phase diagram; in fact, rather than the parameters with respect to which we have actually minimized the energy, the following combinations are considered:

$$w_{(1)}=\pi^2/t^2_{+++};\quad w_{(2)}=\gamma;$$

$$w_{(2,2)}=(\chi\gamma t_{+++})^{1/2};\quad w_{(3)}=t^2_{+++}(\rho\gamma)^{2/3}. \tag{25}$$

The above quantities have a straightforward physical meaning, as they are directly related with the probabilities for a soliton to appear along the chain as an isolated excitation ($w_{(1)}$), as a part of a soliton pair ($2w^2_{(2)}$), as a part of a string made of three adjacent solitons ($3w^3_{(3)}$), and finally as a part of a string made of two soliton pairs separated by one site ($4w^4_{(2,2)}$). From Fig. 7, it becomes evident that the Haldane phase is featured by the occurrence of isolated solitons ($w_{(1)}\neq 0$), as well as of strings made of three adjacent solitons ($w_{(3)}\neq 0$).

This result confirms that, as elicited by the analysis of the phase diagram, the Haldane phase is characterized by our condition (b).

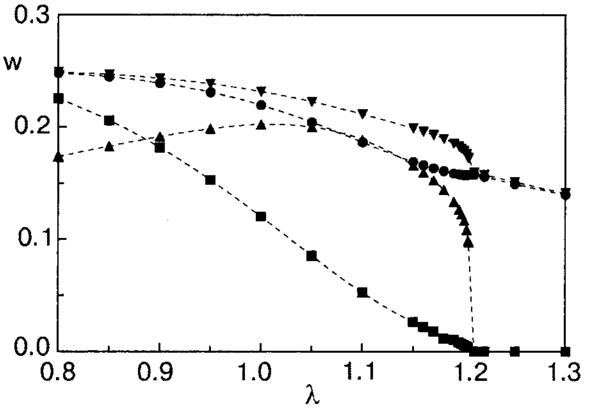

FIG. 7. Parameters $w_{(1)}$ (squares), $w_{(2)}$ (circles), $w_{(3)}$ (upward triangles), and $w_{(2,2)}$ (downward triangles) for $d=0$.

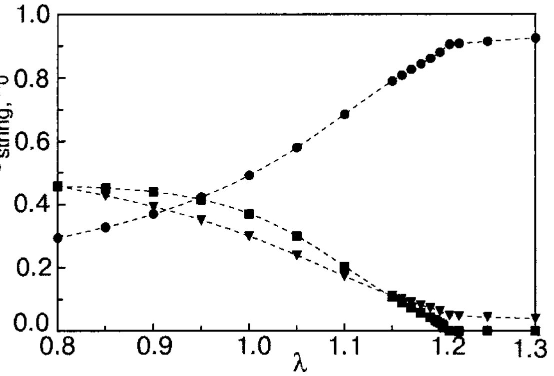

FIG. 8. String order parameters O^x_{string} (squares), O^z_{string} (circles), and soliton density n_0 (triangles) for $d=0$.

Given their essential role, we have also studied the x and z components of the string order parameter, as well as the soliton density $n_0=1-\langle(S^z)^2\rangle$. After KT we expect $O^z_{\text{string}}(\mathcal{H})\neq 0$ in both the Néel and the Haldane phase, and $O^x_{\text{string}}(\mathcal{H})\neq 0$ just in the Haldane phase. In fact, analytical expressions for O^x and O^z may be written[46] in terms of four of the five variational parameters (25), and show that $O^x_{\text{string}}(\mathcal{H})=0$ if $\pi=\rho=0$ or $\chi=t_{+++}=0$, i.e., in phases (a) and (c); $O^z_{\text{string}}(\mathcal{H})>0$ in all phases, asymptotically vanishing as $\rho\to 1$, i.e., in the far large-d phase.

In more detail, we note that $O^x_{\text{string}}=0$ whenever the ground state does not contain strings made of an odd number of adjacent spins; as soon as the shortest string of such type, namely the isolated soliton, appears along the chain, then O^x_{string} becomes finite. The unphysical result $O^z_{\text{string}}>0$ in the (c) phase, vanishing only as $d\to\infty$ rather than everywhere in the large-d phase, is due to our assuming the ground state to belong to the reduced Hilbert space, which actually is licit only in the $\lambda>d$ region.

In Fig. 8 we show O^x_{string}, O^z_{string}, and n_0 as λ varies with $d=0$. We underline that O^x_{string} becomes finite continuously but with discontinuous derivative at the transition (reflecting the behavior of $w_{(1)}$ and $w_{(3)}$ shown in Fig. 7), so that the Néel-Haldane quantum phase transition is recognized as a second-order one. In Fig. 9 we zoom the order parameter O^x_{string} around the critical point: its behavior is seen to be described by a power law $O^x_{\text{string}}\sim(\lambda_c-\lambda)^\beta$, as

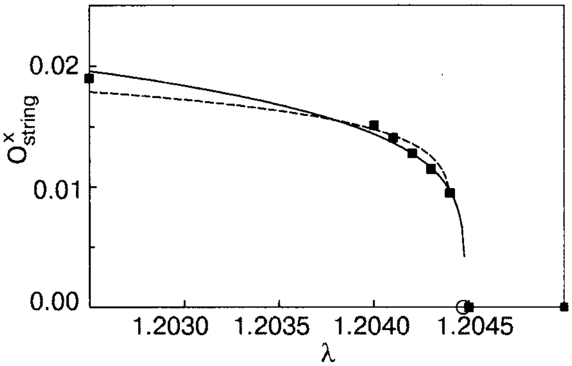

FIG. 9. Critical behavior of O^x_{string} for $d=0$: squares are our results; curves are obtained by best-fit procedure from $O^x_{\text{string}}\sim(\lambda-\lambda_c)^\beta$ with β fixed to 0.125 (dashed curve) and as fitting parameter, resulting in $\beta=0.217$ (solid curve). Both procedures give $\lambda_c=1.2044(5)$, marked by a circle in figure.

expected for a continuous phase transition; our estimated value for the critical exponent is $\beta = 0.217(5)$ as compared to $\beta = 0.125$, corresponding to the Ising model in a transverse field, to whose universality class the Haldane transition is suggested to belong.[42] At the isotropic point $(d=0,\lambda=1)$ we find $O^x_{\text{string}} = 0.3700(5)$, in full agreement with the value obtained by exact diagonalization.[48]

The overall good agreement between our results and the numerical data available, allows us to conclude that the Néel-Haldane transition is a second-order one, and that the string order parameter O^x_{string}, revealing *hidden* order along the x direction, is the appropriate order parameter for the Haldane phase. The disordered ground state featuring the Haldane phase is seen to originate by dissociation of soliton pairs, according to this path. Solitons occur just in pairs in the antiferromagnetically ordered Néel phase; at the Néel-Haldane transition soliton pairs dissociate and the byproducts rearrange into strings consisting of an odd number of solitons. These strings are ultimately responsible for the disorder of the ground state.

IV. TWO-DIMENSIONAL ISOTROPIC HEISENBERG MODEL

The 2D isotropic QHAF on the square lattice is one of the magnetic models most intensively investigated in the last two decades. This is due both to its theoretically challenging properties and to it being considered the best candidate for modeling the magnetic behavior of the parent compounds of some high-T_c superconductors.[2,3]

From a theoretical point of view the fully isotropic Heisenberg model in d dimensions, thanks to the simple structure of its Hamiltonian (whose high symmetry is responsible for most of its peculiar features), may well be considered a cornerstone of the modern theory of critical phenomena, with its relevance extending well beyond the only magnetic systems. The $d=2$ case earned additional interest, representing the boundary dimension separating systems with and without long-range order at finite temperature.[4] The antiferromagnetic coupling adds further appeal, as the classical-like Néel state is made unstable by quantum fluctuations, and the ground state of the system is not exactly known. It can be rigorously proven[19] to be ordered for $S \geqslant 1$; for $S=1/2$ there is no rigorous proof, although evidence for an ordered ground state can be drawn from many different studies (for a review, see, for instance, Ref. 50).

On the experimental side the attention to the properties of 2D QHAF was mainly triggered by the fact that among the best experimental realizations of this model we find several parent compounds of high-T_c superconductors, as, e.g., La_2CuO_4 or $Sr_2CuO_2Cl_2$ (Refs. 51–53), both having spin $S=1/2$. In such materials, as well as in other magnetic compounds with a layered crystal structure, such as La_2NiO_4 (Ref. 54) and K_2NiF_4 (Refs. 52, 53) $(S=1)$, Rb_2MnF_4 (Ref. 55) and $KFeF_4$ (Ref. 56) $(S=5/2)$, or copper formate tetradeuterate (CFTD, $S=1/2$) (Ref. 57), the magnetic ions form parallel planes and interact strongly only if belonging to the same plane. The interplane interaction in these compounds is orders of magnitude smaller than the intraplane one, thus offering a large temperature region where their magnetic behavior is indeed 2D down to those low temperatures where the weak interplane interaction becomes relevant, driving the system towards a 3D ordered phase: an antiferromagnetic Heisenberg interaction and the small spin value make these compounds behave as 2D QHAFs. Even the onset of 3D magnetic long-range order is however strongly affected by the 2D properties of the system: indeed, the observed 3D magnetic transition temperature is comparable with the intraplane interaction energy, i.e., orders of magnitude larger than one would expect solely on the basis of the value of the interplane coupling. Such apparently odd behavior can be easily understood by observing that the establishing of inplane correlations over a characteristic distance ξ effectively enhances the interplane coupling by a factor $(\xi/a)^2$, a being the lattice constant. The latter consideration is one of the reasons explaining why most of the attention, both from the experimental and theoretical point of view, has been paid to the low-temperature behavior of the correlation length ξ of the 2D QHAF (in the following ξ will always be given in units of the lattice constant a).

The 2D QHAF is described by the Hamiltonian

$$\mathcal{H} = \frac{J}{2} \sum_{\mathbf{i},\mathbf{d}} \mathbf{S}_i \cdot \mathbf{S}_{\mathbf{i}+\mathbf{d}}, \tag{26}$$

where J is positive and the quantum spin operators $\mathbf{S}_i$ satisfy $|\mathbf{S}_i|^2 = S(S+1)$. The index $\mathbf{i} \equiv (i_1, i_2)$ runs over the sites of a square lattice, and $\mathbf{d}$ represents the displacements of the 4 nearest-neighbors of each site, $(\pm 1,0)$ and $(0,\pm 1)$.

In addition to the first approximations usually employed to investigate the low-temperature properties of magnetic systems as, e.g., mean-field and (modified) spin-wave theory, the critical behavior of the 2D QHAF was commonly interpreted on the basis of the results obtained by field theory starting from the so-called 2D *quantum nonlinear σ model* (QNLσM),[58] whose action is given by

$$S = \frac{1}{2g} \int d\mathbf{x} \int_0^u d\tau \left(|\nabla \mathbf{n}|^2 + |\partial_\tau \mathbf{n}|^2 \right); \quad |\mathbf{n}|^2 = 1. \tag{27}$$

In the last equation $\mathbf{n}(\mathbf{x})$ is a unitary 3D vector field, $g = c\Lambda/\rho$ and $u = c\Lambda/T$ are the coupling and the imaginary-time cut-off, respectively, and the two parameters ρ and c are usually referred to as *spin stiffness* and *spin-wave velocity*. Despite their names, however, the two parameters ρ and c are just phenomenological fitting constants which can be rigorously related to the proper parameters J and S of the original magnetic Hamiltonian (26) only in the large-S limit.[1,59] The source of nonlinearity in the model of Eq. (27), which is seemingly quadratic in the field variables, is the constraint imposed on the length of the field $\mathbf{n}$.

The relation between the 2D QHAF and the QNLσM was first exploited to interpret the experimental data on cuprous oxides by Chakravarty, Halperin, and Nelson (CHN),[58] who used symmetry arguments to show that the long-wavelength physics of the QHAF is the same of that of the QNLσM; in other words, the physical observables of the two models show the same functional dependence upon T, if the long-wavelength excitations are assumed to be the only relevant ones, as one expects to be at low temperature.

The analysis carried out by CHN on the QNLσM leads one to single out three different regimes, called quantum disordered, quantum critical (QCR), and renormalized classical (RCR), the most striking difference amongst them being the temperature dependence of the spin correlations. If g is such as to guarantee LRO at $T=0$, the QNLσM is in the RCR at very low temperature, and the correlation length ξ behaves as[60]

$$\xi_{3l}=\frac{e}{8}\left(\frac{c}{2\pi\rho}\right)\exp\left(\frac{2\pi\rho}{T}\right)\left[1-\frac{T}{4\pi\rho}\right]. \tag{28}$$

CHN also found that by raising the temperature, any 2D QNLσM with an ordered ground state crosses over from the RCR to the QCR, characterized by a correlation length $\xi \propto \alpha(T)=c/T$.

The first direct comparison between experimental data on spin-1/2 compounds and the prediction of the QNLσM field theory in the RCR gave surprisingly good agreement and caused an intense activity, both theoretical and experimental, in the subsequent years. However, with the accumulation of new experimental data on higher-spin compounds it clearly emerged that the experimentally observed behavior of $\xi(T)$ for larger spin could be reproduced neither by the original simplified (two-loop) form of Eq. (28) given by CHN (which does not contain the term in square brackets) nor by the three-loop result (28) derived by Hasenfratz and Niedermayer (HN);[60] moreover, no trace of QCR behavior was found in pure compounds. The discrepancies observed could be due to the fact that the real compounds do not behave like 2D QHAF or to an actual inadequacy of the theory. In particular the CHN-HN scheme introduces two possible reasons for such inadequacy to occur: the physics of the 2D QHAF is not properly described by that of the 2D QNLσM and/or the two(three)-loop renormalization-group expressions derived by CHN-HN do hold at temperatures lower than those experimentally accessible. After an almost ten-year debate, the latter possibility has finally emerged as the correct one, being strongly supported not only by our own work but also by other independent theoretical approaches,[61] joined with the analysis of the experimental and the most recent quantum Monte Carlo (QMC) data for the 2D QHAF.

The theoretical approach we employed to investigate the 2D QHAF is the effective Hamiltonian method,[62–64] developed within the framework of the *pure-quantum self-consistent harmonic approximation* (PQSCHA) we introduced at the beginning of the 1990s.[65,66] The PQSCHA starts from the Hamiltonian path-integral formulation of statistical mechanics, which allows one to separate in a natural way classical and quantum fluctuations; only the latter are then treated in a self-consistent harmonic approximation, finally yielding an effective classical Hamiltonian whose properties can thereafter be investigated by all the techniques available for classical systems. The idea of separating classical and quantum fluctuations turned out to be fruitful not only in view of the implementation of the PQSCHA, but also in the final understanding of the connection between semiclassical approaches and quantum field theories,[67] which could be possible also thanks to the paper by Hasenfratz[68] about corrections to the field-theoretical results due to cutoff effects.

The PQSCHA naturally applies to bosonic systems, whose Hamiltonian is written in terms of conjugate operators $\hat{q}\equiv(\hat{q}_1,\ldots\hat{q}_N)$, $\hat{p}\equiv(\hat{p}_1,\ldots\hat{p}_N)$ such that $[\hat{q}_m,\hat{p}_n]=i\delta_{mn}$; the method, however, does not require $\mathcal{H}(\hat{p},\hat{q})$ to be standard, i.e., with separate quadratic kinetic $\hat{p}$-dependent and potential $\hat{q}$-dependent terms, and its application may be extended also to magnetic systems, according to the following scheme.[65] The spin Hamiltonian $\mathcal{H}(\mathbf{S})$ is mapped to $\mathcal{H}(\hat{p},\hat{q})$ by a suitable spin-boson transformation; once the corresponding Weyl symbol $\mathcal{H}(\underline{p},\underline{q})$ with $\underline{p}\equiv(\underline{p}_1,\ldots p_N)$ and $\underline{q}\equiv(q_1,\ldots q_N)$ classical phase-space variables, has been determined, the PQSCHA renormalizations may be evaluated, and the effective classical Hamiltonian $\mathcal{H}_{\rm eff}(\underline{p},\underline{q})$ and effective classical function $\mathcal{O}_{\rm eff}(\underline{p},\underline{q})$ corresponding to the observable $\mathcal{O}$ of interest follow. Finally, the effective functions $\mathcal{H}_{\rm eff}(\underline{\mathbf{s}})$ and $\mathcal{O}_{\rm eff}(\underline{\mathbf{s}})$, both depending on classical spin variables $\mathbf{s}$ with $|\mathbf{s}|=1$ and containing temperature- and spin-dependent quantum renormalized parameters, are reconstructed by the inverse of the classical analog of the spin-boson transformation used at the beginning.

In order to successfully carry out such a renormalization scheme, the Weyl symbol of the bosonic Hamiltonian must be a well-behaved function in the whole phase space. Spin-boson transformations, on the other hand, can introduce singularities as a consequence of the topological impossibility of a global mapping of a spherical phase space into a flat one. The choice of the transformation must then be such that the singularities occur for configurations which are not thermodynamically relevant, and whose contribution may be hence be approximated. Most of the methods for studying magnetic systems do in fact share this problem with the PQSCHA; what makes the difference is that by using the PQSCHA one separates the classical contribution to the thermal fluctuations from the pure quantum one, and the approximation only regards the latter, being the former exactly taken into account when the effective Hamiltonian is recast in the form of a classical spin Hamiltonian.

The spin-boson transformation which constitutes the first step of the magnetic PQSCHA is chosen according to the symmetry properties of the original Hamiltonian and of its ground state. In the case of the 2D QHAF both Dyson-Maleev and Holstein-Primakoff transformation can be employed, finally yielding:[63]

$$\frac{\mathcal{H}_{\rm eff}}{J\tilde{S}^2}=\frac{\theta^4}{2}\sum_{\mathbf{i},\mathbf{d}}\mathbf{s_i}\cdot\mathbf{s_{i+d}}+N\mathcal{G}(t), \tag{29}$$

$$\mathcal{G}(t)=\frac{t}{N}\sum_{\mathbf{k}}\ \ln\frac{\sinh f_k}{\theta^2 f_k}-2\kappa^2\mathcal{D}, \tag{30}$$

with the temperature- and spin-dependent parameters

$$\theta^2=1-\frac{\mathcal{D}}{2}, \tag{31}$$

$$\mathcal{D}=\frac{1}{\tilde{S}N}\sum_{\mathbf{k}}\ (1-\gamma_{\mathbf{k}}^2)^{1/2}\mathcal{L}_{\mathbf{k}}, \tag{32}$$

$$f_{\mathbf{k}}=\frac{\omega_{\mathbf{k}}}{2\tilde{S}t},\qquad \mathcal{L}_{\mathbf{k}}=\coth f_{\mathbf{k}}-\frac{1}{f_{\mathbf{k}}}. \tag{33}$$

In the previous equations $\gamma_{\mathbf{k}}=(\cos k_1+\cos k_2)/2$, N is the number of sites of the lattice, and $\mathbf{k}\equiv(k_1,k_2)$ is the wave vector in the first Brillouin zone; $\tilde{S}\equiv S+1/2$ is the effective classical spin length, which naturally follows from the renor-

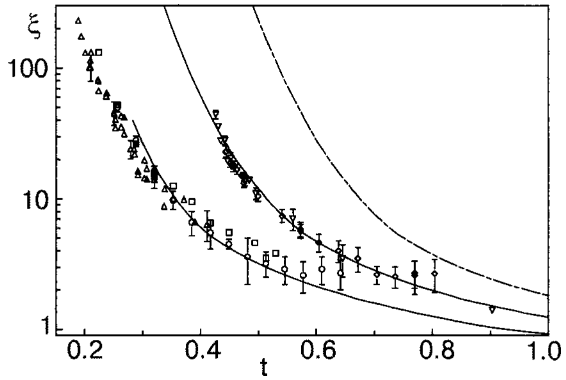

FIG. 10. Correlation length ξ versus t, for $S=1/2$ (leftmost) and $S=1$. The symbols are experimental data; for $S=1/2$: ^{63}Cu NQR data[70] (circles) and neutron scattering data for La_2CuO_4 (squares)[51] and for $Sr_2CuO_2Cl_2$ (up-triangles);[52,53] for $S=1$: neutron scattering data for La_2NiO_4 (down-triangles)[54] and for K_2NiF_4 (diamonds).[52,53] The classical result (dotted-and-dashed line) is also reported.

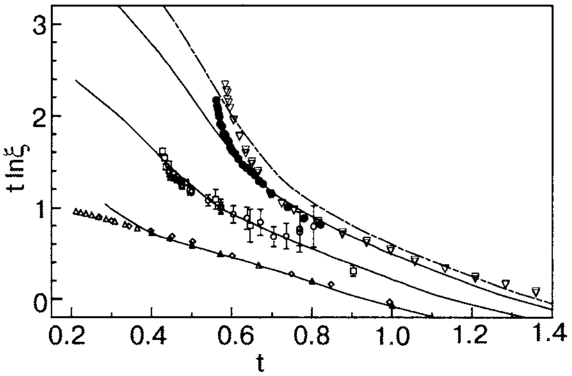

FIG. 11. The function $y(t)=t\ln\xi$ versus t, for (from the rightmost curve) $S=\infty$, 5/2, 1, and 1/2; the up-triangles[71] and the diamonds[72] are quantum MC data for $S=1/2$; also reported are neutron scattering data for La_2NiO_4 (unfilled circles),[54] K_2NiF_4 (squares),[52,53] $KFeF_4$ (filled circles),[56] and Rb_2MnF_4 (down-triangles).[55] The abrupt rising of the experimental data for the $S=5/2$ compounds at $t\simeq 0.65$ is due to the effect of the small, but finite, anisotropies and will be discussed in more detail in Sec. 5.

malization scheme, and $t\equiv T/J\widetilde{S}^2$ is the reduced temperature defined in terms of the energy scale $J\widetilde{S}^2$. The renormalization scheme is closed by the self-consistent solution of the two coupled equations $\omega_{\mathbf{k}}=4\kappa^2(1-\gamma_{\mathbf{k}}^2)^{1/2}$ and $\kappa^2=\theta^2-t/(2\kappa^2)$. The pure-quantum renormalization coefficient $\mathcal{D}=\mathcal{D}(S,t)$ takes the main contribution from the high-frequency part (short-wavelength) of the spin-wave spectrum, because of the appearance of the Langevin function $\mathcal{L}_{\mathbf{k}}$. $\mathcal{D}$ measures the strength of the pure-quantum fluctuations, whose contribution to the thermodynamics of the system is the only approximated one in the PQSCHA scheme. The theory is hence quantitatively meaningful as far as $\mathcal{D}$ is small enough to justify the self-consistent harmonic treatment of the pure-quantum effects. In particular, the simple criterion $\mathcal{D}<0.5$ is a reasonable one to assess the validity of the final results.

The most relevant information we get from Eq. (29) is that the symmetry of the Hamiltonian is left unchanged, so that from a macroscopic point of view the quantum system essentially behaves, at an actual temperature t, as its classical counterpart does at an effective temperature $t_{\text{eff}}=t/\theta^4(S,t)$. This allows us to deduce the behavior of many observables (but not all!—see Refs. 62–64 for details) directly from the behavior of the corresponding classical quantities. This is the case of the correlation length, which turns out to be given simply by

$$\xi(t)=\xi_{\text{cl}}(t_{\text{eff}}) \tag{34}$$

so that once $\theta^4(S,t)$ has been evaluated, the only additional information we need is the classical $\xi_{\text{cl}}(t)$, which is available from *classical* Monte Carlo (MC) simulation and analytical asymptotic expressions[69] as $t\rightarrow 0$.

Sample results obtained by PQSCHA are shown in the figures. In Fig. 10 the correlation length for $S=1/2$ and $S=1$ is compared with experimental data; a similar comparison, including MC data for $S=1/2$ and experimental data on $S=5/2$ compounds $KFeF_4$ and Rb_2MnF_4 is made in Fig. 11, but along the vertical axis the quantity $t\ln\xi$ is plotted in order to better appreciate the deviation from the predicted RCR behavior, that would correspond to a straight line at low t. From the last picture one can easily see that both PQSCHA curves and experimental data for $S\geqslant 1$ (including the exact $S=\infty$ classical result) display a change of slope at intermediate temperature, followed by a curvature inversion at lower t. On the other hand, by looking at the $S=1/2$ case it becomes clear why the QNLσM approach gave such a good agreement when first used to fit the experimental data. The change in both the slope and the curvature of $t\ln\xi$ is less pronounced and possibly occurs at lower temperatures, the lower the spin: in the $S=1/2$ case, it is difficult to say whether these features are still present or not, but, if yes, they occur in a temperature region where the extremely high value of ξ ($\approx 10^4$) makes both the experimental and the simulation data more difficult to obtain.

After having realized that the field theoretical prediction by CHN could not be applied to the $S\geqslant 1$ 2D QHAF in the temperature range probed by the experiments, the following questions were waiting for a satisfactory answer: (i) the real range of applicability of the asymptotic three-loop expression (28) at different S, and (ii) the possible extension of the PQSCHA results to lower temperature, both in view of (iii) a comprehensive description of the behavior of the correlation length of the 2D QHAF in the entire range of temperature and spin values.

A substantial contribution to settle this conundrum came only from QMC simulations for higher spin values able to probe the very large correlation length region:[73] indeed, high-precision Monte Carlo data for $S=1$ and moderate correlation length could still be very well interpreted by PQSCHA and did not display the RCR asymptotic behavior, as shown[64] in Fig. 12, where we compared our curves for ξ and the staggered susceptibility χ^* with QMC data obtained by Harada *et al.*[74]

QMC results for ξ by Beard and coworkers[73] showed unambiguously that the three-loop Eq. (28) holds only for temperatures low enough to ensure an extremely large correlation length, e.g., $\xi\gtrsim 10^5$ for $S=1$, $\xi\gtrsim 10^{12}$ for $S=3/2$, and generally cosmological correlation lengths for $S>3/2$, thus definitely excluding any possibility of employing QNLσM results to interpret available experimental data.

In Ref. 68, Hasenfratz showed why cutoff effects, which

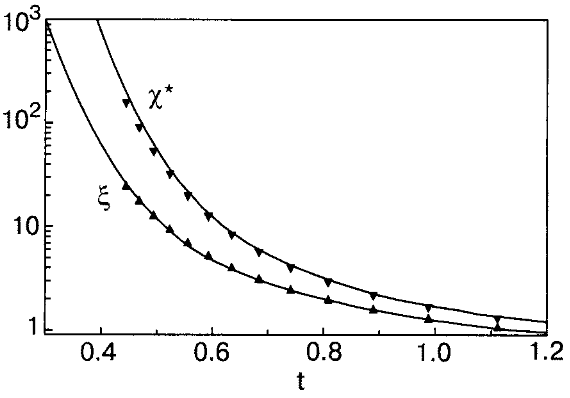

FIG. 12. Correlation length ξ and staggered susceptibility $\chi^* \equiv \chi/\tilde{S}^2$ versus t for $S=1$. Symbols are QMC data from Ref. 74.

are so devious for $S=1/2$, significantly modify the correlation length for $S \geqslant 1$. Reaching such goal was possible only going back to a direct mapping between the QHAF and the QNLσM, and the resulting cutoff-corrected field-theoretical outcome is[68]

$$\xi_H(T,S)=\xi_{3l}(T,S)\mathrm{e}^{-C(T,S)}, \tag{35}$$

where $C(T,S)$, defined in Eq. (14) of Ref. 68, is an integral of familiar spin-wave quantities over the first Brillouin zone.

With this correction, which is the leading order in the spin-wave expansion for the cutoff correction, it is possible to obtain numerically accurate agreement with QMC data down to $\xi \gtrsim 10^3$ for all S.

In our most recent paper[67] about 2D QHAF we showed that by employing the explicit expression for $C(T,S)$, and by substituting in Eq. (28) the spin stiffness ρ and the spin-wave velocity c given by the mapping of QHAF onto the QNLσM, the leading terms of the result (35) not only can be cast in the form $\xi_H(T,S)=\xi_{3l}^{\mathrm{cl}}(t_{\mathrm{eff}}^H)$, in strict analogy with the PQSCHA expression (34), but the effective temperature t_{eff}^H is defined through a renormalization constant which is again a function of the pure-quantum fluctuations only! Such a remarkable and unexpected feature of the cutoff-corrected field-theory prediction suggested that we replace the perturbative expression ξ_{3l}^{cl} with the exactly known classical ξ_{cl}, thus getting the results presented in Fig. 13.

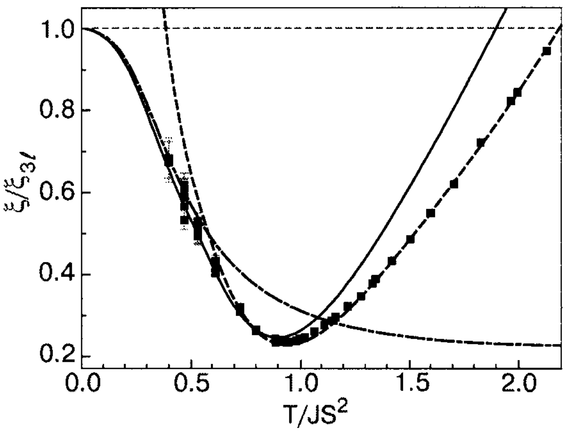

FIG. 13. Ratio ξ/ξ_{3l} versus T/JS^2 for $S=5/2$. Solid line: $\xi_{\mathrm{cl}}(t_{\mathrm{eff}}^H)$; dotted-and-dashed line: $\xi_H \simeq \xi_{3l}^{\mathrm{cl}}(t_{\mathrm{eff}}^H)$; dashed line: standard PQSCHA result; symbols are QMC data.[67]

It is thus made clear that the main features of the quantum correlation length at intermediate temperatures are due to essentially classical nonlinear effects, which cannot be taken into account by perturbative approaches. Moreover, the effective exchange constant that defines the effective temperature t_{eff}^H is seen to depend on the same pure-quantum renormalization coefficients defined by the PQSCHA, according to an expression which is very similar (equal) to that found by the latter approach in its standard (low-T) version: the behavior of ξ in the full temperature and spin-value ranges can thus be quantitatively described by Eq. (34) without any adjustable fitting parameter.

The results obtained by the PQSCHA about the correlation length and other static quantities can also represent the needed information to be inserted within other frameworks, like *mode-coupling* theory, to interpret experiments probing dynamic quantities, like nuclear magnetic resonance (NMR): an example of the successful combination of PQSCHA and mode-coupling theory is given in Ref. 57.

V. TWO-DIMENSIONAL ANISOTROPIC HEISENBERG MODEL

While the theoretical debate mentioned in the previous Section has been mainly dedicated to the isotropic 2D QHAF, real compounds are not actually well described by the isotropic model when the temperature is low: indeed, the Mermin-Wagner theorem[4] states that a finite-temperature transition cannot occur in the 2D isotropic QHAF, while the experimental evidence of a transition suggests that 3D correlations and anisotropy effects, as well as a combination of both, must be considered. Easy-axis (EA) or easy-plane (EP) anisotropies turn out to be fundamental in the analysis of the critical behavior.

A. 2D antiferromagnet with easy-axis anisotropy

Several works (see Ref. 75 for a review) have shown that many additional interaction mechanisms may be taken into account by inserting proper anisotropy terms in the magnetic Hamiltonian; in particular, the transition observed in K_2NiF_4 (Ref. 76) ($S=1$), Rb_2FeF_4 (Ref. 76) ($S=2$), K_2MnF_4 (Ref. 77) and Rb_2MnF_4 (Ref. 76) ($S=5/2$), and others is seen to be possibly due to an easy-axis anisotropy. Such anisotropy has been often described in the literature through an external staggered magnetic field in order to allow for a qualitative description of the experimental data. However, this choice lacks the fundamental property of describing a genuine phase transition, as the field explicitly breaks the symmetry and makes the model ordered at all temperatures. To preserve the symmetry under inversion along the easy axis, it is actually appropriate to insert an exchange anisotropy term in the spin Hamiltonian. Spontaneous symmetry breaking then manifests itself as a phase transition between ordered and disordered states. The EA-QHAF Hamiltonian then reads

$$\mathcal{H}=\frac{J}{2}\sum_{\mathbf{i},\mathbf{d}}\left[\mu(S_{\mathbf{i}}^x S_{\mathbf{i}+\mathbf{d}}^x+S_{\mathbf{i}}^y S_{\mathbf{i}+\mathbf{d}}^y)+S_{\mathbf{i}}^z S_{\mathbf{i}+\mathbf{d}}^z\right], \tag{36}$$

where $\mathbf{i}=(i_1,i_2)$ runs over the sites of a square lattice, $\mathbf{d}$ connects each site to its four nearest neighbors, $J>0$ is the exchange integral, and μ is the EA anisotropy parameter ($0 \leqslant \mu < 1$). Again, $J\tilde{S}^2 \equiv J(S+1/2)^2$ sets the overall energy scale, and $t=T/J\tilde{S}^2$ is the reduced temperature. The model reduces to the isotropic QHAF when $\mu=1$. Note that a canonical transformation reversing the x and y spin components of one sublattice is equivalent to setting $\mu \rightarrow -\mu$, so that the physical properties of the model are even functions of μ. The $\mu=0$ case is called *Ising limit*, not to be confused with the genuine Ising model,[78] reproduced by Eq. (36) with $\mu=0$ and $S=1/2$. Despite being a very particular case of Eq. (36), the 2D Ising model on the square lattice is a fundamental point of reference for the study of the thermodynamic properties of the EA-QHAF. A renormalization-group analysis[79] of the classical model predicted the occurrence of an Ising-like transition at a finite temperature $t_c^{\rm cl}(\mu)$ of the order of unity for any value of μ, no matter how near to the isotropic value $\mu=1$; this analysis has received the support of several Monte Carlo simulations.[80–83]

As for the quantum case, up to a few years ago no information was available about the value of the critical temperature $t_c(\mu,S)$ as a function of anisotropy and spin, save the fact that $t_c(0,1/2)=0.567J$ (Onsager solution)[78] and $t_c(1,S)=0$ (isotropic limit). As a consequence, it was also uncertain whether or not the small anisotropy ($1-\mu \simeq 10^{-2}$) observed in real compounds could be responsible for transitions occurring at critical temperatures of the order of J, also accounting for the fact that quantum fluctuations are expected to lower the critical temperature with respect to the classical case.

Over the last few years our group developed a quantitative analysis of several thermodynamic properties of the model, by means of the effective Hamiltonian method[65,66] for spin $S \geqslant 1$ and by means of quantum Monte Carlo simulations[84] in the case $S=1/2$.

The effective Hamiltonian[85–87] for the EA-QHAF is expressed as

$$\frac{\mathcal{H}_{\rm eff}}{J\tilde{S}^2}=\frac{j_{\rm eff}}{2}\sum_{\mathbf{i},\mathbf{d}} [\mu_{\rm eff}(s^x_{\mathbf{i}} s^x_{\mathbf{i}+\mathbf{d}}+s^y_{\mathbf{i}} s^y_{\mathbf{i}+\mathbf{d}})+s^z_{\mathbf{i}} s^z_{\mathbf{i}+\mathbf{d}}], \tag{37}$$

and shows a weaker renormalized exchange $j_{\rm eff}(t,\mu)<1$ and easy-axis anisotropy $\mu_{\rm eff}(t,\mu)>\mu$, besides an additional free-energy term that is not reported. By means of $\mathcal{H}_{\rm eff}$ a series of thermodynamic quantities was studied:[85,88] internal energy, specific heat, staggered magnetization, staggered correlation function, staggered correlation length, staggered susceptibility. This required extensive classical Monte Carlo simulations, as varying the temperature gives an effective system with different effective anisotropy $\mu_{\rm eff}(t,\mu)$. The quantum phase diagram reported in Fig. 14 could be built up[87,89] in a simpler way starting from the knowledge of the classical phase diagram and using a relation that follows from the form of Eq. (37),

$$t_c(\mu,S)=j_{\rm eff}(t,\mu,S)\,t_c^{\rm cl}(\mu_{\rm eff}(t,\mu,S)). \tag{38}$$

In the region of very weak anisotropy, which is the most important in view of the characterization of experimentally accessible materials, we verified that the Ising-like transition temperature decreases very slowly (logarithmically) towards its vanishing value in the isotropic limit, so that t_c remains substantially of the order of unity.

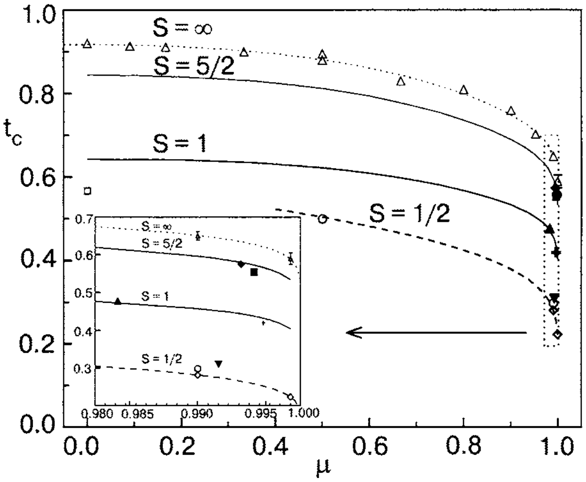

FIG. 14. Critical temperature versus anisotropy μ for the 2D easy-axis antiferromagnet. Dotted line: the fit of $t_c^{\rm cl}(\mu)$ built up from classical MC data[82,83,87] (unfilled triangles). Solid lines: PQSCHA result for $S=1$ and 5/2. Quantum MC data (unfilled circles[90] and diamonds[84]) for $S=1/2$, asymptotically described by $t_c(\mu)=2.49/\ln[70/(1-\mu)]$ (dashed line), and exact result for the Ising model, $\mu=0$ (unfilled square). Filled symbols are experimental data for the compounds $\rm YBa_2Cu_3O_6$ (down triangle),[91] $\rm K_2NiF_4$ (cross),[92,93] $\rm Rb_2NiF_4$ (up triangle),[94] $\rm Rb_2MnCl_4$ (circle),[95] $\rm Rb_2MnF_4$ (diamond).[92,96] In the inset the region of weak anisotropy is enlarged.

As a sample of the various results that were obtained, in Fig. 15 we report the comparison of the results of Ref. 85 with the experimental data[97] for the correlation length of the $S=5/2$ magnet $\rm Rb_2MnF_4$, which results are quite well described by the anisotropic model with $J=7.42$ K and $\mu=0.9942$. $\rm Rb_2MnF_4$ is known to behave as a 2D magnet both above and below the observed transition,[76] so that the critical behavior is not contaminated by the onset of 3D order and a clean characterization of the transition is possible. In Ref. 85, we have compared our theoretical results also with the neutron-scattering experimental data for the staggered magnetization, staggered susceptibility, and correlation length of $\rm Rb_2MnF_4$ and found excellent agreement both for the overall temperature behavior and for the value of the

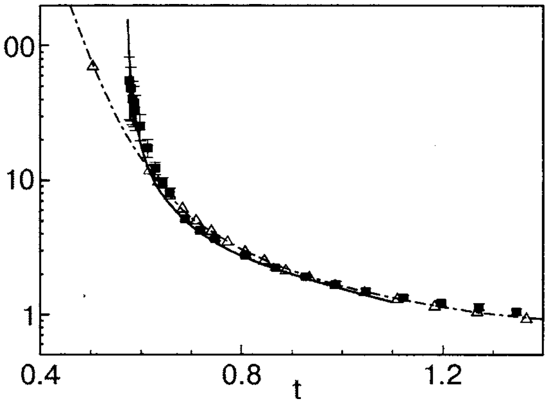

FIG. 15. Correlation length versus t for $S=5/2$, $\mu=0.9942$ (full curve) and $\mu=1$ (isotropic, dotted-and-dashed curve); the symbols are neutron scattering data[97] for $\rm Rb_2MnF_4$. The triangles are quantum Monte Carlo data[98] for the isotropic model.

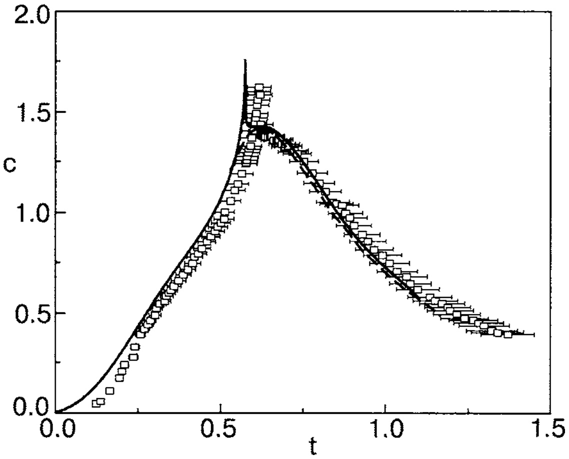

FIG. 16. Specific heat versus $t=T/J\tilde{S}^2$ for $S=5/2$. Mn-f-2U experiments (squares),[100] EA-QHAF with $\mu=0.9942$ (solid line),[87,88] isotropic QHAF (dashed line). Note that the correct anisotropy for this compound is estimated to be $\mu=0.981$. Error bars are due to the experimental uncertainly on J for Mn-f-2U.

critical temperature, which coincides perfectly with that derived from the experimental analysis, $T_c=38.4$ K (i.e., $t_c=0.575$).

Another quantity that shows a signature of the anisotropy and of the Ising transition is the specific heat: in Fig. 16, a comparison with experimental data is shown in the case of the $S=5/2$ compound Mn-formate di-urea (Mn–f–2U),[88] whose anisotropy can be estimated, solely from knowledge of the exchange integral and the measured transition temperature, to be $\mu=0.981$. The comparison reveals the existence of a crossover from a high-temperature 2D-Heisenberg regime to a critical 2D-Ising regime that triggers the observed[99] 3D phase transition at $T_N=3.77$ K.

Finally, for the strongest quantum case, $S=1/2$, we have used the continuous-time quantum Monte Carlo method based on the loop algorithm.[84] The general outcome of the numerical simulations is that the thermodynamics of 2D quantum antiferromagnets is extremely sensitive to the presence of weak easy-axis anisotropies of the order of those of real compounds. For instance, in Fig. 17 it is shown that for $\mu=0.99$ the uniform susceptibility, which is a noncritical quantity, undoubtedly shows a characteristic anisotropic behavior with a different temperature dependence of the transverse and longitudinal branches: the former displays a minimum and the latter monotonically goes to zero, as expected for an EA antiferromagnet.

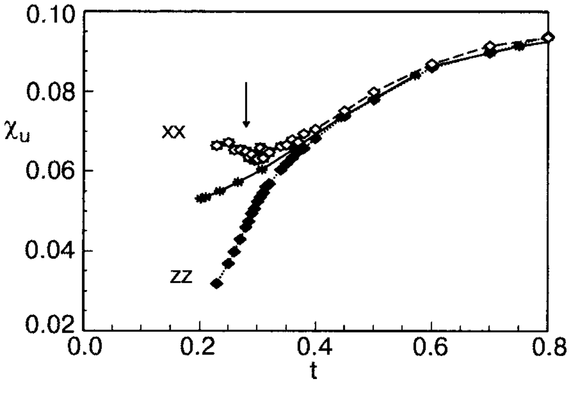

FIG. 17. Uniform susceptibility of the EA model for $\mu=0.99$ from quantum Monte Carlo simulations.[84] Filled diamonds: longitudinal branch; unfilled diamonds: transverse branch; stars: data for the isotropic model.[101] The lines are a guide to the eye. The arrow indicates the estimated critical temperature.

This behavior results from the anisotropy-induced spin ordering, which makes the system more sensitive to the application of a transverse magnetic field than a longitudinal one. Both the minimum of the in-plane component and the decrease of the longitudinal component are close to the transition, a feature also peculiar to the Ising model. Results for the critical temperature at $S=1/2$ are already included in Fig. 14.

B. 2D antiferromagnet with easy-plane anisotropy

In the case of an easy-plane anisotropy the Mermin-Wagner theorem still holds, so that no finite-temperature transition to a phase with a finite order parameter may occur. However, a BKT transition,[102,103] related to the existence of vortex-like topological excitations, is known to characterize the class of the easy-plane models. The reference system for the easy-plane class is the *planar rotator model*, or *XY model*, defined in terms of two-component spins: above the critical temperature t_c the system is disordered, with exponentially decaying correlation functions; in the region $0<t<t_c$ the system is in a critical phase with vanishing magnetization and power-law decaying correlators (quasi-long-range order); at $t=0$ the magnetization acquires a finite value and the system is ordered.

The observation of clear signatures of BKT critical behavior in real magnets is a controversial issue. However, it can explain the properties of several layered compounds[53,104–106] whose high-temperature phase can be described by a purely 2D Heisenberg Hamiltonian, with an exchange interaction often displaying weak EP anisotropies, on the order of $10^{-2}-10^{-4}$ times the dominant isotropic coupling.[105,106] Symmetry and universality arguments suggest that the EP anisotropy drives the system towards a BKT behavior at finite temperature, and the enhanced intraplane correlations trigger the transition to the observed 3D ordered state. As a consequence, 2D critical behavior in close proximity of the would-be BKT transition is masked by these 3D effects.

The EP-QHAF Hamiltonian reads

$$\mathcal{H}=\frac{J}{2}\sum_{\mathbf{i},\mathbf{d}}\left[S_{\mathbf{i}}^{x}S_{\mathbf{i}+\mathbf{d}}^{x}+S_{\mathbf{i}}^{y}S_{\mathbf{i}+\mathbf{d}}^{y}+\lambda S_{\mathbf{i}}^{z}S_{\mathbf{i}+\mathbf{d}}^{z}\right], \qquad (39)$$

where λ is the easy-plane anisotropy parameter $(0\leqslant\lambda<1)$. Again, $J\tilde{S}^2\equiv J(S+1/2)^2$ sets the overall energy scale and $t=T/J\tilde{S}^2$ is the reduced temperature. When $\lambda=1$ the model reduces to the isotropic QHAF. Note that a canonical transformation reversing the x and y spin components of one sublattice is equivalent to setting $(J,\lambda)\rightarrow(-J,-\lambda)$, so that negative values of λ $(-1<\lambda\leqslant 0)$ correspond to the EP ferromagnet. The $\lambda=0$ case is called the *XY model* or *XX*0 *model*. However, at variance with the planar rotator model, out-of-plane fluctuations are present both in the classical and in the quantum EP models. Nevertheless, if $|\lambda|<1$, the classical EP model still undergoes a BKT phase transition.[107]

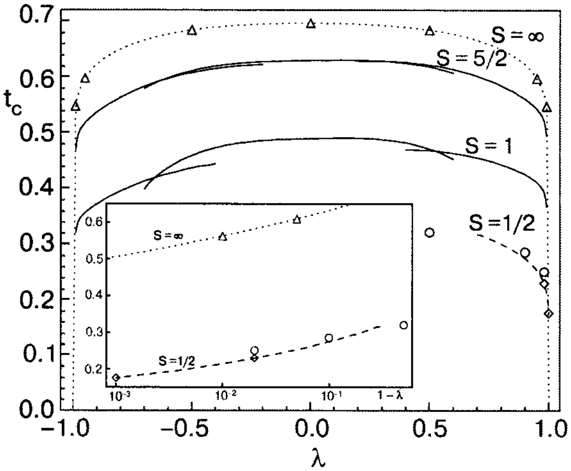

FIG. 18. BKT critical temperature versus anisotropy λ for the easy-plane model with $S=1/2,1,5/2,\infty$. The triangles report the classical ($S=\infty$) MC data[110] used to construct the curve for $t_c^{\rm cl}(\lambda)$ and hence the renormalized curves for $S=1$ and 5/2, the curves obtained through the Holstein-Primakoff ($\lambda \lesssim 0.5$) and the Villain ($\lambda \gtrsim 0.5$) spin-boson transformation, are seen to be connected in a fairly smooth way. The diamonds are our QMC data[84] for $S=1/2$, while the circles are earlier QMC results.[113] The inset expands the nearly isotropic region, in which the expected logarithmic behavior $t_c(\lambda) \sim (a-\ln|1-\lambda|)^{-1}$ is fitted by the dashed curve.

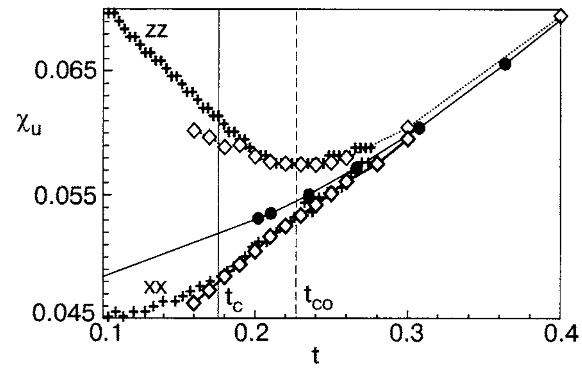

FIG. 19. Out-of-plane (zz) and in-plane (xx) uniform susceptibility χ_u for $\lambda=0.999$. Diamonds are our QMC results; crosses are experimental data[119,120] for $\rm Sr_2CuO_2Cl_2$. The circles report the result for the isotropic QHAF. The vertical lines mark the 3D transition temperature $t_c=0.176$ and the crossover temperature $t_{co}=0.227$.

Monte Carlo simulations of the classical systems[108–111] confirm that the planar and the XXZ model share the same qualitative behavior, but the value of the transition temperature of the planar model[112] shrinks by 22% in the $XX0$ model[110,111] (i.e., with $\lambda=0$), as a consequence of out-of-plane fluctuations. A renormalization group calculation[107] predicts that the transition temperature vanishes logarithmically as the isotropic limit $|\lambda| \to 1$ is approached, and this was also verified in classical MC simulations.[110] Experiments[53,54] and quantum MC simulations[113] indicated that the qualitative behavior of the BKT transition is preserved in the quantum system, with only quantitative modifications of the critical parameters due to the quantum fluctuations.

We applied the effective Hamiltonian formalism[65,66] to the EP-QHAF, finding that it was necessary[87,114] to resort to the Villain or to the Holstein-Primakoff transformation, depending on whether the anisotropy is strong or weak, respectively. While the above approach gives reliable results (with a smooth enough connection at intermediate anisotropy) for spin $S \geqslant 1$, we adopted quantum Monte Carlo simulations[84,88,115–117] in the case $S=1/2$. The effective Hamiltonian[87,114,118] for the EP-QHAF, in terms of classical spins, takes the form

$$\frac{\mathcal{H}_{\rm eff}}{J\tilde{S}^2}=\frac{j_{\rm eff}}{2}\sum_{\mathbf{i},\mathbf{d}}\left[s_{\mathbf{i}}^x s_{\mathbf{i+d}}^x+s_{\mathbf{i}}^y s_{\mathbf{i+d}}^y+\lambda_{\rm eff} s_{\mathbf{i}}^z s_{\mathbf{i+d}}^z\right], \tag{40}$$

and displays a weaker renormalized exchange $j_{\rm eff}(t,\lambda)<1$ and easy-plane anisotropy $\lambda_{\rm eff}(t,\lambda)>\lambda$ (an additional free-energy term is not reported). In analogy to the EA case, the BKT transition temperature can be obtained by renormalization of the classical one using the self-consistent relation

$$t_c(\lambda,S)=j_{\rm eff}(t,\lambda,S)\,t_c^{\rm cl}(\lambda_{\rm eff}(t,\lambda,S)). \tag{41}$$

In Fig. 18, the phase diagram of the EP-QHAF is reported, including the QMC results for $S=1/2$. It is seen that the BKT transition temperature stays large (i.e., comparable to the exchange constant) also for very weak EP anisotropy.

However, as explained above, the problem of detecting the incipient BKT transition requires looking for signatures of XY behavior in a region above the transition. We have shown[115] that a suitable quantity is the uniform susceptibility $\chi_u^{\alpha\alpha}$, which has in-plane ($\alpha=x,y$) and out-of-plane ($\alpha=z$) components and is noncritical, i.e., it does not show singularities at t_c. Figure 19 shows indeed that χ_u^{zz} deviates from the isotropic χ_u and displays a minimum. A similar feature is also present in other quantities[84,115] and occurs around a temperature $t_{co}(\lambda)$ that can be generally defined as the minimum of $\chi_u^{zz}(t,\lambda)$. The pronounced deviation of χ_u^{zz} from the isotropic behavior is due to a simple statistical reason. The uniform susceptibility arises from *spin canting*: two antiferromagnetically coupled spins in an infinitesimal magnetic field **h** minimize their energy when they are located almost orthogonally to **h** and slightly canted in its direction, thus giving a linear response; if they are locally parallel to **h** the response is instead negligible. When for $t \gtrsim t_{co}$ the anisotropy becomes effective, the fraction of spins aligned in the EP rapidly increases compared to that of the isotropic case ($\sim 2/3$), and the response to a field along z (i.e., χ_u^{zz}) is proportionally larger.

The layered cuprate $\rm Sr_2CuO_2Cl_2$ is a good realization[53] of the EP-QHAF model, with $J=1450$ K; considering the spin-wave gap renormalization, its bare anisotropy is estimated to be $1-\lambda \simeq 0.0014$. Experimental data for the uniform susceptibility of this compound[119,120] are reported in Fig. 19. They agree excellently with our results for $\lambda=0.999$: the position of the minimum of χ_u^{zz} gives $t_{co}=0.227(15)$. Close to the critical region the experimental data are affected by the 3D nature of the ordering of the real magnet: the Néel transition is observed at $t_N=0.176(10)$ and compares well with the theoretical estimate $t_c(1-\lambda=0.0014)=0.179(10)$, confirming that 3D ordering is induced by the incipient intralayer BKT transition.

It is worthwhile to mention that in the *triangular* lattice the easy-plane antiferromagnet has very peculiar behavior, already at the classical level, due to the frustration effect of accommodating three antiferromagnetic spins on a plaquette. Indeed, the minimum energy corresponds to a configuration with the three sublattices aligned in the easy plane at equal angles $2\pi/3$. As clockwise and counterclockwise plaquette vorticities are possible, this configuration is twofold degenerate and there is chiral symmetry which corresponds to an Ising-like order parameter. Therefore both a BKT and an Ising transition coexist in the system. We have studied the triangular antiferromagnet both in the classical[121] and in the quantum[122] case, constructing the phase diagram for varying anisotropy and showing that the transitions occur at slightly different temperatures.

C. 2D antiferromagnet in an applied Zeeman field

Interesting behavior is shown by the 2D Heisenberg antiferromagnet when a magnetic field is applied. Indeed, a frustration phenomenon occurs, as antiferromagnetism tends to antialign spins while the field tends to align them with itself: in the classical system[123] it appears that the minimum-energy configuration is the one with the spins almost orthogonal to the field and canted in its direction. Therefore, provided the field is not strong enough to overcome the exchange and to saturate the magnetization, it acts as an effective easy-plane anisotropy, and one expects to observe BKT behavior. Remarkably, as this can be induced in a real quasi-2D antiferromagnetic system by means of an applied field, the strength of the effective anisotropy is in this case tunable. Even though 2D criticality just acts as a trigger for 3D ordering, by observing that the critical temperature follows the predicted behavior with field, an experiment could realize an objective observation of genuine 2D behavior.

The 2D QHAF in a uniform magnetic field is described by the Hamiltonian

$$\mathcal{H}=\frac{J}{2}\sum_{\mathbf{i},\mathbf{d}} \mathbf{S}_{\mathbf{i}}\cdot\mathbf{S}_{\mathbf{i}+\mathbf{d}}-g\mu_B\mathbf{H}\cdot\sum_{\mathbf{i}} \mathbf{S}_{\mathbf{i}}^z, \tag{42}$$

where $\mathcal{H}$ is the applied Zeeman field, μ_B is the Bohr magneton, and g is the gyromagnetic ratio.

We have studied[124,125] the $S=1/2$ 2D QHAF in an uniform magnetic field by means of the QMC method based on the worm algorithm. Our results confirmed that an arbitrarily small field is able to induce a BKT transition and an extended XY phase above it, as in the case of an easy-plane exchange anisotropy. The field-induced XY behavior becomes more and more marked for increasing fields, while for strong fields the antiferromagnetic behavior along the field axis is nearly washed out, so that the system behaves as a planar rotator model with antiferromagnetism surviving in the orthogonal plane only; the BKT critical temperature, as reported in Fig. 20 (where $t\equiv T/J$ and $h\equiv 2g\mu_B H/J$), vanishes as the field reaches the saturation value h_c and the effective rotator length goes to zero. We have therefore shown that the model in a moderately strong field represents an ideal realization of the XY model and that XY behavior can be detected by measuring standard noncritical quantities, such as the specific heat or the induced magnetization. An experimental realization of the XY model in purely magnetic systems and a systematic investigation of the dynamics of vortex/antivortex excitations is therefore possible.

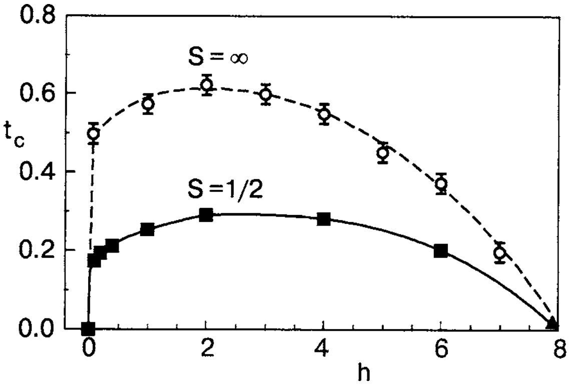

FIG. 20. Phase diagram of the $S=1/2$ 2D QHAF in a magnetic field. Unfilled symbols refer to the classical limit of the model;[123] the triangle[126] and the squares[124] are QMC results.

VI. FRUSTRATION IN THE 2D QUANTUM J_1-J_2 HEISENBERG MODEL

The study of frustrated quantum spin systems is one of the most challenging and exciting topics in theoretical magnetism because of the possible existence of a nonmagnetic zero-temperature phase. A very extensively investigated, yet largely debated model is the so-called J_1-J_2 Heisenberg model with competing antiferromagnetic couplings ($J_1,J_2>0$) between nearest neighbors (nn) and next-nearest neighbors (nnn)

$$\mathcal{H}=J_1\sum_{\mathrm{nn}} \mathbf{S}_{\mathbf{i}}\cdot\mathbf{S}_{\mathbf{j}}+J_2\sum_{\mathrm{nnn}} \mathbf{S}_{\mathbf{i}}\cdot\mathbf{S}_{\mathbf{j}}, \tag{43}$$

where the spin operators are defined on a periodic lattice with $N=L\times L$ sites; hereafter $\alpha=J_2/J_1$ defines the frustration ratio.

In the classical limit ($S\to\infty$) the minimum energy configuration has conventional Néel order with magnetic wave vector $\mathbf{Q}=(\pi,\pi)$ for $\alpha<0.5$. Instead, for $\alpha>0.5$, the antiferromagnetic order is established independently in the two sublattices, with the two staggered magnetizations free to rotate with respect to each other. One of the two families of *collinear* states, with pitch vectors $\mathbf{Q}=(\pi,0)$ or $(0,\pi)$, are selected by an order-by-disorder mechanism as soon as thermal or quantum fluctuations are taken into account. As a result, for $\alpha>0.5$ the classical ground state breaks not only the spin rotational and translational invariance of the Hamiltonian—as the conventional Néel phase—but also its invariance under $\pi/2$ lattice rotations, the resulting degeneracy corresponding to the group $O(3)\times Z_2$. Remarkably, the additional *discrete* Z_2 symmetry can, in principle, be broken at finite temperatures without violating the Mermin-Wagner theorem. On this basis, in a seminal paper,[127] Chandra, Coleman, and Larkin (CCL) proposed that the 2D J_1-J_2 model could sustain an Ising phase transition at finite temperature, with an order parameter directly related to the Z_2 degree of freedom induced by frustration. They also provided quantitative estimates of the critical temperatures in the large-α limit for both the classical and the quantum cases.

This transition in the classical model has been established by an extensive Monte Carlo investigation.[128] In the quantum case, the occurrence of a low-temperature phase with a discrete broken symmetry has been the subject of debates in connection with the discovery of three vanadate compounds (Li_2VOSiO_4, Li_2VOGeO_4, and $VOMoO_4$) whose relevant magnetic interactions involve nearest and next-nearest spin-1/2 V^{4+} ions on weakly coupled stacked planes. In particular, NMR and μSR measurements on Li_2VOSiO_4 (Ref. 129) indicate the occurrence of a transition to a low-temperature phase with collinear order at $T_N \simeq 2.8$ K. However, in the experiments with vanadate compounds, structural distortions and interlayer and anisotropy effects are likely to come into play,[130] and on the other hand the theoretical investigation cannot rely on the insight provided by quantum Monte Carlo methods, as their reliability in the presence of frustration is strongly limited (see the review articles in Refs. 131 and 132).

A complete study of the thermodynamic properties of the quantum J_1-J_2 model in its collinear phase has been pursued within the PQSCHA scheme[65] described in Sec. 4, by which the thermodynamics is rephrased in terms of a classical effective Hamiltonian with renormalized parameters depending on the spin value, temperature, and frustration. It is possible to show that, to $O(1/S)$, the effective Hamiltonian can be recast in a form preserving all the symmetries of the original model, and that reads (except for uniform terms):

$$\mathcal{H}^{\mathrm{eff}}=J_1^{\mathrm{eff}}\widetilde{S}^2\sum_{\mathrm{nn}} \mathbf{s_i}\cdot\mathbf{s_j}+J_2^{\mathrm{eff}}\widetilde{S}^2\sum_{nnn} \mathbf{s_i}\cdot\mathbf{s_j}, \tag{44}$$

where $\mathbf{s}_i$ are classical vectors of length 1, $\widetilde{S}=S+1/2$ is the effective spin length, and $J_1^{\mathrm{eff}}=(\theta_x^2+\theta_y^2)\theta_2^2J_1/2$ and $J_2^{\mathrm{eff}}=\theta_2^4J_2$ are the quantum-renormalized exchange integrals, with spin-, temperature-, and frustration-dependent renormalization parameters θ_x, θ_y, and θ_2.

The occurrence of the transition[127] in the quantum case can be directly addressed within our approach by calculating the critical temperatures as functions of the spin and of the frustration ratio.[133] Using a simple scaling argument, one can relate the critical temperatures in the quantum case $T_c(S,\alpha)$ to those of the classical model $T_c^{\mathrm{cl}}(\alpha)$ through the following self-consistent relation:[87,122]

$$T_c(S,\alpha)=j_1^{\mathrm{eff}}(T,S,\alpha)T_c^{\mathrm{cl}}(\alpha^{\mathrm{eff}}(T_c,S,\alpha)), \tag{45}$$

where $j_1^{\mathrm{eff}}=J_1^{\mathrm{eff}}\widetilde{S}^2/J_1$ and $\alpha^{\mathrm{eff}}=J_2^{\mathrm{eff}}/J_1^{\mathrm{eff}}$. The classical transition temperature, $T_c^{\mathrm{cl}}(\alpha)$ is accurately known through extensive MC simulations for $\alpha \leqslant 2$; it vanishes for $\alpha \rightarrow 2$ and grows more or less linearly for $\alpha > 1$.

The behavior of the transition temperature versus frustration ratio is plotted in Fig. 21 for different values of the spin length. In order to represent the whole interval of $\alpha \in [1/2,\infty]$, in Fig. 21 we have plotted both the MC and the CCL estimates of the classical critical temperatures as a function of $\alpha/(1+\alpha)$. The mismatch between the MC and CCL predictions is a minor flaw that can be corrected by slightly modifying CCL's criterion for the determination of the transition temperature, as explained in Ref. 128. Remarkably, while for large α the transition temperature vanishes for $\alpha \rightarrow \infty$ for any value of the spin, in the opposite limit the critical temperatures vanish on approaching a critical value $\alpha_c > 0.5$ that increases as S decreases, thus confirming the existence of a nonmagnetic phase in the regime of high frustration. In particular for $S=1/2$, $\alpha_c=0.6$, in agreement with the previous estimates of the zero-temperature quantum critical point.[132]

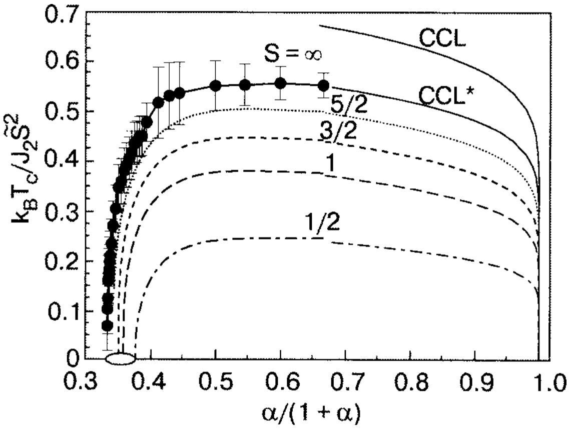

FIG. 21. Renormalized critical temperature of the CCL transition for various values of the spin. Classical data (*) are taken from Ref. 128. The solid lines on the right are the CCL and the CCL* prediction for the classical and $S=1/2$ case (see text). The ellipse on the horizontal axis marks the nonmagnetic (spin-liquid) phase between $\alpha_c(S=\infty)=0.5$ and $\alpha_c(S=1/2)\simeq 0.6$.

VII. CONCLUSIONS

The activity in magnetism of the Condensed Matter Theory group in Florence[134] stems from the early work on two-magnon Raman scattering in the seventies, and has grown up over the years with the collaboration of several scientists. In this paper we summarize the relevant theoretical work that concerns antiferromagnetic models. This activity has been mainly concentrated on low-dimensional systems and has found one of its main motivations in the intent of interpreting the data collected in experiments on real materials. Among the prominent subjects, we have reported about soliton-excitation effects in one-dimensional systems and critical and near-critical behavior and phase transitions in two-dimensional systems. Besides that, we have also addressed some intriguing theoretical problems where fundamental aspects of quantum mchanics come into play, as, e.g., the ground state of antiferromagnetic chains with integer spin or the possible quantum critical regime predicted from the field-theory treatment of the two-dimensional antiferromagnetic Heisenberg model.

[*] E-mail: ruggero.vaia@isc.cnr.it

---

[1] F. D. M. Haldane, Phys. Rev. Lett. **50**, 1153 (1983); Phys. Rev. A **93**, 464 (1983).
[2] A. Sokol and D. Pines, Phys. Rev. Lett. **71**, 2813 (1993).
[3] S. Chakravarty, in *High Temperature Superconductivity*, K. S. Bedell, D. Coffey, D. E. Meltzer, D. Pines, and J. R. Schrieffer (eds.), Addison Wesley, Redwood City (1990).
[4] N. D. Mermin and H. Wagner, Phys. Rev. Lett. **17**, 1133 (1966).
[5] P. A. Fleury, Int. J. Magnetism **1**, 75 (1970).
[6] R. Loudon, Adv. Phys. **17**, 243 (1968); M. G. Cottam and D. J. Lockwood, *Light Scattering in Magnetic Solids*, Wiley, New York (1986).
[7] P. A. Fleury, Phys. Rev. **180**, 591 (1969).
[8] U. Balucani and V. Tognetti, Riv. Nuovo Cimento **6**, 39 (1976).
[9] R. J. Elliott and M. Thorpe, J. Phys. C **2**, 1630 (1969).
[10] U. Balucani and V. Tognetti, Phys. Rev. B **8**, 4247 (1973).
[11] U. Balucani, M. H. Lee, and V. Tognetti, Phys. Rep. **373**, 409 (2003).

[12] F. Barocchi, P. Mazzinghi, V. Tognetti, and M. Zoppi, Solid State Commun. **25**, 241 (1978).

[13] S. R. Chinn, R. W. Davies, and H. J. Zeiger, AIP Conf. Proc. **5**, 317 (1972).

[14] H. Mori, Prog. Theor. Phys. **33**, 423 (1965); **34**, 399 (1965).

[15] U. Balucani and V. Tognetti, Phys. Rev. B **16**, 271 (1977).

[16] U. Balucani, M. G. Pini, and V. Tognetti, Nuovo Cimento B **46**, 81 (1978).

[17] V. E. Korepin, N. M. Bogoliubov, and A. G. Izergin, *Quantum Inverse Scattering Method and Correlation Functions*, Cambridge Univ. Press (1993).

[18] H. J. Mikeska, J. Phys. C **11**, L29 (1978); **13**, 2913 (1980).

[19] F. Currie, J. A. Krumhansl, A. R. Bishop, and S. E. Trullinger, Phys. Rev. B **22**, 477 (1980).

[20] T. Schneider and E. Stoll, Phys. Rev. B **22**, 5317 (1980).

[21] F. Borsa, M. G. Pini, A. Rettori, and V. Tognetti, Phys. Rev. B **28**, 5173 (1983).

[22] S. W. Lovesey, U. Balucani, F. Borsa, and V. Tognetti (eds.), *Magnetic Excitations and Fluctuations*, Vol. 54 of Springer Series in Solid State, Springer Verlag, Berlin (1984).

[23] E. H. Lieb, T. D. Schultz, and D. C. Mattis, Ann. Phys. (N.Y.) **16**, 407 (1961).

[24] I. Affleck, T. Kennedy, E. H. Lieb, and H. Tasaki, Phys. Rev. Lett. **59**, 799 (1987); Commun. Math. Phys. **115**, 477 (1988).

[25] D. P. Arovas, A. Auerbach, and F. D. M. Haldane, Phys. Rev. Lett. **60**, 531 (1988).

[26] I. Affleck, J. Phys.: Condens. Matter **1**, 3407 (1989).

[27] M. Takahashi, Phys. Rev. Lett. **62**, 2313 (1989).

[28] W. J. L. Buyers, R. M. Morra, R. L. Armstrong, M. J. Hogan, P. Gerlach, and K. Hirakawa, Phys. Rev. Lett. **56**, 371 (1986).

[29] M. Steiner, K. Kakurai, J. K. Kjems, D. Petitgrand, and R. Pynn, J. Appl. Phys. **61**, 3953 (1987).

[30] M. Date and K. Kindo, Phys. Rev. Lett. **63**, 1424 (1990).

[31] P. Gaveau, J. P. Boucher, L. P. Regnault, and J. P. Renard, Europhys. Lett. **12**, 647 (1990).

[32] L. C. Brunel, T. Brill, I. Zaliznyak, J. P. Boucher, and J. P. Renard, Phys. Rev. Lett. **69**, 1699 (1992).

[33] R. Botet, R. Jullien, and M. Kolb, Phys. Rev. B **28**, 3914 (1983).

[34] J. B. Parkinson and J. C. Bonner, Phys. Rev. B **32**, 4703 (1985).

[35] M. P. Nightingale and H. W. J. Blöte, Phys. Rev. B **33**, 659 (1986).

[36] T. Kennedy, J. Phys.: Condens. Matter **2**, 5737 (1990).

[37] T. Sakai and M. Takahashi, Phys. Rev. B **42**, 1090 (1990).

[38] T. Delica, K. Kopinga, H. Leschke, and K. K. Mon, Europhys. Lett. **15**, 55 (1991).

[39] H. Koehler and R. Shilling, J. Phys.: Condens. Matter **4**, 7899 (1992).

[40] H.-J. Mikeska, Chaos, Solitons, Fractals **5**, 2585 (1995).

[41] H.-J. Mikeska, Europhys. Lett. **19**, 39 (1992).

[42] G. Gomez-Santos, Phys. Rev. Lett. **63**, 790 (1989).

[43] T. Kennedy and H. Tasaki, Phys. Rev. B **45**, 304 (1992); Commun. Math. Phys. **147**, 431 (1992).

[44] M. den Nijs and K. Rommelse, Phys. Rev. B **50**, 3907 (1994).

[45] H. Tasaki, Phys. Rev. Lett. **66**, 798 (1991).

[46] H.-J. Mikeska and P. Verrucchi, Phys. Rev. B **52**, 3571 (1995).

[47] O. Golinelli, Th. Joliceur, and R. Lacaze, Phys. Rev. B **50**, 3037 (1994).

[48] N. Elstner and H.-J. Mikeska, Phys. Rev. B **50**, 3907 (1994).

[49] E. J. Neves and J. F. Perez, Phys. Lett. **114A**, 331 (1986).

[50] E. Manousakis, Rev. Mod. Phys. **63**, 1 (1991).

[51] M. A. Kastner, R. J. Birgeneau, G. Shirane, and Y. Endoh, Rev. Mod. Phys. **70**, 897 (1998).

[52] M. Greven, R. J. Birgeneau, Y. Endoh, M. A. Kastner, B. Keimer, M. Matsuda, G. Shirane, and T. R. Thurston, Phys. Rev. Lett. **72**, 1096 (1994).

[53] M. Greven, R. J. Birgeneau, Y. Endoh, M. A. Kastner, M. Matsuda, and G. Shirane, Z. Phys. B: Condens. Matter **96**, 465 (1995).

[54] K. Nakajima, K. Yamada, S. Hosoya, Y. Endoh, M. Greven, and R. J. Birgeneau, Z. Phys. B: Condens. Matter **96**, 479 (1995).

[55] Y. S. Lee, M. Greven, B. O. Wells, R. J. Birgeneau, and G. Shirane, Eur. Phys. J. B **5**, 15 (1998).

[56] S. Fulton, S. E. Nagler, L. M. N. Needham, and B. M. Wanklyn, J. Phys.: Condens. Matter **6**, 6667 (1994); S. Fulton, R. A. Cowley, A. Desert, and T. Mason, J. Phys.: Condens. Matter **6**, 6679 (1994).

[57] P. Carretta, T. Ciabattoni, A. Cuccoli, E. Mognaschi, A. Rigamonti, V. Tognetti, and P. Verrucchi, Phys. Rev. Lett. **84**, 366 (2000).

[58] S. Chakravarty, B. I. Halperin, and D. R. Nelson, Phys. Rev. B **39**, 2344 (1989).

[59] I. Affleck, Nucl. Phys. B **257**, 397 (1985).

[60] P. Hasenfratz and F. Niedermayer, Phys. Lett. B **268**, 231 (1991).

[61] N. Elstner, A. Sokol, R. R. P. Singh, M. Greven, and R. J. Birgeneau, Phys. Rev. Lett. **75**, 938 (1995); N. Elstner, Int. J. Mod. Phys. B **11**, 1753 (1997).

[62] A. Cuccoli, V. Tognetti, P. Verrucchi, and R. Vaia, Phys. Rev. Lett. **77**, 3439 (1996).

[63] A. Cuccoli, V. Tognetti, P. Verrucchi, and R. Vaia, Phys. Rev. B **56**, 14456 (1997).

[64] A. Cuccoli, V. Tognetti, P. Verrucchi, and R. Vaia, Phys. Rev. B **58**, 14151 (1998).

[65] A. Cuccoli, R. Giachetti, V. Tognetti, R. Vaia, and P. Verrucchi, J. Phys.: Condens. Matter **7**, 7891 (1995).

[66] A. Cuccoli, V. Tognetti, P. Verrucchi, and R. Vaia, Phys. Rev. A **45**, 8418 (1992).

[67] B. B. Beard, A. Cuccoli, R. Vaia, and P. Verrucchi, Phys. Rev. B **68**, 104406 (2003).

[68] P. Hasenfratz, Eur. Phys. J. B **13**, 11 (2000).

[69] M. Falcioni and A. Treves, Nucl. Phys. B **265**, 671 (1986); S. Caracciolo and A. Pelissetto, Nucl. Phys. B **420**, 141 (1994).

[70] P. Carretta, A. Rigamonti, and R. Sala, Phys. Rev. B **55**, 3734 (1997).

[71] J.-K. Kim, D. P. Landau, and M. Troyer, Phys. Rev. Lett. **79**, 1583 (1997); private communication.

[72] M. S. Makivić and H.-Q. Ding, Phys. Rev. B **43**, 3562 (1991).

[73] B. B. Beard, R. J. Birgeneau, M. Greven, and U.-J. Wiese, Phys. Rev. Lett. **80**, 1742 (1998); B. B. Beard, Nucl. Phys. Proc. Suppl. **83–84**, 682 (2000).

[74] K. Harada, M. Troyer, and N. Kawashima, J. Phys. Soc. Jpn. **67**, 1130 (1998).

[75] J. Kanamori, in *Magnetism*, Vol. 1, G. T. Rado and H. Suhl (eds.), Academic Press, New York (1963).

[76] R. J. Birgeneau, H. J. Guggenheim, and G. Shirane, Phys. Rev. B **1**, 2211 (1970).

[77] R. J. Birgeneau, H. J. Guggenheim, and G. Shirane, Phys. Rev. B **8**, 304 (1973).

[78] L. Onsager, Phys. Rev. **65**, 117 (1944).

[79] M. Bander and D. L. Mills, Phys. Rev. B **38**, 12015 (1988).

[80] J. D. Patterson and G. L. Jones, Phys. Rev. B **3**, 131 (1971).

[81] K. Binder and L. P. Landau, Phys. Rev. B **13**, 1140 (1976).

[82] P. A. Serena, N. García, and A. Levanyuk, Phys. Rev. B **47**, 5027 (1993).

[83] M. E. Gouvêa, G. M. Wysin, S. A. Leonel, A. S. T. Pires, T. Kamppeter, and F. G. Mertens, Phys. Rev. B **59**, 6229 (1999).

[84] A. Cuccoli, T. Roscilde, V. Tognetti, P. Verrucchi, and R. Vaia, Phys. Rev. B **67**, 104414 (2003).

[85] A. Cuccoli, V. Tognetti, T. Roscilde, P. Verrucchi, and R. Vaia, Phys. Rev. B **62**, 3771 (2000).

[86] A. Cuccoli, T. Roscilde, V. Tognetti, R. Vaia, and P. Verrucchi, J. Magn. Magn. Mater. **226–230**, 562 (2001).

[87] A. Cuccoli, T. Roscilde, V. Tognetti, R. Vaia, and P. Verrucchi, Eur. Phys. J. B **20**, 55 (2001).

[88] A. Cuccoli, T. Roscilde, V. Tognetti, R. Vaia, and P. Verrucchi, J. Appl. Phys. **93**, 7637 (2003).

[89] A. Cuccoli, V. Tognetti, T. Roscilde, P. Verrucchi, and R. Vaia, Braz. J. Phys. **30**, 697 (2000).

[90] H.-Q. Ding, J. Phys.: Condens. Matter **2**, 7979 (1990).

[91] J. Rossat-Mignod, L. P. Regnault, C. Vettier, P. Burlet, J. Y. Henry, and G. Lapertot, Physica B **169**, 58 (1991).

[92] H. W. de Wijn, L. R. Walker, and R. E. Walstedt, Phys. Rev. B **8**, 285 (1973).

[93] J. Skalyo, Jr., G. Shirane, R. J. Birgeneau, and H. J. Guggenheim, Phys. Rev. Lett. **23**, 1394 (1969).

[94] K. Nagata and Y. Tomono, J. Phys. Soc. Jpn. **36**, 78 (1974).

[95] B. Schröder, V. Wagner, N. Lehner, K. A. M. Kesharwani, and R. Geick, Phys. Status Solidi B **97**, 501 (1980).

[96] R. A. Cowley, G. Shirane, R. J. Birgeneau, and H. J. Guggenheim, Phys. Rev. B **15**, 4292 (1977).

[97] Y. S. Lee, M. Greven, B. O. Wells, R. J. Birgeneau, and G. Shirane, Eur. Phys. J. B **5**, 15 (1998).

[98] B. B. Beard, Nucl. Phys. B, Proc. Suppl. **83–84**, 682 (2000).

[99] K. Takeda, H. Deguchi, T. Hoshiko, and K. Yamagata, J. Phys. Soc. Jpn. **58**, 3489 (1989).

[100] K. Takeda, M. Mito, K. Nakajima, K. Kakurai, and K. Yamagata, Phys. Rev. B **63**, 024425 (2001).

[101] J.-K. Kim and M. Troyer, Phys. Rev. Lett. **80**, 2705 (1998).

[102] V. L. Berezinskii, Zh. Éksp. Teor. Fiz. **59**, 907 (1970) [Sov. Phys. JETP **32**, 493 (1971)].

[103] J. M. Kosterlitz and D. J. Thouless, J. Phys. C **6**, 1181 (1973); J. M. Kosterlitz, J. Phys. C **7**, 1046 (1974).
[104] B. J. Suh, F. Borsa, L. L. Miller, M. Corti, D. C. Johnston, and D. R. Torgeson, Phys. Rev. Lett. **75**, 2212 (1995).
[105] See, e.g., L. J. de Jongh (ed.), *Magnetic Properties of Layered Transition Metal Compounds*, Kluwer, Dordrecht (1990).
[106] D. C. Johnston, in *Handbook of Magnetic Materials*, Vol. 10, K. H. J. Buschow (ed.), Elsevier Science, New York (1997).
[107] S. B. Khokhlachev, Zh. Éksp. Teor. Fiz. **70**, 265 (1976).
[108] C. Kawabata and A. R. Bishop, Solid State Commun. **42**, 595 (1982).
[109] R. W. Gerling and D. P. Landau, in *Magnetic Excitations and Fluctuations*, S. W. Lovesey, U. Balucani, F. Borsa, and V. Tognetti (eds.), Spinger Verlag, Berlin (1984).
[110] A. Cuccoli, V. Tognetti, and R. Vaia, Phys. Rev. B **52**, 10221 (1995).
[111] H. G. Evertz and D. P. Landau, Phys. Rev. B **54**, 12302 (1996).
[112] R. Gupta and C. Baillie, Phys. Rev. B **45**, 2883 (1992).
[113] H. Q. Ding and M. S. Makivić, Phys. Rev. B **42**, 6827 (1990); **45**, 491 (1992); H.-Q. Ding, Phys. Rev. Lett. **68**, 1927 (1992); Phys. Rev. B **45**, 230 (1992).
[114] L. Capriotti, A. Cuccoli, V. Tognetti, R. Vaia, and P. Verrucchi, Physica D **119**, 68 (1998)
[115] A. Cuccoli, T. Roscilde, R. Vaia, and P. Verrucchi, Phys. Rev. Lett. **90**, 167205 (2003).
[116] A. Cuccoli, T. Roscilde, V. Tognetti, R. Vaia, and P. Verrucchi, J. Appl. Phys. **93**, 7640 (2003).
[117] A. Cuccoli, T. Roscilde, V. Tognetti, R. Vaia, and P. Verrucchi, J. Magn. Magn. Mater. **272–276**, e651 (2004).
[118] A. Cuccoli, V. Tognetti, P. Verrucchi, and R. Vaia, Phys. Rev. B **51**, 12840 (1995).
[119] D. Vaknin, L. L. Miller, J. L. Zaretsky, and D. C. Johnston, Physica C **274**, 331 (1997).
[120] D. Vaknin, S. K. Sinha, C. Stassis, L. L. Miller, and D. C. Johnston, Phys. Rev. B **41**, 1926 (1990).
[121] L. Capriotti, R. Vaia, A. Cuccoli, and V. Tognetti, Phys. Rev. B **58**, 273 (1998).
[122] L. Capriotti, A. Cuccoli, V. Tognetti, P. Verrucchi, and R. Vaia, Phys. Rev. B **60**, 7299 (1999).
[123] D. P. Landau and K. Binder, Phys. Rev. B **24**, 1391 (1981).
[124] A. Cuccoli, T. Roscilde, R. Vaia, and P. Verrucchi, Phys. Rev. B **68**, 060402 (2003).
[125] A. Cuccoli, T. Roscilde, R. Vaia, and P. Verrucchi, J. Magn. Magn. Mater. **272–276**, 884 (2004).
[126] O. F. Syljuåsen, Phys. Rev. B **61**, 846 (2000).
[127] P. Chandra, P. Coleman, and A. I. Larkin, Phys. Rev. Lett. **64**, 88 (1990).
[128] C. Weber, L. Capriotti, G. Misguich, F. Becca, M. Elhajal, and F. Mila, Phys. Rev. Lett. **91**, 177202 (2003).
[129] R. Melzi, P. Carretta, A. Lascialfari, M. Mambrini, M. Troyer, P. Millet, and F. Mila, Phys. Rev. Lett. **85**, 1318 (2000); R. Melzi, S. Aldrovandi, F. Tedoldi, P. Carretta, P. Millet, and F. Mila, Phys. Rev. B **64**, 24409 (2001).
[130] P. Carretta, R. Melzi, N. Papinutto, and P. Millet, Phys. Rev. Lett. **88**, 47601 (2002); P. Carretta, N. Papinutto, C. B. Azzoni, M. C. Mozzati, E. Pavarini, S. Gonthier, and P. Millet, Phys. Rev. B **66**, 094420 (2002).
[131] V. N. Kotov, J. Oitmaa, O. P. Sushkov, and W. H. Zheng, Philos. Mag. B **80**, 1483 (2000).
[132] L. Capriotti, Int. J. Mod. Phys. B **15**, 1799 (2001).
[133] L. Capriotti, A. Fubini, T. Roscilde, and V. Tognetti, Phys. Rev. Lett. **92**, 157202 (2004).
[134] See the group homepage http://www.fi.infn.it/cmtg/.

This article was published in English in the original Russian journal. Reproduced here with stylistic changes by AIP.

LOW TEMPERATURE PHYSICS VOLUME 31, NUMBERS 8–9 AUGUST–SEPTEMBER 2005

Quantum information storage and state transfer based on spin systems

Z. Song*

Department of Physics, Nankai University, Tianjin 300071, China

C. P. Sun†

Department of Physics, Nankai University, Tianjin 300071, China; Institute of Theoretical Physics, Chinese Academy of Sciences, Beijing, 100080, China

(Submitted December 23, 2004)
Fiz. Nizk. Temp. **31**, 907–917 (August–September 2005)

The idea of quantum state storage is generalized to describe the coherent transfer of quantum information through a coherent data bus. In this universal framework, we comprehensively review our recent systematical investigations to explore the possibility of implementing the physical processes of quantum information storage and state transfer by using quantum spin systems, which may be an isotropic antiferromagnetic spin ladder system or a ferromagnetic Heisenberg spin chain. Our studies emphasize the physical mechanisms and the fundamental problems behind the various protocols for the storage and transfer of quantum information in solid state systems. [DOI: 10.1063/1.2008129]

I. INTRODUCTION

The current development of quantum information science and technology demands optimal systems serving as long-lived quantum memories, through which the quantum information carried by a quantum system with short decoherence time can be coherently transferred.[1] In this sense a quantum channel or a quantum data bus is needed for perfect transmission of quantum states. In this article, we will demonstrate that both the quantum information storage and the quantum state transfer can be uniquely described in a universal framework.

There exist some schemes[2–5] concerning the quantum storage of photon states, and there are also some efforts devoted to the universal quantum storage for a qubit (a basic two-level system) state, which is necessary in quantum computation. For example, most recently an interesting protocol[6–8] was presented to reversibly map the electronic spin state onto the collective spin state of the surrounding nuclei. Because of the long decoherence time of the nuclear spins, the information stored in them can be robustly preserved. It was found that,[9] only under two homogeneous conditions with low excitations, such many-nuclei system approximately behaves as a single-mode boson to serve as an efficient quantum memory.

The low-excitation condition requires a ground state with all spins oriented, which can be prepared by applying a magnetic field polarizing all spins along the same direction. With the concept of spontaneous symmetry breaking (SSB), one can recognize that a ferromagnetic Heisenberg spin chain usually has a spontaneous magnetization, which naturally offers a ground state of this kind. In event of SSB, the intrinsic interaction between spins will strongly correlate with the nuclei to form the magnon, a collective mode of spin wave, even without any external magnetic field. With these considerations, Wang, Li, Song, and Sun[10] explored the possibility of using a ferromagnetic quantum spin system, instead of the free nuclear ensemble, to serve as a robust quantum memory. A protocol was presented to implement a quantum storage element for the electronic spin state in a ring array of interacting nuclei. Under appropriate control of both the electron and the external magnetic field, an arbitrary quantum state of the electronic spin qubit, either a pure or a mixed state, can be coherently stored in the nuclear spin wave and then read out in the reverse process.

On the other hand, designed for a more realistic quantum computing, a scalable architecture of quantum network should be based on the solid state system.[11,12] However, the intrinsic feature of solid state based channels, such as the finiteness of the correlation[13,14] and the environment induced noise (especially the low-frequency noise) may block this scalability. Fortunately, analytical study shows that a spin system possessing a commensurate structure of energy spectrum matched with the corresponding parity can ensure the perfect state transfer.[15–17] Based on this fact, an isotropic antiferromagnetic spin ladder system can be pre-engineered as a novel robust kind of quantum data bus.[18] Because the effective coupling strength between the two spins connected to a spin ladder is inversely proportional to the distance of the two spins, the quantum information can be transferred between the two spins separated by a longer distance. Another example of the near-perfect transfer of quantum information was given to illustrate an application of the theorem. The proposed protocol of such near-perfect quantum state transfer utilizes a ferromagnetic Heisenberg chain with uniform coupling constant but in an external parabolic magnetic field.[17]

The present paper will give a broad overview of the present situation of the our investigations mentioned above on quantum state storage and quantum information coherent transfer based on quantum spin systems. We will understand the physical mechanisms and the fundamental problems behind these protocols in the view of a unified conception, the generalized quantum information storage.

II. GENERALIZED QUANTUM STORAGE AS A DYNAMIC PROCESS

For the dynamic process recording and reading quantum information carried by quantum states, we first describe the idea of generalized quantum storage, which was also introduced in association with the Berry's phase factor.[19] Let M be a quantum memory possessing a subspace spanned by $|M_n\rangle$ ($n=1,2,\ldots,d$, $\langle M_n|M_m\rangle=\delta_{nm}$), which can store the quantum information of a system S with basis vectors $|S_n\rangle$, $n=1,2,\ldots,d$. If there exists a controlled time evolution interpolating between the initial state $|S_n\rangle\otimes|M\rangle$ and the final state $|S\rangle\otimes|M_n\rangle$ for each index n and arbitrarily given states $|S\rangle$ and $|M\rangle$, we define the usual quantum storage by using a factorized evolution of time T_m

$$|\Phi(T_m)\rangle=U(T_m)|\Phi(0)\rangle=|S\rangle\otimes|M_n\rangle, \tag{1}$$

starting from the initial state $|\Phi(0)\rangle=|S_n\rangle\otimes|M\rangle$. The corresponding readout process is an inverse evolution of time T_f ($>T_m$)

$$|\Phi(T_f)\rangle=U(T_f)|\Phi(0)\rangle=|S_n\rangle\otimes|M\rangle. \tag{2}$$

In this sense, writing an arbitrary state $|S(0)\rangle=\Sigma_n c_n|S_n\rangle$ of S into M with the initial state $|M\rangle$ of quantum memory can be realized as a controlled evolution from time $t=0$ to $t=T_m$

$$\sum_n c_n|S_n\rangle\otimes|M\rangle\rightarrow|S\rangle\otimes\sum_n c_n|M_n\rangle. \tag{3}$$

The readout process from M is another controlled evolution from time $t=T_m$ to $t=T_f$:

$$|S\rangle\otimes\sum_n c_n|M_n\rangle\rightarrow\sum_n c_n|S_n\rangle\otimes|M\rangle. \tag{4}$$

Obviously, the combination of these two processes forms a cyclic evolution in which a state totally returns to the initial one.

However, in the view of the decoding approach, one does not need "totally return" to revive the information of initial state, and a difference is allowed by the *n-independent* unitary transformation $W=W_S\otimes 1$, namely,

$$|S\rangle\otimes W_M\sum_n c_n|M_n\rangle\rightarrow\Big(W_S\sum_n c_n|S_n\rangle\Big)\otimes|M\rangle. \tag{5}$$

This is a quantum dynamic process (QDP) for recording and reading, which defines a quantum storage. Because the factor W_S is known to be independent of the initial state, it can be easily decoded from $W_S\Sigma_n c_n|S_n\rangle$ by the inverse transformation of W_S. We notice that the quantum storage usually relates to two quantum subsystems.

We will show as follows that the quantum state transfer can be understood as a generalized quantum storage with three subsystems, the input one with the Hilbert space S^A, the data bus with D, and the output one with S^B. As illustrated in Fig. 1, the two subsystems S^A and S^B are located at two distant locations A and B, respectively. Then the Hilbert space of the total system can be written as

$$S_T=S^A\otimes D\otimes S^B\equiv S^A\otimes M, \tag{6}$$

where $M=D\otimes S^B$ can be regarded as the generalized quantum memory with the memory space spanned by $|M_n\rangle=|D\rangle\otimes U_B|S_n^B\rangle$. Here $|D\rangle$ is a robust state of the data bus and U_B represents some local unitary transformations with respect to B, which are independent of the initial state. With this notation, the quantum state transfer indeed can be regarded as a generalized QDP.

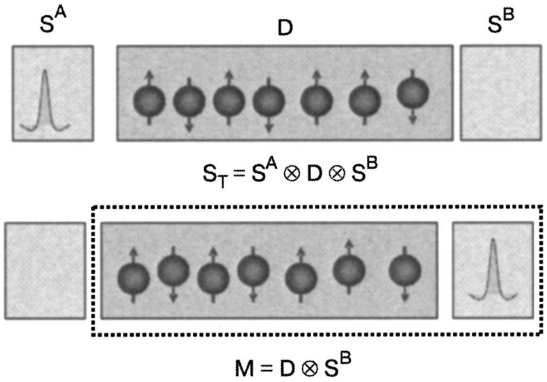

FIG. 1. Demonstration of quantum state transfer as a process of generalized quantum information storage by grouping the data bus D and the target subsystem S^B as a generalized quantum memory.

In fact, if one inputs a state of $|S^A\rangle=\Sigma_n c_n|S_n^A\rangle$ localized at A at $t=0$, the initial state of whole system can be written as

$$|\psi(0)\rangle=\sum_n c_n|S_n^A\rangle\otimes|M\rangle, \tag{7}$$

where $|M\rangle=|D\rangle\otimes U_B|S^B\rangle$. The quantum state transfer can be usually described as a factorized time evolution at time $t=T_f$

$$|\psi(T_f)\rangle=|S\rangle\otimes|D\rangle\otimes\sum_n c_n U_B|S_n^B\rangle=|S\rangle\otimes\sum_n c_n|M_n\rangle \tag{8}$$

with $|M_n\rangle=|D\rangle\otimes U_B|S_n^B\rangle$. The above equations just demonstrate that the quantum state transfer is essentially a generalized quantum memory with $W_M=(1\otimes U_B)$. In this sense the revisable quantum state transfer can be regarded as a general readout process.

Now we would like to remark on the differences between generalized quantum state storage and other two types of quantum processes, quantum teleportation and quantum copy. In fact, quantum teleportation is theoretically perfect, yielding an output state which revives the input with a fidelity $F=1$. Actually one of necessary procedure in teleportation is to measure the Bell state at location A, which will induce wave packet collapse. On the other way around, the quantum state storage process is always on time evolution without any measurement. As for quantum copy the initial state remains unchanged during its copy and can be generated in a dynamic process.

III. QUANTUM STATE TRANSFER IN SPIN SYSTEMS

A robust quantum information processing based on solid state system is usually implemented in a working space spanned by the lowest states, which are well separated from other dense spectra of high excitations. In this sense the energy gap of the solid state system is an important factor we should take into account. The decoherence induced by the environmental noise can also destroy the robustness of quantum information processing, such as the low-frequency (e.g., $1/f$) noise prevalent in solid state devices.

People believe that the gap of the data bus can suppress the stay of transferred state in the middle way in order to enhance the fidelity, but the large gap may result in a shorter correlation length. The relationship between correlation length and the energy gap is usually established in the system with translational symmetry. So we need to consider some modulated-coupling systems or artificially engineered irregular quantum spin systems where the strong correlation between two distant site can be realized.

A. Theorem for the perfect quantum state transfer

Quantum mechanics shows that perfect state transfer is possible. To sketch our central idea, let us first consider a single-particle system with the usual spatial reflection symmetry (SRS) in the Hamiltonian H. Let P be the spatial reflection operator. The SRS is implied by $[H,P]=0$. Now we prove that at time π/E_0 any state $\psi(\mathbf{r})$ can evolve into the reflected state $\pm\psi(-\mathbf{r})$ if the eigenvalues ε_n match the parities p_n in the following way:

$$\varepsilon_n=N_nE_0,p_n=\pm(-1)^{N_n} \tag{9}$$

for arbitrary positive integer N_n and

$$H\varphi_n(\mathbf{r})=\varepsilon_n\varphi_n(\mathbf{r}),\quad P\varphi_n(\mathbf{r})=p_n\varphi_n(\mathbf{r}). \tag{10}$$

Here $\varphi_n(\mathbf{r})$ is the common eigen wave function of H and P, $\mathbf{r}$ is the position of the particle. We call Eq. (9) the spectrum-parity matching condition (SPMC). The proof of the above rigorous conclusion is a simple but heuristic exercise in basic quantum mechanics. In fact, for the spatial reflection operator, $P\psi(\mathbf{r})=\pm\psi(-\mathbf{r})$. For an arbitrarily given state at $t=0$, $\psi(\mathbf{r},t)|_{t=0}$, it evolves to

$$\psi(\mathbf{r},t)=\exp(-iHt)\psi(\mathbf{r})=\sum_n C_n\exp(-iN_nE_0t)\varphi_n(\mathbf{r}) \tag{11}$$

at time t, where $C_n=\langle\varphi_n|\psi\rangle$. Then at time $t=\pi/E_0$, we have

$$\psi\left(\mathbf{r},\frac{\pi}{E_0}\right)=\sum_n C_n(-1)^{N_n}\varphi_n(\mathbf{r})=\pm P\psi(\mathbf{r}) \tag{12}$$

that is $\psi(\mathbf{r},\pi/E_0)=\pm\psi(-\mathbf{r})$. This is just the central result[20] discovered for quantum spin system that the evolution operator becomes a parity operator $\pm P$ at some instant $t=(2n+1)\pi/E_0$, that is $\exp(-iH\pi/E_0)=\pm P$. From the above arguments we have the consequence that if the eigenvalues $\varepsilon_n=N_nE_0$ of a 1D Hamiltonian H with spatial reflection symmetry are odd-number spaced, i.e., N_n-N_{n-1} are always odd, any initial state $\psi(x)$ can evolve into $\pm\psi(-x)$ at time $t=\pi/E_0$. In fact, for such 1D systems, the discrete states alternate between even and odd parities. Consider the odd-number-spaced eigenvalues $\varepsilon_n=N_nE_0$. The next-nearest level must be even-number spaced; then the SPMC is satisfied. Obviously, the 1D SPMC is more realizable for the construction of the model Hamiltonian to perform perfect state transfer.

Now, we can directly generalize the above analysis to many particle systems. For the quantum spin chain, one can identify the above SRS as the middle inversion of spins with respect to the center of the quantum spin chain. As the discussion in Ref. 20, we write spin inversion operation

$$P\Psi(s_1,s_2,\dots,s_{N-1},s_N)=\Psi(s_N,s_{N-1},\dots,s_2,s_1) \tag{13}$$

for the wave function $\Psi(s_1,s_2,\dots,s_{N-1},s_N)$ of the spin chain. Here, $s_n=0,1$ denotes the spin values of the nth qubit.

B. Perfect state transfer in modulated coupling system

Based on the above analysis, in principle, perfect quantum state transfer is possible in the framework of quantum mechanics. According to SPMC, many spin systems can be pre-engineered for perfect quantum states transfer. For instance, two-site spin-1/2 Heisenberg system is the simplest example which meets the SPMC. Recently, Christandl *et al.*[15,16] proposed an N-site XY chain with an elaborately designed modulated coupling constants between two nearest-neighbor sites, which ensures a perfect state transfer. It is easy to find that this model corresponds the SPMC for the simplest case $N_n=n$. A natural extension of the application of the theorem leads to discover other models with $N_n\neq n$. Following this idea, a new class of different models whose spectrum structures obey the SPMC exactly were proposed for perfect state transfer. Consider an N-site spin-1/2 XY chain with the Hamiltonian

$$H=2\sum_{i=1}^{N-1} J_i[S_i^xS_{i+1}^x+S_i^yS_{i+1}^y], \tag{14}$$

where S_i^x, S_i^y, and S_i^z are Pauli matrices for the ith site, and J_i is the coupling strength for the nearest-neighbor interaction. For the open boundary condition, this model is equivalent to the spinless fermion model. The equivalent Hamiltonian can be written as

$$H=\sum_{i=1}^{N-1} J_i^{[k]}a_i^\dagger a_{i+1}+\text{h.c.}, \tag{15}$$

where $a_i^\dagger$, a_i are the fermion operators. This describes a simple hopping process in the lattice. According to the SPMC, we can present different models (labeled by different positive integer $k\in 0,1,2,\dots$) through pre-engineering of the coupling strength as $J_i=J_i^{[k]}=\sqrt{i(N-i)}$ for even i and $J_i=J_i^{[k]}=\sqrt{(i+2k)(N-i+2k)}$ for odd i. By a straightforward calculation, one can find the k-dependent spectrum $\varepsilon_n=-N+2(n-k)-1$ for $n=1,2,\dots,N/2$, and $\varepsilon_n=-N+2(n+k)-1$ for $n=N/2+1,\dots,N$. The corresponding k-dependent eigenstates are

$$|\varphi_n\rangle=\sum_{i=1}^{N} c_{ni}|i\rangle=\sum_{i=1}^{N} c_{ni}a_i^\dagger|0\rangle, \tag{16}$$

where the coefficients c_{ni} can be explicitly determined by the recurrence relation presented in Ref. 18.

It is obvious that the model proposed in Ref. 15 is just the special case of our general model with $k=0$. For arbitrary k, one can easily check that it meets the our SPMC by a straightforward calculation. Thus we can conclude that these spin systems with a set of pre-engineered couplings $J_i^{[k]}$ can serve as the perfect quantum channels that allow the qubit information transfer.

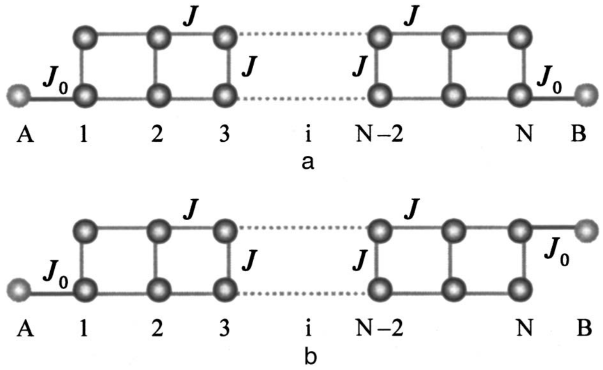

FIG. 2. Two qubits A and B connect to a $2\times N$-site spin ladder. The ground state of H with a-type connection (a) is singlet (triplet) when N is even (odd), while for the b-type connection (b), one should have the opposite result.

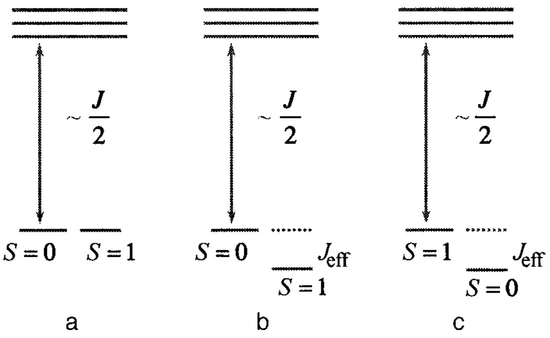

FIG. 3. Schematic illustration of the energy levels of the system. When the connections between two qubits and the medium are switched off ($J_0=0$), the ground states are degenerate (a). When J_0 switches on, the ground state(s) and the first excited state(s) are either singlet or triplet. This is approximately equivalent to that of two coupled spins (b), (c).

C. Near-perfect state transfer

In real many-body systems, the dimension of the Hilbert space increases exponentially with the size N. For example, for an N-site spin-1/2 system the dimension is $D=2^N$, and the symmetry of the Hamiltonian cannot help so much. So it is almost impossible to obtain a model to be exactly engineered. In the above arguments we just show the possibility to implement the perfect state transfer of any quantum state over arbitrary long distances in a quantum spin chain. It sheds light into the investigation of near-perfect quantum state transfer. There is a naive way that one selects some special states to be transported, which is a coherent superposition of commensurate part of the whole set of eigenstates.

For example, we consider a truncated Gaussian wave packet for an anharmonic oscillator with lower eigenstates to be harmonic. It is obvious that such system allows some special states to transfer with high fidelity. We can implement such approximate harmonic system in a natural spin chain without the pre-engineering of couplings but in the presence of a modulated external field. Another way to realize near perfect state transfer is to achieve the entangled states and fast quantum states transfer of two spin qubits by connecting two spins to a medium which possesses a spin gap. A perturbation method, the Fröhlich transformation, shows that the interaction between the two spins can be mapped to the Heisenberg type coupling.

Spin ladder. We sketch our idea with the model illustrated in Fig. 2. The whole quantum system we consider here consists of two qubits (A and B) and a $2\times N$-site two-leg spin ladder. In practice, this system can be realized by an engineered array of quantum dots.[21] The total Hamiltonian $H=H_m+H_q$ contains two parts, the medium Hamiltonian

$$H_M=J\sum_{\langle ij\rangle\perp}\mathbf{S}_i\cdot\mathbf{S}_j+J\sum_{\langle ij\rangle\|}\mathbf{S}_i\cdot\mathbf{S}_j \tag{17}$$

describing the spin-1/2 Heisenberg spin ladder consisting of two coupled chains, and the coupling Hamiltonian

$$H_q=J_0\mathbf{S}_\Lambda\cdot\mathbf{S}_L+J_0\mathbf{S}_B\cdot\mathbf{S}_R \tag{18}$$

describing the connections between qubits A, B and the ladder. In the term H_M, i denotes a lattice site on which one electron sits, $\langle ij\rangle_\perp$ denotes nearest-neighbor sites on the same rung, and $\langle ij\rangle_\|$ denotes nearest neighbors on either leg of the ladder. In the term H_q, L and R denote the sites connecting to the qubits A and B at the ends of the ladder. There are two types of connection between $\mathbf{S}_A$ ($\mathbf{S}_B$) and the ladder, which are illustrated in Fig. 2. According to Lieb's theorem,[22] the spin of the ground state of H with the connection of type a is zero (one) when N is even (odd), while for the connection of type b, one should have the opposite result. For the two-leg spin ladder H_M, analytical analysis and numerical results have shown that the ground state and the first excited state of the spin ladder have spin 0 and 1, respectively.[13,14] It is also shown that there exists a finite spin gap $\Delta=E_1^M-E_g^M\sim J/2$ between the ground state and the first excited state (see Fig. 3). This fact has been verified by experiments[13] and is very crucial for our present investigation.

Thus, it can be concluded that the medium can be robustly frozen to its ground state to induce the effective Hamiltonian $H_{\text{eff}}=J_{\text{eff}}\mathbf{S}_A\cdot\mathbf{S}_B$ between the two end qubits. With the effective coupling constant J_{eff} to be calculated in the following, this Hamiltonian depicts the direct exchange coupling between two separated qubits. As the famous Bell states, H_{eff} has singlet and triplet eigenstates $|j,m\rangle_{AB}$: $|0,0\rangle=1/\sqrt{2}(|\uparrow\rangle_A|\downarrow\rangle_B-|\downarrow\rangle_A|\uparrow\rangle_B)$ and $|1,1\rangle=|\uparrow\rangle_A|\uparrow\rangle_B$, $|1,-1\rangle=|\downarrow\rangle_A|\downarrow\rangle_B$, $|1,0\rangle=1/\sqrt{2}(|\uparrow\rangle_A|\downarrow\rangle_B+|\downarrow\rangle_A|\uparrow\rangle_B)$, which can be used as a channel to share entanglement for a perfect quantum communication in a longer distance.

The above central conclusion can be proved with both analytical and numerical methods as follows. To deduce the above effective Hamiltonian we use $|\psi_g\rangle_M$ ($|\psi_\alpha\rangle_M$) and E_g (E_α) to denote ground (excited) states of H_M and the corresponding eigenvalues. The zero-order eigenstates $|m\rangle$ can then be written in a joint way as

$$\begin{aligned}|j,m\rangle_g&=|j,m\rangle_{AB}\otimes|\psi g\rangle_M,\\ |\psi_\alpha^{jm}(s^z)\rangle&=|j,m\rangle_{AB}\otimes|\psi_\alpha\rangle_M.\end{aligned} \tag{19}$$

Here we have considered that the z component $S^z=S_M^z+S_A^z+S_B^z$ of the total spin is conserved with respect to the connection Hamiltonian H_q. Since S_M^z and S_M^2 commute with H_M, we can label $|\psi_g\rangle_M$ as $|\psi_g(s_M,s_M^z)\rangle_M$, and then $s^z=m+s_M^z$ can characterize the non-coupling spin state $|\psi_\alpha^{jm}(s^z)\rangle$.

When the connections between the two qubits and the medium are switched off, i.e., $J_0=0$, the degenerate ground states of H are just $|j,m\rangle_g$ with the degenerate energy E_g and spin 0, 1, respectively, which is illustrated in Fig. 3a. When the connections between the two qubits and the medium are switched on, the degenerate states with spin 0,1 (Ref. 23) should split as illustrated in Fig. 3b, c. In the case with $J_0 \ll J$ at lower temperature $kT<J/2$, the medium can be frozen to its ground state, and then we have the effective Hamiltonian

$$H_{\text{eff}} \sim \sum_{j',m',j,m,s^z} \frac{|{}_g\langle j,m|H_q|\psi_\alpha^{j'm'}(s^z)\rangle|^2}{E_g-E_\alpha} |j,m\rangle_{gg}\langle j,m|$$

$$= J_{\text{eff}}.\text{Diag.}\left(\frac{1}{4},\frac{1}{4},\frac{1}{4},-\frac{3}{4}\right)+\varepsilon \tag{20}$$

where

$$J_{\text{eff}}=\sum_\alpha \frac{J_0^2[L(\alpha)R^*(\alpha)+R(\alpha)L^*(\alpha)]}{E_g-E_\alpha},$$

$$\varepsilon=\sum_\alpha \frac{3J_0^2[|L(\alpha)|^2+|R(\alpha)|^2]}{4(E_g-E_\alpha)}. \tag{21}$$

This just proves the above effective Heisenberg Hamiltonian (5). Here the matrix elements of interaction $K(\alpha) = {}_M\langle \psi_g|S_K^z|\psi_\alpha(1,0)\rangle_M$ $(K=S,L)$ can be calculated only for the variables of the data bus medium. We also remark that, because S^z and S^2 are conserved for H_q, the off-diagonal elements in the above effective Hamiltonian vanish.

To sum up so far, we have shown that at lower temperature $kT<J/2$, H can be mapped to the effective Hamiltonian H_{eff}, which seemingly depicts the direct exchange coupling between two separated qubits. Notice that the coupling strength has the form $J_{\text{eff}} \sim g(L)J_0^2/J$, where $g(L)$ is a function of $L=N+1$, the distance between the two qubits concerned. Here we take the $N=2$ case as an example. According to Eq. (21) one can get $J_{\text{eff}}=-(1/4)J_0^2/J$ and $(1/3)J_0^2/J$ when A and B connect the plaquette diagonally and adjacently, respectively. This result is in agreement with the theorem[22] about the ground state and the numerical result when $J_0 \ll J$. In general cases, the behavior of $g(L)$ versus L is very crucial for quantum information since $L/|J_{\text{eff}}|$ determines the characteristic time of quantum state transfer between the two qubits A and B. In order to investigate the profile of $g(L)$, a numerical calculation is performed for the systems $L=4,5,6,7,8,10$, with $J=10,20,40$ and $J_0=1$. The spin gap(s) between the ground state(s) and first excited state(s) is (are) calculated, corresponding to the magnitude of J_{eff}. The numerical result is plotted in Fig. 4, which indicates that $J_{\text{eff}} \sim 1/(LJ)$. It implies that the characteristic time of quantum state transfer linearly depends on the distance and then guarantees the possibility of realizing the entanglement of two separated qubits in practice.

In order to verify the validity of the effective Hamiltonian H_{eff}, we need to compare the eigenstates of H_{eff} with those reduced states from the eigenstates of the whole system. In general the eigenstates of H can be written formally as

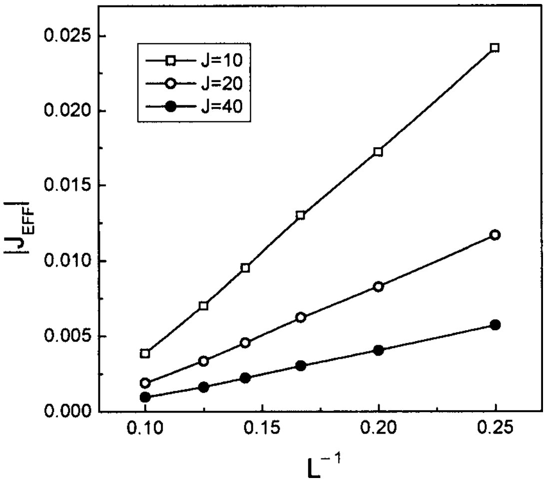

FIG. 4. The spin gaps obtained by numerical method for the systems $L=4,5,6,7,8,10$ with $J=10,20,40$ and $J_0=1$ are plotted, corresponding to the magnitude of J_{eff}. It indicates that $J_{\text{eff}} \sim 1/(LJ)$.

$$|\psi\rangle=\sum_{jm} c_{jm}|j,m\rangle_{AB}\otimes|\beta_{jm}\rangle_M \tag{22}$$

where $\{|\beta_{jm}\rangle_M\}$ is a set of vectors of the data bus, which is not necessarily orthogonal. Then we have the condition $\Sigma_{jm}|c_{jm}|_M^2\langle\beta_{jm}|\beta_{jm}\rangle_M=1$ for normalization of $|\psi\rangle$. In this sense the practical description of the $A-B$ subsystem of two quits can only be given by the reduced density matrix

$$\rho_{AB}=\text{Tr}_M(|\psi\rangle\langle\psi|)=\sum_{jm} |c_{jm}|^2|j,m\rangle_{AB}\langle j,m|$$

$$+\sum_{j'm'\neq jm} c_{j'm'}^* c_{jmM}\langle\beta_{j'm'}|\beta_{j,m}\rangle_M|j,m\rangle_{AB}\langle j',m'| \tag{23}$$

where Tr_M means the trace over the variables of the medium. By a straightforward calculation we have

$$|c_{11}|^2=|c_{1-1}|^2=\left\langle \psi\left|\left(\frac{1}{4}+S_A^z\cdot S_B^z\right)\right|\psi\right\rangle,$$

$$|c_{00}|^2=\left\langle \psi\left|\left(\frac{1}{4}-\mathbf{S}_A\cdot\mathbf{S}_B\right)\right|\psi\right\rangle, \tag{24}$$

$$|c_{10}|^2=1-2|c_{11}|^2-|c_{00}|^2.$$

Now we need a criterion to judge how close the practical reduced eigenstate is to the pure state for the effective two-site coupling H_{eff}. As we noticed, it has the singlet and triplet eigenstates $|j,m\rangle_{AB}$ in the subspace spanned by $|0,0\rangle_{AB}$ with $S^z=S_A^z+S_B^z=0$, we have $|c_{11}|^2=|c_{10}|^2=|c_{1-1}|^2=0$, $|c_{00}|^2=1$; for the triplet eigenstate $|1,0\rangle_{AB}$ we have $|c_{11}|^2 =|c_{1-1}|^2=|c_{00}|^2=0$, $|c_{10}|^2=1$. With the practical Hamiltonian H, the values of $|c_{jm}|^2$, $i=1,2,3,4$ are calculated numerically for the ground state $|\psi_g\rangle$ and first excited state $|\psi_1\rangle$ of finite system(s) $L=4,5,6,7,8,10$ with $J=10,20,40$ $(J_0=1)$ in the $S^z=0$ subspace, which are listed in the Table 1a, b, c of Ref. 17. It shows that, at lower temperature, the realistic interaction leads to results for $|c_{jm}|^2$ which are very close to that described by H_{eff}, even if J is not so large in comparison with J_0.

We assert that the above tables reflect all the facts distinguishing the difference between the results about the entanglement of two end qubits generated by $H_{\rm eff}$ and H. Though we have ignored the off-diagonal terms in the reduced density matrix, the calculation of the fidelity $F(|j,m\rangle)\equiv {}_M\langle j,m|\rho_{AB}|j,m\rangle_M=|c_{jm}|^2$ further confirms our observation that the effective Heisenberg type interaction of two end qubits can approximate the realistic Hamiltonian very well. Then the quantum information can be transferred between the two ends of the $2\times N$-site two-leg spin ladder, that can be regarded as the channel to share entanglement with separated Alice and Bob. Physically, this is just due to a large spin gap existing in such a perfect medium, whose ground state can induce a maximal entanglement of the two end qubits. We also pointed out that our analysis is applicable for other types of medium systems as data buses, which possess a finite spin gap. Since $L/|J_{\rm eff}|$ determines the characteristic time of quantum state transfer between the two qubits, the dependence of $J_{\rm eff}$ upon L becomes important and relies on the appropriate choice of the medium.

In conclusion, we have presented and studied in detail a protocol for quantum state transfer. Numerical results show that the isotropic antiferromagnetic spin ladder system is a perfect medium through which the interaction between two separated spins is very close to the Heisenberg type of coupling, with a coupling constant inversely proportional to the distance, even if the spin gap is not so large compared to the couplings between the input and output spins and the medium.

Spin chain in modulated external magnetic field. Let us consider the Hamiltonian of a $(2N+1)$-site spin-1/2 ferromagnetic Heisenberg chain

$$H=-J\sum_{i=1}^{2N}\mathbf{S}_i\cdot\mathbf{S}_{i+1}+\sum_{i=1}^{2N+1}B(i)S_i^z \tag{25}$$

with the uniform coupling strength $-J<0$, but in the parabolic magnetic field

$$B(i)=2B_0(i-N-1)^2 \tag{26}$$

where B_0 is a constant. In single-excitation invariant subspace with the fixed z component of the total spin, $S^z=N-1/2$, this model is equivalent to the spinless fermion hopping model with the Hamiltonian

$$H=-\frac{J}{2}\sum_{i=1}^{2N}(a_i^\dagger a_{i+1}+\text{h.c.})+\frac{1}{2}\sum_{i=1}^{2N+1}B(i)a_i^\dagger a_i \tag{27}$$

where for simplicity we have neglected a constant in the Hamiltonian. For the single-particle case with the basis set $\{|n\rangle=|0,0,\ldots,1^{n'\rm th},0,\ldots\rangle, n=1,2,\ldots\}$, which is just the same as that of the Hamiltonian of a Josephson junction in the Cooper-pair number basis[24] for $E_J=J$, $E_c=2B_0$, analytical analysis and numerical results have shown that the lower energy spectrum is indeed quasi-harmonic in the case $E_J\gg E_c$ (Ref. 24). Although the eigenstates of the Hamiltonian (25) do not satisfy the SPMC precisely, especially in the high-energy range, there must exist some Gaussian wave packet states expanded by the lower eigenstates. This kind of state can be transferred with high fidelity.

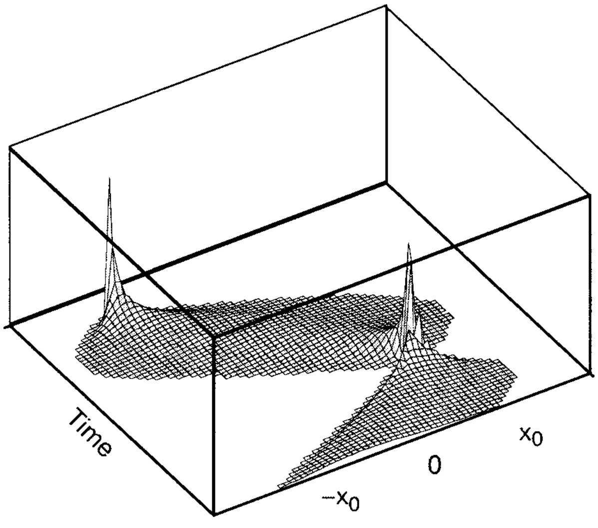

FIG. 5. Schematic illustration of the time evolution of a Gaussian wave packet. It shows that the near-perfect state transfer over a long distance is possible in the quasi-harmonic system.

We consider a Gaussian wave packet at $t=0$, $x=N_A$ as the initial state

$$|\psi(N_A,0)\rangle=C\sum_{i=1}^{2N+1}\exp\left(-\frac{1}{2}\alpha^2(i-N_A-1)^2\right)|i\rangle \tag{28}$$

where $|i\rangle$ denotes the state with $2N$ spins in the down state and only the ith spin in the up state, and C is the normalization factor. The coefficient $\alpha^2=4\ln 2/\Delta^2$ is determined by the width Δ of the Gaussian wave packet. The state $|\psi(0)\rangle$ evolves to $|\psi(t)\rangle=\exp(-iHt)|\psi(N_A,0)\rangle$ at time t, and the fidelity for the state $|\psi(0)\rangle$ transferring to the position N_B is defined as

$$F(t)=|\langle\psi(N_B,0)|\exp(-iHt)|\psi(N_A,0)\rangle|. \tag{29}$$

In Fig. 5 the evolution of the state $|\psi(0)\rangle$ is illustrated schematically. From the investigation of Ref. 25, we know that for small $N_A=-N_B=-x_0$, where N_B is the mirror counterpart of N_A, but in the large Δ limit, if we take $B_0=8(\ln 2/\Delta^2)^2$, $F(t)$ has the form

$$F(t)=\exp\left[-\frac{1}{2}\alpha^2N_A^2\left(1+\cos\frac{2t}{\alpha^2}\right)\right] \tag{30}$$

which is a periodic function of t with the period $T=\alpha^2\pi$ and has maximum of 1. This is in agreement with our above analysis. However, in quantum communication, what we are concerned with is the behavior of $F(t)$ in the case of the transfer distance $L\gg\Delta$, where $L=2|N_A|=2|N_B|$. For this purpose the numerical method is performed for the case $L=500$, $\Delta=2,4,6$ and $B_0=8(\ln 2\Delta^2)^2\lambda$. The factor λ determines the maximum fidelity, and then the optimal field distribution can be obtained numerically. In Fig. 2a, b, c of Ref. 18 the functions $F(t)$ are plotted for different values of λ. It shows that for the given wave packets with $\Delta=2$, 4, and 6 there exists a range of λ within which the fidelities $F(t)$ are up to 0.748, 0.958, and 0.992, respectively. For finite distance, the maximum fidelity decreases as the width of Gaussian wave packet increases. On the other hand, the strength of the external field also determines the value of the optimal fidelity for a given wave packet. There exists an optimal

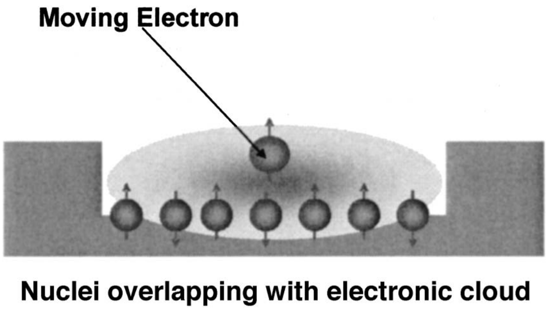

FIG. 6. The electronic spin state onto the collective spin state of the surrounding nuclei ensemble in a quantum well.

external field to obtain maximal fidelity, while the period of $F(t)$ is close to $T=\alpha^2\pi$. This shows a difference from the ideal system, i.e., continuous harmonic systems, in which the fidelity is independent of the strength of the external field. Numerical results indicate that it is possible to realize near-perfect quantum state transfer over a longer distance in a practical ferromagnetic spin chain system.

In summary, we have shown that a perfect quantum transmission can be realized through a universal quantum channel provided by a quantum spin system with spectrum structure, in which each eigenenergy is commensurate and matches with the corresponding parity. According to this SPMC for the a mirror inversion symmetry,[20] we can implement the perfect quantum information transmission with several novel pre-engineered quantum spin chains. For more practical purpose, we prove that an approximately commensurate spin system can also realize near-perfect quantum state transfer in a ferromagnetic Heisenberg chain with uniform coupling constant in an external field. The fidelity for the system in a parabolic magnetic field has been studied by a numerical method. The external field plays a crucial role in the scheme. It induces a lower quasi-harmonic spectrum, which can drive a Gaussian wave packet from the initial position to its mirror counterpart. The fidelity depends on the initial position (or distance L), the width Δ of the wave packet, and the magnetic field distribution $B(i)$ via the factor λ. Thus for given L and Δ, proper selection of the factor λ can achieve the optimal fidelity. Finally, we conclude that it is possible to implement near-perfect Gaussian wave packet transmission over a longer distance in many-body system.

IV. QUANTUM STORAGE BASED ON THE SPIN CHAIN

Recently a universal quantum storage protocol[6–8] was presented to reversibly map the electronic spin state onto the collective spin state of the surrounding ensemble of nuclei in a quantum well (see Fig. 6). Because of the long decoherence time of the nuclear spins, the information stored in them can be robustly preserved.

When all nuclei (with spin operators $I_x^{(i)}$, $I_y^{(i)}$, $I_z^{(i)}$) of spin I_0 are coupled with a single electron spin with strength g_i, a pair of collective operators[9]

$$B=\frac{\Sigma_{i=1}^{N} g_i I_-^{(i)}}{\sqrt{2I_0\Sigma g_j^2}} \tag{31}$$

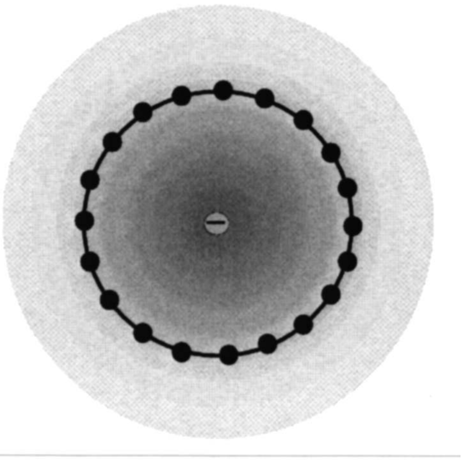

FIG. 7. The configuration geometry of the nuclei-electron system. The nuclei are arranged in a circle within a quantum to form a ring array. To turn on the interaction one can push a single electron towards the center of the circle along the axis perpendicular to the plane.

and its conjugate B^+ are introduced to depict the collective excitations in ensemble of nuclei with spin I_0 from its polarized initial state

$$|G\rangle=|-NI_0\rangle=\prod_{i=1}^{N}|-I_0\rangle_i$$

which denotes the saturated ferromagnetic state of ensemble of nuclei. There is an intuitive argument that if the g_i have different values, while the distribution is "quasi-homogeneous," B and $B^\dagger$ can also be considered as boson operators satisfying $[B,B^+]\to 1$ approximately.

Song, Zhang, and Sun analyzed the universal applicability of this protocol in practice.[9] It was found that only under two homogeneous conditions with low excitations does the many-nuclei system behave approximately as a single-mode boson and can its excitation serve as an efficient quantum memory. The low-excitation condition requires a ground state with all spins oriented, which can be prepared by applying a magnetic field polarizing all spins along a single direction. With consideration of the spontaneous symmetry breaking for all spins oriented, a protocol for a quantum storage element was proposed utilizing a ferromagnetic quantum spin system, instead of the free nuclear ensemble, to serve as a robust quantum memory.

The configuration of the quantum storage element is illustrated in Fig. 7. The nuclei are arranged in a circle within a quantum to form a spin ring array. A single electron is just localized at the center of the ring array, surrounded by the nuclei. The interaction of the nuclear spins is assumed to exist only between the nearest neighbors while the external magnetic field B_0 threads through the spin array. Then the electron-nuclei system can be modeled by a Hamiltonian $H=H_e+H_n+H_{\text{en}}$. It contains the electronic spin Hamiltonian $H_e=g_e\mu_B B_0\sigma^z$, the nuclear spin Hamiltonian

$$H_n=g_n\mu_n B_0\sum_{l=1}^{N} S_l^z-J\sum_{l=1}^{N}\mathbf{S}_l\cdot\mathbf{S}_{l+1} \tag{32}$$

with the Zeeman splitting and the ferromagnetic interaction $J>0$, and the interaction between the nuclear spins and the electronic spin

$$H_{\mathrm{en}}=\frac{\lambda}{2N}\sigma^{+}\sum_{l=1}^{N}S_{l}^{-}+\mathrm{h.c.} \tag{33}$$

Here g_e (g_n) is the Lande g factor of the electron (nuclei), and μ_B (μ_N) is the Bohr magneton (nuclear magneton). The Pauli matrices S_l^- and σ^+ represent the nuclear spin of the lth site and the electronic spin, respectively. The denominator N in Eq. (33) originates from the envelope normalization of the localized electron wave function.[6–8] The hyperfine interactions between nuclei and electron are proportional to the envelope function of localized electron. The electronic wave function is supposed to be cylindrically symmetric, e.g., the s-wave component. Thus the coupling coefficient $\lambda \propto |\psi(\mathbf{r})|^2$ is homogeneous for all the N nuclei in the ring array.

To consider the low spin-wave excitations, the discrete Fourier transformation defines the bosonic operators

$$b_k=\frac{1}{\sqrt{N}}\sum_{l=1}^{N}\exp\left(i\frac{2\pi kl}{N}\right)S^{-l}, \tag{34}$$

in the large N limit. Then one can approximately diagonalize the Hamiltonian (32) as

$$H_T=H_N+\sum_{k=1}^{N-1}\omega_k b_k^{\dagger}b_k$$

where H_N is a Jaynes-Cummings (JC) type Hamiltonian

$$H_N=\omega_N b_N^{\dagger}b_N+\frac{\Omega}{2}\sigma^{z}+\lambda\sqrt{\frac{s}{2N}}(\sigma^{+}b_N+\sigma^{-}b_N^{\dagger}). \tag{35}$$

Then we obtain the dispersion relation for the magnon or spin-wave excitation

$$\omega_k=g_n\mu_nB_0+2Js-2Js\cos\frac{2\pi k}{N}. \tag{36}$$

The above results show that H_T contains only the interaction of the Nth magnon with the electronic spin, and the other $N-1$ magnons decouple with it. Here the frequency of the boson $\omega_N=g_n\mu_nB_0$ and the two-level spacing $\Omega=2g^{*}\mu_BB_0$ can be modulated by the external field B_0 simultaneously.

The process of quantum information storage can be implemented in the invariant subspace of the electronic spin and the Nth magnon. Now we can describe the quantum storage protocol based on the above spin-boson model. Suppose the initial state of the total system is prepared so that there is no excitation in the N nuclei at all, while the electron is in an arbitrary state $\rho_e(0)=\Sigma_{n,m=\pm}\rho_{nm}|n\rangle\langle m|$, where $|+\rangle$ ($|-\rangle$) denotes the electronic spin up (down) state. The initial state of the total system can then be written as

$$\rho(0)=\rho_b(0)\otimes|0_N\rangle\langle 0_N|\otimes\rho_e(0) \tag{37}$$

in terms of $\rho_b(0)=|\{0\}\rangle_{N-1}\langle\{0\}|$, where $|n_1,n_2,\ldots,n_{N-1}\rangle\equiv|\{n_k\}\rangle_{N-1}$ ($k=1,2,\ldots,N-1$) denotes the Fock state of the other $N-1$ magnons. If we set $B_0=0$, at $t=T\equiv(\pi/\lambda)\sqrt{N/2s}$, the time evolution from $\rho(0)$ is just described as a factorized state

$$\rho(T)=\rho_b(0)\otimes w_F\otimes|-\rangle\langle -|, \tag{38}$$

where $w_F=\Sigma_{n,m=0,1}w_{nm}|n_N\rangle\langle m_N|$ is the storing state of the Nth magnon with

$$w_{nm}=\rho_{nm}\exp\left[\frac{i}{2}(m-n)\pi\right]. \tag{39}$$

Here, to simplify our expression, we have denoted $\rho_{++}\equiv\rho_{00}$, $\rho_{\pm}\equiv\rho_{01}$, $\rho_{-+}\equiv\rho_{10}$, $\rho_{-}\equiv\rho_{11}$. The difference between w_F and $\rho_e(0)$ is only an unitary transformation independent of the stored initial state $\rho_e(0)$.

So far we have discussed the ideal case with homogeneous coupling between the electron and the nuclei, that is, the coupling coefficients are the same constant λ for all the nuclear spins. However, the inhomogeneous effect of coupling coefficients has to be taken into account if what our concern extends beyond the s-wave component, where the wave function is not strictly cylindrically symmetric. In this case, the quantum decoherence induced by the so-called quantum leakage has been extensively investigated for the atomic ensemble based quantum memory.[26] We now discuss the similar problems for the magnon-based quantum memory.

In the general case the $\lambda_l\propto|\psi(\mathbf{r}_l)|^2$, where $\psi(\mathbf{r}_l)$ is the envelope function of the electron at site $\mathbf{r}_l$, vary with the positions of the nuclear spins. In this case, the Hamiltonian contains terms other than the interaction between the spin and Nth mode boson, that is, the inhomogeneity induced interaction

$$V=\lambda\sqrt{\frac{s}{2N}}\left(\sigma_{+}\sum_{k=1}^{N-1}\chi_k b_k+\mathrm{h.c.}\right) \tag{40}$$

should be added in our model Hamiltonian H_T, where

$$\chi_k=\sum_{l=1}^{N}\frac{\lambda_l}{\lambda N}\exp(i2\pi kl/N).$$

For a Gaussian distribution of λ_l, e.g., $\lambda_l=(\lambda/\sqrt{2\pi}\sigma)\exp\times(-(l-1)^2/(2\sigma^2))$ with width σ and $\lambda_1=\lambda$, the corresponding inhomogeneous coupling is described by

$$\chi_k=\frac{1}{N}\sum_{l-1=0}^{N-1}\frac{1}{\sqrt{2\pi}\sigma}\exp\left(\frac{-(l-1)^2}{2\sigma^2}+i\frac{2\pi kl}{N}\right). \tag{41}$$

Figure 8 shows the magnitude of χ_k for different Gaussian distributions of λ_l with different widths σ. It indicates that the modes near 1 and $N-1$ have a stronger coupling with the electron. When the interaction gets more homogenous (with larger σ) the coupling coefficients χ_k for all the modes from 1 to $N-1$ become smaller. When the distribution is completely homogeneous, all the couplings with the $N-1$ magnon modes vanish, and then we obtain the Hamiltonian H_T.

In the following we will adopt a rather direct method to analyze the decoherence problem of our protocol resulting from dissipation. If N is so large that the spectrum of the quantum memory is quasicontinuous, this model is similar to the "standard model" of quantum dissipation for the vacuum induced spontaneous emission.[27] The $N-1$ magnons will induce the quantum dissipation of the electronic spin with a decay rate

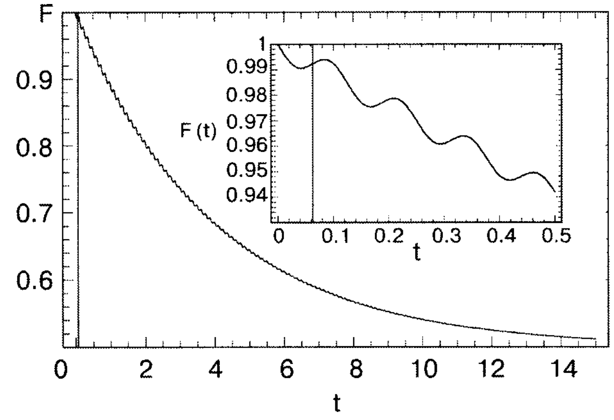

FIG. 8. The fidelity $F(t)$ in the large N limit. The vertical line indicates the instant $\pi/2g$ at which the quantum storage is just implemented. Here $\gamma/g = 1/50$. The inset shows the decaying oscillation with details of $F(t)$ in a small region near the instant $\pi/2g$.

$$\gamma = 2\pi \sum_{k=1}^{N} \frac{\lambda^2 s |\chi_k|^2}{2N} \delta\left(\omega_k - 2\lambda \sqrt{\frac{s}{2N}} \right). \tag{42}$$

Let $|\Psi\rangle$ be the ideal evolution governed by the expected Hamiltonian H_T without dissipation and $|\Psi'\rangle$ be the realistic evolution governed by the Hamiltonian with dissipation. Supposeing that the initial state of the electron is $(|+\rangle + |-\rangle)/\sqrt{2}$, we can analytically calculate the fidelity

$$\begin{aligned} F(t) &= |\langle \Psi | \Psi' \rangle| \\ &= \frac{1}{2}\left[1 + \exp\left(-\frac{\gamma}{2} t \right) \right] \sec \phi (\cos gt \cos(\Delta_1' t + \phi) \\ &\quad + \sin gt \sin \Delta_1' t), \end{aligned} \tag{43}$$

where

$$\phi = \arcsin \sqrt{2N_\gamma^2/\lambda^2 s}, \quad g = \lambda \sqrt{s/2N} \quad \text{and} \quad \Delta_1' = \sqrt{g^2 - \gamma^2}.$$

Figure 8 shows the curve of the fidelity $F(t)$ changing with time t. We can see that the fidelity exhibits a exponential decay behavior with a sinusoidal oscillation. At the instance when we have just implemented the quantum storage process, the fidelity is about $1 - \pi\gamma/8$. Therefore, the deviation from the ideal case with homogeneous couplings is very small for $\gamma/g \ll 1$. Since the ring-shape spin array with inhomogeneous coupling is just equivalent to an arbitrary Heisenberg spin chain in the large N limit, the above arguments means that an arbitrary Heisenberg chain can be used for quantum storage following the same strategy addressed above if γ/g is small, i.e., the inhomogeneous effect is not very strong.

On the other hand, if N is small, the spectrum of the quantum memory is discrete enough to guarantee the adiabatic elimination of the $N-1$ magnon modes, i.e., $\lambda \sqrt{s/2N} \chi_k / |\omega_k| \ll 1$ for the $N-1$ magnon modes. As a consequence of this adiabatic elimination, quantum decoherence or dephasing can result from the mixing of different magnon modes.

We acknowledge the collaborations with P. Zhang, Yong Li, Y. D. Wang, B. Chen, X. F. Qian, T. Shi, Ying Li and R.Xin, which have resulted in our systematic research on quantum spin-based quantum information processing. We acknowledge the support of the CNSF (Grants Nos. 90203018, 10474104, 10447133), the Knowledge Innovation Program (KIP) of the Chinese Academy of Sciences, and the National Fundamental Research Program of China (No. 2001GB309310).

*E-mail: songtc@nankai.edu.cn
†E-mail: suncp@itp.ac.cn

---

[1] D. P. DiVincenzo and C. Bennet, Nature (London) **404**, 247 (2000) and references therein.
[2] M. D. Lukin, Rev. Mod. Phys. **75**, 457 (2003).
[3] M. Fleischhauer and M. D. Lukin, Phys. Rev. Lett. **84**, 5094 (2000); Phys. Rev. A **65**, 022314 (2002).
[4] C. P. Sun, Y. Li, and X. F. Liu, Phys. Rev. Lett. **91**, 147903 (2003).
[5] E. Pazy, I. DAmico, P. Zanardi, and F. Rossi, Phys. Rev. B **64**, 195320 (2001).
[6] J. M. Taylor, C. M. Marcus, and M. D. Lukin, Phys. Rev. Lett. **90**, 206803 (2003).
[7] A. Imamoglu, E. Knill, L. Tian, and P. Zoller, Phys. Rev. Lett. **91**, 017402 (2003).
[8] M. Poggio *et al.*, Phys. Rev. Lett. **91**, 207602 (2003).
[9] Z. Song, P. Zhang, T. Shi, and C. P. Sun, Phys. Rev. B **71**, 205314 (2005).
[10] Y. D. Wang, Y. Li, Z. Song, and C. P. Sun, cond-mat/0409120, submitted to Phys. Rev. A (2004).
[11] D. P. DiVincenzo, D. Bacon, J. Kempe, G. Burkard, and K. B. Whaley, Nature (London) **408**, 339 (2000).
[12] S. Bose, Phys. Rev. Lett. **91**, 207901 (2003).
[13] E. Dagotto and T. M. Rice, Science **271**, 618 (1996).
[14] S. White, R. Noack, and D. Scalapino, Phys. Rev. Lett. **73**, 886 (1994); R. Noack, S. White, and D. Scalapino, Phys. Rev. Lett. **73**, 882 (1994).
[15] M. Christandl, N. Datta, and J. Landahl, Phys. Rev. Lett. **92**, 187902 (2004).
[16] M. Christandl, N. Datta, T. C. Dorlas, A. Ekert, A. Kay, and A. J. Landahl, Phys. Rev. A **71**, 032312 (2005); quant-ph/0411020.
[17] T. Shi, Ying Li, Z. Song, and C. P. Sun, Phys. Rev. A **71**, 032309 (2005).
[18] Ying Li, T. Shi, B. Chen, Z. Song, and C. P. Sun, Phys. Rev. A **71**, 022301 (2005).
[19] C. P. Sun, P. Zhang, and Y. Li, quant-ph/0311052; Y. Li, P. Zhang, P. Zanardi, and C. P. Sun, Phys. Rev. A **70**, 032330 (2004).
[20] C. Albanese, M. Christandl, N. Datta, and A. Ekert, Phys. Rev. Lett. **93**, 230502 (2004); quant-ph/0405029.
[21] D. Loss and D. P. DiVincenzo, Phys. Rev. A **57**, 120 (1998); B. E. Kane, Nature (London) **393**, 133 (1998).
[22] E. Lieb, Phys. Rev. Lett. **62**, 1201 (1989); E. Lieb and D. Mattis, J. Math. Phys. **3**, 749 (1962).
[23] Z. Song, Phys. Lett. A **231**, 135 (1997); Z. Song, Phys. Lett. A **233**, 135 (1997).
[24] Yu. Makhlin, G. Schon, and A. Shnirman, Rev. Mod. Phys. **73**, 357 (2001).
[25] T. Shi, B. Chen, Z. Song, and C. P. Sun, Commun. Theor. Phys. **43**, 795 (2005).
[26] C. P. Sun, S. Yi, and L. You, Phys. Rev. A **67**, 063815 (2003).
[27] W. H. Louisell, *Quantum Statistical Properties of Radiation*, Wiley, New York (1990).

This article was published in English in the original Russian journal. Reproduced here with stylistic changes by AIP.

LOW TEMPERATURE PHYSICS VOLUME 31, NUMBERS 8–9 AUGUST–SEPTEMBER 2005

Localized-magnon states in strongly frustrated quantum spin lattices

J. Richter*

Institut für Theoretische Physik, Universität Magdeburg, P.O. Box 4120, D-39016 Magdeburg, Germany

(Submitted January 19, 2005)
Fiz. Nizk. Temp. **31**, 918–928 (August–September 2005)

Recent developments concerning localized-magnon eigenstates in strongly frustrated spin lattices and their effect on the low-temperature physics of these systems in high magnetic fields are reviewed. After illustrating the construction and the properties of localized-magnon states we describe the plateau and the jump in the magnetization process caused by these states. Considering appropriate lattice deformations fitting to the localized magnons we discuss a spin-Peierls instability in high magnetic fields related to these states. Last but not least we consider the degeneracy of the localized-magnon eigenstates and the related thermodynamics in high magnetic fields. In particular, we discuss the low-temperature maximum in the isothermal entropy versus field curve and the resulting enhanced magnetocaloric effect, which allows efficient magnetic cooling from quite large temperatures down to very low ones. © *2005 American Institute of Physics.* [DOI: 10.1063/1.2008130]

I. INTRODUCTION

The interest in quantum spin antiferromagnetism has a very long tradition; see, e.g., Ref. 1. Stimulated by the recent progress in synthesizing magnetic materials with strong quantum fluctuations,[2] particular attention has been paid to low-dimensional quantum magnets showing novel quantum phenomena like spin-liquid phases, quantum phase transitions or plateaus and jumps in the magnetization process. However, quantum spin systems are of interest in their own right as examples of strongly interacting quantum many-body systems.

We know from the Mermin-Wagner theorem[3] that thermal fluctuations are strong enough to destroy magnetic long-range order (LRO) for Heisenberg spin systems in dimension $D<3$ at any finite temperature T. For $T=0$, where only quantum fluctuations are present, the situation seems to be more complicated. While for one-dimensional (1D) antiferromagnets, in general, the quantum fluctuations are strong enough to prevent magnetic LRO, the competition between interactions and fluctuations is well balanced in two dimensions, and one meets magnetic LRO as well as magnetic disorder at $T=0$, depending on the details of the lattice.[4–8] It was pointed out many years ago by Anderson and Fazekas[9,10] that competition of magnetic bonds for instances due to triangular configurations of antiferromagnetically interacting spins may influence this balance and can lead to disordered ground-state phases in two-dimensional (2D) quantum antiferromagnets. In the context of spin glasses this competition of bonds, later called frustration, was discussed in great detail. These studies on spin glasses have shown that frustration may have an enormous influence on the ground state and thermodynamic properties[11] of spin systems.

The investigation of frustration effects in spin systems, especially in combination with strong quantum fluctuations, is currently a hot topic in solid state physics. We mention some interesting features like quantum disorder, incommensurate spiral phases, "*order by disorder*" phenomena to name a few, which might appear in frustrated systems. The theoretical study of frustrated quantum spin systems is challenging and is often faced with particular problems. While for unfrustrated systems a wide class of well developed many-body methods are available, at least some of them, e.g., the powerful quantum Monte Carlo method, fail for frustrated systems. Furthermore several important exact statements like the Marshall-Peierls sign rule[12] and the Lieb-Mattis theorem[13] are not generally valid if frustration is present (see, e.g., Refs. 14, 15).

On the other hand, the investigation of strongly frustrated magnetic systems surprisingly led to the discovery of several new exact eigenstates. To find exact eigenstates of quantum many-body systems is, in general, a rare exception. For spin systems one has only a few examples. The simplest example for an exact eigenstate is the fully polarized ferromagnetic state, which becomes the ground state of an antiferromagnet in a strong magnetic field. Furthermore the one- and two-magnon excitations above the fully polarized ferromagnetic state also can be calculated exactly (see, e.g., Ref. 1). An example for non-trivial eigenstates is Bethe's famous solution for the 1D Heisenberg antiferromagnet (HAFM).[16] Some of the eigenstates found for frustrated quantum magnets are of quite simple nature and their physical properties, e.g., the spin correlation functions, can be calculated analytically. Note that such states are often eigenstates of the unfrustrated system, too, but they are irrelevant for the physics of the unfrustrated system if they are lying somewhere in the spectrum. However, the interest in these eigenstates comes from the fact that they may become ground states for particular values of frustration. Therefore these exact eigenstates play an important role either as ground states of real quantum magnets or at least as ground states of idealized models which can be used as reference states for more complex quantum spin systems.

Two well-known examples for simple eigenstates of strongly frustrated quantum spin systems are the Majumdar-Gosh state of the 1D J_1–J_2 spin-half HAFM[17] and the orthogonal dimer state of the Shastry-Sutherland model.[18] Both eigenstates are product states built by dimer singlets. They become ground states only for strong frustration. These eigenstates indeed play a role in realistic materials. The Majumdar-Ghosh state has some relevance in quasi-1D spin-Peierls materials like $\mathrm{CuGeO_3}$ (see, e.g., Ref. 19). The orthogonal dimer state of the Shastry-Sutherland model is the magnetic ground state of the quasi-two-dimensional $\mathrm{SrCu_2(BO_3)_2}$ compound.[20] Other frustrated spin models in one, two or three dimensions are known which have also dimer-singlet product states as ground states (see, e.g., Refs. 21–24). Note that these dimer-singlet product ground states have gapped magnetic excitations and lead therefore to a plateau in the magnetization m at $m=0$. Recently it has been demonstrated for the 1D counterpart of the Shastry-Sutherland model[22,25–27] that more general product eigenstates containing chain fragments of finite length can lead to an infinite series of magnetization plateaus.[26] Finally, we mention the so-called frustrated Heisenberg star, where also exact statements on the ground state are known.[28]

In this paper we review recent results concerning a new class of exact eigenstates appearing in strongly frustrated antiferromagnets, namely the so-called localized-magnon states. These states have been detected as ground states of certain frustrated antiferromagnets[29–31] in a magnetic field, and their relevance for physical properties of a wide class of frustrated magnets has been discussed in Refs. 7 and 29–37.

II. LOCALIZED MAGNON STATES

We consider a Heisenberg *XXZ* antiferromagnet for general spin quantum number s in a magnetic field h

$$\hat{H}=\sum_{\langle ij\rangle} J_{ij}\left\{\Delta \hat{S}_i^z\hat{S}_j^z+\frac{1}{2}(\hat{S}_i^+\hat{S}_j^-+\hat{S}_i^-\hat{S}_j^+)\right\}-h\hat{S}^z,$$

$$J_{ij}\geqslant 0. \tag{1}$$

The magnetization $M=\hat{S}^z=\Sigma_i\hat{S}_i^z$ commutes with the Hamiltonian and is used as a relevant quantum number to characterize the eigenstates of $\hat{H}$. Let us consider strong magnetic fields exceeding the saturation field h_{sat}. Then the system is in the fully polarized ferromagnetic eigenstate $|\mathrm{FM}\rangle=|+s,+s,+s,+s,+s\ldots\rangle$, which will be considered as the magnon vacuum state, i.e. $|0\rangle=|\mathrm{FM}\rangle$. The one-magnon states above this vacuum are given by

$$|1\rangle=\frac{1}{c}\sum_i^N a_iS_i^-|0\rangle;\quad (\hat{H}-E_{FM})|1\rangle=w_i(\mathbf{k})|1\rangle, \tag{2}$$

where E_{FM} is the energy of the fully polarized ferromagnetic state $|\mathrm{FM}\rangle$ and c is a normalization constant. For several strongly frustrated lattices one observes flat dispersion modes $w_i(\mathbf{k})=\mathrm{const}$ of the lowest branch. One example is shown in Fig. 1. Here we mention that there is some relation to the flat-band ferromagnetism in electronic systems discussed by Mielke and Tasaki; see Refs. 38–40.

Consequently, one can construct localized states by an appropriate superposition of extended states with different $\mathbf{k}$ vectors. The general form of these localized states can be written as[30,31]

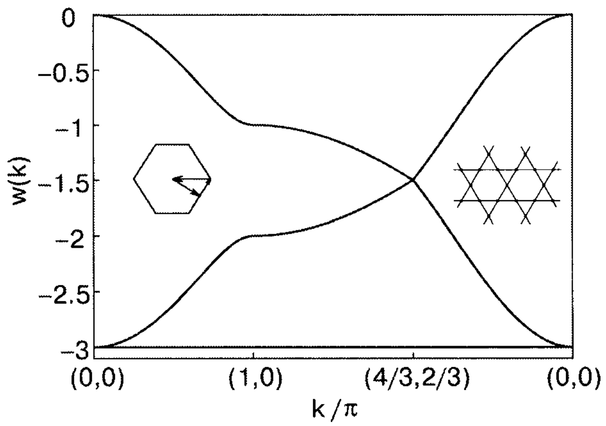

FIG. 1. Excitation energies $w_i(\mathbf{k})$ of the one-magnon states for the isotropic spin-half Heisenberg antiferromagnet [i.e., $J=1$, $\Delta=1$, $s=1/2$, and $h=0$ in Eq. (1)] on the kagomé lattice (right inset). The left inset shows the path in the Brillouin zone corresponding to k values used as x coordinate. This figure was provided by J. Schulenburg.

$$|\mathbf{1}\rangle_L=\frac{1}{c}\sum_i^N a_i\hat{S}_i^-|0\rangle=|\Psi_L\rangle|\Psi_R\rangle,$$

$$a_i\begin{cases}\neq 0 & \forall i\in L\ \ (\text{local})\\ =0 & \forall i\in R\ \ (\text{remainder}),\end{cases} \tag{3}$$

where $|\Psi_L\rangle$ belongs to the localized excitation living on the local region L and $|\Psi_R\rangle$ describes the fully polarized ferromagnetic remainder. We split the Hamiltonian into three parts $\hat{H}=\hat{H}_L+\hat{H}_{L-R}+\hat{H}_R$, where $\hat{H}_L$ contains all bonds J_{il} with $i,l\in L$, $\hat{H}_R$ contains all bonds J_{kj} with $k,j\in R$, and $\hat{H}_{L-R}$ contains all bonds J_{lk} with $l\in L$ and $k\in R$. The requirement that the localized-magnon state $|1\rangle_L$ is simultaneously an eigenstate of all three parts of the Hamiltonian, i.e., $\hat{H}_L|1\rangle_L=e_L|1\rangle_L$, $\hat{H}_R|1\rangle_L=e_R|1\rangle_L$ and $\hat{H}_{L-R}|1\rangle_L=e_{L-R}|1\rangle_L$, leads to two criteria for the exchange bonds J_{ij}, namely[31]

$$\sum_{l\in L} J_{rl}a_l=0\quad \forall r\in R \tag{4}$$

and

$$\sum_{r\in R} J_{rl}=\mathrm{const}\quad \forall l\in L. \tag{5}$$

Equation (4) represents a condition on the bond geometry, whereas Eq. (5) is a condition for the bond strengths and is automatically fulfilled in uniform lattices with equivalent sites. Note, however, that the second condition is not a necessary one, i.e., one can find models with eigenstates of form (3) violating (5); see Ref. 30. This more general case appears

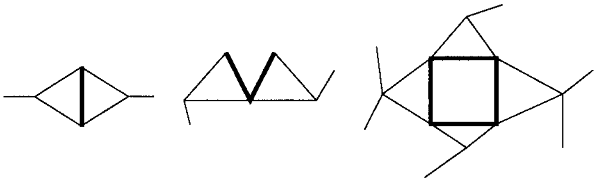

FIG. 2. Typical lattice geometries supporting the localized-magnon states (3). The magnon lives on the restricted area indicated by a thick line.

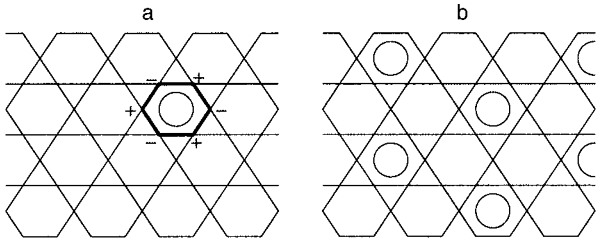

FIG. 3. Localized magnons on the kagomé lattice. One-magnon state indicated by a circle, the + and − signs correspond to the sign of the coefficients $a_i = \pm 1$ [see Eq. (6)] (a). Magnon crystal state corresponding to the maximum filling $n_{\max} = N/9$ of the kagomé lattice with localized magnons (circles) (b). The figures were taken from Ref. 30.

if $|\Psi_L\rangle|\Psi_R\rangle$ is not an individual eigenstate of both $\hat{H}_L$ and $\hat{H}_{L-R}$ but of $(\hat{H}_{L-R} + \hat{H}_L)$. Hence, the geometry condition (4) is the criterion of major importance. A typical geometry fulfilling condition (4) is realized by an even polygon surrounded by isosceles triangles; see Fig. 2. The lowest one-magnon state living on an even polygon has coefficients a_i in $|1\rangle_L$ alternating in sign. But also finite strings of two or three sites attached by appropriate triangles can fulfill the criterion (4); see Fig. 2.

As an example we consider the HAFM (1) on the kagomé lattice,[30] i.e., we have $J_{ij} = 1$ for nearest-neighbor (NN) bonds and $J_{ij} = 0$ otherwise. Its one-magnon dispersion shown in Fig. 1 exhibits one flat mode. The resulting localized magnon lives on a hexagon; see Fig. 3a. Its wave function is

$$|\mathbf{1}\rangle_L^{\text{kagomé}} = \frac{1}{\sqrt{12_S}} \sum_{\substack{i=1\\(i \in \text{hexagon})}}^{6} a_i \hat{S}_i^- |0\rangle, \quad a_i = (-1)^i. \tag{6}$$

Note that the number of hexagons $N/3$ corresponds to the number of states in the flat branch of $w(\mathbf{k})$. Because of the localized nature of the magnon we can put further such magnons on the lattice in such a way that there is no interaction between them. The maximum filling $n_{\max}$ of the kagomé lattice with localized magnons is shown in Fig. 3b. The resulting eigenstate is a magnon "crystal" state with $n_{\max} = N/9$ magnons and a magnetic unit cell three times as large as the geometric one. Therefore the states with $n = \{0,1,2,3,\ldots,N/9\}$ localized magnons represent the class of exactly known product eigenstates with quantum numbers $M = S_z = Ns - n = \{Ns, Ns-1, Ns-2, \ldots, Ns - N/9\}$.

Due to the mutual independence of the localized magnons for $n \leq n_{\max} \propto N$ the energy E_{loc} of the localized-magnon states is proportional to the number n of localized magnons, i.e., at $h=0$ one has $E_{\text{loc}} = E_{FM} - n\varepsilon_1$, where E_{FM} is the energy of the fully polarized (vacuum) state and ε_1 is the energy gain by one magnon. As a results there is a simple linear relation between E_{loc} and the total magnetization M valid for all systems hosting localized magnons:

$$E_{\text{loc}}(M, h=0) = -aN + bsM, \tag{7}$$

where the parameters a and b depend on details of the system like the exchange constant J_{ij}, the anisotropy parameter Δ, the coordination number z of the lattice, etc. For example, for the isotropic spin-half HAFM with NN exchange J on the kagomé lattice one finds[30,35]

$$E_{\text{loc}}(M, h=0) = 2s^2 NJ - 6snJ = -4s^2 NJ + 6sJM. \tag{8}$$

Note that also the spin-spin correlation functions of such states can be easily found.[31]

For the physical relevance of these eigenstates it is crucial that they have lowest energy in the corresponding sector of M. Indeed this can be proved for quite general antiferromagnetic spin models.[29,41]

Since the condition (4) for the existence of localized-magnon states is quite general, one can find a lot of magnetic systems in one, two, and three dimensions having localized-magnon eigenstates.[29–32,35–37,43] To illustrate that we show in Fig. 4 some 1D and in Fig. 5 some 2D and 3D antiferromagnetic spin lattices. But localized-magnon states are observed for frustrated magnetic molecules also.[29]

III. PLATEAUS AND JUMPS IN THE MAGNETIZATION CURVE

As discussed in the previous Section, the localized-magnon states are the lowest states in the corresponding sector of magnetization M. Hence they become ground states in appropriate magnetic fields h. Furthermore we stated that there is a linear relation between the energy of these states E_{loc} and M; cf. Eq. (7). When a magnetic field h is applied the energy reads $E_{\text{loc}}(M,h) = -aN + bsM - hM$, and one has complete degeneracy of all localized-magnon states at the saturation field $h = h_{\text{sat}} = bs$. As a result of this degeneracy the zero-temperature magnetization $m = M/(Ns)$ jumps between the saturation value $m=1$ and the value $1 - n_{\max}/(Ns)$ corresponding to the maximum number $n_{\max}$ of

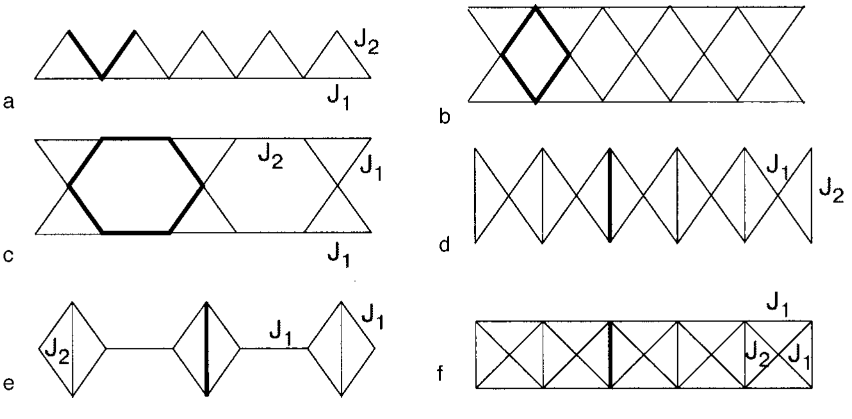

FIG. 4. One-dimensional systems with localized-magnon states. The magnons live on the restricted area indicated by a thick line: sawtooth chain[42,43] (a), kagomé chain I[44] (b), kagomé chain II[45] (c), diamond chain[46] (d), dimer-plaquette chain[22] (e), frustrated ladder[47] (f). Note that there are special restrictions for the exchange integrals to have localized-magnon states as lowest eigenstates in the corresponding sector of M.

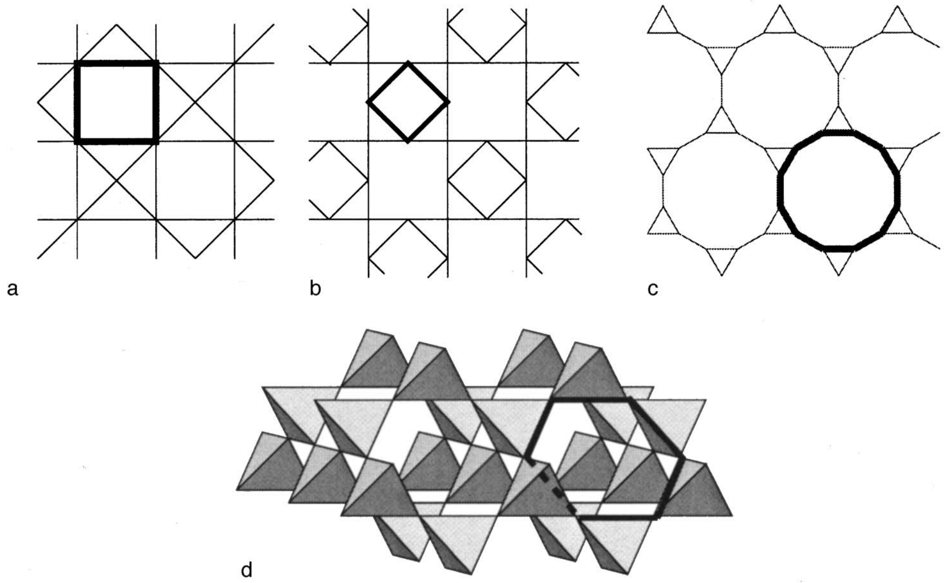

FIG. 5. Two- and three-dimensional antiferromagnets with localized-magnon states. The magnons live on the restricted area indicated by a thick line: planar pyrochlore (checkerboard) lattice[31,48] (a), square-kagomé lattice[37,49] (b), star lattice[7,36] (c), pyrochlore lattice[50] (d).

independent localized magnons. Since $n_{\max}$ is proportional to N but independent of the spin quantum number s, the height of the jump $\delta m = n_{\max}/(Ns)$ goes to zero for $s=\infty$, i.e., the magnetization jump due to the localized-magnon states becomes irrelevant if the spins become classical.

In Fig. 6 we present two examples of the magnetization curves; further examples can be found in Refs. 7, 27, 31, 36, 37. The jumps of height $\delta m = 1/2$ (sawtooth chain) and $\delta m = 2/7$ (kagomé lattice) are well pronounced. Furthermore we see a wide plateau at the foot of the jump for the sawtooth chain. Note that there are general arguments in favor of a plateau just below the jump.[7,51,52] Therefore we might expect a plateau preceeding the jump in all magnetic systems with localized magnon states. Though from Fig. 6 it remains unclear whether there is a plateau for the kagomé lattice, too, a more detailed analysis[32] indeed yields evidence for a finite plateau width of about $\delta h \sim 0.07J$.

IV. MAGNETIC-FIELD INDUCED SPIN-PEIERLS INSTABILITY IN QUANTUM SPIN LATTICES WITH LOCALIZED-MAGNON STATES

The influence of a magnetoelastic coupling in frustrated antiferromagnets on their low-temperature properties is currently widely discussed. Lattice instabilities breaking the translational symmetry are reported for 1D and 2D as well 3D quantum spin systems; see, e.g., Ref. 53. In all those studies the lattice instability was considered at zero field. As discussed already in an early paper by Gross,[54] a magnetic field usually acts against the spin-Peierls transition and might favor a uniform or incommensurate phase. In contrast to those findings, in this Section we discuss a lattice instability in frustrated spin lattices hosting localized magnons for which the magnetic field is essential.[32]

First we point out that due to the localized nature of the

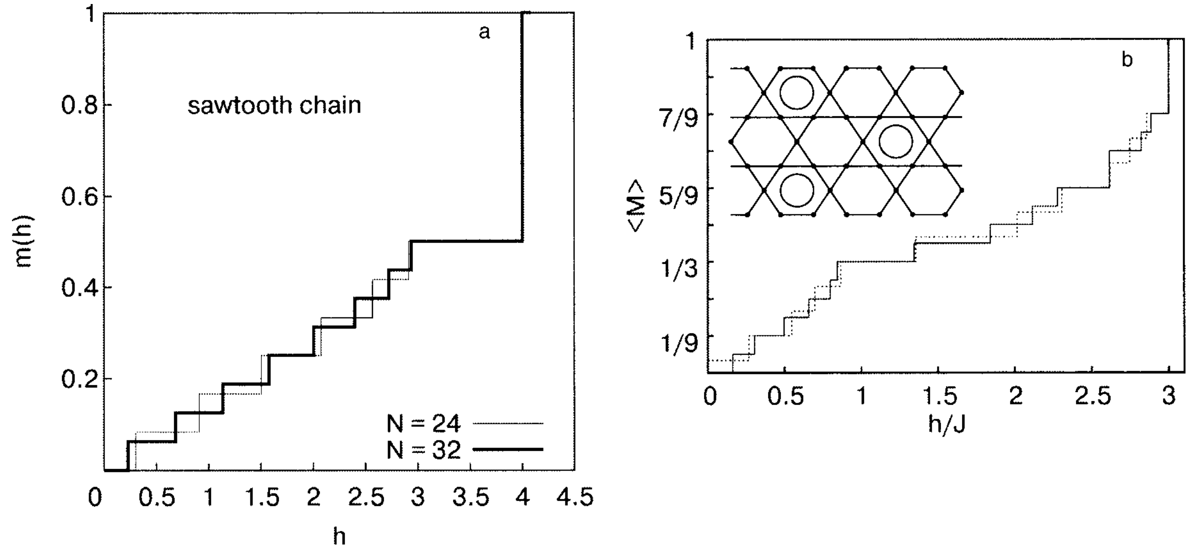

FIG. 6. Panel a: Magnetization versus magnetic field h of the isotropic spin-half Heisenberg antiferromagnet. The sawtooth chain with $J_1=1$ and $J_2=2J_1$; cf. Fig. 4. The figure was taken from Ref. 31. Panel b: The kagomé lattice with $N=27$ (dashed line) and 36 sites (solid line). The inset illustrates the "magnon crystal" state corresponding to maximum filling with localized magnons, where the location of the magnons is indicated by the circles in certain hexagons. The figure was taken from Ref. 8.

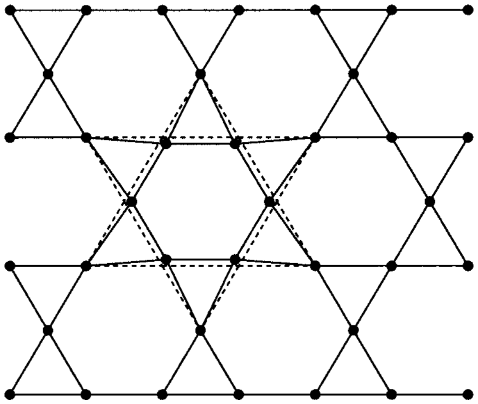

FIG. 7. Kagomé lattice with one distorted hexagon which can host localized magnons. The parts of the lattices before distortions are shown by dashed lines. All bonds in the lattices before distortions have the same length. The figure was taken from Ref. 32.

magnons we have an inhomogeneous distribution of NN spin-spin correlations $\langle \hat{\mathbf{S}}_i \cdot \hat{\mathbf{S}}_j \rangle$.[31] In the case that one magnon is distributed uniformly over the lattice, the deviation of the NN correlation from the ferromagnetic value, i.e. the quantity $\langle \hat{\mathbf{S}}_i \cdot \hat{\mathbf{S}}_j \rangle - 1/4$, is of order $1/N$. On the other hand, for a localized magnon (3) we have along the polygon/line hosting the localized magnon in general actually a negative NN correlation $\langle \hat{\mathbf{S}}_i \cdot \hat{\mathbf{S}}_j \rangle$, and all other NN correlations are positive. For instance for the spin-half HAFM on the kagomé lattice the localized-magnon state (6) leads to $\langle \hat{\mathbf{S}}_i \cdot \hat{\mathbf{S}}_j \rangle = -1/12$ for neighboring sites i and j on a hexagon hosting a magnon and to $\langle \hat{\mathbf{S}}_i \cdot \hat{\mathbf{S}}_j \rangle = +1/6$ for neighboring sites i and j on an attaching triangle. Hence a deformation with optimal gain in magnetic energy will lead to an increase of antiferromagnetic bonds on the polygon/line hosting the localized magnon (i.e., hexagon for the kagomé lattice) and to a decrease of the bonds on the attaching triangles.

Let us discuss the situation for the isotropic spin-half HAFM on the kagomé lattice in more detail. A corresponding deformation which preserves the symmetry of the cell which hosts the localized magnon is shown in Fig. 7. To check the stability of the kagomé lattice with respect to a spin-Peierls mechanism we must compare the magnetic and the elastic energies. For the kagomé lattice the deformation shown in Fig. 7 leads to the following changes in the exchange interactions: $J \to (1+\delta)J$ (along the edges of the hexagon) and $J \to (1-\delta/2)J$ (along the two edges of the triangles attached to the hexagon), where the quantity δ is proportional to the displacement of the atoms and the change in the exchange integrals due to lattice distortions is taken into account in first order in δ. The magnetic energy (8) is lowered by distortions and becomes for one magnon and one corresponding distortion $E_{\text{loc}}(n=1, h=0, \delta) = NJ/2 - 3J - 3\delta J/2$. Considering $n \leqslant n_{\text{max}}$ independent localized magnons and corresponding distortions the energy gain is then $e_{\text{mag}} = -3n\delta J/2$. On the other hand, the elastic energy in the harmonic approximation increases according to $e_{\text{elast}} \propto \delta^2$. Therefore a minimal total energy is obtained for a finite $\delta = \delta^* > 0$. For the kagomé lattice the elastic energy for one distorted cell is $e_{\text{elast}} = 9\gamma\delta^2$ (the parameter γ is proportional to the elastic constant of the lattice). If the localized-magnon states are the ground states of the systems then we have a favorable spin-Peierls distortion with $\delta^* = J/(12\gamma)$. As discussed in the previous Section, we expect a plateau at the foot of the magnetization jump. The spin-Peierls distortion due to localized-magnon states then takes place for the values of the magnetic field belonging to this plateau.

Now the question arises whether the lattice distortion under consideration is stable below and above this plateau, i.e., for $M < N/2 - n_{\text{max}}$ and $M = N/2$. It is easy to check that the lattice distortion illustrated in Fig. 7 is not favorable for the fully polarized vacuum state, i.e. for $M = N/2$. For magnetizations M below this plateau, we are not able to give a rigorous answer, but numerical results for finite kagomé lattices of size $N = 18,27,36,45,54$ indicate that there is no spin-Peierls deformation adopting the lattice distortion shown in Fig. 7 for $M < N/2 - n_{\text{max}}$ (see Ref. 32 for more details).

We mention that the scenario discussed above basically remains unchanged for the anisotropic Hamiltonian (1) with $\Delta \neq 1$ and also for spin quantum numbers $s > 1/2$.[32]

From the experimental point of view the discussed effect should manifest itself most spectacularly as a hysteresis in the magnetization and the deformation of kagomé-lattice antiferromagnets in the vicinity of the saturation field. We emphasize that the discussed spin-Peierls instability in high magnetic fields may appear in the whole class of frustrated quantum magnets in one, two and three dimensions hosting independent localized magnons provided it is possible to construct a lattice distortion preserving the symmetry of the localized-magnon cell.

V. FINITE LOW-TEMPERATURE ENTROPY AND ENHANCED MAGNETOCALORIC EFFECT IN THE VICINITY OF THE SATURATION FIELD

It is well-known that strongly frustrated Ising or classical Heisenberg spin systems may exhibit a huge ground-state degeneracy; see e.g., Refs. 5–7, 55–58. For quantum systems the degeneracy found for classical systems is often lifted due to fluctuations, and the quantum ground state is unique (the so-called "*order from disorder*" phenomenon[60,61]). However, highly frustrated antiferromagnetic quantum spin lattices hosting localized magnons are an example where one finds a huge ground-state degeneracy in a *quantum* system. As discussed in Sec. 3 the localized-magnon states become degenerate at saturation field. As pointed out first in Ref. 7 the degeneracy grows exponentially with system size N. This huge degeneracy and its consequence for the low-temperature physics are discussed in more detail in Refs. 33–35.

For some of the spin systems hosting localized magnons the ground-state degeneracy at saturation and therefore the residual entropy at zero temperature can be calculated exactly by mapping the localized-magnon problem onto a related lattice gas model of hard-core objects.[33–35] These lattice gas models of hard-core objects have been studied over the last decades in great detail (see, e.g., Ref. 59). Let us illustrate this for the sawtooth chain. Here the local areas where the magnons can live are the valleys of the sawtooth chain; see Fig. 4a. Because a certain local area of the lattice can be occupied by a magnon or not, the degeneracy of the

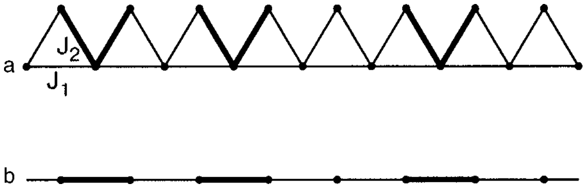

FIG. 8. The sawtooth chain which hosts three localized magnons at fat V parts (a) and the auxiliary lattice used for the exact calculation of the ground-state degeneracy at saturation (b). The localized magnons are eigenstates for $J_2=\sqrt{2(1+\Delta)}J_1$ (Ref. 30). The figure was taken from Ref. 35.

ground state at saturation, $\mathcal{W}$, grows exponentially with N, giving rise to a finite zero-temperature entropy per site at saturation:

$$\frac{S}{N}=\lim_{N\to\infty}\frac{1}{N}\log\mathcal{W}>0. \tag{9}$$

Now we map the original lattice which hosts localized magnons onto an auxiliary lattice which is occupied by hard-core objects, which are rigid monomers and dimers in the case of the sawtooth chain; see Fig. 8. The auxiliary chain (Fig. 8b) consists of $\mathcal{N}=N/2$ sites which may be filled either by rigid monomers or by rigid dimers occupying two neighboring sites. The limiting behavior of $\mathcal{W}$ for $\mathcal{N}\to\infty$ was found by Fisher many years ago:[59]

$$\mathcal{W}=\exp\left(\log\frac{1+\sqrt{5}}{2}\mathcal{N}\right)\approx\exp(0.240606N)$$

$$\to\frac{S}{N}=0.240606. \tag{10}$$

The relevance of this result for experimental studies emerges at low but finite temperatures. In Ref. 33 this mapping was used to obtain a quantitative description of the low-temperature magnetothermodynamics in the vicinity of the saturation field of the quantum antiferromagnet on the kagomé lattice and on the sawtooth chain.

In what follows we report on the extension of the analytical findings for the zero-temperature entropy at the saturation field to finite temperatures and to arbitrary magnetic fields using exact diagonalization data for the sawtooth chain of up to $N=20$ sites.[34,35] In Fig. 9a we show the isothermal entropy versus magnetic field for several temperatures. The presented results show that for several magnetic fields below saturation $h<h_{\rm sat}$ one has a twofold or even threefold degeneracy of the energy levels, leading in a finite system to a

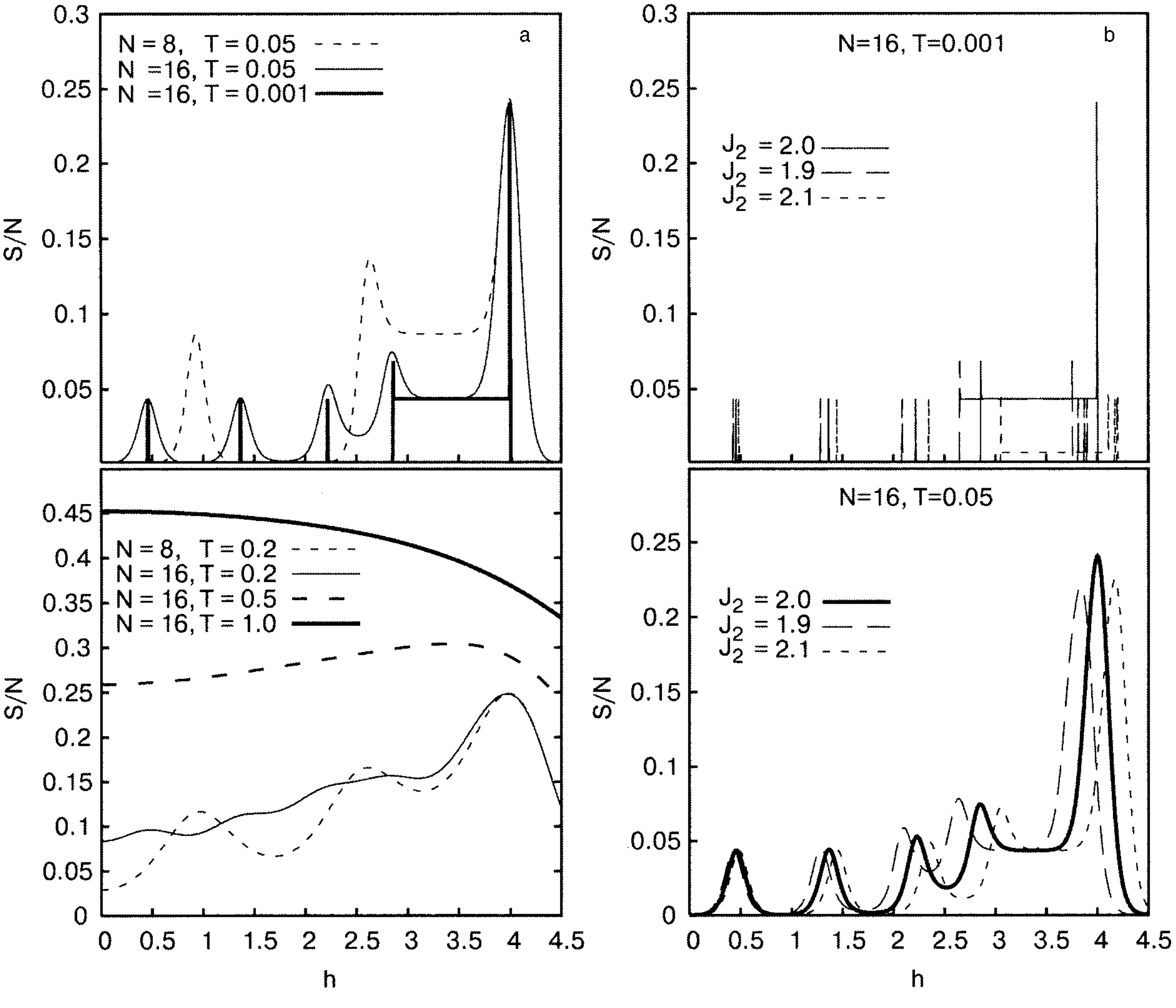

FIG. 9. Field dependence of the isothermal entropy per site for the Heisenberg antiferromagnet on the sawtooth chain of different length ($s=1/2$, $\Delta=1$). $J_1=1$, $J_2=2$, i.e., the condition for bond strengths [Eq. (4)] is fulfilled and the localized-magnon states are exact eigenstates (a). Influence of a deviation from the perfect condition for bond strengths (b). The figures were taken from Ref. 35.

finite zero-temperature entropy per site. Correspondingly one finds in Fig. 9a (upper panel) a peaked structure and moreover a plateau-like area just below $h_{\rm sat}$. However, it is clearly seen in Fig. 9a (upper panel) that the height of the peaks and of the plateau decreases with system size N, leading to $\lim_{N\to\infty}S/N=0$ at $T=0$ for $h<h_{\rm sat}$ and $h>h_{\rm sat}$. Only the peak at $h=h_{\rm sat}=4$ is independent of N and remains finite for $N\to\infty$. At finite but low temperatures this peak survives as a well-pronounced maximum, and it only disappears if the temperature is of the order of the exchange constant; see Fig. 9a (lower panel). Note that the value of the entropy at saturation, which agrees with the analytical prediction (10), is almost temperature independent up to about $T\approx0.2$. Thus, the effect of the independent localized magnons leading to a finite residual zero-temperature entropy is present at finite temperatures $T\lesssim0.2$, producing a noticeable maximum in the isothermal entropy curve at the saturation field. We mention that the numerical results for higher spin quantum numbers s suggest that the enhancement of the entropy at saturation for finite temperatures becomes less pronounced with increasing s.

With respect to the experimental observation of the maximum in the low-temperature entropy at the saturation field in real compounds we are faced with the situation that the condition on bond strengths [see Eq. (4)] under which the localized-magnon states become the exact eigenstates are certainly not strictly fulfilled. For the considered isotropic spin-half HAFM on the sawtooth chain this condition is fulfilled for $J_2=2J_1$; see Fig. 9a. Based on the numerical calculations one is able to discuss the "stability" of the maximum in the entropy against deviation from the perfect condition for bond strengths. In Fig. 9b we show the field dependence of the entropy at low temperatures for the sawtooth chain of $N=16$ sites with $J_1=1$ and $J_2=1.9$ and $J_2=2.1$. Since the degeneracy of the ground state at saturation is lifted when $J_2\neq 2J_1$, the entropy at saturation at very low temperatures (long-dashed and short-dashed curves in the upper panel of Fig. 9b) is not enhanced at the saturation field. However, the initially degenerate energy levels remain close to each other if J_2 deviates only slightly from the perfect value $2J_1$. Therefore with increasing temperature those levels become accessible for the spin system, and one again obtains a maximum in the entropy in the vicinity of saturation at low but nonzero temperatures; see the lower panel in Fig. 9b (long-dashed and short-dashed peaks in the vicinity of saturation). We emphasize that the low-temperature maximum of S/N at saturation is a generic effect for strongly frustrated quantum spin lattices which may host independent localized magnons.

Let us remark that the ground-state degeneracy problem of antiferromagnetic Ising lattices in the critical magnetic field (i.e., at the spin-flop transition point), which obviously do not contain quantum fluctuations, has been discussed in the literature; see, e.g., Ref. 62.

It has been pointed out very recently by Zhitomirsky and Honecker[34,63] that the most spectacular effect accompanying a maximum in the isothermal entropy $S(h)$ is an enhanced magnetocaloric effect. Indeed, the cooling rate for an adiabatic (de)magnetization process is proportional to the derivative of the isothermal entropy with respect to the magnetic field

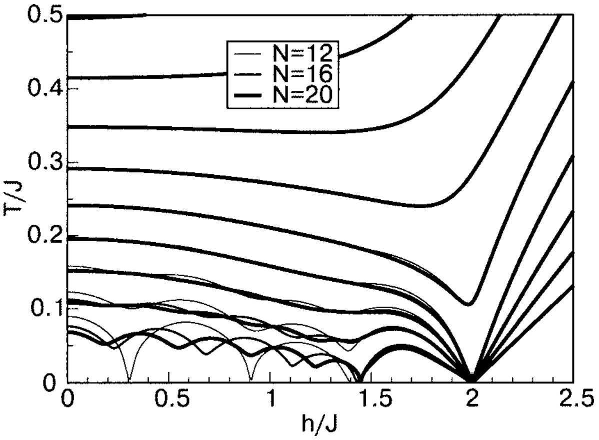

FIG. 10. Lines of constant entropy versus field [i.e., adiabatic (de)magnetization curves] for the Heisenberg antiferromagnet on the sawtooth chain of different length ($s=1/2$, $\Delta=1$, $J_1=J/2$, $J_2=J$). The figure was taken from Ref. 34 with the kind permission of A. Honecker.

$$\left(\frac{\partial T}{\partial h}\right)_S=-T\frac{(\partial S/\partial h)_T}{C}, \tag{11}$$

where C is the specific heat. Again one can calculate the field dependence of the temperature for an adiabatic (de)magnetization process for finite systems by exact diagonalization. Some results for the isotropic spin-half HAFM on the sawtooth chain are shown in Fig. 10. The lowest curves in Fig. 10 belongs to $S/N=0.05$ and $N=12,16,20$, respectively. The other curves correspond to $S/N=0.1,0.15,\ldots,0.4,0.45$. The magnetocaloric effect is largest in the vicinity of the saturation field. In particular, a demagnetization coming from magnetic fields larger than $h_{\rm sat}$ is very efficient. If one starts for $h>h_{\rm sat}$ with an entropy lower than the residual entropy at $h_{\rm sat}$, $S/N=0.240606$ [see Eq. (10)], then one observes even a cooling to $T\to0$ as $h\to h_{\rm sat}$. Thus frustrated magnetic systems hosting localized magnons allow magnetic cooling from quite large T down to very low temperatures. We mention, that the results shown in Fig. 10 also clearly demonstrate that finite-size effects are very small for $h=h_{\rm sat}$ at any temperature. Therefore the above discussion is valid also for large systems $N\to\infty$.

VI. SUMMARY

We have reviewed recent results[29–37] on exact eigenstates constructed from localized magnons which appear in a class of frustrated spin lattices. For these eigenstates several quantities like the energy and the spin-spin correlation can be calculated analytically. The physical relevance of the localized-magnon eigenstates emerges at high magnetic fields where they can become ground states of the spin system.

For frustrated magnetic systems having localized-magnon ground states several interesting physical effects associated with this states may occur. First one finds a macroscopic jump in the zero-temperature magnetization curve at the saturation field $h_{\rm sat}$. This jump is a true quantum effect which vanishes if the spins become classical ($s \rightarrow \infty$). At the foot of the jump one can expect a plateau in the magnetization curve.

Since all localized-magnon states have the same energy at $h = h_{\mathrm{sat}}$ a huge degeneracy of the ground state at saturation is observed which increases exponentially with system size N, thus leading to a nonzero residual zero-temperature entropy. For some of the frustrated spin models hosting localized magnons the residual entropy at saturation field can be estimated exactly. At finite temperatures T the localized-magnon states produce a maximum in the isothermal entropy versus field curve in the vicinity of the saturation field for not too large T. This maximum in the isothermal entropy at h_{sat} leads to an enhanced magnetocaloric effect. If one starts for $h > h_{\mathrm{sat}}$ with an entropy lower than the residual entropy at h_{sat} then one observes even a cooling to $T \rightarrow 0$ as $h \rightarrow h_{\mathrm{sat}}$. This may allow cooling from quite large T down to very low temperatures.

Last but not least, the localized-magnon states may lead to a spin-Peierls instability in strong magnetic fields, for instance for the antiferromagnetic kagomé spin lattice. For this system the magnetic-field driven spin-Peierls instability breaks spontaneously the translational symmetry of the kagomé lattice and appears only in a certain region of the magnetic field near saturation.

We emphasize that the reported effects are generic in highly frustrated magnets. To observe them in experiments one needs frustrated magnets with small spin quantum number s and sufficiently small exchange coupling strength J to reach the saturation field. There is an increasing number of synthesized quantum frustrated spin lattices, e.g., quantum antiferromagnets with a kagomé-like structure.[64–67] Though such materials often do not fit perfectly to the lattice geometry having localized-magnon ground states, the physical effects based on localized magnons states may survive in nonideal geometries (see Sec. 5), which may open the window to the experimental observation of the theoretically predicted effects.

The author is indebted to O. Derzhko, A. Honecker, H.-J. Schmidt, J. Schnack, and J. Schulenburg for the fruitful collaboration in the field of localized-magnon states in frustrated antiferromagnets. Most of the results discussed in the paper are based on common publications with these colleagues. In particular, I thank J. Schulenburg for many valuable discussions and hints. Furthermore I thank H. Frahm for directing my attention to the flat-band ferromagnetism. I also acknowledge the support from the Deutsche Forschungsgemeinschaft (Project No. Ri615/12-1).

[*] E-mail: Johannes.Richter@Physik.Uni-Magdeburg.DE

---

[1] D. C. Mattis, *The Theory of Magnetism I*, Springer-Verlag, Berlin (1991).
[2] P. Lemmens and P. Millet, in *Quantum Magnetism*, Vol. 645 of Lecture Notes in Physics, U. Schollwöck, J. Richter, D. J. J. Farnell, and R. F. Bishop (eds.), Springer-Verlag, Berlin (2004), p. 433.
[3] N. D. Mermin and H. Wagner, Phys. Rev. Lett. **17**, 1133 (1966).
[4] C. Lhuillier, P. Sindzingre, and J.-B. Fouet, Can. J. Phys. **79**, 1525 (2001).
[5] R. Moessner, Can. J. Phys. **79**, 1283 (2001).
[6] G. Misguich and C. Lhuillier, in *Frustrated Spin Systems*, H. T. Diep (ed.), World-Scientific (2004).
[7] J. Richter, J. Schulenburg, and A. Honecker, "Quantum magnetism in two dimensions: from semi-classical Néel order to magnetic disorder," in *Quantum Magnetism*, Vol. 645 of Lecture Notes in Physics, U. Schollwöck, J. Richter, D. J. J. Farnell, and R. F. Bishop (eds.), Springer-Verlag, Berlin (2004), p. 85; see also cond-mat/0412662.
[8] A. Honecker, J. Schulenburg, and J. Richter, J. Phys.: Condens. Matter **16**, S749 (2004).
[9] P. W. Anderson, Mater. Res. Bull. **8**, 153 (1973).
[10] P. Fazekas and P. W. Anderson, Philos. Mag. **30**, 423 (1974).
[11] K. Binder and A. P. Young, Rev. Mod. Phys. **58**, 801 (1986).
[12] W. Marshall, Proc. R. Soc. London, Ser. A **232**, 48 (1955).
[13] E. Lieb and D. Mattis, "Ordering energy levels of interacting spin systems," J. Math. Phys. **3**, 749 (1962).
[14] J. Richter, N. B. Ivanov, and K. Retzlaff, Europhys. Lett. **25**, 545 (1994).
[15] J. Richter, N. B. Ivanov, K. Retzlaff, and A. Voigt, J. Magn. Magn. Mater. **140–144**, 1611 (1995).
[16] H. A. Bethe, Z. Phys. **71**, 205 (1931).
[17] C. K. Majumdar and D. K. Ghosh, J. Math. Phys. **10**, 1399 (1969).
[18] B. S. Shastry and B. Sutherland, Physica B **108**, 1069 (1981).
[19] D. Poilblanc, J. Riera, C. A. Hayward, C. Berthier, and M. Horvatic, Phys. Rev. B **55**, R11941 (1997).
[20] S. Miyahara and K. Ueda, Phys. Rev. Lett. **82**, 3701 (1999).
[21] A. Pimpinelli, J. Phys.: Condens. Matter **3**, 445 (1991).
[22] N. B. Ivanov and J. Richter, Phys. Rev. A **232**, 308 (1997); J. Richter, N. B. Ivanov, and J. Schulenburg, J. Phys.: Condens. Matter **10**, 3635 (1998).
[23] K. Ueda and S. Miyahara, J. Phys.: Condens. Matter **11**, L175 (1999).
[24] H.-J. Schmidt, J. Phys. A **38**, 2133 (2005).
[25] A. Koga, K. Okunishi, and N. Kawakami, Phys. Rev. B **62**, 5558 (2002); A. Koga and N. Kawakami, Phys. Rev. B **65**, 214415 (2002).
[26] J. Schulenburg and J. Richter, Phys. Rev. B **65**, 054420 (2002).
[27] J. Schulenburg and J. Richter, Phys. Rev. B **66**, 134419 (2002).
[28] J. Richter and A. Voigt, J. Phys. A **27**, 1139 (1994); J. Richter, A. Voigt, and S. Krüger, J. Magn. Magn. Mater. **140–144**, 1497 (1995); J. Richter, A. Voigt, and S. Krüger, J. Phys. A **29**, 825 (1996).
[29] J. Schnack, H.-J. Schmidt, J. Richter, and J. Schulenburg, Eur. Phys. J. B **24**, 475 (2001).
[30] J. Schulenburg, A. Honecker, J. Schnack, J. Richter, and H.-J. Schmidt, Phys. Rev. Lett. **88**, 167207 (2002).
[31] J. Richter, J. Schulenburg, A. Honecker, J. Schnack, and H.-J. Schmidt, J. Phys.: Condens. Matter **16**, S779 (2004).
[32] J. Richter, O. Derzhko, and J. Schulenburg, Phys. Rev. Lett. **93**, 107206 (2004).
[33] M. E. Zhitomirsky and H. Tsunetsugu, Phys. Rev. B **70**, 100403(R) (2004).
[34] M. E. Zhitomirsky and A. Honecker, J. Stat. Mech.: Theor. Exp. P07012 (2004).
[35] O. Derzhko and J. Richter, Phys. Rev. B **70**, 104415 (2004).
[36] J. Richter, J. Schulenburg, A. Honecker, and D. Schmalfuss, Phys. Rev. B **70**, 174454 (2004).
[37] J. Richter, J. Schulenburg, P. Tomczak, and D. Schmalfuss, cond-mat/0411673 (2004), submitted to Phys. Rev. B .
[38] A. Mielke, J. Phys. A **24**, 3311 (1991).
[39] H. Tasaki, Phys. Rev. Lett. **69**, 1608 (1992).
[40] A. Mielke and H. Tasaki, Commun. Math. Phys. **158**, 341 (1993).
[41] H.-J. Schmidt, J. Phys. A **35**, 6545 (2002).
[42] T. Nakamura and K. Kubo, Phys. Rev. B **53**, 6393 (1996); D. Sen, B. S. Shastry, R. E. Walstedt, and R. Cava, Phys. Rev. B **53**, 6401 (1996).
[43] V. Ravi Chandra, D. Sen, N. B. Ivanov, and J. Richter, Phys. Rev. B **69**, 214406 (2004).
[44] Ch. Waldtmann, H. Kreutzmann, U. Schollwöck, K. Maisinger, and H.-U. Everts, Phys. Rev. B **62**, 9472 (2000).
[45] P. Azaria, C. Hooley, P. Lecheminant, and A. M. Tsvelik, Phys. Rev. Lett. **81**, 1694 (1998).
[46] H. Niggemann, G. Uimin, and J. Zittartz, J. Phys.: Condens. Matter **9**, 9031 (1997).
[47] F. Mila, Eur. Phys. J. B **6**, 201 (1998); A. Honecker, F. Mila, and M. Troyer, Eur. Phys. J. B **15**, 227 (2000).
[48] S. E. Palmer and J. T. Chalker, Phys. Rev. B **64**, 094412 (2001).
[49] R. Siddharthan and A. Georges, Phys. Rev. B **65**, 014417 (2002); P. Tomczak and J. Richter, J. Phys. A **36**, 5399 (2003).
[50] B. Canals and C. Lacroix, Phys. Rev. Lett. **80**, 2933 (1998).
[51] T. Momoi and K. Totsuka, Phys. Rev. B **61**, 3231 (2000).
[52] M. Oshikawa, Phys. Rev. Lett. **84**, 1535 (2000).
[53] S.-H. Lee, C. Broholm, T. H. Kim, W. Ratcliff II, and S-W. Cheong, Phys. Rev. Lett. **84**, 3718 (2000); Y. Yamashita and K. Ueda, Phys. Rev. Lett. **85**, 4960 (2000); A. Keren and J. S. Gardner, Phys. Rev. Lett. **87**, 177201

(2001); F. Becca and F. Mila, Phys. Rev. Lett. **89**, 037204 (2002); P. Carretta, N. Papinutto, C. B. Azzoni, M. C. Mozzati, E. Pavarini, S. Gonthier, and P. Millet, Phys. Rev. B **66**, 094420 (2002); O. Tchernyshyov, R. Moessner, and S. L. Sondhi, Phys. Rev. Lett. **88**, 067203 (2002); F. Becca, F. Mila, and D. Poilblanc, Phys. Rev. Lett. **91**, 067202 (2003).

[54] M. C. Gross, Phys. Rev. B **20**, 4606 (1979).

[55] G. H. Wannier, Phys. Rev. **79**, 357 (1950).

[56] R. Moessner and S. L. Sondhi, Phys. Rev. B **63**, 224401 (2001).

[57] M. E. Zhitomirsky, Phys. Rev. Lett. **88**, 057204 (2002).

[58] M. Udagawa, M. Ogata, and Z. Hiroi, J. Phys. Soc. Jpn. **71**, 2365 (2002).

[59] M. E. Fisher, Phys. Rev. **124**, 1664 (1961); R. J. Baxter, I. G. Enting, and S. K. Tsang, J. Stat. Phys. **22**, 465 (1980); R. J. Baxter and S. K. Tsang, J. Phys. A **13**, 1023 (1980); R. J. Baxter, J. Phys. A **13**, L61 (1980); R. J. Baxter, *Exactly Solved Models in Statistical Mechanics*, Academic Press, London (1982); R. J. Baxter, Ann. Combinatorics **3**, 191 (1999).

[60] J. Villain, R. Bidaux, J. P. Carton, and R. Conte, J. Phys. A **41**, 1263 (1980).

[61] E. F. Shender, Zh. Éksp. Teor. Fiz. **83**, 326 (1982) (Sov. Phys. JETP **56**, 178 (1982)).

[62] B. D. Metcalf and C. P. Yang, Phys. Rev. B **18**, 2304 (1978).

[63] M. E. Zhitomirsky, Phys. Rev. B **67**, 104421 (2003).

[64] A. P. Ramirez, B. Hessen, and M. Winklemann, Phys. Rev. Lett. **84**, 2957 (2000).

[65] Zenji Hiroi, Masafumi Hanawa, Naoya Kobayashi, Minoru Nohara, Hidenori Takagi, Yoshitomo Kato, and Masashi Takigawa, J. Phys. Soc. Jpn. **70**, 3377 (2001).

[66] A. Fukaya, Y. Fudamoto, I. M. Gat, T. Ito, M. I. Larkin, A. T. Savici, Y. J. Uemura, P. P. Kyriakou, G. M. Luke, M. T. Rovers, K. M. Kojima, A. Keren, M. Hanawa, and Z. Hiroi, Phys. Rev. Lett. **91**, 207603 (2003).

[67] D. Bono, P. Mendels, G. Collin, and N. Blanchard, Phys. Rev. Lett. **92**, 217202 (2004).

This article was published in English in the original Russian journal: Reproduced here with stylistic changes by AIP.

LOW TEMPERATURE PHYSICS VOLUME 31, NUMBERS 8–9 AUGUST–SEPTEMBER 2005

Correlations, spin dynamics, defects: the highly frustrated kagomé bilayer

D. Bono,* L. Limot,† and P. Mendels‡

Laboratoire de Physique des Solides, UMR 8502, Université Paris-Sud, 91405 Orsay, France

G. Collin

Laboratoire Léon Brillouin, CE Saclay, CEA-CNRS, 91191 Gif-sur-Yvette, France

N. Blanchard

Laboratoire de Physique des Solides, UMR 8502, Université Paris-Sud, 91405 Orsay, France

(Submitted March 21, 2005)
Fiz. Nizk. Temp. **31**, 929–951 (August–September 2005)

The compounds $SrCr_{9p}Ga_{12-9p}O_{19}$ and $Ba_2Sn_2ZnGa_{10-7p}Cr_{7p}O_{22}$ are two highly frustrated magnets possessing a quasi-two-dimensional kagomé bilayer of spin-3/2 chromium ions with antiferromagnetic interactions. Their magnetic susceptibility was measured by local nuclear magnetic resonance and nonlocal (SQUID) techniques, and their low-temperature spin dynamics by muon spin resonance. Consistent with the theoretical picture drawn for geometrically frustrated systems, the kagomé bilayer is shown here to exhibit: (i) short range spin-spin correlations down to a temperature much lower than the Curie–Weiss temperature, no conventional long-range transition occurring; (ii) a Curie contribution to the susceptibility from paramagnetic defects generated by spin vacancies; (iii) low-temperature spin fluctuations, at least down to 30 mK, which are a trademark of a dynamical ground state. These properties point to a spin-liquid ground state, possibly built on resonating valence bonds with unconfined spinons as the magnetic excitations.
[DOI: 10.1063/1.2008131]

I. INTRODUCTION

A. Highly frustrated magnets

Anderson's initial proposal of a resonating valence bond (RVB) state was intended as a possible alternative for the Néel ground state of a triangular network with Heisenberg spins coupled by an antiferromagnetic interaction.[1] The RVB state, known also as a "spin-liquid" state because of the short-range magnetic correlations and spin fluctuations down to $T=0$, was also proposed to explain the high-T_c behavior of cuprates[2] and, more recently,[3] of the superconducting compound $Na_xCoO_2 \cdot yH_2O$. Although Anderson's conjecture was proven to be wrong for the triangular network,[4] there is a growing consensus that the RVB state is the ground state of the so-called highly frustrated networks.[5,6] Like the triangular network, the magnetic frustration of these systems is exclusively driven by the triangular geometry of their lattice provided that spins are coupled through an antiferromagnetic (AFM) interaction. This is different from spin glasses, where frustration arises from the randomness of the magnetic interactions.[7] However, compared to a triangular network, these networks have a corner-sharing geometry, as in the two-dimensional kagomé (corner sharing triangles, Fig. 1), the three-dimensional pyrochlore (corner sharing tetrahedra, Fig. 1), and the quasi-two-dimensional kagomé bilayer (corner sharing triangles and tetrahedra, Fig. 2) lattices. The corner-sharing geometry introduces a "magnetic flexibility," thereby enhancing the frustration of these networks (thus the term "highly") and destabilizing the Néel order. A highly frustrated network, and the experimental counterpart known as highly frustrated magnet (HFM), is therefore an ideal candidate to possess a RVB ground state. Moreover, since HFMs are insulators, the experimental investigation of their ground state, and the related theoretical modeling, is greatly simplified by the absence of phenomena such as superconductivity, charge ordering or itinerant magnetism.

The original features of the ground state of the Heisenberg two-dimensional (2D) kagomé network, which is the central issue of this paper, is already apparent through a *classical* description of their magnetism,[8–11] yielding a dynamical ground state with infinite degeneracy. More precisely, the "order by disorder" mechanism selects a coplanar spin arrangement in the ground state. However, the system can swap from one coplanar spin configuration to the other by a rotation of a finite number of spins, with no cost in energy. These zero-energy excitation modes, or soft modes, prevent a selection of one of the coplanar configurations(1) and constitute a low-energy reservoir of magnetic excitations. It results in a finite entropy per spin in the ground state, without, still up to now, any definitive conclusions on a possible long-range order, even at $T=0$.

In a *quantum* description of the magnetism for Heisenberg spins 1/2 on the kagomé network, the magnetic ground state is disordered.[11] It is predicted to be RVB-like, built on a macroscopic number of singlet states.[13,14] If any, a gap between the ground state and the first triplet state is expected to be fairly small, of the order of $J/20$,[15] where J is the AFM interaction between nearest neighbor spins.(2) Most strikingly and similar to the classical case, the corner-sharing geometry and the half-integer spins lead to an exponential density of

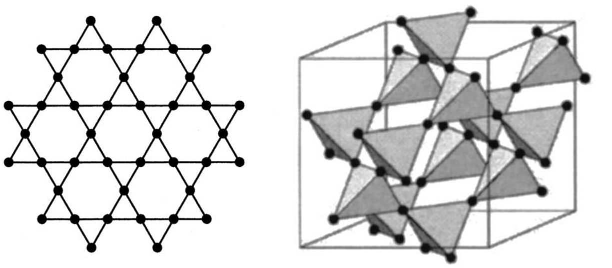

FIG. 1. The kagomé (left) and the pyrochlore (right)[12] corner-sharing lattices. The coordinance of each site is 4 and 6, respectively.

low-lying singlet excitations,[16] with energies smaller than the gap, and to a nonzero entropy per spin at $T=0$.[17] The same conclusions seem to emerge for the AFM pyrochlore lattice.[18] The nature of the magnetic excitations, possibly unconfined spinons, is still an open question.[17,19]

As a major drawback, every additional contribution to the nearest-neighbor AFM interaction, such as next-nearest-neighbor interactions, dipolar interactions, anisotropy, Dzyaloshinskii-Moriya interactions, lattice distortions or magnetic defects generated by the presence of magnetic impurities or spin vacancies, all of which we designate by "disorder," may release the frustration and stabilize an original ground state.[20–25] Experimentally, disorder is present in all HFMs and indeed causes cooperative phase transitions at low temperature, reminiscent of spin glasses or AFM systems. This is typically observed in the jarosites kagomé family, where the disorder is governed by spin anisotropy and by dipolar interactions (Ref. 26).[3)] In the spin-1/2 kagomé compound $[\mathrm{Cu_3(titmb)_2(OCOCH_3)_6}]\cdot\mathrm{H_2O}$, the competition between first- and second-neighbor interactions, respectively ferromagnetic and antiferromagnetic, yields an original ground state, with a double peak in the specific heat and plateaus in the magnetization under particular conditions.[27] In the $S=1$ kagomé staircase $\mathrm{Ni_3V_2O_8}$, the competition between first and second neighbor interactions, combined to Dzyaloshinskii-Moriya interactions and spin anisotropy, produces a very rich field and temperature phase diagram.[28] In three dimensions (3D), dipolar couplings and interactions further than nearest neighbor yield long-range magnetic order at 1 K in the pyrochlore compound $\mathrm{Gd_2Ti_2O_7}$ (Ref. 29). In $\mathrm{Y_2Mo_2O_7}$, lattice distortions have been proposed to relieve the frustration in the ground state.[30] However, some samples, like the pyrochlore $\mathrm{Tb_{2-p}Y_pTi_2O_7}$ (Refs. 31, 32) or the spinel $\mathrm{ZnCr_2O_4}$ (Ref. 33) display spin dynamics down to very low temperature. Anyway, the high spin values and/or the 3D character of the frustrated geometry of these compounds remain far from the ideal Heisenberg kagomé case we are dealing with. Along with the spin-liquid ground state of the ideal systems, the plethoric number of possible ground states in the presence of disorder (including the case of ferromagnetic interactions in the pyrochlore lattice, yielding the frustrated so-called "spin ice" ground state,[34,35] named so as it is equivalent to the order observed for hydrogen atoms in ice $\mathrm{H_2O}$), constitutes one of the rich aspects of the HFMs.

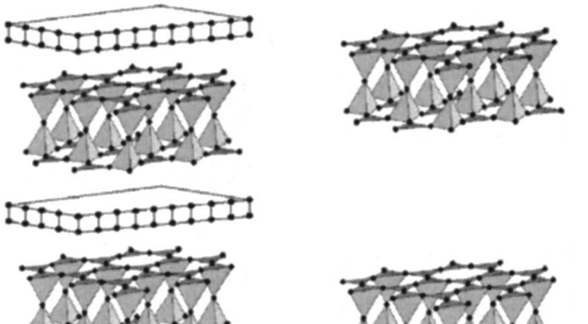

FIG. 2. Kagomé bilayers in SCGO (left) and in BSZCGO (right). There are two different sites in the kagomé bilayer lattice, one of coordinance 5, the other of coordinance 6. The magnetism of both compounds arises from the stacking of magnetically decoupled kagomé bilayers, ensured in SCGO by the presence of the nonmagnetic singlets and in BZSCGO by a large interbilayer distance.

B. SCGO and BSZCGO

Among all HFMs, the chromium-based spin-3/2 kagomé bilayer compounds $\mathrm{SrCr_{9p}Ga_{12-9p}O_{19}}$ [SCGO(p); Ref. 36] and $\mathrm{Ba_2Sn_2ZnGa_{10-7p}Cr_{7p}O_{22}}$ [BSZCGO(p); Ref. 37] are the most likely candidates to possess a spin-liquid ground state. This is not surprising in view of the low spin value, 2D character, and low level of disorder of these compounds compared to other HFMs. They are in fact an experimental realization of a quasi-2D kagomé bilayer of spin-3/2 chromium ions with antiferromagnetic interactions (Fig. 2). Moreover, the AFM interaction between nearest neighboring spins is dominated by a direct overlap exchange resulting in a coupling of $J\sim 40$ K (see Sec. 2). This coupling is almost two orders of magnitude larger than the typical disorder-related interactions, like single-ion anisotropy, estimated to 0.08 K,[38,39] dipolar interactions ~ 0.1 K, or next-nearest-neighbor interactions <1 K. These compounds, however, always have a small amount of substitutional disorder, since a Cr coverage higher than $p=0.95$ and $p=0.97$ cannot be reached in SCGO(p) (Ref. 40) and BSZCGO(p) (Ref. 41), respectively. Hence there are always at least some percent of the magnetic $\mathrm{Cr^{3+}}$ ions which are substituted with nonmagnetic $\mathrm{Ga^{3+}}$ ions. These low amounts of spin vacancies, and the related magnetic defects that they produce, turn out to be insufficient to destroy the spin-liquid behavior of the ground state. We will show that local techniques like nuclear magnetic resonance (NMR) and muon spin relaxation (μSR) are the most suited to probe frustration-related properties in these systems, since they can bypass the magnetic contribution of these defects.

Figure 3 presents a simplified chemical structure for the ideal $p=1$ unit cell of SCGO and of BSZCGO, highlighting the chromium kagomé bilayers.[4)] As can be seen, BSZCGO is a pure kagomé bilayer, contrary to SCGO, where there are two additional chromium sites, labeled Cr(c), between the bilayers. These pairs of Cr spins are coupled by an AFM exchange constant of 216 K with a weak coupling to the kagomé bilayers (~ 1 K).[42] They form an isolated singlet at low temperatures, and the resulting susceptibility is negligible at $T\lesssim 50$ K compared to the susceptibility of the kagomé bilayer in a pure compound. Moreover, the Ga/Cr substitutions are substoechiometric on these sites (see Sec. 2.3.3). The full crystal structure is obtained by the stacking

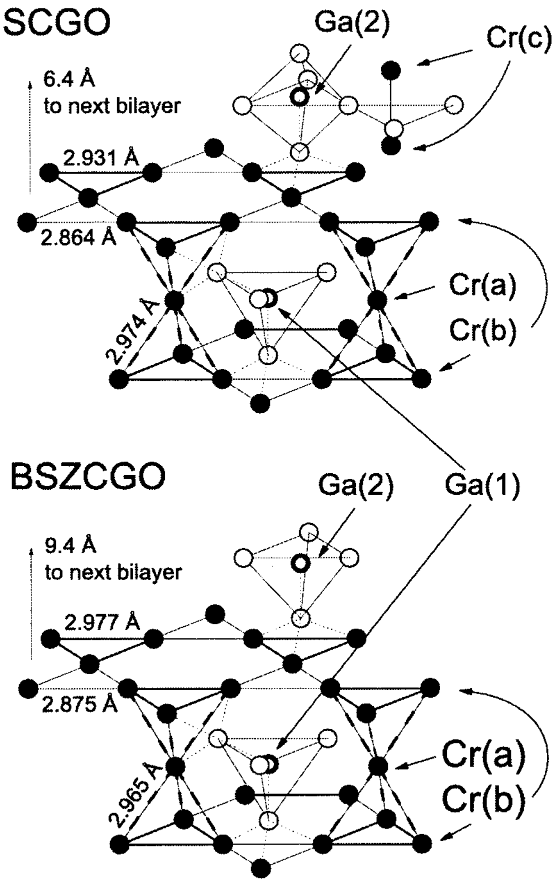

FIG. 3. Cr^{3+} network of SCGO and BSZCGO with their oxygen (○) environments, along with the two Ga^{3+} sites. The dotted lines represent some of the Ga–O–Cr hyperfine coupling paths.

of the unit cells presented in Fig. 3. The magnetism of both compounds arises by magnetically decoupled kagomé bilayers, ensured in SCGO by the presence of the nonmagnetic singlets at low temperature (only weakly affected by the Ga/Cr substitution, see Sec. 2.3.3), and in BSZCGO by the large inter-bilayer distance of 9.4 Å (6.4 Å in SCGO). These compounds can therefore be considered as ideal two-dimensional systems.

Figure 4 shows the typical macroscopic susceptibility

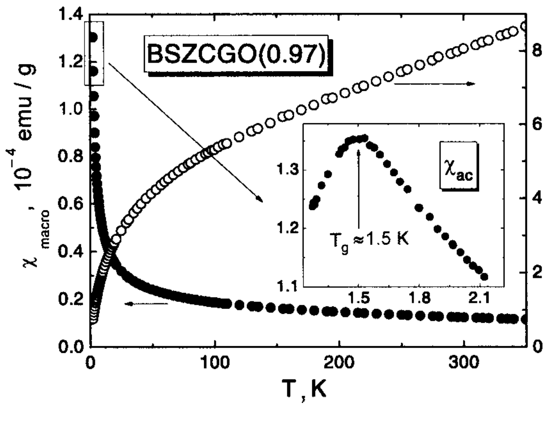

FIG. 4. Macroscopic static susceptibility $\chi_{\rm macro}(T)$ of BSZCGO(0.97) measured with a SQUID under 100 G (left scale) and $\chi^{-1}_{\rm macro}(T)$ (right scale). Inset: ac susceptibility (78 Hz) below 2 K, focusing on the spin-glass-like transition (T_g).

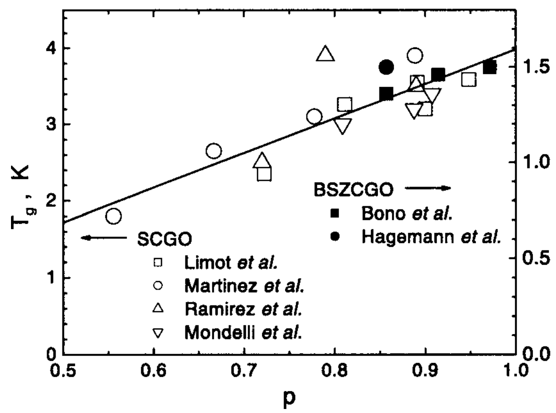

FIG. 5. Collection of spin-glass-like transition temperatures T_g for SCGO and for BSZCGO versus Cr concentration p (our data and from Refs. 37, 38, 50, 51). The line is a guide to the eye.

$\chi_{\rm macro}$ in these compounds. The linearity of $\chi^{-1}_{\rm macro}$ at high temperature and the extrapolation of this line to $\chi^{-1}_{\rm macro}=0$ to a negative temperature is typical of AFM interactions and gives an order of magnitude of the Curie-Weiss temperature $\theta_{CW}=zS(S+1)J/3$ (600 K and 350 K for SCGO and BSZCGO). However, contrary to the case of "conventional" antiferromagnets,[43] no kink is evidenced in $\chi_{\rm macro}$ around θ_{CW}. This is actually one of the common signatures of the frustration in HFMs:[5] the magnetic correlation length cannot increase because of frustration, and mean field theory remains valid for $T\sim\theta_{CW}$. At low temperature, a spin-glass-like transition occurs in both systems, around a freezing temperature $T_g\sim 3$ K in SCGO(p) and 1.5 K in BSZCGO(p) (Fig. 5).

However, the spin-glass transition is unconventional. In fact, in *conventional 3D spin glasses* the nonlinear susceptibility diverges at T_g, the specific heat is proportional to T at low temperature, and T_g is proportional to the number of defects. In *kagomé bilayers*, however, (i) the nonlinear susceptibility diverges at T_g (Ref. 44), but T_g increases as the number of spin vacancies decreases (Fig. 5), indicating that the freezing is related to an intrinsic property of the frustrated bilayer. (ii) The specific heat is proportional to T^2, as in AFM 2D *long-range ordered* systems. Its unusual large value at low temperature unveils a high density of low-lying excitations,[37,44] and its insensitivity to an external magnetic field suggests a large contribution from singlet excitations, which is one of the most striking features predicted for the $S=1/2$ kagomé lattice.[45–47] (iii) Magnetic fluctuations and short-range correlations, consistent with a 2D magnetic network, are encountered at low temperature.[48,49] The kagomé bilayers therefore combine properties of 3D spin glasses, 2D AFM ordering, 2D fluctuating magnetic states and original properties expected in $S=1/2$ kagomé systems.

Given these two temperature scales of the macroscopic susceptibility, θ_{CW} and T_g, Ramírez proposed the definition of a "frustration ratio," $f=\theta_{CW}/T_g$, with $f>10$ in all HFMs.[52] The kagomé bilayers SCGO and BSZCGO, respectively, display $f\sim 150$ and 230,[41] the largest ratios reported so far in compounds where the frustration is driven by corner sharing equilateral triangles.[5] The large frustration, the Heisenberg spins along with the low disorder, make them the archetypes of HFM and maybe the best candidates for a RVB spin-liquid ground state.

We present a review of the magnetic properties of SCGO(p) and BSZCGO(p) *powder samples*, which covers a large range of Cr concentration p. A comparison between samples of different concentration allows us to identify the frustrated and disorder-related magnetic properties of the kagomé bilayer. Through local probes it is then possible to determine the true nature of the bilayer's static susceptibility (by NMR), as well as the bilayer's low-temperature dynamics and ground-state magnetic excitations (by μSR). The outline of the paper is as follows. Section 2 is dedicated to the susceptibility of the kagomé bilayer. It is shown that the susceptibility of the bilayer of SCGO and of BSZCGO can be accessed directly through gallium NMR experiments.[40,41,53–56] Both susceptibilities exhibit a maximum in temperature at $T \sim 40$ K$\sim J$ and decrease below this maximum down to at least $J/4$. This behavior indicates that short range magnetic correlations persist at least down to 10 K, being consistent with the existence of a small spin gap. The comparison of the kagomé bilayer's susceptibility with χ_{macro} shows that the spin vacancies of the bilayer generate paramagnetic defects responsible for the low-temperature Curie upturn observed in the macroscopic susceptibility (both systems have also extra Curie contributions, coming from broken Cr(c) spin pairs in SCGO and from bond length distribution in BSZCGO). Section 3 is dedicated to the μSR study of the low-temperature spin dynamics of these HFMs.[49,56–58] It is shown that magnetic excitations persist down to at least 30 mK (the lowest temperature that could be accessed). This temperature sets an upper limit for the value of a spin gap. A qualitative and quantitative analysis of the data shows that these excitations are possibly coherent unconfined spinons of a RVB ground state. The energy scale T_g would then correspond, in this phenomenological approach, to the signature of this coherent resonating state. A summary and concluding remarks can be found in Sec. 4.

II. FRUSTRATED VERSUS DISORDER-RELATED SUSCEPTIBILITY

A. Gallium NMR in SCGO and BSZCGO

The NMR experiments were performed on ^{69}Ga ($^{69}\gamma/2\pi = 10.219$ MHz/T, $^{69}Q = 0.178 \times 10^{-24}$ cm^2) and ^{71}Ga ($^{71}\gamma/2\pi = 12.983$ MHz/T, $^{71}Q = 0.112 \times 10^{-24}$ cm^2) nuclei in SCGO and BSZCGO using a $\pi/2-\tau-\pi$ spin echo sequence, where γ and Q are, respectively, the gyromagnetic ratio and the quadrupolar moment of the nuclei. The gallium ions are located on two distinct crystallographic sites, labeled Ga(1) and Ga(2) in Fig. 3. As pointed out in Refs. 40, 41, 53, 56, the interest in Ga NMR lies in the coupling between gallium nuclei with their neighboring magnetic Cr^{3+} ions through a Ga-O-Cr hyperfine bridge (Fig. 3). In particular, the ^{69,71}Ga(1) nuclei are exclusively coupled to the Cr^{3+} ions of the kagomé bilayer: to nine chromium ions of the upper and lower kagomé layers [labeled Cr(b) in Fig. 3], and to three chromium ions in the linking site in between the two kagomé layers [labeled Cr(a) in Fig. 3]. Through the NMR of Ga(1), it is possible to probe locally the magnetic properties of the kagomé bilayers of both HFMs. This is the central topic of the NMR study presented in this paper.

TABLE I. Quadrupole parameters for the ^{71}Ga sites in SCGO[40,53] and in BSZCGO.[41] Notice that $^{69}\nu_Q = (^{69}Q/^{71}Q)^{71}\nu_Q \approx 1.59^{71}\nu_Q$. Quadrupole effects are therefore more pronounced for the ^{69}Ga isotope than for the ^{71}Ga.

	Ga site	$^{71}\nu_Q$ (MHz)	η
SCGO	Ga(1)	2.9(2)	0.005(6)
	Ga(2)	20.5(3)	0.050(35)
BSZCGO	Ga(1)	3.5(1.0)	0.60(15)*
	Ga(2)	12.0(5)	0.04(3)

*Determined using point charge simulation.

Before going any further, we briefly recall some relationship between the contribution of each gallium nucleus to the Ga(1) NMR line and its local magnetic environment in order to underline what can be exactly probed through Ga(1) NMR. We suppose first that the susceptibility in the kagomé bilayer varies from chromium site to chromium site and label it, in a generic manner, by χ. A Ga(1) at site i will contribute to the NMR spectrum at a position depending upon the number of the nearest neighbors (NN) occupied chromium sites and their susceptibility χ. This corresponds to the shift K^i in the NMR spectrum for a gallium at site i:

$$K^i = \sum_{\text{occupied NN Cr}(a,b)} A\chi, \tag{1}$$

where A is the hyperfine constant (the chemical shift is neglected here). The average shift, K, of the NMR line, is simply related to the average $\overline{K^i}$ over all the gallium sites. Hence, it is practically proportional to the average susceptibility χ_{kag} of the kagomé bilayer. On the other hand, the distribution of K^i around K defines the magnetic width of the Ga NMR line and reflects the existence of a distribution of χ. As we show in the following sections, the NMR width probes a susceptibility related to disorder in BSZCGO and in SCGO.

Along with this hyperfine interaction, the ^{69,71}Ga Hamiltonian in SCGO and in BSZCGO has a quadrupolar contribution. The quadrupole interaction of gallium nuclei in both SCGO and BSZCGO is a consequence of the coupling of the nucleus to the electric field gradient (EFG) produced by the surrounding electronic charges. Following the usual notations, the nuclear Hamiltonian may be expressed as

$$\mathcal{H} = -\gamma\hbar\mathbf{I}(\bar{1}+\bar{K})\mathbf{H}_0 + \frac{h\nu_Q}{6}\left[3I_z^2 - I^2 + \eta(I_x^2 - I_y^2)\right], \tag{2}$$

where $\mathbf{H}_0$ is the applied magnetic field, ν_Q is the quadrupolar frequency, and $0 \leqslant \eta \leqslant 1$ is the asymmetry parameter. The principal axes of the shift tensor $\bar{K}$ are collinear with the direction of the nuclear spin operators I_x, I_y, and I_z.

As shown in Fig. 3, the gallium sites of both HFMs have different crystallographic environments. Some simple arguments can be used to anticipate differences concerning their spectra (Table I):

(i) The Ga(1) sites of both HFMs have a nearly tetrahedral oxygen environment. Given this nearly cubic symmetry, the EFG is small, i.e., ν_Q is small. However, whereas the Ga(1) site of SCGO is occupied only by Ga^{3+} ions, the

Ga(1) site of BSZCGO is randomly occupied either by Zn^{2+} or by Ga^{3+} ions. As a consequence, point charge simulations of the EFG on the Ga(1) site of BSZCGO show that there is a large distribution of η and ν_Q, contrary to the Ga(1) of SCGO.

(ii) The Ga(2) site of SCGO is surrounded by a bipyramid of 5 oxygen ions, whereas the Ga(2) of BSZCGO lies in an oxygen-elongated tetrahedron. As both environments lack cubic symmetry, the quadrupolar frequency is large. For this site, point charge simulations yield a ν_Q that is twice as large in SCGO as in BSZCGO.

(iii) The ratio Ga(1):Ga(2) is 2:1 in SCGO, whereas it is 1:2 in BSZCGO. Consequently, the relative spectral weight of the Ga(1) and Ga(2) sites will be opposite in the two compounds.

An extensive study of the ^{69,71}Ga NMR spectra in SCGO was presented in Refs. 40 and 53. It allowed identification of the NMR lines and extraction of the parameters of the nuclear Hamiltonian, among them the quadrupolar parameters given in Table I. It was shown that the Ga NMR spectrum of both isotopes is the sum of the Ga(1) and Ga(2) sites, plus a small extra contribution related to the presence of the nonstoichiometric gallium substituted on the chromium sites [labeled Ga(sub) in Fig. 8]. A similar analysis allowed identification of the NMR lines in BSZCGO and determination of the related parameters of the nuclear Hamiltonian,[41] also listed in Table I.

Aside from the Ga-substituted sites, the Ga NMR spectrum displays four sets of lines corresponding to the two isotopes distributed on both Ga(1) and Ga(2) sites. In a powder sample, as used here, for a given site and a given isotope, the line shape results from the distribution of the angles between the magnetic field and the EFG principal axes. This yields singularities rather than well defined peaks (the so-called powder line shape), as in the Ga NMR spectra of SCGO(0.95) and of BSZCGO(0.97) presented in Fig. 6.

Powder-pattern simulations for two different rf frequencies ($\nu_l = 40$ MHz and 84 MHz) are presented in Fig. 7, using the parameters of Table I. They agree perfectly with the experimental NMR spectra and clearly show that the BSZCGO spectrum is more intricate than the SCGO one, because of the more pronounced quadrupolar contribution. This is probably the reason why the Ga(sub) line cannot be resolved in BSZCGO, contrary to SCGO.

Most of the SCGO data were acquired in a field-sweep spectrometer with an rf frequency $\nu_l \approx 40$ MHz, because then the ^{69,71}Ga(1) NMR lines can be isolated, as shown in Fig. 7.[40] At high temperatures (Fig. 8a) the NMR line shape remains unaltered and shifts with decreasing temperature. At low temperature ($T < 50$ K), the line broadens with decreasing temperature (Fig. 8b). The ^{69,71}Ga(1) shift is still qualitatively visible down to 5 K, where the Ga NMR signal is lost (see below). Fits of the low-temperature spectra (using a convolution of a high-temperature unbroadened spectrum with a Gaussian) allow one to extract quantitatively the shift and the width of the NMR lines for all the samples studied ($0.72 \leqslant p \leqslant 0.95$). All display similar shifts with temperature, but different broadening, the line shape increasing with Ga/Cr substitution at a given temperature.[40]

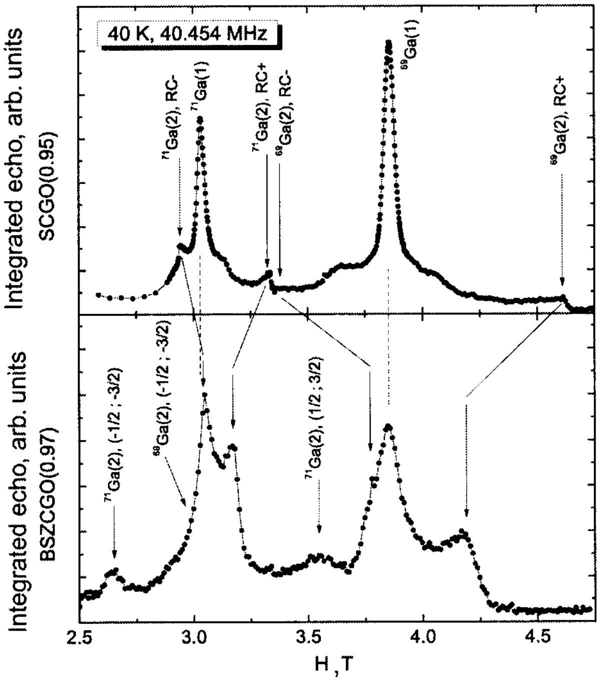

FIG. 6. Comparison of the ^{69,71}Ga NMR spectra in SCGO and BSZCGO obtained by sweeping the field with a constant frequency $\nu_l \approx 40$ MHz, at $T = 40$ K. The arrows point the quadrupolar singularities for the Ga(1) and Ga(2), respectively, located inside and outside the bilayers (Fig. 3). "CL" indicates the central line ($1/2 \leftrightarrow -1/2$ transition) singularities. The continuous and dashed lines show the shift of the in-range singularities of the Ga sites, from one system to the other. We cannot identify the first order satellites of the Ga(1) in BSZCGO on this spectrum.

In the case of BSZCGO, it can be seen from Fig. 7 that it is advantageous to work at a frequency higher than 40 MHz, in order to isolate the Ga(1) contribution.5) Field-sweep ^{71}Ga NMR experiments were performed at an rf frequency $\nu_l \approx 84$ MHz. At high temperature (Fig. 9a) a ^{71}Ga(1) shift is evidenced, similar to the one in SCGO.6) At low temperature, the ^{71}Ga(1) and ^{71}Ga(2) lines broaden and start to overlap. However, the two lines can be resolved by exploiting the different transverse relaxation times T_2 of the two gallium sites ($T_{2,\mathrm{Ga(1)}} \sim 20$ μs, $T_{2,\mathrm{Ga(2)}} \sim 200$ μs). The first step consists in using a large time separation between the two rf pulses ($\tau = 200$ μs) in order to eliminate the Ga(1)

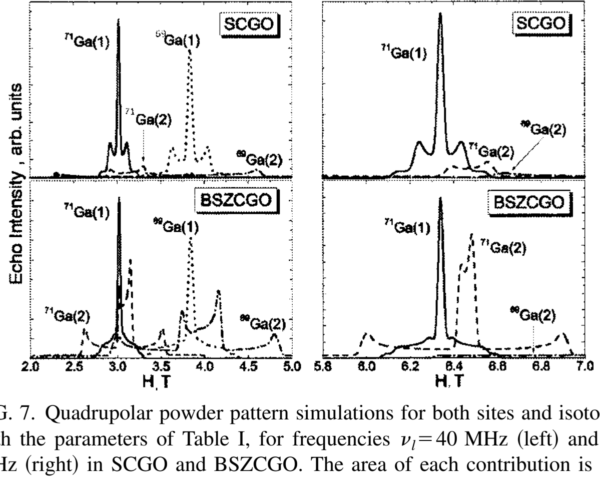

FIG. 7. Quadrupolar powder pattern simulations for both sites and isotopes with the parameters of Table I, for frequencies $\nu_l = 40$ MHz (left) and 84 MHz (right) in SCGO and BSZCGO. The area of each contribution is obtained considering the stoichiometry of each site in the samples and the natural abundance of each isotope. The full NMR spectra are obtained by adding all the contributions (not shown).

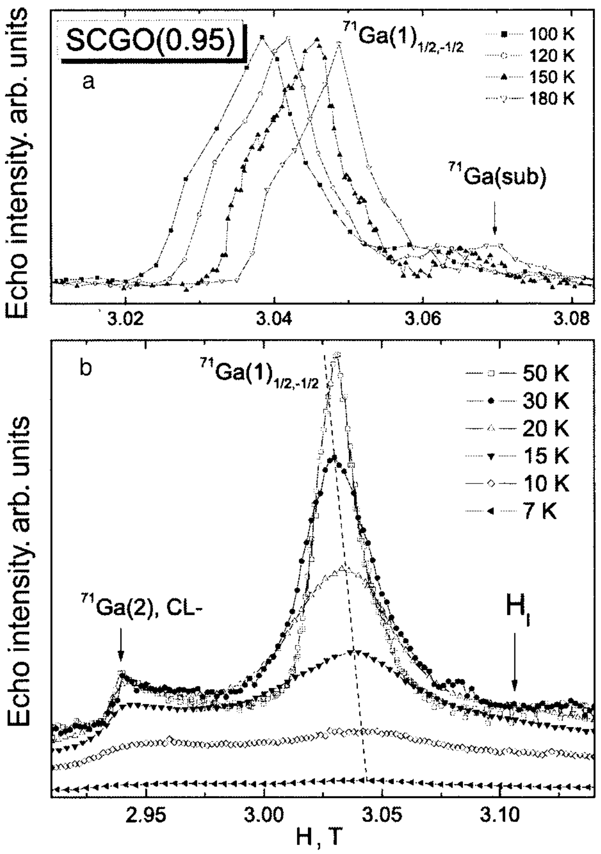

FIG. 8. ^{71}Ga spectra in SCGO ($H_l = 2\pi\nu_l/^{71}\gamma$). a—High temperature. The ^{71}Ga(2) contribution appears as a flat background in this field range. b—Low temperature, lines are broadened. The ^{71}Ga(2) contribution remains flat at the position of the ^{71}Ga(1) line, which shifts to higher fields in this temperature region when the temperature decreases.

contribution. The isolated Ga(2) line is extracted using a Gaussian convolution of the quadrupolar powder pattern. In the second step, a short time separation is employed between the pulses ($\tau \approx 10\ \mu$s) so that the Ga(1) contribution is recovered. The Ga(1) line is finally isolated by subtracting the long-τ spectrum corrected in intensity to account for the shorter time separation employed.[7)] Such a procedure can be employed down to 10 K. The width and the shift of the Ga(1) line can then be extracted from a fit using a $^{71}\nu_Q = 3.5$ MHz quadrupolar powder pattern convoluted by a Gaussian line shape, and are little affected by the uncertainty on $^{71}\nu_Q$. The ratio between the intensities of the Ga(2) and Ga(1) lines (integrated area below the lines) was found to stay close to 2 down to 10 K, in agreement with the 2:1 stoichiometric ratio for the Ga(2) and Ga(1) sites of BSZCGO.

The temperature dependence of the intensity of the ^{71}Ga(1) NMR line, which corresponds to the number of detected ^{71}Ga(1) nuclei, is presented in Fig. 10 for SCGO. A similar trend is observed in BSZCGO, with larger error bars due to the preponderant Ga(2) contribution. As temperature decreases the spin dynamics slows down, and results in a decreasing longitudinal relaxation time T_1 (see Sec. 3), hence in a progressive loss of the NMR signal below 15 K. Such a wipeout is reminiscent of the one observed in spin glasses at temperatures near T_g.[59] However, contrary to spin glasses, where ultimately the signal is recovered below T_g, there is no evidence for such a recovery in SCGO, nor in BSZCGO.

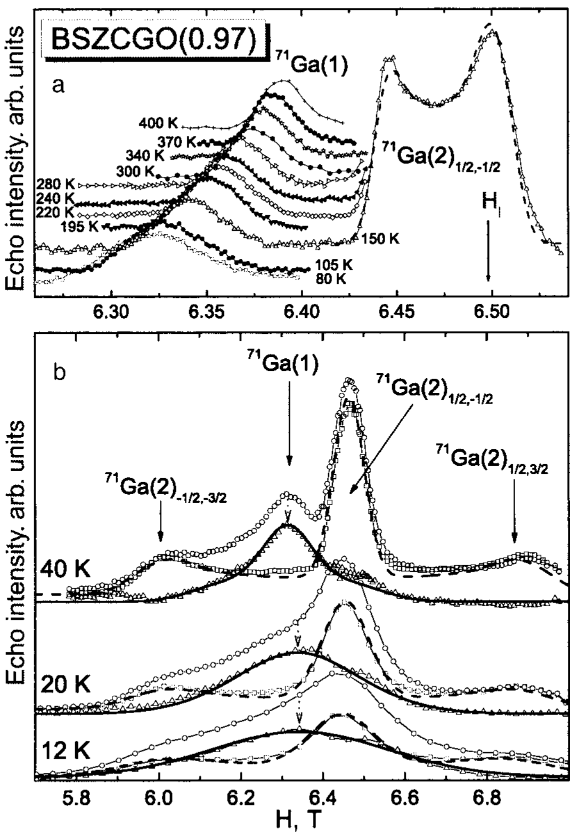

FIG. 9. ^{71}Ga spectra in BSZCGO. a—High temperature. The ^{71}Ga(2) first-order quadrupolar contribution appears as a flat background in this field range at the ^{71}Ga(1) line position. b—Low temperature, lines are broadened. ○ and □ are the short and the rescaled long spectra, respectively. △ is for the Ga(1) contribution, given by their subtraction. The dotted arrows point at the center of the Ga(1) line, which shifts to higher fields when T decreases. Continuous (dashed) lines are Gaussian broadened ^{71}Ga(1) [^{71}Ga(2)] quadrupolar powder pattern simulations, with $\nu_Q = 3.5$ MHz (12 MHz) and $\eta = 0.6$ ($\eta = 0.04$).

B. Susceptibility of the kagomé bilayer

The kagomé bilayer susceptibility χ_{kag} is probed through the shift K of the ^{69,71}Ga(1) NMR lines,[40,41,54] presented in

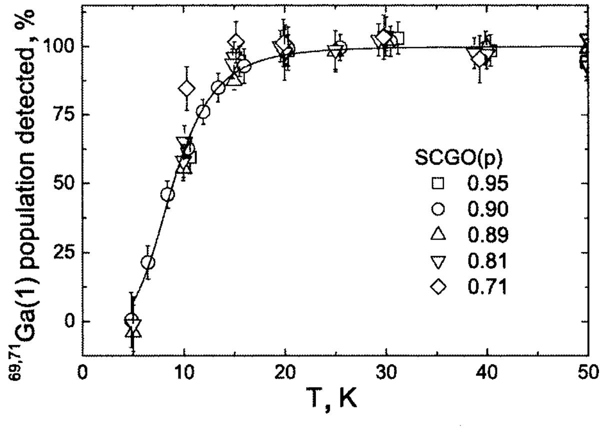

FIG. 10. NMR signal intensity in several SCGO(p) samples. A loss of ^{69,71}Ga sites is observed for $T \lesssim 5T_g$ ($\sim$16 K). The line is a guide to the eye.

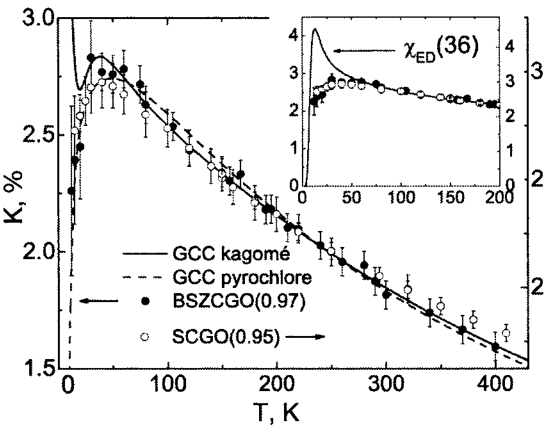

FIG. 11. Shift of the ^{71}Ga(1) line in SCGO and BSZCGO. Lines are GCC calculations (see text). Inset: Full scale down to 0. The line is the 36 spin $S=1/2$ cluster calculation mentioned in the text (χ_{ED}).

Fig. 11 for the purest samples of both systems in a temperature range displaying no significant loss of intensity ($T \gtrsim 10$ K). The shift (and χ_{kag}) increases when the temperature decreases to 45 K, where a maximum is reached, and then decreases again as the temperature is lowered. This behavior is common to both systems and is field- and dilution-independent.[54] Most importantly, it is quite clear from Fig. 12 that there is a discrepancy between the low-temperature behavior of χ_{kag} and of χ_{macro}. Instead of a maximum, the susceptibility probed by SQUID measurements follows a Curie-like law at low temperature. This establishes that χ_{macro} is a two-component susceptibility,8) resulting from the sum of the kagomé bilayer's susceptibility and, as evidenced in Sec. 2.3, of a susceptibility related to magnetic defects (χ_{def}):

$$\chi_{macro}=\chi_{kag}+\chi_{def}. \tag{3}$$

Concerning the high-temperature ($T \geqslant 80$ K) behavior of K, a phenomenological Curie–Weiss law, $K=C_{NMR}/(T+\theta_{NMR})$, is an accurate fit, yielding $\theta_{NMR}=(440\pm5)$ K and (380 ± 10) K, respectively, for SCGO(0.95) and BSZCGO(0.97). The "Curie–Weiss" constant C_{NMR} found from the fit is 20% larger in SCGO than in BSZCGO, which indicates that hyperfine couplings are stronger in SCGO, likely because of the shorter Ga–O–Cr bonds (Fig. 3). Although very commonly employed to extract information from the HFMs susceptibility, this phenomenological law is a rather crude approximation, since the linear behavior of the inverse of the susceptibility is expected to hold, within a mean field approach, only when $T \gtrsim 2\theta_{NMR}$, which is not the case here. From θ_{NMR}, one can therefore only grossly estimate the coupling constants J of the kagomé bilayers. In the absence of any prediction for $S=3/2$, we used the high temperature series expansion of χ_{kag}, derived for an $S=1/2$ kagomé lattice, to correct θ_{NMR} by a factor of 1.5.[60] The coupling constant is finally extracted from the mean-field relation $\theta_{NMR}=1.5zS(S+1)J/3$. The coordinance is $z=5.14$ and corresponds to the average number of nearest neighbors for a chromium ion of the bilayer. The couplings then read $J=45$ K and 40 K for SCGO and BSZCGO, respectively. These values are consistent with the couplings observed in other chromium-based compounds,[61,62] and they indicate that the Cr–Cr AFM interaction stems from the direct overlap between orbitals of neighboring chromium ions, rather than from an oxygen-mediated superexchange coupling. A direct interaction results in a coupling J very sensitive to the Cr–Cr distance (d), and follows a phenomenological law:[40]

$$\delta J/\delta d=450 \text{ K/Å}. \tag{4}$$

The slightly stronger coupling found in SCGO compared to BSZCGO results then, following this viewpoint, from the shorter Cr–Cr bond lengths of its kagomé bilayer (Fig. 3).

We now turn to the low-temperature behavior of χ_{kag}, and in particular we discuss the maximum around 45 K. The first possible interpretation of this maximum is the existence of a spin gap. Such a gap Δ is an important issue for the kagomé bilayer, since it would be the signature of the existence of a singlet ground state, found in the theoretical quantum description of an $S=1/2$ kagomé layer.[15] Its value is predicted to be $\Delta \approx J/20$, and should be of the same order for higher spins.9) Since Ga NMR cannot access temperatures lower than 10 K, which for SCGO and BSZCGO corresponds to $J/4$, we cannot conclude whether the maximum in temperature is related to a gap. From an experimental point of view, its observation would require temperatures $T<\Delta$ in order to observe the exponential decrease predicted for the susceptibility.[47] In the inset of Fig. 11, we compare our experimental data to the susceptibility computed with exact diagonalization on a 36 spin $S=1/2$ kagomé cluster.[19] We see that the position of the predicted maximum does not match the experimental one. Also, the sharp peak of the susceptibility of the calculation is not seen in χ_{kag}. Clearly, larger cluster sizes and the kagomé bilayer geometry are needed for a better comparison to the NMR data. For the time being, it may be safely concluded, that the behavior of the NMR shift, hence of χ_{kag}, is consistent only with a spin gap smaller than $J/10$.

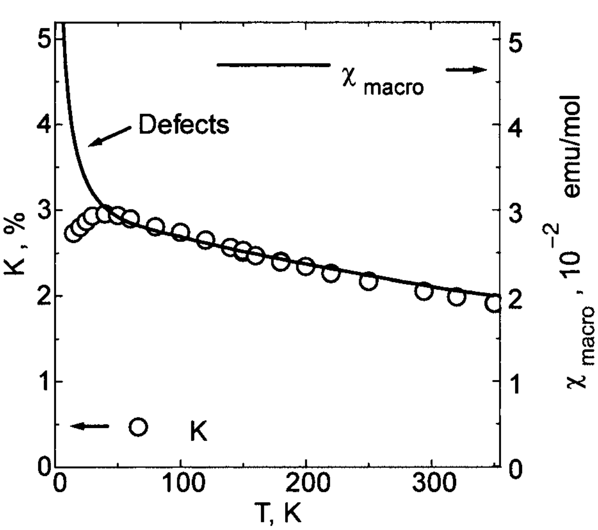

FIG. 12. K (left) and χ_{macro} (right) for SCGO(0.95). The NMR shift and the SQUID susceptibility do not follow exactly the same law at high temperature, since χ_{macro} also probes the susceptibility of the Cr(c)–Cr(c) spin pairs of SCGO (a detailed analysis can be found in Fig. 13 of Ref. 40).

Rather than the signature of a gap, the maximum in χ_{kag} was assigned in Ref. 54 to the signature of a moderate increase of the spin-spin correlations of the kagomé bilayer which, however, must remain short ranged given the absence of any phase transition. This conclusion was confirmed by neutron measurements on SCGO for temperatures ranging from 200 K down to 1.5 K,[63] and by susceptibility calculations performed on the kagomé and the pyrochlore lattices with Heisenberg spins, in which the spin-spin correlation length is kept of the order of the lattice parameter.[64] These calculations, using the so-called "generalized constant coupling" method (GCC),[64] consist in computing the susceptibility of isolated spin-clusters (triangles for the kagomé and tetrahedra for the pyrochlore) and in coupling these clusters following a mean field approach. In the case of the pyrochlore lattice, an exponential decrease of the susceptibility is obtained at low temperature. In this case, the ground state of a cluster is non-magnetic and the spin gap is between the $S=0$ ground state and the magnetic $S=1$ excited states. In the case of the kagomé lattice, the ground state of the triangle is magnetic ($S_{\text{total}}=1/2$) which gives rise to the nonphysical divergence in the susceptibility as $T\rightarrow 0$, due to the choice of a particular cluster.[64] The GCC simulations for the $S=3/2$ kagomé and pyrochlore lattices, in between which the kagomé bilayer's susceptibility is expected to lie, are presented in Fig. 11. As shown, they agree with the data down to $T=40\text{ K}\ll\theta_{\text{NMR}}$, yielding a maximum and a behavior around the maximum in agreement with the experimental findings. From the simulations, the values of θ_{CW} are 260 K for SCGO(0.95) and 235 K for BSZCGO(0.97), which correspond to $J=40$ K and $J=37$ K, close to the previous values obtained through the high-temperature Curie–Weiss law.

In conclusion, the GCC computation fits quite well the data down to $T\sim J\ll\theta_{CW}$, where $J\approx 40$ K. It only shows that the strongest underlying assumption of this cluster mean-field approach is relevant, i.e., the spin-spin correlation length is of the order of the lattice parameter, which prevents any magnetic transition to a long range ordered state.

C. Defect-related susceptibility

In this section, we focus on the defects contribution to the susceptibility. The NMR linewidth and the SQUID data at low temperature show that the paramagnetic susceptibility χ_{def} observed in χ_{macro} comes from the dilution of the kagomé bilayer and from other kinds of defects, namely the Cr(c) pairs in SCGO and bond defects in BSZCGO. The Ga(1) NMR width not only enables to evidence that the vacancy of a spin on the network, i.e. the dilution, generates a paramagnetic defect, but also allows to shed light on the more fundamental question concerning the extended nature of the defects. We first present the experimental facts concerning the magnetic defects, as measured quantitatively through the NMR linewidth and the SQUID susceptibility χ_{macro} and then elaborate on their nature in both compounds.

1. NMR linewidth

The Ga(1) NMR linewidth of SCGO and of BSZCGO was measured for various Cr-concentrations p. Figure 13 presents the typical p-dependence of the linewidth in both samples—in the figure, only for SCGO. In agreement with the qualitative presentation of the raw spectra in Sec. 2.1, the width increases as temperature drops and is well described by $1/T$ Curie law (lines in Fig. 13). It is very sensitive to the lattice dilution, similarly to the low-temperature behavior of χ_{macro} (see Fig. 16), but differs from the NMR shift. The perfect scaling of the widths of the two ^{69,71}Ga(1) isotopes (e.g., SCGO(0.95) in Fig. 13) underlines the magnetic origin of the low-temperature broadening.

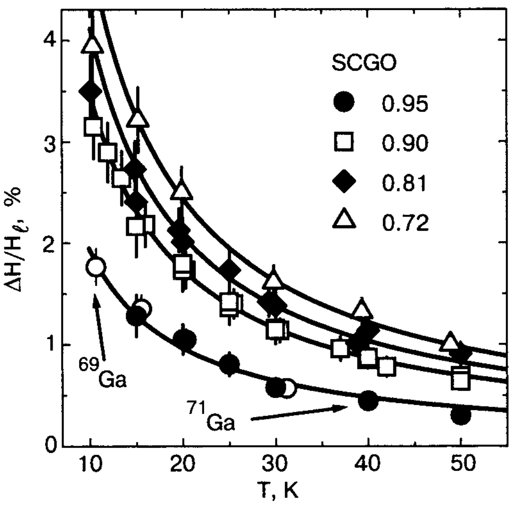

FIG. 13. Ga(1) NMR width versus temperature for SCGO samples of different Cr concentration. The width ΔH is normalized by the reference field $H_l=\nu_l/^{69,71}\gamma$ to superimpose the results from the two gallium isotopes (as explicitly shown for $p=0.95$). The solid lines are $\propto 1/T$ Curie-like fits.

Figure 14 presents the linewidth obtained for SCGO(0.95) and for a comparable dilution in BSZCGO(0.97). Surprisingly, the Curie upturn in BSZCGO(0.97) is four times larger than in SCGO(0.95). This ratio cannot be explained by a higher hyperfine coupling constant for BSZCGO, since, as mentioned in Sec. 2.2, the constants C_{NMR} obtained from the high-temperature Curie-Weiss analysis of the shift in SCGO and BSZCGO point to the opposite variation. Further insight concerning this mismatch between the two HFMs can be gained by plotting the widths as a function of dilution at a given temperature (inset of Fig. 14). In SCGO the width extrapolates to 0 when $p=1$, which shows that the width is only related to dilution. On the contrary, in BSZCGO the width reaches an

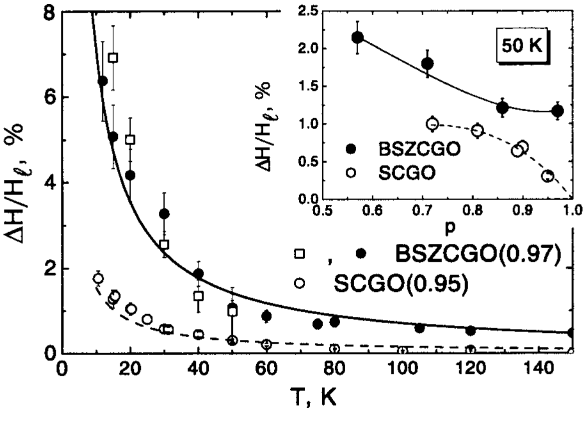

FIG. 14. Magnetic contribution to the NMR linewidth $\Delta H/H_l$. For BSZCGO(0.97), the data for ^{71}Ga(2) (□) are rescaled by a factor of 6, corresponding to the ratio of the coupling constants deduced from the high-temperature shifts. ● are for $\Delta H/H_l[^{71}\text{Ga}(1)]$. The lines are $\propto 1/T$ Curie-like fits. Inset: p dependence of $\Delta H^{71}[^{71}\text{Ga}(1)]$ at 50 K for SCGO(p) and BSZCGO(p). The lines are a guide to the eye.

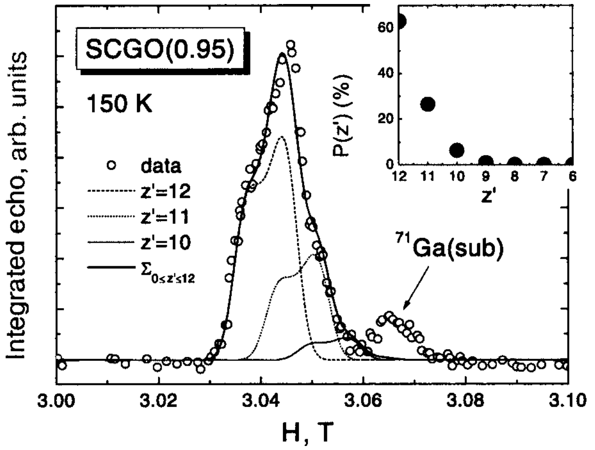

FIG. 15. ^{71}Ga(1) spectrum at 150 K in SCGO(0.95) ($\nu_l \approx 40$ MHz). The lines are quadrupolar powder pattern simulations with the parameters of Table I, shifted with a value proportional to z', the number of NN Cr^{3+} for a site. Their area is weighted by the probability $P(z')$ when $p = 0.95$, presented in the inset.

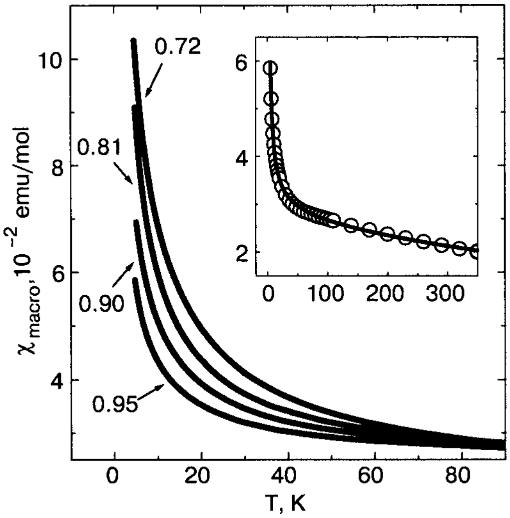

FIG. 16. Low-temperature macroscopic susceptibility (SQUID) for some SCGO Cr concentrations. Inset: SCGO (0.95) data (circles) fitted with Eq. (5).

asymptotic nonzero value for $0.86 \leqslant p < 1$. As a first assumption, one could wonder whether the dilution of the lattice is larger than the nominal one. This can be ruled out since (i) the expected evolution of the line shape with p is found at 300 K (see the following) (ii) muon spin relaxation measurements indicate a regular evolution of the dynamical properties with p (Sec. 3). Therefore, the increased low-temperature upturn in BSZCGO comes from dilution-independent paramagnetic defects, which are not present in SCGO.

We may already rule out possible scenarios which could be responsible for the low-temperature broadening. For instance, the broadening generated by the suppression of chromium ions in the nuclear environment. Such a distribution is present in the Ga(1) NMR spectra of SCGO and of BSZCGO, but is only responsible for a minor broadening of the line as shown in Fig. 15 for SCGO(0.95). This broadening mechanism results from the fact that each Ga(1) nucleus has a probability $P(z')$ (inset of Fig. 15) to have z' chromium neighbors ($0 \leqslant z' \leqslant 12$). Assuming that the Ga/Cr substitution does not affect the Ga–O–Cr hyperfine couplings and that all the chromium ions have the same susceptibility, the shift of a Ga(1) nucleus surrounded by z' neighboring chromium ions is then proportional to z', according to Eq. (1). To construct the spectrum, each gallium nucleus is associated to a quadrupole line simulated with the parameters of Table I, with a shift reflecting its Cr environment and an intensity weighted by the total number of gallium nuclei having the same environment, i.e., weighted by $P(z')$. The simulated line perfectly matches the experimental Ga(1) NMR line at 150 K (Fig. 15). However, the broadening resulting from this distribution scales with the susceptibility, hence with the shift K. Since K decreases at low temperature, this broadening mechanism cannot explain the low-temperature upturn of the width. For the same reason, a spatial distribution of the hyperfine constant, which yields also a width $\propto K$, cannot justify the broadening observed and also has to be ruled out.[10)] Even if a such refined analysis is not possible in BSZCGO because of a stronger broadening than SCGO, similar conclusions are derived for this compound.[56] Hence, the explanation for the low-temperature broadening must be searched elsewhere (see Sec. 2.3.3).

2. SQUID

The SQUID measurements were carried out over a wide range of Cr concentrations ($0.29 \leqslant p \leqslant 0.97$) for temperatures down to 1.8 K (no difference was observed between the field cooled (FC) and zero-field cooled (ZFC) susceptibility above the freezing temperature T_g in a field of 100 G). Figure 16 presents the typical low-temperature macroscopic susceptibility of these HFMs. Like the NMR linewidth, the susceptibility exhibits a low-temperature upturn, increasing with growing dilution. In Sec. 2.2, by a comparison between the NMR shift and the macroscopic susceptibility, we established that χ_{macro} must be a two-component susceptibility, and, in particular, that it should possess, compared to the shift, a paramagnetic susceptibility χ_{def} to explain its low-temperature upturn. The dilution-dependent upturn of χ_{macro} in Fig. 16 therefore establishes that χ_{def} is related to the Ga/Cr substitution in SCGO(p). However, we also know from NMR that there also exist extra paramagnetic contributions, related to intrinsic defects in BSZCGO, for example.

In order to quantify the low-temperature dependence of the susceptibility, we follow Ref. 65 and fit χ_{macro} by a two component expression:

$$\chi_{\text{macro}} = \frac{C}{T+\theta} + \frac{C_{\text{def}}}{T+\theta_{\text{def}}}. \tag{5}$$

The first Curie–Weiss term roughly takes into account the contribution from the kagomé bilayer and governs the behavior of χ_{macro} at high temperature. The second term, the more relevant for this section, also *a priori* Curie–Weiss, quantifies the contribution of χ_{def}. A more accurate fit of χ_{macro} would consist in using a low-temperature susceptibility mimicking the NMR shift. Such a fit, however, yields the same qualitative results as presented below.

From these fits (e.g., inset of Fig. 16), an effective moment per Cr^{3+} is extracted, $p_{\text{eff}} = 4.1 \pm 0.2/\mu_B$ in both SCGO[40] and BSZCGO, close to the $3.87/\mu_B$ expected for

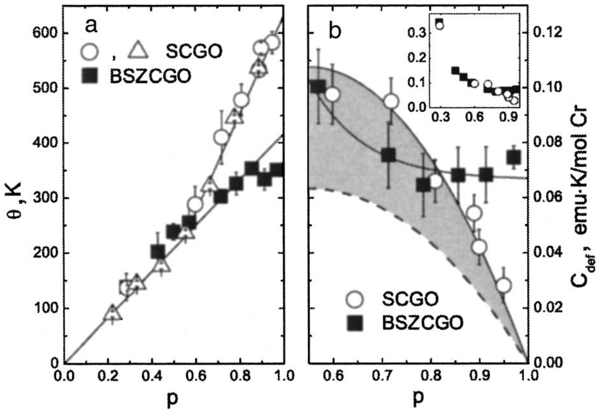

FIG. 17. Fits of the SQUID data (Eq. (5)). a—△ come from Ref. 50. The lines are a guide to the eye. b—The dashed line represents the kagomé bilayers defects contribution to $C_{\mathrm{def}}(p)$ in SCGO(p), the other lines are a guide to the eye. The gray area represent the Cr(c) contribution in $C_{\mathrm{def}}(p)$ for SCGO(p) (see text). Inset: same data as (b) for a broader range of p.

$S=3/2$ spins. In BSZCGO, the Curie-Weiss temperature is found to increase with p (Fig. 17a), in agreement with mean-field theory. From the linear variation, following the procedure described in Sec. 2.2, we extract $J=40$ K,[41] consistent with our NMR results. However, two linear regimes of $\theta(p)$ are observed for SCGO(p), below and above $p\sim 0.55$. This was first reported in Ref. 50 and cannot be understood in terms of simple mean field theory. Taking into account a third term in Eq. (5), corresponding to the susceptibility of the Cr(c) pairs in SCGO, derived in Ref. 40 and vanishingly small below 50 K, does not affect this result.

The second term in Eq. (5) is introduced to fit the low-temperature behavior of the defects. For all samples studied, it is close to a pure Curie law, within error bars. The values of the Curie constants C_{def} extracted are presented in Fig. 17b. A p dependence qualitatively similar to the NMR width is found and C_{def} extrapolates again to 0 for $p=1$ in SCGO, whereas it displays a finite value in BSZCGO. When the Cr concentration is $\leqslant 0.8$, the dependency of C_{def} is qualitatively the same in both systems (inset of Fig. 17b).

To give an order of magnitude, this term represents, for the purest samples, a number of $S=1/2$ paramagnetic spins equal to the number of spin vacancies in SCGO(p) [40] and to 15–20% of the number of Cr^{3+} spins in BSZCGO(p).[41]

3. Paramagnetic defects: discussion

The NMR and the macroscopic susceptibility measurements indicate that there are paramagnetic defects in SCGO and BSZCGO. Some of them are related to the spin vacancies in the kagomé bilayers and affect the neighboring chromium ions in such a way that their overall behavior is paramagnetic. These defects therefore yield information on how the correlated spin network of the kagomé bilayer responds to the presence of the vacancy. In the following, we discuss this point as well as the presence of other types of defects in both compounds.

The second type of defects results from lattice imperfections in BSZCGO, and from the dilution of the spin-pair sites in SCGO. Unfortunately, in the case of BSZCGO the second type of defects dominates the paramagnetic response, and in this compound, on the contrary of SCGO, a fine analysis of the spin-vacancy defects cannot be carried out, even by Ga(1) NMR.

A. Spin vacancies. In AFM systems such as the 1D spin chains[66,67] the quasi-2D spin ladders[68] and the 2D cuprates[69] it is now well established that a vacancy (or a magnetic impurity) generates a long range oscillating magnetic perturbation and creates a paramagnetic-like, i.e., not necessarily $\propto 1/T$, component in the macroscopic susceptibility. The symmetric broadening of the NMR line observed in these systems is related to the oscillating character of the perturbation. The dilution effects of the kagomé bilayer would then be described by the same physics of these correlated systems.

In SCGO, the symmetric feature of the Ga(1) NMR line indicates that spin vacancies induce a perturbation extended in space. This rules out descriptions of the defect in terms of uncorrelated paramagnetic centers,[65,70] since the broadening of the line would then be asymmetric. Hence, given the AFM interactions of the kagomé bilayer, the perturbation was assigned to a staggered polarization of the network.[40] The exact diagonalization of 36 spin 1/2 clusters on the kagomé lattice with spin vacancies by Dommange *et al.* confirms this interpretation.[23] They show that within an RVB ground state, the spin-spin correlations around a vacancy are enhanced, and that the magnetization is staggered around it, a picture that should also hold for higher spin values. However, it seems that the image of a simple envelope of the staggered magnetization, like the Lorentzian now granted in high-T_c cuprates[69], is not correct here since this localization of singlets around the vacancies shifts the staggered cloud from the nonmagnetic impurity. Although the agreement is qualitative at the moment, further work is required within this framework for a quantitative modeling of the NMR lineshape.

B. Bond disorder in BSZCGO. We previously saw that in BSZCGO(p), low-temperature macroscopic susceptibility and NMR width data can be both satisfactorily accounted for, only if a novel p-independent defect-like contribution is taken into consideration, a result somehow surprising in view of the close similarity between the kagomé bilayers of SCGO and BSZCGO. The only major change lies in the 1:1 random occupancy of the Ga(1) site by Ga^{3+} or Zn^{2+} ions which induces different electrostatic interactions with the neighboring ions. As an example, distances to O^{2-} in a tetrahedral environment vary from $r_{\mathrm{Ga}^{3+}\text{-}\mathrm{O}^{2-}}=0.47$ Å to $r_{\mathrm{Zn}^{2+}\text{-}\mathrm{O}^{2-}}=0.60$ Å which is at the origin of a change of the average Ga(1)-O bonds, from 1.871 Å for SCGO[42] to 1.925 Å in BSZCGO.[42] Similarly, one expects that the Cr^{3+} will be less repelled by Zn^{2+} than by Ga^{3+}, which certainly induces magnetic bond-disorder, i.e., a modulation of exchange interactions J between neighboring Cr^{3+}. From Eq. (4), one can estimate that a modulation as low as 0.01 Å in the Cr^{3+}-Cr^{3+} distances would yield a 10% modulation of J.

The presence of nonperfect equilateral triangles classically induces a paramagnetic component in the susceptibility of the frustrated units.[70] The fact that we do not observe any extra Curie variation as compared to SCGO(p) in the average susceptibility, probed through the NMR shift K (Fig. 11), indicates that such unbalanced exchange interactions only induce a staggered response in the same manner as spin vacancies. Whether this could be connected with the localization of singlets in the vicinity of defects and a staggered cloud around them, like for spin vacancies, should be more deeply explored. This might highlight the relevance of a RVB approach to the physics of the kagomé network. Further insight into the exact nature of the defects likely requires a better determination of the bond disorder through structural studies at low T, to avoid the usual thermal fluctuations at room T.

C. Broken spin pairs in SCGO. The Ga/Cr substitution on a Cr(c) site of SCGO could in principle break a Cr(c)-Cr(c) spin pair and free a paramagnetic spin, which then could contribute to the paramagnetic upturn of χ_{macro}. However, this contribution turns out to be small. The fact that the broken spin-pair susceptibility is small, can be deduced by comparing NMR and SQUID measurements for SCGO and BSZCGO. The starting point is to notice that the crossing between the variation of the Curie constants C_{def} of both samples determined by the fits of Eq. (5) to the macroscopic susceptibility (Fig. 17b), is not observed in the NMR width (inset of Fig. 14). Considering from our NMR analysis that there is a 20% difference between the hyperfine coupling, we can evaluate that the scaling factor between $\Delta H/H_l(p)$ and $C_{\text{def}}(p)$ should be 20% larger in BSZCGO(p) than in SCGO(p). An error of 10% comes from the possible difference between the bilayer susceptibility measured with NMR and SQUID, since the Ga(1) nuclei do not probe stoichiometrically the magnetic sites Cr(b) and Cr(a).[11)] We first determine the scaling factor $[\Delta H/H_l(p)]/C_{\text{def}}(p)$ in BSZCGO(p), where 100% of the magnetic ions belong to the kagomé bilayers. With the same ratio, the $\Delta H/H_l(p)$ data for SCGO(p) therefore yield a lower $C_{\text{def}}(p)$ than the measured one, outside the error bars (dashed line in Fig. 17b). This difference is likely due to dilution of the Cr(c) pairs in SCGO(p). Their contribution, which is not probed with the Ga(1) NMR (gray area in Fig. 17b), corresponds to a $0.04p$ Cr^{3+} $S=3/2$ paramagnetic term, whereas a $2p/9$ proportion would be expected in the case of a stoichiometrically substituted sample. This substoichiometric contribution of the Cr(c) site is consistent with neutron diffraction measurements.[40]

III. SPIN DYNAMICS AND MAGNETIC EXCITATIONS

A. Muon: an appropriate probe of dynamics

We mentioned that an abrupt loss of the Ga(1)-NMR intensity occurs below 10 K (Fig. 10). Hence, Ga(1)-NMR cannot be employed to probe the low-temperature magnetic properties of SCGO and of BSZCGO. This is unfortunate, since the low-temperature spin dynamics reveal information that, in particular, gives a clue as to the ground state of these systems. On the contrary, due to the smaller coupling of the muon to the electronic moments and a shorter time window than the NMR one, the μSR technique has proven to be a leading tool for the study of quantum dynamical states in a vast family of fluctuating systems.

The electronic dynamics is commonly probed, either for NMR or for μSR, through the measurements of the longitudinal relaxation time, necessary to recover the thermodynamic equilibrium after the excitation of the nuclear spin or the muon spin systems. However, while the out-of-equilibrium state is reached using rf pulses in NMR, the muon spin system is already in an excited state. Indeed, muons (μ^+, $S=1/2$) are implanted in the sample, 100% spin polarized along the z axis. Therefore, the muon spins always depolarize to reach the Boltzmann distribution and μSR can be performed in zero external field, contrary to conventional NMR.[71] The time dependence of their *polarization* $P_z(t)$ along the z axis is studied through their decay into a positron[72] and is directly linked to both the spin fluctuations [the time correlation function of the local field H_μ is usually exponential, i.e., $\langle \mathbf{H}_\mu(0)\cdot\mathbf{H}_\mu(t)\rangle/\langle H_\mu(0)^2\rangle=\exp(-\nu t)$] and the (random) local field distribution, characterized by a width Δ/γ_μ (γ_μ is the muon gyromagnetic ratio). The longitudinal relaxation time is related to the spin-correlation function through

$$1/T_1 \sim \int_0^\infty \langle \mathbf{S}(0)\cdot\mathbf{S}(t)\rangle \cos(\gamma_\mu H_{LF} t)\,dt.$$

Zero-field and longitudinal-field (LF) μSR experiments, where the external field H_{LF} is applied along the z axis, allow for instance to distinguish magnetic (randomly or ordered) frozen states from dynamical ones.[73,74] Moreover, whereas specific heat is sensitive to all kinds of excitations, including low-lying singlets at low temperature in the kagomé bilayer samples,[46] the muons probe *magnetic* excitations *only*, with a specific range of frequencies ($\sim 10^9$ Hz) sitting in a typical time window (10 ns–10 μs) in between NMR and neutron experiments.

We present here our μSR study of the spin dynamics in SCGO(p) and BSZCGO(p).[56,58] We first show that while conventional μSR polarization functions can be used in the whole temperature range for the very diluted samples and in the high-temperature regime ($T \gtrsim 3T_g$) for the purest ones, they cannot be used satisfactorily in the low-temperature regime in the latter case ($p \gtrsim 0.7$). Moreover, in this first step, we qualitatively show that the magnetic state of all the samples is dynamical down to the experimental limit of 30 mK (Sec. 3.2). We further use a model independent analysis of the data, simply taking the time necessary for the muon spin polarization to decrease down to the value $1/e$. The comparison between SCGO and BSZCGO clearly shows a correlation between the muon spin relaxation rate and T_g, suggesting that this freezing temperature is not an impurity phase. On the contrary, it seems to be closely linked to the slowing down of the spin dynamics in the bulk sample (Sec. 3.3). Finally, a phenomenological model for the muon relaxation, based on sporadic dynamics due to spin excitations in a singlet sea, proposed by Uemura *et al.*,[49] is extended to all fields and temperature range. Its connection to the RVB picture is discussed, and we argue that such coherent states might mediate the interactions between "impurities," which induce the spin-glass freezing (Sec. 3.4).

B. Conventional approaches

1. High-temperature behavior

At high temperature, a conventional paramagnetic behavior is found for all the samples, with a stretched exponential variation of $P_z(t)=\exp[-(\lambda t)^\beta]$. Figure 18 shows that as expected, $\beta\rightarrow 1$ in the dense magnetic cases[74] (in our case,

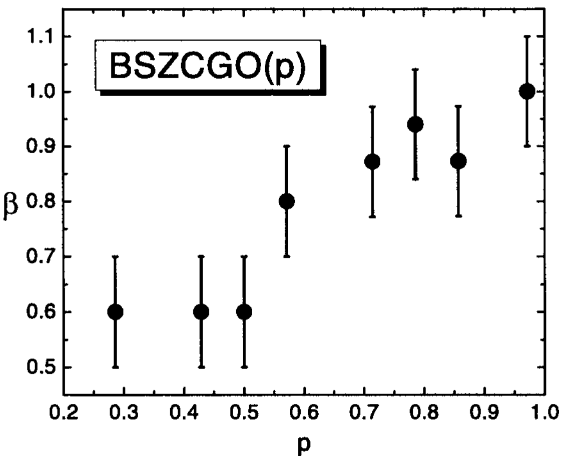

FIG. 18. Exponent $\beta(p)$ in BSZCGO(p) using the relaxation function $P_z(t) = \exp[-(\lambda t)^{\beta}]$ appropriate for the fast fluctuations limit at high temperature ($T \geqslant 10$ K).

with a high coverage of the kagomé bilayer lattice by Cr^{3+}) and $\beta \rightarrow 0.5$ in the dilute cases[73] (i.e., with a low coverage).

We can give here an estimate of the fluctuation frequency in this temperature range and of the NMR time window which would be required to measure this spin dynamics. At ~50 K, the muon relaxation rate is $\lambda \sim 0.03\ \mu s^{-1}$ and $0.01\ \mu s^{-1}$ in SCGO(0.95) and BSZCGO(0.97). In this appropriate fast fluctuating paramagnetic limit, the fluctuation rate can be estimated from $\nu \sim \sqrt{zJS/k_B\hbar} \sim 2\cdot 10^{13}\ s^{-1}$ (Ref. 49) using the coupling $J \approx 40$ K determined previously by NMR, and the average number $z = 5.14$ of Cr nearest neighbors. We extract $\Delta = \sqrt{\lambda\nu/2} \sim 600\ \mu s^{-1}$ and $300\ \mu s^{-1}$, which corresponds to an average field at the muon sites of 7000 G and 3500 G for SCGO and BSZCGO, respectively.

Since the relationship between the longitudinal relaxation time T_1 measured in NMR and μSR is

$$T_1^{NMR}/T_1^{\mu SR} \sim [\Delta/({}^{71}\gamma\,{}^{71}A)]^2,$$

where ${}^{71}A \sim 70$ kOe/μ_B is the hyperfine coupling constant of the ^{71}Ga nuclei obtained from NMR experiments, we can estimate that $T_1^{NMR}/T_1^{\mu SR} \sim 5$. This is consistent with our data $T_1^{NMR} \sim 100\ \mu s$ at high temperature and establishes that below 5 K, the relaxation must be $T_1^{NMR} \sim 1\ \mu s$, which is nonmeasurable as it lies out of the NMR time window. Such a small relaxation time is responsible for the wipeout of the Ga–NMR intensity (Fig. 10).

2. Failure of conventional approaches at low temperature for the purest samples

The derivation of zero field and longitudinal field μSR relaxation functions is presented in Refs. 73 and 74 for textbook cases. We first rule out the possibility of some static freezing as the source of the muon relaxation. Two options can be considered. (i) In *randomly* frozen (static) magnetic states, the major results are the following: first, the muon spin polarization displays a "1/3 tail" in zero external field, i.e., $P_z(t \geqslant 5/\Delta) \rightarrow 1/3$. Indeed, 1/3 of the frozen magnetic internal fields are statistically parallel to z and do not contribute to the muon spin depolarization. Second, $P_z(t)$ is "decoupled," i.e., does not relax, for longitudinal fields $H_{LF} \gtrsim 10\Delta/\gamma_{\mu}$. (ii) In the case of *ordered* magnetic states

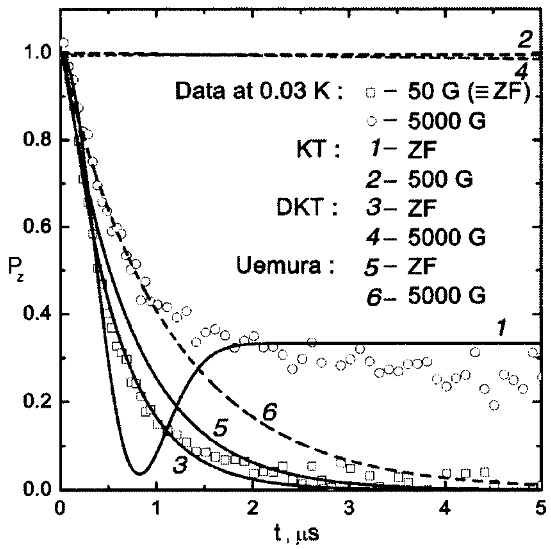

FIG. 19. BSZCGO(0.97) data at 0.03 K. The lines are fits with different models (see text). We used $\Delta \approx 2\ \mu s^{-1}$, $4\ \mu s^{-1}$ ($\nu \approx 17\ \mu s^{-1}$), and $65\ \mu s^{-1}$ ($\nu \approx 600\ \mu s^{-1}$), for the static, dynamic and "Uemura" cases, respectively.

and powder samples, the "1/3 tail" is still observed in zero field experiments for the same reasons, but oscillations appear in $P_z(t)$, which correspond to well defined local fields.

One should notice that nuclear moments which appear static on the μSR time window always contribute to the time-evolution of the polarization. A small longitudinal field of the order of a few 10s of G ($\Delta_{ND} \sim 0.1\ \mu s^{-1}$) is commonly applied to "decouple" this contribution. In other words, since the electronic and dipolar contributions are multiplied, such a contribution, if any, "disappears," and only the electronic contribution, not perturbed by such low fields, is measured. Hence, experiments performed at $H_{LF} \sim 100$ G are roughly equivalent to a zero-field measurement without nuclear dipoles.

Figure 19 shows $P_z(t)$ measured in BSZCGO(0.97) at 0.03 K for $H_{LF} = 50$ G and for $H_{LF} = 5000$ G. Neither oscillations nor a 1/3 tail are observed when $H_{LF} = 50$ G. Although not emphasized in the figure, one can note that the initial polarization is Gaussian, which is even clearer in SCGO(p).[49] In the *static* case such a shape is observed in dense magnetic randomly frozen systems, where the polarization is given by the Gaussian Kubo-Toyabe (KT) function.[73] We fitted our data at short times with this function in zero field, and plot the expected polarization when $H_{LF} = 500$ G in Fig. 19, which is found to be completely decoupled. This contrasts with our experimental finding, i.e., the polarization at 5000 G is hardly decoupled. *The lack of a 1/3 tail, the absence of oscillations and of a decoupling effect show that the magnetic state of BSZCGO(0.97) is fluctuating at 0.03 K.* All these considerations remain valid in both SCGO(p) and BSZCGO(p) compounds when $p \gtrsim 0.6$.

The computation of the *dynamical* relaxation functions is based on a strong collision approximation.[73] Using the corresponding dynamical Kubo-Toyabe (DKT) function, analytically derived by Keren[75] for $\nu \geqslant \Delta$, allows us to fit the zero field data on the whole time range (Fig. 19). Again, the experimental data is much less sensitive to the applied field $H_{LF} = 5000$ G than the expected polarization.

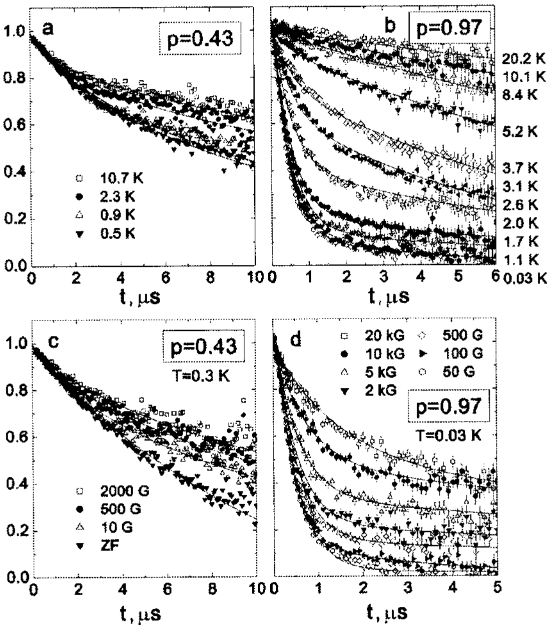

FIG. 20. a,b—Temperature-dependence of the muon polarization $P_z(t)$ in BSZCGO under weak H_{LF} (10 G for $p=0.43$ and 100 G for $p=0.97$). Notice the different time scales for both samples. c,d—H_{LF} dependence at base temperature. The line for $p=0.43$, ZF, is a square-root exponential times the Kubo-Toyabe function in zero field ($\Delta_{ND}\sim 0.08\ \mu s^{-1}$), accounting for the nuclear dipole contribution. The other lines are fits described in the text.

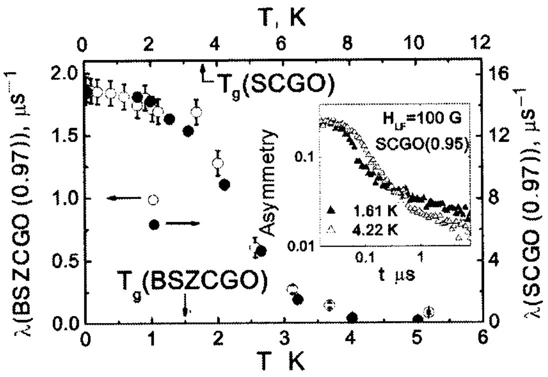

FIG. 21. Comparison of the evolution of the muon spin relaxation rate λ versus T in BSZCGO(0.97) and SCGO(0.95), from a $1/e$ analysis. Inset: recovery of a part of the asymmetry at low temperature and long times in SCGO(0.95) below T_g (log-log scale).

This so-called "undecouplable Gaussian line shape" was first reported in Ref. 49 for SCGO(0.89) and further in other kagomé compounds[57,76,77] or spin singlet compounds like the doped Haldane chain $Y_{2-x}Ca_xBaNiO_5$ (Ref. 78). Uemura *et al.*[49] proposed a relaxation model, presented further in this paper, which captures some of the facets of this relaxation. For now, we just notice that this model cannot justify our data for all fields (Fig. 19), even if it shows a lower decoupling effect, consistent with our (and previous) observations. Before going further with more complex models (Sec. 3.4), we will first, in the following, give qualitative arguments to characterize the low-temperature magnetism of our samples.

In order to illustrate the evolution of the properties with p, we present two typical low and high occupations p of the kagomé bilayers in Fig. 20 which emphasize the qualitative differences for various frustrated network coverage rates p. In addition to the high-temperature behavior already commented, the evolution of $P_z(t)$ at low temperature is markedly different. For $p=0.97$ the relaxation rate increases by more than two orders of magnitude to reach a temperature-independent value for $T\lesssim T_g\approx 1.5$ K (Fig. 20b), with the undecouplable character presented above. For a low coverage rate, $p=0.43$, we also find a dynamical state but, at variance with the previous case, only a weak temperature-dependence is observed. Also, the polarization displays a square root exponential decay for *all* temperatures (Fig. 20a) and for any longitudinal field H_{LF} (Fig. 20c). A weak plateau of the relaxation rate is still observed below 0.5 K but is no more present for $p=0.3$, where $P_z(t)$ is found to be weakly temperature- and H_{LF}-dependent. This is typical of the pure paramagnetic fast fluctuations limit for dilute magnetic systems, which contrasts with the results of SQUID measurements showing that strongly frustrated antiferromagnetic interactions are still present. This is the so-called "cooperative paramagnetism."

C. Model-independent basic analysis

As a first step to a quantitative analysis, we estimate the muon spin relaxation rate λ using the $1/e$ point of the polarization $P_z(t)$, as discussed in Ref. 57. This allows one to single out information about two important issues using a simple model-independent analysis: the role of the spin-glass-like transition and the impact of the spin vacancies on the dynamics.

From high temperature, λ increases by more than two orders of magnitude down to T_g for both kagomé bilayers at their highest level of purity, to reach a relaxation rate plateau $\lambda_{T\to 0}$ for $T\lesssim T_g$.[49,57] Using a temperature-scale twice larger for SCGO(0.95) than in BSZCGO(0.97), the temperature dependence of λ of both samples perfectly scales on the temperature axis, as shown in Fig. 21.12) This ratio is very close to the 2.3(2) ratio between their freezing temperatures T_g, which points to a link between the formation of the spin-glass-like state and the presence of fluctuations. This seems to be a quite common feature of various systems with a singlet ground state.[49,57,76–78]

In Fig. 22 we report the variation of $\lambda_{T\to 0}(T)$ for various BSZCGO(p) samples and compare them to SCGO(p).[49,57]

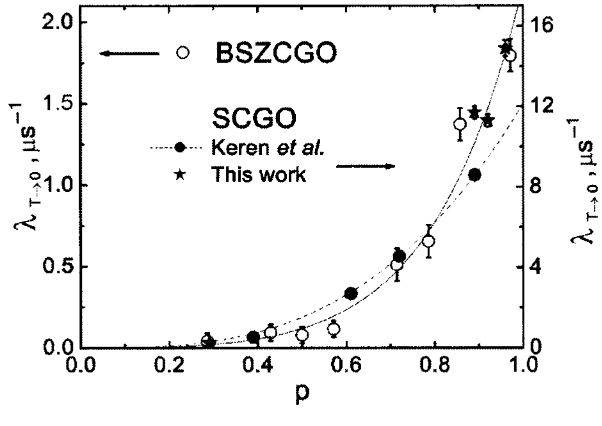

FIG. 22. The p dependence of $\lambda_{T\to 0}$ for BSZCGO(p) (unfilled symbols) and SCGO(p) (filled symbols). Continuous (dashed) lines are $\sim p^3+1.9(3)p^6$ ($\propto p^3$; Ref. 57) fits.

Although additional p-independent defects are dominant in BSZCGO(p), as evidenced by SQUID and NMR measurements, it is very surprising to find, for the two systems, a very similar quantitative low-temperature relaxation rate $\lambda_{T\to 0}$ with increasing Cr concentration over the *entire p* range studied. Therefore we conclude that *only* defects related to *dilution* of the frustrated magnetic network influence the relaxation rate.

In a classical framework, a coplanar arrangement with zero-energy excitation modes, involving spins on hexagons, was proposed in the literature to be selected at low temperature.[79] Inelastic neutron scattering experiments on SCGO and the spinel compound $ZnCr_2O_4$ are indications in favor of such excitations.[33,48] Therefore, one expects the muon spin relaxation to scale with the number of fully occupied hexagons, $\propto p^6$. In Fig. 22, the BSZCGO(p) data altogether with our SCGO($p\geqslant 0.89$) samples indicate that $\lambda_{T\to 0}(p)$ is well accounted for by adding a dominant p^6 term to the p^3 term proposed for SCGO($p\leqslant 0.89$) in Ref. 57. In a case of purely dipolar couplings of the muon with the electronic magnetic moments, the average of the local dipolar field is given by $\Delta\propto\langle\Sigma_i 1/r_i^3\rangle\propto p$, where the sum is made over the Cr^{3+} ions, r_i is the distance between the muon and the ith position, and $\langle\cdot\rangle$ is the average over the muon positions. One therefore obtains $\lambda(p)\sim\Delta(p)\propto p$ in the case of slow fluctuations, and

$$\lambda(p)\sim 2\Delta(p)^2\nu/(\nu^2+\gamma_\mu^2 H_{LF}^2)\propto p^2$$

in the case of fast fluctuations, i.e., $\lambda(p)\propto p^\eta$, with $\eta\leqslant 2$, which is not consistent with our data. This indicates that the relaxation is not induced by single spin excitations but rather *collective* excitation processes extending at least on triangles and/or hexagons. However, these excitations still involve only a finite number of spins since the increase of spin vacancies only affect smoothly the spin dynamics. On the contrary, a more pronounced effect is observed in the $S=1/2$ kagomé-like compound volborthite.[77]

D. RVB ground state with coherent unconfined spinons

Finding a phenomenological model reproducing the polarization $P_z(t)$ for *all* fields, *all* temperatures, and *all* dilutions has been for long a pending challenge in the analysis of these μSR experiments in kagomé frustrated antiferromagnets. In the quantum framework of a singlet ground state, one needs unpaired spins, i.e., isolated magnetic moments, in order to generate magnetic excitations responsible for the muon spin relaxation. Such excitations can be ascribed to unconfined spinons,[19] for which the location of spin 1/2 varies in time with no loss of coherence of the excited state (Fig. 23). Hence, a given muon spin couples to a spin only a short fraction ft of the time t after implantation, and one can use a model of "sporadic" field fluctuations to describe $P_z(t)$.

This was the initial guess by Uemura *et al.* to account for the weakness of the field dependence of $P_z(t)$ at low temperature in SCGO(0.89),[49] although the spins are $S=3/2$. In the absence of any theoretical predictions, we will just assume that the mechanism is comparable. This polarization is given by a "sporadic" dynamical Kubo-Toyabe function, $P_z^K(ft,\Delta,H_{LF},\nu)$, which rewrites simply as $P_z^K(t,f\Delta,H_{LF},\nu)$. Δ/γ_μ is the local field created on the muon site by a paramagnetic neighboring released spin with a fluctuation frequency ν and a corresponding exponential time correlation function $\exp(-\nu t)$. Δ is therefore related to the muon location in the unit cell and its average is assumed to be p-independent for a given system but is expected to vary from BSZCGO to SCGO. The Gaussian at early times, the weakness of the field dependence and a dynamical relaxation down to 0 are altogether related to the f factor and $\nu\sim\Delta$. In addition to this sporadic relaxation, we found that a more conventional Markovian relaxation needs to be introduced to fit the long-times tail ($t\gtrsim 3\ \mu$s) for all fields and temperatures. We therefore write

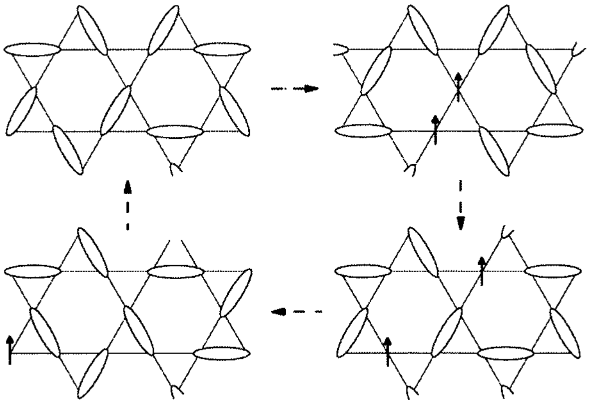

FIG. 23. Schematic representation of the creation and deconfinement of a spinon in a RVB ground state on a kagomé lattice.

$$P_z(t)=xP_z^K(t,f\Delta,fH_{LF},f\nu)+(1-x)e^{-\lambda t},\qquad(6)$$

where x represents the weight of the short-time sporadic dynamical function, associated with the spinons dynamics. In the following, we first detail how all these parameters can be reliably deduced from the data and sketch a physical picture consistent with our results.

We first present our analysis for $T\ll T_g$ in BSZCGO(p). In order to limit the number of free parameters, we make the minimal assumption that the external field does not influence the dynamics of the coherent spinon term. The dynamics (ν) and the average dipolar field created by a spinon on a muon site (Δ) are shared for all p and H_{LF}. For low fields, x is found close to 1 for the purest samples (Fig. 20a,b), making λ' a nonrelevant fitting parameter. It also enables us to determine ν and Δ when $H_{LF}<500$ G, for various p. The parameter f is adjusted for each p and its variation accounts for the evolution of $\lambda_{T\to 0}(p)$. On the contrary, the high-field data enable us to monitor the evolution of x with H_{LF} and to determine a value for λ. We could not extend the fits below $p=0.71$ since the weak field dependence prevents an unambiguous determination of the parameters.

We find perfect fits of our data (Fig. 20d) with $\nu\sim 1000\ \mu s^{-1}$, $\Delta\sim 350\ \mu s^{-1}\sim\gamma_\mu\times 4$ kG and an average value of $f\sim 0.006$. We find a nearly flat p-independent long-time relaxation rate for $T\ll T_g$ ($\lambda'\sim 0.05\ \mu s^{-1}$, ★ in Fig. 24d). An important finding is that x is of the order of p at low fields (Fig. 24a,b). This may be related to the theoretical computations showing that the correlations are enhanced around spin vacancies in the kagomé lattice,[23] which would destroy locally the spin-liquid state. Besides, x decreases appreciably for $H_{LF}\sim 10$ kG whatever the value of p. We can

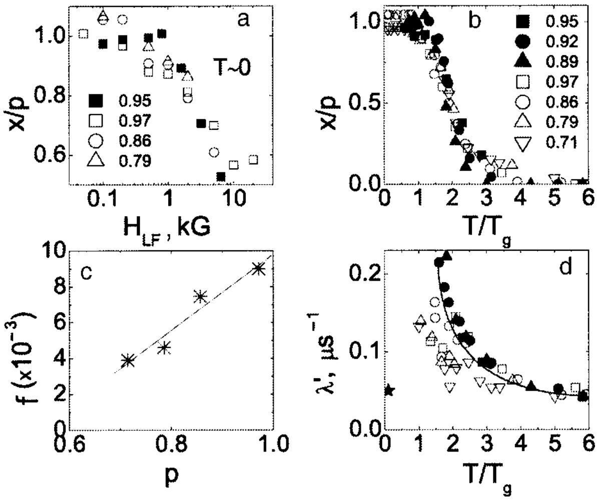

FIG. 24. Fitting parameters of Eq. (6) for BSZCGO and SCGO (unfilled and filled symbols); f is common for both systems.

associate this decrease to the existence of an energy scale ~ 1 K, which is of the order of T_g. Finally, we observe a linear variation of f with p (Fig. 24c), and f tends to vanish around $p\sim 0.5$, a limit consistent with our classical approach (Fig. 22). Indeed, since we find $\nu\sim\Delta$ when $T\rightarrow 0$, the relationship $f(p)\Delta\sim\lambda_{T\rightarrow 0}(p)$ is expected. This indicates that even far from the substituted sites, the coherent state is somehow affected, e.g., the density of spinons could be smaller.

As suggested by the similar p variation of $\lambda_{T\rightarrow 0}$ in both BSZCGO(p) and SCGO(p), we assume that the excitation modes are identical in both systems, i.e., f and ν are kept the same for comparable p. We find $\Delta\sim 1200\ \mu\text{s}^{-1}$ for our SCGO($p\geqslant 0.89$) samples, in agreement with previous work on SCGO(0.89).[49] It is quite rewarding to find that a *common* physical picture underlies all the sets of data at low temperature for *both* kagomé bilayers.

We now extend the fits of the muon spin polarization $P_z(t)$ to the whole temperature range (Fig. 20b), fixing f to its low-temperature value in order to limit the number of free parameters. It would also, phenomenologically, mean that once a spinon is created, its deconfinement process remains temperature independent, which is a quite reasonable assumption from a quantum point of view. As expected from the change of shape around T_g (Refs. 49, 57), the weight x of the sporadic term decreases to finally enter a high-temperature regime (Fig. 24b) with an exponential muon relaxation ($x\rightarrow 0$). The similarity between the field and temperature dependence of x indicates that the sporadic regime is destroyed with an energy of the order of the freezing temperature T_g. Figure 22b displays a sharp crossover from one state to the other between T_g and $3T_g$, corresponding to the steep decrease of λ (Fig. 21), for both BSZCGO(p) and SCGO(p). For $T>T_g$, ν and λ' (Fig. 24d) decrease by one order of magnitude up to $10T_g$.

At high temperature, it is natural to think in terms of paramagnetic fluctuating spins. At lower temperatures, λ seems to diverge at T_g and below, the weight of the exponential term at low fields ($1-x\sim 1-p$) could correspond to localized frozen spins, reflecting the glassy component measured by SQUID. It is noteworthy that T_g does not increase with $1-p$ but rather decreases, opposite to the case of canonical spin glasses. We could further confirm the existence of such a frozen component in SCGO($p=0.95-0.89$), since a clear recovery of a small part ($\sim 4\%$) of the asymmetry is found at long times (e.g., Fig. 21, inset). It is observed for $t\sim 100\lambda^{-1}$, which is out of the experimental range for BSZCGO(p).

To summarize, the picture based on a coherent RVB state, which magnetic excitations are mobile fluctuating spins 1/2 on the kagomé lattice, explains well the data, provided that (i) these excitations can be generated even for $T\rightarrow 0$. This underlines the smallness of the "magnetic" gap, if any, typically $\Delta<J/1000$; (ii) an energy scale related to T_g (fields of the order of 10 kG or, equivalently, temperatures of the order of T_g, which vary very little with p) is high enough to destroy the coherent RVB type state; (iii) the substitution defects are accounted for by an additional classical relaxation process.

E. Spin-glass-like transition

The "intrinsic" spin-glass-like transition at T_g is one of the most puzzling observation in these frustrated magnets. Indeed, the origin of such a spin-glass state in a disorder-free system still awaits for a complete understanding, although recent theoretical approaches catch some of the facets of this original ground state.[80] The most realistic model, presented by Ferrero *et al.* in Ref. 81, uses the so-called "dimerized" approach,[14,16] i.e., considers a geometry of the kagomé lattice with two different kinds of equilateral triangles, corresponding to the Cr(b) layers in SCGO(p) and BSZCGO(p) (Fig. 3). It predicts a spin-glass-like transition in the $S=1/2$ kagomé lattice, related to the freezing of the chirality, with $T_g\sim 0.5J'$. Here J' is the largest coupling in the kagomé planes (corresponding to the thick lines in Fig. 3). Although $0.05J$ is of the order of magnitude of the experimental T_g, the very similar values of the Cr–Cr bonds in both systems and Eq. (4) do not permit prediction of a factor 2 in T_g.

From our μSR results, we propose an other interpretation which still awaits for theoretical confirmation. We find no energy gap for the spin 1/2 excitations. This could explain quite well why the transition to the spin-glass state is fairly independent of p. Indeed, in this framework, spinons could mediate the interactions between magnetic defects localized around spin vacancies. This is corroborated by all the scaling properties in T/T_g. The transition to the spin-glass state would correspond then to the formation of the coherent singlet state rather than any interaction strength between defects. The bond defects inherent to BSZCGO(p) probably decrease the value of this coherent state energy scale since it is more favorable to create localized singlets in this geometry. This is qualitatively consistent with the twice lower spin-glass transition temperature in this family.

F. Extension to other compounds?

We already noticed that the μSR undecouplable Gaussian line shape, altogether with a plateau of the relaxation rate, have been reported in other compounds, and now elaborate about the possible links between these systems.

The other kagomé compounds, volborthite[77,82,83] and Cr jarosite[76] display the same properties as the kagomé bilayers and our phenomenological model seems correct.

Kojima *et al.* already noticed the similarity between the doped Haldane chain $Y_{2-x}Ca_xBaNiO_5$ and SCGO(0.89).[78,84] However, contrary to the kagomé bilayers, the relaxation function becomes more "conventional" when the system becomes purer, i.e., the muon spin relaxation function is a square root exponential in the pure system at low temperature. It is not surprising since in the pure Haldane chain one expects a valence bond crystal.[78,84] Therefore no magnetic excitation are allowed at low temperature and no depolarization is expected in μSR. However, mobile excitations are added when the chains are doped,[85] i.e., the muon spin relaxation becomes unconventional. This corresponds to the data and is consistent with our unconfined spinon phenomenological model.

Finally, Fukaya *et al.* reported the same behavior in $Sr(Cu_{1-x}Zn_x)_2(BO_3)_2$ for $x=0$ and 0.02.[86] This system displays, theoretically and experimentally, an exact singlet dimer state and its intrinsic susceptibility vanishes for $T\lesssim 3$ K.[87,88] Nonetheless, a CW term, corresponding to 0.72% of $S=1/2$ impurities with respect to the Cu sites, is observed below 4 K,[87] which is finally comparable, from the macroscopic susceptibility aspect, to the former cases of pure volborthite and pure $Y_2CaBaNiO_5$. However, according to us, there is today no clue about the possibility of mobile excitations in this magnetic network with a few percent of defects.

We conclude that *all* these systems display (i) a theoretical and/or experimental singlet ground state; (ii) a defect term observed through a low temperature CW like upturn in the macroscopic susceptibility; (iii) a spin-glass-like transition of this defect term at a temperature T_g (but $Sr(Cu_{1-x}Zn_x)_2(BO_3)_2$;1)) (iv) a plateau of the muon spin relaxation rate below T_g.

It is important to notice that the clear experimental correlation between the muon spin relaxation rate plateau and the spin-glass-like transition is strongly against a pure muon-induced effect argument for this plateau. Even if the muon has indeed an effect on the physics of these compounds, the λ plateau below T_g shows that a bulk transition occurs at this temperature, i.e., that this freezing cannot be due to isolated impurities.

Theoretical approaches are now required to link a possible unconfined spinons state to a spin-glass-like behavior and a relaxation plateau of the implanted muon spins. They could therefore corroborate our phenomenological approach.

IV. CONCLUSION

With Heisenberg spins and nearest neighbor couplings of the order of 40 K, the kagomé bilayers of SCGO and BSZCGO are today the archetypes of highly frustrated magnets. The comparison between SQUID and NMR experiments on the two slightly different compounds SCGO and BSZCGO allows us to isolate the intrinsic properties of the frustrated kagomé bilayer geometry and to understand better the role of the (non)magnetic defects. We find that *defects* localized in the frustrated network induce a spatially extended response of the magnetic system, consistent with theoretical predictions. This response generates a Curie-like upturn in the macroscopic susceptibility at low temperature. However, local measurements of the susceptibility, using Ga NMR, show that the *intrinsic* susceptibility of the kagomé bilayers decreases below 45 K, a temperature of the order of J. This behavior was also predicted theoretically and is consistent with short-ranged spin-spin correlations, on the order of the lattice parameter. We cannot give a definitive conclusion about the existence of a spin gap with NMR experiments because the gallium nuclei cannot be probed by NMR at low temperature. However a maximum value of $\sim J/10$ is found for such a gap.

We measured the spin dynamics using muon spin relaxation experiments, down to 30 mK. We find that both systems SCGO and BSZCGO display a dynamical magnetic state down to this temperature, unconventional for the purest samples. Very simple considerations show that the spin-glass-like state, measured at $T_g \ll \theta_{CW}$ with macroscopic susceptibility techniques, is correlated to the slowing down of the Cr spin dynamics in the whole sample. The data are well accounted by a description based on unconfined spinons as the magnetic excitations and we suggest that this phenomenological approach remains valid for several spin singlet compounds at low temperature. Indeed, they all display striking similar aspects such as a spin-glass transition of the magnetic defect channel in the macroscopic susceptibility and an undecouplable Gaussian line shape with a relaxation rate plateau of the muon polarization below this spin-glass transition.

In all these systems the fast depolarization of the muon down to the experimental limit of $T\sim 30$ mK underlines the existence of magnetic excitations at low temperature and hence the weakness of an hypothetical unconfined spinon gap. An other spin dynamics study with neutron spin echo technique is in progress and could give more details about this $T\rightarrow 0$ spin-liquid state.[89]

We thank H. Alloul, F. Bert, J. Bobroff, R. J. Cava, D. Huber, A. Keren, C. Lhuillier, M. Mekata, G. Misguich, R. Moessner, C. Mondelli, H. Mutka, B. Ouladdiaf, C. Payen, P. Schiffer and P. Sindzingre for fruitful discussions. We also wish to thank A. Amato, C. Baines, and A.D. Hillier, our μSR local contacts, whose outstanding efforts have made these experiments possible.

The μSR experiments were performed at the Swiss Muon Source, Paul Scherer Institute, Villigen, Switzerland, and financially supported by the Federal Office for Education and Science, Berne, Switzerland, as well as at the ISIS facility, Rutherford Appleton Laboratory, Didcot, United Kingdom.

Part of this work was financially supported by the EC IHP Program for large scale facilities and by the EC Framework Programmes V and VI.

We are grateful to the muon beamline groups and to the technical staff of Laboratoire de Physique des Solides, Orsay.

---

[*] Present address: Kamerlingh Onnes Laboratory, Leiden University, P.O. Box 9504, 2300 RA Leiden, The Netherlands.

[†] Present address: Institut für Experimentelle und Angewandte Physik, Christian-Albrechts-Universität zu Kiel, D-24098 Kiel, Germany.

[‡] E-mail: mendels@lps.u-psud.fr

1)This is different from the situation encountered in spin glasses, where the cooling history finishes by selecting one of the numerous local minima present in the free energy.

2) We define the Hamiltonian as $\mathcal{H}=J\Sigma_{\langle i,j\rangle}\mathbf{S}_i\cdot\mathbf{S}_j$, where i,j are the nearest neighbors.

3) The $S=3/2$ Cr jarosite is the only exception.[76]

4) The official labeling is as follows for SCGO [BSZCGO]: Ga(4f) [Ga(2d)] for Ga(1), Ga(4e) [Ga(2c)] for Ga(2), Cr(1a) [Cr(2a)] for Cr(a), Cr(12k) [Cr(6i)] for Cr(b) and Cr(4f$_{vi}$) for Cr(c) in SCGO. We used simplified notations for clarity in the comparison of the two systems.

5) Since the Ga(2) line of BSZCGO is governed by quadrupolar effects, its width is $\propto \nu_Q^2/\nu_l$.[90] Therefore this line is broader at low field. On the contrary, the quadrupolar frequency of the Ga(1) is smaller and the linewidth is proportional to the applied external field.

6) Notice that the high-temperature analysis of both ^{71}Ga(1) and ^{71}Ga(2) lines in BSZCGO allows us to compare their shifts, which yields an estimate of the chemical shift of 0.15(3)%.

7) We checked that the transverse relaxation time T_2 is homogeneous over the whole ^{71}Ga(2) line. Its shape is hence used for the subtraction whereas its intensity is multiplied by $\sim\exp[2(\tau_l-\tau_s)/T_2^{71}]$.

8) In the case of SCGO, $\chi_{\rm macro}$ is a three-component susceptibility, the third contribution coming from the Cr(c)-Cr(c) spin pairs, which we drop here for clarity.

9) C. Lhuillier, private communication.

10) A dipolar broadening due to the diluted paramagnetic defects[91] would be too small to justify the broadening of the ^{69,71}Ga spectra.

11) The Ga(1) nuclei are coupled to 9 Cr(b) and 3 Cr(a). The measured susceptibility is hence $\chi_{\rm kag,NMR}\propto 9\chi_b+3\chi_a$, where χ_b and χ_a are the Cr(b) and Cr(a) susceptibilities. On the other hand, the macroscopic susceptibility probes these susceptibilities with their stoichiometric ratio, i.e., $\chi_{\rm kag,macro}\propto 6\chi_b+\chi_a$ (Ref. 55). A small difference between the ratios χ_b/χ_a would yield a slightly different ratio $[\Delta H/H_l(p)]/C_{\rm def}(p)$.

12) We attribute the factor of 8 between λ in the two systems to a different coupling of the muon spin to the Cr spins. Transverse field experiments show for instance a larger linewidth in SCGO(0.95) than in BSZCGO(0.91) despite a lower defect term.[41] On the other hand, Δ, which is mainly created by dipolar interactions in μSR, is $\Delta\propto\Sigma 1/r^3$, where the sum is over all the spins in the lattice and r is the distance between the muon site and these spins.[73] Usually, the muon is located near an O^{2-} ion.[92] In a very simplified approach, we computed Δ, considering that the muon would be located on the O^{2-} sites, as an average, and find $\Delta\approx 1100\ \mu s^{-1}$ and $800\ \mu s^{-1}$ in SCGO(1) and BSZCGO(1). This is in perfect agreement with the high-temperature evaluation of Δ. Since $\lambda\propto\Delta^2$ in the fast fluctuation limit and $\lambda\propto\Delta$ in the static limit, we expect, with this simple approach, that λ will be 1.5–2 times larger in SCGO(p). The missing factor of 4 may either come from a more complex muon sites distribution, due to the O^{2-} ions around the Cr(c) sites, or to a different dynamics range, as suggested by neutron spin echo.[89]

13) To our knowledge, no FC-ZFC magnetization data have been published about Sr(Cu$_{1-x}$Zn$_x$)$_2$(BO$_3$)$_2$.

---

[1] P. W. Anderson, Mater. Res. Bull. **8**, 153 (1973).

[2] P. W. Anderson, Science **235**, 1196 (1987).

[3] G. Baskaran, Phys. Rev. Lett. **91**, 097003 (2003).

[4] B. Bernu, P. Lecheminant, C. Lhuillier, and L. Pierre, Phys. Rev. B **50**, 10048 (1994).

[5] A. P. Ramirez, in *Handbook on Magnetic Materials*, K. J. H. Busch (ed.), Elsevier Science, Amsterdam (2001), Vol. 13, p. 423.

[6] R. Stewart (ed.), Proceedings of the Highly Frustrated Magnetism 2003 Conference, Grenoble, France (2004), J. Phys.: Condens. Matter **16**, S553–922 (2004).

[7] K. Binder and A. P. Young, Rev. Mod. Phys. **58**, 801 (1986).

[8] D. A. Huse and A. D. Rutenberg, Phys. Rev. B **45**, 7536 (1992).

[9] J. T. Chalker, P. C. W. Holdsworth, and E. F. Shender, Phys. Rev. Lett. **68**, 855 (1992).

[10] I. Ritchey, P. Chandra, and P. Coleman, Phys. Rev. B **47**, 15342 (1993).

[11] G. Misguich and C. Lhuillier, in *Frustrated Spin Systems*, H. T. Diep (ed.), World Scientific, Singapore (2003), cond-mat/0310405, and references therein.

[12] R. Moessner, Can. J. Phys. **79**, 1283 (2001).

[13] C. Zeng and V. Elser, Phys. Rev. B **51**, 8318 (1995).

[14] M. Mambrini and F. Mila, Eur. Phys. J. B **17**, 651 (2000).

[15] C. Waldtmann, H. U. Everts, B. Bernu, C. Lhuillier, P. Sindzingre, P. Lecheminant, and L. Pierre, Eur. Phys. J. B **2**, 501 (1998).

[16] F. Mila, Phys. Rev. Lett. **81**, 2356 (1998).

[17] G. Misguich, D. Serban, and V. Pasquier, Phys. Rev. B **67**, 214413 (2003).

[18] B. Canals and C. Lacroix, Phys. Rev. Lett. **80**, 2933 (1998).

[19] C. Lhuillier and P. Sindzingre, in *Quantum Properties of Low-Dimensional Antiferromagnets*, Y. Ajiro and J. P. Boucher (eds.), Kyushu University Press, Fukuoka (2001), p. 111, cond-mat/0212351.

[20] S. E. Palmer and J. T. Chalker, Phys. Rev. B **62**, 488 (2000).

[21] O. Tchernyshyov, R. Moessner, and S. L. Sondhi, Phys. Rev. Lett. **88**, 067203 (2002).

[22] M. Elhajal, B. Canals, and C. Lacroix, Phys. Rev. B **66**, 014422 (2002).

[23] S. Dommange, M. Mambrini, B. Normand, and F. Mila, Phys. Rev. B **68**, 224416 (2003).

[24] M. E. Zhitomirsky, A. Honecker, and O. A. Petrenko, Phys. Rev. Lett. **85**, 3269 (2000).

[25] J.-C. Domenge, P. Sindzingre, and C. Lhuillier, cond-mat/0502414.

[26] A. S. Wills, Can. J. Phys. **79**, 1501 (2001).

[27] Y. Narumi, K. Katsumata, Z. Honda, J. C. Domenge, P. Sindzingre, C. Lhuillier, Y. Shimaoka, T. C. Kobayashi, and K. Kindo, Europhys. Lett. **65**, 705 (2004).

[28] G. Lawes, M. Kenzelmann, N. Rogado, K. H. Kim, G. A. Jorge, R. J. Cava, A. Aharony, O. Entin-Wohlman, A. B. Harris, T. Yildirim *et al.*, Phys. Rev. Lett. **93**, 247201 (2004).

[29] N. P. Raju, M. Dion, M. J. P. Gingras, T. E. Mason, and J. E. Greedan, Phys. Rev. B **59**, 14489 (1999).

[30] A. Keren and J. Gardner, Phys. Rev. Lett. **17**, 177201 (2001).

[31] J. A. Hodges, P. Bonville, A. Forget, A. Yaouanc, P. Dalmas de Réotier, G. André, M. Rams, K. Królas, C. Ritter, P. C. M. Gubbens *et al.*, Phys. Rev. Lett. **88**, 077204 (2002).

[32] A. Keren, J. S. Gardner, G. Ehlers, A. Fukaya, E. Segal, and Y. J. Uemura, Phys. Rev. Lett. **92**, 107204 (2004).

[33] S. H. Lee, C. Broholm, W. Ratcliff, G. Gasparovic, Q. Huang, T. H. Kim, and S. W. Cheong, Nature (London) **418**, 856 (2002).

[34] M. Harris, Nature (London) **399**, 311 (1999).

[35] A. P. Ramirez, A. Hayashi, R. J. Cava, R. Siddhartan, and B. S. Shastry, Nature (London) **399**, 333 (1999).

[36] X. Obradors, A. Labarta, A. Isalgué, J. Tejada, J. Rodríguez, and M. Pernet, Solid State Commun. **65**, 189 (1988).

[37] I. S. Hagemann, Q. Huang, X. P. A. Gao, A. P. Ramirez, and R. J. Cava, Phys. Rev. Lett. **86**, 894 (2001).

[38] A. P. Ramirez, G. P. Espinosa, and A. S. Cooper, Phys. Rev. B **45**, 2505 (1992).

[39] H. Ohta, M. Sumikawa, M. Motokawa, H. Kikuchi, and H. Nagasawa, J. Phys. Soc. Jpn. **65**, 848 (1996).

[40] L. Limot, P. Mendels, G. Collin, C. Mondelli, B. Ouladdiaf, H. Mutka, N. Blanchard, and M. Mekata, Phys. Rev. B **65**, 144447 (2002).

[41] D. Bono, P. Mendels, G. Collin, and N. Blanchard, Phys. Rev. Lett. **92**, 217202 (2004).

[42] S. H. Lee, C. Broholm, G. Aeppli, T. G. Perring, B. Hessen, and A. Taylor, Phys. Rev. Lett. **76**, 4424 (1996).

[43] L. J. de Jongh and A. R. Miedema, Adv. Phys. **50**, 947 (2001).

[44] A. P. Ramirez, G. P. Espinosa, and A. S. Cooper, Phys. Rev. Lett. **64**, 2070 (1990).

[45] P. Lecheminant, B. Bernu, C. Lhuillier, L. Pierre, and P. Sindzingre, Phys. Rev. B **56**, 2521 (1997).

[46] A. P. Ramirez, B. Hessen, and M. Winklemann, Phys. Rev. Lett. **84**, 2957 (2000).

[47] P. Sindzingre, G. Misguich, C. Lhuillier, B. Bernu, L. Pierre, C. Waldtmann, and H. U. Everts, Phys. Rev. Lett. **84**, 2953 (2000).

[48] C. Broholm, G. Aeppli, G. P. Espinosa, and A. S. Cooper, Phys. Rev. Lett. **65**, 3173 (1990).

[49] Y. J. Uemura, A. Keren, K. Kojima, L. P. Le, G. M. Luke, W. D. Wu, Y. Ajiro, T. Asano, Y. Kuriyama, M. Mekata *et al.*, Phys. Rev. Lett. **73**, 3306 (1994).

[50] B. Martínez, F. Sandiumenge, A. Rouco, A. Labarta, J. Rodríguez-Carvajal, M. Tovar, M. T. Causa, S. Galí, and X. Obradors, Phys. Rev. B **46**, 10786 (1992).

[51] C. Mondelli *et al.*, private communication.

[52] A. P. Ramirez, Annu. Rev. Mater. Sci. **24**, 453 (1994).

[53] A. Keren, P. Mendels, M. Horvatić, F. Ferrer, Y. J. Uemura, M. Mekata, and T. Asano, Phys. Rev. B **57**, 10745 (1998).

[54] P. Mendels, A. Keren, L. Limot, M. Mekata, G. Collin, and M. Horvatić, Phys. Rev. Lett. **85**, 3496 (2000).

[55] L. Limot, P. Mendels, G. Collin, C. Mondelli, H. Mutka, and N. Blanchard, Can. J. Phys. **79**, 1393 (2001).

[56] D. Bono, P. Mendels, G. Collin, and N. Blanchard, J. Phys.: Condens. Matter **16**, S817 (2004).
[57] A. Keren, Y. J. Uemura, G. Luke, P. Mendels, M. Mekata, and T. Asano, Phys. Rev. Lett. **84**, 3450 (2000).
[58] D. Bono, P. Mendels, G. Collin, N. Blanchard, F. Bert, A. Amato, C. Baines, and A. D. Hillier, Phys. Rev. Lett. **93**, 187201 (2004).
[59] D. E. MacLaughlin and H. Alloul, Phys. Rev. Lett. **36**, 1158 (1976).
[60] A. B. Harris, C. Kallin, and A. J. Berlinsky, Phys. Rev. B **45**, 2899 (1992).
[61] K. Motida and S. Miyahara, J. Phys. Soc. Jpn. **28**, 1188 (1970).
[62] E. J. Samuelsen, M. T. Hutchings, and G. Shirane, Physica (Amsterdam) **48**, 13 (1970).
[63] C. Mondelli, K. Andersen, H. Mutka, C. Payen, and B. Frick, Physica B **267–268**, 139 (1999).
[64] A. J. Garcia-Adeva and D. L. Huber, Phys. Rev. B **63**, 174433 (2001).
[65] P. Schiffer and I. Daruka, Phys. Rev. B **56**, 13712 (1997).
[66] M. Takigawa, N. Motoyama, H. Eisaki, and S. Uchida, Phys. Rev. B **55**, 14129 (1999).
[67] F. Tedoldi, R. Santachiara, and M. Horvatic, Phys. Rev. Lett. **83**, 412 (1999).
[68] M. Azuma, Z. Hiroi, M. Takano, K. Ishida, and Y. Kitaoka, Phys. Rev. Lett. **73**, 3463 (1994).
[69] S. Ouazi, J. Bobroff, H. Alloul, and W. A. MacFarlane, Phys. Rev. B **70**, 104515 (2004).
[70] R. Moessner and A. J. Berlinsky, Phys. Rev. Lett. **83**, 3293 (1999).
[71] A. Abragam, *Principles of Nuclear Magnetism*, Clarendon Press, Oxford (1961).
[72] S. L. Lee, S. H. Kilcoyne, and R. Cywinski (eds.), *Muon Science: Muons in Physics, Chemistry and Materials*, Proceedings of the Fifty-First Scottish Universities Summer School in Physics, August 1998, Scottish Universities Summer School in Physics & Institute of Physics Publishing, Bristol and Philadelphia (1999).
[73] R. S. Hayano, Y. J. Uemura, J. Imazato, N. Nishida, T. Yamazaki, and R. Kubo, Phys. Rev. B **20**, 850 (1979).
[74] Y. J. Uemura, T. Yamazaki, D. R. Harshman, M. Senba, and E. J. Ansaldo, Phys. Rev. B **31**, 546 (1985).
[75] A. Keren, Phys. Rev. B **50**, 10039 (1994).
[76] A. Keren, K. Kojima, L. P. Le, G. M. Luke, W. D. Wu, Y. J. Uemura, M. Takano, H. Dabkowska, and M. J. P. Gingras, Phys. Rev. B **53**, 2451 (1996).
[77] A. Fukaya, Y. Fudamoto, I. M. Gat, T. Ito, M. I. Larkin, A. T. Savici, Y. J. Uemura, P. P. Kyriakou, G. M. Luke, M. T. Rovers *et al.*, Phys. Rev. Lett. **91**, 207603 (2003).
[78] K. Kojima, A. Keren, L. P. Le, G. M. Luke, B. Nachumi, W. D. Wu, Y. J. Uemura, K. Kiyono, S. Miyasaka, H. Takagi *et al.*, Phys. Rev. Lett. **74**, 3471 (1995).
[79] A. Chubukov, Phys. Rev. Lett. **69**, 832 (1992).
[80] F. Mila and D. Dean, Eur. Phys. J. B **26**, 301 (2002).
[81] M. Ferrero, F. Becca, and F. Mila, Phys. Rev. B **68**, 214431 (2003).
[82] Z. Hiroi, M. Hanawa, N. Kobayashi, M. Nohara, H. Takagi, Y. Kato, and M. Takigawa, J. Phys. Soc. Jpn. **70**, 3377 (2001).
[83] F. Bert, D. Bono, P. Mendels, J. C. Trombe, P. Millet, A. Amato, C. Baines, and A. Hillier, J. Phys.: Condens. Matter **16**, S829 (2004).
[84] K. Kojima, Ph. D. thesis, The University of Tokyo (1995).
[85] B. Ammon and M. Imada, Phys. Rev. Lett. **85**, 1056 (2000).
[86] A. Fukaya, Y. Fudamoto, I. M. Gat, T. Ito, M. I. Larkin, A. T. Savici, Y. J. Uemura, P. P. Kyriakou, G. M. Luke, M. T. Rovers *et al.*, Physica B **326**, 446 (2003).
[87] H. Kageyama, K. Yoshimura, R. Stern, N. V. Mushnikov, K. Onizuka, M. Kato, K. Kosuge, C. P. Slichter, T. Goto, and Y. Ueda, Phys. Rev. Lett. **82**, 3168 (1999).
[88] K. Kodama, M. Takigawa, M. Horvatić, C. Berthier, H. Kageyama, Y. Ueda, S. Miyahara, F. Becca, and F. Mila, Science **298**, 395 (2002).
[89] H. Mutka *et al.*, in preparation.
[90] M. H. Cohen and F. Reif, Solid State Phys. **5**, 321 (1957).
[91] R. E. Walstedt and L. R. Walker, Phys. Rev. B **9**, 4857 (1974).
[92] J. H. Brewer, R. F. Kiefl, J. F. Carolan, P. Dosanjh, W. N. Hardy, S. R. Kreitzman, Q. Li, T. M. Riseman, P. Schleger, H. Zhou *et al.*, Hyperfine Interact. **63**, 177 (1990).

This article was published in English in the original Russian journal. Reproduced here with stylistic changes by AIP.

LOW TEMPERATURE PHYSICS VOLUME 31, NUMBERS 8–9 AUGUST–SEPTEMBER 2005

Ordering in two-dimensional Ising models with competing interactions

G. Y. Chitov*

Department 7.1-Theoretical Physics, University of Saarland, Saarbrücken D-66041, Germany;
Department of Physics and Astronomy, Laurentian University, Sudbury, ON, P3E 2C6 Canada

C. Gros

Department 7.1-Theoretical Physics, University of Saarland, Saarbrücken D-66041, Germany;
Institute for Theoretical Physics, Frankfurt University, Frankfurt 60438, Germany

(Submitted February 28, 2005)
Fiz. Nizk. Temp. **31**, 952–967 (August–September 2005)

We study the 2D Ising model on a square lattice with additional non-equal diagonal next-nearest neighbor interactions. The cases of classical and quantum (transverse) models are considered. Possible phases and their locations in the space of three Ising couplings are analyzed. In particular, incommensurate phases occurring only at non-equal diagonal couplings, are predicted. We also analyze a spin-pseudospin model comprised of the quantum Ising model coupled to XY spin chains in a particular region of interactions, corresponding to the Ising sector's super-antiferromagnetic (SAF) ground state. The spin-SAF transition in the coupled Ising-XY model into a phase with co-existent SAF Ising (pseudospin) long-range order and a spin gap is considered. Along with destruction of the quantum critical point of the Ising sector, the phase diagram of the Ising-XY model can also demonstrate a re-entrance of the spin-SAF phase. A detailed study of the latter is presented. The mechanism of the re-entrance, due to interplay of interactions in the coupled model, and the conditions of its appearance are established. Applications of the spin-SAF theory for the transition in the quarter-filled ladder compound NaV_2O_5 are discussed. © *2005 American Institute of Physics.* [DOI: 10.1063/1.2008132]

I. INTRODUCTION

The role of competing interactions in ordering is a fascinating problem of condensed matter physics. One of the most canonical examples of such systems are frustrated Ising models which demonstrate a plethora of critical properties, far from being exhaustively studied. (For a review see Ref. 1.) The frustrations1) can be either geometrical, like, e.g., in the Ising model on a triangular lattice, or they can be brought about by the next-nearest neighbor (NNN) interactions. Competing interactions (frustrations) can, e.g., result in new phases, change the Ising universality class, or even destroy the order at all. Another interesting aspect of the criticality in frustrated Ising models is an appearance of quantum critical point(s) (QCP) at special frustration points of model's high degeneracy, and related quantum phase transitions.[2]

Inclusion of a transverse field (Ω) brings an extra scale into the game, giving raise to a new and complicated critical behavior. The Ising models with $\Omega=0$ and $\Omega\neq 0$ are also often called classical and quantum, respectively. For a review on the Ising models in transverse field (IMTF) see Ref. 3. Most studies of the frustrated quantum Ising models are restricted to their ground-state properties, when mapping of the d-dimensional quantum model at $T=0$ onto its $(d+1)$-dimensional classical counterpart helps to analyze the ground-state phase diagram of the former. For the NNN 2D models we are interested in, there has been a considerable effort on the quantum anisotropic NNN Ising (ANNNI) model, reviewed in Ref. 3. The studies of some other 2D frustrated transverse Ising models have appeared only recently.[4,5]

Our interest in the subject comes from the earlier work on a quantum Ising model coupled to the spin chains.[6] This kind of coupled so-called spin-pseudospin (or spin-orbital) models appear in context of the phase transition in NaV_2O_5, which has inspired a great experimental and theoretical effort in recent years. (For a review see Ref. 7.) Going deeper into analysis, we came to realize that the Ising sector of the problem is in fact the 2D transverse NN and NNN Ising model on a square lattice. It turns out that even its classical counterpart ($\Omega=0$) has been studied[1] only for the case of equal NNN couplings, $J_1=J_2$. The elementary plaquette of this lattice with the notations for couplings is shown in Fig. 1. To the best of our knowledge, this 2D NN and NNN Ising model in transverse field is a complete *terra incognita* even at $J_1=J_2$.

So, as the first step, we find the ground-state phase diagram of the classical ($\Omega=0$) Ising model at arbitrary couplings $J_\Box, J_1, J_2$. Along with the three ordered phases found earlier by Fan and Wu[8] for the case $J_1=J_2$—ferromagnetic (FM), antiferromagnetic (AF), and super-antiferromagnetic (SAF)—the model has a fourth phase which can occur if the sign of $(J_1/J_2)=-1$. We call it super-ferro-antiferromagnetic (SFAF).[9] From mean-field-type arguments we predict also the existence of an incommensurate (IC) phase at $T>0$ in this model. The 2D IC phase is also called floating.[10] Similar phase is known for the well-studied 2D ANNNI model.[1,10,11] We present a qualitative temperature phase diagram for the regions of the coupling space where the IC phase is located. Note that the three phases—SAF, SFAF, IC—can occur only in the presence of competing in-

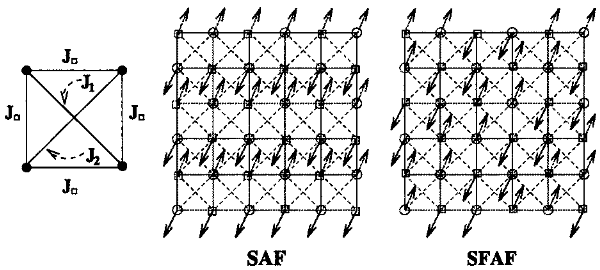

FIG. 1. Couplings on an elementary plaquette in the NN and NNN 2D Ising model (1). Ordering patterns in the super-antiferromagnetic (SAF) and super-ferro-antiferromagnetic (SFAF) phases.

teractions in the Ising model, and the latter two occur only if $J_1 \neq J_2$.

This analysis of the classical Ising model lays the groundwork for venturing into its study in presence of a transverse field. The role of transverse field is subtle. A more straightforward aspect is that its increase above certain critical value can eventually destroy the ordered state of the classical model, and in the ground state the transverse field results in appearance of a QCP. This is similar to the well-understood quantum NN Ising model. Another particularly interesting aspect in the role of transverse field is that it can lift degeneracy of the ground state and stabilize new phases at finite temperature in a highly frustrated model, like, e.g., the antiferromagnetic isotropic triangular Ising model,[4,5] which is disordered at any $T>0$ when $\Omega=0$.

The behavior of the systems with infinitely degenerate ground states (with or without a finite ground-state entropy per spin) can be quite complicated in the presence of transverse field. It lies beyond the scope of the present work, and definitely cannot be understood from the mean-field analysis we apply in this study. For the NN and NNN Ising model we only identify the lines (planes) in the space of couplings $(J_\Box, J_1, J_2)$ where the model is highly degenerate, and in their neighborhood we expect some new exotic phases generated by $\Omega \neq 0$ to appear.

From mapping of the NN and NNN IMTF at $T=0$ onto its classical 3D counterpart, we qualitatively predict the (mean-field) ground-state phase boundaries of the quantum model in the coupling space $(J_\Box, J_1, J_2)$. In particular, it follows from our analysis that in the presence of transverse field the IC ground-state phase can penetrate into some parts of the FM, AF, SAF regions of the classical model $(\Omega=0)$.

Finally, we consider the coupled spin-pseudospin model. It is proposed to analyze the transition in NaV_2O_5. This material provides a unique example of a correlated electron system, where the interplay of charge and spin degrees of freedom results in a phase transition into a phase with coexistent spin gap and charge order. NaV_2O_5 is the only known so far quarter-filled ladder compound. Each individual rung of a ladder is occupied by single electron which is equally distributed between its left/right sites in the disordered phase. At $T_c=34$ K this compound undergoes a phase transition when a spin gap opens, accompanied by charge ordering.[7]

The problem of the electrons in NaV_2O_5 localized on the rungs of the 2D array of ladders is mapped onto the coupled spin-pseudospin model on an effective square lattice. The Ising sector of this model is given by the Hamiltonian of the NN and NNN IMTF, and the Ising variables (called pseudospins for this case) represent physically the charge degrees of freedom. We model the spin sector by the array of the XY spin chains. The 2D long-range charge order in NaV_2O_5 is identified as the SAF phase of the Ising model, and we restrict our analysis to the SAF region of the couplings $(J_\Box, J_1, J_2)$. The coupled model is handled by combining the mean-field treatment of its Ising sector with the use of exact results available for the XY spin chains. Since the SAF state is only fourfold degenerate, the mean-field predictions for the Ising sector of the coupled model are expected to be at least qualitatively correct.

The mean-field equations for the coupled model are, with some minor modifications, the same as we have obtained earlier.[6] A striking feature of the coupled model is that it *always* orders from the charge-disordered spin-gapless state into the phase of co-existent SAF charge order and spin gap. We call this the spin-SAF transition. By *always* we mean that the critical temperature of the spin-SAF transition is nonzero for all Ising couplings within the whole considered SAF region. In other words, the QCP of the IMTF is destroyed, and this is due to the spin-charge (-pseudospin) coupling.

This property of the spin-SAF transition and the parameters of the spin-SAF phase were studied earlier,[6] so in this work we only reinstate some points and stress the distinctions pertinent to the present model.

The other remarkable feature of the coupled model's phase diagram is re-entrance, which was not well understood in our earlier work.[6] Now we carry out an analytical study of the re-entrance and establish the conditions when it can occur. This analysis allows us to understand the detailed mechanism of this interesting phenomenon generated by competing interactions.

The rest of the paper is organized as follows. Section 2 contains our results on the ordering in the 2D NN and NNN Ising model at $\Omega=0$ and $\Omega \neq 0$. The results on the spin-SAF transition in the coupled model are presented in Sec. 3. The final Sec. 4 presents the summary and discussion.

II. 2D NEAREST- AND NEXT-NEAREST-NEIGHBOR ISING MODEL

We consider the 2D Ising model on a square lattice with the Hamiltonian

$$H=\frac{1}{2}\sum_{\langle \mathbf{i},\mathbf{j}\rangle} J_\Box \mathcal{T}^x_{\mathbf{i}}\mathcal{T}^x_{\mathbf{j}}+\frac{1}{2}\sum_{\langle\langle \mathbf{k},\mathbf{l}\rangle\rangle} J_{\mathbf{kl}}\mathcal{T}^x_{\mathbf{k}}\mathcal{T}^x_{\mathbf{l}}, \tag{1}$$

where the bold variables denote lattice vectors, the first (second) sum includes only nearest neighbors (next-nearest neighbors) of the lattice, respectively. Spins along the sides of an elementary plaquette interact via the NN coupling $J_\Box$, while spins along plaquette's diagonals interact via the NNN couplings $J_{\mathbf{kl}}=J_{1,2}$ (see Fig. 1). The way we defined the Hamiltonian corresponds to antiferromagnetic couplings for $J_\Box>0$ and ferromagnetic for $J_\Box<0$.

Ground-state phases

There is no exact solution of the model (1). Its possible ordered phases and critical properties have been studied within various approaches for equal diagonal couplings $J_1 = J_2$ (see Ref. 1 for a review and references on the original literature). We will consider arbitrary Ising couplings $(J_1, J_2, J_\square)$, so the model (1) can be either frustrated or not (see footnote 1). The ground-state phase diagram can be found from energy arguments, as was first done by Fan and Wu[8] for $J_1 = J_2$. (Their phase diagram is shown in Fig. 3c.) From direct counting of the ground-state energies of possible spin arrangements we construct the phase diagram for $J_1 \neq J_2$. Along with the phases found by Fan and Wu—ferromagnetic, antiferromagnetic, and super-antiferromagnetic—there is a fourth phase which can occur if J_1 and J_2 have opposite signs. The name of the SAF phase comes from viewing it as two superimposed antiferromagnetic lattices (one lattice of circled sites and another of squared sites in Fig. 1). In the SAF state there are two frustrated bonds $J_\square$ per plaquette and its energy is fourfold degenerate, since each of the superimposed lattices can be flipped independently. In addition to the two SAF states with alternating ferromagnetic order along the horizontal chains (one of these is shown in Fig. 1), there are two states with the vertical ferromagnetic order.

The new fourth phase shown in Fig. 1 can be viewed as two superimposed lattices, each of which is ordered ferromagnetically along one side (e.g., $J_2 < 0$) and antiferromagnetically along the other (e.g., $J_1 > 0$). So we will call it super-ferro-antiferromagnetic (SFAF).[9] The SFAF state also has two frustrated plaquette's bonds and fourfold degeneracy. The ordering pattern shown in Fig. 1 changes only by a lattice spacing shift over flipping of the sublattices. The direction of the ferromagnetic order is determined by the ferromagnetic diagonal.

The ground-state phases in the space $(J_1, J_2, J_\square)$ are shown in Fig. 2. In order to facilitate perception of this picture, we also present in Figs. 3 and 4 several plane projections of the 3D Fig. 2. In the first quadrant $(J_1, J_2 > 0)$ in the region $J_1 + J_2 > |J_\square|$ lying between two frustration planes (FP)

$$J_1 + J_2 = |J_\square|: \quad \text{FP} \tag{2}$$

the ground state of the model is SAF. A continuous transition from the paramagnetic (PM) to the SAF phase occurs at some critical temperature $T_c > 0$. From the arguments known for the case $J_1 = J_2$ (Ref. 12; see also Ref. 13 for a more general symmetry analysis of the Ginzburg-Landau functional) this transition is nonuniversal: the critical indices depend continuously on the couplings $J_\square, J_1, J_2$.

In the region $J_1 > J_\square$ of the fourth quadrant $(J_1 > 0, J_2 < 0)$ lying between the other pair of frustration planes

$$J_1 = |J_\square|: \quad \text{FP}' \tag{3}$$

the ground state is SFAF. The same arguments[12,13] suggest nonuniversality of the PM→SFAF transition.

In the regions lying above (beneath) the frustration planes FP and FP′, and above (beneath) the basal plane $J_\square = 0$ in the third quadrant, the ground state is a usual AF (FM), respectively. The transition PM→AF (FM) belongs to the 2D Ising universality class. The second quadrant $J_1 < 0, J_2 > 0$, not shown in Fig. 2, is obtained by reflection in the plane $J_1 = J_2$. In the AF (FM) state the number of frustrated (diagonal) bonds per plaquette is two in the first quadrant, one in the second and the fourth, and zero in the third.

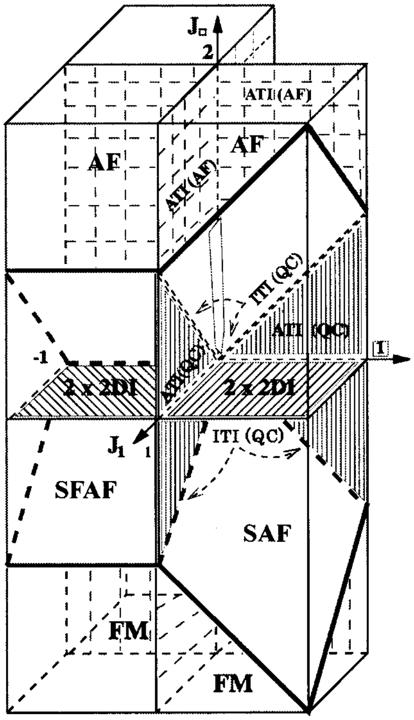

FIG. 2. Phase diagram of the ground states (GS) of the model (1). For visualization purposes it is drawn within the $(-1,1) \times (-1,1) \times (-2,2)$ parallelepiped. The SAF GS lies between the frustration planes $J_1 + J_2 = |J_\square|$. The SFAF GS lies between the frustration planes $J_1 = |J_\square|$. The AF GS (FM GS) lies above (beneath) the frustration planes and above (beneath) the basal plane in the third quadrant, respectively. The second quadrant (not shown) is obtained by a reflection in the $J_1 = J_2$ plane. Different sectors shown by hatched and twiggy lines on the exactly solvable planes $J_\square = 0$ are explained in the text.

Transitions at finite temperature should be absent on the frustration planes FP/FP′ where the model is highly degenerate. We are not aware of studies of the ground state in these cases and cannot say at the moment whether the system possesses some kind of a long-range order at zero temperature or not, except a rather trivial line $J_\square = J_1 = 0, J_2 < 0$ of the FP′ planes crossing where the model becomes a set of decoupled Ising chains, and four special lines on the FP planes where it becomes the exactly-solvable isotropic triangular Ising (ITI) model. The latter case will be discussed momentarily.

Exactly-solvable limits

In the 3D space $(J_1, J_2, J_\square)$ besides the frustration planes FP and FP′, there are three special planes where one of the couplings is zero. On these planes the model (1) reduces to the exactly solvable cases.

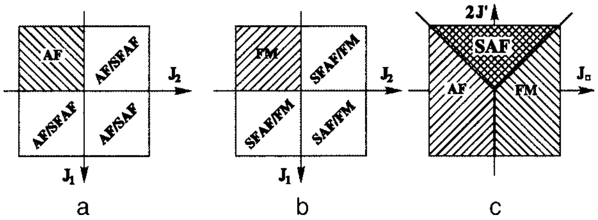

FIG. 3. Plane projections of the 3D diagram shown in Fig. 2. (a): Upper part $J_\square > 0$, view from the top. (b): Lower part $J_\square < 0$, view from the top. (c): Compactification of 3D Fig. 2 in the special case $J_1 = J_2 \equiv J'$.[8]

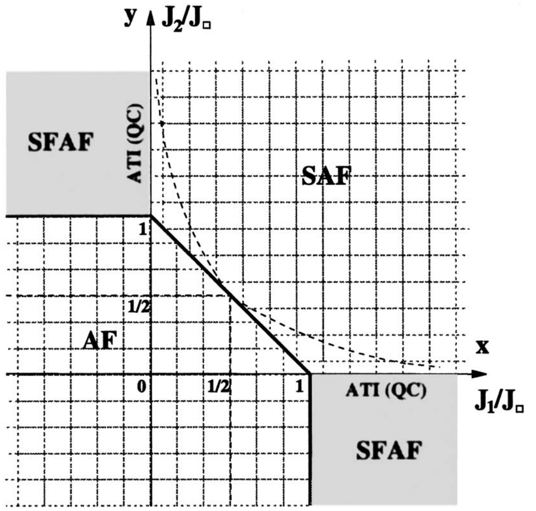

FIG. 4. Plane phase diagram for the ratios of the couplings, corresponding to the 3D Fig. 2 at $J_\square > 0$. The phase boundaries (thick solid lines) correspond to the frustrations planes FP and FP′. The thick dashed lines (online) indicate the boundaries of the incommensurate global minima locus ($y > 1/2$, $x > 1/2$, $y < 1/4x$) discussed in the text. The case $J_\square < 0$ can be obtained by the substitutions $J_{1,2}/J_\square \mapsto J_{1,2}/|J_\square|$, AF→FM in this figure.

Let us start with the upper part ($J_\square > 0$) of the SAF region

$$J_\square < J_1 + J_2 . \tag{4}$$

On the SFAF–SAF boundary $J_2 = 0$ the model is equivalent to the anisotropic Ising model on a triangular lattice (ATI), for which exact results are available.[14–17] The antiferromagnetic ($J_\square, J_1 > 0$) ATI model with one strong bond $J_1 > J_\square$ is disordered at any nonzero temperature.[17] It orders only at $T = 0$, i.e., it is quantum critical (QC). The highly degenerate ground state (however with a vanishing zero-temperature entropy per site) can be viewed as a 2D array of antiferromagnetically ordered (along the strong bond J_1) correlated chains. The oscillating (with a period of four lattice spacings) power-law decay of the spin-spin correlation function along $J_\square$ directions[17] indicate on the preference of the ferromagnetic order along the "missing" diagonal J_2. This resembles the SFAF state, however any couple of adjacent J_1 chains is uncorrelated. We label this state occurring on two sectors of the $J_1 = 0$ (or $J_2 = 0$) planes as ATI (QC) on the phase diagram (Fig. 2). Since the critical behavior of the ATI model with two equal weak ferromagnetic bonds $|J_\square| < J_1$ is equivalent to the totally antiferromagnetic ATI model,[17] the ATI (QC) state smoothly continues into the lower ($J_\square < 0$) part of the SFAF–SAF boundary.

The sectors $J_2 = 0$, $J_1 > 0$ (and $1 \leftrightarrow 2$) above the FP $J_1 + J_2 = J_\square$ correspond to the antiferromagnetic ATI model with one weak bond $J_1 < J_\square$. It is known[17] to have only two phases and to order at finite temperature. T_c(PM→AF) as a function of couplings is also known exactly. The sectors $J_2 = 0$, $J_1 < 0, J_\square > 0$ (and $1 \leftrightarrow 2$) correspond to the antiferromagnetic ATI model which is not even frustrated, and T_c(PM→AF)>0 at any $J_\square > 0$. The PM→AF transition in the ATI model belongs to the 2D Ising class. So, except for the SFAF–SAF boundary, the ordered phase on the exactly-solvable "triangulation" planes $J_1 = 0$ (or $J_2 = 0$) is the same as the AF ground state in the interior in this region of the phase diagram.

The situation on the "triangulation" planes in the lower part ($J_\square < 0$) of the phase diagram is exactly analogous to the upper part, with an obvious replacement AF↔FM.

Note that the ground states change on the lines where the triangulation and frustration planes cross. To put it differently, these are the lines of quantum phase transitions. The AF (FM) phase disappears in the limit $J_1 \to |J_\square| - 0$ ($J_2 = 0$). Also, the zero-temperature AF in-chain order (ATI (QC)) described above disappears in the limit $J_1 \to |J_\square| + 0$ ($J_2 = 0$) as well. The ITI model $J_1 = J_\square$ is disordered at any nonzero temperature (indicated as ITI (QC) in Fig. 2). Its ground state, albeit having finite entropy per site, possesses periodic (with a period of three lattice spacings) long-range order.[16]

The basal plane $J_\square = 0$ in Fig. 2 corresponds to the case when Hamiltonian (1) represents two decoupled identical NN Ising models residing on two superimposed lattices (shown by circles and squares in Fig. 1). Diagonal couplings $J_{1,2}$ are the NN couplings of these Ising models. This is the only exactly-solvable limit (labeled by 2×2DI in Fig. 2) within the SFAF (or SAF) region of the phase diagram. In this limit the PM→SAF (or SFAF) phase transition enters into the 2D Ising universality class.

Incommensurate (floating) phase

So far we have discussed the ground-state phases of the model and the critical behavior on the boundaries of these phases with the disordered phase, as well as on the special planes (lines). However, there is also a possibility that ordering into the ground-state phases of Fig. 2 happens not necessarily from the PM phase, but from some other one(s) occurring at nonzero temperature. A very simple analysis indicates that this indeed can take place in our model. Fourier-transforming the Hamiltonian (1) we obtain (we set the lattice spacing to unity)

$$H = \sum_{\mathbf{q}} J(\mathbf{q}) T^x(\mathbf{q}) T^x(-\mathbf{q}), \tag{5}$$

$$J(\mathbf{q}) = J_\square(\cos q_x + \cos q_y) + J_1 \cos(q_x - q_y) + J_2 \cos(q_x + q_y),$$

where $\mathbf{q}$ runs within the first Brillouin zone $|q_{x,y}| \leqslant \pi$. At mean-field level, a minimum of $J(\mathbf{q})$ in $\mathbf{q}$ space defines the wave vector $\mathbf{q}_0$ of the critical freezing mode $T^x(\mathbf{q}_0)$, i.e., the order parameter $\langle T^x_{\mathbf{m}} \rangle \propto \cos(\mathbf{q}_0 \cdot \mathbf{m} + \varphi)$ below a certain critical temperature T_c. In different regions ($J_1, J_2, J_\square$) of the ground-state phase diagram (Fig. 2) we find a minimum at $\mathbf{q}^{\mathrm{F/A}} = (0,0)/(\pi,\pi)$ giving the FM/AF order parameter and two minima $\mathbf{q}_{1,2}^{\mathrm{SAF}} = (\pi,0)/(0,\pi)$ giving two components of the SAF order parameter. (The latter represent two possible ordering patterns of the SAF phase and via some transformation can be related to magnetizations of the superimposed sublattices.[12]) The important point is that the positions of the *commensurate* (C) extrema $\mathbf{q}^\#$ (# = F, A, SAF) of $J(\mathbf{q})$ do not depend on the couplings.

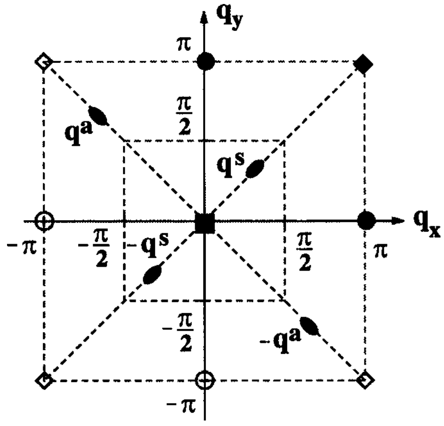

FIG. 5. Positions of extrema of $J(\mathbf{q})$ (5) in the Brillouin zone. Open symbols connected to their bold counterparts by a reciprocal lattice vector. Incommensurate extrema $\pm\mathbf{q}^{a,s}$ (7), (8) (shown for the case $J_1>0$, $J_2<0$) exist if conditions (6) are satisfied.

There are however two other pairs of extrema $\pm\mathbf{q}^{s,a}$ which exist if

$$|J_\square|<2|J_1| \quad \text{and/or} \quad 2|J_2|. \tag{6}$$

These extrema lie on the diagonal of the Brillouin zone. $\mathbf{q}^{s,a}$ are generically *incommensurated* (IC) and depend on the couplings as

$$q_x^s=-q_y^s=\arccos\left(-\frac{J_\square}{2J_2}\right), \tag{7}$$

$$q_x^a=-q_y^a=\arccos\left(-\frac{J_\square}{2J_1}\right). \tag{8}$$

In Fig. 5 we show the positions of all extrema of $J(\mathbf{q})$ within the Brillouin zone. In the SFAF ground-state region (e.g., in the fourth quadrant $J_1>0$, $J_2<0$ shown in Fig. 2) the pair of extrema $\pm\mathbf{q}^a$ (8) gives global minima of $J(\mathbf{q})$ (the other pair of solutions (8) $\pm\mathbf{q}^s$, when it exists, corresponds to maxima), and $|q_x^a|=|q_y^a|>\pi/2$. As we see, two IC modes $\pm\mathbf{q}^a$ could give components of the SFAF ground-state order parameter's wave vectors $\pm\mathbf{q}^{\mathrm{SFAF}}=\pm(\pi/2,-\pi/2)$ only if $J_\square=0$. (In the second quadrant of the SFAF region when $J_1<0$, $J_2>0$, the vectors $\mathbf{q}^s$ and $\mathbf{q}^a$ exchange their roles. Because of the $J_1\leftrightarrow J_2$ symmetry, in the following, for concreteness, we will always discuss the fourth quadrant.)

The locus of the IC global minima does not coincide with the SFAF ground-state region, but overlaps with the neighboring FM, AF, and SAF phases. The minimum J $(\pm\mathbf{q}^a)$ is located between two planes $|J_\square|=2J_1$ in the fourth quadrant, and in two regions of the half of the first quadrant $(J_2<J_1)$: (i) between $J_\square=+2J_1$ and $J_\square=+2\sqrt{J_1J_2}$; (ii) $+\mapsto-$. The regions of the IC minima in the other half $(J_2>J_1)$ of the first quadrant (as in the second quadrant) are obtained from the described above by $J_1\leftrightarrow J_2$, $\mathbf{q}^a\rightarrow\mathbf{q}^s$. On the plane phase diagram shown in Fig. 4 this locus is restricted by the lines $y=1/2$, $x=1/2$, $y=1/4x$, shown by the dashed lines.

So we can conclude that at finite temperature the model possesses an IC phase and there is an IC–C phase transition where the IC wave vector $\mathbf{q}^a$ locks into one of the (commensurate) ground-state phase vectors. As in 2D the IC phase has only an algebraic long-range order; it is called floating.[10] The origin of the IC floating phase in our model is frustration (competing interactions). Such phase is well known from another example of frustrated Ising model, i.e., the ANNNI model which was intensively studied in the past.[1,10,11] In that model the floating phase locks into the antiphase which has the wave vector $\mathbf{q}=(0,\pi/2)$. (The antiphase is the analog of our SFAF phase.) The ANNNI model also provides an example showing that the mean-field (minimization) analysis does not work well in defining boundaries between the floating and commensurate phases in 2D, and the extend of the IC phase is less than the mean field suggests.2)

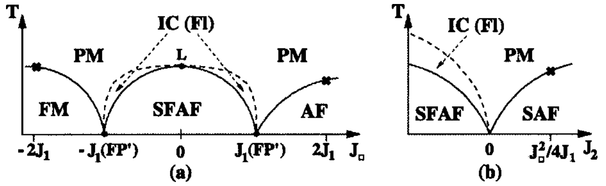

FIG. 6. Qualitative temperature phase diagram. The IC floating (Fl) phase lies beneath the dashed lines. Crosses indicate the borders of the IC minima locus. (a): For fixed $J_1>0$, $J_2<0$. On the plane $J_\square=0$ the floating phase must be absent. We assume that it disappears smoothly at $J_\square=0$, resulting in a Lifshitz point (L). (b): The same for fixed $J_1>0$, $|J_\square|<J_1$.

We will not attempt to locate exactly the phase boundaries at finite temperature in this study. Following Domany *et al.*[13] in classification of the ordered phases by commensurability p, i.e., the ratio of superstructure's period and lattice spacing along a given direction, we can label the phases as follows: $\mathrm{F}\mapsto1\times1$; $\mathrm{AF}\mapsto2\times2$; $\mathrm{SAF}\mapsto1\times2$ (or 2×1); $\mathrm{SFAF}\mapsto4\times4$.3) From mapping of the 2D IC-C phase transition to the Kosterlitz–Thouless problem, it is established[10,18] that there is no such (continuous) transition for commensurate phases with small $p^2<8$. From this result with the proviso of continuity of phase transition(s) in the model, we conclude that the IC floating phase cannot "spill" beyond the SFAF $(p=4)$ ground-state region of the phase diagram, even if a naive (mean-field) analysis suggests that within the F, AF, and SAF regions there are some parts where it could be possible (see Fig. 4). The only high-temperature phase in which the latter three regions have a common border is the disordered PM.

Combining this with the known exact critical properties of the model on the special planes discussed above, we end up with the qualitative finite-temperature phase diagram shown in Fig. 6. Since on the plane $J_\square=0$ the model (1) is just two decoupled Ising lattices, the floating phase must be absent. Mean-field arguments suggest that the floating phase disappears exactly at $J_\square=0$, giving rise to a Lifshitz point (L). Note that the floating phase does not appear if the diagonal couplings are equal even at the mean-field level (see Fig. 4), which agrees with known, more sophisticated analyses of this case.[1]

The model in transverse field

Now we turn to the analysis of the NN and NNN Ising Hamiltonian H (1) in the presence of a transverse field. The total Hamiltonian of the Ising model in transverse field (IMTF) reads

$$H_{\mathrm{IMTF}}=H-\Omega\sum_i \mathcal{T}_i^z. \tag{9}$$

The Ising operators are normalized to satisfy the spin algebra

$$[\mathcal{T}_i^\alpha,\mathcal{T}_j^\beta]=i\delta_{ij}\varepsilon_{\alpha\beta\gamma}\mathcal{T}_i^\gamma. \tag{10}$$

There is no exact solution of the transverse 2D Ising model even for the case of NN couplings only ($J_1=J_2=0$). The ground-state phase diagram of the Hamiltonian (9) can be analyzed from the known mapping of the d-dimensional IMTF at zero temperature onto the $(d+1)$-dimensional Ising model at a given (nonzero) "temperature."[3] In our case the 2D NN and NNN IMTF maps onto the 3D Ising model comprised of the 2D layers (1) coupled *ferromagnetically* in the third (Trotter) direction with the coupling $J_T\propto-\ln\coth\Omega<0$. For such a $(2+1)$-dimensional model a mean-field analysis gives a qualitatively correct diagram of the ground-state phases of the 2D IMTF.[3] The new coupling J_T does not bring any additional frustration to the 2D NN and NNN model. Analysis of $J_3(q_x,q_y,q_T)=J_T\cos q_T+J(q_x,q_y)$, where $J(q_x,q_y)$ is given by (5), shows that J_T does not modify the domains of the global minima in the $(J_1,J_2,J_\square)$ space, adding only a trivial $q_T=0$ third component to the two-dimensional vectors $\mathbf{q}^\#$ discussed above (cf. Fig. 5.) The temperature phase diagram of the 3D Ising model with the spectrum $J_3(q_x,q_y,q_T)$ (if we label the phases according to the in-plane ordering pattern defined by the 2D vectors $\mathbf{q}^\#$) looks similar to that shown in Fig. 6, with one very important distinction: the above-mentioned argument related to phase's commensurability p does not apply in 3D, so the IC region is not restricted to lie above the SFAF phase, but can spill into the neighboring regions of the $(J_1,J_2,J_\square)$ space. From the mean-field arguments, the IC region is given by the locus of the IC minima $J(\pm\mathbf{q}^{a/s})$ defined in the previous Section. So the IC phase, instead of being locked between the special planes FP′ and $J_2=0$ as shown in Fig. 6a and 6b, respectively, can spread up to the locus boundaries shown by the crosses. From the equivalence between the zero-temperature d-dimensional IMTF (quantum Ising) and the $(d+1)$-dimensional classical Ising model, we infer that the ground-state phase diagram of the former on the plane $(\Omega/J,J_\#)$ should have the same structure as the described above $(T,J_\#)$ diagram of the latter. So we expect the transverse field to generate the IC ground-state phase not only in the SFAF region of the Ising coupling space, but also in the neighboring parts of the F, AF, and SAF regions. From minimization arguments the latter are restricted by the dashed lines on the plane diagram in Fig. 4 and by the crosses in Fig. 6.

From analogies with the ANNNI model, we rather expect this "IC region" to be filled with infinitely many commensurate phases with different p,[10,11] but detailed analysis of this question, as well as the full *finite-temperature* phase diagram of the transverse model (9), need a separate study.

In the rest of the paper we will be particularly interested in the SAF region of the coupling space, and restrict ourselves to the couplings

$$J_\square^2<4J_1J_2,\quad (J_1,J_2)>0. \tag{11}$$

According to Fig. 4, it means that we choose the couplings to lie above the hyperbola $y=1/4x$. The first condition in (11) ensures that the couplings lie in the region where $\mathbf{q}_{1,2}^{\mathrm{SAF}}=(0,\pi)/(\pi,0)$ provide a global minimum of model's spectrum, so the phase with the IC solutions $\mathbf{q}^{a/s}$ does not intervene. The second in the above conditions stipulates that even if $J_\square=0$ we stay away from the planes where our model becomes the triangular Ising. A transverse field can generate exotic temperature phases in that model. Such phases have been found[4,5] in the particular case of the isotropic (antiferromagnetic) transverse triangular Ising model.[4)]

From mapping between the quantum and classical Ising models we conclude that at zero temperature our IMTF with the couplings satisfying (11) possesses a single QCP which separates the SAF and PM ground-state phases. The mean field predicts a two-phase PM/SAF diagram. The critical temperature T_c of the second-order PM–SAF phase transition evolves smoothly from the QCP $T_c(J/\Omega_{\mathrm{cr}})=0$ to the asymptotic limit $T_c(\infty)$ of the classical model (see dashed curve in Fig. 8, where $g\equiv(J_1+J_2)/\Omega$). It is also known that the mean field gives a qualitatively correct phase diagram for the IMTF when $d\geqslant2$.[3] Thus we argue that the mean-field result shown by the dashed curve in Fig. 8 *does* represent the phase diagram of the IMTF (1), (9), (11), while its quantitative aspects, e.g., the exact value of the QCP, should be corrected via more accurate treatments.

III. COUPLED SPIN-PSEUDOSPIN MODEL

Now we turn to the analysis of the IMTF (1), (9) coupled to the quantum spins (**S**) residing on the same sites of the lattice as the Ising spins do. The latter we will call pseudospins from now on. Such coupled spin-pseudospin (or spin-orbital) models emerge in various contexts, most notably the Jahn–Teller transition-metal compounds[19] or many kinds of low-dimensional quantum magnets. For a recent short overview and more references, see Ref. 6.

Models of the type we study in the present work appear in analysis of the quarter-filled ladder compound $\mathrm{NaV_2O_5}$. The Hamiltonian of this material can be mapped onto a spin-pseudospin model with spins and pseudospins residing on the same rung of a ladder.[20–22] The ladders form a 2D lattice. The long-range pseudospin order $\langle T_i^x\rangle\neq0$ represents physically the charge disproportionation between left/right sites on a rung below T_c.

This system was analyzed on the effective triangular lattice shown by solid lines in Fig. 7a.[20,22] However, in the case of $\mathrm{NaV_2O_5}$ the Ising couplings generated by Coulomb repulsion are antiferromagnetic and $J_1>J_\square$. Since the triangular Ising model with one strong side is disordered,[17] one needs an extra coupling (J_2-diagonal) to stabilize the observed SAF long-range order. In our earlier study[6] we took J_1 into account explicitly, while the other diagonal J_2 was effectively generated via the spin-pseudospin coupling.[5)]

In this work we take into account the Ising couplings $J_\square,J_1,J_2$ between neighboring sites of the effective lattice, as shown in Fig. 7a. Then such effective lattice can be mapped onto the square lattice shown in Fig. 7b with the NN and NNN Ising couplings. For $\mathrm{NaV_2O_5}$ all $J_\#>0$, so the model is frustrated. As follows from the geometry of the

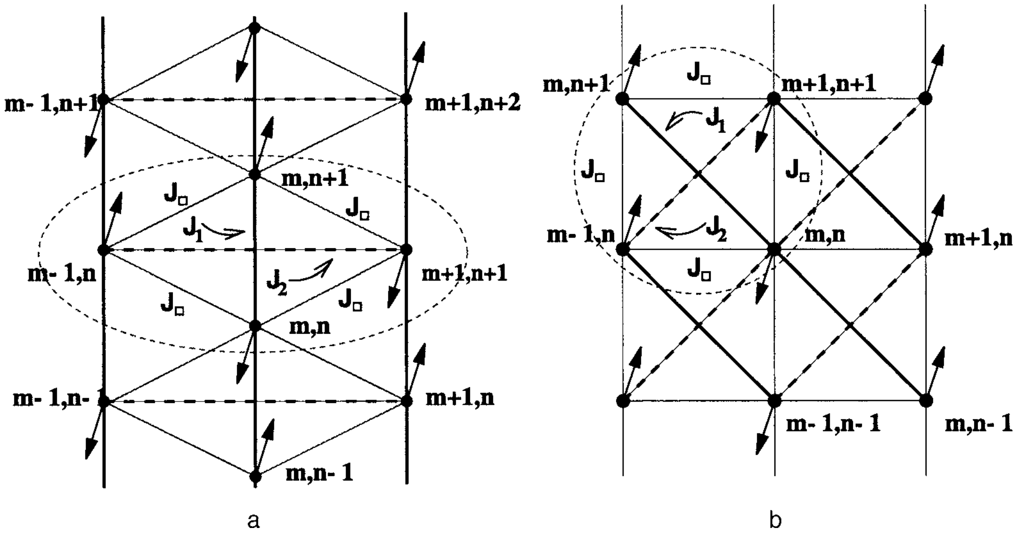

FIG. 7. 2D effective lattice of coupled ladders. A vertical line and a represent dot a single ladder and its rung where pseudospin $\mathcal{T}_{mn}$ and spin $\mathbf{S}_{mn}$ (not shown) reside. In the region encircled by the dashed line the Ising couplings between pseudospins are indicated. Two pseudospins from the $(m-1)$-th and $(m+1)$-th ladders are coupled not only by J_2 (bold dashed line) but also via the dimerization constant ε. The $\mathcal{T}^x_{mn}$-ordering pattern shown corresponds to the SAF phase (a). The same after mapping on a square lattice (b).

original NaV$_2$O$_5$ lattice, J_2 is the weak diagonal and J_1 is the largest coupling:

$$J_2 < J_\square < J_1 . \tag{12}$$

We assume $J_\square$ to be small enough not only to lie beneath the frustration plane (2), but to satisfy a more stringent condition (11). Then according to the above analysis, the IMTF with these couplings has a two-phase (PE-SAF) diagram with a QCP.[6)] In the literature on NaV$_2$O$_5$ its charge order is called the "zig-zag phase," what characterizes the antiferroelectric order in a single ladder only. In fact, the two-dimensional long-range charge order in NaV$_2$O$_5$ is SAF. For a detailed explanation of this point, including interpretation of the experimental crystallographic data on the charge order[23] in terms of the Ising pseudospins; see Ref. 24.

In the following we will work with dimensionless quantities: Hamiltonians $\mathcal{H}=H/\Omega$, temperature $T\to T/\Omega$, and Ising couplings $g_\# \equiv J_\# /\Omega$. With the site labeling shown in Fig. 7, the IMTF Hamiltonian is:

$$\mathcal{H}_{\mathrm{IMTF}} = \sum_{m,n} \Bigg\{ -\mathcal{T}^z_{mm} + \frac{1}{2}\big[g_\square (\mathcal{T}^x_{mn}\mathcal{T}^x_{m+1,n+1} + \mathcal{T}^x_{mn} x \mathcal{T}^x_{m+1,n}) + g_1 \mathcal{T}^x_{mn}\mathcal{T}^x_{m,n+1} + g_2 \mathcal{T}^x_{mn}\mathcal{T}^x_{m+2,n+1}\big] \Bigg\} . \tag{13}$$

For the decoupled spin sector of the total Hamiltonian we take into account only the strongest coupling between spins on the NN rungs of a ladder. In terms of the effective lattice (cf. Fig. 7) this translates into a set of decoupled Heisenberg chains with the usual antiferromagnetic spin exchange J. These parallel chains are oriented along the J_1-diagonals.

As we infer from our previous work on a simpler version of the IMTF Hamiltonian,[6] there are two spin-pseudospin interaction terms resulting in two qualitatively distinct aspects of model's criticality: the inter-ladder spin-pseudospin interaction $\propto \varepsilon$, and the in-ladder spin-pseudospin interaction $\propto \lambda$. The former, in terms of the equivalent square lattice, linear over difference of the charge displacement operators $\mathcal{T}^x$ on the NNN sites along the weak J_2 diagonal, is responsible for the simultaneous appearance of the SAF order and the spin gap, as well as for the destruction of the IMTF QCP.[7)] The latter, quadratic in the NNN charge operators along the J_1-diagonal, is responsible for the re-entrance. With all these terms the total effective Hamiltonian reads

$$\mathcal{H} = \mathcal{H}_{\mathrm{IMTF}} + \sum_{m,n} \mathbf{S}_{mn}\mathbf{S}_{m,n+1}\big[J + \lambda \mathcal{T}^z_{m,n}\mathcal{T}^z_{m,n+1} + \varepsilon (\mathcal{T}^x_{m+1,n+1} - \mathcal{T}^x_{m-1,n}) \big] . \tag{14}$$

The dimensionless couplings J,λ,ε in the Hamiltonian (14) are positive, and the spin operators satisfy the same algebra (10) as the pseudospins (while S and $\mathcal{T}$ commute). The sums above run through $1 \leqslant m \leqslant \mathcal{M}$ and $1 \leqslant n \leqslant \mathcal{N}$. For brevity we will use the notation $D_{mn} \equiv \mathbf{S}_{mn}\cdot \mathbf{S}_{m,n+1}$. In this study we consider the model with the XY spin sector:

$$D_{mn} = S^x_{mn} S^x_{m,n+1} S^y_{mn} S^y_{m,n+1} . \tag{15}$$

The range of couplings under consideration will be restricted to

$$(J,\lambda) \lesssim g_1 , \quad \varepsilon \lesssim \max J,\lambda . \tag{16}$$

Spin-SAF phase transition

We treat the Hamiltonian (14) following conventional wisdom of molecular-field approximations (MFA).[26] In the present version of MFA the pseudospins are decoupled and averaged with the density matrix $\rho^{\mathcal{T}} \propto \exp(-\beta \mathbf{h}_{mn}\cdot \mathcal{T}_{mn})$, where $\mathbf{h}_{mn}$ is the Weiss (molecular) field, while the spin sector is treated exactly via a Jordan-Wigner transformation.

The details are presented in Ref. 6. Similar to the pure IMTF with couplings (11) we assume the possibility of the SAF order in the coupled model (14). So we take the following ansätze for the Ising pseudospin averages (i.e., the charge ordering parameters in terms of the real physical quantities)

$$\langle \mathcal{T}^z_{mn} \rangle = m_z, \tag{17}$$

$$\langle \mathcal{T}^x_{mn} \rangle = (-1)^{m+n} m_x. \tag{18}$$

It is easy to see from the Hamiltonian (14) that ansatz (18) creates a dimerization in the spin sector, therefore a natural assumption for the dimerization operator average is

$$\langle D_{mn} \rangle = -[t + (-1)^{m+n}\delta]. \tag{19}$$

With the new coupling

$$g \equiv g_1 + g_2 \tag{20}$$

the molecular-field equations and results derived in Ref. 6 for the case $g_2 = g_\square = 0$ (i.e., $g = g_1$) can be applied here. Some of them we reproduce in this paper in order to make it more self-contained, and for the use in what follows as well.

The average quantities are determined by the system of four coupled equations

$$m_z = \frac{1}{2}\,\frac{1 + 2\lambda t m_z}{\mathfrak{n}} \tanh \frac{\beta \mathfrak{n}}{2}, \tag{21a}$$

$$m_x = \frac{m_x}{2}\,\frac{g + 2\varepsilon\eta}{\mathfrak{n}} \tanh \frac{\beta \mathfrak{n}}{2}, \tag{21b}$$

$$t = \frac{1}{\pi}\int_0^{\pi/2} d\varphi \frac{\cos^2\varphi}{\xi(\varphi)} \tanh \tilde{\beta}\xi(\varphi) \equiv \frac{1}{\pi} t_n(\Delta, \tilde{\beta}), \tag{21c}$$

$$\eta = \frac{\Delta}{\pi m_x}\int_0^{\pi/2} d\varphi \frac{\sin^2\varphi}{\xi(\varphi)} \tanh \tilde{\beta}\xi(\varphi) \equiv \frac{\Delta}{\pi m_x} \eta_n(\Delta, \tilde{\beta}), \tag{21d}$$

where $\eta = \sqrt{h_x^2 + h_z^2}$ is the absolute value of the Ising molecular field

$$h_z = 1 + 2\lambda t m_z, \tag{22a}$$

$$h_x = g m_x + 2\varepsilon\delta. \tag{22b}$$

The other auxiliary parameters are defined as follows:

$$\delta \equiv m_x \eta, \tag{23a}$$

$$\xi(\varphi) \equiv \sqrt{\cos^2\varphi + \Delta^2 \sin^2\varphi}, \tag{23b}$$

$$\Delta \equiv \frac{2\varepsilon m_x}{J + \lambda m_z^2}, \tag{23c}$$

$$\tilde{\beta} \equiv \frac{\beta}{2}(J + \lambda m_z^2). \tag{23d}$$

At some critical temperature T_c the coupled model undergoes a phase transition. It is a second-order transition, with the thermodynamic behavior of the physical quantities predicted by the Landau theory of phase transitions.[6] With the spin-pseudospin (-charge) coupling ε present, the SAF charge order $m_x \neq 0$ and the spin gap $\Delta_{\mathrm{SG}} = 2\varepsilon m_x$ appear simultaneously below T_c. By analogy with the spin-Peierls transition, when the Peierls phonon instability (freezing) creates the spin gap, it is natural to call this type of transition the *spin-super-antiferroelectric* (*spin-SAF*) transition.

It is worth noting an important property of the Hamiltonian (14): in the other domains of Ising couplings (not considered in our analysis of the coupled model) where the Ising sector of (14) can order into, e.g., FM, AF, or SFAF phase, the dimerization (gap) in the spin sector does not occur.

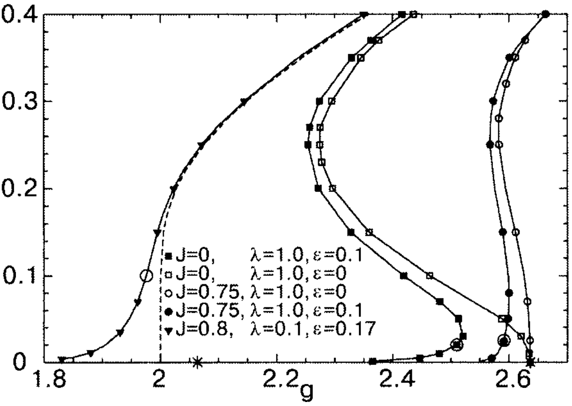

FIG. 8. Critical temperature of the PE-SAF phase transition as a function of the Ising coupling g at different values of J, λ, ε from the numerical solution of Eqs. (21). The dashed line corresponds to the pure IMTF ($J = \lambda = \varepsilon = 0$). Two stars on the abscissa show the positions of critical couplings $g_\lambda = 2.0627$ (2.6366) for $\lambda = 0.1$ (1.0), respectively. The large unfilled circles on the curves with $\varepsilon \neq 0$ indicate the right boundary of the exponential BCS regime (25). At large values of g (not shown) all curves $T_c(g)$ approach the asymptotic line $T_c = g/4$.

The behavior of $T_c(g)$ in the coupled model (14) shows two striking new features in comparison to the pure IMTF: re-entrance and destruction of the QCP.[6] In the absence of the spin-charge coupling ε, the model (14) has a QCP at

$$g_\lambda \equiv 2\left(1 + \frac{\lambda}{\pi}\right), \tag{24}$$

where T_c vanishes (see Fig. 8). λ renormalizes the QCP in comparison with the pure IMTF value $g = 2$. The coupling ε responsible for the spin gap generation also destroys the QCP, resulting in the exponential behavior of T_c in the region $g \leqslant g_\lambda$, where the model would have been disordered at any temperature if $\varepsilon = 0$. This constitutes an important feedback from the spins on the charge degrees of freedom, allowing the very possibility of the model to order at all. Approximate analytical solutions for $T_c(g)$ in the regime of strong Ising couplings and the BCS regime are:[6]

$$T_c \approx \begin{cases} \dfrac{g}{4}, \quad g \gg g_\lambda, \\[2ex] \dfrac{\mathbb{A}\tilde{J}}{2} \exp\left[-\dfrac{\pi \tilde{J}}{4\varepsilon^2}(g_\lambda - g)\right], \quad \text{BCS regime,} \end{cases} \tag{25}$$

where $\mathbb{A} \equiv 8/[\pi \exp(1-\gamma)] \approx 1.6685$, $\gamma \approx 0.5772$ is Euler's constant, and

$$\tilde{J} \equiv J + \frac{\lambda}{4}. \tag{26}$$

The boundary where the low-temperature BCS regime sets in and the related formulas are applicable, is given approximately by the condition:

$$\text{BCS regime:} \quad g < g_\lambda + \frac{4\varepsilon^2}{\pi \tilde{J}}. \tag{27}$$

The BCS regime has many analogies with the standard theory of superconductivity, apart from the exponential dependence of T_c on couplings. In particular, several physical quantities (order parameter, BCS ratio, specific heat jump) manifest certain "universal" behavior near T_c, similar to that known from the BCS theory.[6]

Another peculiarity of $T_c(g)$ found earlier[6] from the numerical solution of Eqs. (21) is re-entrance in the intermediate regimeg $g\sim g_\lambda$. The re-entrance occurs in the coupled model with the QCP ($\varepsilon=0$), while when $\varepsilon\neq 0$ the critical temperature can even manifest a double re-entrant behavior before it reaches the BCS regime (see Fig. 8). A detailed analysis of the coupled model in the regime of re-entrance was not done previously. We will address this in the next subsection, mainly analytically, in order to get more insight on the underlying physics and, in particular, to establish conditions when the re-entrance can occur.

Re-entrance

Let us first reproduce some earlier formulas[6] for the reader's convenience. At $T\leqslant T_c$ one equation from the pair (21a,b) can be written in the form

$$m_z^{-1}=g+\frac{4\varepsilon^2}{\pi(J+\lambda m_z^2)}\eta_n-\frac{2\lambda}{\pi}t_n,\quad T\leqslant T_c. \tag{28}$$

At $T=T_c$ we have Eqs. (21a) as

$$m_z=\frac{1}{2}\tanh\frac{\beta_c}{2}\left(1+\frac{2\lambda m_z}{\pi}t_n\right), \tag{29}$$

and parameters t_n, η_n are given by Eqs. (21c,d) with $\Delta=0$. The latter two functions have the following expansions:[6]

$$t_n(0,x)\approx\begin{cases}\dfrac{\pi}{4}x\left(1-\dfrac{1}{4}x^2\right)+\mathcal{O}(x^5), & x<1,\\[2ex] 1-\dfrac{\pi^2}{24}\dfrac{1}{x^2}+\mathcal{O}(1/x^4), & x>1,\end{cases} \tag{30}$$

and

$$\eta_n(0,x)\approx\begin{cases}\dfrac{\pi}{4}x\left(1-\dfrac{1}{12}x^2\right)+\mathcal{O}(x^5), & x<1,\\[2ex] \ln\mathbb{A}x+\dfrac{\pi^2}{48}\dfrac{1}{x^2}+\mathcal{O}(1/x^4), & x>1.\end{cases} \tag{31}$$

Case $\varepsilon=0$; re-entrance with QCP

As one can easily see from Eqs. (28), (29) there is no re-entrance when $\lambda=0$. This is a well-known fact for the pure IMTF, both on the mean-field level and beyond the MFA.[3,26] To study the re-entrance analytically and in particular, to establish whether there is some minimal value of λ when it appears, we should distinguish between two asymptotic regimes of the mean-field equations. Let us first consider the regime (it can occur only if $\tilde{J}<1$) when ($T_c\equiv 1/\beta_c$)

$$\frac{1}{2}\tilde{J}<T_c<\frac{1}{2}. \tag{32}$$

(In all regimes of couplings the re-entrance occurs at $T_c<1/2$.) By carrying out the leading-term expansions of the functions in Eqs. (28), (29) we obtain

$$g=2+4\exp(-1/T_c)+\frac{\lambda\tilde{J}}{4T_c} \tag{33}$$

for a single-valued function $g(T_c)$. The nonmonotonic (i.e., re-entrant) behavior of $T_c(g)$ is related to the existence of an extremum of $g(T_c)$. The coupling $g_{\min}$ which defines the minimal value of g for the order in m_x to be possible (in the pure IMTF with $\lambda=0$ this was the QCP) and which at the same time is the left border of the re-entrant region

$$g_{\min}<g<g_\lambda, \tag{34}$$

is defined from the minimum of the function $g(T_c)$ (33). This point corresponds to the critical temperature

$$T_*=\ln^{-1}\kappa_{\mathrm{o}},\quad \kappa_{\mathrm{o}}\equiv\frac{16}{\lambda\tilde{J}} \tag{35}$$

for which

$$g_{\min}\approx 2+\frac{4}{\kappa_{\mathrm{o}}}(1+\ln\kappa_{\mathrm{o}}). \tag{36}$$

The consistency of the solution (35) with (32) implies the condition

$$2<\ln\kappa_{\mathrm{o}}<\frac{2}{\tilde{J}}. \tag{37}$$

The other regime corresponds to the case when

$$T_c<\min\{1/2,\tilde{J}/2\}. \tag{38}$$

Proceeding in the same way as above, we obtain for $g(T_c)$ in this case:

$$g=g_\lambda+4\exp(-g_\lambda/2T_c)-\frac{\lambda\pi}{3\tilde{J}^2}T_c^2. \tag{39}$$

Let us point out that the conditions (32), (38) determine two different regimes ($x<1$ or $x>1$) of the asymptotics (30), (31) which we apply to obtain $g(T_c)$ as (33) or (39). So if $\tilde{J}<1$ there are regions of T_c where condition (32) is satisfied, then the approximation (33) applies. However, at sufficiently low temperatures ($T_c<\tilde{J}/2$) we inevitably enter the other regime (38) where the asymptotics (30), (31) change ($x<1\mapsto x>1$), and the function $g(T_c)$ crosses over from (33) to (39). If, on the contrary, $\tilde{J}$ is large, then condition (32) never applies, and the approximation (39) describes the whole region $T_c<1/2$.

Extrema T_* of the function $g(T_c)$ (39) are determined by the transcendental equation

$$\exp(-g_\lambda/2T_*)=\frac{\lambda\pi}{3g_\lambda\tilde{J}^2}T_*^3. \tag{40}$$

This equation always has a trivial solution $T_*'=0$ corresponding to the (local) maximum of $g(T_c)$. This is the QCP, and the curve $T_c(g)$ approaches the QCP normally to the abscissa (see Fig. 8). Two nontrivial solutions of (40) exist if the couplings satisfy the condition

$$\tilde{J} > \mathbb{C}_1 \lambda^{1/2} g_\lambda , \tag{41}$$

where

$$\mathbb{C}_1 \equiv \sqrt{\frac{\pi}{24}\left(\frac{e}{3}\right)^3} \approx 0.3121. \tag{42}$$

There is only one solution within the validity region of the approximation (39), and it corresponds to the minimum of $g(T_c)$. If the couplings satisfy (41) then

$$u \equiv \ln 3 + \frac{1}{3} \ln a_{\text{o}} > 1, \tag{43}$$

$$a_{\text{o}} \equiv \frac{24\tilde{J}^2}{\pi \lambda g_\lambda^2},$$

and the minimum can be found analytically as

$$T_* \approx \frac{g_\lambda}{6}\left(\frac{1}{u} - \frac{\ln u}{u^2}\right). \tag{44}$$

For the left border of the re-entrant region we obtain

$$g_{\min} = g_\lambda - \frac{\lambda \pi}{3\tilde{J}^2} T_*^2 + \frac{4\lambda\pi}{3 g_\lambda \tilde{J}^2} T_*^3. \tag{45}$$

The above equations agree well with the numerical solutions of the MFA (21) at different values of couplings (from comparison of the asymptotics (33), (39) and the numerical curves at various couplings and temperatures we found the deviations $\sim 5\%$ at most). More importantly, the analytical results of this subsection allows us to understand in detail the interplay of the scales provided by a model's couplings and the temperature, resulting in the re-entrance. Let us explain this on the example of two characteristic numerical curves shown in Fig. 8.

The curve shown for $J=0$, $\lambda=1$, $\varepsilon=0$ ($\tilde{J}=0.25$) corresponds to the case of small $\tilde{J}$. At $T_c \gtrsim \tilde{J}/2 = 0.125$ it is well described by the equations for the regime (32). Its re-entrant behavior and, in particular, the minimum $g_{\min}$ is due to the last term on the right-hand side of (33). At lower temperatures $T_c \lesssim 0.125$ the asymptotics (33) is not applicable, the curve is described by (39). Note that since $\mathbb{C}_1 \lambda^{1/2} g_\lambda \approx 0.8229$, the condition (41) for the minimum is broken, and the asymptotics (39) describes the featureless low-temperature evolution of this curve towards the maximum at the QCP.

The second curve in Fig. 8 with $J=0.75$, $\lambda=1$, $\varepsilon=0$ ($\tilde{J}=1$) corresponds to the case of large $\tilde{J}$. The whole re-entrant region ($T_c<0.4$), including the position of the minimum $g_{\min}$ ($\mathbb{C}_1 \lambda^{1/2} g_\lambda \approx 0.8229$) is described by the interplay of the last two terms on the right-hand side of Eq. (39). Comparison of Eqs. (36), (45) also allows one to understand the more pronounced re-entrant behavior for the case of smaller J.

As we see from our analysis of Eqs. (33), (39) in the both regimes (32), (38), the re-entrant behavior on the phase diagram occurs at any $\lambda \neq 0$.

Case $\varepsilon \neq 0$; double re-entrance, no QCP

The absence of re-entrance at $\lambda=0$ can be proven rigorously. Indeed, combining Eqs. (28) and (29), we obtain the equation

$$m_z^{-1} = g + \frac{4\varepsilon^2}{\pi J} \eta_n\left(0, \frac{J}{2} \ln \frac{1+2m_z}{1-2m_z}\right) \tag{46}$$

which has one and only one solution $m_z \in [0,1/2]$ for a given value of g. This solution in its turn provides a unique value of T_c via Eq. (29), and thus no re-entrance.

At $\lambda \neq 0$ continuous evolution of $T_c(g)$ between the regime of strong Ising coupling and the BCS regime [cf. Eq. (25)] can occur either with a double re-entrance [i.e., with one minimum and one maximum of $g(T_c)$] within the re-entrant region

$$g_{\min} < g < g_{\max} , \tag{47}$$

or without re-entrance. In the latter case the function $T_c(g)$ [or $g(T_c)$] has only an inflexion point (see Fig. (8)).

Following the analysis given in the previous subsection, we obtain for the case of small $\tilde{J}$ in the regime (32)

$$g = 2 + 4\exp(-1/T_c) + \frac{\lambda \tilde{J} - 2\varepsilon^2}{4T_c}. \tag{48}$$

Again, the re-entrant behavior is conditional on the existence of a minimum of $g(T_c)$. It exists if, at least,

$$\varepsilon < \frac{1}{\sqrt{2}} \sqrt{\lambda \tilde{J}} \approx 0.7071 \sqrt{\lambda \tilde{J}}. \tag{49}$$

The unique minimum of $g(T_c)$ (48) defines the left border of the re-entrance region $g_{\min}$ and corresponds to the critical temperature T_* given by Eqs. (35), (36) with $\kappa_0 \mapsto \kappa$, and

$$\kappa \equiv \frac{16}{\lambda \tilde{J} - 2\varepsilon^2}. \tag{50}$$

The consistency imposes a constraint analogous to (37), more stringent than the "minimal requirement" (49).

The other regime (38) is described by the approximation

$$g = g_\lambda + 4\exp(-g_\lambda/2T_c) - \frac{\pi T_c^2}{3\tilde{J}^3}(\lambda \tilde{J} + \varepsilon^2) - \frac{4\varepsilon^2}{\pi \tilde{J}} \ln \frac{\mathbb{A}\tilde{J}}{2T_c}. \tag{51}$$

As we have explained in the previous subsection for the case $\varepsilon=0$, the asymptotics (48) is applicable only for small $\tilde{J}$ at the intermediate temperatures (32), while (51) can be applied at arbitrary low temperatures, including the BCS region. The latter, given by the exponential dependence in (25), can be recovered if we retain only the first and last (leading) terms on the right-hand side of Eq. (51).

In the regime (38) the re-entrance occurs if the equation for extrema of (51)

$$\exp(-g_\lambda/2T_*) = \frac{\pi T_*}{3 g_\lambda \tilde{J}^3}\left[(\lambda \tilde{J} + \varepsilon^2) T_*^2 - \frac{6\varepsilon^2 \tilde{J}^2}{\pi^2}\right] \tag{52}$$

has nontrivial solutions. Note in making comparison of Eq. (52) to its counterpart (40) at $\varepsilon=0$, that coupling ε destroys the QCP,[6] as is immediately seen from (51). So the trivial solution $T_*=0$ of Eq. (52) corresponds to the unphysical singularity of g. As follows from (52), (38), nontrivial solutions are possible if, at least,

$$\varepsilon<\frac{\pi}{2\sqrt{6}}\frac{1}{\sqrt{1-\pi^2/24}}\sqrt{\lambda\tilde{J}}\approx0.8357\sqrt{\lambda\tilde{J}}. \tag{53}$$

If this condition is satisfied, the transcendental equation (52) has at least one solution, corresponding to maximum of $g(T_c)$. To leading order in ε, it occurs at the temperature

$$T'_*\approx\frac{\sqrt{6}}{\pi}\left(\frac{\tilde{J}}{\lambda}\right)^{1/2}\varepsilon \tag{54}$$

and the coupling

$$g_{\max}\approx g_\lambda-\frac{4\varepsilon^2}{\pi\tilde{J}}\ln\frac{\mathbb{A}\pi\sqrt{\lambda\tilde{J}}}{2\sqrt{6}\varepsilon}. \tag{55}$$

If the couplings meet both the conditions (41) and

$$\varepsilon<\mathbb{C}_2 g_\lambda\left(\frac{\lambda}{\tilde{J}}\right)^{1/2}, \tag{56}$$

where

$$\mathbb{C}_2\equiv\frac{\pi}{2}\sqrt{\frac{47-13\sqrt{13}}{36}}\approx0.0936, \tag{57}$$

then a second solution of (52) (T''_*), corresponding to minimum of $g(T_c)$, exists. This minimum, located between

$$T'_*<T''_*<\frac{g_\lambda}{6} \tag{58}$$

is given approximately by Eq. (44), where u in (43) is modified by $a_0\mapsto a$, and

$$a\equiv\frac{24\tilde{J}^3}{\pi g_\lambda^2(\lambda\tilde{J}+\varepsilon^2)}. \tag{59}$$

For validity of expansion (44) we assume $u>1$.

The analytical results of this subsection allows us to describe the behavior of the coupled model at $\varepsilon\neq0$, following from the MFA equations (21), both qualitatively and quantitatively. Two counterparts ($\varepsilon=0.1$) of the numerical curves discussed in the previous subsection are shown in Fig. 8. For this case of small ε, re-entrance is possible, according to conditions (49), (53). The re-entrant behavior at the temperatures $T_c\gtrsim T'_*$ is not modified essentially by the presence of new coupling ε as compared to the case $\varepsilon=0$, and is in fact controlled by couplings J,λ,g. Since we have already discussed it in detail for the case $\varepsilon=0$, we will not dwell on it any more. In the low-temperature regime (51) coupling ε changes drastically the behavior of $g(T_c)$ at $T_c\lesssim T'_*$, creating a maximum at $g(T'_*)$ described well by the approximation (54) and turning $g(T_c)$ away from the QCP towards the BCS region. For the BCS regime Eq. (25) provides a virtually exact solution.

As follows from the inequalities (49), (53), (56) an increase of ε can suppress the re-entrance even at $\lambda\neq0$. The necessary conditions (49), (53) for extrema of the two asymptotics (48), (51) are close, albeit with a rather small mismatch of the coefficient. Conditions for re-entrance are more stringent, since they require the consistency between the solutions for extrema and the validity ranges of the appropriate asymptotics. The (overestimated) critical value $\varepsilon_0\sim0.7\sqrt{\lambda\tilde{J}}$ gives a good simple estimate for the boundary where the re-entrance disappears from the whole curve $g(T_c)$, whether $\tilde{J}>1$ or $\tilde{J}<1$. An example of the curve $T_c(g)$ without re-entrance is shown in Fig. 8.

To summarize our analysis of the re-entrance for the cases $\varepsilon=0$ and $\varepsilon\neq0$: it reveals the robustness of this phenomenon in the coupled model (14) and its underlying mechanism, namely, competition between different scales defined by the couplings J,λ,ε,g and the temperature. These competing scales (interactions) are not related to the Ising frustration which is present in the model as well $[(J_\square,J_1,J_2)>0]$, since the latter is not accounted for explicitly by our mean-field equations. This competing mechanism for the re-entrance appears to be robust and not being an artifact of the MFA. Re-entrant phases due to competing interactions are known also, e.g., from exact solution of the Ising model on the Union Jack lattice,[27] or from analyses of decorated Ising models.[28]

It is not clear for us at the moment how the proposed re-entrance can be observed. NaV_2O_5 is, up-to-date, the only known compound with the spin-SAF transition and does not show re-entrance. This is in agreement with our estimates for the parameters for the effective Hamiltonian for this compound. They give its g located on the disordered side of the (destroyed) QCP, and the re-entrance on the whole curve $T_c(g)$ would be only very weak (i.e., localized near $g\sim g_\lambda$), if any. It appears experimentally that, e.g., external pressure cannot modify the in-plane parameters of NaV_2O_5 strongly enough, such that re-entrance would be generated. The variations of the interlayer couplings under pressure, on the other hand, generate various types of order (including devil's staircase) with regard to the plane stacking, while the in-plane SAF order remains unaffected.[24,29]

IV. SUMMARY AND DISCUSSION

We study the 2D Ising model on a square lattice with nearest-neighbor ($J_\square$) and unequal next-nearest neighbor ($J_{1,2}$) interactions. The cases of classical and quantum models are considered.

We find the ground-state phase diagram of the classical Ising model at arbitrary $J_\square,J_1,J_2$. Along with the three ordered phases—ferromagnetic, antiferromagnetic, and SAF—known for $J_1=J_2$,[8] in a more general case $J_1\neq J_2$ there is a region of the coupling space with the super-ferro-antiferromagnetic (or 4×4) ground-state phase and an incommensurate phase at finite temperature, not reported before. The three phases—SAF, SFAF, IC—can occur only in the presence of competing interactions (frustrations) on the Ising model's plaquette.

A particularly interesting conclusion from the analysis of the quantum model's phase boundaries is that transverse field

Ω can stabilize the IC ground-state phase [located for $\Omega = 0$ in the region with sign $(J_1/J_2) = -1$] in some parts of the AF and SAF regions of the coupling space where $(J_1, J_2) > 0$ but $J_1 \neq J_2$. These regions, along with vicinities of the special planes of degeneracy (triangulation and frustration) in coupling space, are good candidates for the quantum model to demonstrate a very nontrivial critical behavior. Leaving this for a future work, we hope that our findings will inspire additional interest in this model. Taking into account only one simple example of a mapping shown in Fig. 7, it is clear the model with $J_1 \neq J_2$ is not so exotic.

We analyze the IMTF coupled to the XY spin chains in the restricted (SAF) region of $(J_\Box, J_1, J_2)$ where the IMTF has a simple two-phase (disordered-SAF) diagram with a QCP, similar to that of the transverse NN model. Our interest in this model is motivated by the problem of the phase transition in the quarter-filled ladder compound NaV_2O_5. The predictions of the mean-field equations for the critical properties of the coupled spin-pseudospin model do not differ essentially from our earlier results for a simpler Hamiltonian.[6] Due to the spin-pseudospin coupling ε, the QCP of the NN and NNN IMTF is destroyed, and in the whole SAF region (11) of Ising couplings the spin-pseudospin model undergoes the spin-SAF transition. We should point out, that albeit the exponential BCS regime (25) on the disordered side of the IMTF QCP $g < g_\lambda$ formally extends up to $g = 0$, decreasing g, i.e., $J_1 + J_2$, will eventually remove us from the coupling region (11) where the SAF pseudospin solution of the MFA equations is applicable.

We perform a detailed analytical study of re-entrance in the coupled model. In particular, we establish the conditions when it can occur. The analytical results not only agree well with the direct numerical calculations in various regimes, but allows us to understand the physical mechanism of re-entrance due to interplay of competing interactions in the coupled model.

In this work we gain more insights on the transition in the spin-pseudospin model, and we can sharpen our previous statements concerning the applications to NaV_2O_5.[6] The present analysis of Ising sector allows us to identify the 2D long-range charge order in that compound as the SAF phase. As follows from known results on the ordering of the frustrated 2D Ising model into the SAF phase,[1] the spin-SAF transition has non-universal coupling-dependent critical indices. Experiments indicate rather wide regions of the two-dimensional structural (charge-ordering) fluctuations characterized by the critical index $\beta \approx 0.17-0.19$,[30–32] close to $\beta = 1/8$ of the 2D Ising model. Due to known difficulties in extracting critical indices from experimental data, it seems problematic to diagnose the deviations from universality caused by $0 < J_\Box / J_1 < 1$. (Note that in the limit $J_\Box$ the PM-SAF transition enters into the 2D Ising universality class, and for NaV_2O_5, due to its geometry, the ratio $J_\Box / J_1$ should be small.)

On the theoretical side, the critical indices of the PM-SAF transition as functions of couplings in the NN and NNN Ising model have been calculated by various methods only at $J_1 = J_2$.[1] The critical exponents are unknown for the case $J_1 \neq J_2$, and it appears to be an interesting problem to study.

Another very interesting issue we addressed recently in a separate study,[24] is the 3D nature of the transition in NaV_2O_5. According to the correlation lengths measurements,[30] upon approaching $T_c = 34$ K the 2D crossover of the pretransitional structural fluctuations occurs somewhere at $T \sim 50$ K. The model considered in the present work deals with a single plane, leaving aside the question of charge ordering along the third (stacking) direction. The phase transition in NaV_2O_5 quadruples the unit cell in the stacking direction, and the recent x-ray experiments, carried out deep in the ordered phase[23,33] revealed peculiar stacking ordering patterns of the super-antiferroelectrically charge-ordered planes. In addition, the pressure can change these patterns and even generate a multitude of higher-order commensurate superstructures in the stacking direction (devil's staircase).[29] To explain these phenomena we proposed a 3D extension of the Ising sector with additional competing couplings between the nearest and next-nearest planes.[24] In the limit $J_\Box$ the Ising sector reduces to two identical interpenetrating decoupled 3D ANNNI models. Although inclusion of the competing interlayer couplings accommodates the explanation for the observed stacking charge order in the framework of the spin-SAF (in-plane) mechanism of the transition in NaV_2O_5, a deeper understanding of the critical properties of a very complicated model with the 3D Ising sector warrants further study.

We are grateful to D. I. Khomskii, E. Orignac, and P. N. Timonin for helpful discussions. This work is supported by the German Science Foundation. G.Y.C. also acknowledges support from a LURF grant.

---

[*] E-mail: gchitov@laurentian.ca

1) We use the term "frustration" in a broad sense,[1] meaning only that there is no spin arrangement on an elementary plaquette which can satisfy all bonds.

2) The well-studied ANNNI phase diagram with the FM and antiphase ground states[1,10,11] is an analog of the lower part of the fourth quadrant (FM-SFAF) of our diagram in Fig. 2.

3) According to this notation, the antiphase of the 2D ANNNI model is (1×4). For the same reasons we give for our case, the floating phase of that model exists only within the antiphase ground-state region.

4) By analogy with the triangular Ising case of Refs. 4 and 5, we expect the transverse field to bring about new exotic phases near the frustration planes FP, FP$'$, where the ground state of our model is also infinitely degenerate.

5) A linear coupling $\propto \varphi(\mathcal{T}_1 \mp \mathcal{T}_2)$ with some Gaussian mode φ results in an effective anti-/ferrro-magnetic interaction between $\mathcal{T}_1$ and $\mathcal{T}_2$. Such terms can create or renormalize the couplings of the Ising effective Hamiltonian. In his context the Ising model with two NNN couplings of different signs is less academic than it might appear.

6) Since in applications to NaV_2O_5 the Ising pseudospins T represent charge displacements, the appropriate names for the phases are "paraelectric" (PE) and "super-antiferrolelectric." We keep the same abbreviation SAF for the latter.

7) This type of coupling is allowed by the symmetry of the original NaV_2O_5 lattice.[6] Numerical estimates of ε from a microscopic Hamiltonian are given in Ref. 25. Note also that ε effectively couples the spin chains.

---

[1] R. Liebmann, *Statistical Mechanics of Periodic Frustrated Ising Systems*, Springer, Berlin (1986).

[2] S. Sachdev, *Quantum Phase Transitions*, Cambridge University Press, Cambridge (1999).

[3] B. K. Chakrabarti, A. Dutta, and P. Sen, *Quantum Ising Phases and Transitions in Transverse Ising Models*, Springer, Berlin (1996).

[4] R. Moessner and S. L. Sondhi, Phys. Rev. B **63**, 224401 (2001).

[5] M. V. Mostovoy, D. I. Khomskii, J. Knoester, and N. V. Prokof'ev, Phys. Rev. Lett. **90**, 147203 (2003).

[6] G. Y. Chitov and C. Gros, Phys. Rev. B **69**, 104423 (2004).

[7] P. Lemmens, G. Güntherodt, and C. Gros, Phys. Rept. **375**, 1 (2003).

[8] C. Fan and F. Y. Wu, Phys. Rev. **179**, 560 (1969).

[9] Such a state, with the name of (4×4) superstructure, was described before, e.g., by D. P. Landau and K. Binder, Phys. Rev. B **31**, 5946 (1985). It can also occur in the 2D Ising model when, along with NN and NNN, the third-neighbor interactions are included.

[10] P. Bak, Rep. Prog. Phys. **45**, 587 (1982).

[11] W. Selke, Phys. Rep. **170**, 213 (1988).

[12] S. Krinsky and D. Mukamel, Phys. Rev. B **16**, 2313 (1977).

[13] E. Domany, M. Schick, J. S. Walker, and R. B. Griffiths, Phys. Rev. B **18**, 2209 (1978).

[14] G. H. Wannier, Phys. Rev. **79**, 357 (1950); Errata: Phys. Rev. B **7**, 5017 (1973).

[15] R. M. F. Houtappel, Physica (Amsterdam) **16**, 425 (1950).

[16] J. Stephenson, J. Math. Phys. **11**, 413 (1970).

[17] J. Stephenson, J. Math. Phys. **11**, 420 (1970).

[18] S. N. Coppersmith, D. S. Fisher, B. I. Halperin, P. A. Lee, and W. F. Brinkman, Phys. Rev. B **25**, 349 (1982); Phys. Rev. Lett. **46**, 549 (1981); Erratum: Phys. Rev. Lett. **46**, 869 (1981).

[19] K. I. Kugel and D. I. Khomskii, Usp. Fiz. Nauk **136**, 621 (1982) [Sov. Phys. Usp. **25**, 231 (1982)].

[20] M. V. Mostovoy and D. I. Khomskii, Solid State Commun. **113**, 159 (1999).

[21] D. Sa and C. Gros, Eur. Phys. J. B **18**, 421 (2000).

[22] M. V. Mostovoy, D. I. Khomskii, and J. Knoester, Phys. Rev. B **65**, 064412 (2002).

[23] S. Grenier, A. Toader, J. E. Lorenzo, Y. Joly, B. Grenier, S. Ravy, L. P. Regnault, H. Renevier, J. Y. Henry, J. Jegoudez, and A. Revcolevschi, Phys. Rev. B **65**, 180101(R) (2002).

[24] G. Y. Chitov and C. Gros, J. Phys.: Condens. Matter **16**, L415 (2004).

[25] C. Gros and G. Y. Chitov, Europhys. Lett. **69**, 447 (2005).

[26] R. Blinc and B. Žekž, *Soft Modes in Ferroelectrics and Antiferroelectrics*, North-Holland, Amsterdam (1974).

[27] V. G. Vaks, A. I. Larkin, and Y. N. Ovchinnikov, Zh. Éksp. Teor. Fiz. **49**, 1180 (1965) [Sov. Phys. JETP **22**, 820 (1966)].

[28] E. H. Fradkin and T. P. Eggarter, Phys. Rev. A **14**, 495 (1976).

[29] K. Ohwada, Y. Fujii, N. Takesue, M. Isobe, Y. Ueda, H. Nakao, Y. Wakabayashi, Y. Murakami, K. Ito, Y. Amemiya, H. Fujihisa, K. Aoki, T. Shobu, Y. Noda, and N. Ikeda, Phys. Rev. Lett. **87**, 086402 (2001).

[30] S. Ravy, J. Jegoudez, and A. Revcolevschi, Phys. Rev. B **59**, 681 (1999).

[31] B. D. Gaulin, M. D. Lumsden, R. K. Kremer, M. A. Lumsden, and H. Dabkowska, Phys. Rev. Lett. **84**, 3446 (2000).

[32] Y. Fagot-Revurat, M. Mehring, and R. K. Kremer, Phys. Rev. Lett. **84**, 4176 (2000).

[33] S. van Smaalen, P. Daniels, L. Palatinus, and R. K. Kremer, Phys. Rev. B **65**, 060101 (2002).

This article was published in English in the original Russian journal. Reproduced here with stylistic changes by AIP.

LOW TEMPERATURE PHYSICS VOLUME 31, NUMBERS 8–9 AUGUST–SEPTEMBER 2005

Frustrated vortex in a two-dimensional antiferromagnet

M. M. Bogdan*

B. Verkin Institute for Low Temperature Physics and Engineering, National Academy of Sciences of Ukraine, pr. Lenina 47, Kharkov 61103, Ukraine

(Submitted April 6, 2005)
Fiz. Nizk. Temp. **31**, 968–973 (August–September 2005)

The interaction of a magnetic vortex with the frustration created by a magnetic defect is investigated in a discrete Heisenberg model of a two-dimensional antiferromagnet with easy-plane anisotropic exchange. Numerical solutions are obtained for the static Landau-Lifshitz equations describing the spin distribution in a system with magnetic frustration and a vortex. It is found that the energy of the magnet is minimum in the case when the center of the vortex coincides with the position of the magnetic impurity. It is shown that as a result of the attraction between the vortex and frustration, a two-dimensional solitonic bound state localized at the magnetic defect—a frustrated vortex—arises in the magnet. The energy of such a vortex is lower than that of the free vortex, and this effect can be manifested in features of the behavior of the EPR linewidth in two-dimensional magnets. © *2005 American Institute of Physics.* [DOI: 10.1063/1.2008133]

I. INTRODUCTION

The class of quasi-two-dimensional antiferromagnets comprising metalorganic compounds can evidently be supplemented by high-T_c superconductors in the magnetically ordered phase.[1] The CuO_2 planes in high-T_c superconducting compounds such as $YBa_2Cu_3O_{6+x}$ and $La_{2-x}Sr_xCuO_{4-y}$ are two-dimensional Heisenberg layers of antiferromagnetically coupled copper spins with a value close to 1/2.[2] The superexchange J between Cu^{2+} ions takes place through the oxygen ions O^{2-}. These almost isotropic two-dimensional layers are coupled by a weak exchange $J_\perp \ll J$ of the same order as the easy-plane magnetic anisotropy.[3] It is known[4] that the electronic state of the CuO_2 planes and, hence, the character of the magnetic exchange between Cu^{2+} ions depend substantially on the oxygen content in high-T_c superconductors. In particular, it has been established for lanthanum and yttrium superconductors that variation of the oxygen concentration leads to the formation of "holes" in the CuO_2 plane. These "holes" are charge carriers in the superconducting phase,[5] and in the opinion of Aharony and co-authors,[2] their localization at the oxygen in the magnetic phase leads to a change in character of the superexchange between the Cu^{2+} ions, from antiferromagnetic with $J \approx 1000$ K to ferromagnetic with $J' \approx -3000$ K.[3] The resulting frustration[6] destroys the long-range magnetic order.

The quantum description of these phenomena is a very laborious task,[7] and for that reason the analytical approach usually turns to the framework of classical Heisenberg models.[8] In the Heisenberg XYZ model the magnetic interactions in the copper planes in $YBa_2Cu_3O_{6+x}$ are described by a Hamiltonian of the form

$$H_0 = J \sum_{\mathbf{r},\mathbf{a}} [S^x_{\mathbf{r}} S^x_{\mathbf{r}+\mathbf{a}} + \eta S^y_{\mathbf{r}} S^y_{\mathbf{r}+\mathbf{a}} + \lambda S^z_{\mathbf{r}} S^z_{\mathbf{r}+\mathbf{a}}], \tag{1}$$

on a square lattice, where $\mathbf{S}_\mathbf{r}$ is the classical spin, the summation is over lattice sites and nearest neighbors, the constant $\lambda < 1$ corresponds to easy-plane anisotropy, and the constant η is introduced to take into account a weak anisotropy in the plane: $1-\eta \ll 1-\lambda \ll 1$. It will be understood that the results obtained below are applicable primarily to yttrium compounds, for which $\lambda \approx 0.99$, whereas for lanthanum compounds it is important to take the Dzyaloshinski–Moriya interaction into account as well. For yttrium compounds, since the spins of two nearest-neighbor copper planes interact antiferromagnetically with an exchange $J_\perp$, we shall assume when studying the static configurations that the nearest spins in different planes are pairwise antiparallel.

The static spin distributions are solutions of the following Landau-Lifshitz equations:

$$\mathbf{S}_\mathbf{r} \times \mathbf{F}_\mathbf{r} = 0, \quad \mathbf{F}_\mathbf{r} = -\frac{\delta H}{\delta \mathbf{S}_\mathbf{r}}, \tag{2}$$

where $\mathbf{F}_\mathbf{r}$ is the effective field at site $\mathbf{r}$, and H is the Hamiltonian of the magnetic system. In the presence of a bond defect (the exchange constant between two spins has a different sign from the interaction in the host matrix), as a result of frustration, the ground state can be nonuniform (in the XY model this is a threshold effect in the parameter J'/J).[7] Such a state, with a nonuniform distribution of the antiferromagnetic vector field localized near the defect is called a Villain ground state.[6] On the other hand, such a localized spin structure can also be interpreted naturally as a two-dimensional magnetic soliton localized at the defect. Therefore, the term magnetic frustration has come to denote a solitonic spin distribution arising near an effective frustrated bond.[2] Such frustrations can influence the magnetic characteristics of high-T_c superconducting (HTSC) compounds, in particular, the temperature of the Néel phase transition in $YBa_2Cu_3O_{6+x}$ (Ref. 9), and can contribute to the susceptibility of the crystals. Direct experimental measurement of the susceptibility of the CuO_2 planes is difficult because of the large values of the exchange constants J and J'. However, it has become possible to estimate the susceptibility of the

CuO_2 layers in an indirect way thanks to the discovery of a new class of HTSC compounds containing rare-earth (R) ions: $GaBa_2Cu_3O_{6+x}$, $Nd_{2-x}Ce_xCuO_4$, etc.,[10,11] in which the rare-earth ions neighbor the CuO_2 planes. A soliton approach to the treatment of questions related to the structure of magnetic frustrations in the CuO_2 layers of HTSC compounds and their rare-earth analogs in the presence of magnetic field was proposed in Refs. 12 and 13; the contribution of frustrations to the magnetic susceptibility of magnets was investigated, and the magnetic fields induced by the field of a frustration in the rare-earth ion layers were found. Since the characteristic interactions in the rare-earth layers are substantially smaller than the exchange J in the CuO_2 plane, the magnetic properties of the planes containing the Ga, Nd, etc. ions are studied by conventional techniques. Susceptibility measurements in compounds of the class R_2CuO_4 have revealed[11] weak ferromagnetism, one of the causes of which may be that frustrations having a magnetic moment are present in the CuO_2 planes. Since frustrations in the CuO_2 planes influence the magnetic ordering in the adjacent rare-earth layers,[13] one expects that frustration contributions will also be manifested in magnetic resonance experiments.

On the other hand, it is well known that magnetic vortex solitons can exist in two-dimensional isotropic and easy-plane magnets.[14,15] In the case of weak anisotropy these vortices have a structure with spin components that come out of the plane.[16] Such solitons can contribute to the EPR line broadening in quasi-two-dimensional magnets.[17,18] Their interaction with magnetic and nonmagnetic defects of substitution has become a topic of research only recently.[19–23]

In this paper we investigate the character of the interaction of a magnetic frustration and a vortex in an easy-plane antiferromagnet and predict the formation of their bound state—a *frustrated vortex*. Such nonlinear excitations can contribute to the resonance and thermodynamic characteristics of quasi-two-dimensional magnets and HTSC compounds in the magnetically ordered phase.

II. TWO-DIMENSIONAL HEISENBERG MAGNET WITH A FRUSTRATING IMPURITY

The use of a planar model for describing magnetic frustration,[2,8,12] raises the question of the correctness of replacing the almost isotropic Heisenberg Hamiltonian customarily used for HTSC compounds by the XY model. The important circumstance that calls the applicability of such an approximation into question is this: two-dimensional solitons—magnetic vortices—can exist in easy-plane magnets.[14,16] If the anisotropy is not small, then the vortex spin configuration is planar. In the almost isotropic case, which corresponds to the CuO_2 plane, the vortex configuration acquires spin components that come out of the plane. This naturally raises the questions of how the magnetic frustrations will behave in an almost isotropic Heisenberg model, and what will be the nature of the interaction of a frustration and a magnetic vortex in such a system?

To answer these questions, we formulate the following classical model describing the interaction of the spin of a hole and the spins of the copper in the CuO_2 plane (see also Ref. 7). The Hamiltonian (1) is supplemented with a term appropriate to such an interaction:

$$H=H_0+H_{\rm fr}, \quad H_{\rm fr}=\tilde{J}\mathbf{S}_h\cdot(\mathbf{S}_{\mathbf{r}_1}+\mathbf{S}_{\mathbf{r}_2}), \tag{3}$$

where $\mathbf{S}_h$ is a hole spin, and the exchange $\tilde{J}$ between the hole spin and a copper spin is assumed, for the sake of definiteness, to be antiferromagnetic, i.e., $\tilde{J}>0$. (We recall that all of the spins have been replaced by classical unit vectors, and their absolute value $S=1/2$ is subsumed in the renormalization of the exchange constants.) This model explicitly takes into account the interaction of the magnetic impurity with the spins of the host and admits a transition in terms of this parameter to the defectless case, $\tilde{J}\to 0$. We note that the static Landau-Lifshits equation for the hole spin,

$$\mathbf{S}_h\times(\mathbf{S}_{\mathbf{r}_1}+\mathbf{S}_{\mathbf{r}_2})=0 \tag{4}$$

has the obvious solution in accordance with the fact that the hole spin is antiparallel to the sum of the copper spin vectors:

$$\mathbf{S}_h=-\frac{\mathbf{S}_{\mathbf{r}_1}+\mathbf{S}_{\mathbf{r}_2}}{|\mathbf{S}_{\mathbf{r}_1}+\mathbf{S}_{\mathbf{r}_2}|}. \tag{5}$$

Therefore, in the proposed model the frustrated contribution of the hole to the interaction between the statically distributed copper spins is equal to $H_{\rm fr}=-\tilde{J}|\mathbf{S}_{\mathbf{r}_1}+\mathbf{S}_{\mathbf{r}_2}|$. We note that the effective interaction of the copper spins via the hole spins turns out to be of a ferromagnetic character independently of the initial sign of the interaction of the hole spin and copper spin (see also Ref. 2). Here we note that, unlike the models using the frustrated bond approximation,[2,8] which lead to results that are equivalent for ferro- and antiferromagnets to within a change of the signs of the exchange constants, the present model pertains specifically to antiferromagnets, since it is due to the inevitable frustrating influence of an interstitial magnetic impurity on the antiferromagnetic ordering of the host spins.

The solution (5) of equation (4) suggests a numerical algorithm that permits effective solution of the static equation (2) in the general case. An iterative method of solving the static Landau–Lifshitz equations for arbitrary values of the spins S and arbitrary interactions governing the equilibrium state of the system (in particular, spin distributions like two-dimensional magnetic frustrations and vortices) is based upon the following idea. It follows from Eq. (2) that the vector $\mathbf{S}_\mathbf{r}$ should always be parallel to the effective field $\mathbf{F}_\mathbf{r}$, and the elementary iteration step can therefore be written as

$$\mathbf{S}_\mathbf{r}^{i+1}=S\cdot\mathbf{F}_\mathbf{r}^i/F_\mathbf{r}^i, \tag{7}$$

where $F_\mathbf{r}^i$ is the length of the vector $\mathbf{F}_\mathbf{r}^i$, and the index i is the number of the iteration. If the initial spin distribution if sufficiently close in form to a magnetic frustration or vortex, then the iterative calculation converges very rapidly and leads to a stable solution of Eqs. (2).

III. INTERACTION OF A MAGNETIC FRUSTRATION AND A VORTEX IN A TWO-DIMENSIONAL ANTIFERROMAGNET

In this paper we report a numerical investigation of the equilibrium spin configurations in the framework of the discrete Heisenberg model (3) on a 41×40 spin matrix (n,m) (the lattice constant is taken equal to unity). First we obtained solutions describing magnetic frustrations; they turned

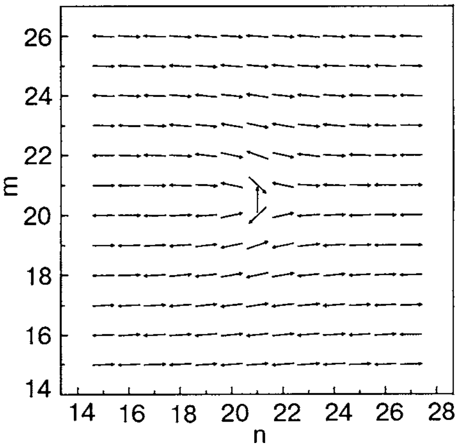

FIG. 1. A 13×12 fragment of the spin distribution at a magnetic frustration. The positions of the central spins are the sites (21,20) and (21,21), between which is located the spin of a magnetic impurity.

out to be practically the same as in the planar model,[2,8,12,13] i.e., localized in the easy plane at for arbitrarily weak anisotropy (see Fig. 1). This circumstance permits a complete justification of the use of the planar model for calculating the structure of the frustrations in the presence of magnetic field.[12,13] We note that in the purely isotropic case ($\eta=\lambda=1$), all the spins of the frustration also lie in a single plane, but there is degeneracy with respect to rotation of that plane around an arbitrary axis. In the frustration model with interaction (3) a nonuniform ground state arises at arbitrarily small values of the parameter $W=\tilde{J}/J$. For $W=0$ the energy of the uniform antiferromagnetic ground state of a 41×40 matrix of spins in units of J has the value $E_0=-3199$. The energy of the system with frustration, E_{fr}, initially falls off quadratically as a function of the parameter W but then, after $W\approx 3$, its decline becomes practically linear (Fig. 2). Thus the energy of the system with frustration is lowered by an amount $\Delta E_{\mathrm{fr}}=E_{\mathrm{fr}}-E_0$, which is naturally called the self-energy of a frustration. For example, for $W=3$ the energy $\Delta E_{\mathrm{fr}}=-2.08$.

The proposed numerical method is efficient for calculating the structure of a vortex with components that come out from the easy plane, since in that case the spin distributions in the course of the iterations converge rapidly to the stable solutions. As the initial distribution for the vortex in the calculations we used approximate analytical expressions for easy-plane vortices from Ref. 16. The numerical calculation for the energy of a free vortex (i.e., in the system without a frustrating impurity, $W=0$) for a 41×40 spin matrix gives $\Delta E_v=E_v-E_0=9.51$.

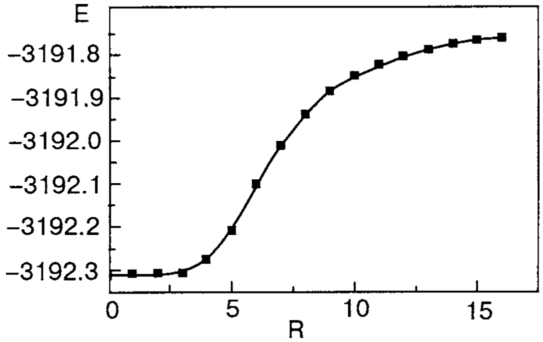

FIG. 3. Energy of an antiferromagnet containing a vortex and a frustration, measured in units of J, as a function of the distance between their centers.

The next step consists in the calculation of the interaction of a magnetic vortex and a frustration in the framework of the proposed model. For this the problem is stated for the following physical situation: a hole is introduced into a system of spins with a vortex at the center and is moved to different distances from the center of the vortex. It was assumed in the calculations that the anisotropy constants $\eta=1$ and $\lambda=0.99$, and the ratio of exchange constants $W=3$. For the stable configuration obtained, the energy of the system was found. Figure 3 shows the dependence of that energy on the distance R between the hole spin and vortex center. It is seen that the interaction is of an attractive character. It follows from an analysis of the spin distributions obtained that at large distances between the hole spin and vortex center the presence of frustration is practically unnoticeable (see Fig. 4), and outwardly the vortex differs little from the free vortex.[16] At the same time, the vortex turns out to be strongly deformed in the energetically most favorable state, when the vortex center lies on the axis between two copper spins, coinciding precisely with the position of the hole spin (Fig. 5). Such a bound state of the magnetic vortex and an impurity spin is naturally called a *frustrated vortex*. The strong frustrating influence of the magnetic impurity on the deviation of the components of the vortex from the easy plane is clearly seen in Fig. 6, which shows the modulus of the $S_{\mathbf{r}}^z$ components of the host spins.

To find the energy ΔE_{fv} of a frustrated vortex, one must subtract from the total energy $E_{fv}=-3192.31$ the energy

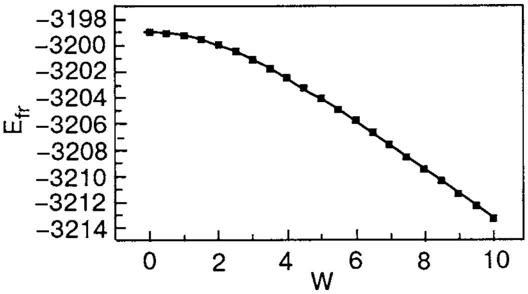

FIG. 2. Energy of an antiferromagnet with frustration E_{fr}, measured in units of J, as a function of the frustration interaction parameter W.

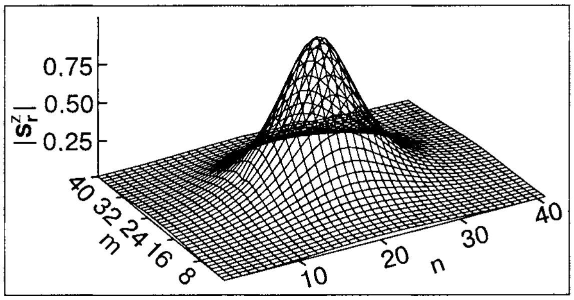

FIG. 4. Modulus of the projection $S_{\mathbf{r}}^z$ on the coordinates in an antiferromagnet containing a vortex and a magnetic frustration in the case when the impurity spin is located between sites (11,20) and (11,21).

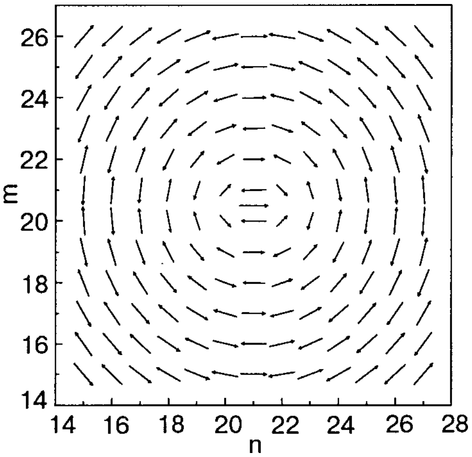

FIG. 5. A 13×12 fragment of the distribution of the projections of spins in a frustrated vortex. The arrows indicate the components of the vectors $\mathbf{S}_\mathbf{r}$ in the XY plane. The impurity spin is located in the middle between sites (21,20) and (21,21).

$E_{\rm fr} = -3201.08$ of a nonuniform ground state of the system with an isolated frustration. The energy obtained, $\Delta E_{fv} = 8.77$, is less than the energy ΔE_v of a free vortex by the amount of the binding energy, $\Delta E_b = -0.74$, which amounts to around 8% of the vortex energy. As is seen in Fig. 3, these calculations are equivalent to finding the binding energy in a frustrated vortex by subtracting from E_{fv} (the total energy at $R=0$) the energy of the system with the magnetic frustration removed to a large distance and the free vortex.

Returning to the initial physical statement of the problem, we emphasize that introducing a hole into a $\mathrm{CuO_2}$ plane containing a free vortex leads to the formation of their bound state—a frustrated vortex, and lowers the energy of the system as a whole by an amount $\Delta E = -2.82$, which consists of the energy of a frustration and the binding energy.

Thus, for given dimensions of the lattice (or density of vortices and holes) and values of the exchange interactions, a numerical estimate of the energy of a frustrated vortex shows that the decrease of the system energy due to the introduction of a hole into it and the localization of the vortex at the hole is of the order of 30% of the energy of a free vortex.

Such a decrease might be detected in EPR experiments in layered magnets—rare-earth analogs of HTSC compounds. Upon localization of the magnetic impurity at a site in a metalorganic antiferromagnet one observes temperature broadening of the EPR line. One of the possible explanations for this is that this broadening of the resonance line includes a contribution from magnetic vortices.[17] An estimate of the energy of the vortices can be obtained from the temperature dependence of the EPR linewidth.[18] In HTSC compounds EPR directly on the copper ions is not observed; this remains one of the unexplained mysteries of the physics of high-temperature superconductivity.[24,25] This may be because of the very strong broadening of the resonance line in these compounds, which may include a contribution from magnetic vortices. The resonance *is* observed in the rare-earth analogs of HTSC compounds,[11] and the contribution of frustrated vortices might be observed indirectly through the fields induced in the planes of the rare-earth ions, as in the simpler case of a replica of a magnetic frustration.[13] It should be noted, however, that for further generalization of the results to the lanthanum compounds $\mathrm{La_{2-x}Sr_xCuO_{4-y}}$ it is necessary to take the Dzyaloshinski–Moriya interaction into account in a consistent way, and also the possible motion of the holes, which requires consideration of more-complex spin Hamiltonians.[26,27]

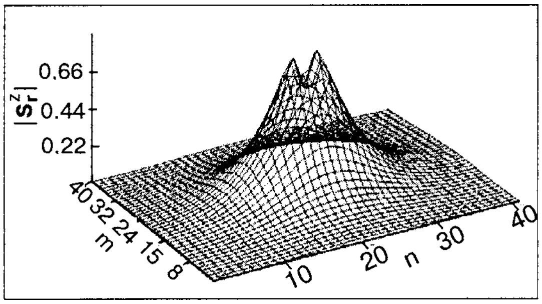

FIG. 6. Frustrated vortex with center of localization at a magnetic defect. The dependence of the modulus of the projection $S_\mathbf{r}^z$ on the coordinates is shown.

IV. CONCLUSIONS

We have formulated a discrete classical Heisenberg model of a two-dimensional antiferromagnet with easy-plane anisotropy of the exchange with an interstitial magnetic impurity. Such a model can describe the behavior of magnetic copper layers of the HTSC compound $\mathrm{YBa_2Cu_3O_{6+x}}$ with holes in the $\mathrm{CuO_2}$ planes. We have investigated the interaction of a magnetic frustration and a magnetic vortex in the framework of this model and obtained the following results.

1. We have proposed an efficient algorithm for numerical solution of the static Landau–Lifshitz equations for calculation of the equilibrium stable spin configurations of magnetic systems with an arbitrary character of the spin interactions.

2. The solutions of the Landau–Lifshitz equations corresponding to magnetic frustration and a magnetic vortex with spin components coming out of the easy plane have been found numerically, and the energy characteristics of these solutions have been calculated as functions of the model parameters.

3. We have shown that the energy of a magnet containing a vortex and frustration is minimum in the case when the center of the vortex coincides with the position of the hole. As a result of the attraction between the vortex and frustration a two-dimensional bound state localized at the magnetic defect—a *frustrated vortex*—appears. The energy of such a vortex is lower than that of the free vortex.

4. This effect can be detected in EPR experiments, since an estimate of the energy of magnetic vortices can be obtained from the temperature dependence of the resonance linewidth, to which these nonlinear excitations give an exponential contribution.

Thus in two-dimensional antiferromagnetic systems with interstitial impurities (such as holes in HTSC compounds) the magnetic frustrations and vortices can form bound states having a substantial influence on the thermodynamics and resonance properties of these systems.

The author thanks N. F. Kharchenko and J. M. Tranquada for helpful discussions and advice.

[*] E-mail: bogdan@ilt.kharkov.ua

---

[1] L. J. de Jongh and A. R. Miedema, Adv. Phys. A **23**, 1 (1974).
[2] A. Aharony, R. J. Birgeneau, A. Coniglio, M. A. Kastner, and H. E. Stanley, Phys. Rev. Lett. **60**, 1330 (1988).
[3] J. M. Tranquada, A. H. Moudden, A. I. Goldman, P. Zolliker, D. E. Cox, G. Shirane, S. K. Sinha, D. Vaknin, D. C. Johnston, M. S. Alvarez, A. J. Jacobson, J. T. Lewandowski, and J. M. Newsam, Phys. Rev. B **38**, 2477 (1988).
[4] J. M. Tranquada, S. M. Heald, A. R. Moodenbaugh, and Xu Youwen, Phys. Rev. B **38**, 8893 (1988).
[5] V. J. Emery, Phys. Rev. Lett. **58**, 2794 (1987).
[6] J. Villain, J. Phys. C **10**, 4793 (1977).
[7] R. J. Gooding and A. Mailhot, Phys. Rev. B **44**, 11852 (1991).
[8] J. Vannimenus, S. Kirkpatrick, F. D. M. Haldane, and C. Jayaprakash, Phys. Rev. B **39**, 4634 (1989).
[9] M. M. Bogdan and A. S. Kovalev, Fiz. Nizk. Temp. **16**, 1576 (1990) [Sov. J. Low Temp. Phys. **16**, 887 (1990)].
[10] H. Takagi, S. Uchida, and Y. Tokura, Phys. Rev. Lett. **62**, 1197 (1989).
[11] R. D. Zysler, M. Tovar, C. Rettori, D. Rao, H. Shore, S. B. Oseroff, D. C. Vier, S. Schultz, Z. Fisk, and S-W. Cheong, Phys. Rev. B **44**, 9467 (1991).
[12] M. M. Bogdan, A. S. Kovalev, and A. A. Stepanov, Fiz. Nizk. Temp. **18**, 838 (1992) [Low Temp. Phys. **18**, 591 (1992)].
[13] A. S. Kovalev and M. M. Bogdan, Fiz. Tverd. Tela (St. Petersburg) **35**, 1773 (1993) [Phys. Solid State **35**, 886 (1993)].
[14] A. M. Kosevich, B. A. Ivanov, and A. S. Kovalev, *Nonlinear Waves of Magnetization. Dynamical and Topological Solitons* [in Russian], Naukova Dumka, Kiev (1983).
[15] A. A. Belavin and A. M. Polyakov, JETP Lett. **22**, 245 (1975).
[16] M. E. Gouvea, G. M. Wysin, A. R. Bishop, and F. G. Mertens, Phys. Rev. B **39**, 11840 (1989).
[17] F. Waldner, J. Magn. Magn. Mater. **31–34**, 1203 (1983).
[18] F. Waldner, J. Magn. Magn. Mater. **54–57**, 873 (1986).
[19] C. E. Zaspel, T. E. Grigereit, and J. E. Drumheller, Phys. Rev. Lett. **74**, 4539 (1995).
[20] C. E. Zaspel, C. M. McKennan, and S. R. Snaric, Phys. Rev. B **53**, 11317 (1996).
[21] K. Subbaraman, C. E. Zaspel, and J. E. Drumheller, J. Appl. Phys. **79**, 101 (1996).
[22] K. Subbaraman, C. E. Zaspel, and J. E. Drumheller, Phys. Rev. Lett. **80**, 2201 (1998).
[23] M. M. Bogdan and C. E. Zaspel, Phys. Status Solidi **189**, 983 (2002).
[24] F. Mehran and P. W. Anderson, Solid State Commun. **71**, 29 (1989).
[25] P. Simon, J. M. Bassat, Y. Henrion, B. Rives, J. P. Loup, P. Odier, and S. B. Oseroff, Physica C **235–240**, 1647 (1994).
[26] R. J. Gooding, N. M. Salem, R. J. Birgeneau, and F. C. Chou, Phys. Rev. B **55**, 6360 (1997).
[27] R. J. Gooding and A. Mailhot, Phys. Rev. B **48**, 6132 (1993).

Translated by Steve Torstveit

LOW TEMPERATURE PHYSICS VOLUME 31, NUMBERS 8–9 AUGUST–SEPTEMBER 2005

Fermionic versus bosonic descriptions of one-dimensional spin-gapped antiferromagnets

S. Yamamoto* and K. Funase

Division of Physics, Hokkaido University, Sapporo 060-0810, Japan

(Submitted January 31, 2005)
Fiz. Nizk. Temp. **31**, 974–983 (August–September 2005)

In terms of spinless fermions and spin waves, we describe the magnetic properties of a spin-1/2 ferromagnetic-antiferromagnetic bond-alternating chain which behaves as a Haldane-gap antiferromagnet. On the one hand, we employ the Jordan–Wigner transformation and treat the fermionic Hamiltonian within the Hartree–Fock approximation. On the other hand, we employ the Holstein–Primakoff transformation and modify the conventional spin-wave theory so as to restore the sublattice symmetry. We calculate the excitation gap, the specific heat, the magnetic susceptibility, magnetization curves, and the nuclear spin-lattice relaxation rate with varying bond alternation. These schemes are further applied to a bond-alternating tetramerized chain which behaves as a ferrimagnet. The fermionic language is particularly stressed as a useful tool for investigating one-dimensional spin-gapped antiferromagnets, while the bosonic one works better for ferrimagnets. © *2005 American Institute of Physics.*
[DOI: 10.1063/1.2008134]

I. INTRODUCTION

Haldane[1,2] sparked renewed interest in one-dimensional Heisenberg antiferromagnets, predicting that their low-energy structures should vary qualitatively depending on whether the constituent spins are integral or fractional. A magnetic excitation gap immediately above the ground state, which is referred to as the Haldane gap, was indeed observed in quasi-one-dimensional spin-1 Heisenberg antiferromagnets such as $\mathrm{CsNiCl_3}$ (Ref. 3) and $\mathrm{Ni(C_2H_8N_2)_2NO_2(ClO_4)}$ (Refs. 4, 5). A rigorous example of such a massive phase was also given theoretically.[6,7] Significant numerical efforts[8–12] were dovoted to detecting the Haldane gap in the higher-spin systems. Competition between massive and massless phases in low-dimensional quantum magnets was extensively studied especially by the nonlinear-sigma-model quantum field theory,[13–23] and a wide variety of spin gaps-energy gaps in magnetic excitation spectra-were further predicted. There followed stimulative findings, including quantized plateaux in zero-temperature magnetization curves,[24–26] gap formation in coupled spin chains[27,28] and the dramatic crossover from one- to two-dimensional quantum antiferromagnets,[29] and an antiferromagnetic excitation gap with a ferromagnetic background.[30–33]

Besides the sigma-model study, analytic approaches played a crucial role in revealing the nature of Haldane-gap antiferromagnets. The valence-bond-solid model[13,14] stimulated considerable interest in matrix-product representation[34–40] of the Haldane phase. The Lieb–Schultz–Mattis theorem[41] was generalized[24] to clarify a mechanism for gap formation in a magnetic field. However, these arguments were essentially restricted to the ground-state behavior and can hardly be extended to finite-temperature properties. Numerical tools such as quantum Monte Carlo and density-matrix renormalization-group techniques are indeed useful for such a purpose, but an analytic strategy is still indispensable to low-temperature thermodynamics especially of spin-gapped antiferromagnets, where grand canonical sampling is hardly feasible numerically. Then we are led to describe massive spin chains in terms of conventional languages such as the Jordan–Wigner fermions and the Holstein–Primakoff spin waves.

The Jordan–Wigner transformation is an efficient approach to low-dimensional quantum magnetism. Spin-1/2 arrays with uniform[42] and alternating[43–45] antiferromagnetic exchange interactions between nearest neighbors were thus investigated and their energy structures, magnetization curves, and thermodynamic properties were indeed revealed well. Two-leg antiferromagnetic spin ladders were also discussed within this scheme[46,47] and the interchain-coupling effect on the lowest-lying excitation was elucidated. More refined fermionization was further proposed for coupled spin chains. Ordering spinless fermions along a snake-like path, Dai and Su[48] succeeded in interpreting massive and massless excitations with varying number of the ladder legs. Their idea was generalized to investigate zero-temperature magnetization curves[49] and thermodynamic quantities.[50] In such circumstances, we consider fermionizing an spin-1/2 ferromagnetic-antiferromagnetic bond-alternating chain, which converges to the spin-1 antiferromagnetic Heisenberg chain as the ferromagnetic coupling tends to infinity and therefore reproduces many of observations common to Haldane-gap antiferromagnets.

Bosonic theory has significantly been developed for one-dimensional quantum magnets in recent years. While the Schwinger-boson mean-field theory is unable to distinguish fractional-spin chains from integral-spin ones, it is still useful in predicting the asymptotic dependence of the Haldane gap on spin quantum number[51] and explaining quantum phase transitions of Haldane-gap antiferromagnets in a field.[52] The Schwinger-boson representation was further applied to ferrimagnetic spin chains[53,54] and ladders.[55] It was a major breakthrough leading to the subsequent development of the spin-wave theory in low dimensions[56–62] that Takahashi[63] gave a spin-wave description of the one-dimensional ferromagnetic thermodynamics introducing an additional constraint on the number of spin waves. This modified spin-wave scheme was further applied to spin-gapped antiferromagnets[50,64,65] and qualitatively improved for one-dimensional ferrimagnets.[66,67] The antiferromagnetic modified spin-wave theory is less quantitative than the ferrimagnetic version,[54,68] but it enlighteningly interpreted novel observations such as the temperature dependence of the Haldane gap[64,65] and the field dependence of the nuclear spin-lattice relaxation rate.[69] Such spin-wave understanding is well supported by other analytic descriptions.[70–72] As for finite-temperature calculation of spin-gapped antiferromagnets, the Schwinger-boson mean-field theory is of no use, while the modified spin-wave theory maintains its validity to a certain extent.[54] Thus, we apply the modified spin-wave scheme to the spin-1/2 ferromagnetic-antiferromagnetic bond-alternating chain with particular emphasis on a comparison between fermionic and bosonic descriptions of spin-gapped antiferromagnets.

Our theoretical attempt is much motivated by existent bond-alternating chain compounds such as $\mathrm{IPACuCl_3}$ [IPA $=$isopropylammonium$=(\mathrm{CH_3})_2\mathrm{CHNH_3}$] (Ref. 73) and $(4\text{-BzpipdH})\mathrm{CuCl_3}$ [4-BzpipdH$=$4-benzylpiperidinium $=\mathrm{C_{12}H_{18}N}$] (Ref. 74).

These materials behave as spin-1 Haldane-gap antiferromagnets at low temperatures,[75–78] while such spin-1 features are broken up into paramagnetic spin 1/2′s with increasing temperature.[79–81] Besides the thermal crossover from quantum spin 1′s to classical spin 1/2′s, their enriched ground-state properties[82–86] and novel edge states[87] are of great interest to both theoreticians and experimentalists.

II. FORMALISM

We consider the ferromagnetic-antiferromagnetic bond-dimeric spin-1/2 Heisenberg chain, whose Hamiltonian is given by

$$\mathcal{H}=\sum_{n=1}^{N}\left[(J_{AF}\mathbf{S}_{2n-1}\cdot\mathbf{S}_{2n}-J_F\mathbf{S}_{2n}\cdot\mathbf{S}_{2n+1})\right.$$
$$\left.-g\mu_BH(S^z_{2n-1}+S^z_{2n})\right]. \tag{1}$$

The ground-state properties[88–91] and low-lying excitations[92] of this model were well investigated by numerical tools and variational schemes. In particular, the string order parameter originally defined for spin-1 Heisenberg chains[93] was generalized to this system[88–90] and the breakdown of a hidden $Z_2\times Z_2$ symmetry was extensively argued.[84,85] As the ferromagnetic coupling tends to infinity, the string order remains finite and the Haldane gap converges to that originating in decoupled singlet dimers.

On the other hand, the thermodynamic properties have much less been calculated so far[87,94] and there is no guiding theory for extensive experimental findings. Employing two different languages, we calculate various thermal quantities and give rigorous information on their low-temperature behavior.

A. Fermionic approach

In accordance with the bond dimerization, we introduce two kinds of spinless fermions through the Jordan-Wigner transformation

$$S^+_{2n-1}=a^\dagger_n\exp\left[i\pi\left(\sum_{m=1}^{n-1}a^\dagger_m a_m+\sum_{m=1}^{n-1}b^\dagger_m b_m\right)\right],$$
$$S^+_{2n}=b^\dagger_n\exp\left[i\pi\left(\sum_{m=1}^{n}a^\dagger_m a_m+\sum_{m=1}^{n-1}b^\dagger_m b_m\right)\right],$$
$$S^z_{2n-1}=a^\dagger_n a_n-\frac{1}{2},\quad S^z_{2n}=b^\dagger_n b_n-\frac{1}{2}. \tag{2}$$

Decomposing the fermionic Hamiltonian at the Hartree-Fock level, we obtain a mean-field Hamiltonian as

$$\mathcal{H}_{HF}=E_0+(J_{AF}-J_F)$$
$$\times\sum_{n=1}^{N}\left[\left(d_b-\frac{1}{2}\right)a^\dagger_n a_n+\left(d_a-\frac{1}{2}\right)b^\dagger_n b_n\right]$$
$$+J_{AF}\sum_{n=1}^{N}\left[\left(\frac{1}{2}-p_{AF}\right)a^\dagger_n b_n+\mathrm{H.c.}\right]$$
$$-J_F\sum_{n=1}^{N}\left[\left(\frac{1}{2}-p_F\right)b^\dagger_n a_{n+1}\mathrm{H.c.}\right]$$
$$-g\mu_BH\sum_{n=1}^{N}(a^\dagger_n a_n+b^\dagger_n b_n), \tag{3}$$

where $d_a=\langle a^\dagger_n a_n\rangle_{HF}$, $d_b=\langle b^\dagger_n b_n\rangle_{HF}$, $p_{AF}=\langle b^\dagger_n a_n\rangle_{HF}$, $p_F=\langle a^\dagger_{n+1}b_n\rangle_{HF}$, and

$$E_0=\left[J_{AF}\left(\left|p_{AF}\right|^2-d_ad_b-\frac{1}{4}\right)-J_F\left(\left|p_F\right|^2-d_ad_b+\frac{1}{4}\right)\right.$$
$$\left.+g\mu_BH\right]N, \tag{4}$$

with $\langle\ldots\rangle_{HF}$ denoting the thermal average over the Hartree-Fock eigenstates. Defining the Fourier transformation as

$$a_n=\frac{1}{\sqrt{N}}\sum_k \mathrm{e}^{ik(n-1/4)}a_k,$$
$$b_n=\frac{1}{\sqrt{N}}\sum_k \mathrm{e}^{ik(n+1/4)}b_k \tag{5}$$

and then a unitary transformation as

$$\begin{pmatrix}a_k\\ b_k\end{pmatrix}=\begin{pmatrix}u_k & v_k\mathrm{e}^{i\theta_k}\\ v_k\mathrm{e}^{-i0_k} & -u_k\end{pmatrix}\begin{pmatrix}\alpha_k\\ \beta_k\end{pmatrix}, \tag{6}$$

where

$$u_k=\sqrt{\frac{1}{2}\left(1-\frac{\eta}{\sqrt{\eta^2-|\gamma_k|^2}}\right)},$$
$$v_k=\sqrt{\frac{1}{2}\left(1+\frac{\eta}{\sqrt{\eta^2+|\gamma_k|^2}}\right)},$$

$$\gamma_k \equiv |\gamma_k| \mathrm{e}^{i\theta_k} = J_{AF}\left(\frac{1}{2} - p_{AF}\right)\mathrm{e}^{ik/2} - J_F\left(\frac{1}{2} - p_F^*\right)\mathrm{e}^{-ik/2},$$

$$\xi = \frac{1}{2}(J_{AF} - J_F)(d_a + d_b - 1),$$

$$\eta = \frac{1}{2}(J_{AF} - J_F)(d_a - d_b), \tag{7}$$

and twice the lattice constant is set equal to unity, we can diagonalize the Hamiltonian as

$$\mathcal{H}_{HF} = E_0 + \sum_k (\varepsilon_k^+ \alpha_k^\dagger \alpha_k + \varepsilon_k^- \beta_k^\dagger \beta_k), \tag{8}$$

where the dispersion relations are given by

$$\varepsilon_k^\pm = \xi \pm \sqrt{\eta^2 + |\gamma_k|^2} - g\mu_B H. \tag{9}$$

In terms of the fermion distribution functions $\bar{n}_k^\pm = [\mathrm{e}^{\varepsilon_k^\pm / k_B T} + 1]^{-1}$, the internal energy, the total magnetization, and the magnetic susceptibility are expressed as

$$E = E_0 + \sum_k \sum_{\sigma = \pm} \varepsilon_k^\sigma \bar{n}_k^\sigma, \tag{10}$$

$$M = \sum_k \sum_{\sigma = \pm} \bar{n}_k^\sigma - N, \tag{11}$$

$$\chi = \frac{(g\mu_B)^2}{k_B T} \sum_k \sum_{\sigma = \pm} \bar{n}_k^\sigma (1 - \bar{n}_k^\sigma), \tag{12}$$

respectively. Another quantity of wide interest is the nuclear spin-lattice relaxation rate $1/T_1$. Considering the electronic-nuclear energy-conservation requirement, the Raman process usually plays a leading role in the relaxation, which is formulated as

$$\frac{1}{T_1} = \frac{4\pi(g\mu_B \hbar \gamma_N)^2}{\hbar \Sigma_m \mathrm{e}^{-E_m/k_B T}} \sum_{m,m'} \mathrm{e}^{-E_m/k_B T} \left| \langle m' | \sum_n (A_n S_{2n-1}^z + B_n S_{2n}^z) | m \rangle \right|^2 \delta(E_{m'} - E_m - h\omega_N), \tag{13}$$

where A_n and B_n are the dipolar coupling constants between the nuclear and electronic spins, $\omega_N = \gamma_N H$ is the Larmor frequency of the nuclei, with γ_N being the gyromagnetic ratio, and the summation Σ_m is taken over all the electronic eigenstates m with energy E_m. Assuming the Fourier components of the coupling constants to have little momentum dependence as $\Sigma_n \exp(ikn) A_n \equiv A_k \simeq A$ and $\Sigma_n \exp(ikn) B_n \equiv B_k \simeq B$, we obtain the fermionic expression of the Raman relaxation rate as

$$\frac{1}{T_1} = \pi(g\mu_B h \gamma_N)^2 / \hbar N^2 \times \sum_{k,k'} [A^2 + B^2 + 2AB\cos(\theta_{k'} - \theta_k)] \times \sum_{\sigma = \pm} \bar{n}_k^\sigma (1 - \bar{n}_{k'}^\sigma) \delta(\varepsilon_{k'}^\sigma - \varepsilon_k^\sigma - h\omega_N). \tag{14}$$

B. Bosonic approach

Next we consider a single-component bosonic representation of each spin variable at the cost of the rotational symmetry. We start from the Holstein-Primakoff transformation

$$S_{4n-4+\tau}^+ = \sqrt{2S - a_{\tau:n}^\dagger a_{\tau:n}}\, a_{\tau:n},$$

$$S_{4n-4-\tau}^z = S - a_{\tau:n}^\dagger a_{\tau:n},$$

$$S_{4n-2+\tau}^+ = b_{\tau n}^\dagger \sqrt{2S - b_{\tau:n}^\dagger b_{\tau:n}},$$

$$S_{4n-2+\tau}^z = -S + b_{\tau:n}^\dagger b_{\tau:n}, \tag{15}$$

where $\tau = 1,2$; that is, we assume the chain to consist of four sublattices. Under the large-S treatment, the Hamiltonian can be expanded as

$$\mathcal{H} = -2(J_F + J_{AF})S^2 N + E_1 + E_0 + \mathcal{H}_1 + \mathcal{H}_0 + O(S^{-1}), \tag{16}$$

where E_i and H_i give the $O(S^i)$ quantum corrections to the ground-state energy and the dispersion relations, respectively. The naivest diagonalization of the Hamiltonian (16), whether up to $O(S^1)$ or up to $O(S^0)$, results in diverging sublattice magnetizations even at zero temperature. In order to suppress the quantum as well as thermal divergence of the number of bosons, we consider minimizing the free energy constraining the sublattice magnetizations to be zero:[56–58]

$$\sum_{n=1}^{N} \sum_{\tau=1,2} (a_{\tau:n}^\dagger a_{\tau:n} + b_{\tau:n}^\dagger b_{\tau:n}) = 4SN. \tag{17}$$

Within the conventional spin-wave theory, spins on one sublattice point predominantly up, while those on the other predominantly down. The condition (17) restores the sublattice symmetry. In order to enforce the constraint (17), we first introduce a Lagrange multiplier and diagonalize

$$\mathcal{H} = \mathcal{H} + J_{AF} \nu S \sum_{n=1}^{N} \sum_{\tau=1,2} (a_{\tau:n}^\dagger a_{\tau:n} + b_{\tau:n}^\dagger b_{\tau:n}). \tag{18}$$

We define the Fourier transformation as

$$a_{\tau:n} = \frac{1}{\sqrt{N}} \sum_k \mathrm{e}^{-ik(n - 5/8 + \tau/4)} a_{\tau:k},$$

$$b_{\tau:n} = \frac{1}{\sqrt{N}} \sum_k \mathrm{e}^{ik(n - 1/8 + \tau/4)} b_{\tau:k}, \tag{19}$$

and then the Bogoliubov transformation as

$$\begin{pmatrix} a_{1:k} \\ a_{2:k} \\ b_{1:k}^\dagger \\ b_{2:k}^\dagger \end{pmatrix} = \begin{pmatrix} \psi_{1:k}^+ & \psi_{1:k}^- & -\psi_{4:k}^{+*} & -\psi_{4:k}^{-*} \\ \psi_{2:k}^+ & \psi_{2:k}^- & -\psi_{3:k}^{+*} & -\psi_{3:k}^{-*} \\ -\psi_{3:k}^+ & -\psi_{3:k}^- & \psi_{2:k}^{+*} & \psi_{2:k}^{-*} \\ -\psi_{4:k}^+ & -\psi_{4:k}^- & \psi_{1:k}^{+*} & \psi_{1:k}^{-*} \end{pmatrix} \begin{pmatrix} \alpha_{1:k} \\ \beta_{1:k} \\ \alpha_{2:k}^\dagger \\ \beta_{2:k}^\dagger \end{pmatrix} \tag{20}$$

where four times the lattice constant is set equal to unity. We determine the coefficients $\psi_{i:k}^\pm$ so as to diagonalize $\mathcal{H}$ up to order $O(S)$ and take $\mathcal{H}_0$ into account in the calculation perturbationally.[95] Then the Hamiltonian (16) is written as

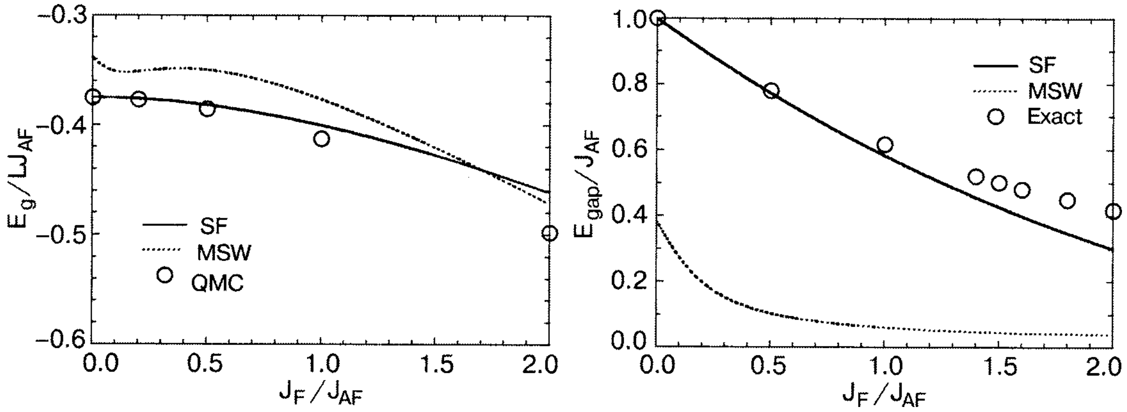

FIG. 1. The spinless-fermion (SF), modified-spin-wave (MSW), quantum Monte Carlo (QMC), and numerical-diagonalization (Exact) calculations of the ground-state energy (the left) and the excitation gap immediately above the ground state (the right) for the bond-alternating dimerized chain, where $L=2N$ is the number of spins.

$$E_1=-2J_{AF}(1+\gamma+\nu)SN+J_{AF}\sum_k\sum_{\sigma=\pm}\omega_k^\sigma,$$

$$E_0=2J_{AF}[2\Delta(\Lambda-\gamma\Gamma)-(1+\gamma)\Delta^2-\gamma\Gamma^2-\Lambda^2],$$

$$\mathcal{H}_1=J_{AF}\sum_k\sum_{\tau=1,2}(\omega_k^+\alpha_{\tau k}^\dagger\alpha_{\tau k}+\omega_k^-\beta_{\tau,k}^\dagger\beta_{\tau,k}),$$

$$\mathcal{H}_0=J_{AF}\sum_k\sum_{\tau=1,2}(\delta\omega_k^+\alpha_{\tau:k}^\dagger\alpha_{\tau:k}+\delta\omega_k^-\beta_{\tau:k}^\dagger\beta_{\tau:k})$$
$$+\mathcal{H}_{\mathrm{irrel}}+\mathcal{H}_{\mathrm{quart}}, \tag{21}$$

where $\gamma=J_F/J_{AF}$,

$$\omega_k^\sigma=S\sqrt{(1+\gamma+\nu)^2-1+\gamma^2+2\sigma\chi_k},$$

$$\delta\omega_k^\sigma=[(\Lambda-\gamma\Gamma)-(1+\gamma)\Delta)]\left(1+\frac{\sigma\gamma}{\chi_k}\right)\frac{1+\gamma+\nu}{\lambda_k^\sigma}$$
$$-\gamma(\Delta+\Gamma)\frac{\gamma+\sigma\chi_k}{\lambda_k^\sigma}+(\Delta-\Lambda)\frac{\sigma\chi_k+\gamma\sin^2\frac{k}{2}}{\sigma\chi_k\lambda_k^\sigma},$$

$$\Gamma=\frac{1}{4N}\sum_k\sum_{\sigma=\pm}\left[\left(1+\frac{\sigma\gamma}{\chi_k}\right)\frac{1+\gamma+\nu}{\lambda_k^\sigma}-1\right]$$
$$\times\frac{(1+\gamma+\nu)\sigma\chi_k\cos^2\frac{k}{2}-\gamma(\gamma+\sigma\chi_k)\lambda_k^\sigma\sin^2\frac{k}{2}}{\chi_k^2+\gamma(\gamma+2\sigma\chi_k)\sin^2\frac{k}{2}},$$

$$\Lambda=\frac{1}{4N}\sum_k\sum_{\sigma=\pm}\frac{\sigma\chi_k+\gamma\sin^2\frac{k}{2}}{\sigma\chi_k\lambda_k^\sigma},$$

$$\Delta=\frac{1}{4N}\sum_k\sum_{\sigma=\pm}\left[\left(1+\frac{\sigma\gamma}{\chi_k}\right)\frac{1+\gamma+\nu}{\lambda_k^\sigma}-1\right], \tag{22}$$

with $\lambda_k^\sigma=\omega_k^\sigma/S$ and $\chi_k=[(1+\gamma+\nu)^2-\sin^2(k/2)]^{1/2}$. $\mathcal{H}_{\mathrm{irrel}}$ and $\mathcal{H}_{\mathrm{quart}}$ in $\mathcal{H}_0$ contain off-diagonal one-body terms such as $\alpha_{\tau:k}\beta_{\tau:k}$ and residual two-body interactions, respectively, both of which are neglected in the perturbational treatment.

At finite temperatures we replace $\alpha_{\tau:k}^\dagger\alpha_{\tau:k}$ and $\beta_{\tau:k}^\dagger\beta_{\tau:k}$ by their canonical averages $\langle\alpha_{\tau:k}^\dagger\alpha_{\tau:k}\rangle\equiv\bar{n}_{\tau:k}^+$ and $\langle\beta_{\tau:k}^\dagger\beta_{\tau:k}\rangle\equiv\bar{n}_{\tau:k}^-$, respectively, which are expressed as $\bar{n}_{\tau:k}^\pm\equiv\bar{n}_k^\pm=[\mathrm{e}^{J_{AF}(\omega_k^\sigma+\delta\omega_k^\sigma)/k_BT}-1]^{-1}$. Here the Lagrange multiplier ν is determined through

$$\sum_k\sum_{\sigma=\pm}\left(1+\frac{\sigma\gamma}{\chi_k}\right)\frac{1+\gamma+\nu}{\lambda_k^\sigma}(1+2\bar{n}_k^\sigma)=2N(1+2S). \tag{23}$$

Then the internal energy and the magnetic susceptibility are given by[96]

$$E=E_g+2\sum_k\sum_{\sigma=\pm}\tilde{\omega}_k^\sigma\bar{n}_k^\sigma,$$

$$\chi=\frac{2(g\mu_B)^2}{3k_BT}\sum_k\sum_{\sigma=\pm}\bar{n}_k^\sigma(\bar{n}_k^\sigma+1), \tag{24}$$

where $E_g=-2(J_F+J_{AF})S^2N+E_1+E_0$.

III. CALCULATIONS

First we calculate the ground-state energy E_g and the lowest excitation gap E_{gap} and compare them with numerical findings in Fig. 1. The spinless fermions are much better than the modified spin waves at describing both quantities. As J_F goes to zero, the fermionic findings are refined and end up with the exact values $E_g/N=-3J_{AF}/4$ and $E_{\mathrm{gap}}=J_{AF}$. The modified spin waves considerably underestimate the spin gap. They can not distinguish massive spin chains from massless critical ones[54] to begin with, but they are still useful in qualitatively investigating dependences of the Haldane gap on temperature and spin quantum number.[65]

Secondly we calculate the thermodynamic properties. Figure 2 shows the temperature dependences of the zero-field specific heat and magnetic susceptibility. Due to the significant underestimate of the spin gap, the modified spin-wave description is much less quantitative than the fermionic one at low temperatures. Furthermore, the modified spin waves completely fail to reproduce the antiferromagnetic Schottky-type peak of the specific heat. Because of the Lagrange multiplier ν, which turns out to be a monotonically increasing function of temperature, the dispersion relations (22) lead to endlessly increasing energy and thus nonvanishing specific heat at high temperatures. The spinless fermions succeed in

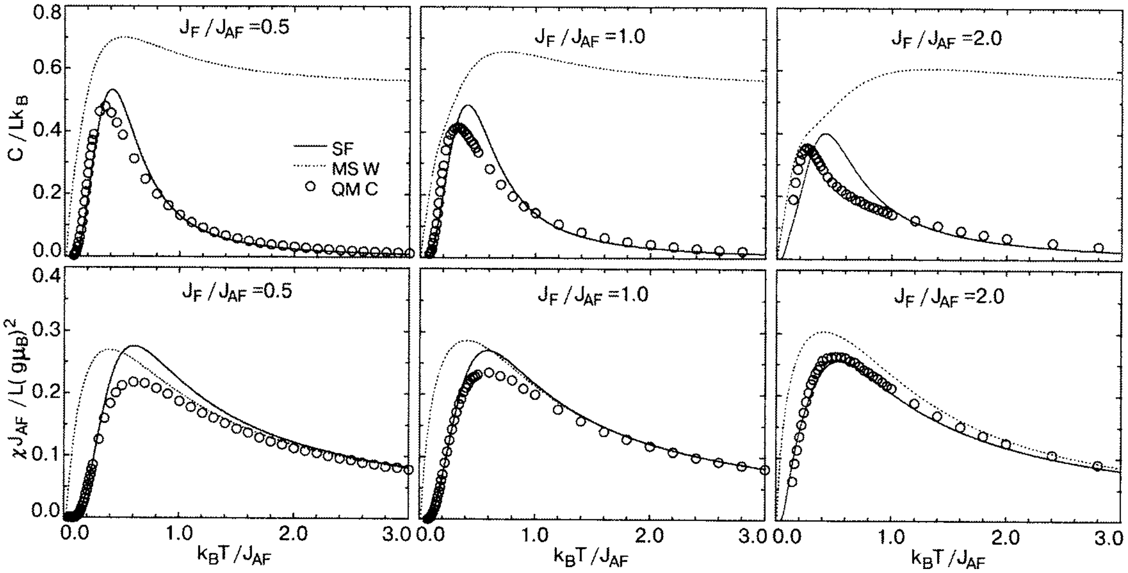

FIG. 2. The spinless-fermion (SF), modified-spin-wave (MSW), and quantum Monte Carlo (QMC) calculations of the specific heat (the upper three) and the magnetic susceptibility (the lower three) as functions of temperature for the bond-alternating dimerized chain, where $L=2N$ is the number of spins.

reproducing the overall thermal behavior. The present approaches have the advantage of giving the low-temperature behavior analytically. Equation (9) shows that the dispersion relation of the low-lying excitations reads

$$\varepsilon_k^{\pm}\simeq\pm(E_{\rm gap}+J_{AF}vk^2)-g\mu_BH, \tag{25}$$

provided $g\mu_BH<E_{\rm gap}$, where

$$E_{\rm gap}=\sqrt{J_{AF}^2\tilde{p}_{AF}^2+J_F^2\tilde{p}_F^2+2J_FJ_{AF}\tilde{p}_F\tilde{p}_{AF}},$$

$$2E_{\rm gap}v=J_F\tilde{p}_F\tilde{p}_{AF}, \tag{26}$$

with $\tilde{p}_F=\mathrm{Re}\,p_F-1/2$ and $\tilde{p}_{AF}=\mathrm{Re}\,p_{AF}-1/2$. Then the low-temperature properties are calculated as

$$\frac{C}{Nk_B}\simeq\sqrt{\frac{k_BT}{\pi vJ_{AF}}}\,\mathrm{e}^{-E_{\rm gap}/k_BT}\left[\left(\frac{E_{\rm gap}}{k_BT}\right)^2+\frac{E_{\rm gap}}{k_BT}+\frac{3}{4}\right],$$

$$\frac{\chi J_{AF}}{(g\mu_B)^2N}\simeq\sqrt{\frac{J_{AF}}{\pi vk_BT}}\,\mathrm{e}^{-E_{\rm gap}/k_BT}. \tag{27}$$

These features are found in the antiferromagnetic Heisenberg two-leg ladder as well[50,72] and can be regarded as common to spin-gapped antiferromagnets. The power-law prefactor to the activation-type temperature dependence, which can hardly be extracted from numerical findings, is essential in estimating the spin gap experimentally.

Next we consider the total magnetization as a function of an applied field and temperature. We compare the fermionic description of magnetization curves with numerical findings in Fig. 3. The spinless fermions again work very well. Quantum Monte Carlo sampling becomes less and less feasible with decreasing temperature, while we have no difficulty in calculating Eq. (11) even at zero temperature. The ground-state magnetization turns out to behave as $M\propto(H-H_c)^{1/2}$ near the critical field $g\mu_BH_c=E_{\rm gap}$ (Ref. 97). Magnetization plateaus of multi-leg spin ladders[49] and mixed spin chains[98] are also well interpreted in terms of the spinless fermions. On the contrary, in the modified spin-wave theory, the number of sublattice bosons are kept constant and therefore we have no quantitative information on the uniform magnetization as well as the staggered one. Though the Schwinger-boson mean-field theory,[51,54,99,100] which consists of a rotationally invariant bosonic representation, still works with an applied field and/or existent anisotropy[52,101,102] to a certain extent but rapidly loses its validity with increasing temperature.[54]

Thus we are fully convinced that the spinless fermions are superior to the modified spin waves in investigating quantum and thermal properties of spin-gapped antiferromagnets. Lastly in this section, we calculate the nuclear spin-

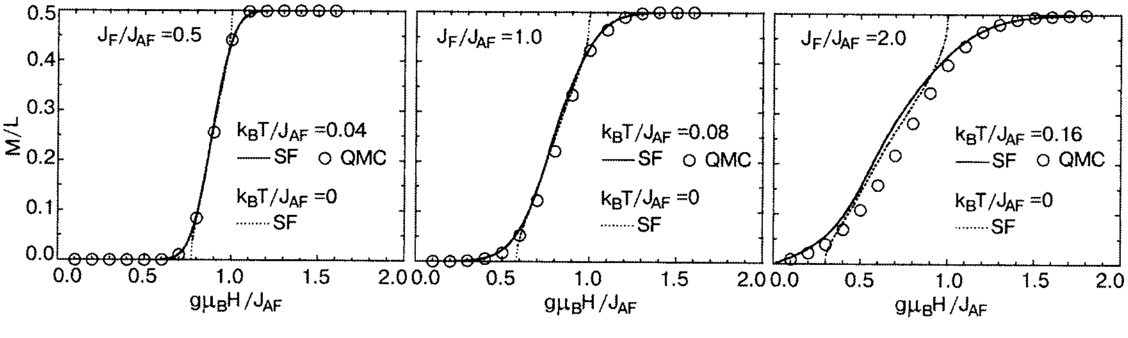

FIG. 3. The spinless-fermion and quantum Monte Carlo calculations of magnetization curves for the bond-alternating dimerized chain, where $L=2N$ is the number of spins.

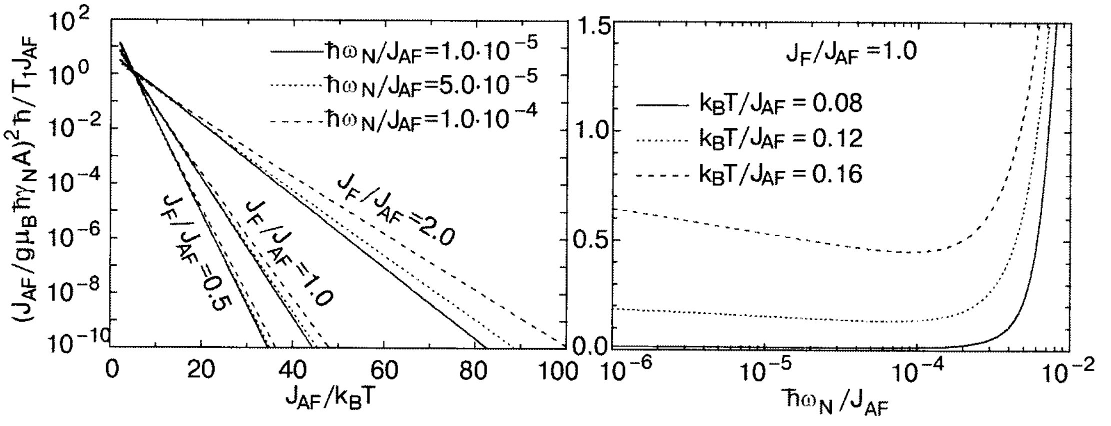

FIG. 4. The spinless-fermion calculations of the nuclear spin-lattice relaxation rate as a function of temperature (the left) and an applied magnetic field (the right) for the bond-alternating dimerized chain.

lattice relaxation rate $1/T_1$ in terms of the spinless fermions in an attempt to stimulate further experimental interest in this system. If we again employ the approximate dispersion (25) at moderate fields and temperatures, $k_BT \ll E_{\mathrm{gap}} - g\mu_B H$, Eq. (14) can be further calculated analytically as

$$\frac{1}{T_1} \simeq \frac{(g\mu_B\hbar\gamma_N)^2}{2\pi\hbar v J_{AF}}(A+B)^2 \mathrm{e}^{-E_{\mathrm{gap}}/k_BT} \times \cosh\frac{g\mu_B H}{k_BT} K_0\left(\frac{\hbar\omega_N}{2k_BT}\right), \tag{28}$$

where K_0 is the modified Bessel function of the second kind and behaves as $K_0(x) \simeq \ln 2 - \gamma - \ln x$ for $0 < x \ll 1$ with γ being Euler's constant. Considering the significant difference between the electronic and nuclear energy scales ($\hbar\omega_N \lesssim 10^{-5}$ J), there usually holds the condition $\hbar\omega_N \ll k_BT$. At low temperatures, $1/T_1$ also exhibits an increase of the activation type but with logarithmic correction, which is much weaker than the power correction in the case of the susceptibility. Such a pure spin-gap-activated temperature dependence of $1/T_1$, which is shown in Fig. 4, should indeed be observed experimentally, unless magnetic impurities mask the intrinsic properties. Equation (28) further reveals a unique field dependence of $1/T_1$: *With increasing field*, $1/T_1$ *first decreases logarithmically and then increases exponentially*, which is visualized in Fig. 4. The initial logarithmic behavior comes from the Van Hove singularity peculiar to one-dimensional energy spectra and may arise more generally from a nonlinear dispersion relation at the band bottom. Therefore, besides spin-gapped antiferromagnets, one-dimensional ferromagnets and ferrimagnets may exhibit a similar field dependence.[69,72,103,104] Relaxation-time measurements on spin-gapped chain antiferromagnets such as IPACuCl$_3$ and (4-BzpipdH)CuCl$_3$ are strongly encouraged.

IV. BOND-ALTERNATING FERRIMAGNETIC CHAIN

Before closing our comparative study, we briefly mention a bond-alternating but ferrimagnetic chain calculated within the same schemes. We take another interest in the ferromagnetic-ferromagnetic-antiferromagnetic-antiferromagnetic bond-tetrameric spin-1/2 Heisenberg chain, whose Hamiltonian is given by

$$\mathcal{H} = \sum_{n=1}^{N} [J_{AF}(\mathbf{S}_{4n-3}\cdot\mathbf{S}_{4n-2} + \mathbf{S}_{4n-2}\cdot\mathbf{S}_{4n-1}) - J_F(\mathbf{S}_{4n-1}\cdot\mathbf{S}_{4n} + \mathbf{S}_{4n}\cdot\mathbf{S}_{4n+1})]. \tag{29}$$

Cu(3$-$Clpy)$_2$(N$_3$)$_2$[3-Clpy=3-chloropyridine=C$_5$ClH$_4$N] (Ref. 105) is well described by this Hamiltonian[106] and behaves as if it is a ferrimagnet of alternating spins 3/2 and 1/2.[68] In the conventional spin-wave scheme, the spin deviations in each sublattice, $\langle a^\dagger_{\tau:n} a_{\tau:n}\rangle$ and $\langle b^\dagger_{\tau:n} b_{\tau:n}\rangle$, diverge in the antiferromagnetic ground state but stay finite in the ferrimagnetic one. Without quantum divergence of the sublattice magnetization, it is not necessary to diagonalize the effective Hamiltonian (29). In an attempt to keep the dispersion relations free from temperature, we may simply diagonalise the original Hamiltonian (18) and then introduce a Lagrange multiplier so as to minimize the free energy.[54] For ferrimagnets such an idea is much superior to the original antiferromagnetic modified spin-wave scheme.[56–58]

Figure 5 shows the thus-modified spin-wave calculations as well as the Hartree–Fock calculations in terms of the spinless fermions in comparison with numerical findings. The ferrimagnetic modified spin waves work very well, contrasting with the antiferromagnetic ones. They reproduce the Schottky-type peak of the specific heat and the ferrimagnetic minimum of the susceptibility-temperature product at intermediate temperatures. Although the modified spin-wave description of the antiferromagnetic increase of χT is somewhat moderate, it converges into the paramagnetic value $S(S+1)/3$ at high temperatures. The description is more and more refined with decreasing temperature and is expected to be accurate at sufficiently low temperatures.[67] The $T^{1/2}$ initial behavior of C and the T^{-2}-diverging behavior of χ are both correctly reproduced.[66] Besides static properties, T_1 measurements[107] on a ferrimagnetic chain compound NiCu(C$_7$H$_6$N$_2$O$_6$)(H$_2$O$_3$)$\cdot$2H$_2$O was elaborately interpreted in terms of the modified spin waves.[108]

On the other hand, the spinless fermions misread the low-temperature properties of ferrimagnetic chains. A fatally weak point of their description is the onset of a Néel-ordered state. With increasing J_F, the transition temperature T_c goes up and the applicability of the Hartree-Fock fermions is reduced. Indeed the fermionic description is not so bad away

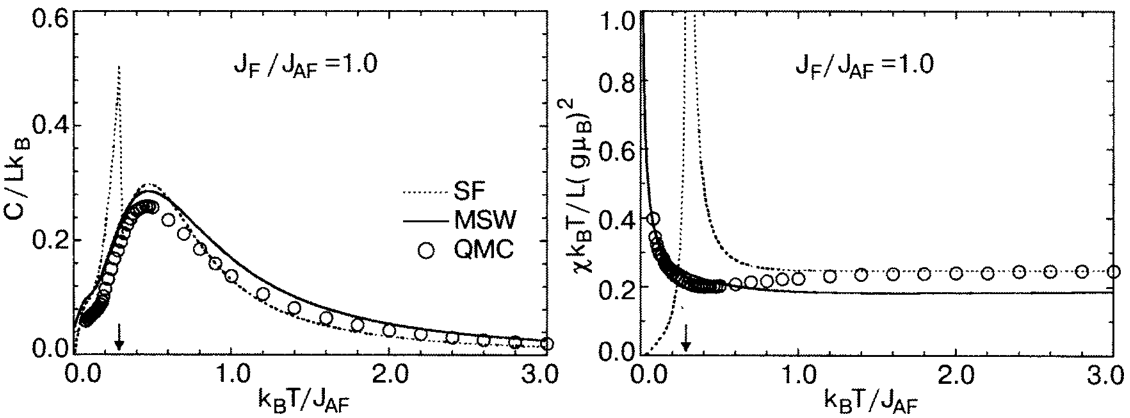

FIG. 5. The spinless-fermion, modified-spin-wave, and quantum Monte Carlo calculations of the specific heat (the left) and the magnetic susceptibility (the right) as functions of temperature for the bond-alternating tetramerized chain, where $L \equiv 4N$ is the number of spins. The Hartree-Fock fermions encounter a paramagnetic-to-Néel-ordered phase transition with decreasing temperature and the transition temperature is indicated by arrows.

upward from T_c, but it is much less complementary to numerical tools in ferrimagnetic systems.

V. SUMMARY

We have comparatively discussed fermionic and bosonic descriptions of the bond-dimeric Heisenberg chain as an example of spin-gapped antiferromagnets. The fermionic language is based on the Jordan–Wigner spinless fermions within the Hartree–Fock approximation, while the bosonic formulation consists of constraining the Holstein–Primakoff bosons to restore the sublattice symmetry. The spinless fermions well describe both ground-state and finite-temperature properties. The zero-field specific heat and magnetic susceptibility behave as

$$C \propto (k_B T)^{-3/2} \mathrm{e}^{-E_{\mathrm{gap}}/k_B T}$$

and

$$\chi \propto (k_B T)^{-1/2} \mathrm{e}^{-E_{\mathrm{gap}}/k_B T},$$

respectively, at sufficiently low temperatures, while the relaxation rate behaves as

$$1/T_1 \propto \mathrm{e}^{-E_{\mathrm{gap}}/k_B T} \cosh(g\mu_B H/k_B T)[0.80908 - \ln(\hbar \omega_N / k_B T)]$$

at moderately low temperatures and fields. On the other hand, the modified spin waves give much poorer findings. In particular, they significantly underestimate the spin gap and fail to reproduce the Schottky-type peak of the specific heat. The same schemes have further been applied to the bond-tetrameric ferrimagnetic chain, where the modified spin waves work very well and are superior to the spinless fermions both qualitatively and quantitatively. The fermionic language is useful in describing disordered ground states and their excitations, whereas the bosonic one in depicting ordered ground states and their fluctuations.

The modified spin-wave theory is fully applicable to higher-spin systems. The Jordan–Wigner transformation can also be generalized to higher-spin systems,[109] where spin-1 chains, for instance, are mapped onto an extended $t-J$ model of strongly correlated electrons. However, the *double-graded* Hubbard operators such as $\tilde{c}_{n,\uparrow} \equiv (1 - c_{n,\downarrow}^{\dagger} c_{n,\downarrow}) c_{n,\uparrow}$ demand that we should treat the fermion and boson degrees of freedom in the same footing.[99,110–112] The present naive fermionic representation is highly successful for spin-1/2 gapped antiferromagnets, including various bond-alternating and/or coupled chains. It is complementary to numerical tools especially at low temperatures and allows us to readily infer both static and dynamic properties of spin-gapped antiferromagnets.

The authors are grateful to H. Hori for valuable comments. This work was supported by the Ministry of Education, Culture, Sports, Science and Technology of Japan, and the Iketani Science and Technology Foundation.

[*] E-mail: yamamoto@mary.sci.hokudai.ac.jp

---

[1] F. D. M. Haldane, Phys. Lett. A **93**, 464 (1983).
[2] F. D. M. Haldane, Phys. Rev. Lett. **50**, 1153 (1983).
[3] W. J. L. Buyers, R. M. Morra, R. L. Armstrong, M. J. Hogan, P. Gerlach, and K. Hirakawa, Phys. Rev. Lett. **56**, 371 (1986).
[4] J. P. Renard, M. Verdaguer, L. P. Regnault, W. A. C. Erkelens, J. Rossat-Mignod, and W. G. Stirling, Europhys. Lett. **3**, 945 (1987).
[5] K. Katsumata, H. Hori, T. Takeuchi, M. Date, A. Yamagishi, and J. P. Renard, Phys. Rev. Lett. **63**, 86 (1989).
[6] T. Affleck, T. Kennedy, E. H. Lieb, and H. Tasaki, Phys. Rev. Lett. **59**, 799 (1987).
[7] T. Affleck, T. Kennedy, E. H. Lieb, and H. Tasaki, Commun. Math. Phys. **115**, 477 (1988).
[8] S. Yamamoto, Phys. Rev. Lett. **75**, 3348 (1995).
[9] U. Schollwoeck and Th. Jolicoeur, Europhys. Lett. **30**, 493 (1995).
[10] S. Yamamoto, Phys. Lett. A **213**, 102 (1996).
[11] Y.-I. Wang, S. Qin, and L. Yu, Phys. Rev. B **60**, 14529 (1999).
[12] S. Todo and K. Kato, Phys. Rev. Lett. **87**, 047203 (2001).
[13] I. Affleck, Nucl. Phys. B **257**, 397 (1985).
[14] I. Affleck, Nucl. Phys. B **265**, 409 (1986).
[15] G. Sierra, J. Phys. A: Math. Gen. **29**, 3299 (1996).
[16] G. Sierra, Phys. Rev. Lett. **77**, 3443 (1996).
[17] T. Fukui and N. Kawakami, Phys. Rev. B **55**, R14709 (1997).
[18] T. Fukui, M. Sigrist, and N. Kawakami, Phys. Rev. B **56**, 2530 (1997).
[19] T. Fukui and N. Kawakami, Phys. Rev. B **56**, 8799 (1997).
[20] T. Fukui and N. Kawakami, Phys. Rev. B **57**, 398 (1998).
[21] A. Koga, S. Kumada, N. Kawakami, and T. Fukui, J. Phys. Soc. Jpn. **67**, 622 (1998).
[22] K. Takano, Phys. Rev. Lett. **82**, 5124 (1999).
[23] K. Takano, Phys. Rev. B **61**, 8863 (2000).
[24] M. Oshikawa, M. Yamanaka, and I. Affleck, Phys. Rev. Lett. **78**, 1984 (1997).
[25] K. Totsuka, Phys. Lett. A **228**, 103 (1997).
[26] D. C. Cabra, A. Honecker, and P. Pujol, Phys. Rev. Lett. **79**, 5126 (1997).
[27] E. Dagotto, J. Riera, and D. Scalapino, Phys. Rev. B **45**, R5744 (1992).
[28] S. Gopalan, T. M. Rice, and M. Sigrist, Phys. Rev. B **49**, 8901 (1994).

[29]E. Dagotto and T. M. Rice, Science **271**, 618 (1996).
[30]A. K. Kolezhuk, H.-J. Mikeska, and S. Yamamoto, Phys. Rev. B **55**, R3336 (1997).
[31]G.-S. Tian, Phys. Rev. B **56**, 5355 (1997).
[32]S. Maslov and A. Zheldev, Phys. Rev. B **57**, 68 (1998).
[33]Y. Takushima, A. Koga, and N. Kawakami, Phys. Rev. B **61**, 15189 (2000).
[34]W.-D. Feritag and E. Möller-Hartmann, Z. Phys. B **83**, 381 (1991).
[35]A. Klömper, A. Schadschneider, and J. Zittartz, Z. Phys. B **87**, 281 (1992).
[36]A. Klömper, A. Schadschneider, and J. Zittartz, Europhys. Lett. **24**, 293 (1993).
[37]K. Totsuka and M. Suzuki, J. Phys. A: Math. Gen. **27**, 6443 (1994).
[38]K. Totsuka and M. Suzuki, J. Phys.: Condens. Matter **7**, 1639 (1995).
[39]S. Yamamoto, Phys. Lett. A **225**, 157 (1997).
[40]S. Yamamoto, Int. J. Mod. Phys. B **12**, 1795 (1998).
[41]E. H. Lieb, T. Schultz, and D. J. Mattis, Ann. Phys. (N.Y.) **16**, 407 (1961).
[42]L. N. Bulaevskii, Sov. Phys. JETP **16**, 685 (1963).
[43]L. N. Bulaevskii, Sov. Phys. JETP **17**, 684 (1963).
[44]V. M. Kontorovich and V. M. Tsukernik, Sov. Phys. JETP **26**, 687 (1968).
[45]A. A. Zvyagin, Sov. Phys. Solid State **32**, 181 (1990).
[46]M. Azzouz, Phys. Rev. B **48**, 6136 (1993).
[47]M. Azzouz, L. Chen, and S. Moukouri, Phys. Rev. B **50**, 6233 (1994).
[48]X. Dai and Z. Su, Phys. Rev. B **57**, 964 (1998).
[49]H. Hori and S. Yamamoto, J. Phys. Soc. Jpn. **71**, 1607 (2002).
[50]H. Hori and S. Yamamoto, J. Phys. Soc. Jpn. **73**, 549 (2004).
[51]D. P. Arovas and A. Auerbach, Phys. Rev. B **38**, 316 (1988).
[52]H. Xing, G. Su, S. Gao, and J. Chu, Phys. Rev. B **66**, 054419 (2002).
[53]C. Wu, B. Chen, X. Dai, Y. Yu, and Z.-B. Su, Phys. Rev. B **60**, 1057 (1999).
[54]S. Yamamoto, Phys. Rev. B **69**, 064426 (2004).
[55]X. Y. Chen, Q. Jiang, and W. Z. Shen, J. Phys.: Condens. Matter **15**, 915 (2003).
[56]M. Takahashi, Phys. Rev. B **40**, 2494 (1989).
[57]J. E. Hirsch and S. Tang, Phys. Rev. B **40**, 4769 (1989).
[58]S. Tang, M. E. Lazzouni, and J. E. Hirsch, Phys. Rev. B **40**, 5000 (1989).
[59]V. Y. Irkhin, A. A. Katanin, and M. I. Katsnelson, Phys. Rev. B **60**, 1082 (1999).
[60]S. Yamamoto and T. Nakanishi, Phys. Rev. Lett. **89**, 157603 (2002).
[61]M. Kollar, I. Spremo, and P. Kopietz, Phys. Rev. B **67**, 104427 (2003).
[62]H. Hori and S. Yamamoto, J. Phys. Soc. Jpn. **73**, 1453 (2004).
[63]M. Takahashi, Phys. Rev. Lett. **58**, 168 (1987).
[64]S. M. Rezende, Phys. Rev. B **42**, 2589 (1990).
[65]S. Yamamoto and H. Hori, J. Phys. Soc. Jpn. **72**, 769 (2003).
[66]S. Yamamoto and T. Fukui, Phys. Rev. B **57**, R14008 (1998).
[67]S. Yamamoto, T. Fukui, K. Maisinger, and U. Schollwöck, J. Phys.: Condens. Matter **10**, 11033 (1998).
[68]T. Nakanishi and S. Yamamoto, Phys. Rev. B **65**, 214418 (2002).
[69]S. Yamamoto and H. Hori, J. Phys. Soc. Jpn. **73**, 822 (2004).
[70]Th. Jolicoeur and O. Golinelli, Phys. Rev. B **50**, 9265 (1994).
[71]J. Sagi and I. Affleck, Phys. Rev. B **53**, 9188 (1996).
[72]M. Troyer, H. Tsunetsugu, and D. Würtz, Phys. Rev. B **50**, 13515 (1994).
[73]L. P. Battaglia, A. B. Corradi, G. Marcotrigiano, L. Menabue, and G. C. Pellacani, Inorg. Chem. **19**, 125 (1980).
[74]S. A. Roberts, D. R. Bloomquist, R. D. Willett, and H. W. Dodgen, J. Am. Chem. Soc. **103**, 2603 (1981).
[75]H. Manaka, I. Yamada, and K. Yamaguchi, J. Phys. Soc. Jpn. **66**, 564 (1997).
[76]M. Hagiwara, Y. Narumi, K. Kindo, T. Kobayashi, H. Yamakage, K. Amaya, and G. Schumauch, J. Phys. Soc. Jpn. **66**, 1792 (1997).
[77]H. Manaka, I. Yamada, Z. Honda, H. A. Katori, and K. Katsumata, J. Phys. Soc. Jpn. **67**, 3913 (1998).
[78]H. Manaka, I. Yamada, N. V. Mushnikov, and T. Goto, J. Phys. Soc. Jpn. **69**, 675 (2000).
[79]H. Manaka and I. Yamada, Phys. Rev. B **62**, 14279 (2000).
[80]H. Manaka, I. Yamada, M. Hagiwara, and M. Tokunaga, Phys. Rev. B **63**, 144428 (2001).
[81]H. Manaka, I. Yamada, Y. Miyajima, and M. Hagiwara, J. Phys. Soc. Jpn. **72**, 2694 (2003).
[82]K. Hida, Phys. Rev. B **45**, 2207 (1992).
[83]K. Hida, Phys. Rev. B **46**, 8268 (1992).
[84]M. Kohmoto and H. Tasaki, Phys. Rev. B **46**, 3486 (1992).
[85]M. Yamanaka, Y. Hatsugai, and M. Kohmoto, Phys. Rev. B **48**, 9555 (1993).
[86]K. Okamoto, D. Nishino, and Y. Saika, J. Phys. Soc. Jpn. **62**, 2587 (1993).
[87]K. Funase and S. Yamamoto, Phys. Lett. A **334**, 220 (2005).
[88]S. Takada, J. Phys. Soc. Jpn. **61**, 428 (1992).
[89]K. Hida and S. Takada, J. Phys. Soc. Jpn. **61**, 1879 (1992).
[90]K. Hida, J. Phys. Soc. Jpn. **62**, 439 (1993).
[91]T. Sakai, J. Phys. Soc. Jpn. **64**, 251 (1995).
[92]K. Hida, J. Phys. Soc. Jpn. **63**, 2514 (1994).
[93]M. den Nijs and K. Rommelse, Phys. Rev. B **40**, 4709 (1989).
[94]K. Hida, J. Phys. Soc. Jpn. **67**, 1416 (1998).
[95]S. Yamamoto, T. Fukui, and T. Sakai, Eur. Phys. J. B **15**, 211 (2000).
[96]M. Takahashi, Prog. Theor. Phys. Suppl. **87**, 233 (1986).
[97]T. Sakai and M. Takahashi, Phys. Rev. **57**, R8091 (1998).
[98]S. Yamamoto and T. Sakai, J. Phys.: Condens. Matter **11**, 5175 (1999).
[99]A. Auerbach and D. P. Arovas, Phys. Rev. Lett. **61**, 617 (1988).
[100]S. Sarker, C. Jayaprakash, H. R. Krishnamurthy, and M. Ma, Phys. Rev. B **40**, 5028 (1989).
[101]C. J. De Leone and G. T. Zimanyi, Phys. Rev. B **49**, 1131 (1994).
[102]M.-R. Li, Y.-J. Wang, and C.-D. Gong, Z. Phys. B **102**, 129 (1997).
[103]S. Yamamoto, J. Phys. Soc. Jpn. **69**, 2324 (2000).
[104]H. Hori and S. Yamamoto, Phys. Rev. B **68**, 054409 (2003).
[105]A. Escuer, R. Vicente, M. S. E. Fallah, M. A. S. Goher, and F. A. Mautner, Inorg. Chem. **37**, 4466 (1998).
[106]M. Hagiwara, Y. Narumi, K. Minami, K. Kindo, H. Kitazawa, H. Suzuki, N. Tsujii, and H. Abe, J. Phys. Soc. Jpn. **72**, 943 (2003).
[107]N. Fujiwara and M. Hagiwara, Solid State Commun. **113**, 433 (2000).
[108]H. Hori and S. Yamamoto, J. Phys.: Condens. Matter **16**, 9023 (2004).
[109]C. D. Batista and G. Ortiz, Phys. Rev. Lett. **86**, 1082 (2001).
[110]Y. Suzumura, Y. Hasegawa, and H. Fukuyama, J. Phys. Soc. Jpn. **57**, 2768 (1987).
[111]G. Kotliar and J. Liu, Phys. Rev. B **38**, 5142 (1988).
[112]D. Yoshioka, J. Phys. Soc. Jpn. **58**, 32 (1989).

This article was published in English in the original Russian journal. Reproduced here with stylistic changes by AIP.

LOW TEMPERATURE PHYSICS VOLUME 31, NUMBERS 8–9 AUGUST–SEPTEMBER 2005

Superconductivity and normal state properties of non-centrosymmetric $CePt_3Si$: a status report

E. Bauer*

Institut für Festkörperphysik, Technische Universität Wien, A-1040 Wien, Austria

I. Bonalde

Centro de Física, Instituto Venezolano de Investigaciones Científicas, Apartado 21874, Caracas, 1020-A, Venezuela

M. Sigrist

Theoretische Physik, ETH-Hönggerberg, 8093 Zürich, Switzerland

(Submitted March 1, 2005)
Fiz. Nizk. Temp. **31**, 984–994 (August–September 2005)

Ternary $CePt_3Si$ crystallizes in the tetragonal $P4mm$ structure which lacks a center of inversion. Antiferromagnetic order sets in at $T_N \approx 2.2$ K followed by superconductivity (SC) below $T_c \approx 0.75$ K. Large values of $H'_{c2} \approx -8.5$ T/K and $H_{c2}(0) \approx 5$ T were derived, referring to Cooper pairs formed out of heavy quasiparticles. The mass enhancement originates from Kondo interactions with a characteristic temperature $T_K \approx 8$ K. $CePt_3Si$ follows the general features of correlated electron systems and can be arranged within the Kadowaki–Woods plot next to the unconventional SC UPt_3. NMR and μSR results show that both magnetic order and SC coexist on a microscopic scale without having spatial segregation of both phenomena. The absence of an inversion symmetry gives rise to a lifting of the degeneracy of electronic bands by spin-orbit coupling. As a consequence, the SC order parameter may have uncommon features as indicated from a very unique NMR relaxation rate $1/T_1$ and a linear temperature dependence of the penetration depth λ. © *2005 American Institute of Physics.*

[DOI: 10.1063/1.2008135]

I. INTRODUCTION

Electron correlations in solids are a "magic door" to the discovery of unexpected features and phases of metals, intermetallics and oxides at low temperatures. Of particular importance are phase transitions at $T=0$. Critical fluctuations associated with such a phase transition can lead to strong renormalization of normal metallic properties and novel exotic phases may emerge from these strongly fluctuating environments. One of the most exciting features in this context is the occurrence of superconductivity (SC).

The appearance of SC in such a scenario can deviate from the common BCS type in many essential aspects. Strong correlation effects responsible for the heavy electron behavior from narrow f-electron bands, may hamper the possibility of conventional Cooper pairing, i.e., pairing in the most symmetric (s-wave) form as it is favored by electron-phonon interaction. In turn, magnetic fluctuation may provide the necessary attractive interaction in a different angular momentum channel. This means that Cooper pairs may have either spin-singlet or spin-triplet configuration and the orbital angular momentum may lead to a highly anisotropic gap with zero nodes. Almost all previously studied SC exhibiting strong electron correlations in the normal state region are characterized by a center of inversion in its crystal structure. This allows us to distinguish spin-singlet and spin-triplet components of the SC order parameter and consider them separately. Superconductivity in materials having no inversion symmetry is rare. This lack of a inversion center invalidates some aspects of the scheme of symmetry classification and leads to a mixture of singlet and triplet pairing in general.

A recently discovered example in this respect is $CePt_3Si$ with the tetragonal space group $P4mm$ (No. 99),[1] the first heavy fermion SC without a center of inversion. The absence of inversion symmetry induces peculiar band splittings, as we will discuss below, which are detrimental to certain kinds of Cooper pairing channels. In particular, spin triplet pairing becomes unlikely under these circumstances.[2]

The aim of the present paper is to provide a review of results of current research dedicated to the various physical properties of $CePt_3Si$ in both the normal and superconducting states and to locate the system in the standard generic phase diagram of heavy fermion compounds.

This paper is organized as follows. After a discussion of normal state properties of $CePt_3Si$, the SC features of $CePt_3Si$ are examined before theoretical considerations concerning the SC order parameter are made.

II. RESULTS AND DISCUSSION

A. Normal state properties

Physical properties of ternary $CePt_3Si$ are dominated by the onset of long range, presumably antiferromagnetic order below $T_N \approx 2.2$ K, followed by SC below $T_c = 0.75$ K. This intriguing coincidence of two ordering phenomena in $CePt_3Si$ have to be considered in the context of crystal electric field (CEF) splitting and Kondo interaction which sub-

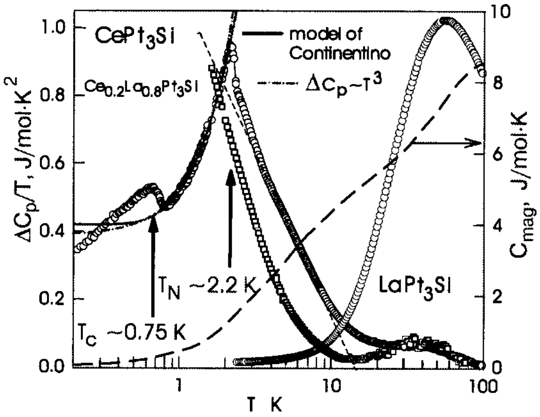

FIG. 1. Temperature-dependent magnetic contribution to the specific heat, ΔC_p of CePt$_3$Si plotted as $\Delta C_p/T$ on a logarithmic temperature scale (filled circles). The phonon contribution to define ΔC_p is taken from $C_p(T)$ of LaPt$_3$Si (filled diamonds). The long-dashed line represents the magnetic entropy (right axis). The short-dashed line is a guide to the eye and roughly indicates the non-Fermi liquid behavior. The solid line is a fit according to Eq. (1) and the dotted-and-dashed line is a fit according to $\Delta C_p \sim T^3$.

stantially modify Hund's $j=5/2$ ground state of the Ce ion. The response of the system associated with the mutual interplay of these mechanisms will be highlighted below.

Substantial information concerning the magnetic and the paramagnetic properties of CePt$_3$Si can be deduced from the temperature-dependent magnetic contribution to the specific heat $C_{\mathrm{mag}}(T)$. The latter may be defined by the difference ΔC_p between CePt$_3$Si and isostructural nonmagnetic reference LaPt$_3$Si, with $\Delta C_p \sim C_{\mathrm{mag}}$. Plotted in Fig. 1 is $\Delta C_p/T$ versus T of CePt$_3$Si together with the raw data of LaPt$_3$Si. The low temperature behavior of the latter can be accounted for in terms of the Debye model with $\theta_D = 255$ K together with a Sommerfeld value $\gamma \approx 9\ \mathrm{mJ/mol \cdot K^2}$. $\Delta C_p(T)$ of CePt$_3$Si defines three regimes: the SC state of CePt$_3$Si below $T_c = 0.75$ K; the magnetically ordered range below $T_N \approx 2.2$ K, and the paramagnetic region above T_N. This region is characterized by a Schottky-like anomaly with a weak local maximum around 40 to 50 K. Such numbers imply a CEF level approximately 100 K above the ground state doublet. However, since $C_p(T)$ of LaPt$_3$Si slightly exceeds the specific heat data of CePt$_3$Si, $\Delta C_p(T) \sim C_{\mathrm{mag}}(T)$ becomes negative, and hence a reliable evaluation of CEF level scheme is not possible, at least, considering this quantity only. The integrated entropy S_{mag} (right axis, Fig. 1) reaches $R \ln 2$ around 25 K, and the entropy of 8.7 $\mathrm{J/mol \cdot K^2}$ integrated up to 100 K is slightly less than $R \ln 4 = 11.5\ \mathrm{J/mol \cdot K^2}$. These results confirm again that the ground state of Ce^{3+} ions is a doublet with the first excited level above about 100 K. The twofold degeneracy of the ground state doublet, however, is lifted by magnetic order as well as by Kondo type interaction spreading entropy to higher temperatures.

The second interesting aspect in the paramagnetic temperature range of CePt$_3$Si is an almost logarithmic tail of $\Delta C_p/T$ above T_N, extrapolating to about 12 to 13 K. The logarithmic temperature dependence observed just above the magnetic transition may be considered as hint of non-Fermi liquid (nFl) behavior. Therefore, it is a unique observation at ambient pressure that non-Fermi liquid behavior, magnetic ordering and eventually a SC transition consecutively arises on the same sample upon lowering the temperature. To corroborate the nFl property deduced for CePt$_3$Si from the specific heat data and to exclude short range order effects and inhomogeneities above the magnetic phase transition, $C_p(T)$ was studied for diluted Ce$_{0.2}$La$_{0.8}$Pt$_3$Si as well. Results are shown in Fig. 1 as ΔC_p versus $\ln T$ (squares). This diluted sample—without magnetic ordering—exhibits a similar logarithmic contribution to the specific heat, like the parent CePt$_3$Si, and thus establishes this feature as an intrinsic property.

In order to analyze in more detail the magnetically ordered region of CePt$_3$Si, a model by Continentino[3] is applied for the specific heat well below T_{mag}:

$$C_{\mathrm{mag}}(T) = g \Delta_{SW}^{7/2} T^{1/2} \exp(-\Delta_{SW}/T) \left[1 + \frac{39}{20} \left(\frac{T}{\Delta_{SW}} \right) + \frac{51}{32} \left(\frac{T}{\Delta_{SW}} \right)^2 \right]. \tag{1}$$

This expression is based on antiferromagnetic magnons with a dispersion relation $\omega = \sqrt{\Delta_{SW}^2 + D^2 k^2}$, where Δ_{SW} is the spin-wave gap and D is the spin-wave velocity; $g \propto 1/D^3 \propto 1/\Gamma^3$, and Γ is an effective magnetic coupling between the Ce ions. A least squares fit of Eq. (1) to the data below T_N (solid line, Fig. 1) reveals $\Delta_{SW} \approx 2.7$ K, a reasonable gap value with respect to the ordering temperature. A recent neutron diffraction study carried out on CePt$_3$Si confirmed antiferromagnetic ordering below $T_N \approx 2.2$ K with a wave vector $\mathbf{k} = (0,0,1/2)$, i.e., doubling of the magnetic unit cell along the **c** direction.[4] A second model calculation with simple antiferromagnetic spin waves, yielding $C_{\mathrm{mag}} \propto T^3$, again gives reasonable agreement with the heat capacity data. Using both models, one can estimate a Sommerfeld coefficient of 0.42 and 0.39 $\mathrm{J/mol \cdot K^2}$ for the former and latter model, respectively. Such figures are in excellent agreement with an extrapolation of high field specific heat data where SC is already suppressed by the applied magnetic field. These strongly enhanced Sommerfeld values characterize CePt$_3$Si as a typical heavy fermion compound.

Considering Kondo type interactions to be responsible for the significant renormalization of electrons, the temperature dependent magnetic entropy $S_{\mathrm{mag}}(T)$ allows one to estimate the Kondo temperature T_K. Applying results derived from the renormalization group technique[5] for effective spin-1/2 systems to $S_{\mathrm{mag}}(T)$ derived for CePt$_3$Si yields $T_K \approx 7.2$ K. A second possible estimate for T_K follows from the competition of the RKKY interaction and the Kondo effect, which leads to a significant reduction of the specific heat jump at $T = T_N$. Following the procedure developed in Ref. 6 gives $T_K \approx 9$ K, in reasonable agreement with the previous estimate.

The temperature-dependent electrical resistivity $\rho(T)$ of CePt$_3$Si is plotted in Fig. 2a together with $\rho(T)$ of isostructural LaPt$_3$Si. $\rho(T)$ of CePt$_3$Si drops to zero from a residual value of 5.8 $\mu\Omega \cdot$cm with $T_c^{\mathrm{mid}} = 0.75$ K, thus indicating superconductivity. At high temperatures, $\rho(T)$ is characterized by a negative logarithmic contribution, followed by pronounced curvatures around 75 K and 15 K, which may reflect crystal electric field effects in the presence of Kondo type interactions. Further evaluation of $\rho(T)$ requires knowl-

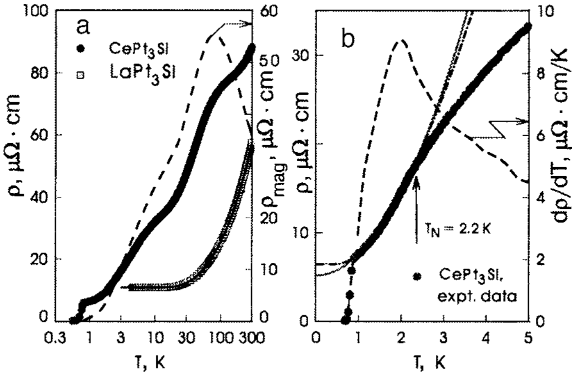

FIG. 2. Temperature-dependent electrical resistivity ρ of $CePt_3Si$ and $LaPt_3Si$ plotted on a logarithmic temperature scale. The magnetic contribution $\rho_{\mathrm{mag}}(T)$ (dashed line) refers to the right axis (a). Low-temperature details of $\rho(T)$ of $CePt_3Si$. The solid and the dotted-and-dashed lines are least squares fits (see text) and the dashed-line shows $d\rho(T)/dT$ (b).

edge of the phonon contribution ρ_{ph} which, in a first approximation, may be derived from homologous and isotypic $LaPt_3Si$. $LaPt_3Si$ is metallic in the temperature range measured and $\rho(T)^{\mathrm{La}}=\rho_0^{\mathrm{La}}+\rho_{\mathrm{ph}}^{\mathrm{La}}(T)$ (ρ_0 is the residual resistivity) can simply be accounted for in terms of the Bloch Grüneisen model with the Debye temperature $\theta_D\approx 160$ K [solid line, Fig. 2a] and $\rho_0=10.7\ \mu\Omega\cdot$cm. According to Matthiessen's rule, $\rho(T)$ of $CePt_3Si$ can be expressed as $\rho(T)^{\mathrm{Ce}}=\rho_0^{\mathrm{Ce}}+\rho_{\mathrm{ph}}^{\mathrm{Ce}}(T)+\rho_{\mathrm{mag}}(T)$. The temperature-dependent magnetic contribution to the resistivity, $\rho_{\mathrm{mag}}(T)$, then follows simply from the difference of $\rho(T)^{\mathrm{Ce}}$ and $\rho(T)^{\mathrm{La}}$, assuming $\rho_{\mathrm{ph}}^{\mathrm{Ce}}\approx\rho_{\mathrm{ph}}^{\mathrm{La}}$. Furthermore, ρ_0^{La} is subtracted. $\rho_{\mathrm{mag}}(T)$ exhibits a distinct logarithmic contribution for $T>100$ K; the maximum around 80 K may indicate the overall crystal field splitting of the $j=5/2$ Ce $4f^1$ state (dashed line, Fig. 2a, right axis).

Figure 2b exhibits low-temperature features of the electrical resistivity of $CePt_3Si$. Besides the onset of superconductivity, there is a distinct change of the slope in $\rho(T)$ around 2 K, which becomes more evident from a $d\rho/dT$ plot [right axis, Fig. 2b]. In the context of the specific heat study, this anomaly is interpreted as a signature of the onset of long-range magnetic order. A least-squares fit according to $\rho=\rho_0+AT^2$ reveals the residual resistivity $\rho_0=5.2\ \mu\Omega\cdot$cm and a material-dependent constant $A=2.35\ \mu\Omega\cdot$cm/K^2.

To account for the magnetically ordered region of $CePt_3Si$ in more detail, the above indicated model of Continentino can be adopted for the temperature dependent electrical resistivity, where conduction electrons are scattered on antiferromagnetic magnons[3]

$$\rho=\rho_0+A\Delta_{SW}^{3/2}T^{1/2}\exp(-\Delta_{SW}/T)\left[1+\frac{2}{3}\left(\frac{T}{\Delta_{SW}}\right)+\frac{2}{15}\left(\frac{T}{\Delta_{SW}}\right)^2\right]. \tag{2}$$

Again, Δ_{SW} is the spin-wave gap. A least squares fit of Eq. (2) to the experimental data above T_c and below the ordering temperature yields an equally good agreement (dot-and-dash line, Fig. 2b) as the earlier model (solid line, Fig. 2b). The spin gap obtained from this fit, $\Delta_{SW}=2.77$ K, agrees excellently with that value obtained from specific-heat analysis.

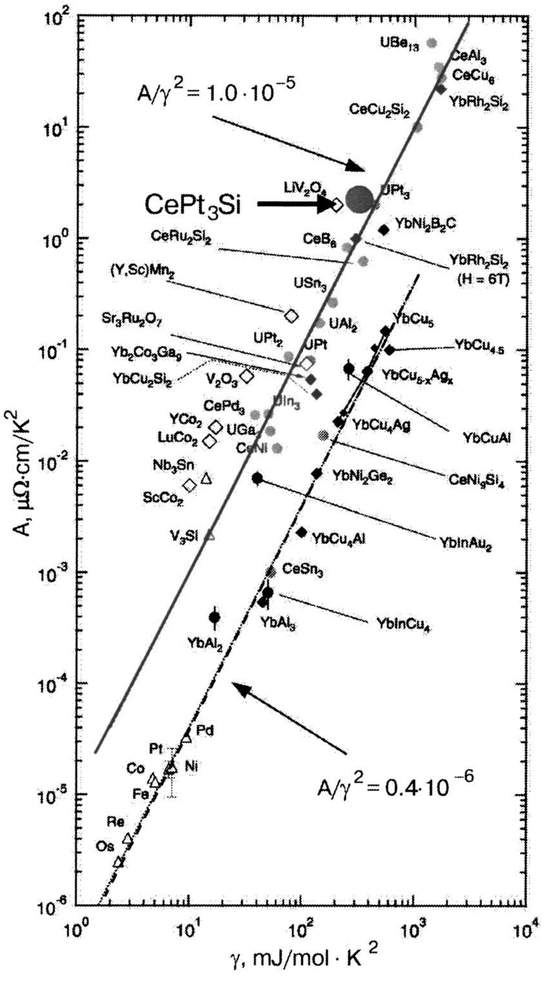

FIG. 3. A plot of the T^2 coefficient of the electrical resistivity A versus the T-linear specific heat coefficient γ. Solid and dashed lines represent $A/\gamma^2=1\times10^{-5}\ \mu\Omega\cdot\mathrm{cm}\cdot\mathrm{mol}^2\,\mathrm{K}^2\,\mathrm{mJ}^{-2}$ and $A/\gamma^2=0.4\times10^{-6}\ \mu\Omega\cdot\mathrm{cm}\cdot\mathrm{mol}^2\,\mathrm{K}^2\,\mathrm{mJ}^{-2}$ (figure taken from Ref. 8).

The coefficient A derived is much larger than usually observed for simple metals like K or Cu, and thus evidences again that the low temperature state of $CePt_3Si$ is dominated by heavy quasiparticles. In fact, considering the electron-electron interaction in terms of the Barber model indicates $A\propto(N(E_F))^2$, where $N(E_F)$ is the electronic density of states at the Fermi energy. Since also the Sommerfeld value depends on the same quantity, it is natural to arrange certain systems according their A and γ values. Such a classification was made for the first time by Kadowaki and Woods,[7] and many highly correlated electron systems have been shown to satisfy this scheme.[8] A closer inspection yields for the ratio $A/\gamma^2=1\times10^{-5}\ \mu\Omega\cdot\mathrm{mol}^2\cdot\mathrm{K}^2\cdot\mathrm{mJ}^{-2}$. Arranging $CePt_3Si$ in such a Kadowaki-Woods plot, see Fig. 3, obviously shows that the present compound is found at the very same site as the unconventional superconductor UPt_3.

Temperature-dependent magnetic susceptibility provides information concerning the effective magnetic moments μ_{eff} involved in a particular system, the interaction strength between these moments via the paramagnetic Curie temperature θ_p, and about phase transitions present in a certain

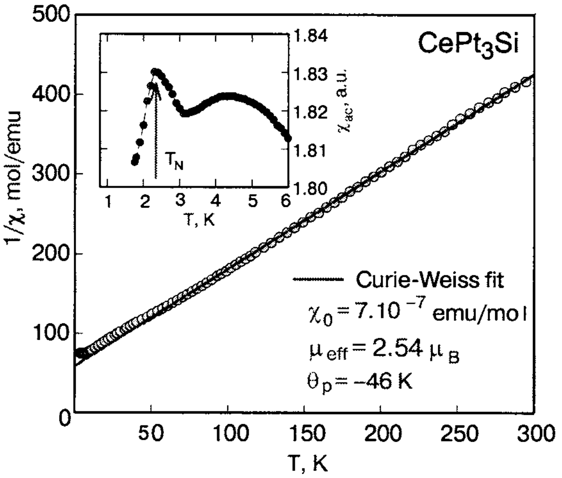

FIG. 4. Temperature-dependent susceptibility of $CePt_3Si$ plotted as $1/\chi$ versus T. The solid line is a least-squares fit according to the modified Curie-Weiss law. The inset shows the low temperature behavior deduced from an ac susceptibility study (Ref. 9).

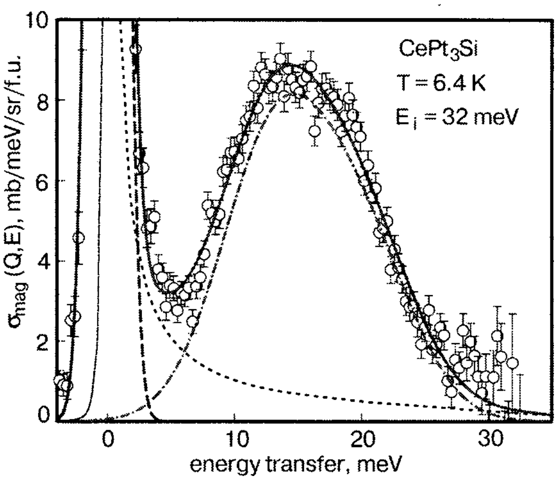

FIG. 5. Magnetic scattering obtained at 6.4 K with the incident energy of 35 meV. The dashed line is for the elastic component with FWHM = 2.4 meV while the short-dashed line represents the quasi-elastic component with FWHM = 0.8 meV. The dotted-and-dashed line is for the sum of two Lorentzian components centered at 13 and 20 meV with FWHM = 10.0 meV (Ref. 17).

sample. Results taken from a SQUID measurement performed at $\mu_0 H = 1$ T are shown in Fig. 4 together with an ac susceptibility measurement in the inset of this figure. At elevated temperatures, $\chi(T)$ of $CePt_3Si$ exhibits a Curie-Weiss behavior—and the anomaly around 2.2 K (inset, Fig. 4) indicates a magnetic phase transition. To account qualitatively for the region above about 50 K, a least-squares fit according to the modified Curie-Weiss law, i.e.,

$$\chi = \chi_0 + \frac{C}{T + \theta_p} \tag{3}$$

was applied. χ_0 represents a temperature independent Pauli-like susceptibility and C is the Curie constant.

Results of this procedure are shown by the solid line in Fig. 4. The effective magnetic moment deduced from the Curie constant C matches the theoretical value associated with the 3+ state of cerium, thereby implying a rather stable magnetic moment. The paramagnetic Curie temperature $\theta_p \approx -46$ K is large and negative, being indicative of strong antiferromagnetic interactions. In the Kondo picture, already adopted to explain the large Sommerfeld value γ, the value of θ_p suggests a Kondo temperature of the order of 10 K $(T_K \approx |\theta_p|/4)$.

Very large values of θ_p ($H \| [100]$ and $H \| [001]$) were also deduced from a previous investigation[4] of single crystalline $CePt_3Si$, confirming the substantial antiferromagnetic interaction strength.

For better understanding of the magnetic ground state and expected localized character of Ce $4f$ electrons, neutron inelastic scattering experiments were performed. In order to accurately and reliably determine magnetic scattering from the magnetic moments of Ce, both $CePt_3Si$ and $LaPt_3Si$ were investigated in powder form under identical conditions. For a proper phonon subtraction, two well-established methods were used,[10] yielding almost identical results.

The intensity shown in Fig. 5 for a sample temperature $T = 6.4$ K is expected to be solely of magnetic origin as the phonon contribution has been subtracted from the data. In order to account for the excitations observed, the standard CEF Hamiltonian for Ce^{3+} with C4v point symmetry is considered:

$$H_{CEF} = B_2^0 O_2^0 + B_4^0 O_4^0 + B_4^4 O_4^4. \tag{4}$$

B_l^m and O_l^m are the CEF parameters and the Steven operators, respectively. Due to CEF effects, the 6-fold degenerate ground state of the Ce^{3+} ions is split in tetragonal symmetry into 3 doublets. Applying Eq. (4) to the data shown in Fig. 5 reveals CEF parameters $B_2^0 = -0.4972$ meV, $B_4^0 = 0.0418$ meV, and $B_4^4 = 0.2314$ meV. These parameters are consistent with levels at $\Delta_1 = 13$ and $\Delta_2 = 20$ meV and permit a reasonably good description of the magnetic scattering (solid line, Fig. 5). Keeping the CEF parameters unchanged, the data obtained at 94 K are equally well explained. Moreover, the two CEF excitations centred at 13 and 20 meV are also consistent with the heat capacity data as discussed above. We furthermore studied low energy excitations using lower incident energy to find a weak feature around 1.4 meV. The dispersion of that intensity at $T = 5$ K, particularly around $Q = 0.8$ Å^{-1} is a signature for the development of short-ranged magnetic correlations and can be considered as origin of the anomalous behavior of the specific heat above magnetic ordering. At higher temperatures ($T \approx 30$ K) scattering becomes Q-independent. This feature is completely absent in non-magnetic $LaPt_3Si$. Unlike our study performed at the instrument HET of ISIS (UK), the inelastic neutron scattering experiment reported in Ref. 4 indicated two CEF peaks at 1.0 and 24 meV. Based on the latter, a set of CEF parameters was deduced, sufficient to account for isothermal magnetization and the temperature dependent magnetic susceptibility. However, this latter CEF level scheme does not properly describe the temperature dependent magnetic contribution to the specific heat and magnetic entropy. Such a discrepancy is rather serious, since, different to magnetization and susceptibility, not any theoretical model is necessary for the calculation, except basic thermodynamics. In order to get more reliable data for the analysis, particularly at low

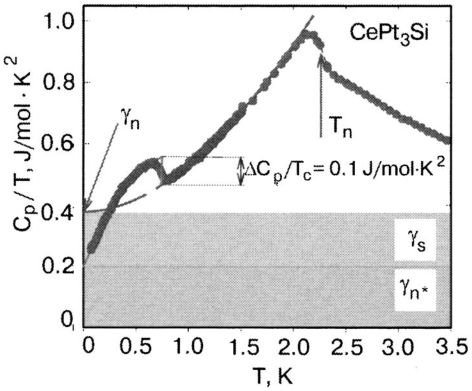

FIG. 6. Temperature-dependent specific heat C_p/T of CePt$_3$Si; the dashed line is a T^3 extrapolation of $C_p(T)$ at 0 T.

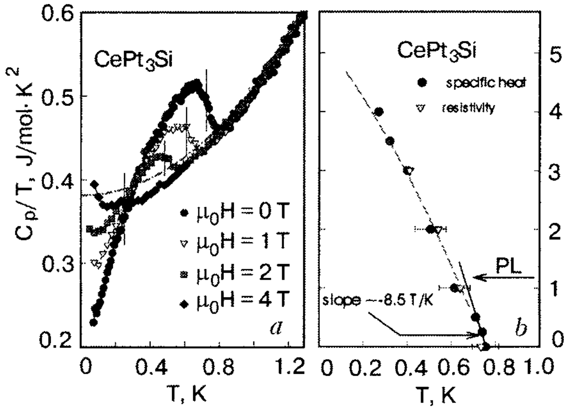

FIG. 7. Temperature-dependent specific heat C_p/T of CePt$_3$Si for various values of applied fields; the dashed line is a T^3 extrapolation of $C_p(T)$ at 0 T (a). Temperature dependence of the upper critical field H_{c2}. The solid straight line yields $H'_{c2}\approx -8.5$ T/K; the dashed line is a guide to the eye (Ref. 1). PL indicates the Pauli-Clogston limiting field (b).

energy excitations, neutron inelastic measurements with high resolution and low incident energy neutrons are in progress.

B. Superconducting properties of CePt$_3$Si

Signs of bulk SC of CePt$_3$Si below $T_c=0.75$ K are numerous: zero resistivity, diamagnetic signal in the susceptibility, a jump in the specific heat and NMR relaxation rate at T_c.

Substantial information concerning the superconducting state is provided by heat capacity data taken at low temperatures for CePt$_3$Si. Results are shown in Fig. 6 as C_p/T versus T. The phonon contribution is negligible in the temperature range shown. Besides the already mentioned magnetic phase transition at $T_N=2.2$ K and the logarithmic contribution above that temperature, the superconducting transition at $T_c\approx 0.75$ K is the most prominent feature.

The Sommerfeld coefficient $\gamma_n\approx 0.39$ J/mol·K^2 of CePt$_3$Si at zero field, obtained from an extrapolation of the antiferromagnetically ordered region, evidences the large effective masses of the charge carriers involved. The extrapolation shown in Fig. 6 (dashed line) satisfies the basic requirement of superconductivity, the entropy balance between the SC and normal state regions. Another careful extrapolation of the heat capacity of data within the superconducting temperature range towards zero yields about $\gamma_n^*\approx 210$ mJ/mol·K^2. This nonvanishing contribution within the SC state may hint at two mechanisms: not all electrons are involved in the SC condensate, rather, roughly half of them ($\gamma_s\approx\gamma_n^*$) are forming normal state long range magnetic order, which then co-exists with superconductivity on a microscopic scale; a somewhat gapless superconducting state. This would cause finite values of the Sommerfeld constant and power laws of the thermodynamic and transport properties instead of an exponential behavior as in typical BCS systems. The coexistence of both states is evidenced from μSR spectroscopy and a superconducting state with nodes in the gap (gapless at certain sites) is supported by magnetic penetration depth $\lambda(T)$ measurements (see below).

The jump of the specific heat anomaly associated with superconductivity, $\Delta C_p/T|_{T_c}\approx 0.1$ J/mol·K^2, leads to $\Delta C_p/(\gamma_n T_c)\approx 0.25$, which is significantly smaller than the figure expected from the BCS theory ($\Delta C_p/(\gamma T_c)\approx 1.43$). Even using the electronic specific heat coefficient in the SC state, $\gamma_s\approx 0.18(1)$ J/mol·K^2, we obtained $\Delta C_p/(\gamma_s T_c)\approx 0.55$ that is still below the BCS value.

Again, two scenarios may explain the substantial reduction of $\Delta C_p/(\gamma T_c)$ with respect to the BCS value; strongly anisotropic gaps yield a reduced magnitude of $\Delta C_p/(\gamma T_c)$ (Ref. 11), and not all electrons condense into Cooper pairs, and the rest stay essentially normal. This may imply that the electrons responsible for normal state features, such as antiferromagnetic order, coexist with those forming the Cooper pairs. In fact, the finite value of $\gamma_s\approx 0.18$ J/mol·K^2 provides evidence that even at $T=0$ K a significant portion of the Fermi surface is still not involved in the SC condensate.

Very recently, a specific-heat study was performed on a well heat-treated polycrystalline CePt$_3$Si sample, revealing two consecutive phase transitions at $T_{c1}\approx 0.8$ and $T_{c2}\approx 0.55$ K. The extreme different field response for both transitions, however, are possibly indicative of two different superconducting states.[12]

The upper critical field $H_{c2}(0)$ and the slope $dH_{c2}/dT\equiv H'_{c2}$ are indispensable quantities for the determination of microscopic parameters describing the superconducting state. The temperature- and field-dependent specific heat $C_p(T,H)$ of CePt$_3$Si is shown for the low-temperature range in Fig. 7a.

The application of magnetic fields reduces T_c, resulting in a rather large change of $dH_{c2}/dT\approx -8.5$ T/K, in good agreement with the conclusion drawn from electrical resistivity [see Fig. 7b]. An extrapolation of $T_c(H)$ towards zero yields $H_{c2}(0)\approx 5$ T, well above the paramagnetic limiting field $H_p\approx 1.1$ T.[1] Furthermore, an estimation of the Sommerfeld coefficient from the high field data gives 0.36 J/mol·K^2, in fair agreement with the value obtained from an extrapolation of the normal state in the zero field data (see Fig. 6). The upturn of C_p/T at the lowest temperatures, that gets stronger with increasing magnetic field, derives from the nuclear contribution of ^{195}Pt.

In order to derive a set of parameters characterizing the superconducting state of CePt$_3$Si the BCS theory is adopted.[13,14] Although substantial deviations from a spherical Fermi surface are expected for tetragonal CePt$_3$Si, reasonable physical parameters can be expected (compare, e.g., Refs. 14 and 15).

The starting parameters are $\gamma_s = 0.18(2)$ J/mol·K^2 (as a lower limit), $H'_{c2} = -8.5$ T/K and $\rho_0 = 5.2$ $\mu\Omega\cdot$cm.

The effective Fermi surface S_s is then computed [Eq. (2) in Ref. 14] as $S_s^{cl} \simeq 3.7\times 10^{20}$ m^{-2} within the clean limit and $S_s^{dl} \simeq 3.5\times 10^{20}$ m^{-2} for the dirty limit. Considering the dirty limit only, one gets $H'_{c2} \approx -0.77$ T/K, a value rather low with respect to the experimentally derived slope $H'_{c2} \approx -8.5$ T/K. This indicates that CePt$_3$Si is not a typical dirty-limit superconductor. Thus, the further calculations are based on clean-limit results. Combining the Fermi surface with γ_s gives the Fermi velocity $v_F \simeq 5300$ m/s and in the context of the residual resistivity, $\rho_0 \simeq 5.2$ $\mu\Omega\cdot$cm, a mean free path $l_{tr} \simeq 8\times 10^8$ m can be estimated. The coherence length ξ_0 for $T \to 0$ was obtained from two independent relations. One follows from the BCS equation, $\xi_0 = 0.18 h v_F/(k_B T_c) \simeq 9.7\times 10^{-9}$ m. A second expression stems from the well known formula $\mu_0 H_{c2} = \Phi_0/(2\pi\xi_0^2)$, yielding $\xi_0 = 8.1\times 10^{-9}$ m, in reasonable agreement with the former.

The evaluation of the Ginzburg-Landau parameter $\kappa_{GL} = \lambda/\xi$ requires knowledge of the thermodynamic critical field $\mu_0 H_c(0) = 26(2)$ mT, which can be calculated from the free energy difference between the superconducting and the normal state:

$$\Delta F(T) = F_n - F_s = \mu_0 H_c^2(T)/2$$
$$= \int_{T_c}^{T}\int_{T_c}^{T'} \frac{(C_s - C_n)}{T''}\, dT''\, dT'.$$

C_s is obtained from the zero-field specific heat, and C_n is taken from the T^3 extrapolation, as indicated by the dashed line in Fig. 6. With $H_{c2}(0) \approx 5$ T one derives a value for $\kappa_{GL} = H_{c2}(0)/\sqrt{2H_c}) \simeq 140$, which, in turn, determines the London penetration depth $\lambda_L(T\to 0) \simeq 1.1\times 10^{-6}$ m. Since the evaluation of the various parameters is based on s-wave models, care has to be taken when using their absolute values; nevertheless the right order of magnitude can be anticipated.

Evaluating Eq. (A.13) of Ref. 14 with $\rho_{\max} \approx 100$ $\mu\Omega\cdot$cm yields $S_{hT} \simeq 3.1\times 10^{21}$ m^{-2}, the Fermi surface at elevated temperatures. The discrepancy between S_s and S_{hT} suggests that only a part of the Fermi surface is involved in forming Cooper pairs while the remaining one engages in normal state magnetic correlations. This finding seems to be convincingly supported from the lessened value of $\Delta C_p/(\gamma T_c)$. In terms of the coexistence of both superconductivity ($T_c = 0.75$ K) and long-range magnetic order ($T_N = 2.2$ K), the downsized specific heat jump at T_c may explain, at least partly, that the Fermi surface is likely to be subdivided into a superconducting part (related to γ_s) and a normal-state region. Microscopic evidence for the latter conclusion can be found from zero-field μSR spectroscopy data obtained in the magnetic phase below and above T_c in the magnetic phase (Fig. 8). At temperatures much above T_N, the μSR signal is a characteristic of a paramagnetic state with a depolarization solely arising from nuclear moments.

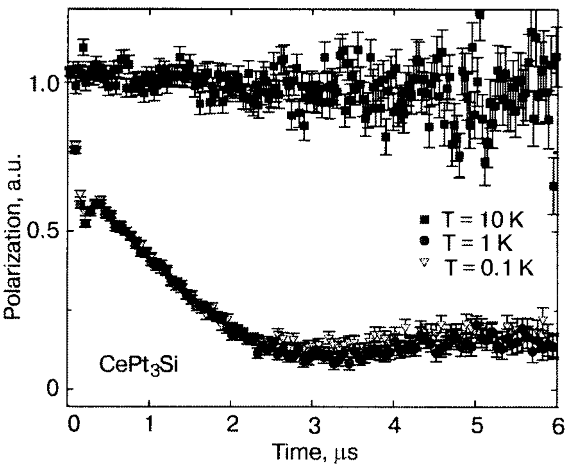

FIG. 8. Zero field depolarization rate of CePt$_3$Si at various temperatures (Ref. 17).

Below T_N the μSR signal indicates that the full sample volume orders magnetically. High statistic runs performed[16] above and below T_c did not show any change of the magnetic signal, supporting the view of a microscopic coexistence between magnetism and SC.

This points to a novel state for SC Ce-based heavy-fermion systems at ambient pressure, for which, to date, magnetism was found to be either absent[18] or strongly competing against SC.[19] The observed coexistence is reminiscent of the situation observed in UPd$_2$Al$_3$,[20] where a model of two independent electron subsets, localized or itinerant, was proposed in view of similar microscopic data.[21]

Additional microscopic information about the SC state can be obtained from the temperature-dependent ^{195}Pt nuclear spin-relaxation rate $1/T_1$.[22] Results in the form of a plot of $(1/T_1T)/(1/T_1T)_{T_c}$ versus T/T_c are shown in Fig. 9 for 8.9 and 18.1 MHz. The relaxation behavior $1/T_1T$ of CePt$_3$Si is reminiscent of a kind of Hebel–Slichter anomaly,[23] indicating coherence effects as in conventional BCS SC. The peak height, however, is significantly smaller than that observed for conventional BCS SC and, additionally, shows no field dependence at the 8.9 MHz ($H\sim 1$ T)

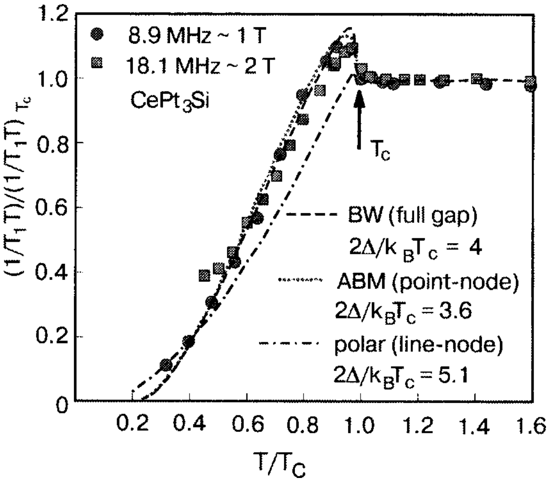

FIG. 9. A plot of $(1/T_1T)/(1/T_1T)_{T_c}$ versus T/T_c at 8.9 MHz ($H\sim 1$ T) and 18.1 MHz ($H\sim 2$ T). The dashed line is for the Balian-Werthamer model (BW isotropic triplet SC state) with a value of $2\Delta/k_BT_c = 4$. The dotted line assumes a point-node model with $2\Delta/k_BT_c = 3.6$, and the dotted-and-dashed line represents a fit by a line-node gap model with $2\Delta/k_BT_c = 5.1$ (Ref. 17).

and 18.1 MHz ($H\sim2$ T) run. Notably, $\mathrm{CePt_3Si}$ is the first HF SC that exhibits a peak in $1/T_1T$ just below T_c.

$1/T_1T$ at $H\sim2$ T seems to saturate at low temperature, which can be assigned to the presence of vortex cores where the normal-state region is introduced. $1/T_1T$ at 8.9 MHz ($H\sim1$ T), however, continues to decrease down to $T=0.2$ K, the lowest temperature yet measured. Neither an exponential law nor the usual T^3 law, reported for most of the unconventional HF SC (see, e.g., Ref. 24 and references cited therein), is observed for the data down to $T=0.2$ K ($\approx0.3T_c$). However, further studies at temperatures below $0.2T_c$ are required to make any definite conclusion on the specific behavior of $1/T_1$.

The nuclear spin-lattice relaxation rate $1/T_1$ in the superconducting state can be expressed as

$$\frac{1}{T_1}=\frac{2\pi A^2}{\hbar}\int_0^\infty[N_s^2(E)+M_s^2(E)]f(E)[1-f(E)]dE, \tag{5}$$

N_s is the density of states and describes the distinct features of an isotropic, polar or axial SC state; M_s is the anomalous density of states arising from coherence effects which can be calculated from

$$M_s(E)=\frac{N(0)}{4\pi}\int_0^{2\pi}\int_0^{\pi}\frac{\Delta(\theta,\varphi)}{\sqrt{E^2-\Delta^2(\theta,\varphi)}}\sin\theta d\theta d\varphi, \tag{6}$$

with $\Delta(0,\varphi)$ the direction-dependent energy gap. M_s is expected to exist only in s-wave superconductors.

To account for the relaxation behavior below T_c in noncentrosymmetric $\mathrm{CePt_3Si}$, three unconventional models were adopted for a description of the temperature dependence of $1/T_1$ at $H\sim1$ T. The dashed line in Fig. 9 represents a fit according to the Balian–Werthamer model (BW isotropic spin-triplet SC state) with $2\Delta/k_BT_c=3.9$.[25] Note that the peak of the BW model in $1/T_1T$ originates from the presence of an isotropic energy gap. The dotted-and-dashed line is a fit using a line-node model with $2\Delta/k_BT_c=5.1$. The dotted line refers to a point-node model with $2\Delta/k_BT_c=3.6$. The models used, however, failed to give satisfactory description of the observed temperature dependence of $1/T_1$ over the entire temperature range.

The data seem to start following the line-node model at the lowest measured temperatures. However, the data are described reasonably well by the BW (nodeless) model just below T_c. The experimentally observed peak in $1/T_1T$ would indicate the presence of an isotropic energy gap, even though a coherence effect—inherent for the isotropic spin-singlet s-wave pairing state—is absent.

In almost all previous studies on either conventional and unconventional SC, it was assumed that the crystal has an inversion center, which allows separate consideration of the even (spin-singlet) and odd (spin-triplet) components of the SC order parameter. In $\mathrm{CePt_3Si}$, however, a center of symmetry is absent. Therefore, the novel relaxation behavior found below T_c hints at a possibly new class of a SC state being realized in noncentrosymmetric heavy fermion compounds.

An important probe of the structure of the superconducting energy gap is the temperature dependence of the magnetic penetration depth $\lambda(T)$. Figure 10 shows results obtained using a tunnel diode oscillator system running at 9.5 MHz, for a polycrystalline $\mathrm{CePt_3Si}$ sample at temperatures down to 0.049 K.[26] Figure 10a depicts the normalized variation of $\Delta\lambda(T)/\Delta\lambda_0$ versus T/T_c in the whole temperature region below T_c. Here $\Delta\lambda(T)=\lambda(T)-\lambda(0.049\text{ K})$ and $\Delta\lambda_0$ is the total penetration depth shift. Figure 10b displays $\Delta\lambda(T)$ versus T/T_c in the low-temperature range $T<0.6T_c$ for polycrystalline $\mathrm{CePt_3Si}$ and Cd samples. Cadmium is a classic s-wave superconductor, for which the low temperature dependence of $\lambda(T)$ is exponential. The inset to Fig. 10b is a close-up of $\Delta\lambda(T)$ versus T/T_c for the $\mathrm{CePt_3Si}$ sample for temperatures $T<0.3T_c$, where it can be clearly seen that the penetration depth data of the $\mathrm{CePt_3Si}$ sample follow a linear temperature behavior below $0.17T_c$. We remark here that the low-temperature behavior of $\lambda(T)$ is not affected by the type of sample (single crystal, powder, etc.) in which the measurement is performed, if the sample is of high quality.[27–29]

For a clean, local superconductor the penetration depth is given by

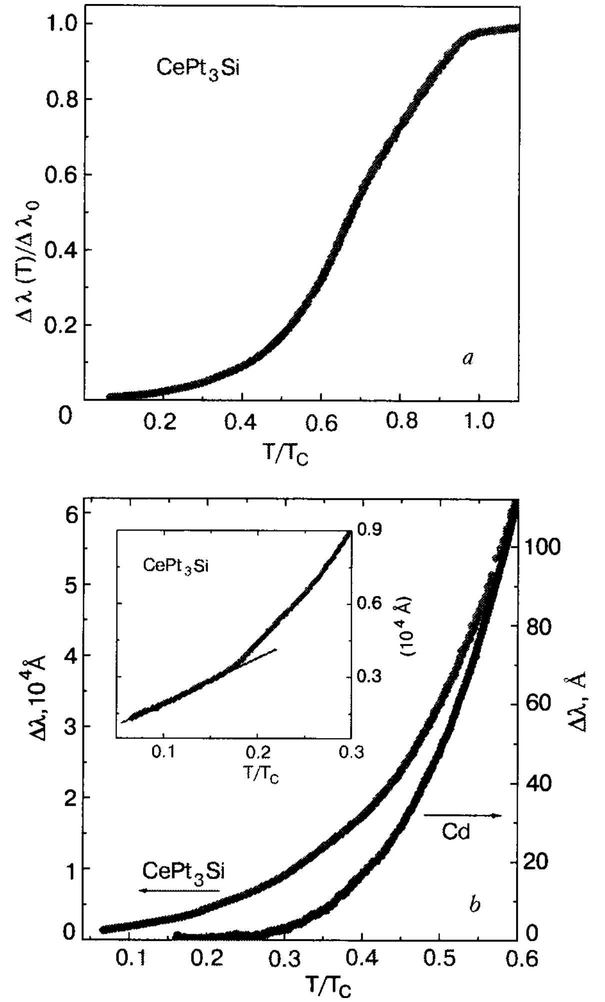

FIG. 10. Normalized variation $\Delta\lambda(T)/\Delta\lambda_0$ versus T/T_c in a polycrystalline $\mathrm{CePt_3Si}$ sample (a). Low-temperature behavior of $\Delta\lambda(T)$ in polycrystalline $\mathrm{CePt_3Si}$ and Cd samples. $\lambda(T)$ is independent of temperature below $0.28T_c$ in cadmium, as expected for an s-wave superconductor. The inset displays a linear low-temperature behavior of $\lambda(T)$ in $\mathrm{CePt_3Si}$ (b).

$$\frac{\lambda^2(0)}{\lambda^2(T)}=\left[1+2\left\langle\int_\Delta^\infty dE\,\frac{\partial f}{\partial E}\,\frac{E}{\sqrt{E^2-\Delta^2(T,\theta,\varphi)}}\right\rangle\right]. \tag{7}$$

Here $\langle ...\rangle$ represents an angular average over the Fermi surface, and f is the Fermi function. Evidently the temperature dependence of $\lambda(T)$ depends on the topology of the gap structure. For line nodes in the energy gap the penetration depth is expected to be linear in the low temperature limit, where the temperature dependence of the energy gap can be neglected. Assuming that CePt$_3$Si is both a clean ($l>\xi_0$) and a local ($\lambda(0)>\xi_0$) superconductor, as was discussed above, the penetration depth experimental result points out to the existence of lines of nodes in the structure of the superconducting pairing state and, hence, to unconventional superconductivity in CePt$_3$Si. For this material with a tetragonal crystal lattice a p-wave pairing symmetry, like $d(k)=\hat{x}k_y-\hat{y}k_x$ proposed earlier by Frigeri *et al.*, will not be consistent with line nodes, because for materials with strong spin-orbit coupling all the spin-triplet states are predicted to have point nodes.[30] Thus, the T-linear variation of the penetration depth suggests possibly a d-wave (spin-singlet) type of pairing symmetry in the energy gap.

A broad shoulder in $\Delta\lambda(T)$ just below T_c, like the one observed in Fig. 10a, is usually associated in polycrystalline samples to intergrain or proximity effects. However, this effect is not expected to be relevant in the present case, because of the high quality of the polycrystalline sample and the very small measuring magnetic fields (about 5 mOe).[27] $\Delta\lambda(T)$ for this sample has an inflection point around 0.52 K temperature that is near to the second superconducting transition (0.55 K) recently found in CePt$_3$Si.[12] Thus, it is tempting to relate the shoulder to this second transition. However, the inflection point—or similar feature—does not seem to be present in preliminary results (obtained by one of the authors) in a sedimented powder sample, where the intrinsic behavior is thought to be more pronounced. Thus, no conclusions can be drawn on the second transition from the present measurements of the penetration depth.

C. Symmetry aspects

Time reversal invariance and inversion symmetry are essential ingredients for superconductivity. They allow us to distinguish pairing with spin singlet and spin triplet configuration and even and odd parity. Due to Fermion antisymmetry of the Cooper pair wavefunction these are uniquely combined into even parity spin singlet and odd parity spin triplet pairing states. The formation of Cooper pairs with vanishing total momentum relies on the availability of degenerate electron states of opposite momentum on the Fermi surfaces. It is generally believed that for spin singlet Cooper pairing time reversal invariance provides the necessary conditions, while spin triplet pairing needs additionally an inversion center.[2] The absence of inversion symmetry removes, however, the distinction of even and odd parity and leads immediately to a mixing also of the spin channels.[31]

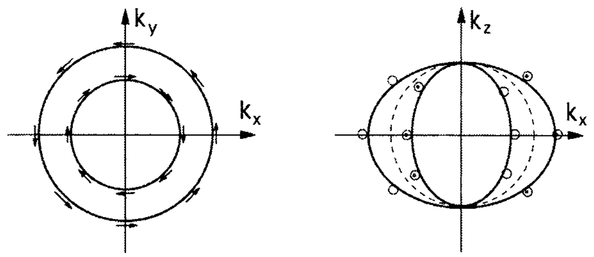

FIG. 11. Fermi surface splitting. The lack of inversion symmetry gives rise to antisymmetric spin-orbit coupling which leads in general to a splitting of the spin degeneracy of the electronic states. The figure depicts schematically the splitting of the Fermi surfaces for the generating point group C_{4v} CePt$_3$Si. The spinor states are **k**-dependent in the way that the spin quantization axes lie perpendicular to the Fermi surface and the z axis with the spin pointing in opposite direction for the two Fermi surfaces. This feature is essential for the possible spin configuration of the pairing states which can be constructed from two electrons on the same Fermi surface.

The absence of inversion symmetry gives rise to antisymmetric spin–orbit coupling. In the case of CePt$_3$Si the generating point group is C_{4v}, which implies that there is no reflection symmetry $z\rightarrow -z$, where z is the fourfold tetragonal rotation axis. This is incorporated into band structure by a Rashba-like term

$$\epsilon_{\mathbf{k}}\sigma_0\rightarrow\epsilon_{\mathbf{k}}\sigma_0+\alpha(\hat{z}\times\mathbf{k})\cdot\boldsymbol{\sigma} \tag{8}$$

with σ_0 as the unit matrix and $\boldsymbol{\sigma}$ as the Pauli matrices in the electron spinor space. The electron bands split into two, yielding two different Fermi surfaces with opposite spinor orientation as depicted in Fig. 11. Obviously there is now a clear restriction on the possible spin configurations for zero momentum Cooper pairs.

The mixing of the spin singlet and spin triplet channel for this electron band structure leads to an non-vanishing spin susceptibility at $T=0$ in any case.[31–33] Thus the absence of paramagnetic limiting would be naturally explained. It was suggested, however, by Kaur and collaborators that in high magnetic fields perpendicular to the z-axis a novel superconducting phase with a helical order parameter could be realized which would leave its traces in the temperature dependence of the upper critical field.[34]

So far the symmetry of the order parameter remains an open question. However, theoretical considerations suggest that the lack of inversion symmetry introduces several complications in the microscopic discussion of superconductivity.[31,32,35–39]

III. SUMMARY

We summarize that non-centrosymmetric CePt$_3$Si is a heavy-fermion SC with $T_c=0.75$ K that orders magnetically at $T_N=2.2$ K. Specific heat, NMR, and μSR studies indicate that superconductivity and long range magnetic order coexist on a microscopic scale and may be originated by two different sets of electrons. The NMR relaxation rate $1/T_1$ shows unexpected features which were neither found before in conventional nor in heavy fermion SC, indicative of very unusual shapes of the SC order parameter. Unconventional SC is backed also by the present penetration depth studies. In fact, the various theoretical scenarios developed for this compound support these conclusions.

This work was supported by the Austrian FWF P16370, P18054, and by FONACIT of Venezuela under Grant No. S1-2001000639.

*E-mail: ernst.bauer@ifp.tuwien.ac.at

---

[1] E. Bauer, G. Hilscher, H. Michor, Ch. Paul, E. W. Scheidt, A. Gribanov, Yu. Seropegin, H. Noel, M. Sigrist, and P. Rogl, Phys. Rev. Lett. **92**, 027003 (2004).

[2] P. W. Anderson, Phys. Rev. B **30**, 4000 (1984).

[3] M. A. Continentino, S. N. de Medeiros, M. T. D. Orlando, M. B. Fontes, and E. M. Baggio-Saitovitch, Phys. Rev. B **64**, 012404 (2001).

[4] N. Metoki, K. Kaneko, T. D. Matsuda, A. Galatanu, T. Takeuchi, S. Hashimoto, T. Ueda, R. Settai, Y. Onuki, and N. Bernhoeft, J. Phys.: Condens. Matter **16**, L207 (2004).

[5] H. U. Desgranges and K. D. Schotte, Phys. Lett. A **91**, 240 (1982).

[6] M. Besnus, M. J. Braghta, A. Hamdaoui, and A. Meyer, J. Magn. Magn. Mater. **104–107**, 1385 (1992).

[7] K. Kadowaki and S. B. Woods, Solid State Commun. **58**, 507 (1986).

[8] N. Tsujii, K. Yoshimura, and K. Kosuge, J. Phys.: Condens. Matter **15**, 1993 (2003).

[9] E. Bauer, R. Lackner, G. Hilscher, H. Michor, M. Sieberer, A. Eichler, A. Gribanov, Y. Seropegin, and P. Rogl, J. Phys.: Condens. Matter **17**, 1877 (2005).

[10] D. T. Adroja, J. G. Park, K. A. McEwen, N. Takeda, M. Ishikawa, and J.-Y. So, Phys. Rev. B **68**, 094425 (2003).

[11] A. P. Makenzie and Y. Maeno, Rev. Mod. Phys. **75**, 657 (2003).

[12] E. W. Scheidt, F. Mayr, G. Eickerling, P. Rogl, and E. Bauer, J. Phys.: Condens. Matter **17**, L121 (2005).

[13] See, for example, M. Tinkham, *Introduction to Superconductivity*, McGraw-Hill, New York (1975).

[14] U. Rauchschwalbe, Physica B **147**, 1 (1987).

[15] R. Movshovich, M. Jaime, J. D. Thompson, C. Petrovic, Z. Fisk, P. G. Pagliuso, and J. L. Sarrao, Phys. Rev. Lett. **86**, 5152 (2001).

[16] A. Amato, E. Bauer, and C. Baines, Phys. Rev. B **71**, 092501 (2005).

[17] E. Bauer, G. Hilscher, H. Michor, M. Sieberer, E. W. Scheidt, A. Gribanov, Yu. Seropegin, P. Rogl, A. Amato, W. Y. Song, J.-G. Park, D. T. Adroja, M. Nicklas, G. Sparn, M. Yogi, and Y. Kitaoka, Physica B **359–361,** 360 (2005).

[18] C. Petrovic, R. Movshovich, M. Jaime, P. G. Pagliuso, M. F. Hundley, J. L. Sarrao, Z. Fisk, and J. D. Thompson, Europhys. Lett. **53**, 354 (2001).

[19] G. M. Luke, A. Keren, K. Kojima, L. P. Le, B. J. Sternlieb, W. D. Wu, Y. J. Uemura, Y. Onuki, and T. Komatsubara, Phys. Rev. Lett. **73**, 1853 (1994).

[20] R. Feyerherm, A. Amato, C. Geibel, F. N. Gygax, P. Hellmann, R. H. Heffner, D. E. MacLaughlin, R. Müller-Reisener, G. J. Nieuwenhuys, A. Schenck, and F. Steglich, Phys. Rev. B **56**, 699 (1997).

[21] R. Caspary, P. Hellmann, M. Keller, G. Sparn, C. Wassilew, R. Köhler, C. Geibel, C. Schank, F. Steglich, and N. E. Phillips, Phys. Rev. Lett. **71**, 2146 (1993)

[22] M. Yogi, Y. Kitaoka, S. Hashimoto, T. Yasuda, R. Settai, T. D. Matsuda, Y. Haga, Y. Onuki, P. Rogl, and E. Bauer, Phys. Rev. Lett. **93**, 027003 (2004).

[23] L. C. Hebel and C. P. Slichter, Phys. Rev. **107**, 901 (1957).

[24] H. Tou, Y. Kitaoka, K. Asayama, C. Geibel, C. Schank, and F. Steglich, J. Phys. Soc. Jpn. **64**, 725 (2003).

[25] R. Balian and N. R. Werthamer, Phys. Rev. **131**, 1553 (1963).

[26] I. Bonalde, W. Brämer-Escamilla, and E. Bauer, Phys. Rev. Lett. **94**, 207002 (2005).

[27] R. B. Goldfarb, M. Lelental, and C. A. Thompson, in *Magnetic Susceptibility of Superconductors and Other Spin Systems*, R. A. Hein (ed.), Plenum Press, New York (1991), p. 49.

[28] T. Xiang, C. Panagopoulos, and J. R. Copper, Int. J. Mod. Phys. B **12**, 1007 (1998); C. Panagopoulos, Phys. Rev. Lett. **79**, 2320 (1997).

[29] F. Manzano, A. Carrington, N. E. Hussey, S. Lee, A. Yamamoto, and S. Tajima, Phys. Rev. Lett. **88**, 047002 (2002).

[30] M. Sigrist and K. Ueda, Rev. Mod. Phys. **63**, 239 (1991).

[31] L. P. Gor'kov and E. I. Rashba, Phys. Rev. Lett. **87**, 037004 (2001).

[32] P. A. Frigeri, D. F. Agterberg, and M. Sigrist, New J. Phys. **6**, 931 (2004).

[33] L. N. Bulaevski, A. A. Guseinov, and A. I. Rusinov, Sov. Phys. JETP **44**, 1243 (1976).

[34] R. P. Kaur, D. F. Agterberg, and M. Sigrist, cond-mat/0408149.

[35] K. V. Samokhin, E. S. Zijlstra, and S. K. Bose, Phys. Rev. B **69**, 094514 (2004).

[36] P. A. Frigeri, D. F. Agterberg, A. Koga, and M. Sigrist, Phys. Rev. Lett. **92**, 097001 (2004).

[37] V. P. Mineev, Int. J. Mod. Phys. B **18**, 2963 (2004).

[38] I. A. Sergienko and S. Curnoe, Phys. Rev. B **70**, 144522 (2004).

[39] S. S. Saxena and P. Monthoux, Nature (London) **427**, 799 (2004).

This article was published in English in the original Russian journal. Reproduced here with stylistic changes by AIP.

LOW TEMPERATURE PHYSICS VOLUME 31, NUMBERS 8–9 AUGUST–SEPTEMBER 2005

Antiferromagnetism and superconductivity of the two-dimensional extended *t*-*J* model

C. T. Shih,* J. J. Wu, and Y. C. Chen

Department of Physics, Tunghai University, Taichung, Taiwan

C. Y. Mou and C. P. Chou

Department of Physics, National Tsing Hua University, Hsinchu, Taiwan

R. Eder

Institut für Festkörperphysik, Forschungszentrum Karlsruhe, Germany

T. K. Lee

Institute of Physics, Academia Sinica, Nankang, Taiwan

(Submitted January 13, 2005)
Fiz. Nizk. Temp. **31**, 995–1001 (August–September 2005)

The mechanism of high-temperature superconductivity (HTS) and the correlation between the antiferromagnetic long-range order (AFLRO) and superconductivity (SC) are the central issues of the study of HTS theory. SC and AFLRO of the hole-doped two-dimensional extended t-J model are studied by the variational Monte Carlo method. The results show that SC is greatly enhanced by the long-range hopping terms t' and t'' for the optimal and overdoped cases. The phase of coexisting SC and AFM in the t-J model disappears when t' and t'' are included. It is concluded that the extended t-J model provides a more accurate description for HTS than the traditional t-J model does. The momentum distribution function $n(\mathbf{k})$ and the shape of Fermi surface play critical roles for establishing the phase diagram of HTS materials. *© 2005 American Institute of Physics.* [DOI: 10.1063/1.2008136]

I. INTRODUCTION

The two-dimensional (2D) t-J model was proposed to provide the mechanism of superconductivity (SC)[1,2] right after the discovery of high-temperature superconductivity (HTS). This idea quickly gained momentum when variational calculations showed that the doping dependence of pairing correlation[3,4] and the phase diagram of the antiferranagnetic long-range order (AFLRO) and SC seem to agree with experimental results fairly well.[5] However, the calculation beyond variational method showed that SC of the pure 2D t-J model was not large enough to explain such high transition temperature of the cuprates.[6] Up to now, this issue has still not been settled.[7–9]

Interplay between the d-wave SC and AFLRO is another one of the critical issues in the physics of HTS.[10,11] Early experimental results showed the existence of AFLRO at temperature lower than the Néel temperature T_N in the insulating perovskite parent compounds of the cuprates. When charge carriers are doped, AFLRO is destroyed quickly and then SC appears. In most thermodynamic measurements for hole doped cuprates, AFLRO does not coexist with SC[12] and disappears completely around doping density $\delta_h \sim 5\%$. However, recent experiments such as muon spin rotation and elastic neutron scattering show that the spin density wave (SDW) may compete, or coexist with SC.[13–18] These results suggest that AFLRO may coexist with SC, but the possibility of inhomogeneous phases is not completely ruled out.

For the theoretical part of this issue, analytical and numerical studies of the t-J model show that at half-filling, the d-wave resonating valence bond (RVB) state with AFLRO is a good trial wave function (TWF) and that SC is absent due to the constraint of no double occupancy. Upon doping, the carriers become mobile and SC sets in while AFLRO is quickly suppressed. However, AFLRO will survive until the hole density $\delta_h > 10\%$, which is much larger than the critical density observed by experiments. SC and AFLRO coexist in the very underdoped regime.[5,19–22]

The discrepancies imply that the t-J model may be insufficient to describe the physics of HTS. On the other hand, there are several experimental and theoretical studies suggesting the presence of the next- and third-nearest-neighbor hopping terms t' and t'' in cuprates. For example, the topology of the large Fermi surface (FS) and the single-hole dispersion studied by angle-resolved photoemission spectroscopy (ARPES), and the asymmetry of phase diagrams of the electron- and hole-doped cuprates can be understood by introducing these terms.[23]

It is suggested that the longer range hopping terms may play important roles on the mechanism of HTS. Results of band-structure calculations[24,25] and experimental analysis[26] show that T_c is enhanced by the next-nearest neighbor hopping t'/t, and the highest $T_{c,\max}$ for different monolayer hole doped cuprates strongly correlates with t'/t. However, this contradicts with previous results[27,28] of exact calculations that for the hole doped systems, introducing t' into the t-J model will suppress pairing.

We will discuss the model and the trial wave function in Sec. 2, and the variational Monte Carlo (VMC) method results for SC, AFLRO, and the shape of the Fermi surface in Sec. 3. At last we will make a summary in Sec. 4.

II. THE MODEL AND THE WAVE FUNCTIONS

The Hamiltonian of the extended t-J model is

$$H=H_t+H_J=-\sum_{ij} t_{ij}(\tilde{c}^{\dagger}_{i,\sigma}\tilde{c}_{j,\sigma}+\text{H.c.})$$
$$+J\sum_{\langle i,j\rangle}\left(\mathbf{S}_i\cdot\mathbf{S}_j-\frac{1}{4}n_in_j\right), \qquad (1)$$

where $t_{ij}=t,\ t',\ t''$, and 0 for sites i and j that are nearest, next nearest, and third nearest neighbors and other sites, respectively. $\langle i,j\rangle$ in H_J means the spin-spin interaction occurs only for nearest neighbors. $\tilde{c}_{i,\sigma}=(1-n_{i,-\sigma})c_{i,\sigma}$ satisfies the no-double-occupancy constraint. At half-filling, the system is reduced to the Heisenberg Hamiltonian H_J. As carriers are doped into the parent compound, H_t is included in the Hamiltonian.

To solve the ground-state wave function of this Hamiltonian, three mean-field order parameters are introduced:[21,29] the staggered magnetization $m_s=\langle S^z_A\rangle=-\langle S^z_B\rangle$, where the lattice is divided into A and B sublattices, the uniform bond order parameters $\chi=\langle\Sigma_\sigma c^{\dagger}_{i\sigma}c_{j\sigma}\rangle$, and the d-wave RVB (d-RVB) order parameter $\Delta=\langle c_{j\downarrow}c_{i\uparrow}-c_{j\uparrow}c_{i\downarrow}\rangle$, if i and j are n.n. sites in the x direction, and $-\Delta$ for the y direction. The Lee-Shih wave function, which is the mean-field ground-state wave function, is

$$|\Psi_{LS}\rangle=P_d\left(\sum_{\mathbf{k}\in SBZ}(A_{\mathbf{k}}a^{\dagger}_{\mathbf{k}\uparrow}a^{\dagger}_{-\mathbf{k}\downarrow}+B_{\mathbf{k}}b^{\dagger}_{\mathbf{k}\uparrow}b^{\dagger}_{-\mathbf{k}\downarrow})\right)^{N_s/2}|0\rangle, \qquad (2)$$

where N_s is the total number of sites and

$$A_{\mathbf{k}}=(E^{(1)}_{\mathbf{k}}+\xi_{\tilde{\mathbf{k}}})/\Delta_{\mathbf{k}},\quad B_{\mathbf{k}}=-(E^{(2)}_{\mathbf{k}}-\xi^{+}_{\mathbf{k}})/\Delta_{\mathbf{k}}$$

with

$$E^{(1)}_{\mathbf{k}}=(\xi^{-\,2}_{\mathbf{k}}+\Delta^2_{\mathbf{k}})^{1/2},\quad E^{(2)}_{\mathbf{k}}=(\xi^{+\,2}_{\mathbf{k}}+\Delta^2_{\mathbf{k}})^{1/2}.$$

Here $\Delta_{\mathbf{k}}=\frac{3}{4}J\Delta(\cos k_x-\cos k_y)$. The energy dispersions for the two SDW bands are

$$\xi^{\pm}_{\mathbf{k}}=\pm[(\varepsilon_{\mathbf{k}}+\mu)^2+(Jm_s)^2]^{1/2}-\mu'$$

with

$$\varepsilon^{\mathbf{k}}=-2\left(t\delta+\frac{3}{8}J\chi\right)(\cos k_x+\cos k_y).$$

$$a_{\mathbf{k}\sigma}=\alpha_{\mathbf{k}}c_{\mathbf{k}\sigma}+\sigma\beta_{\mathbf{k}}c_{\mathbf{k}+\mathbf{Q}\sigma}$$

and $b_{\mathbf{k}\sigma}=-\sigma\beta_{\mathbf{k}}c_{\mathbf{k}\sigma}+\alpha_{\mathbf{k}}c_{\mathbf{k}+\mathbf{Q}\sigma}$, where $\mathbf{Q}=(\pi,\pi)$,

$$\alpha^2_{\mathbf{k}}=\frac{1}{2}\{1-[(\varepsilon_{\mathbf{k}}+\mu')/(\xi^{+}_{\mathbf{k}}+\mu')]\},$$

$$\beta^2_{\mathbf{k}}=\frac{1}{2}\{1+[(\varepsilon_{\mathbf{k}}+\mu')/(\xi^{+}_{\mathbf{k}}+\mu')]\},$$

are the operators of the lower and upper SDW bands, respectively,

$$\mu'=\mu+4t'_v\cos k_x\cos k_y+2t''_v(\cos 2k_x+\cos 2k_y),$$

where μ is the chemical potential determining the number of electrons, and t'_v and t''_v are variational parameters corresponding to the next and third nearest neighbor hoppings. t'_v and t''_v are not necessarily equal to the bare values t' and t'' because the constraint strongly renormalizes the hopping amplitude. Note that the summation in Eq. (2) is taken over the sublattice Brillouin zone (SBZ). The operator P_d enforces the constraint of no doubly occupied sites for cases with finite doping.

For the half-filled case, $\mu=t'=t''=0$ and the optimal variational energy of this trial wave function (TWF) obtained by tuning Δ and m_s in the VMC simulation is -0.332 J per bond, which is within 1% of the best estimate of the ground-state energy of the Heisenberg model.[30] For the case of pure AFLRO without Δ, the energy per bond is about 3 to 4% higher.

Upon doping, there are two methods of modifying the TWF: one is to use a nonzero μ to control the filling of the SDW bands,[29] the other is to create charge excitations from the half-filled ground states.[31] For the former method, the TWF is optimized by tuning Δ, m_s, t'_v, t''_v, and μ. Note that for larger doping densities, AFLRO disappears ($m_s=0$) and the wave function reduces to the standard d-RVB wave function. For the latter method, the wave function is the "small Fermi pocket" state $|\Psi_p\rangle$:

$$|\Psi_p\rangle=P_d\left(\sum_{\mathbf{k}\in SBZ,\mathbf{k}\notin Q_p}(A_{\mathbf{k}}a^{\dagger}_{\mathbf{k}\uparrow}a^{\dagger}_{-\mathbf{k}\downarrow}+B_{\mathbf{k}}b^{\dagger}_{\mathbf{k}\uparrow}b^{\dagger}_{-\mathbf{k}\downarrow})\right)^{N_s/2}|0\rangle. \qquad (3)$$

The $\mathbf{k}$-points in Q_p are the momenta of the electron singlet pairs (with momenta and spin $(\mathbf{k}\uparrow,-\mathbf{k}\downarrow)$ removed from the half-filled FS. Thus the number of holes is twice of the number of $\mathbf{k}$-points in Q_p, μ, t'_v and t''_v are identical to zero in Eq. (2) because the size and shape of FS are determined by the choice of Q_p. Note that no matter what $\mathbf{k}$'s are chosen in Q_p, the total momentum of the wave function is zero. The $\mathbf{k}$'s can be viewed as "hidden quantum numbers" of the wave function.

In general, for the ground state the set Q_p should be determined variationally. As we expected, it agrees well with the rigid band picture for very underdoped systems.[31] For example, there is only one point in the two-hole system.

The variational energies for several choices of $\mathbf{k}$ in a 12×12 lattice are shown in Fig. 1. It can be seen that for both the $(t',t'')=(-0.1,0.05)t$ (full circles) and $(t',t'')=(-0.3,0.2)t$ (open circles) cases, the $\mathbf{k}$ with lowest energy is $(\pi/2,\pi/2)$. The $\mathbf{k}$'s with the second-lowest energy are $(2\pi/3,\pi/3)$ and $(\pi/2,\pi/3)$ for $(t',t'')=(-0.1,0.05)t$ and $(t',t'')=(-0.3,0.2)t$, respectively.

According to the rigid-band assumption, we expect that the best choice of Q_p for the 4-hole system is $\{(\pi/2,\pi/2),(-\pi/2,\pi/2)\}$. And the Q_p's for the 6-hole system with

$$(t',t'')=(-0.3,0.2)t\ \text{ and}(t',t'')=(-0.1,0.05)t$$

are

$$\{(\pi/2,\pi/2),(-\pi/2,\pi/2),(\pi/2,\pi/3)\},$$

and

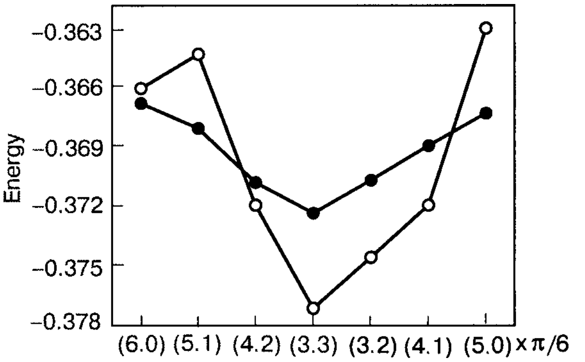

FIG. 1. Energies for two holes in a 12×12 lattice for $J/t=0.3$, $(t',t'')=(-0.1,0.05)t$ (filled circles) and $(t',t'')=(-0.3,0.2)t$ (unfilled circles). **k** is the "hidden quantum number" corresponding to the momentum of the pair removed from the half-filled Fermi surface. Note that the total momenta of all the wave functions are zero.

$$\{(\pi/2,\pi/2),(-\pi/2,\pi/2),(2\pi/3,\pi/3)\},$$

respectively.

Figure 2 shows the choices of Q_p's for several doping densities (0–10 holes) for the $(t',t'')=(-0.3,0.2)t$ case. The validity of the rigid-band picture has been checked by comparing several Q_p's for the same number of holes for these very underdoped cases.

Another issue is that the choice of Q_p may change the total symmetry of the wave function. For example, Fig. 2e shows that Q_p for 8 holes is

$$\{(\pi/2,\pi/2),(-\pi/2,\pi/2),(\pi/2,3),(-\pi/2,-\pi/3)\}.$$

We can also choose

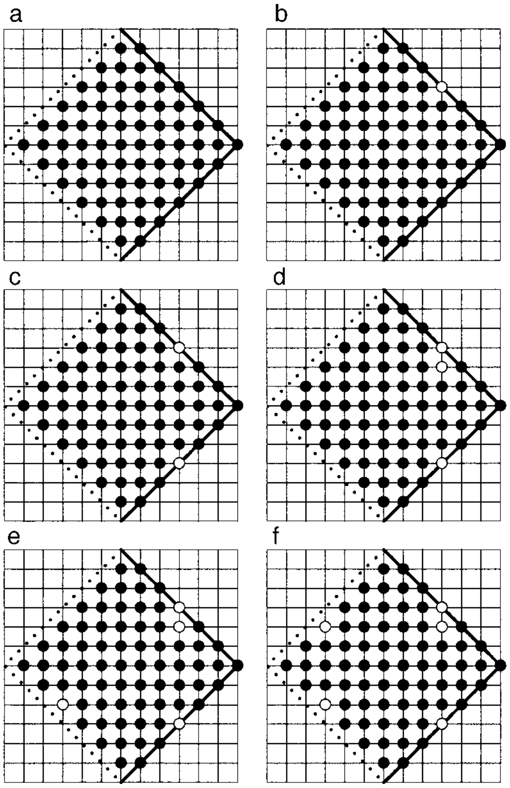

FIG. 2. Choices of Q_p (unfilled circles) for several doping densities for $t'/t=-0.3$ and $t''/t=0.2$ in **k** space. The filled circles are the occupied **k**-points: 0 (a), 2 (b), 4 (c), 6 (d), 8 (e), 10 (f) holes.

$$Q_p=\{(\pi/2,\pi/2),(-\pi/2,\pi/2),(\pi/2,\pi/3),(\pi/3,\pi/2)\}.$$

The variational energies of these two wave functions, long-range pair-pair correlation, and staggered magetization are almost identical (within error bars). Since $\mathbf{k}=(\pm\pi/2,\pm\pi/3)$ and $(\pm\pi/3,\pm\pi/2)$ are all degenerate for the two-hole system, the wave function could also be degenerate for those Q_p's with **k**-points $(\pm\pi/2,\pm\pi/2)$ and any two of $\mathbf{k}=(\pm\pi/2,\pm\pi/3)$ and $(\pm\pi/3,\pm\pi/2)$ for the 8-hole system. This conjecture has been verified numerically. Thus the best TWF should be a linear combination of all these wave functions. For simplicity, we choose only one of the Q_p in the following calculation. The properties of SC and AFLRO are not affected by this simplification.[32]

III. RESULTS AND DISCUSSION

The staggered magnetization

$$\langle M\rangle=\frac{1}{N_s}\left\langle\sum_j \mathrm{e}^{i\mathbf{Q}\cdot\mathbf{R}_j}S^z_{\mathbf{R}_j}\right\rangle, \tag{4}$$

the momentum distribution function

$$n(\mathbf{k})=\frac{1}{N_s}\sum_{ij\sigma}\mathrm{e}^{i\mathbf{k}\cdot(\mathbf{R}_i-\mathbf{R}_j)}\langle c^\dagger_{i\sigma}c_{j\sigma}\rangle, \tag{5}$$

and the d-wave pair-pair correlation

$$P_d(\mathbf{R})=\frac{1}{N_s}\left\langle\sum_i \Delta^\dagger_{\mathbf{R}_i}\Delta_{\mathbf{R}_i+\mathbf{R}}\right\rangle, \tag{6}$$

where

$$\Delta_{\mathbf{R}_i}=c_{\mathbf{R}_i\uparrow}(c_{\mathbf{R}_i+\hat{\mathbf{x}}\downarrow}+c_{\mathbf{R}_i-\hat{\mathbf{x}}\downarrow}-c_{\mathbf{R}_i+\hat{\mathbf{y}}\downarrow}-c_{\mathbf{R}_i-\hat{\mathbf{y}}\downarrow})$$

are measured for $J/t=0.3$ and (a) $t'=t''=0$, (b) $(t',t'')=(-0.3,0.2)t$ and (c) $(t',t'')=(-0.1,0.05)t$ cases for the 12×12 lattice with periodic boundary condition. P_d^{ave} is the averaged value of the long-range part ($|\mathbf{R}|>2$) of $P_d(\mathbf{R})$. The optimal wave function for different densities are determined by minimizing the variational energies among $|\Psi_p(m_s,\Delta,\{Q_p\})\rangle$ and $|\Psi_{LS}(m_s,\Delta,t'_v,t''_v,\mu)\rangle$. We will discuss the results for these three cases in this section.

A. $t'=t''=0$

It can be seen in Fig. 3a that in the underdoped region for the $J/t=0.3$, $t'=t''=0$ case, AFLRO coexists with SC for density smaller than $\delta_c\sim 10\%$. The δ_c is smaller than the weak-coupling mean-field result $\sim 15\%$,[21] but is still larger than the phase boundary of AFLRO determined by experiments ($\delta_c<5\%$). The energies of $|\Psi_{LS}\rangle$ are lower than those of $|\Psi_P\rangle$ for all doping densities in this case. This result is also consistent with the results reported by Himeda and Ogata.[22] Comparison of the VMC result with that of the weak-coupling one seems to indicate that the rigorous no-double-occupancy constraint suppresses the AFLRO faster than the constraint-relaxed mean-field approximation.

P_d^{ave} shows a dome-like shape which agrees well with the experiments except in the slightly doped AFLRO region. It is well known that the variational method usually overestimates the order parameters. Our previous studies using calculations beyond VMC show that P_d^{ave} will be suppressed greatly when the wave function is projected to the true

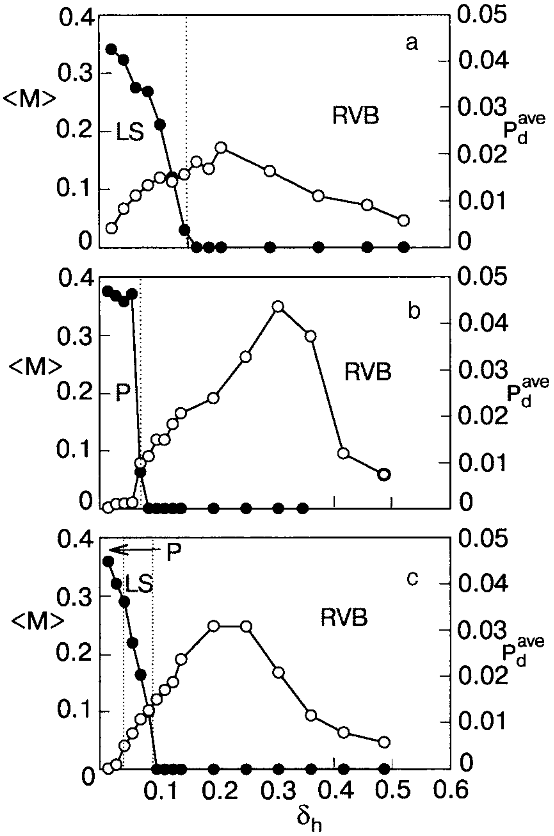

FIG. 3. $\langle M\rangle$ (filled circles) and P_d^{ave} (unfilled circles) for $J/t=0.3$: $t'=t''=0$ (a), $(t',t'')=(-0.3,0.2)t$ (b), and $(t',t'')=(-0.1,0.05)t$ (c) for a hole-doped 12×12 lattice. The vertical dashed lines show the critical doping densities of level crossing. P ($|\Psi_P\rangle$), LS ($|\Psi_{LS}\rangle$), and RVB ($|\Psi_{LS}\rangle$ with $m_s=0$) represent the best TWFs of each region.

ground state. Note that the two-hole binding energy becomes positive (no binding) in the thermodynamic limit.[6]

B. $t'/t=-0.3$ and $t''/t=0.2$

Now we examine the phase diagram for $J/t=0.3$, $t'/t=-0.3$, and $t''/t=0.2$, parameters for YBCO and BSCO compounds. The results are shown in Fig. 3b. It was found that level crossing occurs at $\delta_c\sim0.06$. For $\delta_h<0.06$, $|\Psi_P\rangle$ is the ground-state wave function and $\langle M\rangle$ is a little larger than in the $t'=t''=0$ case, while P_d^{ave} is suppressed by one order of magnitude. Thus there is AFLRO but no SC in this regime. For δ_h larger than 0.06, the RVB state ($m_s=0$ in $|\Psi_{LS}\rangle$) optimizes the energy. P_d^{ave} increases, and $\langle M\rangle$ drops sharply to zero. Unlike the $t'=t''=0$ case, there is no region optimized by $|\Psi_{LS}\rangle$ with nonzero m_s. In conclusion, there is no coexistence of AFLRO and SC for the $(t',t'')=(-0.3,0.2)t$ case.

To show that $|\Psi_{LS}\rangle$ and $|\Psi_P\rangle$ belong to two different types of wave function, we calculate their overlap. $\langle\Psi_{LS}|\Psi_P\rangle/(|\Psi_{LS}||\Psi_P|)$ is only 0.0113(4).[33] The near-orthogonality of the two wave functions implies that the ground-state wave functions switch at the critical density.

The result that the critical δ_h for negative t'/t is smaller than that of the $t'=0$ case is consistent with the results evaluated by exact diagonalization,[35,36] and the suppression of coexistence of AFLRO and SC is consistent with the slave-boson mean-field theory.[37]

For a little larger doping density $0.06<\delta_h<0.15$, it can be seen that P_d^{ave} starts to grow but is still smaller than that in the $t'=t''=0$ case. The suppression of P_d^{ave} by t' and t'' in the underdoped regime is consistent with the results[27,28] obtained the density matrix renormalization group (DMRG) method. Interestingly, for even larger δ_h, P_d^{ave} grows greatly and reaches the maximum at $\delta_h\sim30\%$, and the SC region extends to $\delta_h\sim0.4$. The maximal P_d^{ave} is larger than the $t'=t''=0$ value at the same density by almost one order of magnitude, and about 2.5 times larger than the maximum of the optimal value of the $t'=t''=0$ case. The enhancement of P_d^{ave} may come from the deformation of the Fermi surface. The electron occupation at the **k**-points near $(\pi,0)$ is increased by a negative t'. The results from exact diagonalization and slave-boson mean-field theory also show similar behavior.[34]

The great enhancement of pairing due to t' may provide a possible mechanism for HTS. But the doping density $\delta_{\max}$ with maximal P_d^{ave} is too large ($\sim30\%$) in comparison with experiments (15%). This discrepancy may disappear for the real ground state of the extended *t*-*J* model. From our experience, if we do the calculation beyond VMC, the amplitude of P_d^{ave} will be suppressed and $\delta_{\max}$ will move to a smaller value.[6] If this trend is true for the *t*-*J* type models, we expect that $\delta_{\max}$ may move toward the more physical value. This conjecture will be investigated in the future.

C. $t'/t=-0.1$ and $t''/t=0.05$

For the lanthanum materials with $t'/t=-0.1$ and $t''/t=0.05$, the behaviors are more complex. It can be seen from Fig. 3c that for hole density $\delta_h<4\%$, $|\Psi_P\rangle$ optimizes the variational energy, and the phase in this region is ARFLO but not SC. For $4\%<\delta_h<10\%$, $|\Psi_{LS}\rangle$ is the best TWF with nonzero m_s and Δ. AFLRO and SC coexist in the ground state of this density interval. At even larger dopings, m_s in $|\Psi_{LS}\rangle$ vanishes and the phase becomes pure SC. The maximum of the SC dome is at $\delta_h\sim20\%$, and the maximal P_d^{ave} is about 1.5 times larger than the $t'=t''=0$ value.

Since the phase transition comes from the level crossing of the two classes of states $|\Psi_P\rangle$ and $|\Psi_{LS}\rangle$, it is a first-order phase transition. It is quite natural to have inhomogeneity in the system near the critical point.[38] It may also lead to other more novel inhomogeneous states such as a stripe phase.[39] Another interesting result of our study is that the noncoexistence of SC and AFLRO is much more robust for systems with larger values of t'/t and t''/t, such as YBCO and BSCO.[25] For LSCO, where t'/t and t''/t are smaller, the tendency toward coexistence is larger and the possibility of an inhomogeneous phase will become much more likely.

D. Shape of the Fermi surface

Figure 4 shows the FS of both under- and overdoped systems with the parameter sets we discussed above. For the underdoped systems ($\delta_h=6/144$), there is a large FS for the $t'=t''=0$ case (Fig. 4a) and a clear "Fermi pocket" for the $t'/t=-0.3$, $t''/t=0.2$ case (Fig. 4b), whose ground-state wave function is $|\Psi_P\rangle$. The shape of the FS for $t'/t=-0.1$ and $t''/t=0.05$ (Fig. 4c) is placed between the previous two cases. The ground-state wave function is $|\Psi_{LS}\rangle$ but the

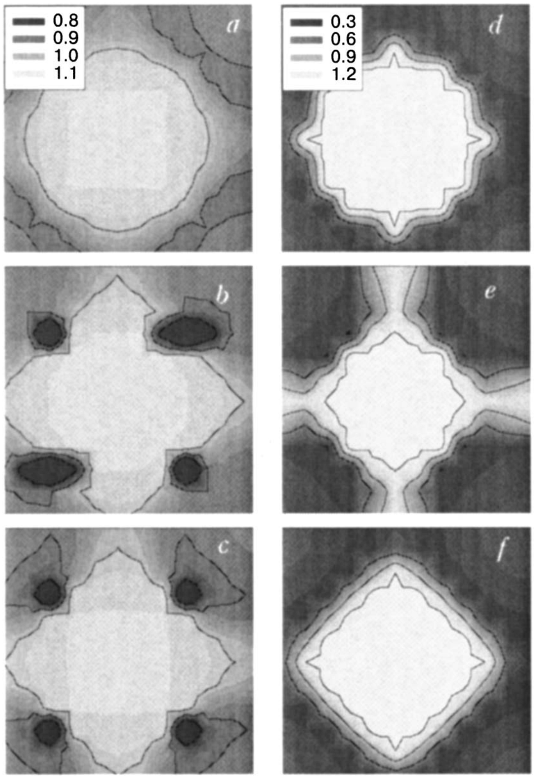

FIG. 4. Contour maps of $n(\mathbf{k})$: $t'=t''=0$ (a), (d); $(t',t'')=(-0.3,0.2)t$ (b),(e); $(t',t'')=(-0.1,0.05)t$ (c),(f). The hole densities are 6/144 for (a), (b), (c), and 44/144 for (d), (e), (f), respectively.

pocket-like feature is still obvious. Lack of a large FS is one of the possible reasons for the suppression of P_d^{ave} by t' in the underdoped region.

For the overdoped systems ($\delta_h=44/144$), the ground-state wave functions for all the three cases are $|\Psi_{LS}\rangle$. They all have large FSs but with different shapes determined mainly by the parameters t'_v and t''_v. It is clear that the distortion of the FS makes $n(\mathbf{k}=(\pi,0))$ for the $t'/t=-0.3$ and $t''/t=0.2$ (Fig. 4e) case much larger than the other two. The shapes of the FS for $t'=t''=0$ (Fig. 4d) and $t'/t=-0.1$ and $t''/t=0.05$ (Fig. 4f) are similar and the occupations near $(\pi,0)$ are both small. For the d-wave SC, the electron pairs with momenta near $(\pi,0)$ contribute to SC most. Thus P_d^{ave} for $t'/t=-0.3$ and $t''/t=0.2$ case is much larger than the other two.

Our results show that P_d^{ave} is closely correlated with $n(\mathbf{k})$ and thus with the shape of the FS. Figure 5 plots the maximal possible value of P_d^{ave} for all doping densities as a function of t'. The maximal P_d^{ave} is proportional to t' in the range $0\geqslant t'\geqslant-(0.3\text{–}0.4)$. Beyond these values pairing is no longer enhanced. Coincidentally, these values are about the same value of t'/t for mercury cuprates, as estimated by Pavarini *et al.*,[25] but much larger than those reported in Ref. 24. Among all the cuprate series, mercury cuprate has held the record of having highest T_c for almost a decade.

The decrease of P_d^{ave} for $-t'\geqslant0.4$ in the overdoped regime such as $\delta=0.31$ is also likely a consequence of the change of the FS. $n(\mathbf{k}=(\pi,0))$ is almost saturated at $-t'=0.4$ and remains unchanged for larger $-t'$. It is not difficult to recognize that as $-t'$ becomes much larger than t, electrons will occupy separate regions around $\mathbf{k}=(\pm\pi,0)$ and $\mathbf{k}=(0,\pm\pi)$. Hence the FS becomes disjoint pieces. Although at $-t'/t=0.4$ the FS is still connected, this tendency is already observed. The density of states starts to decrease, and this is probably the reason for the suppression of pairing beyond $-t'/t\geqslant0.4$.

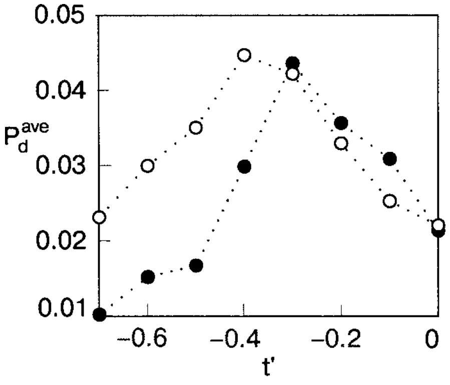

FIG. 5. Maximal P_d^{ave} for different t' with $t''=-t'/2$ for 8×8 (unfilled circles) and 12×12 (filled circles) lattices.

IV. SUMMARY

In summary, a new wave function $|\Psi_P\rangle$ is proposed for the extended t-J model for very low hole densities. The size and shape of the FS and of $|\Psi_P\rangle$ are determined by the choice of pairs with the momenta $\mathbf{k}\in Q_p$ removed from the half-filled system. The chosen $\mathbf{k}$'s are around the $(\pi/2,\pi/2)$ region in $\mathbf{k}$ space for hole-doped materials. The behavior of $|\Psi_P\rangle$ is very different from that of $|\Psi_{LS}\rangle$ which optimizes the energy for the t-J model. In contrast to $|\Psi_P\rangle$, the FS for the states of $|\Psi_{LS}\rangle$ is controlled by the chemical potential μ and the effective long-range hopping terms t'_v and t''_v.

There are three remarkable effects of t' and t'' for the extended t-J model. First, the critical density where AFLRO vanishes is moved to more physical values. Second, the phase of coexisting AFLRO and SC is suppressed. If t' and t'' are large enough (corresponding to the YBCO or BSCO materials), the coexisting phase will disappear. Third, P_d^{ave} is enhanced for the optimal and overdoped region, and suppressed for the underdoped region. This resolves the conflict between the DMRG and band structure calculation results. The enhancement of P_d^{ave} can be explained by the electron occupation near $(\pi,0)$ and FS. These results offer a possible mechanism for HTS.

The work is supported by the National Science Council in Taiwan with Grant Nos. NSC-93-2112-M-029-001-, 93-2112-M-007-009-, 93-2112-M-001-018-, and 93-2112-M029-009. Part of the calculations are performed in the IBM P690 and PC clusters in the National Center for High-Performance Computing in Taiwan, and the PC clusters of the Department of Physics and Department of Computer Science and Engineering of Tunghai University, Taiwan. We are grateful for their help.

[*]E-mail: ctshih@mail.thu.edu.tw

---

[1] P. W. Anderson, Science **235**, 1196 (1987).
[2] F. C. Zhang and T. M. Rice, Phys. Rev. B **37**, 3759 (1988).

[3] C. Gros, Phys. Rev. B **38**, 1196 (1988).

[4] F. C. Zhang, C. Gros, T. M. Rice, and H. Shiba, Supercond. Sci. Technol. **1**, 36 (1988).

[5] T. K. Lee and S. P. Feng, Phys. Rev. B **38**, 11809 (1988).

[6] C. T. Shih, Y. C. Chen, H. Q. Lin, and T. K. Lee, Phys. Rev. Lett. **81**, 1294 (1998).

[7] S. Sorella, G. B. Martins, F. Becca, C. Gazza, L. Capriotti, A. Parola, and E. Dagotto, Phys. Rev. Lett. **88**, 117002 (2002).

[8] T. K. Lee, C. T. Shih, Y. C. Chen, and H. Q. Lin, Phys. Rev. Lett. **89**, 279702 (2002).

[9] S. Sorella, A. Parola, F. Becca, L. Capriotti, C. Gazza, E. Dagotto, and G. Martins, Phys. Rev. Lett. **89**, 279703 (2002).

[10] P. W. Anderson, *The Theory of Superconductivity in the High-T_c Cuprates*, Princeton University Press, Princeton, NJ (1997).

[11] S. C. Zhang, Science **275**, 1089 (1997).

[12] C. M. A. Kastner, R. J. Birgeneau, G. Shirane, and Y. Endoh, Rev. Mod. Phys. **70**, 897 (1998).

[13] B. Lake, H. M. Rønnow, N. B. Christensen, G. Aeppli, K. Lefmann, D. F. McMorrow, P. Vorderwisch, P. Smeibidl, N. Mangkorntong, T. Sasagawa, M. Nohara, H. Takagi, and T. E. Mason, Nature (London) **415**, 299 (2002).

[14] R. I. Miller, R. F. Kiefl, J. H. Brewer, J. E. Sonier, J. Chakhalian, S. Dunsiger, G. D. Morris, A. N. Price, D. A. Bonn, W. H. Hardy, and R. Liang, Phys. Rev. Lett. **88**, 137002 (2002).

[15] J. E. Sonier, K. F. Poon, G. M. Luke, P. Kyriakou, R. I. Miller, R. Liang, C. R. Wiebe, P. Fournier, and R. L. Greene, Phys. Rev. Lett. **91**, 147002 (2003).

[16] Y. Sidis, C. Ulrich, P. Bourges, C. Bernhard, C. Niedermayer, L. P. Regnault, N. H. Andersen, and B. Keimer, Phys. Rev. Lett. **86**, 4100 (2001).

[17] J. A. Hodges, Y. Sidis, P. Bourges, I. Mirebeau, M. Hennion, and X. Chaud, Phys. Rev. B **66**, 020501(R) (2002).

[18] H. A. Mook, P. Dai, S. M. Hayden, A. Hiess, J. W. Lynn, S.-H Lee, and F. Doǧan, Phys. Rev. B **66**, 144513 (2002).

[19] G. J. Chen, R. Joynt, F. C. Zhang, and C. Gros, Phys. Rev. B **42**, R2662 (1990).

[20] T. Giamarchi and C. Lhuillier, Phys. Rev. B **43**, 12943 (1991).

[21] M. Inaba, H. Matsukawa, M. Saitoh, and H. Fukuyama, Physica C **257**, 299 (1996).

[22] A. Himeda and M. Ogata, Phys. Rev. B **60**, R9935 (1999).

[23] A. Damascelli, Z. Hussain, and Z.-X. Shen, Rev. Mod. Phys. **75**, 473 (2003).

[24] R. Raimondi, J. H. Jefferson, and L. F. Feiner, Phys. Rev. B **53**, 8774 (1996); L. F. Feiner, J. H. Jefferson, and R. Raimondi, Phys. Rev. Lett. **76**, 4939 (1996).

[25] E. Pavarini, I. Dasgupta, T. Saha-Dasgupta, O. Jepsen, and O. K. Andersen, Phys. Rev. Lett. **87**, 047003 (2001).

[26] K. Tanaka, T. Yoshida, A. Fujimori, D. H. Lu, Z.-X. Shen, X.-J. Zhou, H. Eisaki, Z. Hussain, S. Uchida, Y. Aiura, K. Ono, T. Sugaya, T. Mizuno, and I. Terasaki, Phys. Rev. B **70**, 092503 (2004).

[27] S. R. White and D. J. Scalapino, Phys. Rev. B **60**, R753 (1999).

[28] G. B. Martins, J. C. Xavier, L. Arrachea, and E. Dagotto, Phys. Rev. B **64**, 180513 (2001).

[29] T. K. Lee and C. T. Shih, Phys. Rev. B **55**, 5983 (1997).

[30] S. Liang, B. Doucot, and P. W. Anderson, Phys. Rev. Lett. **61**, 365 (1988).

[31] T. K. Lee, C. M. Ho, and N. Nagaosa, Phys. Rev. Lett. **90**, 067001 (2003).

[32] Note that $n(\mathbf{k})$ will depend on the choice of these Q_p because there will be dips for the unoccupied **k**'s.

[33] C. T. Shih, Y. C. Chen, C. P. Chou, and T. K. Lee, Phys. Rev. B **70**, 220502(R) (2004).

[34] C. T. Shih, T. K. Lee, R. Eder, C. Y. Mou, and Y. C. Chen, Phys. Rev. Lett. **92**, 227002 (2004).

[35] T. Tohyama and S. Maekawa, Phys. Rev. B **49**, 3596 (1994).

[36] R. J. Gooding, K. J. E. Vos, and P. W. Leung, Phys. Rev. B **49**, 4119 (1994).

[37] H. Yamase and H. Kohno, Phys. Rev. B **69**, 104526 (2004).

[38] J. Burgy, M. Mayr, V. Martin-Mayor, A. Moreo, and E. Dagotto, Phys. Rev. Lett. **87**, 277202 (2001).

[39] A. Himeda, T. Kato, and M. Ogata, Phys. Rev. Lett. **88**, 117001 (2002).

This article was published in English in the original Russian journal. Reproduced here with stylistic changes by AIP.

LOW TEMPERATURE PHYSICS VOLUME 31, NUMBERS 8–9 AUGUST–SEPTEMBER 2005

Shift of the basal planes as the order parameter of transitions between the antiferromagnetic phases of solid oxygen

E. V. Gomonay*

N. N. Bogolyubov Institute of Theoretical Physics, National Academy of Sciences of Ukraine, ul. Metrologicheskaya 14-b, Kiev 03143, Ukraine; National Technical University of Ukraine "Kiev Polytechnical Institute," pr. Pobedy 37, Kiev 03506, Ukraine

V. M. Loktev†

N. N. Bogolyubov Institute of Theoretical Physics, National Academy of Sciences of Ukraine, ul. Metrologicheskaya 14-b, Kiev 03143, Ukraine

(Submitted January 31, 2005)
Fiz. Nizk. Temp. **31**, 1002–1019 (August–September 2005)

A phenomenological model in the spirit of Landau theory is constructed and used to analyze the phase stability conditions and the conditions for phase transitions between the various magnetocrystalline structures of solid oxygen over a wide range of pressure, temperature, and external magnetic field. [DOI: 10.1063/1.2008137]

I. INTRODUCTION

The discovery of antiferromagnetism as a physical phenomenon is inextricably connected to the Kharkov period of activity of L. V. Shubnikov and L. D. Landau. There can be no doubt that the experimental discovery of a new magnetic phase transformation between identical crystal structures not manifesting a macroscopic magnetic moment **M** or, in modern terminology, a paramagnet-antiferromagnet transition, belongs to Trapeznikov and Shubnikov, who observed an anomaly of the heat capacity of anhydrous ferrous chloride and linked it to the magnetic properties of this substance.[1] Landau, apparently learning of this research from the authors prior to publication of the results, laid out the basic concepts of the antiferromagnetic state. Based on these concepts, he developed a phenomenological theory of such a magnetic state of the crystal, in which one ferromagnetic sublattice is exactly compensated by another, so that, on the whole, spontaneous magnetization of macroscopic regions (ferromagnetism) does not arise after the transition.[2] It would later be found that the class of antiferromagnets, in which, by definition, the total magnetization $\mathbf{M}=0$ although the mean spins $\langle \mathbf{S_n} \rangle \neq 0$ at the sites **n** are finite and ordered, includes an enormous number of both metallic and insulating systems, with an extremely great diversity of magnetic structures (see, e.g., Ref. 3).

Among the antiferromagnetic insulators a special place is held by solid oxygen. First, it is one of a very few molecular magnets (if not the only one), since the O_2 molecule has spin $S=1$ in its ground state. Second, also uniquely, the antiferromagnetism of this cryocrystal is realized in a uniform (homomolecular) medium. Third and last, the equilibrium phases (α, β, and γ) of this crystal in the absence of external pressure P display different magnetic properties, and the magnetic (exchange) component makes a real contribution to the intermolecular interaction, significantly stabilizing the crystal structure of the α and β phases of solid oxygen.[4]

It should be noted that research on the thermal properties—the heat capacity,[5] thermal expansion,[6] and thermal conductivity[7,8]—of solid O_2 has not only confirmed the results of the pioneering magnetic measurements of Borovik-Romanov *et al.*[9,10] but also yielded new results, in particular, on the order of the α-β transition. It is now accepted (though not conclusively proven) that it is a first-order, close to second-order, transition, and it occurs not only between different crystal structures but also between different magnetic orderings. While the lowest-temperature ($T \leqslant 23$ K) phase at $P=0$, the monoclinic α phase, is characterized by a collinear two-sublattice magnetic structure with easy-axis anisotropy, the rhombohedral β phase is an example of a three-sublattice 120° magnetic structure with easy-plane anisotropy and correlation-type (short-range) ordering. This triangular structure in solid O_2 was predicted by one of the authors[11] and is known as the Loktev structure.

A theory of the magnetocrystalline phase transformation between the spin-collinear α phase and the spin-noncollinear β phase was proposed in Ref. 12, based on taking into account the dependence of the exchange (Heisenberg) pair interaction on the intermolecular distance in the framework of the linear theory of elasticity. That theory showed that the magnetoelastic transition arising in such a model can provide a correct description of both the crystal and magnetic structures of the α and β phases on the qualitative (and even semiquantitative) level. Nevertheless, a treatment of the β phase as an antiferromagnet with long-range dipolar magnetic order does not completely fit in with the modern view of the magnetism of easy-plane structures in crystals of reduced dimensionality.

The point is that, to a significant degree, β oxygen is among those degenerate two-dimensional magnetic systems that cannot exhibit an isotropic magnetoelastic gap, and so long-range spin ordering in the usual sense cannot arise in it (see, e.g., Ref. 13). However, it has been shown[14–16] that in view of the above-listed special properties of the Loktev structure, which can exist as right or left polarized, the sign of the polarization (and not the Néel order) can be preserved in it over macroscopic distances. This introduces a physical characteristic that can serve as a measure of the ordering in the absence of long-range vector order. This ordering is called "correlation ordering," since it is of the nature of highly developed short-range correlations corresponding completely to the Loktev structure. These correlations admit description in the framework of the Landau phenomenological approach.

By the mid-1980s to the early 1990s it seemed that the basic experimental and theoretical research on the magnetic and structural features of solid oxygen had been done, and the most important physical parameters characterizing the crystal and magnetic (sub)lattices had been determined. But the development of high-pressure technique substantially expanded the realm of standard problems in the physics of cryocrystals, ushering in the study of new crystal structures arising under external mechanical pressure in substances that had seemingly been studied already. Again, by virtue of its molecular structure and unusually strong magnetic interactions, solid oxygen has turned out to be a unique system among cryocrystals in that diverse phases, both magnetic and nonmagnetic, arise at high pressure, which differ in their crystal structure and electronic properties, as well.

A comprehensive and exhaustive review of the experimental data concerning the thermodynamic properties of the solid phases of O_2 and the existing theoretical models was recently given by Freiman and Jodl.[17] Without going into the details presented in that review, let us note that the theoretical studies of this topic have predominantly taken a microscopic or semi-microscopic approach based on a concrete form for the intermolecular interaction potentials. Approaches of this type, which to a certain extent includes the studies mentioned above,[12,14–16] have succeeded, for example, in elucidating the leading role of magnetic interactions in the α-β transition and, through analysis of the lattice dynamics, have led to the prediction of a jumplike change of the lattice parameters at the α-β and α-δ transitions.[18] A good complement to these microscopic models, which permit rather exact calculation of the parameters of the crystal in the framework of some restrictions on the range of the interactions, the forms of the potentials, etc., is the phenomenological (in essence, thermodynamic) theory, which gives a quantity picture of the phase transitions and the features that appear on the macroscopic observables at those transitions. Below we attempt to treat the sequence of phase transformations in solid oxygen specifically from the standpoint of the general phenomenological theory in the spirit of the Landau theory of phase transitions, which, as far as we know, has not been applied to solid O_2 before. The approach is based on general symmetry concepts without recourse to a concrete form of the intermolecular interaction, in conformity with Occam's razor—simplicity without trivialization. A feature of the proposed approach is that the thermodynamic potential is of a form for which one can take into account the finite (and non-small) lattice distortions arising in solid oxygen under pressure, which are not describable in the framework of the standard theory of elasticity. We shall also consider the question of the influence of external magnetic field on the structure of the phases and the macroscopic properties of their lattices in different ranges of pressure and temperature.

II. CHOICE OF THE ORDER PARAMETER

Solid oxygen, as we have said, is a unique physical system in which the character of the magnetic ordering has a substantial influence on the crystal structure; the relative displacements of the atoms at phase transitions induced by external pressure are so large that the lattice strain tensor cannot be considered small, and the standard harmonic approximation is insufficient to describe it. In addition, from a symmetry standpoint not all the Fedorov (space) groups of the observed phases are in a subgroup relationship (for example, the β and δ phases, the space groups of which are D_{3d}^5 and D_{2h}^{23}, respectively). All of these features make it a nontrivial problem to choose the order parameter (or parameters) and the form of the corresponding thermodynamic potential adequate to describe the whole sequence of transitions between the β, α, and δ phases of solid oxygen (we begin with the lattice of β-O_2 as the most symmetric of these phases).

A. Order parameter of the structural phase transition

All three phases considered below, the α and β phases and the δ phase that arises under pressure, have a layered structure in which the oxygen molecules can all be considered to be oriented parallel to each other and perpendicular to the close-packed atomic planes.[19] The molecules solidify in such a position exclusively on account of quantum (valence and exchange) interactions, since the other substantial interaction—the quadrupole-quadrupole—leads to a noncollinear mutual orientation of the molecules.[4]

If we ignore the distortions of vectors lying in the basal plane and the relatively small changes of the interplane distances, then it seems obvious that each of the phases in the sequence of phase transitions $\beta \rightarrow \alpha \rightarrow \delta$ can be obtained and in reality arises through a simple shift of the hexagonal close-packed planes relative to each other (see Fig. 1), from an initial right-angle stacking (i.e., stacking such that in the direction perpendicular to the planes the atoms are located one above the other).

The initial "unshifted" ordering of the hexagonal planes can be regarded as some virtual (not observed in reality) phase (the paraphase, in the terminology of Ref. 20), the symmetry group D_{6h}^1 of which includes the symmetry groups of the β, α, and δ phases as subgroups.

Choosing the reference unit cell to be one constructed on the basis vectors of the lattice of the paraphase, one can describe all the experimentally observed changes of the crystallographic structure with the use of a uniform finite-strain tensor containing five independent components (since the twofold symmetry axis in the basal plane is preserved). As the finite distortions one can choose, e.g., the relative change of the lengths of the basis vectors, the distortion of the basal plane determined by the hexagonality parameter $(\&hab - a)/a$, and the relative displacement of the close-packed planes $\xi = c \cos \beta / a$, where a, b, c, β specify in the general case a monoclinic lattice with mutually perpendicular vectors **a**, **b** in the basal plane. Only the last of these listed parameters (independently of its magnitude) can be used to describe the sequence of phase transitions between the β, α, and δ phases using general symmetry arguments in accordance with the canons of Landau theory. The quantity ξ,

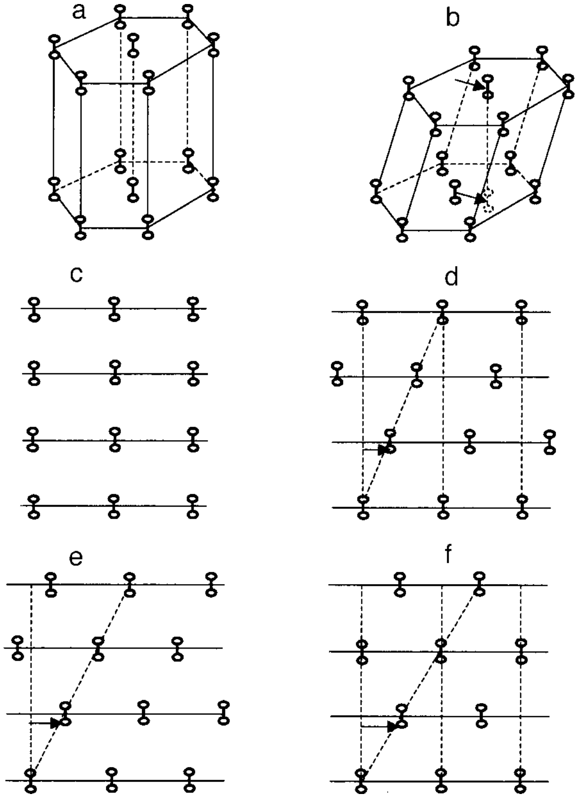

FIG. 1. Crystal structure of the antiferromagnetic phases of solid oxygen: hypothetical nonmagnetic paraphase (a,c), β-O_2 (b,d), α-O_2 (e), and δ-O_2 (f). The arrows indicate the direction of the shift (the vector $\mathbf{u}$). The horizontal lines on diagrams (c)–(f) correspond to the close-packed basal planes.

which need not be small, is considered below as an order parameter for these transitions.

For a rigorous symmetry analysis instead of the parameter ξ we consider the relative displacement vector $\mathbf{u}$ characterizing the mutual position of two adjacent planes in the different phases (upon a displacement of the order of $|\mathbf{u}| \propto \xi$ along one of the twofold axes). Since the states in which two parallel atomic planes are displaced by a vector multiple of the lattice period are physically equivalent and in essence identical, the vector $\mathbf{u}$ is defined up to a translation vector of the lattice in the basal plane.1) This imposes certain symmetry restrictions on the dependence of the internal energy on $\mathbf{u}$.

For example, let us consider the interaction potential $V^{(12)}(\mathbf{u})$ of two adjacent close-packed planes, which, by virtue of the periodicity properties mentioned above, can be written in the form of a series

$$V^{(12)}(\mathbf{u}) = \sum_{n,m} V_{nm}^{(12)} \exp(i\mathbf{g}_{nm}\mathbf{u}) \tag{1}$$

in the reciprocal lattice vectors $\mathbf{g}_{nm} = n\mathbf{b}_1 + m\mathbf{b}_2$, parallel to the basal plane. The functions $\psi_{nm} = \exp(i\mathbf{g}_{nm} \cdot \mathbf{u})$ form a representation of the symmetry point group of the "unshifted" paraphase, and their linear combinations can be chosen as the order parameter of the phase transitions described.2) For the sequence of transitions between the β, α, and δ phases considered in this paper it is sufficient to choose as the order parameters of the structural transition the functions $\psi_{01}, \psi_{10}, \psi_{\bar{1}1}$, the transformations of which under the operations of the group D_{6h}^1 are presented in Table I. The indicated order parameter is uniform in the sense that the relative displacement of any two adjacent planes is identical in both magnitude and direction.3)

TABLE I. Transformation of the functions ψ_{nm}, $n,m = 0,1$, under the operations of the generating elements of the group D_{6h}^1.

1	$6_{[001]}$	$2_{[1\bar{1}0]}$	$\bar{1}$
ψ_{01}	ψ_{10}	ψ_{01}^*	ψ_{01}^*
ψ_{10}	$\psi_{\bar{1}1}^*$	$\psi_{\bar{1}1}^*$	ψ_{10}^*
$\psi_{\bar{1}1}$	ψ_{01}	ψ_{10}^*	$\psi_{\bar{1}1}^*$

B. Description of the magnetic structure

In accordance with the experimental data currently available, which are presented rather completely in Freiman and Jodl's review,[17] the spin moments localized on the oxygen molecules form a noncollinear triangular structure in the basal plane, with short-range order in the β phase (Fig. 2a) and an antiferromagnetic collinear structure in the α and δ phases (Fig. 2b). The mutual orientation of the moments in adjacent close-packed layers is not uniquely determined and can be parallel or antiparallel (see, e.g., Ref. 21). A symmetry analysis of the two-dimensional magnetic structures compatible with hexagonal ordering of the atoms (molecules) within the plane was carried out in the papers by Vitebskii *et al.*,[14–16,22] and it was shown in a paper by Gaididei and one of the authors[12] that the wave vectors specifying the magnetic superlattices of the α and β phases correspond to a minimum of the quasi-classical magnetic energy of the crystal when the only exchange interactions taken into account are those between nearest neighbors in the basal plane. We note that those results remain valid for the δ phase in the two-dimensional approximation.

However, for studying the mutual influence of the magnetic and structural phase transitions arising in solid oxygen under pressure it is important to take into account not only the intralayer but also the interlayer exchange interaction, which is more sensitive to the relative shift of adjacent atomic planes. Accordingly, we shall classify the magnetic structures of the β, α, and δ phases in irreducible representations of the symmetry group of the paraphase, D_{6h}^1, i.e., a substantially three-dimensional rather than a two-dimensional lattice, and we write the wave vectors of the magnetic superstructures in terms of the vectors $\mathbf{b}_1 = (2\pi/a, 2\pi/\sqrt{3}a, 0)$, $\mathbf{b}_2 = (0, 4\pi/\sqrt{3}a, 0)$, $\mathbf{b}_3(0,0,2\pi/c)$ of

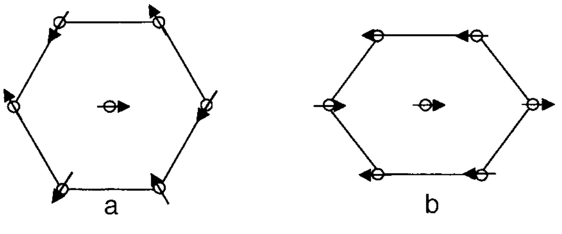

FIG. 2. Orientation of the magnetic moments of solid oxygen in the basal plane of the β phase (a) and of the α and δ phases (b).

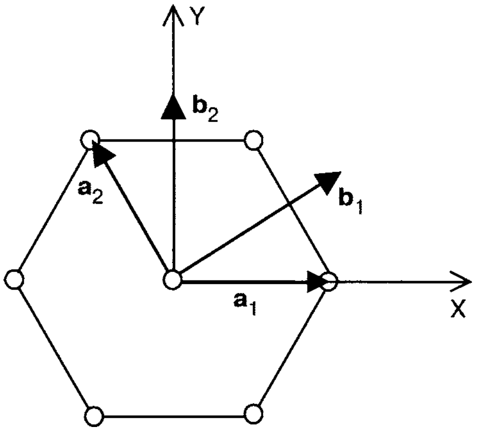

FIG. 3. Orientation of the direct and reciprocal lattices in the basal plane.

the reciprocal lattice of the hexagonal lattice with vectors $\mathbf{a}_1=(a,0,0)$, $\mathbf{a}_2=(-a/2,\sqrt{3}a/2,0)$, $\mathbf{a}_3=(0,0,c)$ (see Fig. 3).

The experimentally observed phases are compatible with the following representations of the magnetization vector $\mathbf{M}(\mathbf{r}_j)$ at the point $\mathbf{r}_j$:

1. In the β phase (Fig. 2a)

$$\mathbf{M}^{(\beta)}(\mathbf{r}_j)=\mathrm{Re}[(\mathbf{l}_1^{(\beta)}+i\mathbf{l}_2^{(\beta)})\exp(i\mathbf{q}_\beta\cdot\mathbf{r}_j)],$$

where the orthogonal vectors $\mathbf{l}_1^{(\beta)},\mathbf{l}_2^{(\beta)}$ satisfy the normalization conditions

$$(\mathbf{l}_1^{(\beta)})^2+(\mathbf{l}_2^{(\beta)})^2=M_0^2,$$

where M_0 is the saturation magnetization per unit volume. These vectors can be regarded as a two-component4) order parameter, and the transition wave vector $\mathbf{q}_\beta$ coincides with the representation of one of the single-ray stars (in Kovalev's notation)[23] of the group D_{6h}^1: $\mathbf{k}_{13}=(\mathbf{b}_1+\mathbf{b}_2)/3$ or $\mathbf{k}_{15}=(\mathbf{b}_1+\mathbf{b}_2)/3+\mathbf{b}_3/2$. The antiferromagnetic vectors $\mathbf{l}_1^{(\beta)},\mathbf{l}_2^{(\beta)}$ can also be regarded as the nonzero linear combinations of sublattice magnetic moments that determine the transition to the magnetically ordered phase, the number of sublattices being equal to three or six, depending on the star ($\mathbf{k}_{13}$ and $\mathbf{k}_{15}$, respectively), of the transition.

2. In the α and β phases (Fig. 2b)

$$\mathbf{M}^{(\alpha)}(\mathbf{r}_j)=\sum_{k=1}^{3}\mathbf{l}_k^{(\alpha)}\exp(i\mathbf{q}_k^{(\alpha)}\cdot\mathbf{r}_j)$$

and

$$\mathbf{M}^{(\delta)}(\mathbf{r}_j)=\sum_{k=1}^{3}\mathbf{l}_k^{(\delta)}\exp(i\mathbf{q}_k^{(\delta)}\cdot\mathbf{r}_j). \qquad (2)$$

The antiferromagnetic vectors $\mathbf{l}_k^{(\alpha)}$, $k=1,2,3$ form the three-component order parameter, corresponding to the star $\mathbf{k}_{12}=\mathbf{b}_1/2$ with the three arms

$$\mathbf{q}_1^{(\alpha)}=\frac{\mathbf{b}_1}{2},\quad \mathbf{q}_2^{(\alpha)}=-\frac{\mathbf{b}_2}{2},\quad \mathbf{q}_3^{(\alpha)}=\frac{\mathbf{b}_2-\mathbf{b}_1}{2},$$

and each of the antiferromagnetic vectors corresponds to one of the arms. Analogously, the vectors $\mathbf{l}_k^{(\delta)}$, $k=1,2,3$ correspond to the three-arm star $\mathbf{k}_{14}=(\mathbf{b}_1+\mathbf{b}_3)/2$, with the arms

$$\mathbf{q}_j^{(\delta)}=\mathbf{q}_j^{(\alpha)}+\frac{\mathbf{b}_3}{2}.$$

The channel of a possible transition contains only one of the three arms (i.e., only one of the vectors $\mathbf{l}_{1,2,3}^{(\alpha)}$ is nonzero), and in this case the normalization conditions reduce to the relation $(\mathbf{l}_k^{(\alpha)})^2=M_0^2$ (analogously for the δ phase). In practice the different antiferromagnetic vectors ($\mathbf{l}_1^{(\alpha)},\mathbf{l}_2^{(\alpha)}$, or $\mathbf{l}_3^{(\alpha)}$) correspond to different domains of the same magnetically ordered phase. As to a description in terms of magnetic sublattices, according to the experimental data in the α phase the number of such sublattices is two (the star $\mathbf{k}_{12}$), while in the δ phase it is four (the star $\mathbf{k}_{14}$).

The star pairs ($\mathbf{k}_{13},\mathbf{k}_{15}$) and ($\mathbf{k}_{12},\mathbf{k}_{14}$) correspond to the same antiferromagnetic ordering of magnetic moments in the basal plane of the crystal but differ in respect of the mutual orientation of the spins in adjacent planes: parallel for the stars $\mathbf{k}_{12}$ and $\mathbf{k}_{13}$, and antiparallel for $\mathbf{k}_{15}$ and $\mathbf{k}_{14}$. As we have said above, the majority of experiments done to date do not permit an unambiguous determination of the type of star ($\mathbf{k}_{13}$ or $\mathbf{k}_{15}$) that characterizes the magnetic structure in the β phase. Contributing to this is the absence of long-range order in the basal planes themselves, although the short-range order corresponds unambiguously to the Loktev structure (see Ref. 17). As to the collinear magnetic structure of the α and δ phases, the spin configurations we have chosen above agree not only with the direct magnetic measurements[21] but also permit explanation of the observed[19] jump of the order parameter at the α-δ transition (see below). Nevertheless, it should be kept in mind that a two-sublattice magnetic structure is also compatible with the lattice of the δ phase.

Upon application of an external magnetic field a macroscopic moment arises in the crystal. In the exchange approximation the magnetization vector $\mathbf{m}$ transforms according to the unit irreducible representation, corresponding to the vector $\mathbf{k}=0$. In the description in terms of a multi-sublattice model the vector $\mathbf{m}$ is equal to the sum of the magnetic moments of all the sublattices.

III. THERMODYNAMIC POTENTIAL

On the phenomenological level the sequence of magnetostructural transitions between low-temperature phases of solid oxygen can be described on the basis of the Landau theory of phase transitions, i.e., by analysis of the corresponding thermodynamic potential Φ (the Gibbs potential in the presence of external fields and the Helmholtz free energy in the absence of field).

In view of the the strong coupling between the magnetic and structural subsystems of solid oxygen, as internal parameters describing the thermodynamic state of the crystal one can choose the magnetic moment density $\mathbf{M}^{(k)}(\mathbf{r})$ ($k=\beta,\alpha,\delta$), the structure functions ψ_{nm} (which depend on the shift vector of the atomic planes), the specific volume v of the crystal, and the components of the strain tensor u_{jk}. As the variables responsible for the phase transitions (primary order parameter), besides the magnetic vectors $\mathbf{l}_j^{(k)}$ ($j=1,2,3$), we choose the real part of the functions $\psi_{01},\psi_{10},\psi_{\bar{1}1}$ and the relative volume change $\Delta v/v$, and the remaining combinations will be assumed to be secondary order parameters.5) The main parameters responsible for the phase transitions and the accompanying parameters are listed in Table II.

TABLE II. Primary and secondary order parameters implementing irreducible representations of the group D_{6h}^1 of the paraphase.

Primary OP	Secondary OP	IR
$\mathrm{Re}\,(\psi_{01}+\psi_{10}+\psi_{\bar{1}1})$, $\Delta v/v$	$u_{xx}+u_{yy}$, u_{zz}	A_{1g}
$\mathrm{Re}\,(\psi_{01}+\psi_{10}-2\psi_{\bar{1}1})$, $\mathrm{Re}\,(\psi_{01}-\psi_{10})$	$\{(u_{xx}-u_{yy}),2u_{xy}\}$, $\{u_{xz},u_{yz}\}$	E_{1g}

The thermodynamic potential represented as a function of the internal and external parameters can be written in the form of a sum of terms Φ_{mag} and Φ_{str} which depend only on the magnetic and only on the structural parameters, respectively, and also a term Φ_{int} that takes the interaction between them into account:

$$\Phi=\Phi_{\mathrm{str}}+\Phi_{\mathrm{mag}}+\Phi_{\mathrm{int}}. \tag{3}$$

In principle, the thermodynamic potential Φ contains yet another component associated with the orientation of the oxygen molecules. However, we have not written it down because it does not directly influence the sequence of magnetostructural phase transitions under consideration, although by changing from phase to phase (and also with changes in temperature and pressure) it can contribute to the observed values of the coefficients of volume expansion, etc. (see below).

To take into account the features of the phase transitions observed in solid oxygen, we write the structure (lattice) potential Φ_{str} in the form

$$\begin{aligned}\Phi_{\mathrm{str}}=&-K_2(v)[\cos 2\pi\xi_1+\cos 2\pi\xi_2+\cos 2\pi(\xi_1-\xi_2)]\\&+\frac{1}{4}K_4[\cos 4\pi\xi_1+\cos 4\pi\xi_2+\cos 4\pi(\xi_1-\xi_2)]\\&+f(v,T)+P\frac{\Delta v}{v}.\end{aligned} \tag{4}$$

In this expression the quantities $2\pi\xi_{1,2}\equiv\mathbf{b}_{1,2}\cdot\mathbf{u}$ are proportional to the projections of the shift vector **u** onto the vectors of the hexagonal lattice, $f(v,T)$ is some function of the specific volume v and temperature T which models the dependence of the internal energy of the crystal on the interatomic distances, and P is the external hydrostatic pressure.

Expression (4) is in essence an analog of the Landau-theory expansion of the thermodynamic potential in powers of the order parameter, which is invariant with respect to the symmetry operations of the most symmetric of the phases. However, unlike the orthodox theory, here the expansion is in periodic functions of the shift vector **u** [actually in Fourier harmonics; cf. formula (1)], where it is assumed that the coefficients $K_2,K_4,\ldots$ of the expansion fall off in magnitude with increasing number of the harmonic, so that, as usual, it is sufficient to keep only the first few terms of the series. In the limit of small strains, these coefficients can be expressed in terms of the shear modulus$^{6)}$ c_{44} and the anharmonicity constants.

Formula (4) differs from the standard Landau approach in another way as well. Usually for description of a phase transition due to a change of temperature, it is sufficient to assume that one of the expansion coefficients (for example, K_2) has a power-law dependence on temperature, while the other coefficients are assumed constant. For solid oxygen one can choose the main parameter "controlling" the phase transformations to be the specific volume v, since both the value of the exchange magnetic interactions and the interaction between adjacent atomic planes depend substantially on the intermolecular distances and, as a consequence, on v. That is the reason why we have assumed that the coefficient K_2 depends on the external parameters indirectly, through the relative volume change $\Delta v/v$. From a thermodynamic point of view, however, the volume itself is an internal parameter of the crystal, and for establishing the relation with temperature and pressure the function f has been introduced in (4). In spite of the fact that with variation of the external parameters the specific volume of solid oxygen varies very strongly and the quantity $\Delta v/v$ certainly cannot be considered a small parameter, this function can be approximated to good accuracy by the expression

$$f\left(\frac{\Delta v}{v},T\right)=\frac{1}{2\chi_T}\left(\frac{\Delta v}{v}\right)^2-\frac{1}{\chi_T}\left(\frac{\Delta v}{v}\right)\int_0^T\beta_P(T')dT', \tag{5}$$

where the "bare" (not including the contributions due to the phase transitions) coefficient of thermal expansion $\beta_P(T)$ at constant pressure and the isothermal compliance χ_T generally speaking change on going from one temperature and pressure range to another,$^{7)}$ and the volume change is reckoned from some reference state, e.g., from the state with $T=0$, $P=0$. The presence of an integral in the last term in (5) is due to the fact that, according to the experimental data, the coefficient of thermal expansion depends substantially on temperature. In the limit of a weak dependence $\beta_P(T)\approx\mathrm{const}$, expression (5) agrees with the analogous contribution to the free energy in the Landau model.[30] In an analogous way the coefficient K_2 can be assumed to be a linear function of volume, with a phenomenological coefficient

$$K_2(v)\equiv K_0-\lambda_v\frac{\Delta v}{v}.$$

In expression (4) for the structural contribution to the free energy of solid oxygen only two of the five independent parameters governing the finite strain of the crystal (see above) are taken into account explicitly: the relative displacement vector of adjacent planes, since it determines the order parameter of the phase transitions β-α-δ, and the relative volume change, since this parameter is isomorphic to the external parameters—the temperature and pressure.

When only the exchange interactions are taken into account, the magnetic energy can be written in the form of a sum

$$\begin{aligned}\Phi_{\mathrm{mag}}=&-J(\mathbf{k}_{13})\sum_{j=1}^{2}(\mathbf{l}_j^{(\beta)})^2-J(\mathbf{k}_{12})\sum_{j=1}^{3}(\mathbf{l}_j^{(\alpha)})^2\\&-J(\mathbf{k}_{14})\sum_{j=1}^{3}(\mathbf{l}_j^{(\delta)})^2-\mathbf{m}\cdot\mathbf{H},\end{aligned} \tag{6}$$

where $J(\mathbf{k}_j)>0$, $j=12,13,14$ are the Fourier components of the exchange integral with the corresponding wave-vector representatives of the stars (see Sec. 2.2). The last term in (6) arises on account of the the interaction of the macroscopic magnetic moment **m** with the external magnetic field **H**.

The phenomenological quantities $J(\mathbf{k}_j)$ include a contribution from the exchange excitation both between nearest and, generally speaking, between more remote neighbors in the basal plane, and also the interlayer exchange. However, taking into account the experimentally established[17] fact that the exchange interaction between nearest neighbors is dominant, we can assume approximately that $J(\mathbf{k}_{12})=J(\mathbf{k}_{13})=J(\mathbf{k}_{14})=J_0$.

The interaction between the magnetic and structural subsystems, as we have said, is of a magnetoelastic nature and, in accordance with the symmetry of the paraphase, is modeled by the potential:

$$\begin{aligned}\Phi^{\text{int}}=&\Lambda^{(\beta)}\frac{\Delta v}{v}\sum_{j=1}^{2}(\mathbf{l}_j^{(\beta)})^2+\Lambda^{(\alpha)}\frac{\Delta v}{v}\sum_{j=1}^{3}(\mathbf{l}_j^{(\alpha)})^2\\&+\Lambda^{(\delta)}\frac{\Delta v}{v}\sum_{j=1}^{3}(\mathbf{l}_j^{(\delta)})^2-\Lambda_{\parallel}^{(\alpha)}[(\mathbf{l}_1^{(\alpha)})^2\cos 2\pi\xi_1\\&+(\mathbf{l}_2^{(\alpha)})^2\cos 2\pi\xi_2+(\mathbf{l}_3^{(\alpha)})^2\cos 2\pi(\xi_1-\xi_2)]\\&-\Lambda_{\parallel}^{(\delta)}[(\mathbf{l}_1^{(\delta)})^2\cos 2\pi\xi_1+(\mathbf{l}_2^{(\delta)})^2\cos 2\pi\xi_2\\&+(\mathbf{l}_3^{(\delta)})^2\cos 2\pi(\xi_1-\xi_2)]-\Lambda_{\perp}^{(\alpha)}\{(u_{xx}-u_{yy})(\mathbf{l}_1^{(\alpha)})^2\\&+2u_{xy}[(\mathbf{l}_2^{(\alpha)})^2-(\mathbf{l}_3^{(\alpha)})^2]\}-\Lambda_{\parallel}^{(\delta)}\{(u_{xx}-u_{yy})(\mathbf{l}_1^{(\alpha)})^2\\&+2u_{xy}[(\mathbf{l}_2^{(\alpha)})^2-(\mathbf{l}_3^{(\alpha)})^2]\}.\end{aligned}\tag{7}$$

The coefficients $\Lambda^{(k)}$ $(k=\beta,\alpha,\delta)$ are responsible for the volume effect arising at the transition between different magnetic phases, while the terms with the coefficients $\Lambda_{\parallel}^{(\alpha)}$ and $\Lambda_{\parallel}^{(\delta)}$ are responsible for the magnetoelastic contribution, which describes the change of the interlayer exchange interaction upon a mutual displacement of the basal planes. The last two terms, with $\Lambda_{\perp}^{(\alpha)}$ and $\Lambda_{\perp}^{(\delta)}$, describe the result of Ref. 12 for the dependence of the intraplane exchange interaction on the corresponding intraplane shift of the rhombic strain (see Ref. 12), $u_{xx}-u_{yy}$, which lifts the degeneracy of the intermolecular distances in the basal plane. Unlike the exchange constants $J(\mathbf{k}_j)$ introduced above, all of the coefficients of the magnetoelastic interaction that appear in expression (7) are governed predominantly by the long-range structural order. For our model it is important that these coefficients are substantially different for the collinear (α and δ phases) and triangular (β phase) magnetic structures.

IV. EQUILIBRIUM PHASES AND TRANSITIONS BETWEEN THEM

For determination of the thermodynamic equilibrium phases and the conditions of their stability we use the standard condition of a minimum of the free energy potential (3), namely:

$$\frac{\partial\Phi}{\partial x_p}=0,\quad \left\|\frac{\partial^2\Phi}{\partial x_p\partial x_q}\right\|>0\tag{8}$$

with respect to the parameters $\xi_{1,2}$, $\Delta v/v$, $\mathbf{l}_j^{(k)}$, $k=\beta,\alpha$; $j=1,2,3$ [all denoted x_p in Eq. (8)]. Here it is unnecessary to minimize the free energy with respect to the wave vectors of the magnetic superstructures, since only those of them corresponding to the observed magnetic structures have been taken into account in expression (4).

Analysis of the expressions appearing in Eq. (3) shows that the most symmetric state, which in the given case corresponds to a hypothetical nonmagnetic paraphase, correspond to zero values of the structural and magnetic parameters:

$$\xi_1=\xi_2=0,\quad \mathbf{l}_{1,2}^{(\beta)}=\mathbf{l}_{1,2,3}^{(\alpha)}=0.\tag{9}$$

This unobserved phase will not be considered further.

The less-symmetric β, α, and δ phases, which nevertheless preserve the symmetry with respect to twofold rotation around one of the directions $\mathbf{a}_1-\mathbf{a}_2$, $\mathbf{a}_1+2\mathbf{a}_2$, or $2\mathbf{a}_1+\mathbf{a}_2$ in the basal plane, correspond to three equivalent sets of parameters with

$$1)\ \xi_1=-\xi_2,\quad 2)\ \xi_1=2\xi_2,\quad 3)\ 2\xi_1=\xi_2.\tag{10}$$

In the β phase all of the states indicated in (10) are physically indistinguishable, and the multivaluedness arises because of additional symmetry of the paraphase—the close-packed state of two adjacent hexagonal planes can be obtained with the aid of a shift along any of the directions indicated above.[8)]

In the α and δ phases the different states (10) correspond to different structural domains of the same phase, differing by the direction of the twofold symmetry axis in the basal plane. For definiteness we shall consider the first of the possibilities indicated in Eq. (10), corresponding to the direction $\mathbf{a}_1-\mathbf{a}_2$ (the other two can be analyzed in the same way).

For further analysis we write conditions (8) for a minimum of the potential (3) with respect to the variables $\xi\equiv\xi_2=\xi_1/2$ and $\Delta v/v$ in explicit form (the analogous conditions for the magnetic vectors $\mathbf{l}_j^{(k)}$ are trivial and are not shown):

$$\begin{aligned}\frac{\partial\Phi}{\partial\xi}=&4\pi\sin 2\pi\xi\{K_2(v)(1+2\cos 2\pi\xi)\\&-K_4\cos 2\pi\xi(1+2\cos 4\pi\xi)\\&+2[\Lambda_{\parallel}^{(\alpha)}(\mathbf{l}_1^{(\alpha)})^2+\Lambda_{\parallel}^{(\delta)}(\mathbf{l}_1^{(\delta)})^2]\cos 2\pi\xi\}=0;\end{aligned}$$

$$\begin{aligned}\frac{\partial\Phi}{\partial(\Delta v/v)}=&\frac{1}{\chi_T}\frac{\Delta v}{v}-\frac{1}{\chi_T}\int_0^T\beta_P(T')dT'+P+\lambda_v(2\cos 2\pi\xi\\&+\cos 4\pi\xi)+\Lambda^{(\beta)}\sum_{j=1}^{2}(\mathbf{l}_j^{(\beta)})^2+\Lambda^{(\alpha)}(\mathbf{l}_1^{(\alpha)})^2\\&+\Lambda^{(\delta)}(\mathbf{l}_1^{(\delta)})^2=0,\end{aligned}\tag{11}$$

where we have taken into account that in the α and δ phases the magnetic state is determined solely by one antiferromagnetic vector, $\mathbf{l}_1^{(\alpha)}$ and $\mathbf{l}_1^{(\delta)}$, respectively.

The conditions of stability against small perturbations of the parameters are obtained from (8); they have the form

$$\frac{\partial^2\Phi}{\partial\xi^2}=16\pi^2\{K_2(v)(\cos 2\pi\xi+2\cos 4\pi\xi)$$

$$-K_4(\cos 4\pi\xi+2\cos 8\pi\xi)+2[\Lambda_{\parallel}^{(\alpha)}(\mathbf{l}_1^{(\alpha)})^2$$

$$+\Lambda_{\parallel}^{(\delta)}(\mathbf{l}_1^{(\delta)})^2]\cos 4\pi\xi\}>0;$$

$$\frac{\partial^2\Phi}{\partial\xi^2}>\frac{\partial^2\Phi}{\partial\xi\partial(\Delta v/v)}=16\pi^2\chi_T^2\lambda_v^2\sin^2 2\pi\xi(1$$

$$+2\cos 2\pi\xi)^2,\quad \chi_T>0. \tag{12}$$

A. β phase

It is seen from Eqs. (11) that the possible equilibrium values of the order parameter ξ depend on the type of magnetic ordering realized in the crystal. In particular, if it is the triangular Loktev magnetic structure, described by the vectors $\mathbf{l}_{1,2}^{(\beta)}$, with $(\mathbf{l}_1^{(\beta)})^2+(\mathbf{l}_2^{(\beta)})^2=M_0^2$, and $\mathbf{l}_1^{(\alpha)}=\mathbf{l}_1^{(\delta)}=0$, then the first of Eqs. (11) has the solution $\xi=1/3$, corresponding to the β phase, in which the adjacent planes are shifted relative to each other by $(\mathbf{a}_1-\mathbf{a}_2)/3$. The stability of this phase with respect to the long-wave shear vibrations and hydrostatic pressure is determined by the relation

$$K_{\text{eff}}-\lambda_v\left[\int_0^T\beta_P(T')dT'-\chi_T P\right]<0;\quad K_4>0;\quad \chi_T>0, \tag{13}$$

where for convenience we have introduced the effective constant

$$K_{\text{eff}}=K_0-K_4-\frac{3}{2}\chi_T\lambda_v^2+\chi_T\lambda_v\Lambda^{(\beta)}M_0^2. \tag{14}$$

Since, as will be seen from the following, $\lambda_v>0$, the stability conditions (13) are strengthened with increasing temperature and weakened with increasing pressure; taken all together, this is in complete agreement with the observed existence region of the β phase (see Ref. 17).

The appearance (in comparison with the paraphase) of a nonzero order parameter leads to a lowering of the symmetry: the rotations about the sixfold axis vanish, while the rotations about the threefold axis, which are weighted by the operation of translation by the lattice vector $\mathbf{a}_1+\mathbf{a}_2$ in the basal plane, remain. Of the order parameters corresponding to the transition, only those appear which transform according to the irreducible representation A_{g1}, i.e., hydrostatic (isomorphic) compression-extension in the basal plane (the parameter $u_{xx}+u_{yy}$) and the change of the interplane distances (determined by u_{zz}).

The important characteristic of the β phase is the temperature and pressure dependence of the relative volume change of the crystal:

$$\left.\frac{\Delta v}{v}(T,P)\right|_{\beta}=\int_0^E\beta_P(T')dT'-\chi_T P-\chi_T\Lambda^{(\beta)}M_0^2$$

$$+\frac{3}{2}\chi_T\lambda_v. \tag{15}$$

The linear dependence of the specific volume on P is observed experimentally[17] over a wide range of pressures, as can be seen, for example, in Fig. 4. A comparison with experiment also allows one to determine the dependence $\beta_P(T)$. For example, on the basis of an analysis of the data of Ref. 6, at atmospheric pressure

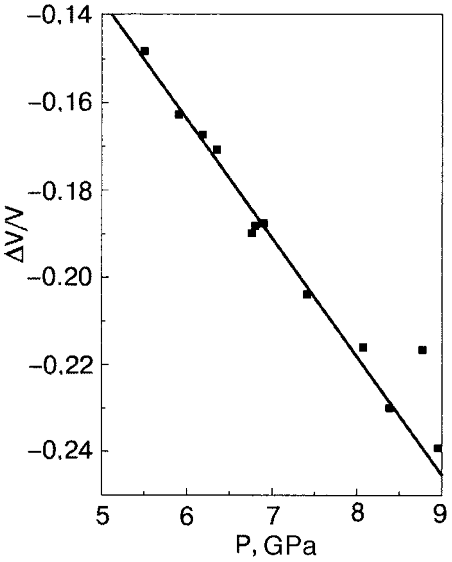

FIG. 4. Pressure dependence of the relative change of the specific volume at room temperature. The points are experimental,[17] the solid line is a linear approximation with the coefficient $\chi_T=0.27\times 10^{-11}$ cm^3/dyn.

$$\beta_P(T)=\begin{cases}1.6\cdot 10^{-4}\ 1/\text{K}, & T<11\ \text{K},\\ 6.66\cdot 10^{-5}T-5.72\cdot 10^{-4}\ 1/\text{K}, & 11\\ \text{K}<T<43.5\ \text{K}.\end{cases} \tag{16}$$

B. α phase and the α-β transition

If the magnetic structure of the crystal is two-sublattice, with $|\mathbf{l}_1^{(\alpha)}|=M_0$, then Eqs. (11) have a solution with an order parameter that, depending on the external parameters, lies in the range $1/3<\xi<1/2$, corresponding to the α phase. The value of ξ is determined by the following equation, which is written for convenience in terms of the variable $\eta\equiv 1+2\cos 2\pi\xi$, which from a macroscopic point of view can be considered to be the order parameter of the phase transitions examined below, since its value in the β phase is equal to zero:

$$\left\{K_{\text{eff}}+[\Lambda_{\parallel}^{(\alpha)}+\chi_T\lambda_v(\Lambda^{(\beta)}-\Lambda^{(\alpha)})]M_0^2\right.$$

$$\left.-\lambda_v\left(\int_0^T\beta_P(T')dT'-\chi_T P\right)\right\}\eta+\frac{3}{2}K_4\eta^2$$

$$-\frac{1}{2}(K_4-\chi_T\lambda_v^2)\eta^3=\Lambda_{\parallel}^{(\alpha)}M_0^2. \tag{17}$$

The structural stability of the α phase with respect to variation of ξ is then determined by the condition

$$K_{\text{eff}}-\lambda_v\left(\int_0^T\beta_P(T')dT'-\chi_T P\right)<K_4-2\Lambda_{\parallel}^{(\alpha)}M_0^2$$

$$-\chi_T\lambda_v(\Lambda^{(\alpha)}-\Lambda^{(\beta)})M_0^2, \tag{18}$$

and the energetic favorability, by the inequality

TABLE III. Values of the main phenomenological coefficients.

Parameter	Value	Notes
χ_T	$3.54\cdot10^{-11}$ cm^2/dyn	at P, atm (Ref.6)
	$0.75\cdot10^{-11}$ cm^2/dyn	at $T=19$ K, $P=1-10$ GPa
	$0.27\cdot10^{-11}$ cm^2/dyn	at $T=300$ K, $P=5-10$ GPa
$\beta_p(\mathrm{T})$	$1.6\cdot10^{-4}$ 1/K	$T<11$ K
	$(0.67\cdot T-5.72)\cdot10^{-4}$ 1/K	11 K $<T<$ 43.5 K
$J_0M_0^2$	$2.6\cdot10^{8}$ erg/cm^3	calculation
$\Lambda_{\parallel}^{(\alpha)}M_0^2$	$-7.4\cdot10^{9}$ erg/cm^3	calculation
$\Lambda^{(\beta)}M_0^2$	$0.82\cdot10^{9}$ erg/cm^3	calculation
$\Lambda^{(\alpha)}M_0^2$	$8.2\cdot10^{9}$ erg/cm^3	calculation
λ_v	$1.0\cdot10^{11}$ erg/cm^3	calculation
M_0	133 G	Ref.17
K_{eff}	$7.1\cdot10^{10}$ erg/cm^3	calculation
K_4	$8.0\cdot10^{10}$ erg/cm^3	calculation

$$\Phi_\alpha-\Phi_\beta=-\frac{1}{2}K_{\mathrm{eff}}\eta^2-\frac{1}{2}K_4\eta^3+\frac{1}{8}(K_4-\chi_T\lambda_v^2)\eta^4+\Lambda_{\parallel}^{(\alpha)}M_0^2\left(\eta-\frac{1}{2}\eta^2\right)+\frac{1}{2\chi_T}\left[\left(\frac{\Delta v}{v}\right)_\beta^2-\left(\frac{\Delta v}{v}\right)_\alpha^2\right]<0, \tag{19}$$

which can be inferred from a comparison of the thermodynamic potentials of the two phases at fixed values of the external parameters (cf. Ref. 12, where similar relations were written for the case $T=0$, $P=0$). The sign of the quantities on the right-hand side of inequality (18) are in essence determined by the interplay of several constants and can be positive or negative. According to our estimates (see Table III), the last term on the right-hand side is negligible, and the first two terms are positive. Thus inequality (18), which determines the stability region of the α phase, is not incompatible with (and is even weaker than) the existence condition of the β phase [Eq. (13)]. In other words, the two phases can coexist in a certain interval of temperature and pressure.

What, then, leads to the observed α-β transition in the framework of the phenomenological description?

As we see from Eq. (17), the "driving force" of this transition, analogous to an "external field," is the possibility of lowering the free energy by a change of the magnetic structure, specifically: owing to the term $\Lambda_{\parallel}^{(\alpha)}$ due to the collinear magnetic ordering, the solution with $\eta=0$, corresponding to the β phase, vanishes on the right-hand side of this equation. Since, when the collinear magnetic order is "switched on," the "driving force" immediately takes on some finite value, the α-β transition must inevitably occur as a first-order transition (although close to second-order in the Landau classification). From a physical standpoint the fact that this magnetostructural transition is close to second-order is apparently due to the fact that the "heavy" (inertial) subsystem—the molecular lattice—can undergo an α-β transformation continuously. However, it does not occur before the initiation of a jumplike rearrangement of the magnetic ordering of the "easy" spin (and hence, electronic) subsystem of the oxygen. We note that the scenario of a smooth α-β transformation was set forth in Ref. 17.

Here it should be emphasized that the isolation of the role of magnetic interactions in the α-β transition is of a conventional character. Actually there is a simultaneous change of the crystalline (a shift and straining of the basal planes) and magnetic (transition from the noncollinear to the collinear structure) subsystems caused by the energetic favorability of the new state. There is no doubt that an important role in this transformation is played by the specific volume change, which in the α phase is described by the expression

$$\left.\frac{\Delta v}{v}(T,P)\right|_\alpha=\left.\frac{\Delta v}{v}(T,P)\right|_\beta-\chi_T(\Lambda^{(\alpha)}-\Lambda^{(\beta)})M_0^2-\frac{1}{2}\chi_T\lambda_v\eta^2, \tag{20}$$

where $(\Delta v/v)_\beta$ is given by formula (15). It is seen that at the transition to the α phase the specific volume of the crystal should decrease in a jump (both terms on the right-hand side are negative). This decrease is due to both the difference of the magnetoelastic volumes effects in the α and β phases [the second term in (20)] and to the incipient shift of the basal planes (the last term).

It is seen from an analysis of expression (7) and Table II that the appearance of $\eta\neq0$ due to the change of the magnetic structure (the appearance of $\mathbf{l}_1^{(\alpha)}\neq0$) also leads to straining of the basal plane (described by the quantity $u_{xx}-u_{yy}$), but a treatment of the corresponding effects is beyond the scope of this paper.

Furthermore, the specific volume v actually causes the effective exchange interaction constants J_{eff} (i.e., the coefficient of M_0^2, which in the given model determines the stability of the magnetic subsystem and the value of the magnetic susceptibility) to depend on the external parameters. We note that in the model adopted [see formulas (4) and (5)] the influence of temperature and pressure are equivalent. However, for definiteness, in considering the α-β transition we shall treat temperature as the control parameter, assuming the pressure to be fixed and equal to atmospheric. The features of the α-β transition arising at other values of the external pressure are discussed below in Sec. 4.3.

The linear character of the dependence $J_{\mathrm{eff}}(v)$ is confirmed, for example, by the the experiments of Refs. 6 and 24, the results of which were used to construct the plots of the inverse magnetic susceptibility (actually $J_{\mathrm{eff}}M_0^2$) as a function of the specific volume change of the crystal in the α and β phases (at atmospheric pressure) in Fig. 5. In accordance with expressions (6) and (7) and with the assumptions made above as to the short-range character of the intraplane exchange interaction, we have for the effective exchange constant

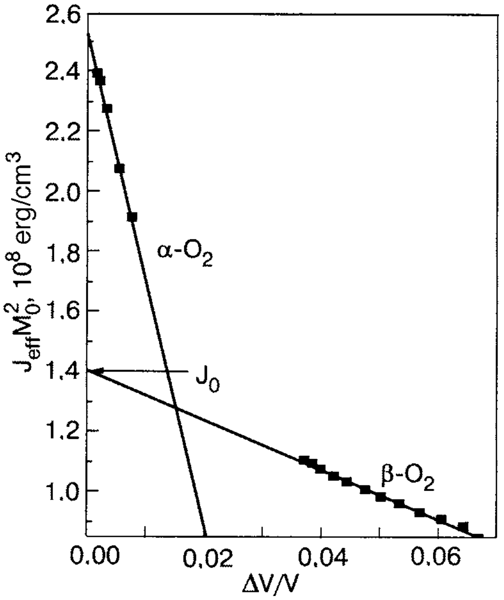

FIG. 5. Dependence of the inverse magnetic susceptibility on the relative volume change, constructed according to the data of Refs. 6 and 24. The solid lines are the theoretical curves calculated according to formula (21) with the parameters $J_0M_0^2=2.54\times10^8$ erg/cm^3, $\Lambda^{(\beta)}M_0^2=0.82\times10^9$ erg/cm^3, $\Lambda^{(\alpha)}M_0^2=8.2\times10^9$ erg/cm^3.

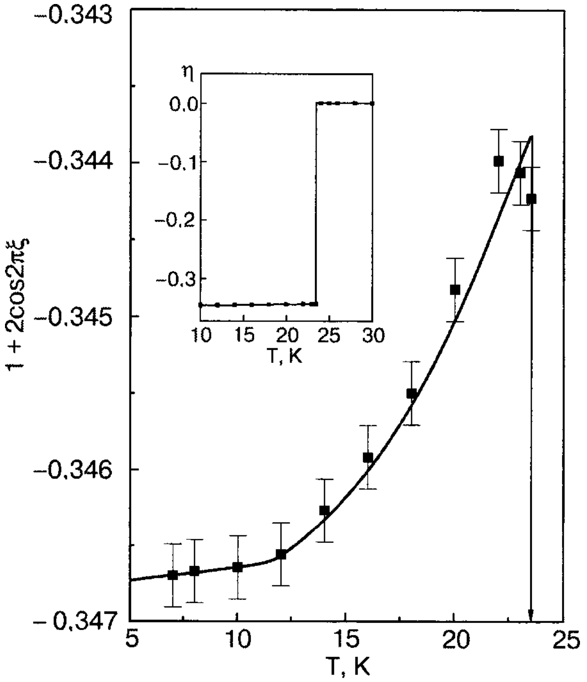

FIG. 6. Temperature dependence of the order parameter $\eta=1+2\cos2\pi\xi$, calculated according to the values of the lattice constants from Ref. 6 (points). The arrow indicates the temperature of the α-β transition. The solid line is the result of a calculation according to formulas (17) and (16). The inset shows the same dependence, which shows the range of variation of η in the α phase.

$$J_{\rm eff}=\begin{cases} J_0+\Lambda_{\parallel}^{(\alpha)}\cos4\pi\xi-\Lambda^{(\alpha)}\Delta v/v, & \alpha-\mathrm{O}_2,\\ J_0-\Lambda^{(\beta)}\Delta v/v, & \beta-\mathrm{O}_2. \end{cases} \tag{21}$$

Approximating the experimental data according to (21) allows one to estimate the values of the constants appearing in it (see Table III). The corresponding value of the "bare" exchange interaction $J_0M_0^2\simeq3\times10^8$ erg/cm^3, which, with allowance for the value of the saturation magnetization $M_0=133$ G (calculated from the data of Ref. 6), gives an estimate for the spin-flip field of the order of 230 T, in complete agreement with the value 227 T given in the review.[17]

From relations (21) and Fig. 5 it is clearly seen that a change of the magnetic structure can occur only with a simultaneous change of the crystal structure. For example, it is obvious that at certain values of the external parameters the spin coefficient that corresponds to the larger (in absolute value) effective exchange interaction constant is realized, since here $\partial^2\Phi/\partial M_0^2>0$. Hence on the basis of formula (21) we obtain the condition of stability of the collinear magnetic structure corresponding to the α phase:

$$(\Lambda^{(\alpha)}-\Lambda^{(\beta)})\frac{\Delta v}{v}-\Lambda_{\parallel}^{(\alpha)}\cos4\pi\xi>0, \tag{22}$$

where the relative change of volume is driven by expression (20). Inequality (22) holds in the case when the order parameter ξ exceeds a certain critical value

$$\xi\geqslant\xi_{\rm cr}\approx\frac{3}{8}+\frac{[\Lambda^{(\alpha)}-\Lambda^{(\beta)}]}{4\pi\Lambda_{\parallel}^{(\alpha)}}\frac{\Delta v}{v}. \tag{23}$$

Thus the transition to the α phase is possible only when conditions (18) and (22) are satisfied simultaneously. The first condition means that the lattice is "soft" enough to shift the required amount under the influence of the comparatively small magnetic forces, and the second means that during such a rearrangement of the lattice the exchange interactions favor the onset of a two-sublattice (type α) and not three-sublattice (type β) magnetic structure. Because of the presence of this mutual influence of the magnetic and lattice subsystems, the phase transition is, as we have said, decidedly first-order: the relative displacement of the close-packed planes varies in a jump from $\xi=1/3$ (in the β phase) to $\xi\geqslant\xi_{\rm cr}$ (in the α phase). The point at which this phase transition occurs at fixed external parameters is determined from the condition of equality of the thermodynamic potentials [see Eq. (19)].

The temperature dependence of the order parameter η introduced in Eq. (17) and calculated according to that formula is shown in Fig. 6 by the solid curve. The values of the phenomenological constants (see Table III) were determined mainly from the dependence of the lattice parameters on pressure (from the data of Ref. 19), and the coefficient of thermal expansion was calculated from the empirical relation (16). The points show the same dependence constructed according to the values[6] of the lattice constants.9) It is seen that the calculated dependence correctly reflects the character of the decline of the order parameter with temperature. The transition to the α phase occurs at the value $\xi=0.367$, which, it must be acknowledged, is in fair agreement (considering the substantial error that unavoidably arises in the calculation of the order parameter) with the value $\xi_{\rm cr}=0.376$ calculated according to formula (23). It should be noted, however, that the range of variation of the order parameter in the α phase is substantially less than its absolute value, as is seen in the inset of Fig. 6.

The temperature dependence of the relative change of the molar volume calculated according to formulas (15), (20), and (16), is shown in Fig. 7. The points are experimen-

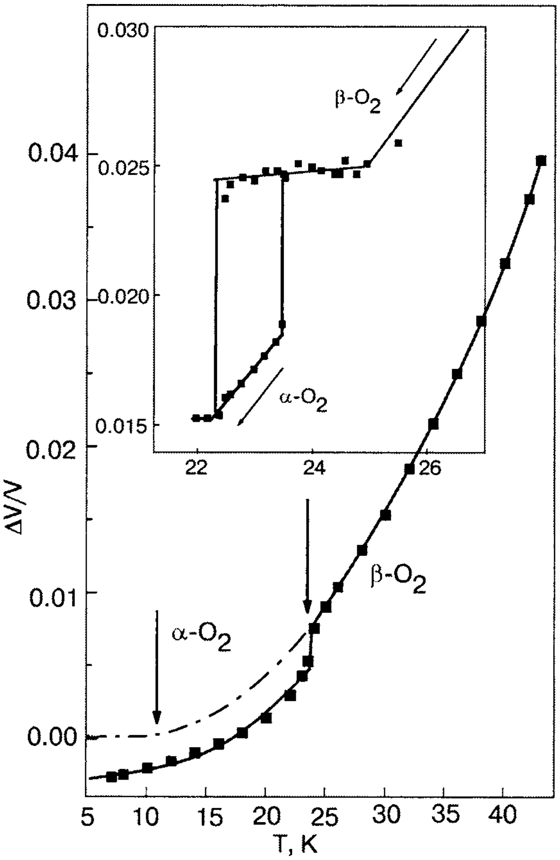

FIG. 7. Temperature dependence of the relative change of the specific volume (at atmospheric pressure). The points are experimental, the solid curve shows the approximation according to formulas (15), (20), and (16). The dashed curve is the extrapolation of the dependence for the β phase into the lower-temperature region. The inset shows the change of the molar volume on cooling in the vicinity of the α-β transition point (according to the data of Ref. 25). The solid curve is an approximation with a single fitting parameter, $\beta_P(T)=3.0\times10^{-3}$ 1/K.

tal data.[6] The dashed line shows the extrapolation of the curve for the β phase into the low-temperature region according to formulas (15) and (16); this corresponds to the thermal expansion of the lattice if the rearrangement of the lattice at the phase transition is not taken into account.

As is seen from a comparison with experiment, the proposed model satisfactorily describes the main features of the observed phase transformation—the jump of the specific volume and the nonlinear dependence on temperature in the transition region.

We note another important circumstance. A symmetry analysis based on the model developed indicates that the α-β transition should be first-order, since a fundamental rearrangement of the magnetic structure occurs (a transition from three-sublattice to two-sublattice; see above). Nevertheless, from an experimental point of view the α-β transition can be first- or second-order,[17] since the heat of transition is small (not more than 100 J/mole, which when expressed per unit volume comes out to 5×10^7 erg/cm^3). However, the evidence pointing to a first-order transition comes not only from qualitative but also from quantitative arguments. For example, it follows from expression (19) that the difference of the thermodynamic potentials of the α and β phases is determined by the difference of two contributions which are close in value: a positive contribution due to the jump of the specific volume [the last term in (19)], the value of which at the transition point $(T=23.5\ \text{K}, P=0)$ equals 8×10^7 erg/cm^3, and a negative contribution due to the appearance of the order parameter (all the other terms), the value of which is 5×10^8 erg/cm^3. Since the estimation of all the phenomenological parameters is rather crude (not better than 10%), the heat of transition thus obtained corresponds to an upper bound on the experimentally observed values.

Another argument in favor of a first-order transition is the coexistence region of the α and β phases predicted by the model, and the consequent possibility of hysteresis effects. The inset in Fig. 7 shows the change of the molar volume on cooling in the vicinity of the α-β transition point, plotted according to the data of Ref. 25. The solid curve corresponds to the theoretical approximation with a coefficient $\beta_P(T)=3.0\times10^{-3}$ 1/K and, apparently, it is precisely in the coexistence region (where the theory of phase transitions is technically correct) that the α phase is described by the same phenomenological parameters as the β phase. On further decrease of temperature the value of the coefficient of thermal expansion $\beta_P(T)$ changes substantially; this cannot be interpreted in the given model.

C. δ phase and phase transitions under pressure

Equation (11) has yet another "crystalline" solution, which formally does not depend on the type of magnetic ordering. If $\xi=1/2$ (or $\eta=-1$) then the crystal structure corresponds to the (orthorhombic) δ phase, in which the molecules in every alternate basal plane lie directly above one another (see Fig. 1f). Also entering the stability condition of the δ phase are the constants determining the magnetoelastic interactions [cf. Eq. (18)]:

$$K_{\text{eff}}-\lambda_v\left(\int_0^T\beta_P(T')dT'-\chi_T P\right)>K_4-2\Lambda_{\parallel}^{(\delta)}M_0^2 -\chi_T\lambda_v(\Lambda^{(\delta)}-\Lambda^{(\beta)})M_0^2. \qquad (24)$$

Analysis of Eqs. (17), (11) and condition (24) shows that there are two ways of getting to the δ phase in solid oxygen: directly from the β phase (through rearrangement of the magnetic structure), and from the α phase (through a gradual shift of the close-packed planes). The parameter that determines which of these paths is realized for given values of the pressure and temperature is again the specific volume of the crystal, the relative change of which (relative to the state with $T=0$, $P=0$) is equal to

$$\frac{\Delta v}{v}(T,P)\bigg|_{\delta}=\frac{\Delta v}{v}(T,P)\bigg|_{\beta}-(\Lambda^{(\delta)}-\chi_T\Lambda^{(\beta)})M_0^2 -\frac{1}{2}\chi_T\lambda_v\,. \qquad (25)$$

Indeed, as we have said, the β phase loses stability because of a change of the magnetic structure. In turn, the collinear magnetic ordering becomes energetically favorable to the Loktev structure only when condition (23) is satisfied. In other words, the value of the basal plane shift that arises simultaneously with the collinear magnetic structure must again exceed a certain critical value that depends on the value of the specific volume. At low pressure and low tem-

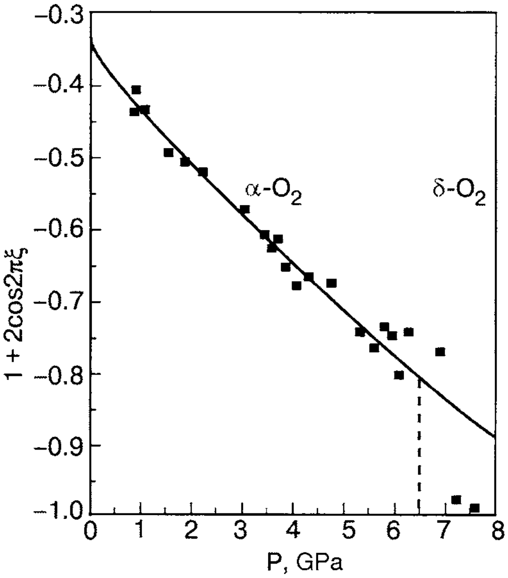

FIG. 8. Pressure dependence of the order parameter $\eta=1+2\cos 2\pi\xi$ at $T=19$ K (points), calculated using the values of the lattice constants from Ref. 19. The solid curve is the theoretical approximation calculated according to formula (17). The dashed line shows the region of the transition between the α and δ phases.

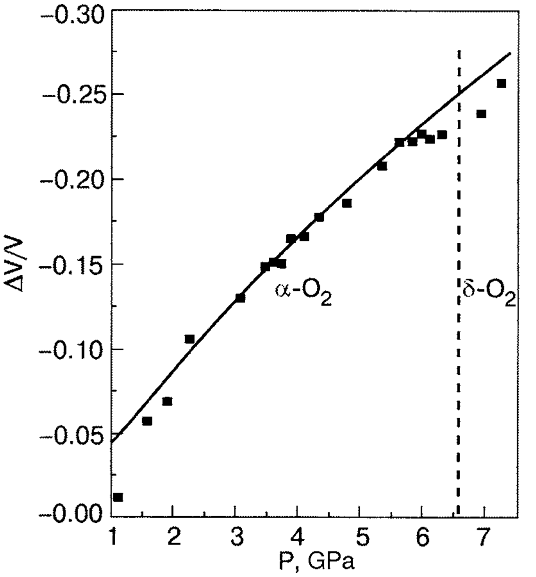

FIG. 9. Pressure dependence of the relative change of the specific volume at $T=19$ K, calculated according to the values of the lattice constants from Ref. 19. The solid curve is the theoretical approximation calculated according to formula (20). The dashed line shows the region of the transition between the α and δ phases.

peratures the value of the critical shift ξ_{cr} lies in the range $3/8<\xi_{\mathrm{cr}}<1/2$, and the unstable β phase transforms only to the α phase. However, with increasing pressure an increase of the negative volume change occurs[10)] [see Eqs. (15) and (25)] and, accordingly, ξ_{cr} grows to a limiting value of 1/2 after the stimulated transition from the β phase to the δ phase occurs under the influence of the magnetic interaction and the magnetic rearrangement. This transition, like the α-β transition, is first-order and should be accompanied by the release of heat [cf. the analogous expression for the α phase, Eq. (19)]:

$$\Phi_\delta-\Phi_\beta=-\frac{1}{2}K_{\mathrm{eff}}+\frac{5}{8}K_4-\frac{1}{8}\chi_T\lambda_v^2-\frac{1}{2}\Lambda_\parallel^{(\delta)}M_0^2+\frac{1}{2\chi_T}\left[\left(\frac{\Delta v}{v}\right)_\beta^2-\left(\frac{\Delta v}{v}\right)_\delta^2\right]. \qquad (26)$$

Let us now consider the question of how the α-δ transition occurs. Analysis of Eq. (17) shows that the value of the order parameter (i.e., the shift vector) depends substantially on the pressure. This fact is illustrated in Fig. 8, which shows the pressure dependence of η at $T=19$ K (the corresponding values of the phenomenological parameters[11)] are given in Table III; $\chi_T=0.75\times10^{-11}$ cm/dyn). It is seen that an increase of pressure causes a gradual (but not small) shift of the close-packed planes. When the limiting value $\xi=1/2$ is reached, the symmetry of the crystal increases to orthorhombic. This also corresponds to the transition to the δ phase.

The critical pressure above which the symmetry of the lattice no longer changes[12)] is calculated as 9 GPa. Generally speaking, such a transition could occur as a second-order transition, since (under the condition that the magnetic structure of the α and δ phases is identical) the two phases are found in a subgroup relationship, and the order parameter can vary in a continuous manner.

The experimental data[19] plotted in Fig. 8 show, however, that in reality the pressure-induced transition from the α to the δ phase occurs earlier, at a pressure of $\simeq$6.5–7 GPa (the transition region is denoted in the figure by the vertical dashed line), and the order parameter changes in a jump at that point. Such behavior of the parameter η permits the assertion that, in accordance with the observations,[21] the magnetic structure of the δ phase, although collinear, is different from that of the α phase (see Sec. 2.2). Formally it follows from this that the corresponding magnetoelastic interaction constants $(\Lambda^{(\alpha)},\Lambda^{(\delta)},\Lambda_\parallel^{(\alpha)},\Lambda_\parallel^{(\delta)})$ in the two phases are different. The condition for loss of stability of the collinear two-sublattice structure containing the α phase, accordingly, has a form analogous to expression (22):

$$(\Lambda^{(\delta)}-\Lambda^{(\alpha)})\frac{\Delta v}{v}+\Lambda_\parallel^{(\alpha)}\cos 4\pi\xi-\Lambda_\parallel^{(\delta)}>0, \qquad (27)$$

which gives the estimate $\Lambda_\parallel^{(\delta)}\simeq-3\times10^9$ erg/cm^3.

The jumplike character of the α-δ transition at high pressures is also discernable on the pressure dependence of the relative volume change shown in Fig. 9. The theoretical curve (solid line) calculated according to formulas (25) and (15) gives good agreement with the experimental data[19] (points) up to 6 GPa, after which a significantly smoother dependence of $\Delta v/v(P)$ is observed.

Thus the α-δ transition occurs as a first-order phase transition. The cause of this, as for the transition between the α and β phases, is a rearrangement of the magnetic structure of the crystal from two collinear sublattices to four.

V. PHASE TRANSITIONS IN THE PRESENCE OF EXTERNAL MAGNETIC FIELD

As we have said more than once, an important role in the sequence of transitions between the α, β, and δ phases of solid oxygen is played by the magnetic interaction. This

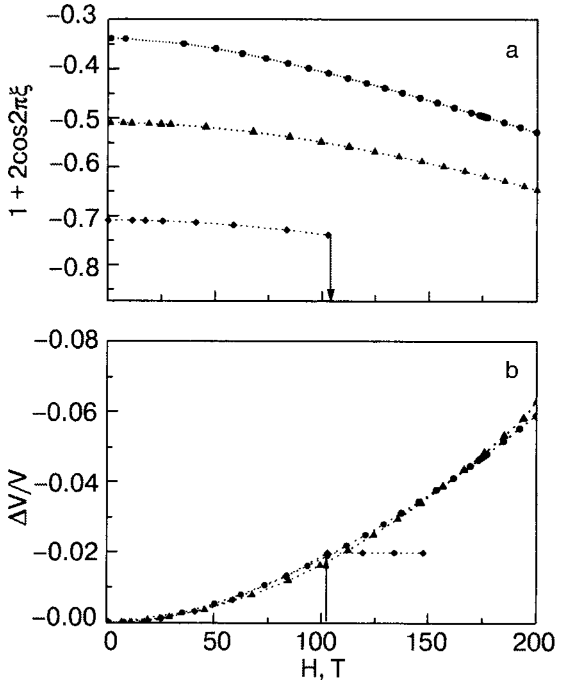

FIG. 10. The value of the order parameter $\eta = 1 + 2\cos 2\pi\xi$ (a) and relative change of the specific volume (b) as functions of the crystal magnetic field at $P = 0$ (●), 2 (▲), and 5 (*****) GPa. Temperature $T = 19$ K; spin-flip field 227 T.

naturally raises the question: Can these transitions be controlled by applying to the crystal an external magnetic field sufficient to alter the magnetic structure of the crystal?

Since all three of the phases of solid oxygen (α, β, δ) discussed in this paper (in the absence of external magnetic field) are compensated antiferromagnets, the application of an external magnetic field will lead, first, to a change of the absolute value of the antiferromagnetic vector. Taking into account the normalization conditions $\mathbf{l}^2 + \mathbf{m}^2 = M_0^2$ ($\mathbf{l}$ is one of the antiferromagnetic vectors introduced above, in the α or δ phase) and $(\mathbf{l}_1^{(\beta)})^2 + (\mathbf{l}_2^{(\beta)})^2 + \mathbf{m}^2 = M_0^2$, and also the relation $\mathbf{m} = \mathbf{H}/H_E$ ($\mathbf{m}$ is the magnetization, $H_E = 227$ T is the collapse field[7]), it is easy to obtain expressions for determining the order parameter and the phase equilibrium conditions in an external field. For this one should make the following substitution in all the formulas obtained previously:

$$M_0^2 \to M_0^2 \left(1 - \frac{H^2}{H_E^2} \right).$$

Thus the magnetic field, as it were, decreases the "driving force" [see expression (17)] that leads to a shift of the basal planes, but it also influences the phase stability conditions [expressions (18) and (24)] and the value of the specific volume [expressions (15), (20), and (25)]. In particular, as an analysis of Eq. (17) shows, the application of a field in the α phase can lead to an additional shift of the basal planes "in the direction" of the δ phase (i.e., to an increase of ξ). The corresponding curves of the order parameter and specific volume as a function of external field for different values of the external pressure ($T = 19$ K), calculated according to formula (17), are shown in Fig. 10. It should be emphasized that the curves shown are more of a qualitative character, since because of the lack of data they do not take into account the contribution to the change in specific volume from the appearance of a mean magnetic moment. Nevertheless, even on the basis of the available data one can conclude that (in any case, in a defectless crystal) the field dependence of the specific volume should be only of a quadratic character. Furthermore, it can be assumed that at high enough pressures, close to the region of the transition to the δ phase, the α-δ structural transition can also be induced by a field (the proposed phase transition point at $P = 5$ GPa is indicated by an arrow in Fig. 10).

The application of a magnetic field at $P = 0$ can lead to a thermomagnetic effect: specifically, a shift of the temperature of the β-α transition by an amount

$$\Delta T = \frac{\Lambda_{\parallel}^{(\alpha)} M_0^2 (1 - \eta)}{\lambda_v \beta_P(T)\, \eta} \left(\frac{H}{H_E} \right)^2, \tag{28}$$

which at a field $H = 20$ T should amount to around 2 K. Interestingly, according to the model, a magnetic field should shift the transition point to higher temperatures, i.e., it seemingly should broaden the existence region of the β phase according to the predictions of Ref. 31, which were based on an analysis of the magnon spectrum. However, as is seen from Eq. (17), the term of a magnetic nature ($\Lambda_{\parallel}^{(\alpha)} M_0^2$) together with the temperature and pressure renormalizes the constant K_{eff}, which determines the stiffness of the crystal with respect to the magnetic "driving force." Ultimately, the sign of ΔT is determined by the balance of the two tendencies indicated, specifically, the weakening of the exchange interaction responsible for the antiparallel ordering of the magnetic moments in the external field and the increase of the compliance of the lattice with respect to a shift of the close-packed planes. Nevertheless, the precise behavior of the lines of phase transitions and their dependence on the external parameters can be established only experimentally. The possibilities of both the microscopic and the phenomenological approaches still remain limited.

It is also not ruled out that the external magnetic field can have a noticeable influence on the value of the shear modulus (and, as a consequence, on the velocity of transverse sound), which is determined by the constant K_{eff}, but the discussion of that question is beyond the scope of this paper.

6. CONCLUSION

In this paper we have analyzed on the basis of a phenomenological model the phase stability conditions and the conditions for phase transitions between different magnetocrystalline structures of solid oxygen over a wide range of pressure, temperature, and external magnetic field.

We have shown that the sequence of observed transitions between the α, β, and δ phases can be described with the use of a single structural order parameter—the shift vector of two adjacent close-packed basal planes. As the main parameter that determines the dependence of the value of the shear vector on the external thermodynamic parameters—the temperature and pressure—one can use the specific volume of the crystal (or, from a microscopic point of view, the change of the intermolecular distances), the change Δv of which can be rather large ($\Delta v \sim v$).

The character of the magnetic ordering also has a substantial influence on the crystal structure. For example, it follows from an analysis of the conditions for a minimum of the thermodynamic potential that collinear ordering is compatible only with the crystal structure of the α and δ phases. Furthermore, the value of the shift vector is also influenced by the character of the collinear magnetic ordering (two- or four-sublattice). The substantial dependence of the structural parameter on the character and form of the magnetic structure is what makes it so that the phase transitions between the β and α phases and between the α and δ phases can occur only as first-order transitions, accompanied by a jumplike change of the value of the shift vector[13)] and also of the specific volume and other observables, e.g., the lattice parameters, the energies of the different elementary excitations, etc.

Since the ''driving force'' of the structural transformations considered is necessarily a change of the magnetic ordering, then we assume that an external magnetic field, by changing the mutual orientation of the spins, can (and should) also lead to a change of the crystal structure. In particular, the proposed model predicts a change of the magnitude of the shift vector and a displacement toward the δ phase on the phase diagram upon application of magnetic field (and pressure) to a crystal found in the α phase. One also expects a noticeable change of the specific volume in a magnetic field, and the character of this dependence should be quadratic. It is not ruled out that the application of magnetic field can lead to displacement of the temperature of the α-β transition, but the lack of available experimental data does not permit an unambiguous determination of whether this displacement is to higher or lower temperatures.

As we have demonstrated, the proposed approach allows one on a qualitative and, under certain conditions (semi-)quantitative level to describe and systematize the rather large amount of experimental material that has been accumulated to date concerning the properties of solid oxygen. However, the domain of applicability of the model is restricted, at minimum, by the assumptions that a number of parameters remain unchanged or change little, and also by the fact that the values of the phenomenological coefficients used are only estimates and not rigorous quantitative values, and, possibly importantly, we have neglected effects due to the change of the mutual orientation of the oxygen molecules. Another important circumstance that can limit the applicability of the phenomenological model is its independence of the dimensionality of the crystal, since the model is essentially based on the self-consistent field theory. At the same time, it is well known that at least the magnetic characteristics of solid O_2 are close to two-dimensional, and that requires a certain care, especially for the description of phase transitions (see Ref. 17). The satisfactory agreement obtained above between the calculated and observed parameters associated with the volume change for practically all the low-temperature phases of solid O_2 is apparently due to the phenomenological allowance for the temperature dependence of the coefficients of volume thermal expansion, which most likely implicitly include the contribution of correlation effects.

On the whole, one can say that the phenomenological approach first proposed by Landau for the description of antiferromagnetically ordered systems remains applicable for such an unusual object from the theoretical and experimental standpoints as solid oxygen, where the coupling of the magnetic and elastic subsystems in principle cannot be neglected. Therefore the Landau phenomenological theory requires a certain modification due to the fact that the value of the relative shifts of the crystal (basal) planes is not small. In this paper we have attempted to go beyond the standard Landau theory, which relies on the smallness of the order parameter and, in particular, the linear theory of elasticity, and to describe the properties of the antiferromagnetic phases of solid oxygen arising under the influence of high pressures.

We are sincerely grateful to Yu. A. Freiman for acquainting us with the content of his review article[17] prior to its publication; that was the stimulus for our studies. Freiman made a number of concrete critical comments that helped us state the results presented above in a more precise way. This work was done partially as part of a plan of scientific research of the National Technical University of Ukraine ''Kiev Polytechnical Institute'' (State Registration No. N105U001280). One of us (E.V.G.) thanks A. A. Malyshenko for financial and technical support during the performance of this study.

[*]E-mail: malyshen@ukrpack.net
[†]E-mail: vloktev@bitp.kiev.ua

[1)] We note that this requirement differs from the condition of translational invariance of the crystal as a whole, since we are talking about the relative shift of only two planes, while the position of the others remains unchanged.

[2)] The idea of choosing a periodic function of the shift vector as the order parameter was put forth in Refs. 26–28.

[3)] Nonuniform shifts of this type usually give rise to the so-called polymorphic structures,[29] the best-known example of which is the case of the fcc and hcp lattices, with layer alternations of $ABCABC\ldots$ and $ABAB\ldots$.

[4)] In the exchange approximation, with accuracy up to rotations of the magnetic moments relative to the crystallographic axes.

[5)] This is meant in the sense that the appearance of the order parameter responsible for the transition entails the appearance of parameters proportional to it which transform according to the same irreducible representation.

[6)] The shear modulus is defined by the value of the second derivative of the potential Φ_{str} with respect to the vector $\mathbf{u}$, taken at the equilibrium value of the latter.

[7)] Such a dependence of the phenomenological coefficients in the case of solid oxygen can be due to both anharmonicity of the intermolecular interaction potential and to dependence on the orientation and degree of overlap of the electron shells of the oxygen molecules. The latter circumstance can turn out to be important at high pressures.

[8)] This degeneracy is lifted if the interaction of planes farther apart than nearest neighbors is taken into account.

[9)] The value of ξ was calculated from the experimental data as follows: $\xi = c \cdot \cos\beta/a$, where the quantities a, b, c, β specify the monoclinic lattice of the α phase.

[10)] We note that in solid oxygen the specific volume changes very strongly; for example, at $T=19$ K and $P=0$ one has $v \simeq 20$ cm^3/mole, while at $P=7$ GPa, $v \simeq 14$ cm^3/mole.

[11)] The values of the coefficients K_{eff}, K_4, $\Lambda_{\parallel}^{(\alpha)}$ were determined by approximating the experimental data[19] by the theoretical dependence (17), while χ_T and λ_v were obtained by approximating the dependence of the specific volume on the external pressure according to formulas (20) and (25).

[12)] We note that a further shift of the basal planes in the same direction would lead to a lowering of the symmetry and to a ''retro'' (from a symmetry standpoint) transition to the α phase.

[13)] If it were possible to ''turn off'' the magnetic interactions that lead to antiferromagnetic order in the solid oxygen crystal (e.g., on account of spin-flip of the magnetic sublattices in an external field), then the phase transitions mentioned could in principle also occur as second-order transitions, with a smooth change of the shift vector.

---

[1] O. N. Trapeznikova and L. W. Shubnikow, Nature (London) **3384**, 378 (1934).

[2] L. D. Landau, *Collected Works* [in Russian], Vol. 1, Nauka, Moscow (1969).

[3] S. V. Vonsovskiĭ, *Magnetism*, Vols. 1 and 2, Wiley, New York (1974), Nauka, Moscow (1971).

[4] B. I. Verkin and A. F. Prikhot'ko (eds.), *Cryocrystals* [in Russian], Naukova Dumka, Kiev (1983).

[5] C. Fagerstroem and A. Hollis, J. Low Temp. Phys. **1**, 3 (1969).

[6] I. N. Krupskiĭ, A. I. Prokhvatilov, Yu. A. Freĭman, and A. I. Erenburg, Fiz. Nizk. Temp. **5**, 271 (1979) [Sov. J. Low Temp. Phys. **5**, 130 (1979)].

[7] B. Verkin, V. Manzhelii, and V. Grigor'ev, *Handbook of Properties of Condensed Phases of Hydrogen and Oxygen*, Hemisphere Publishing Corporation, New York (1991).

[8] A. Jezowski, P. Stachowiak, V. V. Sumarokov, J. Mucha, and Yu. A. Freiman, Phys. Rev. Lett. **71**, 97 (1993).

[9] A. S. Borovik-Romanov, Zh. Éksp. Teor. Fiz. **21**, 1303 (1951)].

[10] A. S. Borovik-Romanov, M. P. Orlova, and P. G. Strelkov, DAN SSSR **99**, 699 (1954).

[11] V. M. Loktev, Fiz. Nizk. Temp. **5**, 295 (1979) [Sov. J. Low Temp. Phys. **5**, 142 (1979)].

[12] Yu. B. Gaididei and V. M. Loktev, Fiz. Nizk. Temp. **7**, 1305 (1981) [Sov. J. Low Temp. Phys. **7**, 634 (1981)].

[13] A. Z. Patashinskiĭ and V. L. Pokrovskiĭ, *Fluctuation Theory of Phase Transitions*, transl. of 1st Russ. ed., Pergamon Press, Oxford (1979), cited 2nd Russ. ed., Nauka, Moscow (1983).

[14] I. M. Vitebskii, V. L. Sobolev, A. A. Chabanov, and V. M. Loktev, Fiz. Nizk. Temp. **18**, 1044 (1992) [Low Temp. Phys. **18**, 733 (1992)].

[15] I. M. Vitebskii, V. L. Sobolev, A. A. Chabanov, and V. M. Loktev, Fiz. Nizk. Temp. **19**, 151 (1993) [Low Temp. Phys. **19**, 107 (1993)].

[16] I. M. Vitebskii and N. M. Lavrinenko, Fiz. Nizk. Temp. **19**, 535 (1993) [Low Temp. Phys. **19**, 380 (1993)].

[17] Y. A. Freiman and H. J. Jodl, Phys. Rep. **401**, 1 (2004).

[18] R. D. Etters, K. Kobashi, and J. Belak, Phys. Rev. B **32**, 4097 (1985).

[19] Y. Akahama, H. Kawamura, and O. Shimomura, Phys. Rev. B **64**, 054105 (2001).

[20] Yu. A. Izyumov and V. N. Syromyatnikov, *Phase Transitions and Symmetry of Crystals* [in Russian], Nauka, Moscow (1984).

[21] I. N. Goncharenko and O. L. Makarova, Phys. Rev. Lett. **93**, 055502 (2004).

[22] I. M. Vitebskii, A. N. Knigavko, and A. A. Chabanov, Fiz. Nizk. Temp. **19**, 542 (1993) [Low Temp. Phys. **19**, 385 (1993)].

[23] O. V. Kovalev, *Irreducible and Induced Representations and Co-Representations of Fedorov Groups* [in Russian], Nauka, Moscow (1986).

[24] G. S. DeFotis, Phys. Rev. B **23**, 4714 (1981).

[25] A. I. Prokhvatilov, N. N. Gal'tsov, and A. V. Raenko, Fiz. Nizk. Temp., **27**, 523 (2001) [Low Temp. Phys. **27**, 391 (2001)].

[26] J. C. Tolédano and P. Tolédano, *The Landau Theory of Phase Transitions*, World Scientific, Singapore (1987).

[27] V. P. Dmitriev, S. B. Rochal, Y. M. Gufan, and P. Tolédano, Phys. Rev. Lett. **60**, 1958 (1988).

[28] P. Tolédano, G. Krexner, M. Prem, H.-P. Weber, and V. P. Dmitriev, Phys. Rev. B **64**, 144104 (2001).

[29] B. I. Nikolin, *Multilayer Structures and Polytypism in Metallic Alloys* [in Russian], Naukova Dumka, Kiev (1984).

[30] L. D. Landau and E. M. Lifshitz, *Theory of Elasticity*, 3rd English ed., Pergamon Press, Oxford (1986), 4th Russ. ed., Nauka, Moscow (1987), p. 28.

[31] A. P. J. Jansen and A. van der Avoird, J. Chem. Phys. **86**, 3597 (1987).

Translated by Steve Torstveit

LOW TEMPERATURE PHYSICS VOLUME 31, NUMBERS 8–9 AUGUST–SEPTEMBER 2005

On the discovery of magnon sidebands in insulating antiferromagnets

R. M. White*

Carnegie Mellon University, Pittsburgh, Pennsylvania 15213, USA

W. M. Yen†

Department of Physics and Astronomy, University of Georgia, Athens, Georgia 30602-2451, USA

(Submitted February 4, 2005)
Fiz. Nizk. Temp. **31**, 1020–1023 (August–September 2005)

In this article, we reconstruct the course of events which led to the discovery and identification of magnon sidebands in the optical spectrum of simple antiferromagnetic insulators. © *2005 American Institute of Physics.* [DOI: 10.1063/1.2008138]

INTRODUCTION

In a recent article in which he summarizes his remarkable career and his many seminal contributions to our understanding of optical properties of the condensed phases,[1] Don McClure writes:

> ...But I was an unreconstructed academic and returned to academic life after receiving an offer from the University of Chicago in 1962. There, among other things, we built a pulsed magnet capable of producing fields of 20 T and saw the Zeeman effect in the triplet states of organic molecules.
>
> More interesting though was the effect of these high fields on the absorption spectrum of MnF_2 and similar transition metal compounds whose thermodynamic properties Willard Stout had been studying. We found that some of the spectra lines were split in the field as expected, but that others were not—a surprise which could be explained in terms of the antiferromagnetic structure of the crystal. While we were learning that there were such things as magnons as well as excitons in these crystals, a group of students of Art Schawlow at Stanford published a paper on the spin-wave sidebands (magnon side bands) of MnF_2. We were in second place again but our paper nicely confirmed their interpretation. We never learned why they picked up MnF_2 just when we did . . . .

The paper McClure alludes to concerned the first observation of a magnon-induced sideband in a magnetically ordered material.[2] The identification of these sidebands by a pair of young students and two post-docs illustrates how serendipity, a touch of good luck and reckless youthful enthusiasm often plays a role in scientific discovery. In this article, we describe the events that led to these developments in the hope that they will answer McClure's curiosity on this subject.

THE STANFORD HANSEN MICROWAVE LABORATORY

The authors became acquainted with each other at Stanford in the Fall 1962; at that time, one of us (RMW) was in midst of his PhD thesis work in Marshall Sparks' theory group while the other (WMY) had just joined Art Schawlow's group in spectroscopy as a Research Associate. Schawlow had arrived earlier in the year at Stanford from Bell Labs and was assigned temporary lab space in the Hansen Microwave Lab and began establishing those programs which were later to be recognized with a Nobel Prize. The Microwave Lab was housed in a "temporary" building dating from the Second World War and the lab was extremely crowded; the forced contact in these close quarters led to considerable socialization between members of the six or seven different research groups utilizing Hansen and resulted in some beneficial interactions, as exemplified by our discovery of magnon sidebands.

Schawlow's interests at the time centered on the optical properties of various dopants in insulating solids which could be used for solid state lasers. Yen and other members of the group were given the task of understanding the thermal dependence of the widths and positions of the sharp line spectra of transition metals and rare earths in solids. These studies resulted in a number of publications in which the thermal broadening and shifts of the spectra were identified as arising from phonon-ion interactions. Of significance to this article, in Imbusch *et al.*,[3] the isotope shifts of the Cr^{3+} R-lines in Al_2O_3 and MgO were related to changes in the phonon frequencies induced by the differences in the masses of the hosts and the reflection of these changes in the phonon sideband structure. In addition, in Yen *et al.*,[4] observation of phonon sideband structure was first reported for a rare earth based material ($^3H_4$ to $^3P_0$ absorption of $LaF_3{:}Pr^{3+}$).

White's thesis involved extending Suhl's theory of spin-wave instabilities in ferrites to antiferromagnets. Although the magnetic properties of antiferromagnets had been described by Néel in 1932, at that time they were more of a curiosity than a material with technological applications as were the ferrites. This is not the case today where antiferromagnets play a critical role in providing the giant magnetoresistance (GMR) so important in magnetic recording heads. White's thesis also explored the possibility of phonon instabilities which developed his appreciation for analogies between magnons and phonons.

THE VARIAN LABS AND THE OASIS

The new Physics Building at Stanford, the Varian Building, was finished in 1963 and Schawlow's spectroscopy group moved over from Hansen. At that time, it was customary for a group of us Physics graduate students and post-docs to stop for a night cap at a local watering spot ("The Oasis" or affectionately "The O") following our usual late evenings at the lab; there normally would be a whole table reserved to accommodate us and both authors were frequent attendees of these gatherings. The topic of conversation at them was wide ranging, even including physics problems at times! On one of these gatherings, about the time the two publications mentioned above were submitted, a discussion on phonon-induced sidebands arose during which White first raised the possibility of observing a magnon-induced sideband; our discourse then shifted to the practicality of observing such a feature in magnetically ordered materials and on the appropriate materials which would allow the observation of these assisted transitions. The first requirement, of course, was that the material possess good optical properties and secondly that its crystalline and magnetic properties be well characterized. At that time there were no obvious ferromagnets with the desired optical properties.

Eventually, White settled on the antiferromagnet, MnF_2, which was being investigated at Bell Labs from the resonance point of view and whose magnetic properties had been established. In fact, Vince Jaccarino once refered to MnF_2 as the "fruit fly" of magnetics research. It is reasonably transparent and has a Néel temperature that is not too low. In addition, the room temperature spectra of the Mn^{2+} in MnF_2 had been determined by Stout.[5]

The "luck" we referred to above also had to do with selecting MnF_2. MnF_2 has the rutile crystal structure, which does not have a center of symmetry between Mn pairs. It is these pairs that are excited in the sideband. This lack of symmetry enables a relatively strong electric dipole transition, without which this effect might not have been observable. This was subsequently pointed out by Tanabe *et al.*[6]

White actually purchased a sample of MnF_2 using his advisor's theory funding to launch this exploration. Crystals and boules of MnF_2 were also listed as available in a catalogue from SemiElements, a small company in Pennsylvania. We purchased a whole boule from this company; though we later obtained samples from Howard Guggenheim (Bell Labs) and from Bob Feigelson (Stanford); curiously, the samples derived from this boule proved to be the best samples we ever investigated. We never learned the origin of the boule as SemiElements went out of business soon after.

Samples in different orientations, σ, π, and α were cut from the boule, and initial surveys of the absorption spectra were done at low temperature using a photographic B&L spectrograph. Initial results were first reported at the 1963 APS Winter Meeting in Berkeley;[7] in that paper, we first reported sharp structure in the vicinity of the first two excited states of Mn^{2+} ($^4T_{1g}$ and $^4T_{2g}$) and very strong absorptions in the $^4A,^4E$ region, but no clearly identifiable magnon-assisted transitions. The paper attracted very little attention, but the preliminary results were encouraging enough to warrant continued interest on our part. Our activities attracted the attention of three members of the Schawlow group, initially Warner Scott and then Darrell Sell and Rick Greene; we began an earnest effort to obtain high resolution, low-temperature spectra of MnF_2 using a scanning spectrometer and electronic detection in the winter of 1964.

1964 was an exceptional active year for both the authors. White had obtained an NSF postdoctoral fellowship and had joined C. Kittel's group at UC Berkeley. Again guided by analogy with phonon sidebands he developed a theory for the shape of the magnon sideband. This characteristic asymmetric line shape became critical in the subsequent identification of the sideband in experimental data.

Yen, on the other hand, had begun a program to investigate optical energy transfer processes in rare earth activated systems and was in the process of interviewing for a permanent position; he was to accept an offer from Wisconsin-Madison in the Spring of 1965. We were able to revisit the MnF_2 only occasionally during this period, but fortunately both Darrell Sell and Rick Greene began to show an increased interest in this problem as 1964 progressed and it eventually became the subject of their PhD theses.

PHYSICS OF QUANTUM ELECTRONICS CONFERENCE AND THE DISCOVERY

These activities produced a small problem for Art Schawlow, since none of his grants provided coverage for these investigations. He discussed these difficulties with Yen just prior to their departure for Puerto Rico to attend the Physics of Quantum Electronics Conference (PQEC, June 28–30, 1965); it was agreed during that discussion that the project would be transferred to Wisconsin when Yen assumed his faculty position there in the Fall of 1965 but that we would continue our investigations at Stanford until our return from the PQEC meeting. Schawlow also was aware that R.E. Dietz, L.F. Johnson and others at Bell Labs had been investigating the properties of magnetically ordered materials and suggested that Yen discuss our ideas with them to resolve any conflicts if any existed. Yen's paper on linewidth studies of energy transfer mechanisms[8] was scheduled in the same session as that of Dietz *et al.* which was entitled "Fluorescence from Magnetic Crystals" (NiF_2, CoF_2, MnF_2).[9] During the question period, Bob Dietz was specifically asked by Yen whether he had observed any effects relatable to the collective magnetic excitations of the simple fluorides he investigated; before he could answer, Willi Lowe of the Hebrew University responded for him and empathetically stated that "magnetic interactions were notoriously weak and there was absolutely no chance they would couple to electronic transitions." It is likely that at that point, Schawlow wrote off our effort as a lost cause.

As noted earlier, however, we had strong and tantalizing hints of sharp structure accompanying the lower ^4T transitions of Mn^{2+} in MnF_2; before his departure for PQEC, Yen, Sell and Greene mapped out a schedule of experimentation during his absence which included He λ-point temperature runs on a high resolution Jarrell–Ash scanning spectrograph with emphasis on the lowest $^4T_{1g}$ state of MnF_2. Yen also scheduled himself for a week of vacation in St. Thomas following the PQEC meeting to extend the time before our efforts at Stanford were to be shut down. As it turns out, the additional week was not needed; Sell's lab book entry for the observation of what would later be definitely identified as magnon sidebands, shown in Fig. 1, was June 29, 1965, likely the very day of the session alluded to above! When these traces were shown to Schawlow in early July, he im-

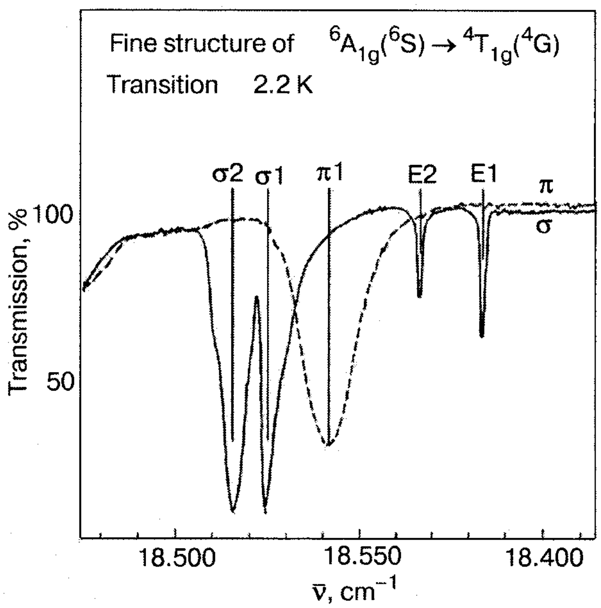

FIG. 1. Absorption spectrum of MnF_2 in the range of 18.550 cm^{-1}. The absorptions E1 and E2 are pure electronic transitions of Mn^{2+}. The absorptions $\sigma1$, $\sigma2$, and $\pi1$ are the first identified magnon-assisted transitions in a magnetic material.

mediately understood the importance of the observation, and shutting down the effort was, of course, never considered again. Schawlow's enthusiasm was also responsible for White returning to Stanford as an Assistant Professor in the fall of 1965.

CONCLUSIONS

A complete description of the magnon sideband phenomenon was published in 1967.[10] The fact that the peak of the sideband is directly related to the frequency of magnons at the Brillouin zone boundary enables one to study these modes quite easily, which previously could only be done by neutron scattering. At least half a dozen theses on various aspects of the spectra of magnetically ordered materials from Stanford and from Wisconsin followed in the following decades; this work contributed to a comprehensive understanding of the static and dynamic optical properties of ordered magnetic systems. These studies included studies on the luminescence properties of pure and doped MnF_2,[11,12] the observation of induced photomagnetism,[13] of magnon-induced broadening of optical transitions,[14] of circular and magnetic circular dichroism[15] and the discovery of biexciton annihilation in this material.[16] And recently, we have been able to identify sublattice splittings in MnF_2 induced by dipolar interactions predicted earlier by one of us (RMW).[17,18]

It is interesting how often new concepts in science appear almost simultaneously in different contexts. While we were looking for what we now call an exciton-magnon excitation in MnF_2 at Stanford, the very similar phenomenon of two-magnon excitation in the infrared was unknowingly being observed in FeF_2 by I. Silvera at Berkeley[19] and later in CoF_2 at Bell Labs.[20] In fact, the Berkeley IR absorption data with its anamolous peak at 154 cm^{-1} was presented in the very same session of the 1963 APS meeting in Berkeley at which we presented our first optical spectra of MnF_2. And, as indicated by McClure's quote at the beginning of this article, his group was also studying the optical spectra of MnF_2 and had been puzzled by the observation of transitions which did not split in a magnetic field.[21] Now that we understand this process we know that all these phenomenon are related, and their existence provides a very useful technique for studying magnon dynamics[22] as well as energy transfer in solids.[23]

[*] E-mail: white@ece.cmu.edu
[†] E-mail: wyen@physast.uga.edu

---

[1] D. S. McClure, J. Lumin. **100**, 47 (2002).
[2] R. L. Greene, D. D. Sell, W. M. Yen, A. L. Schawlow, and R. M. White, Phys. Rev. Lett. **15**, 656 (1965).
[3] G. F. Imbusch, W. M. Yen, A. L. Schawlow, G. E. Devlin, and J. P. Remeika, Phys. Rev. **136**, A 481 (1964).
[4] W. M. Yen, W. C. Scott, and A. L. Schawlow, Phys. Rev. **136**, A 271 (1964).
[5] J. W. Stout, J. Chem. Phys. **31**, 709 (1959).
[6] Y. Tanabe, T. Moriya, and S. Sugano, Phys. Rev. Lett. **15**, 1023 (1965).
[7] W. M. Yen, W. C. Scott, and R. M. White, Bull. Am. Phys. Soc. **II-9**, 715 (1963).
[8] W. M. Yen, R. L. Greene, and W. C. Scott, "Optical linewidth studies of energy transfer mechanisms between impurity ions," *Proceedings of the Physics of Quantum Electronics*, P. L. Kelley, B. Lax, and P. E. Tannenwald (eds.), McGraw-Hill, New York (1966), p. 332.
[9] R. E. Dietz, L. F. Johnson, and H. J. Guggenheim, "Fluorescence of magnetic crystals," *Proceedings of the Physics of Quantum Electronics*, P. L. Kelley, B. Lax, and P. E. Tannenwald (eds.), McGraw-Hill, New York (1966), p. 361.
[10] D. Sell, R. Greene, and R. M. White, Phys. Rev. **158**, 489 (1967).
[11] R. L. Greene, D. D. Sell, R. S. Feigelson, G. F. Imbusch, and H. J. Guggenheim, Phys. Rev. **171**, 600 (1968).
[12] B. A. Wilson, W. M. Yen, J. Hegarty, and G. F. Imbusch, Phys. Rev. B **19**, 4238 (1978).
[13] J. F. Holzrichter, M. L. Report No. 1912, Stanford University, November (1970).
[14] M. W. Passow, D. L. Huber, and W. M. Yen, Phys. Rev. Lett. **23**, 477 (1969).
[15] Y. H. Wong, F. L. Scarpace, C. D. Pfeifer, and W. M. Yen, Phys. Rev. B **9**, 3086 (1974).
[16] B. A. Wilson, J. Hegarty, and W. M. Yen, Phys. Rev. Lett. **41**, 268 (1978).
[17] D. J. Lockwood, R. M. White, and W. M. Yen, Phys. Rev. B **69**, 174413 (2004).
[18] R. M. White, J. Appl. Phys. **36**, 3653 (1965).
[19] I. Silvera and M. Tinkham, Bull. Am. Phys. Soc. **II-9**, 714 (1963).
[20] P. L. Richards, Bull. Am. Phys. Soc. **II-10**, 33 (1965).
[21] P. G. Russell, D. S. McClure, and J. W. Stout, Phys. Rev. Lett. **16**, 176 (1966).
[22] L. D. Rotter, W. M. Dennis, and W. M. Yen, Phys. Rev. B **42**, 720 (1990).
[23] G. P. Morgan and W. M. Yen, "Optical energy transfer in insulators," in *Laser Spectroscopy of Solids*, W. M. Yen (ed.), Vol. 65 of Springer Topics in Applied Physics, Springer-Verlag, Berlin (1989), p. 77.

This article was published in English in the original Russian journal. Reproduced here with stylistic changes by AIP.

LOW TEMPERATURE PHYSICS VOLUME 31, NUMBERS 8–9 AUGUST–SEPTEMBER 2005

Direct optical excitation of two and three magnons in α-Fe_2O_3

Y. Tanabe

Department of Applied Physics, University of Tokyo, 7-3-1 Hongo, Tokyo 113-8656, Japan

Y. Fujimaki, K. Kojima, and S. Uchida

Department of Physics, University of Tokyo, 7-3-1 Hongo, Tokyo 113-8656, Japan

S. Onari and T. Matsuo

Institute of Materials Science, University of Tsukuba, Tsukuba, Ibaraki 304-8573, Japan

S. Azuma and E. Hanamura*

Chitose Institute of Science and Technology and Japan Science and Technology Agency Chitose, Hokkaido 066-8655, Japan

(Submitted December 20, 2004)
Fiz. Nizk. Temp. **31**, 1024–1031 (August–September 2005)

Direct excitation of two and three magnons is observed in mid-infrared absorption and Raman scattering spectra of α-Fe_2O_3 crystals. These polarization characteristics and the spectra themselves are shown to be understood from group-theoretical point of view. The microscopic mechanism of three-magnon excitation is proposed in addition to that of well-known two-magnon excitation process. © *2005 American Institute of Physics.* [DOI: 10.1063/1.2008139]

I. INTRODUCTION

Transition-metal oxide with open d-electron shells have shown many interesting magnetic and transport phenomena of strongly correlated d-electrons.[1] Optical absorption due to phonon-assisted two-magnon excitation was observed for transition-metal oxides of quasi-two-dimensional La_2CuO_4, Nd_2CuO_4, $Sr_2CuO_2Cl_2$,[2] La_2NiO_4,[3] $YBa_2Cu_3O_6$,[4] and two-leg-ladder $(Ca,La)_{14}Cu_{24}O_{41}$ crystals.[5] On the other hand, phonon-assisted particle-hole excitation of the spinons was confirmed in quasi-one-dimensional Sr_2CuO_3 crystal.[6] Here the oscillator strength of the optical phonon makes the optical excitation of two magnons possible through the magnon-phonon interaction.[7]

We have observed direct mid-infrared absorption by two- and three-magnon excitation in α-Fe_2O_3 crystal.[8] This is due to the effective electric dipole moment induced by the combined effect of the electronic transition of the d-electron and the exchange interaction between the neighboring Fe^{3+} ions.[9,10] The magnon energy as well as the absorption coefficient of α-Fe_2O_3 are much larger than those of MnF_2 with Néel temperature $T_N = 67.3$ K and absorption coefficienct of a few cm^{-1} (Refs. 11, 12).

Magnetic properties of α-Fe_2O_3 have been well studied,[13] and the origin of weak ferromagnetism was proposed from the studies of this crystal.[14,15] The magnon dispersion has been obtained from inelastic neutron scattering investigation[16] and also from its theoretical analysis.[17] On the other hand, the phonon structure of α-Fe_2O_3 is also obtained by the infrared reflection spectrum,[18] Raman scattering[19] and lattice dynamics study.[20] Two-magnon Raman scattering in this crystal had been a controversial point but this was also clarified by the effects of pressure and isotope substitution on the Raman spectrum.[21–23] Magnetic structure of this crystal was found to change at Morin temperature $T_M = 261$ K.[24] Below T_M, the four sublattice magnetizations are parallel to the threefold c axis of the corundum structure with the space group $D_{3d}^6(\bar{3}\,2(/m))$, and this phase shows pure antiferromagnetism. Between T_M and the Néel temperature $T_N = 960$ K, the four sublattice magnetizations are almost in the ab plane, and the weak ferromagnetism is induced in the direction of the twofold a axis. Here the space group is monoclinic $C_{2h}(2/m)$.

In the present paper, we shall supplement the previous report on the mid-infrared absorption due to magnons[8] by supplying the observed polarization dependence and temperature dependence of the Raman spectrum. Then we can confirm the assignment of the two-magnon excitation at the D point at the Brillouin zone edge to the effective (exchange) dipole moment $\pi \mathbf{S}_i \cdot \mathbf{S}_j$. This will be given in Sec. 2. The three-magnon excitation was assigned to originate from the effective dipole moment, like in $\pi^{DM} \cdot (\mathbf{S}_i \times \mathbf{S}_j)$.[10] We will give all the terms that contribute to the three-magnon excitation in Sec. 3 and discuss its microscopic mechanism in Sec. 4. Last, Sec. 5 is for conclusion and discussion.

II. MID-INFRARED AND RAMAN SCATTERING SPECTRUM

The samples used were prepared from single crystals of good-quality natural hematite, which were also used in Ref. 8. These crystals have been sliced and polished by using diamond powder and finally by aluminate powder with a diameter 0.1 μm. The samples used have thickness ranging from 50 μm to 140 μm.

The measurement of the mid-infrared absorption spectrum was performed with a Bruker IFS 113 V Fourier-transform spectrometer in the energy range 350 to 2400 cm^{-1}. We observed several prominent features on the high-energy side of the single phonon modes,[18] as shown in

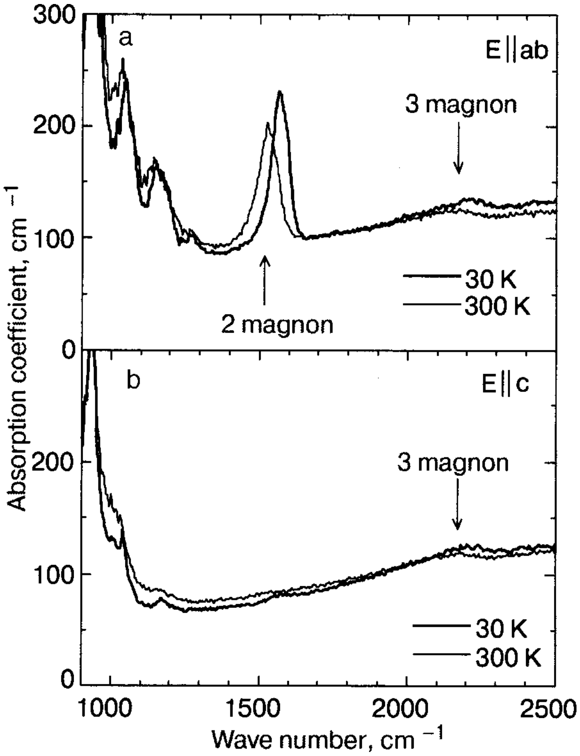

FIG. 1. The polarization dependence of mid-infrared absorption spectrum of α-Fe_2O_3 crystal with a crystal thickness 120 μm at 30 K and 300 K (a). The incident beam is polarized in the *ab* plane and in the *c* direction (b).

Figs. 1 and 2. The first important characteristics is that the absorption peak just above 1500 cm^{-1} shows strong polarization dependence: no signal is observed for $\mathbf{E}\| c$ axis while the strong signal for $\mathbf{E}\perp c$ axis. On the other hand, the signal around 2200 cm^{-1} is observed under both polarizations. Second, both of these peaks show blue shift with decreasing lattice temperatures, e.g., the absorption peak of 1500 cm^{-1} at room temperature shifts to 1570 cm^{-1} at 30 K. Third, three absorption peaks are observed on the high energy side of the single phonon modes,[18] i.e., 1160 cm^{-1}, 1050 cm^{-1}, and 920 cm^{-1}. These energies are almost independent of the lattice temperature in contrast to those at 1500-1 and 2200 cm^{-1}. From these polarization and temperature dependence, we may speculate that the signals at 1500 cm^{-1} and 2200 cm^{-1} come from the elementary excitations different from others.

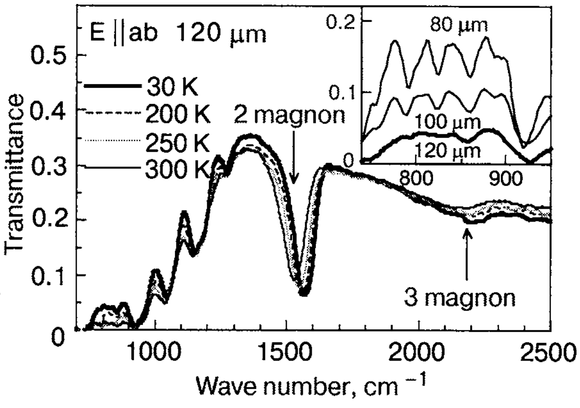

FIG. 2. The temperature dependence of the transmission spectrum for the polarization *E* in the *ab* plane for the same sample thickness 120 μm as in Fig. 1. The inset shows the sample-thickness dependence around 800 cm^{-1} at 30 K. A single E_u magnon is expected at 782 cm^{-1} while combination modes of two phonons are at 780 cm^{-1} (TO_2+LO_3), 805 cm^{-1} (TO_3+LO_2) and 851 cm^{-1} (TO_3+LO_1').

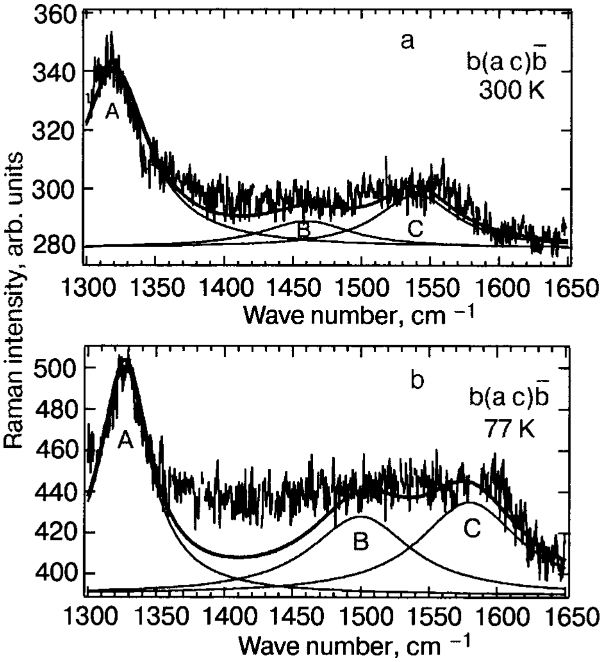

FIG. 3. Raman spectrum of α-Fe_2O_3 at room temperature (a) and 77 K (b) with incident beam 633 nm from He–Ne laser. *A*, *B* and *C* describe Lorentzian fittings with (central wave number, width at half maximum, relative intensity) = (1320 cm^{-1}, 60 cm^{-1}, 60) for *A*, (1460 cm^{-1}, 80 cm^{-1}, 9) for *B*, and (1540 cm^{-1}, 70 cm^{-1}, 18) for *C* in (a), and (1327 cm^{-1}, 45 cm^{-1}, 110) for *A*, (1500 cm^{-1}, 90 cm^{-1}, 38) for *B*, and (1580 cm^{-1}, 90 cm^{-1}, 45) for *C* in (b). The thick solid line describes superposition of Lorentzian curves *A*, *B*, and *C*.

As a matter of fact, on the basis of the assignment of single phonon modes[18] observed by the infrared reflection spectrum and the magnon dispersion obtained from neutron inelastic scattering, we can assign the 1160 cm^{-1} signal to a combination of TO_4 (524 cm^{-1}) + LO_4 (or LO_2') (662 cm^{-1}), the 1050 cm^{-1} signal to that of TO_4 (524 cm^{-1}) + TO_2' (526 cm^{-1}), and the 920 cm^{-1} signal to that of TO_3 (437 cm^{-1}) + TO_2' (494 cm^{-1}). Each of the transverse and longitudinal E_u modes is numbered from the lower to higher energy side, and LO_2' and TO_2' correspond to the A_{2u} modes. The energies of 1500 cm^{-1} and 2200 cm^{-1} are nearly equal to two and three magnons, respectively, obtained from the neutron data.[17] We are interested in the wave number region around 800 cm^{-1} to check whether a single magnon is observed in the absorption spectrum. The transmission spectrum is observed as shown in the inset of Fig. 2 by reducing the sample thickness from 120 μm to 100 and 80 μm.

In order to confirm these assignments, Raman spectrum has been observed with Stokes shift in this energy range. This gives information to supplement the mid-infrared absorption spectrum. Figures 3a, b give the Raman spectrum observed by using He–Ne laser as incident beam at room temperature and nitrogen temperature, respectively. A doublet structure is observed with Stokes shift 1460 cm^{-1} and 1540 cm^{-1} at room temperature, as shown in Fig. 3a, and showing a blue shift similar to that in the mid-infrared absorption spectrum at nitrogen temperature, as shown in Fig. 3b. The stronger signal at 1320 cm^{-1} is almost independent of the lattice temperature and is well assigned to overtone of two LO_4 phonons ($2\times 662\ \mathrm{cm}^{-1}$). These two-phonon excitations at 1160, 1050 and 920 cm^{-1} and at 1320 cm^{-1} obey Loudon's selection rule of combination and overtone modes, respectively, for the infrared and Raman scattering process.[25] The doublet structure around 1500 cm^{-1} is observed under the configuration $b(a,c)\bar{b}$ but not for $b(a,a)\bar{b}$ nor for $b(c,c)\bar{b}$, while the signal at 1320 cm^{-1} is allowed for both configurations. This means that the elementary excitation with doublet structure around 1500 cm^{-1} has the symmetry E_g.

The second task of the present paper is to understand two- and three-magnon excitations both in the mid-infrared and Raman spectrum from both group-theoretical and microscopic points of view. These will be discussed in the following sections.

III. SELECTION RULES

The mid-infrared absorption peak due to two-magnon excitation is observed more strongly than a single magnon absorption. This is expected simply from two reasons: (i) the joint density of states for a pair of excitation $\mathbf{k}$ and $-\mathbf{k}$, which diverges at the high-symmetry points on the Brillouin zone (BZ) edges, becomes much larger than that of a single elementary excitation near the Γ point; (ii) and the two-magnon excitation in the antiferromagnet is accompanied by rather large electronic dipole moment due to the mechanism different from a single magnon excitation, as discussed in Ref. 9. The total symmetry of the two excitons (magnons) at the high-symmetry points of the BZ edge may be determined as given in the literature.[26,27]

The magnetic unit cell of α-Fe_2O_3 consists of four sublattices both below and above T_M. The effective dipole moment to excite two magnons is associated with the antiferromagnetic pair of the neighboring magnetic ions coupled by the superexchange interaction.[9]

Loudon[26,27] has shown how to derive the selection rules for the two-magnon absorption. The procedure is to reduce the representation at the Γ point, whose bases are two-magnon states at the high-symmetry point of the BZ boundary, and to see whether the decomposition contains the representation to which the dipole moment operator belongs. If it does, the excitation of two magnons at the boundary will be allowed, intensified there by the high density of states.

This conventional procedure can be applied to optical excitations of two magnons at high-symmetry points in the Brillouin edge for antiferromagnets with two magnetic sublattices such as in MnF_2. However, in the case of α-Fe_2O_3 where the magnetic unit cell contains four sublattices, we must exclude the processes of two-magnon excitation from the pair with ferromagnetic coupling. As a result, the selection rule is modified as shown in Ref. 10. The modified selection rule for direct optical excitation of two magnons in α-Fe_2O_3 is summarized as follows. Symmetry put in a double bracket on the right-hand side is forbidden, either because the final state is antisymmetric or because it corresponds to the creation of two magnons both within the up- or down-sublattices. In the antisymmetric combination denoted by {}, two contributions cancel out each other.

TABLE I. Representations and excitation energies of magnons at high-symmetry points.

Symmetry point	Representaion	Energy, meV
Γ optical	E_u	97.0
Z acoustic	Z_2	86.8
optical	Z_3	90.9
D acoustic	D_1+D_3	92.0
optical	D_2+D_4	97.1
A acoustic	A_1	96.6
optical	A_1	98.0

(a) Z point with aconstic Z_2 and optical Z_3 magnons:

$$[Z_2^2]=[Z_3^2]=A_{1u}+[[E_g]],\quad \{Z_2^2\}=\{Z_3^2\}=[[A_{2u}]], \tag{1}$$

$$Z_2\times Z_3=A_{1g}+A_{2g}+[[E_u]]; \tag{2}$$

(b) D point with acoustic D_1+D_3 and optical D_2+D_4 magnons:

$$D_1^2+D_3^2=D_2^2+D_4^2=A_{1g}+E_g+[[A_{1g}+E_g]], \tag{3}$$

$$2D_1\times D_3=2D_2\times D_4=2[[A_{2g}+E_g]], \tag{4}$$

$$D_1\times D_2+D_3\times D_4=A_{1u}+E_u+[[A_{1u}+E_u]], \tag{5}$$

$$D_1\times D_4+D_2\times D_3=A_{2u}+E_u+[[A_{2u}+E_u]]; \tag{6}$$

(c) A point with acoustic A_1 and optical A_1 magnons:

$$[A_1^2]=[[A_{1g}+A_{2g}+2E_g]]+A_{1u}+E_u, \tag{7}$$

$$A_1^2=[[A_{2u}+E_u]], \tag{8}$$

for each mode, and

$$A_1\times A_1=A_{1g}+A_{2g}+2E_g+[[A_{1u}+A_{2u}+2E_u]] \tag{9}$$

for the simultaneons excitation of the acoustic and optical mode.

For D_{3d}, the states of allowed electric dipole transition are E_u for a- and b-polarized light and A_{2u} for c polarization, and the allowed states of Raman scattering are E_g and A_{1g}. We have already obtained the eigenvectors at high-symmetry points,[10] and we also have the eigenenergies of the magnon at these points[16] as shown in Table I.

Now we can assign the two-magnon excitation from the experimental results of mid-infrared absorption and Raman scattering as well as from the selection rule together with Table I. First, we can eliminate the contribution from the Z point to the mid-infrared absorption of two-magnon excitation because $[[A_{2u}]]$ in Eq. (1) and $[[E_u]]$ in Eq. (2) come from two magnons within the up- or down-spin sublattices. Furthermore, Raman scattering with E_g symmetry is absent from the contribution at the Z point. Second, the dipole-allowed transition with E_u symmetry is possible from the D and A points, as seen from Eqs. (5), (6), and (7), respectively. However, the doublet structure of E_g Raman scattering is acceptable for the D point because the splitting between two acoustic magnons $D_1 \times D_3$ and two optical magnons $D_2 \times D_4$ in Eq. (3) give the doublet structure of E_g symmetry with a splitting energy of 10 meV, in agreement with the observed value. The Raman signal in Eq. (9) comes from one optical and one acoustic magnon, and the splitting of the two E_g modes may be speculated to be smaller than the splitting 1.4 meV between acoustic and optical magnons. Although we cannot eliminate the possibility to assign the doublet Raman signal to the two-magnon excitation at the A point, two-magnon excitation from the D point looks most probable.

Let us discuss the possibility of this assignment from a numerical standpoint. A combination energy of infrared-active (D_1+D_3) and (D_2+D_4) is 189 meV ($1533\,\mathrm{cm}^{-1}$), while two overtones of Raman-active $D_1^2+D_3^2$ and $D_2^2+D_4^2$ are 184 meV ($1482\,\mathrm{cm}^{-1}$) and 194 meV ($1565\,\mathrm{cm}^{-1}$), respectively. The systematic difference between the observed energies and the sum of corresponding energies given in Table I is about $30\,\mathrm{cm}^{-1}$ and may be attributed to the binding energy of two magnons.[28] While a combination of acoustic and optical magnons $D_1 \times D_4 + D_2 \times D_3$ in Eq. (6) may be excited by both polarized light $\mathbf{E} \perp c$ axis (E_u) and $\mathbf{E} \| c$ axis (A_{2u}), the effective dipole moment of this process is an order of magnitude smaller than that of Eq. (5).[10] Therefore, the mid-infrared absorption due to two-magnon excitation should be observed dominantly under polarization $\mathbf{E} \perp c$ axis through E_u in Eq. (5).

We shall show that three-magnon excitation is accessible by both incident beams with the polarization parallel and perpendicular to the c axis. The three-magnon excitation may be possible for the combination of an optical magnon with E_u symmetry at the Γ point and two magnons at the opposite BZ edges. We may use D points as the BZ edge point with high symmetry. Then the three-magnon excitations have the following symmetry:

$$\begin{aligned} E_u \times (D_1^2+D_3^2) = E_u \times (D_2^2+D_4^2) &= A_{1u}+A_{2u}+2E_u \\ &\quad +[[A_{1u}+A_{2u}+2E_u]], \end{aligned} \tag{10}$$

$$\begin{aligned} E_u \times (D_1 \times D_2 + D_3 \times D_4) &= E_u \times (D_1 \times D_4 + D_2 \times D_4) \\ &= A_{1g}+A_{2g}+2E_g \\ &\quad +[[A_{1g}+A_{2g}+2E_g]]. \end{aligned} \tag{11}$$

As a result, three-magnon excitations $E_u \times (D_1^2+D_3^2)$ and $E_u \times (D_2^2+D_4^2)$ are excited by the incident beam both for polarization parallel (A_{2u}) and perpendicular (E_u) to the c axis. The excitation energy, which is estimated as a sum of the corresponding magnon energies in Table I, extends from 281 meV ($2266\,\mathrm{cm}^{-1}$) to 291 meV ($2349\,\mathrm{cm}^{-1}$). The energy difference of the observed one from these is a little larger than $30\,\mathrm{cm}^{-1}$ (the binding energy of two magnons[28]) and may be attributed to the binding energy of three magnons.

IV. MICROSCOPIC MODEL

The possibility of electric dipole transition due to two- and three-magnon excitation has been confirmed by the group-theoretical consideration and the magnon dispersion obtained by the neutron diffraction. In the two-magnon excitation, the superexchange interaction between the neighboring antiferromagnetic ions is accompanied by the electric dipole transition within the transition-metal ion or the charge-transfer transition between the empty $3d$ orbital of the magnetic ion and the $2p$ orbitals of the surrounding oxygen ion.[9] We use the expression in Ref. 9 to estimate the two-magnon absorption coefficient. The charge transfer excitation gives the absorption coefficient of the order of $10^4\ \mathrm{cm}^{-1}$ around 2 eV. The superexchange interaction is assumed to be of the order of the Néel temperature 960 K (0.1 eV), and we use this value for the off-diagonal exchange matrix element. Then the absorption coefficient for two-magnon excitation is estimated to be of the order of $10^2\ \mathrm{cm}^{-1}$. This value is reasonable to explain the observed results in Fig. 1. The advantage of direct optical excitation of two magnons in α-$\mathrm{Fe_2O_3}$ over $\mathrm{MnF_2}$ is speculated to arise from the large charge-transfer matrix element between the $O(2p)$ and $\mathrm{Fe}^{3+}(3d)$ orbitals, and its low excitation energy ΔE of the order of 2 eV for α-$\mathrm{Fe_2O_3}$. This large matrix element at the same time results in large absorption coefficient of the order of $10^4\ \mathrm{cm}^{-1}$ and high Néel temperature 960 K through the large superexchange integral $2J$. This is in contrast to the Néel temperature of $\mathrm{MnF_2}$, which is 67.3 K.

The dipole moment of two-magnon excitation is described by $\pi(i,j)\mathbf{S}_i \cdot \mathbf{S}_j$. As to the three-magnon excitation, we first remember that Moriya[15] has derived the so-called Dzyaloshinski-Moriya interaction $\mathbf{d} \cdot (\mathbf{S}_i \times \mathbf{S}_j)$ as the (off-diagonal) exchange interaction $-2J\mathbf{S}_i \cdot \mathbf{S}_j$ between the ions i and j, modified by the (off-diagonal) spin-orbit interaction $\lambda(\mathbf{S} \cdot \mathbf{L})$. The magnitude of $\mathbf{d}$ here may be estimated very roughly as $(\lambda/\Delta E) \times (-2J)$, where ΔE is the energy of electronic excitation from the ground $|0\rangle$ to the excited state $|\mathrm{n}\rangle$. This suggests that there may also exist an effective dipole moment such as $\pi^{DM}(i,j) \cdot (\mathbf{S}_i \times \mathbf{S}_j)$, which may be regarded as derived from the exchange dipole moment $\pi(i,j)\mathbf{S}_i \cdot \mathbf{S}_j$ (responsible for the two-magnon absorption) perturbed by the spin-orbit interaction. The magnitude of π^{DM} may then be given roughly by $(\lambda/\Delta E) \times \pi$. Note here that $\mathbf{S}_i \times \mathbf{S}_j$ contains, e.g., a term like $(S_{ix}-iS_{iy})S_{jz}-S_{iz}(S_{jx}-iS_{jy})$ which gives rise to three-magnon excitation.

The expression for the effective dipole moment $\mathbf{P}^{DM}$ of three-magnon excitation is expressed as

$$\mathbf{P}^{(DM)} = \mathbf{P}_{i*j}^{(DM)} + \mathbf{P}_{j*t}^{(DM)}, \tag{12}$$

$$\mathbf{P}_{i*j}^{(DM)} = \sum_n \left(\frac{\langle 00|\mathcal{H}_{\mathrm{so}}|n0\rangle\langle n0|\mathbf{P}_{i*j}|00\rangle}{E_{i0}-E_{in}} + \frac{\langle 00|\mathbf{P}_{i*j}|n0\rangle\langle n0|\mathcal{H}_{\mathrm{so}}|00\rangle}{E_{i0}-E_{in}} \right) \tag{13}$$

with the exchange dipole $\mathbf{P}_{i*j}$ defined in Ref. 9. That is,

$$\mathbf{P}_{i*j} = \sum_{nn'm} \pi(i;n' \leftarrow n, jm)\mathbf{s}_i(n' \leftarrow n) \cdot \mathbf{s}_{jm}, \tag{14}$$

$$\mathbf{s}_i(n' \leftarrow n) = \sum_{mm'} c_{in'm'}^{\dagger} c_{inm} \langle m'|\mathbf{s}|m\rangle. \tag{15}$$

When we assume that the ion i is excited by the light to the lowest orbital state $|n\rangle = |\kappa T_{1g}\nu\rangle$ from its ground state $|0\rangle = |A_{1g}\rangle$, we have the following matrix element:

$$\langle n0|\mathbf{P}_{i*j}|00\rangle=\mathbf{\Pi}(n0,00)\langle S-1M_s^0|\sigma_i|SM_s\rangle\cdot\langle 0|\mathbf{S}_j|0\rangle, \tag{16}$$

$$\mathbf{\Pi}(n0,00)=\sum_{nn'm}\pi(i;n'\leftarrow n,jm)\times\frac{\langle\kappa^4T_{1g}\nu\|\mathbf{s}_i(n'\leftarrow n)\|^6A_{1g}\rangle}{\langle S-1\|\sigma\|S\rangle 2S}. \tag{17}$$

In terms of operator equivalent for off-diagonal elements,[29,30] $\mathcal{H}_{\rm so}$ may be replaced by

$$\langle^6A_{1g}M_s|\mathcal{H}_{\rm so}|\kappa^4T_{1g}M^{0_s}\nu\rangle=\zeta(0n)\langle SM_s|\sigma^\dagger|S-1M_s^0\rangle\cdot\langle A_{1g}|\tau^\dagger|\kappa T_{1g}\nu\rangle, \tag{18}$$

$$\text{where}\quad \zeta(0n)=\frac{\langle^6A_{1g}\|V_{\rm so}\|\kappa^4T_{1g}\rangle}{\langle S\|\sigma^\dagger\|S-1\rangle\cdot\langle A_{1g}\|\tau^\dagger\|\kappa T_{1g}\rangle}, \tag{19}$$

$$\langle\kappa T_{1g}\|\tau\|A_{1g}\rangle=\langle A_{1g}\|\tau^\dagger\|\kappa T_{1g}\rangle=i\sqrt{3}, \tag{20}$$

$$\langle S-1\|\sigma\|S\rangle=-\langle S\|\sigma^\dagger\|S-1\rangle=\sqrt{(2S+1)/2}. \tag{21}$$

The reduced matrix element of the spin-orbit interaction operator $V_{\rm so}$ is found in Ref. 31:

$$\langle^6A_{1g}\|V_{\rm so}\|\kappa^4T_{1g}\rangle=6i\zeta, \tag{22}$$

with ζ being the spin-orbit coupling parameter for the $3d$ orbital. The operator τ is defined as

$$\tau_\nu|A_{1g}\rangle=i|\kappa T_{1g}\nu\rangle, \tag{23}$$

$$\langle A_{1g}|\tau_\nu^\dagger=-i(\kappa T_{1g}\nu|, \tag{24}$$

for $\nu=\alpha,\beta,\gamma$, and

$$\langle n|\mathcal{H}_{\rm so}|0\rangle=\zeta(0n)^*\langle S-1M_s^0|\sigma|SM_s\rangle\cdot\langle\kappa T_{1g}\nu|\tau|A_{1g}\rangle, \tag{25}$$

where $S=5/2$.

We now have

$$\begin{aligned}\mathbf{P}_{i*j}^{(DM)}&=\sum_n\left[\frac{\langle 00|\zeta(0n)\sigma_i^\dagger\cdot\tau_i^\dagger|n0\rangle\langle n0|\mathbf{P}_{i*j}|00\rangle}{E_{i0}-E_{in}}+\frac{\langle 00|\mathbf{P}_{i*j}|n0\rangle\langle n0|\zeta(0n)^*\sigma_i\cdot\tau_i|00\rangle}{E_{i0}-E_{in}}\right]\\&=\sum_n\zeta(0n)\sum_{\alpha\beta}\left[\frac{\mathbf{\Pi}(n0,00)}{E_{i0}-E_{in}}\langle 0|\tau_\alpha^\dagger|n\rangle\sigma_{i\alpha}^\dagger\sigma_{i\beta}S_{j\beta}-\frac{\mathbf{\Pi}(n0,00)^*}{E_{i0}-E_{in}}\langle 0|\tau_\alpha^\dagger|n\rangle\sigma_{i\beta}^\dagger\sigma_{i\alpha}S_{j\beta}\right],\end{aligned} \tag{26}$$

because $\zeta(0n)^*=\zeta(0n)$.

We then obtain

$$\begin{aligned}\mathbf{P}^{(DM)}=&\left[\sum_n i\zeta(0n)\frac{\operatorname{Re}\mathbf{\Pi}(n0,00)}{E_{i0}-E_{in}}\langle 0|\tau_i^\dagger|n\rangle-\sum_m i\zeta(0m)\frac{\operatorname{Re}\mathbf{\Pi}(m0,00)}{E_{j0}-E_{jm}}\langle 0|\tau_j^\dagger|m\rangle\right]\\&\cdot\frac{-1}{2S}(\mathbf{S}_i\times\mathbf{S}_j)+\sum_n i\zeta(0n)\frac{\operatorname{Im}\mathbf{\Pi}(n0,00)}{E_{i0}-E_{in}}\langle 0|\tau_i^\dagger|n\rangle\\&\times\left(\frac{1}{3}\mathbf{S}_j-\frac{1}{S(2S-1)}\mathbf{Q}_i\cdot\mathbf{S}_j\right)\\&+\sum_m i\zeta(0m)\frac{\operatorname{Im}\mathbf{\Pi}(m0,00)}{E_{j0}-E_{jm}}\langle 0|\tau_j^\dagger|m\rangle\\&\times\left(\frac{1}{3}\mathbf{S}_i-\frac{1}{S(2S-1)}\mathbf{Q}_j\cdot\mathbf{S}_i\right),\end{aligned} \tag{27}$$

where we have made use of

$$\sigma_\alpha^\dagger\sigma_\beta=\delta_{\alpha\beta}/6+[S_\alpha,S_\beta]/4S-Q_{\alpha\beta}/2S(2S-1), \tag{28}$$

$$Q_{\alpha\beta}=\frac{1}{2}(S_\alpha S_\beta+S_\beta S_\alpha)-\delta_{\alpha\beta}\frac{1}{3}S(S+1), \tag{29}$$

and

$$(\mathbf{Q}_i\cdot\mathbf{S}_j)_\nu=\sum_\beta Q_{i;\nu\beta}S_{j\beta}. \tag{30}$$

Here we evaluate $\mathbf{\Pi}=(n0,00)$ by choosing $|\kappa T_{1g}a_{+1}\rangle$ in the trigonal basis[32] as $|n\rangle$, because this is the orbital state excited by P_{i*j} of Eq. (13) in the magnetically ordered phase. Expanding the $3d$ orbital in the trigonal field in terms of real ξ, η, ζ and the u,v orbitals in the O_h field,[33] we find that $\mathbf{\Pi}=(n0,00)$ is complex. As a consequence, both the vector product term $(\mathbf{S}_i\times\mathbf{S}_j)$ and the tensor term $\mathbf{Q}_i\cdot\mathbf{S}_j$ and $\mathbf{Q}_j\cdot\mathbf{S}_i$ term in Eq. (27) can contribute to the three-magnon excitation. The three-magnon excitation due to $\mathbf{Q}_i\cdot\mathbf{S}_j$ and $\mathbf{Q}_j\cdot\mathbf{S}_i$ terms as well as $\mathbf{S}_i\times\mathbf{S}_j$ term is always accompanied by the single magnon excitation by $\mathbf{S}_j$ or $\mathbf{S}_i$ with a common coefficient. We have not yet observed clear evidence of the single-magnon excitation around 800 cm^{-1} because the tail part of large absorption coefficient due to single phonons below 700 cm^{-1} prevent clear observation of the single magnon, as shown in the inset of Fig. 2. The first term in Eq. (27) corresponds exactly to $\pi^{DM}(i,j)\cdot(\mathbf{S}_i\times\mathbf{S}_j)$ obtained in Refs. 8 and 10 simply following Moriya's derivation of the DM interaction. These spin operators are rewritten in terms of the magnon creation and annihilation operators through the Bogoliubov transformation. Then we realize that the $\mathbf{S}_i\times\mathbf{S}_j$ term as well as the $\mathbf{Q}_i\cdot\mathbf{S}_j$ and $\mathbf{Q}_j\cdot\mathbf{S}_i$ terms contribute to the three-magnon excitation.[8] Note also that the coefficients of both spin-product operators in the transition dipole moment in Eq. (27) is naturally real. From this derivation, we can answer a question where the oscillator strength of three-magnon excitation comes from. That is, when one of the two Fe^{3+} ions participating in two-magnon excitation is perturbed by off-diagonal elements of the spin-orbit interaction, three-magnon mid-infrared absorption becomes possible using the effective exchange dipole moment $\pi(i,j)$. The magnitude of three-magnon absorption due to this process is estimated as follows. The spin-orbit coupling parameter $\lambda(0n)=\zeta(0n)/2S$ is related to ζ, the atomic one, by $\lambda(0n)=-\zeta/S$. When we use $\zeta=410\ \mathrm{cm}^{-1}$ for Fe^{2+} of magnitude for ζ and the excitation energy $\Delta E=8000\ \mathrm{cm}^{-1}$, $(\lambda(0n)/\Delta E)^2$ is estimated to be of the order of 10^{-2}–10^{-3}. Here either one of the Fe^{3+} ions which contribute to two-magnon excitation may well accompany the third magnon excitation under the additional action of spin-orbit interaction. Taking into account this fact, the ratio of the absorption coefficient $I_{\rm abs}(3\text{ magnons})/I_{\rm abs}(2\text{ magnons})$ is estimated to be of the order of 10^{-2} in agreement with the observed results. At the present stage, we cannot judge theoretically which plays the more important role in the three-magnon excitation, $\mathrm{Re}\,\mathbf{\Pi}$ or $\mathrm{Im}\,\mathbf{\Pi}$ in Eq. (27).

V. CONCLUSION

We conclude that two- and three-magnon excitation is induced around 1500 cm^{-1} and 2200 cm^{-1}, respectively, by the electric dipole moment in the antiferromagnetic α-$\mathrm{Fe_2O_3}$. Two magnons at the D point have been assigned to contribute to the mid-infrared absorption and Raman scattering processes from the polarization dependence and the group-theoretical consideration.

In some crystals with a center of inversion such as the layered perovskites, e.g., $\mathrm{La_2CuO_4}$, the mid-infrared absorption due to two-magnon excitation through the exchange dipole moment is not allowed, but phonon-assisted two-magnon excitation was observed using the oscillator strength of the phonon. However, this is not the case with α-$\mathrm{Fe_2O_3}$, whose unit cell contains four Fe^{3+} ions with, e.g., (1) up, (2) down, (3) down, and (4) up Fe^{3+} spins on the c axis. Although centers of inversion are located at the midpoints between the 2nd and 3rd and between the 4th and 1st Fe^{3+} ions, two magnons may be excited from the antiferromagnetic pair of the 1st and 2nd or 3rd and 4th Fe^{3+} ions, with no inversion symmetry around the midpoints. Note that these are the first-neighbor pairs. Actually, we have more important 3rd- and 4th-neighbor (antiferromagnetic) pairs of ions with larger coupling[16] if we take neighboring unit cells into account. No inversion symmetry is found for each of these pairs, which allows them to make significant contributions to the direct optical excitation of two magnons in this crystal.[10] On the contrary, we find that many layered perovskite crystals such as $\mathrm{La_2CuO_4}$ and $\mathrm{YBa_2CuO_6}$ have the center of inversion between the antiferromagnetic pair of ions, so that only phonon-assisted two-magnon excitations are possible.

The polarization dependence and the absorption spectrum itself of the two-magnon excitation do not change so much above and below the Morin temperature as shown in Figs. 1 and 2, where the sublattice magnetization rotates by $\pi/2$. This may be explained as follows: the magnon dispersion[17] and optical response of two magnons[10] can be well described by Heisenberg model. This is consistent with the fact that the spin anisotropy energy and anisotropic exchange interaction are much smaller than the isotropic exchange energy.[13] As a result, optical response of two- and three-magnon excitation depends only on the relative angle between the neighboring spins but not on the absolute angle of the sublattice magnetization relative to the crystal axis. This can explain the other mystery why the polarization characteristic of two-magnon excitation does not change at T_M.

---

*E-mail: hanamura@photon.chitose.ac.jp

[1] M. Imada, A. Fujimori, and Y. Tokura, Rev. Mod. Phys. **70**, 1039 (1998).
[2] J. D. Perkin, J. M. Graybeal, M. A. Kastner, R. J. Birgeneau, J. P. Falck, and M. Greven, Phys. Rev. Lett. **71**, 1621 (1993); J. D. Perkins, R. J. Birgeneau, J. M. Graybeal, M. A. Kastner, and D. S. Kleinberg, Phys. Rev. B **58**, 9390 (1998).
[3] J. D. Perkins, D. S. Kleinberg, M. A. Kastner, R. J. Birgeneau, Y. Endoh, K. Yamada, and S. Hosoya, Phys. Rev. B **52**, R9863 (1995).
[4] M. Grüninger, D. van der Marel, A. Damascelli, A. Erb, T. Nunner, and T. Kopp, Phys. Rev. B **62**, 12422 (2000).
[5] M. Windt, M. Grüninger, T. Nunner, C. Knetter, K. P. Schmidt, G. S. Uhrig, T. Kopp, A. Freimuth, U. Ammerahl, B. Buchner, and A. Revcolevschi, Phys. Rev. Lett. **87**, 127002 (2001).
[6] H. Suzuura, H. Yasuhara, A. Furusaki, N. Nagaosa, and Y. Tokura, Phys. Rev. Lett. **76**, 2579 (1996).
[7] J. Lorenzana and G. A. Zawatzky, Phys. Rev. B **52**, 9576 (1995); Phys. Rev. Lett. **74**, 1867 (1995).
[8] S. Azuma, M. Sato, Y. Fujimaki, S. Uchida, Y. Tanabe, and E. Hanamura, Phys. Rev. B **71**, 014429 (2005).
[9] Y. Tanabe, T. Moriya, and S. Sugano, Phys. Rev. Lett. **15**, 1023 (1965).
[10] Y. Tanabe and E. Hanamura, J. Phys. Soc. Jpn. **74**, 670 (2005).
[11] S. J. Allen, Jr., R. Loudon, and P. L. Richards, Phys. Rev. Lett. **16**, 463 (1966).
[12] R. Loudon, Adv. Phys. **13**, 423 (1964).
[13] T. Moriya, in *Magnetism I*, G. T. Rado and H. Suhl (eds.), Academic Press, New York and London (1963), chap. 3, and references cited in that article.
[14] I. Dzyaloshinski, J. Phys. Chem. Solids **4**, 241 (1958).
[15] T. Moriya, Phys. Rev. Lett. **4**, 228 (1960).
[16] E. J. Samuelsen and G. Shirane, Phys. Status Solidi **42**, 241 (1970).
[17] E. J. Samuelsen, Physica (Amsterdam) **43**, 353 (1969).
[18] S. Onari, T. Arai, and K. Kudo, Phys. Rev. B **16**, 1717 (1977).
[19] I. R. Beattie and T. R. Gilson, J. Chem. Soc. A **5**, 980 (1970).
[20] W. Kappus, Z. Physik B **21**, 325 (1975). The character table of the Z point in Table 1 contains errors which should be replaced by the correct one in Ref. 34.
[21] T. R. Hart, S. B. Adams, and H. Temkin, in *Proceedings of the 3rd International Conference on Light Scattering in Solids*, M. Balkanski, R. C. C. Leite, and S. P. S. Porto (eds.), Wiley, New York (1976), p. 259.
[22] T. P. Martin, R. Merlin, D. R. Huffman, and M. Cardona, Solid State Commun. **22**, 565 (1977).
[23] M. J. Massey, U. Baier, R. Merlin, and W. H. Weber, Phys. Rev. B **41**, 7822 (1990), and references cited in this paper.
[24] F. J. Morin, Phys. Rev. **78**, 819 (1950).
[25] R. Loudon, Phys. Rev. **137**, A 1784 (1965).
[26] R. Loudon, Adv. Phys. **17**, 243 (1968).
[27] I. Inui, Y. Tanabe, and Y. Onodera, Group Theory and its Applications in Physics (Springer Series in Solid State Sciences 78), Second Corrected Printing, Springer-Verlag, Berlin, Heidelberg and New York (1996), chap. 13.
[28] R. J. Elliot and M. F. Thorpe, J. Phys. **2**, 1630 (1969).
[29] K. Shinagawa and Y. Tanabe, J. Phys. Soc. Jpn. **30**, 1280 (1971).
[30] T. Fujiwara and Y. Tanabe, J. Phys. Soc. Jpn. **32**, 912 (1972).
[31] Y. Tanabe, Suppl. Prog. Theor. Phys. **14**, 17 (1960).
[32] See the appendix of K. Eguchi, Y. Tanabe, T. Ogawa, M. Tanaka, Y. Kawabe, and E. Hanamura, J. Opt. Soc. Am. **22**, (January 2005).
[33] S. Sugano, Y. Tanabe, and H. Kamimura, Multiplets of Transition-Metal Ions in Crystals, Academic, New York (1970).
[34] E. R. Cowley, Can. J. Phys. **47**, 1381 (1969).

This article was published in English in the original Russian journal. Reproduced here with stylistic changes by AIP.

LOW TEMPERATURE PHYSICS VOLUME 31, NUMBERS 8–9 AUGUST–SEPTEMBER 2005

Circular dichroism and Raman optical activity in antiferromagnetic transition-metal fluorides

K. R. Hoffman

Department of Physics, Whitman College, Walla Walla, Washington 99362, USA

D. J. Lockwood*

Institute for Microstructural Sciences, National Research Council, Ottawa, ON K1A 0R6, Canada

W. M. Yen

Department of Physics and Astronomy, University of Georgia, Athens, Georgia 30602, USA

(Submitted February 17, 2005)
Fiz. Nizk. Temp. **31**, 1032–1041 (August–September 2005)

The Raman optical activity (ROA) of magnons in rutile-structure antiferromagnetic FeF_2 ($T_N = 78$ K) is studied as a function of temperature and applied magnetic field. For exciting light incident along the c axis, ROA is observed for magnons but not for phonons. In zero field, a small splitting ($0.09\ \mathrm{cm}^{-1}$) of the two acoustic-magnon branches is observed for the first time by inelastic light scattering. The splitting in applied magnetic field is found to reduce with increasing temperature in accordance with theory. No ROA is detected for two-magnon excitations. In optical absorption measurements performed over thirty years ago, a very small circular dichroism (CD) was observed in the magnon sidebands of other simple rutile antiferromagnetic fluorides (MnF_2 and CoF_2). The origin of this CD was not understood at the time. The Raman studies of the one-magnon Raman scattering in FeF_2 have demonstrated that in zero field the degeneracy of the antiferromagnetic magnon branches is lifted by a weak magnetic dipole-dipole interaction, as predicted by Pincus and Loudon and by White four decades ago. The source of the observed CD in the magnon sidebands can now be traced to this same magnetic-dipole induced splitting. © *2005 American Institute of Physics.*

[DOI: 10.1063/1.2008140]

I. INTRODUCTION

In 1965, the discovery of the one-magnon sideband in the visible absorption spectrum of MnF_2 (Ref. 1) and the two-magnon absorption of the far-infrared spectrum of FeF_2 (Ref. 2) spurred many investigations into the optical properties of antiferromagnetic insulators. The theoretical framework regarding these two processes was developed by Tanabe *et al.*[3] and Allen *et al.*[4] In these materials, coupling between the various intrinsic excitations of the lattice, i.e., excitons, magnons and phonons, leads to the formation of cooperative transitions which can account for much of the spectral structure. An article discussing this work appears elsewhere in this special issue of *Low Temperature Physics*. In addition to absorption and luminescence measurements, magnon lines were also observed in Raman scattering measurements.[5,6] Raman scattering measurements permit the physical properties of magnons to be studied without the additional contributions due to electronic states associated with optical emission or absorption. A comprehensive review of Raman theory and experimental results for antiferromagnets is presented in the book by Cottam and Lockwood.[7]

The magnetic character of the magnon transitions led to the utilization of circularly polarized light to explore the dichroic properties of these materials. In the early 1970s, a series of papers reported on their magnetic circular dichroism (MCD) in an applied magnetic field.[8–10] The authors reported at that time the observation of circular dichroism (CD) in certain magnon sidebands of MnF_2 (Ref. 8) and CoF_2 (Ref. 10) but not in FeF_2 (Ref. 9); CD occurs in the absence of an applied magnetic field and corresponds to zero field MCD though the origins of the dichroism may arise from different sources. The authors were able to eliminate experimental artifacts as the source of the observed CD, but were not able at that time to identify the physical basis for the unexpected observation. Recently, we revisited this problem and showed that the source of the CD is to be found in the dipolar interactions that exist between the antiferromagnetic sublattices, which render them inequivalent.[11]

Raman optical activity (ROA) characterizes the difference in the Raman line intensity when excited with right and left circularly polarized light. The earliest experiments to combine Raman spectroscopy with chirality in solids were performed in the 1970s on CdS under resonance excitation conditions.[12] Attempts were also made to observe a similar effect in antiferromagnetic fluoride materials but the experimental sensitivity was insufficient. At about the same time ROA was also measured in a chiral molecule.[13] The chiral structure of some molecules makes them naturally suited to couple more strongly to either right or left circularly polarized light. The theoretical[14] and experimental developments in this field have been reviewed in the literature.[15,16] A series of Raman papers in the 1980s on the magnetic properties of dilute magnetic semiconductors employed the use of circular polarization to isolate spin flip transitions of Mn ions.[17,18] The improvement in detector sensitivity over a period of twenty years afforded us the opportunity in the 1990s to revisit the question of ROA in antiferromagnetic insulators. We were able to observe ROA in the one-magnon line of FeF_2[19–21] and several phonon lines in rutile-structure materials.[22,23] In addition, we demonstrated for the first time that Raman scattering could be used to measure a zero field splitting of the magnon branches in antiferromagnetic FeF_2.[24] These results were then utilized to reinterpret the CD measurements completed in the early 1970s that were alluded to above.[11]

In the following Sections, we present our current understanding of the dichroic properties of antiferromagnetic insulators possessing the rutile structure. The focus of this review will be on ROA measurements to explore the magnetic properties of these materials. We start with a summary of the zero field dichroism measurements in MnF_2, CoF_2, and FeF_2 because the CD studies prompted one of us (W.M.Y.) to explore the use of ROA in antiferromagnetic fluorides. We then present a more thorough review of the ROA measurements, techniques, and analysis in FeF_2. Here we mention first the work on phonons before focusing on the one- and two-magnon scattering results, including a revised assessment of the results from the temperature dependence and zero magnetic field studies of FeF_2.

II. OPTICAL DICHROISM IN RUTILE ANTIFERROMAGNETS

Dichroism in a material is defined as the difference in the absorption coefficient of a medium for two related polarizations; thus CD arises from the difference in the absorption for right- and left-circularly polarized radiation. When these differences are induced by the application of an external magnetic field, the effect is termed MCD. In both CD and MCD, a unique direction is necessary in order to define the sense of circulation in the circularly polarized light; this is provided by some unique crystalline axis or by the direction of the applied magnetic field. Materials showing CD are normally called "optically active" and such crystals are relatively rare, whereas MCD is quite common in paramagnetic systems possessing a unique axis. MCD is conjugated to Faraday rotation by the Kramers–Kronig relations and constitutes the resonant rather than the dispersive phenomena in the transformation.

The compounds that we wish to discuss here are the common difluorides, MnF_2, CoF_2, and FeF_2, all of which possess the rutile crystal structure. Below the Néel temperature T_N these materials are describable as simple two sublattice antiferromagnets and in principle they are ideal systems on which to study magnetically dichroic phenomena. The ground states of ions in each sublattice as well as the collective magnetic excitations (magnons) are identical to each other in every respect except their polarization. The sole remaining energy degeneracy, which will respond to an applied magnetic field, is that of the two sublattices; hence, the origin of magnetic dichroism in these systems is directly related to the lifting of this energy equivalence both in the electronic (exciton), the spin (magnon) or the combined (magnon sideband) systems.

For simple antiferromagnets in their ordered state, the ground state of each sublattice is non-degenerate and is identical to the other except for their sense of magnetization with respect to the unique crystalline axis. If the state for the "up" or A sublattice is given by $|L,M\rangle$ then the corresponding "down" or B sublattice is represented by $|L,-M\rangle$. For pure electronic transitions, the appropriate dipolar transition operators for circular polarized radiation transform as $L_\pm + 2S_\pm$, where the $(+)$ and $(-)$ subscripts refer to right and left circular polarizations, respectively. If ions in one of the sublattices have a nonvanishing transition probability between two states for one of these operators, then the ions in the opposite sublattice will have an identical element for the corresponding conjugated operator. In the absence of a magnetic field, the sublattices are degenerate in energy and no CD should be observed. However, weak interactions between the sublattices, such as magnetic dipole-dipole interactions, can produce a small anisotropy between the two sublattices that results in CD. At low temperatures, a very small zero-field CD signal was observed in two of the three compounds investigated and it is the origin of these signals that will be addressed in this paper.

III. EXPERIMENTAL RESULTS FOR CIRCULAR DICHROISM MEASUREMENTS

A finite CD was observed at low temperatures in two of the three difluorides studied. Signals were observed in the magnon sidebands of the $^6A_{1g}$ ground state to $^4T_{1g}$ and ($^4A_{1g}$, ^4E_g) absorptions of MnF_2 and of the $^4T_1$ to ^2A, $^2T_1$ (^2P) of CoF_2; no CD signals were observed in FeF_2. As noted earlier, the origins of CD and MCD are different; as a consequence, CD can be subtracted from MCD in order to determine the magnetic field induced splittings. When this is done the, the residual or pure MCD signal can be fitted accurately with a differential line shape; this indicates that in our cases the MCD arise simply from the lifting of the sublattice degeneracy, as per our expectation.

Figure 1 shows the absorption of a magnon sideband of the (^2A, $^2T_1$) transition of CoF_2 along with the observed CD and MCD in a 2 T applied magnetic field. The CD is also purely differential in shape and is estimated to be an additive intrinsic splitting of the order of $\Delta\omega = 0.015\ \mathrm{cm}^{-1}$. The CD in CoF_2 becomes unobservable in the vicinity of 10 K.

Figure 2 shows the absorption spectrum of the so-called σ_1 and σ_2 sidebands accompanying the ground state to $^4T_{1g}$ transition in MnF_2. These transitions are α-polarization active. A small CD signal is observed that is clearly related to this transition. The zero-field splittings for the sidebands were determined to be $\Delta\omega(\sigma_1) = 0.07\ \mathrm{cm}^{-1}$ and $\Delta\omega(\sigma_2) = -0.05\ \mathrm{cm}^{-1}$, respectively.

The negative sign in $\Delta\omega(\sigma_2)$ signifies that the sense of the splitting in this sideband is out of phase with that of σ_1. Such a change in the sense of splitting is also observed when uniaxial stress is applied to MnF_2 along the [110] direction in the basal plane. The behavior of the CD was studied as a function of basal plane stress allowing the intrinsic strain in the basal plane of ordered MnF_2 to be estimated: $\Sigma = \Delta d/d = 1.2\times10^{-5}$. This result highlights the advantages of chiral techniques for exploring interactions in antiferromagnets.

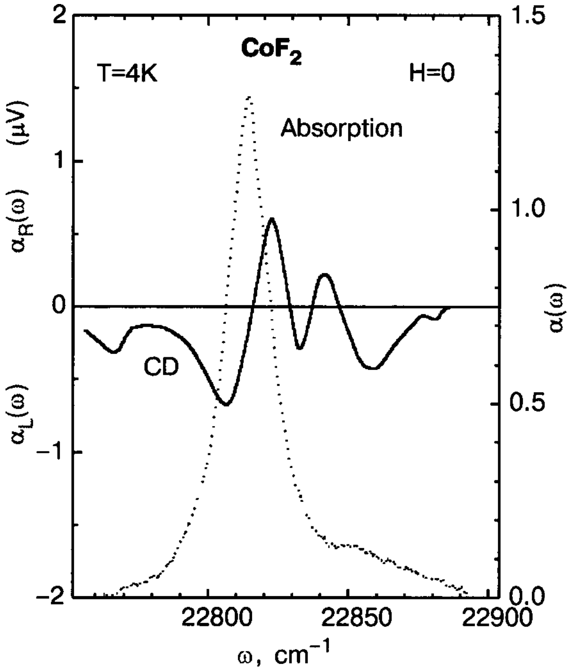

FIG. 1. The CD spectrum of the one-magnon sideband near 22,800 cm^{-1} of CoF_2 at 4 K and the corresponding absorption spectrum of the sideband.

FeF_2 was studied in the 21500–28500 cm^{-1} spectral region. The observed transitions without exception exhibited MCD signals consistent with a simple sublattice splitting and with a linear dependence on magnetic field. No CD signals were encountered in any of the α-active transitions investigated. The sensitivity of our apparatus places an upper limit of 10^{-3} cm^{-1} on any splitting that might occur in this compound at 4 K.

IV. RAMAN OPTICAL ACTIVITY

Raman optical activity is observed experimentally in the difference in a Raman line intensity when excited by right and left circularly polarized light, respectively. The circular intensity difference (CID) is normally used to quantify ROA:[14]

$$\Delta_\alpha = \frac{I_\alpha^R - I_\alpha^L}{I_\alpha^R + I_\alpha^L}, \tag{1}$$

where I_α^R and I_α^L represent the scattered light intensity with α polarization due to incident right (R) or left (L) circularly polarized light. The normalization term permits a simple comparison of data from different spectroscopic systems. One major difficulty of ROA measurements is the sensitivity of the technique to intrinsic or extrinsic depolarization effects. Care must be taken to account for any birefringent effects in the steering and focusing optics. Additionally, the crystal itself can contribute to significant depolarization effects that appear as CID in spectra that normally would not be expected to produce any difference. We will discuss this effect in more detail in the next Section of the paper.

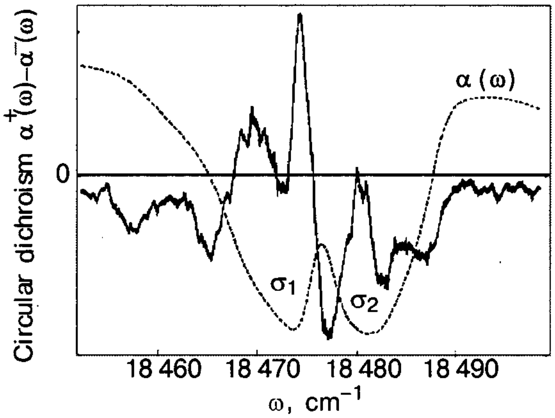

FIG. 2. The absorption and CD spectra of the so-called σ_1 and σ_2 sidebands of MnF_2 at 2 K; these traces connect the observed CD to the magnon sidebands.

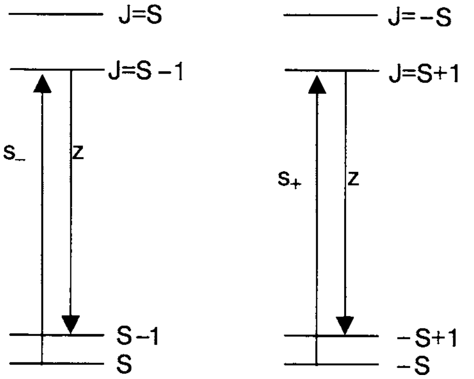

FIG. 3. The electronic levels of the magnetic ions in antiferromagnetically ordered rutile materials responsible for the observed ROA signal. The two sets of lines correspond to the two antiferromagnetic sublattices. In both cases a magnon is generated during the scattering process.

Fundamentally, the source of Raman scattering is the modulation of the induced polarizability of a medium by fundamental excitations in the medium. To couple the incident light to the medium, its susceptibility is expanded in terms of phonon or magnon operators. This results in a modulation of the polarizability at the frequency of the fundamental excitation. In the case of magnons, the inclusion of spin operators results in a change of the overall angular momentum component along the z axis: $\Delta m_j = \pm 1$. Figure 3 illustrates the important mechanism for magnon light scattering from antiferromagnetic fluorides. The energy levels shown in the picture belong to the transition metal ions on the two sublattices. These transitions obey the same selection rules that contribute to CD or MCD signals. The circularly polarized light couples to different sublattices in the Raman process as well, thus providing a way of distinguishing between the two sublattices. The figure shows energy levels for both sublattices in the medium and illustrates that left and right circular polarizations create magnons on different sublattices.

Symmetry arguments can be applied to determine selection rules for the various scattering processes and are summarized in the form of Raman scattering tensors. The scattering tensors for the tetragonal antiferromagnetic fluorides are presented in Table I.

The tensors have been transformed so that they are appropriate for $[R,L,z]$ incident polarizations and $[x,y,z]$ scattered polarizations. The Raman tensors describe the scattered

TABLE I. The Raman tensors for circularly polarized incident light that is analyzed for linearly polarized light scattered at 90°.

$$A_{1g}=\frac{1}{\sqrt{2}}\begin{bmatrix} a & a & 0\\ -ia & ia & 0\\ 0 & 0 & \sqrt{2}b\end{bmatrix}\qquad B_{1g}=\frac{1}{\sqrt{2}}\begin{bmatrix} c & c & 0\\ -ic & ic & 0\\ 0 & 0 & 0\end{bmatrix}\qquad B_{2g}=\frac{1}{\sqrt{2}}\begin{bmatrix} -ie & ie & 0\\ e & e & 0\\ 0 & 0 & 0\end{bmatrix}$$

$$\Gamma_3^+ + \Gamma_4^+\begin{bmatrix} |+1\rangle \\ \hline |-1\rangle\end{bmatrix}=\frac{1}{\sqrt{2}}\begin{bmatrix} 0 & 0 & \pm\sqrt{2}\delta\\ 0 & 0 & i\sqrt{2}\delta^*\\ (\pm\varepsilon+\varepsilon^*) & (\pm\varepsilon-\varepsilon^*) & 0\end{bmatrix}\qquad E_g(1)=\frac{1}{\sqrt{2}}\begin{bmatrix} 0 & 0 & 0\\ 0 & 0 & \sqrt{2}d\\ -id & id & 0\end{bmatrix}\qquad E_g(2)=\frac{1}{\sqrt{2}}\begin{bmatrix} 0 & 0 & \sqrt{2}d\\ 0 & 0 & 0\\ d & d & 0\end{bmatrix}$$

electric field amplitudes and thus the scattered light intensity in a specific polarization is calculated through multiplication of the tensor by its conjugate value. To describe the expected CID spectrum, we need to calculate the difference between two intensity terms. For example, the A_{1g} phonon mode should not generate a CID signal for scattered light polarized along the x axis:

$$\Delta_x(A_{1g})=\frac{I_x^R-I_x^L}{I_x^R+I_x^L}=\frac{a^2-a^2}{a^2+a^2}=0. \tag{2}$$

In the case of the magnon scattering we can calculate the CID for each sublattice separately. In the case of the Γ_3^+ band, we obtain the following CID expression:

$$\Delta_z(\Gamma_3)=\frac{(\varepsilon^*\varepsilon+\varepsilon^{*2}+\varepsilon^*\varepsilon+\varepsilon^2)-(\varepsilon^*\varepsilon-\varepsilon^{*2}+\varepsilon^*\varepsilon-\varepsilon^2)}{(\varepsilon^*\varepsilon+\varepsilon^{*2}+\varepsilon^*\varepsilon+\varepsilon^2)+(\varepsilon^*\varepsilon-\varepsilon^{*2}+\varepsilon^*\varepsilon-\varepsilon^2)}=\frac{\varepsilon^{*2}+\varepsilon^2}{2(\varepsilon^*\varepsilon)}. \tag{3}$$

Likewise for the Γ_4^+ magnon band we get a similar result:

$$\Delta_z(\Gamma_4)=-\frac{\varepsilon^{*2}+\varepsilon^2}{2(\varepsilon^*\varepsilon)}. \tag{4}$$

The negative sign reflects the coupling of left circular polarization to this particular sublattice. Notice that if the energies of the two magnon bands are equal and the line profiles equivalent, the total CID is the sum of these terms and will be zero. The application of a magnetic field lifts the degeneracy of the magnon branches. As a result, the CID of the two branches will no longer completely cancel. This result is analogous to the differences observed between MCD and CD spectra. The important distinction is that the Raman spectra are determined only by the energies of the magnon bands with no interference from the excited states of the ion.

V. RAMAN OPTICAL ACTIVITY EXPERIMENTS

The experimental arrangement, shown in Fig. 4, used the standard 90° Raman scattering geometry. The incident beam was the 488-nm line of a continuous-wave Spectra Physics 166 argon–ion laser. The focused laser power density at the sample was 150 kW/cm^2, well below the damage threshold of the materials used. A Conoptics 370 electro-optic modulator (EOM) was used to alternate between right and left circular polarization. The scattered light was dispersed by a Spex 1401, 0.85-m double monochromator and detected using a cooled RCA 31034-A02 photomultiplier. The signal was measured using a Stanford SR-400 dual-gated photon counter and stored on a computer. The signals counted on the two gates, corresponding to the two incident polarizations, were stored separately, permitting both I^R-I^L and I^R+I^L to be easily calculated. Low temperatures were achieved using a Cryosystems closed-cycle refrigerator. A permanent magnet assembly located inside the refrigerator applied a constant magnetic field parallel to the crystal c axis. The magnets were drilled through so that the incident laser beam could be focused in the crystal collinear with the applied field and allowed to pass on through the refrigerator.

The crystals used in this study were the rutile-structure fluorides FeF$_2$ and MgF$_2$. These materials are uniaxial, with FeF$_2$ undergoing an antiferromagnetic phase transition at $T_N=78$ K. The MgF$_2$ crystal orientation was determined from x-ray Laue diffraction measurements before the cuboid sample was cut (to within a 1° accuracy) and polished. The c-axis orientation for the FeF$_2$ sample was found using a polariscope. In addition, a polished crown glass cube was used as a reference material to check for instrumental artifacts.

Rayleigh and Raman CID in MgF$_2$ and FeF$_2$

Our measurements of the magnon and phonon CID in FeF$_2$ generated several signals that were difficult to understand initially. Figure 5 shows the difference spectrum I^R-I^L as well as the separate I^R and I^L spectra from FeF$_2$ with no applied magnetic field. What is curious about these measurements is that the magnon exhibits no apparent differential scattering but the B_{1g} phonon mode does. When the spectrum is enlarged to encompass all of the phonon modes and the Rayleigh line, we observe a similar CID spectrum for the A_{1g} and B_{2g} modes and the Rayleigh line but the sign of the difference signal is opposite to that of the B_{1g} mode. Referring back to the Raman tensors, no CID is expected from any of the phonon modes nor should Rayleigh scatter-

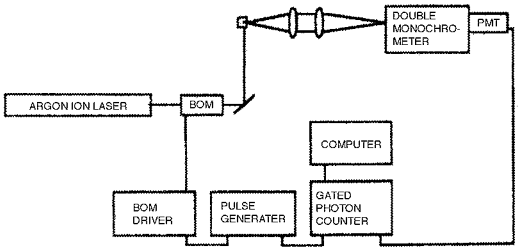

FIG. 4. The experimental setup for the ROA measurements. The laser light was directed vertically through the sample to align the beam path with the entrance slit of the spectrometer.

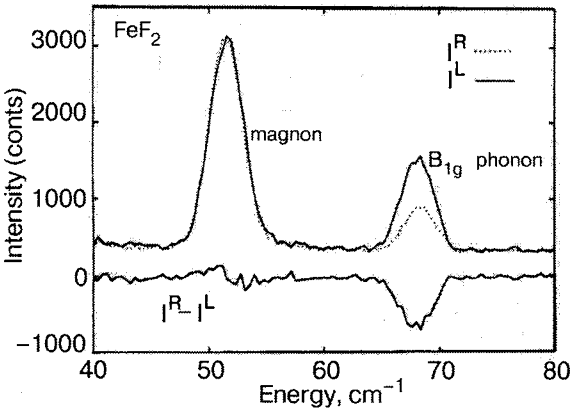

FIG. 5. The ROA spectrum of FeF_2 at 4 K. The presence of a CID spectrum in the B_{1g} phonon mode indicates a misalignment of the incident laser and the crystalline c axis.

ing exhibit CID. MgF_2 is also a rutile-structure fluoride, but it does not exhibit any magnetic ordering. It showed a similar differential scattering pattern. An isotropic glass sample was used to check for instrumental artifacts and none were found.

To explain the CID spectra of the phonons we looked carefully at the effects of birefringence in the crystal on the scattered intensity. Light propagating along the c axis will experience an isotropic index of refraction so that no change in the polarization occurs as it moves through the sample. A slight misalignment results in distinct indices of refraction parallel and perpendicular to the plane containing the c axis. As a result, circularly polarized light becomes elliptically polarized as it moves through the sample. The changes in polarization affect the relative amplitude of the x and y components of the incident light. The crucial point is that changes of I_x and I_y are different for left and right circular polarization so that any scattering that depends on only one of these terms will exhibit a CID spectrum. This result permits a very sensitive tool for aligning the samples for ROA measurements so that intrinsic birefringence effects can be eliminated.

Raman optical activity of magnons in FeF_2

Figure 6 presents the conventional Raman and ROA spectrum of the one-magnon line of FeF_2 in an applied magnetic field. The modest applied field, $B<0.6$ T, is too small to observe the splitting of the magnon branches within the magnon linewidth using conventional (linearly polarized light) Raman techniques. However, the magnon line exhibits a clear CID spectrum. To determine the energy difference between the two branches we fit the data using offset Gaussian line shapes to describe the one magnon scattering peak. In this manner we can calculate the energy difference as a function of temperature. Figure 7 shows the temperature dependence of the frequency splitting between the two magnon branches in FeF_2. As the temperature increases, the energy splitting between the branches decreases, while the linewidth increases resulting in a larger uncertainty for the energy splitting between the branches.

Theoretically,[28] the energy splitting between the two branches is given by

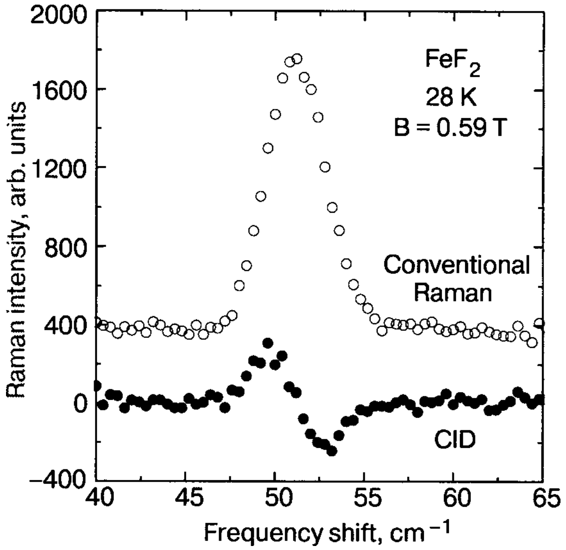

FIG. 6. The low-temperature ROA spectrum of FeF_2 in the presence of an applied magnetic field. The upper trace shows the conventional Raman spectrum. The lower trace is the measured CID spectrum.

$$\Delta\omega(T)=2[g\mu_B-J\chi_{\parallel}]H \tag{5}$$

where H is the applied magnetic field along the crystal c axis, $\chi_{\parallel}$ is the parallel susceptibility per spin site, μ_B is the Bohr magneton, J is the dominant nearest neighbor exchange, and g is the Lande g factor. At low temperatures, $\chi_{\parallel}$ is nearly zero, so

$$\Delta\omega(T=0)=2g\mu_B H \tag{6}$$

whereas at temperatures near T_N, $\chi_{\parallel}=g\mu_B/2J$ so:

$$\Delta\omega(T=T_N)=g\mu_B H. \tag{7}$$

This theory predicts that the splitting between the branches should change by a factor of two when going from low temperature to the phase transition temperature. Using param-

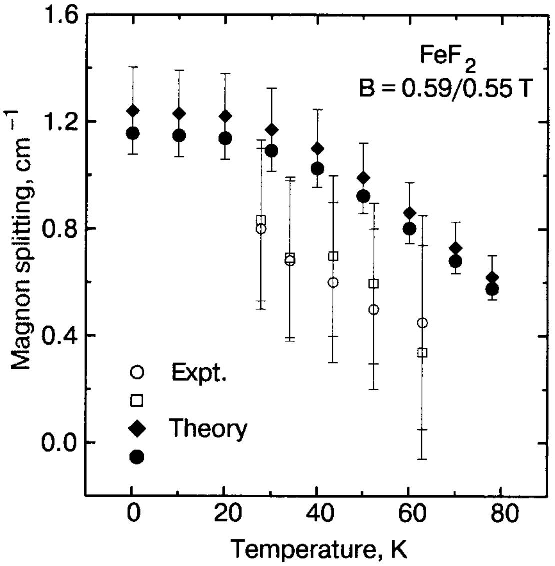

FIG. 7. The temperature dependence of the magnon branch splitting obtained from ROA measurements in FeF_2. The theoretical points are calculated using applied fields of 0.59 (filled diamonds) and 0.55 T (filled circles). The error bars on the theoretical points derive largely from the uncertainty in the applied magnetic field strength.

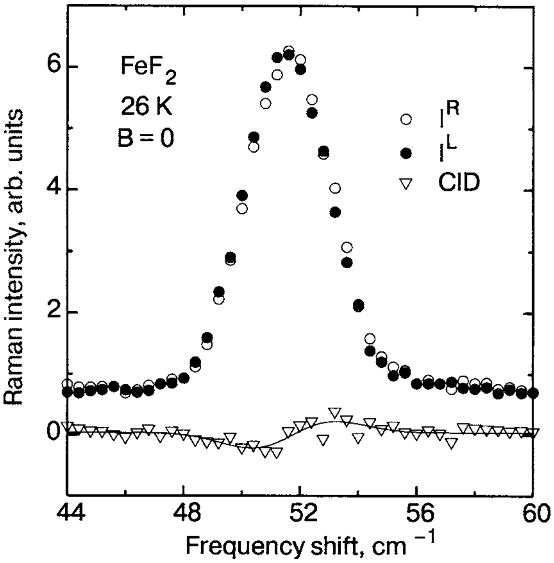

FIG. 8. The zero-field ROA spectrum of the one magnon line in FeF$_2$. The solid line is a fit modeling the small CID apparent in this spectrum.

eters obtained from the experiment or the literature the theoretical curve shown in Fig. 7 was obtained. The theoretical curve accurately describes the temperature variation of the energy splitting between the magnon bands, but overall there is a general offset between the measured data and the theoretical curve. The primary uncertainty for this measurement arises from determining the actual value of the magnetic field inside the refrigerator. The magnetic field of 0.59 T for the permanent magnet gap was measured at room temperature. The magnet will be at a much lower temperature during the Raman measurement, but the affects of the lower temperature on the gap field strength is not known.

These measurements highlight the sensitivity of this technique in measuring magnon branch splittings. The linewidths of the two peaks at 62 K were greater than 10 cm^{-1}, but the separation between the peaks was only 0.4 cm^{-1}.

For a simple antiferromagnet, we would not expect to observe any CID spectrum in zero applied field ROA measurements. However, careful measurements revealed a small but repeatable CID spectrum in FeF$_2$. Figure 8 shows the CID spectrum and the separate I^R and I^L Raman signals of FeF$_2$. Care was taken to eliminate all of the depolarization effects by using the Rayleigh scattering spectrum to ensure alignment of the crystal c axis with the incident laser light. The solid-line fit determined the zero field splitting between the two magnon branches to be $\Delta\omega=(0.09\pm0.02)$ cm^{-1}. To our knowledge this result is the first measurement of a zero field splitting of the magnon branches in antiferromagnets using Raman scattering. Again the high sensitivity and resolution of this technique is highlighted in obtaining this result.

Finally, ROA measurements of the two-magnon scattering peak in FeF$_2$ showed a null result. The lack of any CID signal confirms that the dominant mechanism for two-magnon scattering involves exchange coupled magnons on opposite sublattices. Other possible sources of two-magnon scattering are higher order processes that would be expected to be much weaker than the one-magnon scattering. Multiple spin-flip transitions have been observed in dilute magnetic semiconductors in the paramagnetic phase under resonance excitation conditions.[17,18] These transitions were observed in a forward scattering geometry where the scattered light was analyzed for the circular polarization as well. The intensities of the two spin flip signals are much lower than the single spin flip signals consistent with a higher-order interaction.

VI. MAGNETIC DIPOLE-DIPOLE INTERACTIONS

In 1963 Loudon and Pincus[25] examined the effect of the classical dipole-dipole interaction between magnetic moments on the spin wave spectrum of a simple uniaxial antiferromagnet. In the absence of an applied magnetic field, as discussed above, the spin wave branches are degenerate in these systems. The magnon dispersion relation is given by

$$\omega\equiv\gamma[H_A^2+2H_AH_E+2H_E^2b^2k^2]^{1/2} \tag{8}$$

where $\gamma=g\mu_B$ is the gyromagnetic ratio, H_A is the uniaxial single-ion internal anisotropy field, and H_E is the effective exchange field; k is the wave vector and $b=az^{-1/2}$, with a the nearest-neighbor distance and z the number of nearest neighbors. On inclusion of the dipolar fields, Eq. (8) splits into two modes with their dispersions given by:

$$\omega_1=\gamma[H_A^2+2H_EH_A+2H_E^2b^2k^2]^{1/2}, \tag{9}$$

$$\omega_2=\gamma[H_A^2+2(H_A+H_Eb^2k^2)(H_E+4\pi M_s\sin^2\theta_k)]^{1/2} \tag{10}$$

where M_s is the sublattice magnetization and θ_k is the angle between the easy axis (z) of magnetization and the direction of propagation $\mathbf{k}$ of the spin wave. Only the frequency of the second mode is affected by the dipolar interaction. For spin waves with $\mathbf{k}=0$, Eqs. (9) and (10) reduce to

$$\omega_1=\gamma[H_A(H_A+2H_E)]^{1/2} \tag{11a}$$

$$\omega_2=\gamma[H_A(H_A+2H_E+8\pi M_s\sin^2\theta_0)]^{1/2}. \tag{11b}$$

In the case of longitudinal spin waves $\theta_0=0$, and there is no dipolar effect. For the transverse spin waves, however, $\theta_0=\pi/2$, and the dipolar effects are at a maximum.

Subsequently, Harris[26] has shown that Eq. (10) is an approximate result and has derived the full expression for the spin wave dispersion in the presence of a dipolar field. However, the difference between Eq. (10) and the complete result only becomes important when $4\pi M_s$ is comparable to H_E, which is not the case here.

The Loudon and Pincus calculation is based on a molecular field approach that neglects the affect of the Lorentz field of one sublattice upon the other sublattice. When this effect is included, White[27] showed that the resonant frequencies for $\mathbf{k}=0$ are given by:

$$\omega(k=0)_{1,2}=\pm\gamma\left[H_A\left(H_A-\frac{8}{3}\pi M_s\right)+2H_A(H_E+4\pi M_sN_x)\right]^{1/2}, \tag{12a}$$

$$\omega(k=0)_{3,4}=\pm\gamma\left[H_A\left(H_A-\frac{8}{3}\pi M_s\right)+2H_A(H_E+4\pi M_sN_y)\right]^{1/2} \tag{12b}$$

and for $\mathbf{k}\neq 0$ by

$$\omega(k)_{1,2}=\pm\gamma\Bigg[H_A^2+2H_AH_E+H_E^2(1-\gamma_k^2)+\frac{8}{3}\pi M_s[H_A+H_E(1-\gamma_k)]\Bigg]^{1/2}, \tag{13a}$$

$$\omega(k)_{3,4}=\pm\gamma\Bigg[H_A^2+2H_AH_E+H_E^2(1-\gamma_k^2)+8\pi M_s\left(\frac{1}{3}-\sin^2\theta_k\right)[H_A+H_E(1-\gamma_k)]\Bigg]^{1/2} \tag{13b}$$

where $\mathbf{N}$ is the demagnetization dyadic,[27] and γ_k is defined as $(1/z)\Sigma_\delta\exp(i\mathbf{k}\cdot\boldsymbol{\delta})$, where the $\boldsymbol{\delta}$'s are the vectors to the z nearest neighbors.

Notice that for the uniform spin precession ($\mathbf{k}=0$) in a sphere ($N_x=N_y=N_z=1/3$), the Lorentz field just cancels the surface demagnetizing field. Therefore, there is no shift in the resonant frequency as compared to non-dipolar cases. The symmetric occurrence of N_x and N_y in Eq. (12) is due to the fact that the normal modes labeled 1, 2 and 3, 4 are characterized by net transverse magnetizations that are linearly polarized in the x and y directions, respectively. Notice also that although the 1, 2 spin wave modes are independent of θ they are shifted by the Lorentz field.

Since the samples used in the optical studies had rectangular cross sections in the basal plane, there will be dipolar splittings of the magnons. Thus, from Eq. (12),

$$\Delta\omega_{k=0}=\omega_1-\omega_3=\frac{4\pi M_sH_A(N_x-N_y)}{\sqrt{2H_AH_E+H_A^2}}. \tag{14}$$

The demagnetizing factors are given by integrals over the surface.[27] In order to obtain estimates of these splittings we approximate N_x and N_y by 1/2 and 1/4, respectively, based on the sample dimensions. The parameter values used in the calculations and the resulting splittings are listed for MnF_2, CoF_2, and FeF_2 in Table II.

VII. COMPARISON OF THEORY WITH EXPERIMENT

Optical circular dichroism

The calculated splittings given in Table II are quite small compared with the magnon energies in these compounds. Given the nature of the natural linewidths, splittings of this magnitude are difficult to measure and they have been resolved only recently using Raman spectroscopy.[11,15]

The calculated values for $\Delta\omega$ in MnF_2 and CoF_2 (see Table II) are of similar magnitude to those found experimentally for the magnon sidebands in the visible region: $0.02\ \mathrm{cm}^{-1}$ for CoF_2 and 0.07 and $0.05\ \mathrm{cm}^{-1}$ for MnF_2. Thus the origin of the observed splittings reported in the CD measurements is well encompassed by the effects of the magnetic dipole-dipole interaction in these simple rutile antiferromagnets. The size of the splittings detected by spontaneous magnetic CD cannot be compared directly with those calculated in Table II, as the processes involved in the formation of magnon sidebands are not as simple and direct as those encountered in Raman scattering. For MnF_2, for example, the sideband involves a combination of an exciton on one sublattice with essentially zero dispersion[25] with a magnon on the other with nearly $50\ \mathrm{cm}^{-1}$ dispersion; $\mathbf{k}$ conservation requires the creation of exciton-magnon pairs with equal and opposite wave vectors from throughout the Brillouin zone. Although the splitting is mostly uniform across the Brillouin zone, the CD is, in effect, sampling the derivative of the joint density of states. It follows that an accurate calculation of the CD requires the use of Eq. (13), but the theory needs to be extended to include specific symmetry points in the Brillouin zone and an appropriate summation over the entire zone.

TABLE II. Magnetic parameters at low temperature for various transition-metal fluorides possessing the rutile structure. The calculated dipole-dipole induced splittings, $\Delta\omega_{k=0}$ and $\Delta\omega_{k=\pi/2}$, are also given.

Parameter	MnF_2 [28–30]	FeF_2 [29,31]	CoF_2 [29,32]
Effective spin S	5/2	2	1/2
H_E (T)	51.5	53.313	37.6
H_A (T)	0.84	19.745	9.54
g	2.00	2.25	2.80
γ (cm^{-1}/T)	0.934	1.05	1.31
M_S (T)	0.060	0.056	~0.06
$\Delta\omega_{k=0}$ (cm^{-1})	0.016	0.065	0.083
$\Delta\omega_{k=\pi/2}$ (cm^{-1})	0.02	0.08	0.12

Conceivably, another possible cause of CD in these compounds could be a slight tilting of the spins away from their ordered positions along the c axis. However, at low temperatures and in zero applied magnetic field, all experimental results to date point to collinear spin alignment in all of these compounds.[29]

Raman circular intensity difference

In the Raman equivalent of the CD measurements discussed above, a $\Delta\omega$ of $(0.09\pm0.02)\ \mathrm{cm}^{-1}$ was observed in FeF_2 at low temperatures using a 90° scattering geometry. From Eq. (11), the theoretical splitting for magnons propagating at approximately 45° to the c (z) axis is $\Delta\omega=0.15\ \mathrm{cm}^{-1}$, which, considering the expected large uncertainty in M_s, is in good agreement with the experimental results. Including the Lorenz field correction, Eq. (14) gives $\Delta\omega=0.065\ \mathrm{cm}^{-1}$ (see Table II), which is in even closer agreement with experiment. The zero-field splitting of the magnon branches observed in FeF_2 is thus attributed to the magnetic dipole-dipole interactions that can be important for long wavelength magnons.[27]

Another way to quantitatively describe the interaction is to define it in terms of an effective anisotropy field, H', that is treated in the same manner as an external magnetic field. In this approach the energy of the magnons shows up in much the same form as presented in Eq. (6) except that the splitting is now due to H'.

$$\Delta\omega(T=0)=2\gamma H'=0.09\ \ \mathrm{cm}^{-1}. \tag{15}$$

Using the parameter value $\gamma = 1.05\ \mathrm{cm}^{-1}/T$ (Table II) we calculate the anisotropy field to be: $H' = (0.04 \pm 0.01)$ T.

By comparing Figs. 8 and 6 we see that the CID spectra have opposite signs for the case of $H = H'$ and $H = H_{\mathrm{applied}} + H'$, respectively. Since the energy splitting of the two magnetic sublattices switches sign with the external field, the direction of the applied field must be opposite to the direction of the effective anisotropy field. Going back to the temperature dependence of the magnon branch splitting we can now correct for the presence of the effective anisotropy field in the material. Equation (5) becomes

$$\begin{aligned}\Delta\omega(T) &= 2[g\mu_B - J\chi_{\|}](H_{\mathrm{applied}} - H') \\ &= 2[g\mu_B - J\chi_{\|}](0.55\ \ \mathrm{T}). \qquad (16)\end{aligned}$$

The second theoretical curve shown in Fig. 7 uses this new value for the magnetic field and gives better agreement with the measured data.

8. CONCLUSIONS

The magnon sideband CD observed in rutile-structure antiferromagnets can be quite readily explained as being the result of magnetic dipole-dipole interactions breaking the degeneracy of the two spin wave branches. These optical measurements performed three decades ago are seen now to represent the first observation of such splittings, as first predicted by Loudon and Pincus in 1963. It would be informative to perform further experiments to confirm the $\sin^2\theta$ dependence of the splitting by varying the angle θ_0 from 0 to $\pi/2$, i.e., the incident light direction is varied from along to perpendicular to the easy axis, and also the sample shape effect on the splitting.

The ability to measure an effective anisotropy field in $\mathrm{FeF_2}$ highlights the sensitivity of ROA measurements for determining small splittings between the magnon branches in antiferromagnets. The measurement of such a splitting due to magnetic dipole-dipole interactions in $\mathrm{FeF_2}$ has permitted a final resolution of questions concerning the origins of CD in optical measurements completed over thirty years ago. The high sensitivity of ROA also permits the study of antiferromagnetic branch splittings for low applied magnetic fields.

The precise experimental work of Professor F. L. Scarpace and Dr. Y. H. (Russ) Wong from thirty years ago is noted with appreciation. We thank Professors R. M. White and M. G. Cottam for useful discussions and the National Science Foundation for continued support spanning these three decades.

---

*E-mail: david.lockwood@nrc.ca

[1] R. L. Greene, D. D. Sell, W. M. Yen, A. L. Schawlow, and R. M. White, Phys. Rev. Lett. **15**, 656 (1965).
[2] J. W. Halley and I. Silvera, Phys. Rev. Lett. **15**, 654 (1965).
[3] Y. Tanabe, T. Moriya, and S. Sugano, Phys. Rev. Lett. **15**, 1023 (1965).
[4] S. J. Allen, R. Loudon, and P. L. Richards, Phys. Rev. Lett. **16**, 643 (1966).
[5] P. A. Fleury, S. P. S. Porto, L. E. Cheeseman, and H. J. Guggenheim, Phys. Rev. Lett. **17**, 84 (1966).
[6] P. A. Fleury and R. Loudon, Phys. Rev. **166**, 514 (1968).
[7] M. G. Cottam and D. J. Lockwood, *Light Scattering in Magnetic Solids*, Wiley, New York (1986).
[8] F. L Scarpace, M. Y. Chen, and W. M. Yen, J. Appl. Phys. **42**, 1655 (1971).
[9] M. Y. Chen, F. L. Scarpace, M. W. Passow, and W. M. Yen, Phys. Rev. B **4**, 1332 (1971).
[10] Y. H. Wong, C. D. Pfeifer, and W. M. Yen, in *Magnetism and Magnetic Materials (1972)*, C. D. Graham, Jr. and J. J. Rhyne (eds.), AIP Conference Proc. No. 10, AIP, New York (1973), p. 1960.
[11] D. J. Lockwood, R. M White, and W. M. Yen, Phys. Rev. B **69**, 174413 (2004).
[12] W. M. Yen and Y. Oka, Bussei Kenkyu **13**, 507 (1972).
[13] L. D. Barron, M. P. Bogaard, and A. D. Buckingham, J. Am. Chem. Soc. **95**, 603 (1973).
[14] L. D. Barron and A. D. Buckingham, Mol. Phys. **20**, 1111 (1971).
[15] L. D. Barron, *Molecular Light Scattering and Optical Activity*, Cambridge University Press, Cambridge (1982).
[16] L. D. Barron and L. Hecht, in *Circular Dichroism: Principles and Applications*, J. Nakanishi, N. Berova, and R. W. Woody (eds.), VCH Publishers, New York (1994).
[17] Petrou, D. L. Peterson, S. Venugopalan, R. R. Galazka, A. K. Ramdas, and S. Rodríguez, Phys. Rev. B **27**, 3471 (1983).
[18] D. L. Peterson, D. U. Barthololmew, A. K. Ramdas, and S. Rodríguez, Phys. Rev. B **31**, 7932 (1985).
[19] K. R. Hoffman, W. Jia, and W. M. Yen, Opt. Lett. **15**, 332 (1990).
[20] K. R.;Hoffman, W. Jia, and W. M. Yen, *Proceedings of the 12th International Conference on Raman Spectroscopy*, J. R. Durig and J. F. Sullivan (eds.), Wiley, New York (1990), p. 864.
[21] K. R. Hoffman, W. M. Yen, and D. J. Lockwood, *Proceedings of the 14th International Conference on Raman Spectroscopy*, N. T. Yu and X. Y. Li (eds.), Wiley, Chichester (1994), p. 1078.
[22] K. R. Hoffman, W. M. Yen, and D. J. Lockwood, *Proceedings of the 13th International Conference on Raman Spectroscopy*, W. Kiefer *et al.* (eds.), Wiley, Chichester (1992), p. 766.
[23] K. R. Hoffman, W. M. Yen, D. J. Lockwood, and P. E. Sulewski, Phys. Rev. B **49**, 182 (1994).
[24] D. J. Lockwood, K. R. Hoffman, and W. M. Yen, J. Lumin. **100**, 147 (2002).
[25] R. Loudon and P. Pincus, Phys. Rev. **132**, 673 (1963).
[26] A. B. Harris, Phys. Rev. **143**, 353 (1966).
[27] M. G. Cottam and D. J. Lockwood, *Light Scattering in Magnetic Solids*, Wiley, New York, (1986), Chapter 5.
[28] D. D. Sell, R. L. Greene, and R. M. White, Phys. Rev. **158**, 149 (1967).
[29] R. A. Cowley and W. J. L. Buyers, Rev. Mod. Phys. **44**, 406 (1972).
[30] J. P. Kotthaus and V. Jaccarino, Phys. Rev. Lett. **28**, 1649 (1972).
[31] T. Dumelow, R. E. Camley, K. Abraha, and D. R. Tilley, Phys. Rev. B **58**, 897 (1998).
[32] P. L. Richards, J. Appl. Phys. **35**, 850 (1964).

This article was published in English in the original Russian journal. Reproduced here with stylistic changes by AIP.

LOW TEMPERATURE PHYSICS VOLUME 31, NUMBERS 8–9 AUGUST–SEPTEMBER 2005

Magnetoelasticity and domain structure in antiferromagnetic crystals of the iron-group dihalides

V. M. Kalita, A. F. Lozenko,* S. M. Ryabchenko, and P. A. Trotsenko

Institute of Physics of the National Academy of Sciences of Ukraine, pr. Nauki 46, Kiev 03028, Ukraine

(Submitted December 31, 2004; revised May 4, 2005)
Fiz. Nizk. Temp. **31**, 1042–1058 (August–September 2005)

We study the formation of antiferromagnetic magnetoelastic domains in easy-plane antiferromagnets of the iron-group dihalides, in which the infinite degeneracy of the spatial orientation of the antiferromagnetic vector in the basal plane is lifted on account of the spontaneous magnetostriction. In these crystals the domains differ from each other not only by the direction of the antiferromagnetic vector **L** in them but also by the related directions of the principal axes of the spontaneous magneostrictive strain. The system of antiferromagnetic domains turns out to be identical to the system of elastic domains. It is shown that the processes of magnetization and the induced striction in a magnetic field in the multidomain antiferromagnetic state are interconnected. Data on the field dependence of the induced magnetostriction in the multidomain state of the easy-plane antiferromagnets $CoCl_2$ and $NiCl_2$ are presented and analyzed. It is shown that although the magnetostriction in the cycles of imposition and removal of the magnetic field includes both reversible and irreversible contributions, the reversible being the main one. It is shown that the magnetoelastic-striction domains are responsible for reversibility (equilibrium) of the multidomain state. The field dependence of the magnetostriction of the uniform and multidomain states and the behavior of the magnetization of the crystals are described. For description of the rearrangement of the multidomain state, the approximation of a continuous distribution of domains with respect to the orientations of their **L** vector in the easy plane of the crystal in the absence of external magnetic field. It is shown that the matching of the elastic fields of the system of domains and the elastic fields of defects can bring about the formation of a reversible multidomain state, i.e., it can make such a state energetically favorable. The results of the analysis are in satisfactory agreement with the experimental data. © *2005 American Institute of Physics.* [DOI: 10.1063/1.2008141]

I. INTRODUCTION

Many of the fundamental aspects of the magnetoelasticity resulting from the lowering of the symmetry upon the magnetic ordering of high-symmetry magnets with multiple spatial degeneracy of the directions of the order parameter have not been adequately studied. First and foremost, this applies to the formation of magnetic domains in them. This paper is devoted to an examination of these questions for the example of layered easy-plane antiferromagnetic crystals of iron-group dihalides.

II. BASIC PROPERTIES OF LAYERED ANTIFERROMAGNETIC IRON-GROUP DIHALIDES

A. Properties of the crystals

Easy-plane antiferromagnetic crystals of iron-group dihalides MeX_2 (Me is a metal ion, Co or Ni, and X is a halogen ion, Cl or Br) have a layered crystal structure in which each layer of Me^{2+} metal ions are surrounded by two layers of halogen ions X^-, coupled with the Me^{2+} ions by ionic-covalent bonds. The set of such sandwiches, coupled together by van der Waals bonds, for a crystal. A threefold symmetry axis C_3 passes perpendicular to the layers, and in the basal plane, which coincides with the plane of the layers, there are two sets of twofold axes C_2, three equivalent axes in each. The layeredness leads to anisotropy of the physical properties both in the elastic subsystem of the crystals—the values of the elastic constants in the direction perpendicular to the layer are an order of magnitude smaller than those within the layer—and in the magnetic subsystem—the exchange interactions of the magnetic ions in the layer are much larger than those between ions of adjacent layers. The inter-sandwich stacking of different crystals of this group can be somewhat different. For example, $CoCl_2$ and $NiCl_2$ have spatial symmetry D^5_{3d} (isomorphic to $CdCl_2$),[1] while $CoBr_2$ has space group D^3_{3d} (isomorphic to CdI_2).[2]

The majority of the crystals discussed[3–5] are easy-plane (EP) two-sublattice antiferromagnets (AFMs) with hard axis C_3. The Me^{2+} ions lying in one plane belong to one sublattice, and the ions of adjacent planes belong to the other. Owing to the EP anisotropy $\mathbf{L} \perp C_3$, $\mathbf{L}=\mathbf{s}_1-\mathbf{s}_2$ is the antiferromagnetic vector, and $\mathbf{s}_1$ and $\mathbf{s}_2$ are the sublattice magnetization vectors. The anisotropy due to the departure of the vectors $\mathbf{s}_1$ and $\mathbf{s}_2$ from the EP is much larger than the anisotropy within the EP, and for a number of these crystals it is even large compared to the exchange. As to the anisotropy within the EP, according to the neutron scattering datea[3] the easiest directions for **L** in the EP correspond to the three equivalent C_2 axes of one set (sixfold spatial degeneracy), while the three C_2 axes of the other set are harder, i.e., there is some anisotropy. In $NiCl_2$ this anisotropy, although extremely weak, is nevertheless manifested in the angular dependence of the low-frequency branch of the antiferromagnetic resonance (AFMR),[4] in $CoCl_2$ no such manifestation could be discerned. The assertion that the in-plane anisotropy is extremely weak can also be made from the observations of the magnetization, which is actually independent of the magnetic field direction in the basal plane.[5] Thus the vector **L** can take practically any direction in the easy plane by overcoming this small anisotropy.

One should also take into consideration the possible modification of the in-plane magnetic anisotropy by the fields of defects of the corresponding structure of the AFMs studied. Point defects of a different type (vacancies or impurity atoms) can enhance or weaken the 6-fold anisotropy mentioned and can even cause a change of sign. Dislocations, including screw, and disclinations will also alter the anisotropy mentioned in the region around them. Thus defects can suppress the weak in-plane anisotropy if its local modulation caused by them exceeds its small initial value.

The parameter θ in the Curie-Weiss law for the temperature dependence of the paramagnetic susceptibility and also the temperature of AFM ordering (the Néel temperature T_N) in these crystals is mainly determined by the intralayer ferromagnetic exchange, while the interlayer AFM exchange is considerably weaker.[5]

B. Spontaneous lowering of symmetry. AFMR. Domains

It follows from the neutron diffraction observations that the AFM ordering in $CoCl_2$, $CoBr_2$, and $NiCl_2$ in the presence of orientational degeneracy of the directions of the vector **L** in the plane is accompanied by the separation of the crystal into antiferromagnetic domains[3] with different directions of **L** in the EP. Within each domain **L** is uniform. According to the data of Ref. 3, the values of the angles between directions of **L** are predominantly equal to 60°, reflecting, it would seem, the orientation of **L** within each domain with its easiest axis. However, even the neutron diffraction data do not imply that the distribution functions of the directions of **L** of the different domains are completely concentrated only near these directions, and the residual stresses are not represented. In a magnetic field **H** lying in the EP a gradual transition to a uniform (single-domain) state with $\mathbf{L}\perp\mathbf{H}$ occurs. It is reached in a field H_{ff}, much less than the sublattice collapse fields. When the field is removed the multidomain state is is restored, though not completely. The volume of the domains with **L** normal to the imposed field is greater than the volumes of domains with other orientations of **L**.

AFMR studies of these crystals[4,6–8] have shown that the low-frequency (LF) branch of the AFMR in them has a finite gap, the value of which is much larger than would be expected from the small in-plane anisotropy. Besides the data[4] for $NiCl_2$, where the angular dependence of the frequency of the LF AFMR was found to contain a weak contribution due to the angle between **H** in the EP and the C_2 axes, no manifestations of this anisotropy in the corresponding angular dependences of the frequency of the LF AFMR has been discerned in other crystals of this group. Such behavior of the LF AFMR is typical[9,10] for the spontaneous lowering of the symmetry on account of the magnetoelastic (ME) interaction, in an AFM with infinite spatial degeneracy of the orientations of **L**. A spontaneous anisotropy of the magnetostriction arises in the crystal, with the principal axes of the strain tensor lying in the EP in the directions perpendicular and parallel to **L**. The in-plane magnetoelastic anisotropy due to the magnetostriction lifts the spatial degeneracy for the directions of **L**, leading to the formation of a gap for fast oscillations of **L** and **M** in the plane ($\mathbf{M}=\mathbf{s}_1+\mathbf{s}_2$). Importantly, this "anisotropy" for the crystals studied turns out to be much greater than the initial in-plane magnetic crystallographic anisotropy discussed above.

Comparison of the field of this anisotropy (magnetoelastic field) with the exchange field shows that in order of magnitude the magnetoelastic energy amounts to some percent of the exchange energy. It is expected that when the values of the elastic constants of the crystals are taken into account, the values of the anisotropic spontaneous magnetostriction in them will be anomalously large, as was observed in Ref. 11: it reaches values of $10^{-4}-10^{-3}$. A magnetostriction of similar magnitude observed in rare-earth magnets is sometimes called "giant." [12]

Observation of the LF AFMR in $CoCl_2$ has revealed practically no manifestations of angular dependence (dependence on the direction of **H** in the EP) of the frequency in either the single-or the multidomain state. The magnetic-field dependence of the LF AFMR can be described on the assumption that the value of the MS gap is independent of field at the transition to the single-domain state. Consequently, in the multidomain state, domains with different directions of the MS coexist without creating mutual elastic stresses that influence the value of the gap of the LF AFMR.

The multidomain character is manifested in the magnetization of the structures.[13] At high magnetic fields in the single-domain state the samples behave as Néel two-sublattice AFMs with linear dependence of the magnetization on field. In the multidomain state one observes a nonlinear trend of these dependences with a noticeable decrease of the magnetic susceptibility for $H\rightarrow 0$.[13] These features of the magnetization had not been explained before.

It was shown in Refs. 14–19 that the AFM domains in the crystals studied have a magnetoelastic nature. In those papers, and also in Refs. 20 and 21, it was established that it is the elastic aspect of the multidomain state that is responsible for its essential reversibility. Below we give a brief review of the papers mentioned and carry out additional proofs of the magnetoelastic nature of the AFM domains in layered iron-group dihalides.

C. Causes of the formation of domains in layered AFMs

The formation and stability of AFM domains have been discussed in many papers.[22–25] The multidomain character of the AFM is not due, as in the case of ferromagnets, to magnetostatic fields (of a dipolar nature)[26,27] The cost in exchange energy in the domain walls should make this state energetically unfavorable. Therefore the AFM domains are most often metastable, thermodynamically nonequilibrium, and are not restored after the crystal has been brought to the single-domain state by an external magnetic field.

The AFM domains arising at orientation phase transitions in uniaxial AFMs was studied in Refs. 28 and 29. In a magnetic field the transition from the state with easy-axis

AFM orientation of the sublattice spins to the state with spins tilted toward the field and oriented almost perpendicular to the easy axis, both these states are observed simultaneously, i.e., an intermediate AFM state is realized.[29] This multidomain state formed in the magnetization of an AFM is described with allowance for the magnetostatic energy.

Various mechanisms have been proposed[22] to explain the formation of an equilibrium multidomain state in an AFM, but apparently none of them applies to all AFMs. The most universal, at first glance, is the entropy mechanism,[30] according to which the energy cost due to the exchange interaction in the wall is compensated by a lowering of the free energy $T\Delta S$ owing to the increase in entropy in the multidomain state (T is the temperature and ΔS is the entropy increase). This contribution vanishes at $T\rightarrow 0$, although in a number of cases it does permit an explanation of the formation of an equilibrium multidomain state at high temperatures, close to the Néel point.[22]

In many AFMs the equilibrium (or almost equilibrium) multidomain AFM state exists in the temperature interval from T_N to $T\rightarrow 0$. It is most often linked with the influence of defects. Domains of this kind have been observed by different methods, e.g., they have been visualized optically.[31,32] AFM domains are formed upon twinning of the crystal, when the domain structure is a combination of antiferromagnetic and structural domains. The formation of a multidomain state is possible when the order of succession of the sublattices is disrupted, e.g., in the presence of edge dislocations, when the defect is a half plane of atoms with magnetic moments belonging to one of the magnetic sublattices. In Refs. 33 and 34 it was shown that a screw dislocation in an AFM leads to the formation of a spin disclination, which, when the anisotropy is taken into account, leads to the formation of AFM domains. Defects can also stabilize the multidomain state of a kinetic nature that arises in the course of the AFM ordering, when domains form because there are many centers for the formation of the AFM state at T_N.[35]

The simplest case of the influence of defects on the formation of a multidomain state involves the so-called ''metallurgical defects,'' which, distorting the lattice, locally alter the direction of the anisotropy fields and the local orientations of the vector **L**. We shall not consider that case but restrict the investigation to multidomain states formed as a result of the ME interaction of the magnetic subsystem with the elastic fields of defects in rather perfect crystals, which has been fully studied.

It is not obvious why it is optimal for a system of AFM domains to form in which each of the domains suffers spontaneous ms that is anisotropic in the plane, with different directions of the principal axes of the strictive strains. If the directions of the striction are different in different directions, then stresses should arise on the walls of adjacent domains to counteract the differently directed spontaneous MS in them. And although the directions of the principal axes of the strain tensors can be matched for two adjacent domains, but it cannot be done where more than two domains come together at a point. Such a point is surrounded by elastic stresses that add to the energy cost to the crystal. However, if the place where three or more domains come together coincides with a structural defect, which is also a source of elastic stresses and strains, then the energy cost of the structural defect can be reduced by having the signs of their elastic fields match those of the stresses caused by the junction of the domains. In that case the total energy of the crystal can even decrease provided the cost of the exchange energy in the domain walls is less than the benefit in the elastic energy.

The possibility of stabilization of the multidomain magnetoelastic state owing to the benefit in the surface energy of a sample without any changes of its outward form was considered in Refs. 20 and 21. This mechanism may be applicable to AFM samples of very small size. Therefore, we shall not analyze it in detail here.

In the analysis of the induced MS of the crystal as a whole, it is necessary to distinguish two regions: the low field region, where the observable, aggregate MS is mainly due to rearrangement of the multidomain state, and the high field region, where in the single-domain state the MS that appears is due solely to the rotation of the sublattice magnetizations toward the magnetic field and their ultimate collapse at a field $H_{ff}=2H_E$. For some of the crystals considered, the values of $2H_E$ are small and accessible in experiments.

III. FIELD AND TEMPERATURE DEPENDENCE OF THE INDUCED MAGNETOSTRICTION AND THE MAGNETIZATION OF THE EASY-PLANE AFMs

A. Dependence of the induced MS in crossed magnetic fields

The magnetostriction of $CoCl_2$, $CoBr_2$, and $NiCl_2$ has been studied by means of a capacitive dilatometer.[36] The crystals were grown by the slow cooling of the melt in a sealed quartz ampoule. Prior to sealing, the ampoule containing the ''chemically pure'' (grade ChDA) powder was pumped down at a temperature close to the melting point for dessication. The crystals are easily delaminated along the plane perpendicular to the C_3 axis; the directions of the C_2 axes in the basal plane of the crystals was not monitored. Samples in the form of $5\times5\times1$ mm rectangular slabs were cut from flat wafers obtained by cleaving. The variation of the length of one of the sides of the slab in magnetic field was measured.

To obtain data on the reversible and irreversible (after a cycle of imposition and removal of the magnetic field) parts of the induced MS, we used a system of crossed superconducting magnets. The sample was mounted so that the fields of both coils lay in plane of the sample, one in the direction along the side of the slab measured by the dilatometer, the other perpendicular to it. The maximum magnetic fields equaled 65 and 13 kOe. This set of solenoids made it possible to investigate the MS while rearranging the domain structure and also to determine the part that lies ''hidden'' in the spontaneous MS of the sample before the magnetic field is applied. The sample temperature was set at values ranging from 4.2 to 70 K.

Figure 1 shows the curves of the relative elongation $\varepsilon(H)=\Delta\ell/\ell$ for $CoCl_2$ and $NiCl_2$ (the curve for $CoBr_2$ is analogous to that for $CoCl_2$) in an imposition-removal cycle of the crossed magnetic fields at a temperature of 4.2 K. Here ℓ is the length of the sample and $\Delta\ell$ is its change in the field. Curves *1* and *2* in Fig. 1 correspond, respectively, to

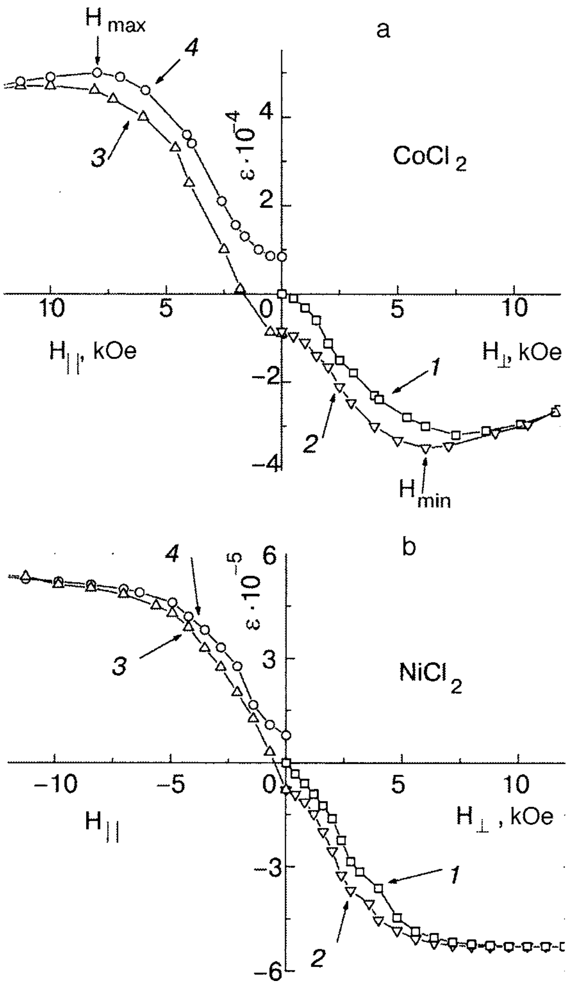

FIG. 1. Relative elongation of $CoCl_2$ (a) and $NiCl_2$ (b) during the imposition and removal of a magnetic field lying in the easy-plane perpendicular to the direction of the measured side of the crystal (curves *1* and *2*) and the subsequent imposition and removal of a field along the measured direction (curves *3* and *4*).

the measurements of $\varepsilon_\perp(H)$ during the imposition and removal of the field H perpendicular to the measured side of the crystal, and curves *3* and *4* to the measurements of $\varepsilon_\parallel(H)$ during the subsequent imposition and removal of a field H along that direction. It is seen that the striction is anisotropic with respect to the field direction and that the curves of the MS thus obtained have the form of hysteresis loops with a remanent MS, the sign of which is determined by the direction of the removed field.

The curves shown in Fig. 1 correspond to the variation of the MS during the rearrangement of the multidomain state and a transition to a uniform state under the influence of magnetic field. In the AFM state an anisotropic spontaneous MS is realized for these samples. However, in the multidomain state the differently directed spontaneous strains of the individual domains average out almost to zero over the crystal as a whole. At high fields the spontaneous MS of the crystal is restored in a transition to the single-domain state. After the field is removed, the multidomain state is largely restored, and the MS decreases to a small remanent striction. This remanent MS is also absent prior to the first imposition of the field. In the multidomain state, as we have said, the AFMR data[11] indicate that the domains individually are spontaneously strained, as is reflected in the observed gap in the spectrum of the LF branch. This means that the domains retain the spontaneous MS without creating substantial stresses on each other, although the spontaneous MS of the whole crystal in the multidomain state is close to zero.

It is also seen in Fig. 1 that the signs of the contribution from the induced MS in the single-domain state are opposite to the signs of the initial spontaneous MS for both crystals and both orientations of the magnetic field. Therefore, the $\varepsilon_\parallel(H)$ curve has a maximum and the $\varepsilon_\perp(H)$ curve a minimum near the field at which the single-domain state is established in the sample. In $NiCl_2$ the $\varepsilon_\parallel(H)$ and $\varepsilon_\perp(H)$ curves are practically antisymmetric at the transition from the multidomain to the single-domain state. In $CoCl_2$, as in $CoBr_2$, this antisymmetry is noticeably distorted. For $CoCl_2$ and $CoBr_2$ the field of the maximum $H_{\max}$ is constant larger than the field of the minimum $H_{\min}$, and $\varepsilon_\parallel(H_{\max})>|\varepsilon_\perp(H_{\min})|$.

These results were explained in Ref. 14 as follows. The strains of different domains add together, forming the strain of the crystal in the direction of measurement. Since for the spontaneous MS the strains of the crystal along **L** and perpendicular to it must be equal in magnitude and opposite in sign, the total spontaneous MS anisotropic in the basal plane for the crystal in the multidomain state averages to zero for $H\approx 0$ if it is assumed that the domains are uniformly distributed over equivalent directions of **L**. After the induced transition of the crystal to the single-domain state for $\mathbf{L}\perp\mathbf{H}$, the dependence of the induced MS on the field is determined solely by the canting of the sublattice magnetizations toward **H**. For the data shown in Fig. 1, this stage begins at $H \geqslant 10$ kOe and ends at $H=H_{ff}$ (the data for $H>H_{ff}$ are not shown in Fig. 1). The differences between the curves during imposition and removal of the field in Fig. 1, corresponding to the remanent spontaneous MS of the crystal as a whole, reflect the partial irreversibility of the rearrangement of the domain structure in this cycle.

B. Field dependence of the MS at low fields

Figure 2 shows the dependence of the MS of the multidomain state of $CoCl_2$ and $NiCl_2$ on the square of the magnetic field strength during the removal of the field at low fields. For $H<2.5$ kOe the curves can be described by the expression

$$\varepsilon_{\parallel,\perp}=\varepsilon_{r\parallel,\perp}+\alpha_{\parallel,\perp}H^2_{\parallel,\perp}, \tag{1}$$

where $\varepsilon_{r\parallel,\perp}$ is the remanent striction in the plane for measurements along ($\parallel$) and transverse to ($\perp$) the magnetic field, $|\varepsilon_{r\parallel}|\cong|\varepsilon_{r\perp}|$, but $\varepsilon_{r\parallel}\cong-\varepsilon_{r\perp}$; $\alpha_\parallel\cong-\alpha_\perp$ are empirical parameters. The $\varepsilon(H)$ curve for the first imposition of the field is also described by Eq. (1), but with $\varepsilon_r=0$. The curves drawn according to Eq. (1) are shown by the solid lines in Fig. 2. The quadratic character of the field dependence of the MS shows that the rearrangement of the multidomain state, i.e., the increase of the volume of domains with the favorable orientations of the sublattice spins (relative to the direction of **H**) and the decrease of the volume of domains with an unfavorable orientation occurs mainly through the motion of domain walls.

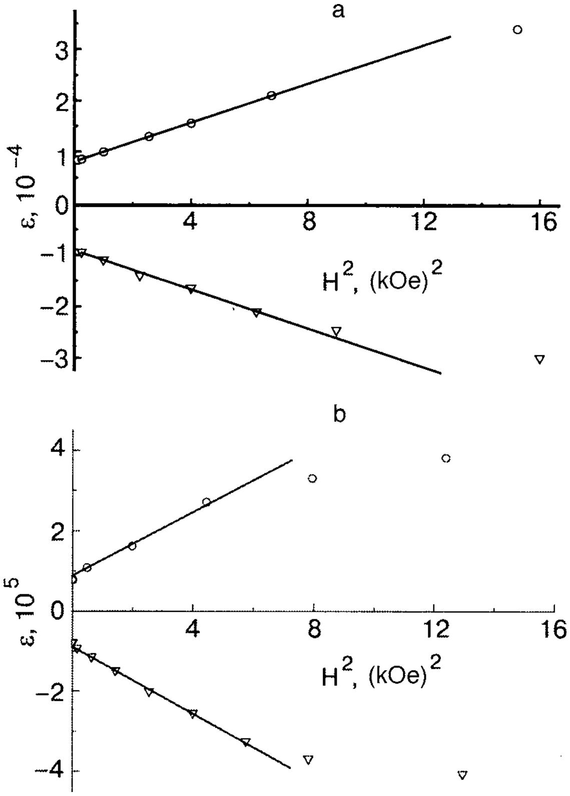

FIG. 2. Dependence of the induced magnetostriction of $CoCl_2$ (a) and $NiCl_2$ (b) versus the square of the magnetic field strength during removal of the field.

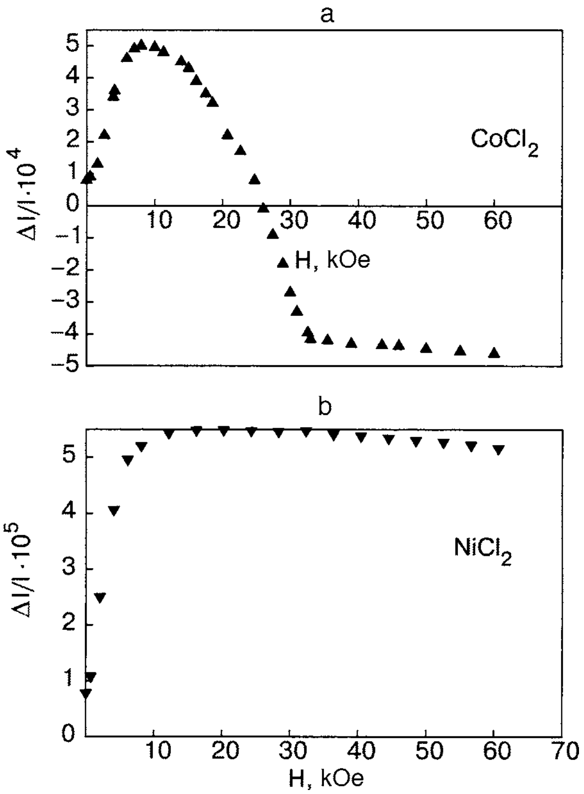

FIG. 3. Field dependence of the magnetostriction of $CoCl_2$ (a) and $NiCl_2$ (b) crystals; the measurements were made during removal of a field lying along the direction of measurement of their relative elongation.

C. Behavior of the MS in the uniform state

The rearrangement of the multidomain state is completed in a magnetic field higher than the characteristic value of the field for bringing the sample to the single-domain state (in our case ≈ 10 kOe), by a transition to a single-domain state with $\mathbf{L}\perp\mathbf{H}$. Figure 3 shows the relative elongation of the crystals as a function of the magnetic field strength for a field $H \leqslant 65$ kOe parallel to the side being measured. The MS of the single-domain state can be described by the expression[17,37]

$$\varepsilon_{\parallel}(H) = \varepsilon^{(S)}(1 - \xi(H/H_{ff})^2), \tag{2}$$

where $\varepsilon^{(S)}$ is the striction that would be realized in the crystal at $H \to 0$ if the sample were in a uniform state, and ξ is an empirical parameter. The value of $\varepsilon^{(S)}$ should be regarded as spontaneous anisotropic MS, which can be obtained from the assumption continuation of the $\varepsilon_{\parallel}(H)$ curve into the region $H \to 0$. For $NiCl_2$ and $CoCl_2$ the cases $\xi < 1$ and $\xi > 1$ are realized, respectively. As was shown in Refs. 14, 17, and 37, this is due to the different relative contribution to the MS from the inter- and intra-sublattice magnetoelastic interactions.

In $CoCl_2$ an orientational phase transition is reached in the given field interval, at $H = H_{ff}$, when the spins of both sublattices become parallel along $\mathbf{H}$. After that, the field dependence of the MS changes in connection with the paraprocess. According to Ref. 1 and our data, $H_{ff} = 32$ kOe in $CoCl_2$. In $NiCl_2$, according to the AFMR data, $H_{ff} = 129$ kOe,[38] and it was not reached in our experiments; we therefore used the published value for H_{ff} in determining the value of the parameter ξ in Eq. (2).

C. Temperature dependence of the MS

Figure 4 shows the field dependence of the relative strain of $CoCl_2$ in the direction along the magnetic field, which was oriented in the EP, for temperatures from 4.2 to 24 K. The influence of temperature is manifested in the value of the MS strain: it decreases with increasing T. The field of the transition to the single-domain state (the region of the maximum on the curves) also decreases with increasing T, as does the field H_{ff}.

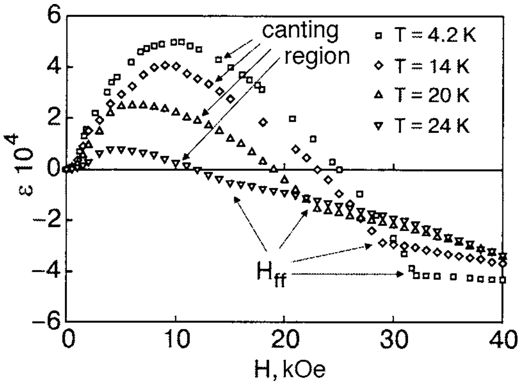

FIG. 4. Field dependence of the magnetostriction of $CoCl_2$ for the first imposition of the magnetic field at different temperatures.

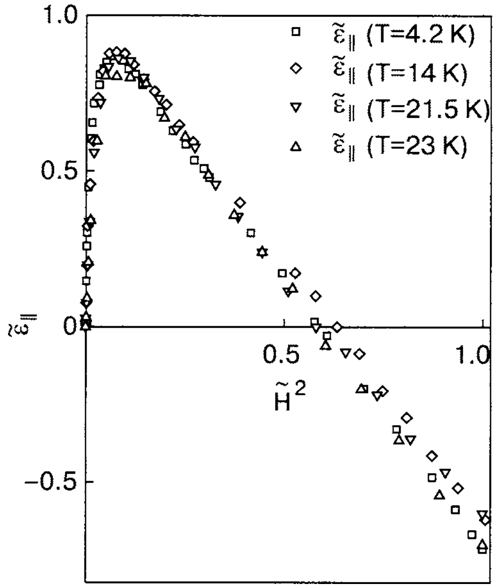

FIG. 5. Magnetostriction $\tilde{\varepsilon}_{\parallel}$ of the uniform state of $CoCl_2$, normalized to its spontaneous value, versus the square of the magnetic field in the plane, normalized to the collapse field, for different temperatures.

Figure 5 shows the MS in $CoCl_2$, normalized to the value of the spontaneous anisotropic MS, i.e., $\tilde{\varepsilon}(T,H)_{\parallel} = \varepsilon(T,H)_{\parallel}/\varepsilon^{(S)}(T)$, for different temperatures as a function of the square of the magnetic field (for field directed parallel to the side being measured), normalized to the square of the collapse field at the corresponding temperature: $\tilde{H}_{\parallel}^2 = H_{\parallel}^2/H_{ff}^2(T)$. It is seen that, when normalized in this way, the curves for different temperatures in the single-domain state all coincide. This means that in the uniform region the MS obeys relation (2) with a parameter ξ this is independent of T. Then the variation of $\varepsilon_{\parallel}(H)$ with temperature should be due to the influence of temperature on $\varepsilon^{(S)}(T)$ and $H_{ff}(T)$ only. This is easy to understand, since the induced MS of the single-domain state is due solely to the canting of the sublattice spins.

In the region where the rearrangement of the multidomain state occurs, the dependence of MS on magnetic field has a different character. Figure 6 shows the dependence of the induced MS of $CoCl_2$ on the square of the magnetic field strength during the first imposition of the field ($\varepsilon_r = 0$). They obey expression (1) but with a coefficient α that depends on T. Here the trend of the MS can be represented in the form

$$\varepsilon_{\parallel,\perp} = \varepsilon^{(S)}(T)\frac{H_{\parallel,\perp}^2}{H_d^2}, \tag{3}$$

where H_d is a parameter having dimensions of magnetic field strength. For agreement with experiment the value of H_d should be chosen the same for all temperatures and equal to 5.7±0.3 kOe. If an entropy mechanism of the multidomain state or a mechanism involving the influence of the surface elastic energy is realized in the crystal, then the parameter H_d would be temperature-dependent.

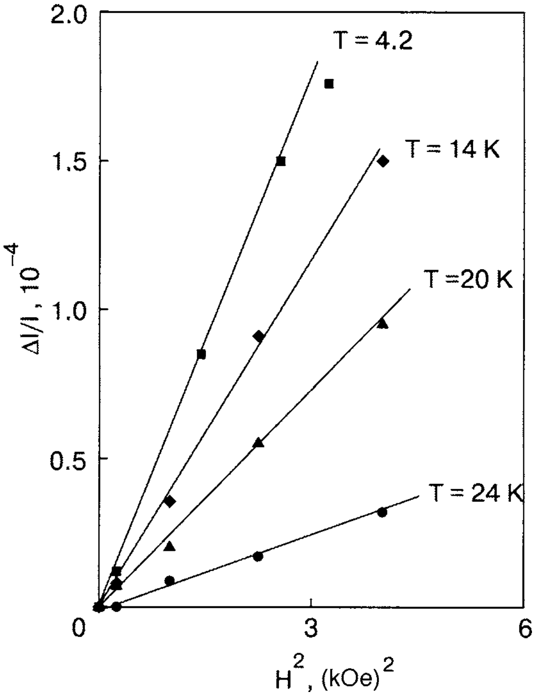

FIG. 6. Magnetostriction of $CoCl_2$ versus the square of the magnetic field during its removal at different temperatures in the region of the multidomain state.

E. Field dependence of the magnetization in the multidomain state

The magnetization was measured using an LDJ-9500 vibrating magnetometer. $NiCl_2$ samples with dimensions of $5 \times 4 \times 0.2$ at the were studied. The applied field did not exceed 12 kOe, which was sufficient for the transformation of $NiCl_2$ from a multidomain to a single-domain state.[17] The samples used in the magnetostriction and magnetization measurements were grown at different times. Because $NiCl_2$ crystals are hygroscopic, the samples were stored in a dessicated medium. In view of the possible differences in the growth and storage conditions, it cannot be said for certain that the samples were identical from the standpoint of the possible number of defects. Measurements made in the cycles of field imposition and removal have shown the absence of remanent magnetization. Consequently, our AFM crystals, like those in Ref. 39, did not have ferromagnetic inclusions.

Figure 7 shows the magnetization curve of a $NiCl_2$ single crystal during the imposition of a field $\mathbf{H} \perp C_3$. It is seen that the magnetization depends nonlinearly on H. The dashed line in Fig. 7 shows the straight line expected for the dependence of the magnetization on H in a single-domain EP AFM with no in-plane anisotropy.[40] The experimental dependence $m(H)$, on the contrary, has a characteristic "sag" below this straight line in the region where the rearrangement of the multidomain structure occurs. Initially the difference between the calculated and experimental $m(H)$ curves grows and the curves diverge from each other, but then (for $H > 5$ kOe) they draw closer together and practically merge at $H \approx 10$ kOe. The $m(H)$ curve of the multidomain state for $H \to 0$ is well approximated by the expression

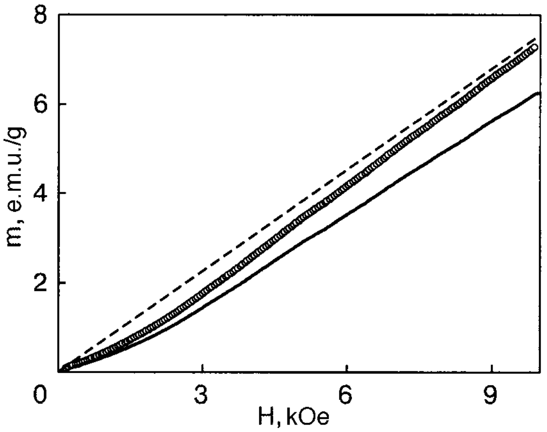

FIG. 7. Magnetization of $NiCl_2$ as a function of the magnetic field lying in the EP. The dots are experimental (result of the first imposition of the field), the dashed line is the expected dependence for a single-domain crystal with reversible domain structure.

$$m=\chi_d H\left(1+\frac{H^2}{H_m^2}\right), \tag{4}$$

where χ_d is the magnetic susceptibility of the multidomain state for $H\rightarrow 0$, and H_m is an empirical parameter. A fitting to experiment gives $\chi_d=0.44$ e.m.u./(g·kOe), $H_m=4.3\pm 0.6$ kOe.

By integrating $m(H)$ over H, one can determine the work done by the magnetic field in magnetizing the crystal. The work done by the field in taking a unit volume of an AFM from the multidomain to the uniform state[18] will be the difference between the work of magnetization of a uniform and a multidomain segment. For the numerical integration we use the experimental dependence shown in Fig. 7. We compute

$$\Delta A=\frac{1}{2\rho}\left[\chi_e H_e^2-\int_0^{H_e} m(H)dH\right], \tag{5}$$

where ρ is the density of the crystal, χ_e is the magnetic susceptibility of the uniform state, which, line the magnetization $m(H)$, is normalized per unit mass of the sample, and H_e is the field at which the uniform state is attained (we used the value $H_e=10$ kOe).

The energy E per unit volume of a multidomain antiferromagnet in a magnetic field can be written as a sum $E=e_1+e_2+e_3+e_4$, where e_1 is the AFM exchange energy, e_2 is the Zeeman contribution, e_3 is the domain-wall energy, and e_4 is the energy of matching of the local elastic fields of defects of the crystal and the elastic strains due to spontaneous MS domains. The local matching of the elastic strains of the spontaneous MS of the domains with defects promote the formation of multiple domains, and therefore e_4 can be called the energy "source" of the multidomain character. An equilibrium multidomain state corresponds to a minimum of the energy E. In that case the energy increments e_3 and e_4 upon the formation of the multidomain state must have opposite signs.

Let us consider the difference of the energies E of a crystal in the states prior to application of the magnetic field and in the field H_e, i.e., $\Delta E=\Delta e_1+\Delta e_2+\Delta e_3+\Delta e_4$. Hence $\Delta A=-[e_3(H=0)+\Delta e_4]$, where we have taken into account that for $H=H_e$ the state of the crystal is uniform (almost uniform for our calculation using $H_e=10$ kOe), $e_3(H=H_e)=0$, and $\Delta e_3=e_3(H=0)-e_3(H=H_e)=e_3(H=0)=e_3$. According to Eq. (5), $\Delta A>0$, and the formation of domain walls is unfavorable for the exchange interactions, and therefore $e_3>0$. It follows from the arguments presented above that $\Delta e_4<0$, and $|\Delta e_4|>e_3$. Since $\Delta e_4=e_4(H=0)-e_4(H_3)$, we obtain $e_4(H=0)<e_4(H_3)$. Such a feature of the energy source e_4 of the multidomain character is a necessary condition for the formation of an equilibrium magnetoelastic multidomain state.

The energy benefit of the multidomain state at $H=0$ can be determined from Eq. (5). Its value is equal to the square of the figure enclosed between the straight line of uniform magnetization and the $m(H)$ curve in Fig. 7. According to our calculations, the ratio of this energy benefit to the exchange energy of the inter-sublattice interactions in $NiCl_2$ equals 5.7×10^{-4}.

Thus one can conclude that in the presence of defects causing local elastic stresses, the multidomain magnetoelastic state is energetically favorable and, consequently, should be reversible, i.e., in a state of thermodynamic equilibrium. That state is realized in the given AFM.

Before turning to an analysis of the multidomain state, let us analyze the behavior of the MS of a uniform state. Moreover, at small values of H_{ff} the contribution from the canting of the sublattice spins in the rearrangement of the multidomain state cannot be neglected.

IV. PHENOMENOLOGICAL DESCRIPTION OF THE MS OF THE UNIFORM STATE

In the phenomenological description of the induced MS of the uniform state we shall assume that its value depends only on the orientation of the sublattice spins.[19,37] We shall take into account only the magnetoelastic interactions which are anisotropic in the easy plane. When the symmetry of these crystals is taken into account, the sum of the magnetoelastic and elastic contributions to the energy can be written in the form

$$\begin{aligned}E=&\sum_{\alpha\geqslant\beta}\gamma_{\alpha\beta}(T)(n_{\alpha x}n_{\beta x}-n_{\alpha y}n_{\beta y})(U_{xx}-U_{yy})\\&+\sum_{\alpha\geqslant\beta}\lambda_{\alpha\beta}(T)(n_{\alpha x}n_{\beta y}+n_{\beta x}n_{\alpha y})U_{xy}+\sum_{\alpha\geqslant\beta}\delta_{\alpha\beta}(T)\\&\times(n_{\alpha x}n_{\beta x}+n_{\alpha y}n_{\beta y})(U_{xx}+U_{yy})+\frac{1}{2}C_{11}(U_{xx}^2\\&+U_{yy}^2)+C_{12}U_{xx}U_{yy}+(C_{11}-C_{12})U_{xy}^2,\end{aligned} \tag{6}$$

where $n_{\alpha x}, n_{\alpha y}$ and $n_{\beta x}, n_{\beta y}$ are the direction cosines of the sublattice magnetization vectors $\mathbf{s}_\alpha$ and $\mathbf{s}_\beta$, the x and y axes lie in the EP, γ, λ, and δ are temperature-dependence parameters of the magnetoelastic interactions, the indices $\alpha,\beta=1,2$ enumerate the sublattices, and the U_{ij} are components of the strain tensor. The terms containing the constants C_{11} and C_{12} describe the elastic contribution to the energy of the crystal. In Eq. (6) the terms with $\alpha=\beta$ and $\alpha\neq\beta$ pertain to the intra- and inter-sublattice magnetoelastic interactions, respectively.

In the uniform state and in a magnetic field oriented in the EP, the spins of both sublattices lie in that plane and are tilted in the same way with respect to **H**. Then the direction cosines in (6) are proportional to H/H_{ff}. The dependence of the strain on H is easily found by minimizing (6) with respect to U_{ij}. The expressions obtained for U_{yy}, when **H** lies along y or x, have the form[14,17,37]

$$U_{yy}(H\|y,x)=-\frac{2\delta_{11}}{C_{11}+C_{12}}\mp\frac{\gamma_{12}}{C_{11}-C_{12}}+\left(\frac{\delta_{12}}{C_{11}+C_{12}}\pm\frac{2\gamma_{11}}{C_{11}-C_{12}}\right)\left(1-2\frac{H^2}{H_{ff}^2}\right), \quad (7)$$

where the upper sign corresponds to $\mathbf{H}\|y$, when the field is parallel to the strain being measured, U_{yy}, and the lower sign to $\mathbf{H}\|x$, when the field is perpendicular to that strain.

In the MS measurements the length of the side of the crystal at $H=0$ is taken as the reference point, and the isotropic contributions to the strain in (7) are not reflected in the measurements. Therefore, expressions for the MS of the relative elongation of the sides of the crystal in the easy plane of an EP AFM in the directions along and transverse to the magnetic field take the form

$$\varepsilon_{d\|,\perp}=\pm\varepsilon^{(S)}\left(1-2(1+\eta_{\|,\perp})\frac{H_{\|,\perp}^2}{H_{ff}^2}\right). \quad (8)$$

Here the MS of the uniform state at $H=0$ should satisfy the relations $\varepsilon_{d\|}(H_{\|}=0)=\varepsilon^{(S)}$ and $\varepsilon_{d\perp}(H_{\perp}=0)=-\varepsilon^{(S)}$, where $\varepsilon^{(S)}=(2\gamma_{11}-\gamma_{12})/(C_{11}-C_{12})$. The values of $\eta_{\|,\perp}$ in (8) are expressed in terms of the parameters of the magnetoelastic interactions:

$$\eta_{\|}=\gamma_{12}/(2\gamma_{11}-\gamma_{12})+\delta_{12}(C_{11}-C_{12})/(2\gamma_{11}-\gamma_{12})\times(C_{11}+C_{12}),$$

$$\eta_{\perp}=\gamma_{12}/(2\gamma_{11}-\gamma_{12})-\delta_{12}(C_{11}-C_{12})/(2\gamma_{11}-\gamma_{12})\times(C_{11}+C_{12}).$$

The dependence (8) is in good agreement with the empirical relation (2).

For $\delta_{12}\neq 0$ and $\gamma_{12}\neq 0$ the derivative

$$\partial\varepsilon_{d\|}(H^2)/\partial(H_{\|}^2)\neq-\partial\varepsilon_{d\perp}(H^2)/\partial(H_{\perp}^2),$$

since $\eta_{\|}\neq\eta_{\perp}$, as it characteristic for $CoCl_2$.[16,19] In that compound $\xi=2(1+\eta_{\|,\perp})>1$, and the intra-sublattice magnetoelastic interactions are dominant. In $NiCl_2$ the slopes of the $\varepsilon_{d\|}(H^2)$ and $\varepsilon_{d\perp}(H^2)$ are, to within the error limits, equal in magnitude and opposite in sign. Here $\xi=2(1+\eta_{\|,\perp})<1$, which corresponds to dominance of the inter-sublattice magnetoelastic interactions which are isotropic in the EP.[17] This difference of the magnetoelastic interactions in these crystals is apparently due to the fact that in $NiCl_2$ the orbital moment of the ions is almost completely frozen, and the single-ion anisotropy is much less than the intra-sublattice exchange.[41] In $CoCl_2$, on the contrary, total freezing of the orbital moment of the ions does not occur, and therefore the single-ion anisotropy in it is comparable to the intra-sublattice exchange,[41–44] and that leads to dominance of the intra-sublattice magnetoelastic interactions.

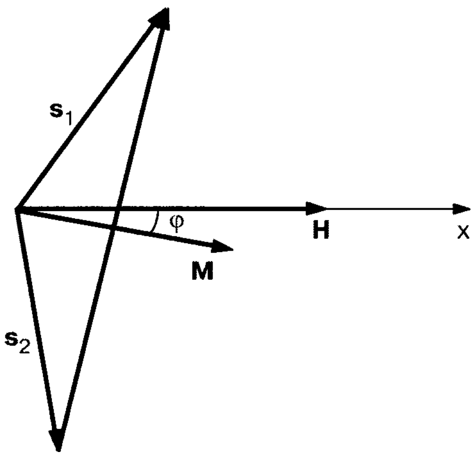

FIG. 8. Scheme of the orientations of $\mathbf{s}_1$ and $\mathbf{s}_2$ and of **L** and **M** of a domain relative to the magnetic field **H**.

V. DESCRIPTION OF THE REARRANGEMENT OF THE MULTIDOMAIN MAGNETOELASTIC STATE OF AN AFM

A. System of magnetoelastic domains in an AFM

It follows from the director presented that for a qualitative discussion of the multidomain nature of these crystals the distribution over orientations of the **L** vectors of the AFM domains in the EP can be treated as continuous. Generally speaking, because of the influence of the small in-plane anisotropy it should be anisotropic, but taking that anisotropy into account, in view of its smallness and the presence of three equivalent "easiest" axes in the EP, it does not affect the magnetic-field dependence of the MS in the multidomain state.[17] We shall therefore disregard the in-plane anisotropy to avoid complicating the calculations. We shall also adopt an approximation of the probability density distribution of the domains over orientations of **L** by assuming that prior to the first application of the field the domains (the **L** vectors in them) are distributed equiprobably over all directions in the EP.

The orientation of the **L** vectors of the domains in the EP will be specified by an angle φ between the magnetic moment vector **M** of the domain and the vector **H** (see Fig. 8), the angle φ being defined in the EP. For $H\to 0$ the angle φ should be taken to be the angle between the direction corresponding to $\lim_{H\to 0}\mathbf{M}$ and the direction of **H**. The density of the domain distribution $p(\varphi)$ we define as the ratio of the volume of domains with orientation φ to the volume of the crystal. It is normalized, i.e., $1/\pi\int_{-\pi/2}^{\pi/2}p(\varphi)d\varphi=1$.

As we have said, the MS of a uniform easy-plane AFM is anisotropy in the easy plane. It is equal to $\varepsilon^{(S)}$ in the direction perpendicular to **L** and to $-\varepsilon^{(S)}$ in the direction along **L**. Using $p(\varphi)$, we write an expression for the MS of the crystal as a whole in the multidomain state:

$$\varepsilon=\frac{1}{\pi}\int_{-\pi/2}^{\pi/2}[\varepsilon_{\|}^{(S)}(H)\cos^2\varphi+\varepsilon_{\perp}^{(S)}(H)\sin^2\varphi]p(\varphi)d\varphi. \quad (20)$$

For a domain with $\varphi\neq 0$ the magnetic field moment **M** is not parallel to **H** and is equal to $|\mathbf{M}|=\chi_e H\cos\varphi$. Its projection on **H** is equal to $M_H=\chi_e H\cos^2\varphi$. Therefore the magnetization of the crystal as a whole will be

$$m=\frac{1}{\pi}\int_{-\pi/2}^{\pi/2}\chi_e H\cos^2\varphi\, p(\varphi)d\varphi. \tag{21}$$

For $NiCl_2$ the field H_{ff} is much greater than the width of the region of fields in which the rearrangement of the multidomain state occurs. Therefore we can assume $\varepsilon_{\parallel}^{(S)}(H)\approx\text{const}$, $\varepsilon_{\parallel}^{(S)}(H)\approx\text{const}$. The MS in $NiCl_2$ is almost completely antisymmetric (see Fig. 1). Therefore $\varepsilon_{\parallel}^{(S)}(H)\approx-\varepsilon_{\perp}^{(S)}(H)=\varepsilon^{(S)}$. Then the relation between the mean magnetization and the MS in the multidomain state will have the form[18]

$$m(H)=\frac{1}{2}\chi_e H\left(1+\frac{\varepsilon_{\parallel}(H)}{\varepsilon^{(S)}}\right). \tag{22}$$

If the experimental values[18] of the relative elongation of the crystal along **H** in the region of rearrangement of the multidomain state, $\varepsilon_{\parallel}(H)$, are substituted into Eq. (22), we obtain a curve for $m(H)$ that is close to the experimental curve for the magnetization of the crystal, presented in Fig. 5. One can also carry out the inverse procedure, substituting $m(H)$ into Eq. (22). Then one can obtain from the magnetization data the expected behavior of the relative elongation of the crystal. The curve thus obtained for the striction also turns out[18] to agree well with the experimental dependence.

Thus the magnetic-field dependences of the magnetization and the MS in the multidomain AFM state are interrelated and reflect the process of the rearrangement of that state under the influence of the field. This is a consequence of the magnetoelastic nature of the AFM domains in these crystals.

At low magnetic fields the domain distribution that gives satisfaction agreement with the experimental data on the field dependences of the MS and magnetization has the form

$$p(\varphi)=\frac{1}{\pi}\left[1+4\left(\frac{\varepsilon_r}{\varepsilon^{(S)}}+\frac{H^2}{H_d^2}\right)\left(\cos^2\varphi-\frac{1}{2}\right)\right]. \tag{23}$$

During the removal of the magnetic field or its repeated imposition in the same direction the dependence of the magnetization at low fields will have the form

$$m=\frac{1}{2}\chi_e H\left(1+\frac{\varepsilon_r}{\varepsilon^{(S)}}+\frac{H^2}{H_d^2}\right). \tag{24}$$

If the remanent striction $\varepsilon_r\to 0$, then the magnetic susceptibility χ_d at the beginning of the rearrangement of the domain structure, for H starting from zero, should be smaller by half than the susceptibility of the uniform state, $\chi_d=\chi_e/2$. The experimental value of χ_d is close to $\chi_e/2$, although it is slightly larger, reflecting the existing irreversible contribution to the structure of the multidomain state. Furthermore, one would expect that $H_d=H_m$. The difference of the values of the parameters H_d and H_m is 15%. As we have said, the crystals used in our investigation of the MS and magnetization were grown at different times, and their defect state, which determines the values of H_d and H_m, could have been different.

B. Reversible and irreversible components of the rearrangement of the multidomain state

The distribution of domains over orientations of their **L** vectors (23) contains two terms. The first is due to ε_r and pertains to the irreversible component of the rearrangement of the multidomain state, while the second is due to the reversible component. The MS of the crystal as a whole can be written as the sum

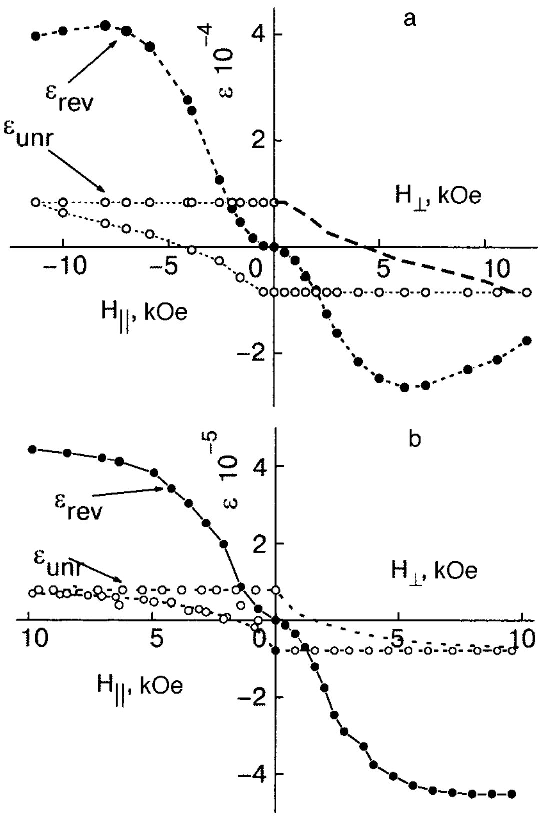

FIG. 9. Field dependence of the reversible ε_{rev} and irreversible ε_{unr} components of the magnetostriction of $CoCl_2$ (a) and $NiCl_2$ (b).

$$\varepsilon(H)=\varepsilon_{\text{rev}}(H)+\varepsilon_{\text{unr}}(H), \tag{25}$$

where $\varepsilon_{\text{rev}}(H)$ is the reversible contribution to the resultant striction, and $\varepsilon_{\text{unr}}(H)$ is the irreversible component; both components depend on the magnetic field and the stage of its imposition-removal cycle, although, starting at a certain value of the applied field, $\varepsilon_{\text{unr}}(H)$ should apparently cease to depend on it. We assume that in the removal of the field the irreversible part of the MS in the whole field interval in which the AFM state exists, remains constant and equal to the remanent MS: $\varepsilon_{\text{unr}}(H)=\varepsilon_r=\text{const}$.

The $\varepsilon_{\text{rev}}(H)$ and $\varepsilon_{\text{unr}}(H)$ curves obtained for $CoCl_2$ and $NiCl_2$ on the basis of these ideas from the experimental data (Fig. 1) are shown in Fig. 9. The reversible component does not have hysteresis in the cycles of imposition and removal of the crossed magnetic fields. For $CoCl_2$ the $\varepsilon_{\text{rev}}(H)$ curve becomes more non-antisymmetric in comparison with the curves obtained directly from experiment, whereas for $NiCl_2$ the $\varepsilon_{\text{rev}}(H)$ curve remains antisymmetric. The irreversible component $\varepsilon_{\text{unr}}(H)$ is hysteretic for both crystals. The closed part of the loop for $\varepsilon_{\text{unr}}(H)$ in Fig. 9 (in the first quadrant) was constructed on the basis of the properties of antisymmetry of the MS at low fields, since the data for that part is missing in Fig. 1.

We approach the magnetization in an analogous way, writing it as the sum

$$m(H)=m_{\text{rev}}(H)+m_{\text{unr}}(H), \tag{26}$$

where $m_{\text{rev}}(H)$ and $m_{\text{unr}}(H)$ are the reversible and irreversible contributions to the resonant magnetization, respectively. We define the irreversible fraction of the MS as the ratio $\delta_{\text{unr}}^{MS}=\varepsilon_r/\varepsilon^{(S)}$. For our NiCl_2 samples $\delta_{\text{unr}}^{(S)}=0.16$. We shall assume that an equal fraction of the sample volume consists of domains that contribute to the irreversible MS. This fraction of the domains during the removal or the repeated imposition of the field in the same direction will be magnetized with the susceptibility χ_e of the uniform state (with $\mathbf{L}\perp\mathbf{H}$). Comparing the experimental value of the magnetic susceptibility χ_d of the multidomain state for $H\to 0$ and its expected value $\chi_e/2$, we find the fraction of the irreversible contribution to the magnetization, $\delta_{\text{unr}}^{m}=2\chi_d/\chi_{\text{e}}-1$. The value obtained for NiCl_2, $\delta_{\text{unr}}^{m}\approx 0.14$ turned out to be close to δ_{unr}^{MS}.

Let us determine the field dependence of the reversible contribution to the magnetization of NiCl_2. The relative volume of domains that contribution to it is $\varepsilon_{\text{rev}}=1-\delta_{\text{unr}}$. A plot of $m_{\text{rev}}(H)$ for NiCl_2 is given in Fig. 7 (m_{rev} was calculated per unit mass of the sample). The magnetic susceptibility of this part of the domains for $H\to 0$ is $\chi_e/2$. The value of H_m determined from $m_{\text{rev}}(H)$ better satisfies the condition $H_d=H_m$.

The increase of the volume of domains with the favorable orientation in magnetic field and the decrease of the volume of the other domains should be regarded first as the result of the motion of the domain wall in the field. The motion occurs on account of the stresses acting on the walls on account of the magnetic field.[19] In equilibrium the pressure exerted on the walls by the field will be compensated by "reaction forces," which ensure equilibrium of the multidomain structure at $H\neq 0$. If a defect lies in the path of the wall, then the wall will bend, and surface forces arise which will prevent further displacement of the wall. The parameters of those, essentially quasi-elastic forces are determined by the characteristics of the elastic interaction of the wall and defects. For each value of the field there exists a certain balance of the volumes of domains with different directions of **L**. If defects are responsible for the multidomain character, then equilibrium in a field corresponds to the appearance of certain elastic stresses in the crystal due to the mismatch of the elastic fields of the defects and the elastic fields of MS strains in the domains.

The irreversible part of the rearrangement of the domains is most likely due to the part of the domains where the orientation **L** is not maintained by counterbalancing quasi-elastic forces. To distinguish the reversible and irreversible components of the rearrangement of the multidomain state, we write the distribution function of the domains in the form of a sum,

$$p(\varphi)=(1-\delta)p_{\text{rev}}(\varphi)+\delta p_{\text{unr}}(\varphi), \tag{27}$$

where δ is the fraction of the volume occupied by domains whose magnetic moment **M** is oriented along the magnetic field and do not cause "reaction forces."

An expression for the distribution function of the domains over the angle φ was obtained in Ref. 19:

$$p_{\text{rev}}(\varphi)=\frac{1}{I(H/H_0)}\exp\left(\frac{H^2}{2H_0^2}\cos^2\varphi\right), \tag{28}$$

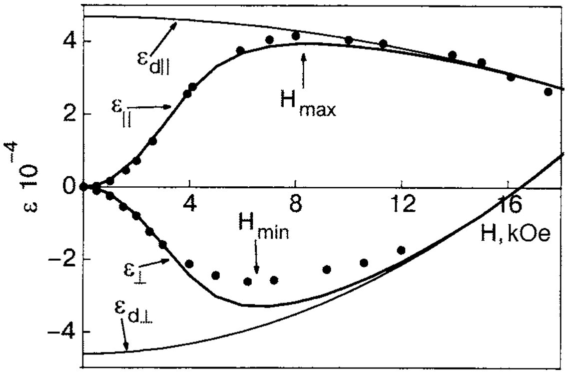

FIG. 10. Field dependence of the model magnetostriction of the uniform $\varepsilon_{d\parallel,\perp}$ and multidomain $\varepsilon_{\parallel,\perp}$ states of CoCl_2. The light solid curves show the dependence of $\varepsilon_{d\parallel,\perp}$, the heavy solid curves $\varepsilon_{\parallel,\perp}$, and the points are experimental.

where

$$H_0=H_d/(2\sqrt{2}) \text{ and}$$

$$I(H/H_0)=\int_{-\pi/2}^{\pi/2}\exp\left(\frac{H^2}{2H_0^2}\cos^2\varphi\right)d\varphi.$$

We see that expression (28) leads to a δ-function-like concentration of the distribution function around $\varphi=0$ as the field increases for $H>H_d$.

C. Rearrangement of the reversible component of the multidomain state

Expression (28) for the density of the distribution function enables one to obtain the field dependence of the reversible part of the relative elongation of the crystal during the imposition of a field over the whose interval of fields of transition of the multidomain state to the uniform state. The field dependence of the reversible MS of the multidomain state in the approximation of an ideal multidomain state ($\varepsilon_{\text{unr}}=0$) will be described by the expression

$$\frac{\varepsilon_{\parallel}(H)}{\varepsilon^{(S)}}=\frac{1}{I(H/H_0)}\int_{-\pi/2}^{\pi/2}\left[\left(1-2(1+\eta_{\parallel})\frac{H^2\cos^2\varphi}{H_{ff}^2}\right)\right.$$
$$\times\cos^2\varphi-\left.\left(1-2(1+\eta_{\perp})\frac{H^2\cos^2\varphi}{H_{ff}^2}\right)\sin^2\varphi\right]$$
$$\times\exp\left(\frac{H^2}{H_0^2}\cos^2\varphi\right)d\varphi. \tag{29}$$

An analogous expression can be written down for the MS perpendicular to the applied field.

For $H/H_0<1$ Eq. (29) gives a quadratic field dependence of the MS, similar to (3).

Figure 10 shows a comparison of the experimental $\varepsilon_{\parallel\,\text{rev}}(H)$ and $\varepsilon_{\perp\,\text{rev}}(H)$ curves for CoCl_2 with the curves $\varepsilon_{\parallel}(H)$ calculated according to formula (29) and $\varepsilon_{\perp}(H)$ calculated by an analogous formula. The parameters $\varepsilon^{(S)}$, H_{ff}, and $\eta_{\parallel}$ were taken from the MS data for the uniform state, H_d from the data for the reversible component of the MS, and the parameter $\eta_{\perp}$ was chosen so as to satisfy the observed degree of non-antisymmetry of the field dependences of the longitudinal and transverse MS in CoCl_2. The thin curves in Fig. 10 show the field dependence of the MS for

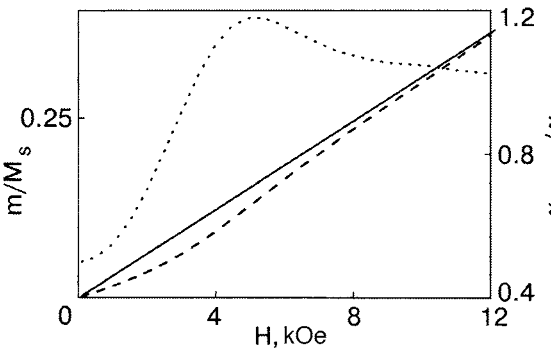

FIG. 11. Model curves of the magnetization, normalized to its limiting value, and magnetic susceptibility, normalized to its value in the uniform state, as functions of the field in the multidomain state.

the uniform state, calculated for the same parameters according to Eq. (8). The calculated curve for the longitudinal MS is in good agreement with the experimental data over the entire range of fields causing rearrangement of the multidomain state. There is some disagreement with experiment for the calculated curve of the transverse MS, but it does not exceed the error of measurement.

Let us use Eq. (28) to calculate the dependence of the magnetization of the crystal as a whole in a magnetic field lying in the EP. If the irreversible component of the rearrangement of the multidomain state is neglected ($\delta=0$), the expression for the magnetization takes the form

$$\frac{m(H)}{M_s}=\frac{1}{I(H/H_0)}\frac{H}{H_{ff}}\int_{-\pi/2}^{\pi/2}\cos^2\varphi\exp\left(\frac{H^2}{2H_0^2}\cos^2\varphi\right)d\varphi, \tag{30}$$

where M_s is the magnetization of the uniform state of the crystal for $H=H_{ff}$.

In Fig. 11 the dashed curve shows $m(H)/M_s$ calculated according to Eq. (30) for the same parameters of the distribution function as were used in the MS calculation. The solid straight line shows $m(H)/M_s$ for a uniform state with $\mathbf{L}\perp\mathbf{H}$. The calculated curve for the multidomain state has a characteristic sag below the dependence for the uniform state and agrees with the experimental data[17] on $m(H)$ for NiCl$_2$ (see Fig. 7).

Differentiation of Eq. (30) with respect to H gives the calculated magnetic susceptibility $\chi_{\text{calc}}(H)$. The dotted curve in Fig. 11 shows a plot of $\chi_{\text{calc}}(H)/\chi_e$. For $H<H_d$ it is proportional to H^2, it has a maximum for $H\sim H_d$, and with further increase in field it tends toward the value for the uniform state χ_e. The maximum on $\chi(H)$ is due to the rapid change of $p(\varphi)$ near $H\approx H_d$. Figure 12 shows the experimentally obtained curve of the magnetic susceptibility for NiCl$_2$.[45]

D. Magnetoelastic mechanisms for the influence of defects on the formation of AFM domains

In the treatment above we assumed an equiprobable distribution function for directions of the **L** vector of the AFM domains at $H=0$. To present a picture of the mutual arrangement of domains, domain walls, and defects for such a distribution is rather difficult. To fill a plane with domains having boundaries with matched MS strains is impossible. At points where more than two domains come together, elastic stresses will arise. However, if those places coincide with the locations of defects of the crystal structure that create a stress of the opposite sign around them, then the additional elastic energy due to these stresses will be lessened, and the system of AFM domains can turn out to be energetically favorable. Let us demonstrate such a situation for the hypothetical example of a distribution of magnetoelastic domains with several equivalent "easiest" directions of the **L** vectors in the EP.

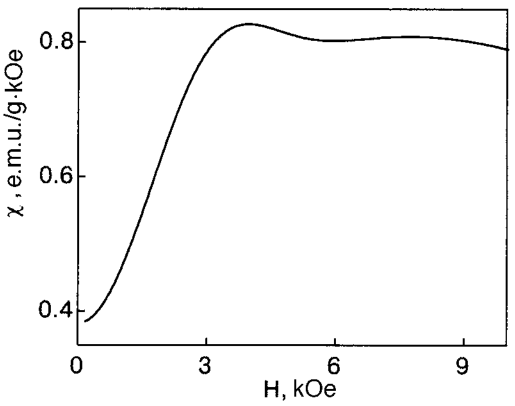

FIG. 12. Dependence of the magnetic susceptibility of NiCl$_2$ on field during its removal in the region in other words rearrangement of the multidomain structure.

Such a structure was considered in Ref. 15 for the case of an equilibrium distribution of domains with **L** vectors lying at an angle of 120° (60°) and is illustrated in Fig. 13. The easy plane of the crystal is represented by a set of hexagons. Their boundaries are shown by solid lines. The spontaneous MS of the hexagons leads, for example, as in the figure, to elongation of the hexagons along their diagonal that is parallel to **L**. An exception is the region where three domains come together, where the uncompensated (for the example shown, tensile) mechanical stresses cannot be eliminated. These regions are formed where domains belonging to different "triads" come together (one such triad is shaded in Fig. 13). As a result of the strain the hexagons become biaxial, with C_3 symmetry of the local extension at those sites.

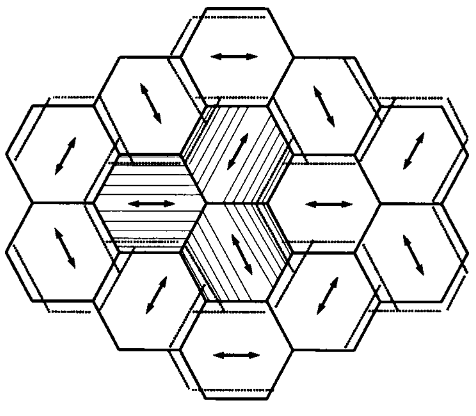

FIG. 13. Hypothetical structure of magnetoelastic domains in an easy plane AFM. The two-headed arrows show the directions of the sublattice magnetizations in the domains. The solid lines show the boundaries of the domains prior to the spontaneous striction, and the dotted lines after. The shaded triad of domains is an element forming the domain walls of the crystal transition.

In the ideal crystal such domain structure in the form of a set of deformed hexagons leaves the domains partially stressed. The presence of the triangles of extension at the points where three domains come together means that the strain does not conserve the volume of the domains. However, the estimates made in Ref. 15 show that the cost in magnetoelastic energy for these nonuniform strains of the hexagons is only a few percent of the magnetoelastic energy of the uniform state. Therefore, the structure illustrated in Fig. 13 can be regarded as a rather good approximation of the ME domains with the minimal elastic stresses and with the minimal cost in elastic energy.

If tensile point defects are placed at junctions of three domains, then the matching of the strains generated by the defects and the ME strains of the domains will lead to partial or complete compensation of the stresses created by these sources. The volume of the region of the crystal deformed by the defect and the energy cost associated with the defect decrease. Point defects that appear during growth increase the elastic energy of a crystal. Superposition of the location of the defects with the junctions of three domains decreases this contribution to the energy, i.e., it makes the multidomain state preferable. Analogous elastic matching can be achieved if the junction of three domains is threaded by disclinations perpendicular to the EP.[46] We emphasize that in both the case of point defects and the case of disclinations the stress that these defects exert on the domain walls is independent of temperature, which account for the observed temperature-importance of the parameter H_d in CoCl_2.

The geometry structure of the domains illustrated in Fig. 13 presupposes the presence of defects isotropically extending the crystal in the EP. In that case the defect does not specify the directions for the **L** vectors in the domains but preserves the orientational degeneracy in the EP. If the spontaneous MS of the domains is opposite in sign, then a region of compression will form at the junctions of three domains. For stabilizing such a structure one needs defects of another type, e.g., vacancies.

The ‘‘triad’’ model has a different distribution function of the domains over orientations of **L** than that considered in Sec. 5.1. Nevertheless, all of the qualitative features of the behavior of the induced MS and magnetization of the crystal in the region of rearrangement of the multidomain state will be present in this model also, although the details will be somewhat different.

The mechanism of surrounding defects by triads of domains does not take into account the actual interaction of the defects, which can promote equilibrium of the multidomain state.

Let us consider the interaction of the defects[19] in the simplest case of a planar isotropic medium, when the energy of interaction between the neighboring defects (numbered i and j) depend only on the distance between them, $e = e(r_{ij})$. Suppose that during the equilibrium of the uniform AFM order a uniform spontaneous anisotropic MS occurs which is is positive and equal to $\varepsilon^{(S)}$ along the x axis and negative, and with the same magnitude, along the y axis, $-\varepsilon^{(S)}$ (both lie in the EP). The total energy of interaction between defects in this case will be

$$E=\sum_{ij} e(r_{ij})=\sum_{ij} e(r_{0ij})+\sum_{ij}\left\{\frac{\partial e}{\partial(x_i-x_j)}(x_{0i}-x_{0j})-\frac{\partial e}{\partial(y_i-y_j)}(y_{0i}-y_{0j})\right\}\varepsilon^{(S)}+\frac{1}{2}\sum_{ij}\left\{\frac{\partial^2 e}{\partial(x_i-x_j)^2}(x_{0i}-x_{0j})^2-2\frac{\partial^2 e}{\partial(x_i-x_j)\partial(y_i-y_j)}(x_{0i}-x_{0j})(y_{0i}-y_{0j})+\frac{\partial^2 e}{\partial(y_i-y_j)^2}(y_{0i}-y_{0j})^2\right\}(\varepsilon^{(S)})^2. \tag{31}$$

The first sum in (31) is equal to the interaction energy E_0 between defects prior to the spontaneous anisotropic MS. In the approximation that the anisotropic strain is independent of the local positions of the defects, the second sum in (31) should be equal to zero. The expression multiplying the square of $\varepsilon^{(S)}$ in the third sum will be denoted by k. The interaction energy between defects after the anisotropic MS takes the form

$$E=E_0+k(\varepsilon^{(S)})^2. \tag{32}$$

If we consider growth defects, which can be assumed almost equilibrium, then the energy of interaction between them will satisfy a minimum principle. In that case $k>0$, and the uniform spontaneous anisotropic MS, which is advantageous for a defectless crystal, increases the interaction energy of the defects. That is, the dependence of the interaction energy of the defects on the magnetostrictive displacements crates a quasi-elastic restoring force.

Since defects cannot move through the crystal, it follows from (32) that they will prevent the formation of the single-domain state of an AFM with anisotropic MS. The crystal will break up into regions with uniform, but differently directed, MS in them. Thus the two mechanisms for the ME interaction of defects and domains promote the equilibrium of the multidomain AFM state.

VI. CONCLUSION

Analysis of the data on the induced MS and magnetization of multidomain AFM state in layered easy-plane AFMs of the ion dihalide group shows that the system of AFM domains in them is due to the ME interactions of spontaneously strained domains and the elastic fields of defects. In the multidomain state the spontaneous MS of the crystal as a whole is close to zero in the absence of magnetic field, while the domains retain their spontaneous MS. The spontaneous lowering of the symmetry upon the establishment of AFM order in the presence of many-fold degeneracy for spatial orientation of the antiferromagnetic vector comes about in the given case through the formation of a nonuniform multidomain state. This multidomain state is reversible in the imposition and removal of magnetic field, i.e., it is a state of thermodynamic equilibrium.

It is known that the spontaneous lowering of the symmetry in an AFM occurs because the uniform anisotropic MS lowers the magnetic energy of the crystal linearly as a function of the magnitude of the strictive strains. In that case the elastic energy of the crystal increases quadratically in those strains. As a result, the total energy of the crystal reaches a minimum at some equilibrium spontaneous MS. In real crystals the elastic energy is supplemented by the interaction between the elastic fields of defects separated by distances much greater than the lattice parameter. Therefore the cost in elastic energy upon spontaneous MS may be lessened if the MS strains are not uniform but matched with the elastic fields of the defects. This may turn out to be sufficient to compensate the cost in exchange energy in the domain walls. In other words, the formation of a multidomain magnetoelastic state in a crystal containing defects is a consequence of the presence of long-range elastic forces due to the defects. This leads to a nonuniform elastically strained state of the crystal, which entails inhomogeneity of the magnetic state. It is that nonuniform state that gives a minimum of the total energy of the crystal upon spontaneous MS. We note that this should be the case not only in easy-plane AFMs but also in ferromagnets with spontaneous magnetostriction. In the latter, however, the formation of the method state is stimulated primarily by the magnetostatic forces, while the contribution due to defects and magnetoelasticity turns out to be secondary or, at least, masked.

[*] E-mail: lozenko@iop.kiev.ua

---

[1] J. W. Leech and A. J. Manuel, Proc. Phys. Soc. London, Sect. B **69**, 210 (1956).

[2] H. Yoshizawa, K. Ubukoshi, and K. Hirakawa, J. Phys. Soc. Jpn. **48**, 42 (1980).

[3] M. K. Wilkinson, J. W. Cable, E. O. Wollan, and W. C. Koehler, Phys. Rev. **113**, 497 (1959).

[4] M. O. Kostryukova and L. M. Kashirskaya, JETP Lett. **9**, 238 (1969).

[5] A. S. Borovik-Romanov, "Antiferromagnetism," in *Progress in Science* [in Russian], Izd-vo AN SSSR, Moscow (1962).

[6] A. F. Lozenko and S. M. Ryabchenko, Zh. Éksp. Teor. Fiz. **65**, 1085 (1973) [Sov. Phys. JETP **38**, 538 (1974)].

[7] K. Katsumata and K. Yamasaka, J. Phys. Soc. Jpn. **34**, 346 (1973).

[8] J. Magarino, J. Tuchendler, A. R. Fert, and J. Gelard, Solid State Commun. **23**, 175 (1977).

[9] A. S. Borovik-Romanov and E. G. Rudashevskiĭ, Zh. Éksp. Teor. Fiz. **47**, 2095 (1964) [Sov. Phys. JETP **20**, 1407 (1965)].

[10] E. A. Turov and V. G. Shavrov, Fiz. Tverd. Tela (Leningrad) **7**, 217 (1965) [Sov. Phys. Solid State **7**, 166 (1965)].

[11] A. F. Lozenko, P. E. Parkhomchuk, S. M. Ryabchenko, and P. A. Trotsenko, Fiz. Nizk. Temp. **14**, 941 (1988) [Sov. J. Low Temp. Phys. **14**, 517 (1988)].

[12] A. K. Zvezdin, V. M. Matveev, A. A. Mukhin, and A. I. Popov, *Rare-Earth Ions in Magnetically Ordered Crystsals* [in Russian], Nauka, Moscow (1985).

[13] D. Billerey, C. Terrier, A. J. Pointon, and J. P. Redoules, J. Magn. Magn. Mater. **21**, 187 (1980).

[14] V. M. Kalita, A. F. Lozenko, S. M. Ryabchenko, and P. A. Trotsenko, Ukr. Fiz. Zh. (Russ. Ed.) **43**, 1469 (1998).

[15] V. M. Kalita and A. F. Lozenko, Fiz. Nizk. Temp. **27**, 489 (2001) [Low Temp. Phys. **27**, 358 (2001)].

[16] V. M. Kalita and A. F. Lozenko, Fiz. Nizk. Temp. **27**, 872 (2001) [Low Temp. Phys. **27**, 645 (2001)].

[17] V. M. Kalita, A. F. Lozenko, and P. A. Trotsenko, Fiz. Nizk. Temp. **28**, 378 (2002) [Low Temp. Phys. **28**, 263 (2002)].

[18] V. M. Kalita, A. F. Lozenko, S. M. Ryabchenko, P. A. Trotsenko, and T. M. Yatkevich, Fiz. Tverd. Tela (St. Petersburg) **46**, 317 (2004) [Phys. Solid State **46**, 326 (2004)].

[19] V. M. Kalita, A. F. Lozenko, S. M. Ryabchenko, and P. A. Trotsenko, Zh. Éksp. Teor. Fiz. **126**, 1209 (2004) [JETP **99**, 1054 (2004)].

[20] E. V. Gomonaj and V. M. Loktev, Fiz. Nizk. Temp. **25**, 699 (1999) [Low Temp. Phys. **25**, 529 (1999)].

[21] H. Gomonay and V. Loktev, J. Phys. C **14**, 3959 (2002).

[22] M. M. Farztdinov, *Physics of Magnetic Domain in Antiferromagnets and Ferrites* [in Russian], Nauka, Moscow (1981).

[23] A. Hubert, *Theorie der Domanenwande in Geordneten Medien*, Springer-Verlag, Berlin (1974), Mir, Moscow (1977).

[24] V. G. Bar'yakhtar, A. E. Borovik, and V. A. Popov, Zh. Éksp. Teor. Fiz. **62**, 2233 (1972) [Sov. Phys. JETP **35**, 1844 (1972)].

[25] A. N. Bogdanov and I. E. Dragunov, Fiz. Nizk. Temp. **24**, 1136 (1998) [Low Temp. Phys. **24**, 852 (1998)].

[26] S. V. Vonsovskiĭ, *Magnetism*, Vols. 1 and 2, Wiley, New York (1974), Nauka, Moscow (1971).

[27] V. G. Bar'yakhtar, A. N. Bogdanov, and D. A. Yablonskiĭ, Usp. Fiz. Nauk **156**, 47 (1988).

[28] L. Neel, Ann. Phys. **3**, 137 (1948).

[29] V. G. Bar'yakhtar, A. E. Borovik, and V. A. Popov, Zh. Éksp. Teor. Fiz. **9**, 634 (1969)].

[30] Y. Y. Li, Phys. Rev. **101**, 1450 (1956).

[31] V. V. Eremenko, N. F. Kharchenko, and L. I. Beliy, J. Appl. Phys. **50**, 7751 (1979).

[32] N. F. Kharchenko and A. V. Belyĭ, Izv. AN SSSR, ser. fiz. **446**, 1451 (1980).

[33] I. E. Dzyaloshinskiĭ, JETP Lett. **25**, 414 (1977).

[34] A. S. Kovalev and A. M. Kosevich, Fiz. Nizk. Temp. **3**, 259 (1977) [Sov. J. Low Temp. Phys. **3**, 125 (1977)].

[35] I. M. Lifshitz, Zh. Éksp. Teor. Fiz. **42**, 1354 (1962) [Sov. Phys. JETP **15**, 939 (1962)].

[36] Z. A. Kazeĭ, M. V. Levanidov, and V. I. Sokolov, Prib. Tekh. Éksp., No. 1, 196 (1982).

[37] V. M. Kalita, A. F. Lozenko, and S. M. Ryabchenko, Fiz. Nizk. Temp. **26**, 671 (2000) [Low Temp. Phys. **26**, 489 (2000)].

[38] J. Gunzbourg, S. Papassimacopoulos, A. Mieden-Gros, and A. Allain, J. Phys. C **32**, 125 (1971).

[39] D. Billerey, C. Terrier, A. J. Pointon, and J. P. Redoules, J. Magn. Magn. Mater. **21**, 187 (1980).

[40] L. Neel' (L. Neél), Izvestiya AN SSSR Ser. Fiz. **21**, 890 (1957).

[41] M. E. Lines, Phys. Rev. **131**, 546 (1963).

[42] V. M. Kalita and A. F. Lozenko, Fiz. Nizk. Temp. **28**, 91 (2002) [Low Temp. Phys. **28**, 66 (2002)].

[43] W. J. De Haas, B. H. Schultz, and J. Koolhaas, Physica **7**, 57 (1940).

[44] C. Starr, F. Bitter, and A. R. Kaufmann, Phys. Rev. **58**, 977 (1940).

[45] V. M. Kalita, A. F. Lozenko, P. A. Trotsenko, and T. M. Yatkevich, Fiz. Nizk. Temp. **30**, 38 (2004) [Low Temp. Phys. **30**, 27 (2004)].

[46] A. M. Kosevich, *Theory of Crystal Lattice*, Wiley, New York (1999), Vishcha Shkola, Kharkov (1987).

Translated by Steve Torstveit

LOW TEMPERATURE PHYSICS VOLUME 31, NUMBERS 8–9 AUGUST–SEPTEMBER 2005

Investigation of the anomalies of the magnetoelectric and magnetoelastic properties of single crystals of the ferroborate $GdFe_3(BO_3)_4$ at phase transitions

A. M. Kadomtseva, Yu. F. Popov,* S. S. Krotov, G. P. Vorob'ev, and E. A. Popova

M. V. Lomonosov Moscow State University, Vorob'evy gory, Moscow 119992, Russia

A. K. Zvezdin

Institute of General Physics, Russian Academy of Sciences, Moscow 119991, Russia

L. N. Bezmaternykh

L. V. Kirensky Institute of General Physics, Siberian Branch of the Russian Academy of Sciences,
Krasnoyarsk 660036, Russia

(Submitted January 21, 2005)
Fiz. Nizk. Temp. **31**, 1059–1067 (August–September 2005)

The transformation of various properties of gadolinium ferroborate single crystals at phase transitions, both spontaneous and induced by magnetic fields up to 200 kOe, is investigated theoretically and experimentally. Particular attention is paid to elucidating the role of magnetoelectric interactions and the change in them at spin-reorientation transitions accompanied by a change of magnetic symmetry. With that goal the magnetoelastic and magnetoelectric properties of the system are investigated over a wide range of temperatures for two orientations of the magnetic field, $H\|c$ and $H\perp c$, and a fundamental difference of the character of the field dependences of the magnetostriction and electric polarization is found. In the framework of a symmetry approach a description of the magnetic structures and their transformations in the system $GdFe_3(BO_3)_4$ is proposed, and an interpretation of the experimentally observed properties is given. © *2005 American Institute of Physics.* [DOI: 10.1063/1.2008142]

INTRODUCTION

Rare-earth ferroborates $RFe_3(BO_3)_4$, isostructural to the natural mineral huntite, have a rhombohedral structure and belong to the hexagonal space group $R32$ (D_3^7).

These compounds have attracted particular interest in recent years in connection with the prospects for their practical use, particularly in laser technique[1,2] and for optical second-harmonic generation,[3] and also because of the discovery of unusual magnetic properties and diverse phase transitions in them.[4–6] According to measurements of the temperature dependence of the magnetic susceptibility[7] and heat capacity,[8] three phase transitions are observed in gadolinium ferroborate: a structural phase transition at $T_C=156$ K, a magnetic ordering of the Fe^{3+} ions at $T_N=38$ K, and a spin-reorientation phase transition at $T_R=10$ K.[7] The existing data in the literature nevertheless do not permit one to reach definite conclusions as to the nature of the phase transitions observed in these compounds.

In regard to the magnetic structure of gadolinium ferroborate the data in the literature are contradictory. In Ref. 9 it was stated on the basis of a study of antiferromagnetic (AFM) resonance that the magnetic phase transition of the Fe^{3+} ion subsystem at T_N corresponds to two-sublattice spin ordering of the easy-plane type, and, as the temperature is lowered below T_R, the interaction of the iron and gadolinium subsystems brings about a reorientation of the Fe^{3+} spins from easy-plane to easy-axis (the c axis). The magnetic unit cell of the system is doubled along the c axis in comparison with the crystalline unit cell in hexagonal coordinates.

In Ref. 7 the magnetic behavior of gadolinium ferroborate was investigated in the framework of three-sublattice ordering (of the triangular type) of the iron subsystem. The spins of the Fe^{3+} ions in the temperature interval $10\ \mathrm{K}<T<38$ K were found to lie in the "easy plane" at an angle of 120° to one another. Below 10 K, according to Ref. 7, under the influence of an interaction with the gadolinium subsystem, the Fe^{3+} spins are reoriented from the easy plane in the direction toward the c axis, forming a cone with axis along c. Since nothing was said about any change in the unit call at the magnetic phase transition, and the system remained antiferromagnetic over the whole temperature interval, the opening angle of the cone (the tilt angle of the Fe^{3+} spins toward the c axis for compensation of the magnetization of the gadolinium subsystem) should "follow" the increase of the magnetic moment of the Ge^{3+} ions with decreasing temperature. For an orientation of the external magnetic field $H\|c$ at $T<10$ K a field-induced reorientation of the Fe^{3+} spins from the c axis to the easy plane was observed.[5,7]

We carried out additional experimental and theoretical investigations of the transformation of various properties of gadolinium ferroborate single crystals at the spontaneous and field-induced phase transitions at high magnetic fields up to 200 kOe. Particular attention was paid to investigation of the role of magnetoelectric interactions and their changes at the spin-reorientation transitions. An interpretation of the antiferromagnetic properties of the system was given in the framework of a thermodynamic approach. Studies of the magnetoelastic and magnetoelectric properties of the system for two

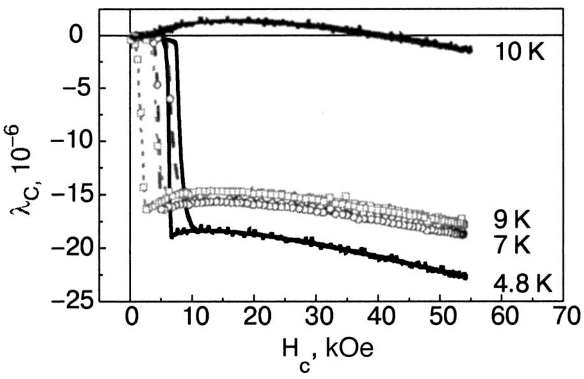

FIG. 1. Isotherms of the dependence of the longitudinal magnetostriction of the $GdFe_3(BO_3)_4$ single crystal for $H\|c$.

orientations of the magnetic field: $H\|c$ and $H\perp c$ (for which at present there is absolutely no information in the literature). We expected that gadolinium ferroborate, which has a noncentrosymmetric space group, would exhibit substantial manifestations of the magnetoelectric interactions and their change at the spin-reorientation transitions, which are accompanied by a change of magnetic symmetry.

EXPERIMENTAL RESULTS

We studied the electric polarization P_i and magnetostriction λ_i as functions of magnetic field up to 200 kOe in the temperature interval 4.2–50 K for $H\|c$ and $H\perp c$ by the technique described in Ref. 10, and also the temperature dependence of the thermal expansion of $GdFe_3(BO_3)_4$.

Figure 1 shows isotherms of the dependence of the longitudinal magnetostriction of the gadolinium ferroborate single crystal at $H\|c$. It is seen that in the low-temperature region $T<10$ K at a certain critical value of magnetic field $H=H^{\text{crit}}(H\|c)$ there are jumps in the magnetostriction, where, according to Refs. 7 and 9, a magnetic-field-induced spin reorientation from the c axis toward the easy plane was observed. At high temperatures $10<T<T_N=38$ K the magnetostriction does not exhibit anomalies and depends quadratically on the field. The threshold fields H^{crit} at which the magnetostriction jumps appear decrease with increasing temperature and agree with the fields at which the magnetization jumps were observed at the field-induced reorientation of the spins from the c axis to the easy plane.[7]

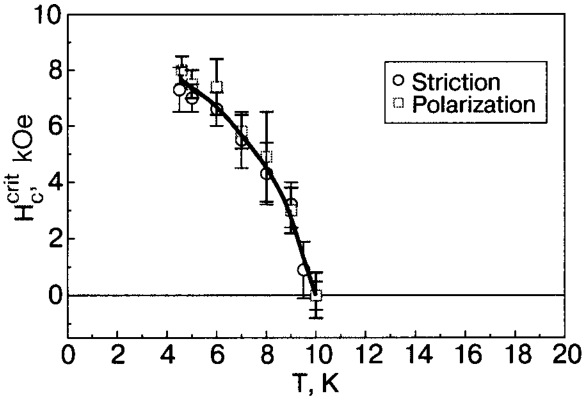

FIG. 3. H-T phase diagram obtained for $GdFe_3(BO_3)_4$ from measurements of the longitudinal magnetostriction and electric polarization for $H\|c$.

Our studies of the magnetoelectric properties of $GdFe_3(BO_3)_4$ single crystals have shown that in the course of the spin-reorientation transition at $T<10$ K for a field orientation $H\|c$ there are also jumps of the electric polarization (Fig. 2), evidently due to the change of the magnetoelectric interactions as a result of the change of magnetic symmetry. The spin-reorientation transition induced by a magnetic field $H\|c$ is accompanied by hysteresis with respect to the the field, which indicates that the transition is a first-order phase transition. Figure 3 shows the H-T phase diagrams obtained from measurements of the magnetoelectric and magnetoelastic properties for $H\|c$, which demonstrated good agreement with the values of the threshold fields. The character of the field dependence of the magnetostriction and electric polarization differs strongly for $H\|c$ and $H\perp c$. Figure 4 shows the dependence of the longitudinal magnetostriction for $H\|a$. It is seen that at $T\sim5$ K the magnetostriction initially depends weakly on field, and then, at $H^{\text{crit}}\sim37$ K, it increases in a jump to 1×10^{-5}. With increasing temperature the threshold field decreases monotonically. Starting at temperatures $T\sim10$ K and on up to 38 K the magnetostriction increases in a sharp jump even in weak magnetic fields ~2 kOe and then behaves monotonically. The magnetic-field dependence of the electric polarization is of an analogous character (Fig. 5), and the threshold fields agree with each other, as is seen on the H-T phase diagrams (Fig. 6) constructed from the data of the $\lambda(H)$ and $P(H)$ measurements. Thus for $H\|c$ and $H\perp c$ a strict correlation of

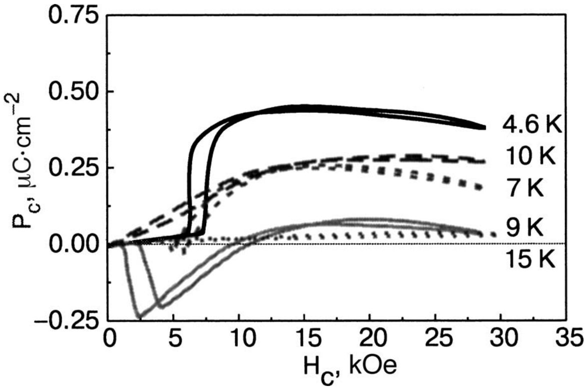

FIG. 2. Isotherms of the longitudinal electric polarization in a gadolinium ferroborate single crystal for $H\|c$.

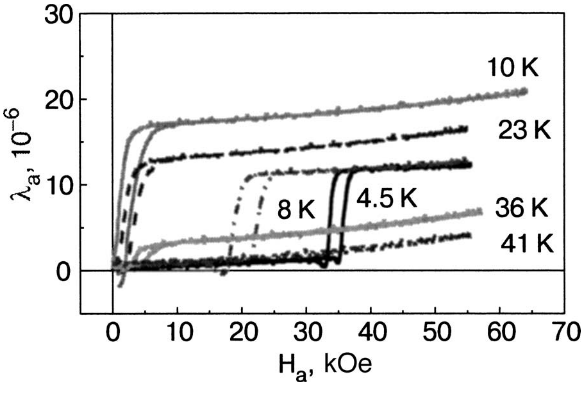

FIG. 4. Isotherms of the longitudinal magnetostriction for a $GdFe_3(BO_3)_4$ single crystal at $H\|a$.

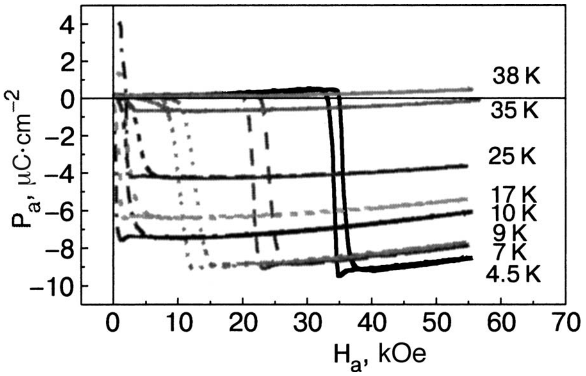

FIG. 5. Curves of the dependence of the electric polarization on magnetic field $H \| a$ for a $GdFe_3(BO_3)_4$ single crystal at various temperatures.

the magnetoelectric and magnetoelastic properties is established. It should be noted that in measurements of the temperature dependence of the thermal expansion we observed a sharp λ-shaped anomaly at a temperature of 156 K (Fig. 7). Recent measurements[11] have shown that at $T=156$ K there is also a jumplike change of the dielectric constant, which apparently indicates the onset of spontaneous electric ordering at that temperature.

THEORETICAL PART

In view of what we have said above, it is best to take a symmetry approach to the theoretical description of the properties of the $GdFe_3(BO_3)_4$ system. On the one hand, it allows one to explain the behavior of that system in a unified way and to identify the active and passive degrees of freedom responsible for the change of its magnetic and crystalline symmetry, the corresponding order parameters, and the interactions of the latter both among themselves (leading to phenomena such as weak ferromagnetism, intrinsic magnetoelectric effect, etc.) and with external fields. At the same time, it is exceptionally efficient for predicting new effects (according to the "possible-impossible" principle from considerations of whether the space-time symmetry in the behavior of a particular system is broken or preserved).

The group-theoretical approach used here (in the spirit of the Landau theory of phase transitions) permits one to describe in an exhaustive way all the possible types of magnetic structures that, depending on the concrete form of the exchange interactions (and also the features of the anisotropic interactions) can appear in the ferroborate $GdFe_3(BO_3)_4$ below the magnetic ordering temperature. We begin with a discussion of the features of the magnetic phase transition at the temperature T_N (at which the moments of the Fe^{3+} ions order). We recall that the unit cell of $RFe_3(BO_3)_4$ in the rhombohedral scheme contains one R^{3+} ion (position $1a$) and three Fe^{3+} ions (position $3d$). If the space diagonal of the elementary rhombohedron is assumed to be directed vertically, then the crystal structure of the $RFe_3(BO_3)_4$ system will be a set of rhombohedrally shifted identical horizontal layers (oblique with respect to the vertical but parallel to each other) alternating along the vertical. The distance between two adjacent equivalent layers is one-third of the vertical period c of the structure, which is the height of the unit cell of $RFe_3(BO_3)_4$ in the hexagonal crystallographic coordinates (Fig. 8). But then the hexagonal unit cell of the $RFe_3(BO_3)_4$ system (which is doubly body-centered and tripled in volume as compared to the rhombohedral cell) contains three formula units $(Z=3)$, or, in other words, three translationally equivalent R^{3+} ions (position $3a$) and, accordingly, nine Fe^{3+} ions (position $9d$). Since the rhombohedral (truly primitive) crystal cell of $GdFe_3(BO_3)_4$ contains

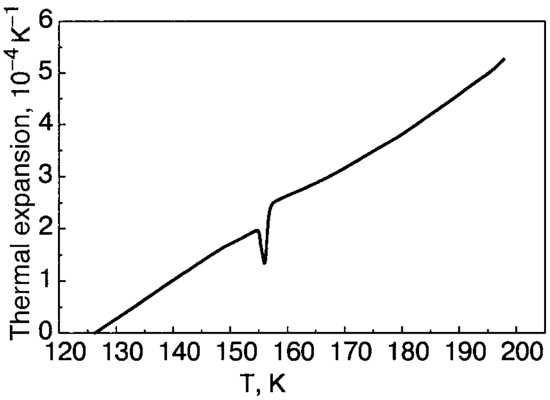

FIG. 7. Dependence of the thermal expansion for a $GdFe_3(BO_3)_4$ single crystal along the c axis in the region of the structural transition $T_C = 156$ K.

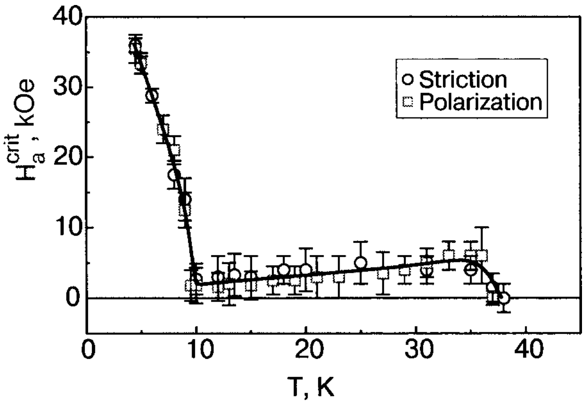

FIG. 6. H-T phase diagram obtained from measurements of the longitudinal magnetostriction and electric polarization for $H \| a$, for the single crystal $GdFe_3(BO_3)_4$.

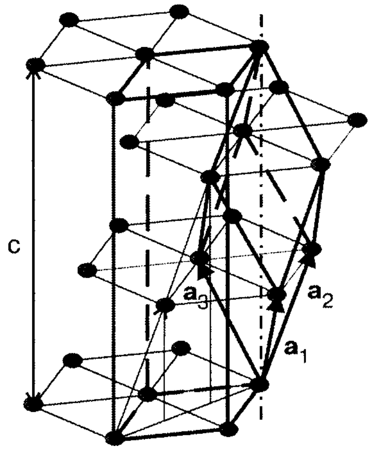

FIG. 8. Fragment of the Bravais lattice of the system $RFe_3(BO_3)_4$ with the rhombohedral (primitive) and hexagonal (unit) cells shown explicitly. The lattice sites (ellipses) correspond to the positions of the R^{3+} ions.

only one R^{3+} ion, which will be magnetic for R=Gd, Nd, and our system is antiferromagnetic at all temperatures below T_N, we shall assume that the elementary translations of the magnetic Bravais lattice $\mathbf{a}_1^m\mathbf{a}_2^m\mathbf{a}_3^m$ of the $GdFe_3(BO_3)_4$ system will be related to the elementary translations $\mathbf{a}_1, \mathbf{a}_2, \mathbf{a}_3$ of its crystal lattice (Fig. 8) by the relations

$$\mathbf{a}_1^m = \mathbf{a}_2 + \mathbf{a}_3, \quad \mathbf{a}_2^m = \mathbf{a}_3 + \mathbf{a}_1, \quad \mathbf{a}_3^m = \mathbf{a}_1 + \mathbf{a}_2. \tag{1}$$

It follows from relations (1) that the magnetic primitive cell of $GdFe_3(BO_3)_4$ will be a rhombohedron doubled in volume in comparison with the high-temperature primitive crystal cell. In fact, the volume V^m of the magnetic cell is found from the relation $V^m = \mathbf{a}_1^m \cdot [\mathbf{a}_2^m \times \mathbf{a}_3^m] = (\mathbf{a}_2 + \mathbf{a}_3) \cdot [(\mathbf{a}_3 + \mathbf{a}_1) \times (\mathbf{a}_1 + \mathbf{a}_2)] = 2V^c$, where V^c is the volume of the primitive crystal cell. In principle, since in our case the appearance of antiferromagnetic order in the system from the standpoint of magnetic symmetry corresponds to a change of the Bravais lattice on account of the appearance of anti-translations in it (doubling of a certain number of primitive translations of the initial crystal lattice), besides the case (1) considered above, in terms of exchange symmetry there are two more possibilities, fundamentally different from the first: 1) when only one of the primitive translations is doubled, while the other two remain unchanged; 2) when some pair of the three translations doubles, while the third translation remains unchanged. One is readily convinced that the two cases mentioned would lead, as a result of a phase transition, to the "loss" of a threefold symmetry axis and, accordingly, to a change of the symmetry class of the system from hexagonal to monoclinic. For the existing ideas about the hierarchy of exchange interactions (intralayer and interlayer), in our system the realization of these possibilities is improbable. For that reason we shall restrict the discussion to case (1). If one is working with the hexagonal unit cell (which is more natural from an experimental standpoint) for this system, the change of magnetic symmetry (1) leads to doubling of the height of the $GdFe_3(BO_3)_4$ unit cell. Since no concrete change of the crystal symmetry (micro- and, accordingly, macroscopic) of the system at $T_C = 156$ K has been established experimentally$^{1)}$ (while such a change could in principle occur with a doubling of the unit cell, as, e.g., in the case of $BiFeO_3$), we assume that the doubling of the unit cell of the $GdFe_3(BO_3)_4$ system occurs at the Néel temperature T_N.

As we have said, at high temperatures the rare-earth ferroborates belong to the rhombohedral space group $R32$ (D_3^7). Taking the change of the unit cell at T_N into account, for describing the magnetic properties of our system (construction of the corresponding irreducible representations of the group $R32$) we consider six Fe^{3+} magnetic moments characterized by spins $\mathbf{S}_1 - \mathbf{S}_6$. The first three of them—$\mathbf{S}_1, \mathbf{S}_2, \mathbf{S}_3$—belong to one horizontal layer, and the other three—$\mathbf{S}_4, \mathbf{S}_5, \mathbf{S}_6$—lie in the adjacent layer parallel to the first at a distance of $c/3$ from it. As is done in Landau theory, in describing the magnetic phase transition it is necessary to go over from the individual spins $\mathbf{S}_1 - \mathbf{S}_6$ to their symmetrized combinations (basis functions of the corresponding irreducible representations of the group $R32$), each of which describes one of the possible types of magnetic ordering—either collinear (in the case of a one-dimensional representation) or noncollinear (for two- and three-dimensional representations). Under the condition that in hexagonal coordinates the vector of the AFM structure appearing at the Néel point is equal to $\mathbf{k} = \{0,0,1/2\}$, we obtain the following relations:

$$\mathbf{B}_1 = \sqrt{3}(\mathbf{S}_1 - \mathbf{S}_2) - \sqrt{3}(\mathbf{S}_4 - \mathbf{S}_5),$$

$$\mathbf{B}_2 = \mathbf{S}_1 + \mathbf{S}_2 - 2\mathbf{S}_3 - \mathbf{S}_4 - \mathbf{S}_5 + 2\mathbf{S}_6,$$

$$\tilde{\mathbf{B}}_1 = \sqrt{3}(\mathbf{S}_1 - \mathbf{S}_2) + \sqrt{3}(\mathbf{S}_3 - \mathbf{S}_5),$$

$$\tilde{\mathbf{B}}_2 = \mathbf{S}_1 + \mathbf{S}_2 - 2\mathbf{S}_3 + \mathbf{S}_4 + \mathbf{S}_5 - 2\mathbf{S}_6,$$

$$\mathbf{L} = \mathbf{S}_1 + \mathbf{S}_2 + \mathbf{S}_3 - \mathbf{S}_4 - \mathbf{S}_5 - \mathbf{S}_6.$$

$$\mathbf{F} = \mathbf{S}_1 + \mathbf{S}_2 + \mathbf{S}_3 + \mathbf{S}_4 + \mathbf{S}_5 - \mathbf{S}_6. \tag{2}$$

TABLE I. Basis functions of the irreducible representations (structural, magnetic, and exchange) of the group $R32$.

D_3^7	Structure	Magnetic	Exchange
Γ_1	u_{ZZ} $u_{XX} + u_{YY}$	$\tilde{B}_{1Y} - \tilde{B}_{2X}$	
Γ_1'		$B_{1Y} - B_{2X}$	
Γ_2	P_Z	$F_Z, \tilde{B}_{1X} + \tilde{B}_{2Y}$	
Γ_2'		$L_Z, B_{1X} + B_{2Y}$	
Γ_3	$\begin{Bmatrix} P_X \\ P_Y \end{Bmatrix}$ $\begin{Bmatrix} u_{XX} - u_{YY} \\ -2u_{XY} \end{Bmatrix}$ $\begin{Bmatrix} u_{YZ} \\ -u_{XZ} \end{Bmatrix}$	$\begin{Bmatrix} F_X \\ F_Y \end{Bmatrix}, \begin{Bmatrix} L_X^2 - L_Y^2 \\ -2L_X L_Y \end{Bmatrix}$ $\begin{Bmatrix} \tilde{B}_{1Z} \\ \tilde{B}_{2Z} \end{Bmatrix}, \begin{Bmatrix} \tilde{B}_{1Y} + \tilde{B}_{2X} \\ \tilde{B}_{1X} - \tilde{B}_{2Y} \end{Bmatrix}$	$\begin{Bmatrix} \mathbf{L}\cdot\mathbf{B}_2 \\ -\mathbf{L}\cdot\mathbf{B}_1 \end{Bmatrix}$ $\begin{Bmatrix} \mathbf{F}\cdot\tilde{\mathbf{B}}_1 \\ -\mathbf{F}\cdot\tilde{\mathbf{B}}_2 \end{Bmatrix}$
Γ_3'		$\begin{Bmatrix} L_X \\ L_Y \end{Bmatrix}, \begin{Bmatrix} B_{1Z} \\ B_{2Z} \end{Bmatrix}$ $\begin{Bmatrix} B_{1Y} + B_{2X} \\ B_{1X} - B_{2Y} \end{Bmatrix}$	$\begin{Bmatrix} \mathbf{F}\cdot\mathbf{B}_2 \\ -\mathbf{F}\cdot\mathbf{B}_1 \end{Bmatrix}, \begin{Bmatrix} \mathbf{L}\cdot\tilde{\mathbf{B}}_2 \\ -\mathbf{L}\cdot\tilde{\mathbf{B}}_1 \end{Bmatrix}$

Note: The primed representations are odd with respect to translation along the c axis.

Since we are interested not only in the magnetic but also the magnetoelastic and magnetoelectric properties of the $GdFe_3(BO_3)_4$ system, in the corresponding column of the table of irreducible representations of the group $R32$ (Table I) we also give the basis functions of the "nonmagnetic" representations (corresponding to structural macro-variables of the system—to the components of the strain tensor and electric polarization vector).

In accordance with formulas (2), the pair of functions $\{\mathbf{B}_1, \mathbf{B}_2\}$, corresponding in the exchange approximation to a two-dimensional representation (odd with respect to a shift by a period along the c axis), will itself describe an exchange-noncollinear AFM structure of the triangular type, with the closest three moments, those belonging to the Fe^{3+} ions found at the center of the sides of the elementary triangle of Gd ions of one layer, directed at an angle of 120° to one another, and the moments of the next-nearest layer antiparallel to the moments of the first layer. Another pair of functions, $\{\tilde{\mathbf{B}}_1, \tilde{\mathbf{B}}_2\}$, corresponding in the exchange approximation to yet another two-dimensional representation (even with respect to vertical translation), will describe another exchange-noncollinear AFM structure, also of the triangular type, that is possible from the standpoint of symmetry. Being ordered (as in pair of functions $\{\mathbf{B}_1, \mathbf{B}_2\}$) antiferromagnetically within each layer, the moments of adjacent layers will be coupled ferromagnetically, and the resulting magnetic structure will be antiferromagnetic, with coincident magnetic and crystal cells. If one goes by the magnetizations of the layers, the function $\mathbf{L}$ describes two-sublattice (and formally speaking, six-sublattice) collinear AFM ordering in which all the moments of one layer are coupled ferromagnetically and those of the next layer are also coupled ferromagnetically among themselves, but are opposite to the moments of the initial layer, etc. (this corresponds to the case $\mathbf{k} = \{0,0,1/2\}$). The function $\mathbf{F}$ is the magnetization vector of the magnetic unit cell. It follows from what we have said that the dominant role of the antiferromagnetic interlayer exchange (brought about by the interaction of nearest spins lying in neighboring layers) leads to the appearance, as the temperature is lowered, first of 1D magnetic ordering along the corresponding helical chains, parallel to the c axis, of iron ions surrounded by distorted oxygen octahedra.[6] Depending on the character of the intralayer exchange of nearest spins of the Fe^{3+} ions (and, hence, the exchange between individual ordered chains)—ferromagnetic or antiferromagnetic—our system on the whole in the exchange approximation will be either a collinear antiferromagnet (which, in the main approximation, exhibits traits of a two-sublattice antiferromagnet) or an exchange-noncollinear antiferromagnet of the triangular type. There are no other possibilities for the aforementioned change of magnetic symmetry (1).

Following Ref. 9, in our discussion below we shall give preference mainly to the case of collinear ordering. Then the magnetic ordering that appears at the temperature T_N will be characterized by a vector $\mathbf{L}$. Nevertheless, for the sake of completeness (since more-detailed studies of the system are still warranted) we shall write the thermodynamic potential of the system (the subsystems of ordering moments of the Fe^{3+} ions) to second order in the exchange approximation with allowance for the characteristic energy of all possible magnetic modes of our system:

$$\Phi_{\mathrm{ex}}^{(2)} = \frac{1}{2}\Lambda_1^{(2)}\mathbf{L}^2 + \frac{1}{2}\Lambda_2^{(2)}(\mathbf{B}_1^2+\mathbf{B}_2^2) + \frac{1}{2}\Lambda_3^{(2)}\mathbf{F}^2 + \frac{1}{2}\Lambda_4^{(2)} \times (\tilde{\mathbf{B}}_1^2+\tilde{\mathbf{B}}_2^2). \tag{3}$$

We obtain the relativistic (magnetically anisotropic) contribution taking into account not only the independent magnetic modes, after explicitly separating out the terms corresponding to the case $\mathbf{k}=\{0,0,1/2\}$,

$$\Phi_{\mathrm{rel.ind}}^{(2)} = \frac{1}{2}\eta_1^{(2)}L_Z^2 + \frac{1}{4}\eta_1^{(4)}L_Z^4 + \frac{1}{2}\eta_2(B_{1Y}-B_{2X})^2 + \frac{1}{2}\eta_3(B_{1X}+B_{2Y})^2 + \frac{1}{2}\eta_4(B_{1Y}+B_{2X})^2 + (B_{1X}-B_{2Y})^2, \tag{4}$$

[in Eq. (4) we have explicitly taken into account the anisotropic contributions of both second and fourth order only for the mode $\mathbf{L}$ of interest to us, which, as we know,[12] will be responsible for possible spin reorientation] but also the mixed contributions ("mixing" the different magnetic modes) of second order, which describe the simplest characteristic interactions of the different magnetic modes of our system,

$$\Phi_{\mathrm{rel.int.}} = \alpha_1[L_X(B_{1Y}+B_{2X}) + L_Y(B_{1X}-B_{2Y})] + \alpha_2 L_Z(B_{1X}+B_{2Y}). \tag{5}$$

Furthermore, we write the main intrinsic (in the absence of magnetic field) magnetoelectric contributions of both exchange and relativistic nature,

$$\Phi_{ME} = \beta_0\{P_X(\mathbf{L}\cdot\mathbf{B}_2) - P_Y(\mathbf{L}\cdot\mathbf{B}_1)\} + \beta_1\{P_X(L_x^2-L_Y^2) - 2P_Y L_X L_Y\} + \beta_2 L_Z(P_X L_Y - P_Y L_X) + \beta_3 P_Z L_Z(B_{1Y}-B_{2X}). \tag{6}$$

We also take into account the simplest magnetoelastic contributions:

$$\Delta\Phi_{\mathrm{Mel}} = \gamma_1^1 u_{ZZ}L_Z^2 + \gamma_1^2 u_{ZZ}(L_X^2+L_Y^2) + \gamma_2^1(u_{XX}+u_{YY})L_Z^2 + \gamma_2^2(u_{XX}+u_{YY})(L_X^2+L_Y^2) + \gamma_3[(u_{XX}-u_{YY}) \times (L_X^2-L_Y^2)] + 4u_{XY}L_X L_Y] + \gamma_4[u_{YZ}(L_X^2-L_Y^2) + 2u_{XZ}L_X L_Y]. \tag{7}$$

The establishment of collinear AFM order in the system at the Néel temperature T_N means, in the ideology of the Landau theory, that the following inequalities hold:

$$\Lambda_1^{(2)}(T_N)=0, \quad \Lambda_2^{(2)}(T_N)>0, \quad \Lambda_3^{(2)}(T_N)>0, \quad \Lambda_4^{(4)}(T_N)>0. \tag{8}$$

Assuming that in the temperature region $10\ \mathrm{K}<T<38\ \mathrm{K}$ the system is an easy-plane antiferromagnet, we must assume that the inequality $\eta_1^{(2)}(T)>0$ holds in that temperature interval. Then the point of the spin-reorientation transition T_R will correspond to the condition $\eta_1^{(2)}(T_R) + \eta_1^{(4)}(T_R)=0$,[12] and the system goes from easy-plane to easy-axis at temperatures $T<T_R$, for which $\eta_1^{(2)}(T) + \eta_1^{(4)}(T)<0$.

It follows from the results of Ref. 8 that as the temperature is lowered in the region $T\sim 20$ K the subsystem of moments of the rare-earth ions Gd will begin to play a role in the magnetism, the interaction of the subsystem of Fe spins with it having a substantial influence on the spin-reorientation transition in our system, although no actual magnetic ordering occurs in the rare-earth subsystem itself. Let us give some special attention to this fact. We start for the temperature region $T>10$ K, i.e., where the system is still an easy-plane antiferromagnet. Since the magnetic unit cell of the $\mathrm{GdFe_3(BO_3)_4}$ system is doubled at the phase transition at the Néel point (and then contains two Gd ions), for describing the interaction of the disordered subsystem of moments of the Gd ions with the ordered system of moments of the Fe ions, we introduce an antiferromagnetic vector $\tilde{\mathbf{L}}$ for the gadolinium subsystem also. Taking into account the symmetry of the sites of the two gadolinium ions in the magnetic unit cell of our system, we easily see that the vectors $\tilde{\mathbf{L}}$ and $\mathbf{L}$ correspond to equivalent representations of the exchange symmetry group of our system, and so the energy of the f-d exchange interaction, $E=\kappa\tilde{\mathbf{L}}\cdot\mathbf{L}$ will be an invariant of the group $R32$. The mean energy of the f-d exchange, averaged over the vector $\tilde{\mathbf{L}}$, i.e., $\langle E\rangle=\kappa\langle\tilde{\mathbf{L}}\rangle\cdot\mathbf{L}$, because of the disordered nature of the gadolinium subsystem, does not itself contribute to the thermodynamic potential of the system. Nevertheless, the antiferromagnetic order induced by the f-d exchange in the gadolinium subsystem can give an effective contribution to the thermodynamic potential on account of the corresponding correlations of the longitudinal (lying in the easy plane) component of the vector $\tilde{\mathbf{L}}$ in the second order of perturbation theory:

$$\Delta\Phi_{\text{cor}}=\kappa^2\frac{1}{\varepsilon}\langle\tilde{L}^2\rangle(L_X^2+L_Y^2), \qquad (9)$$

where ε is the characteristic mean energy of spin waves of the gadolinium subsystem. It is seen that the correlation contribution to the thermodynamic potential of the system will be positive independently of the sign of κ. The physical meaning of the energy $\Delta\Phi_{\text{cor}}$ is that the correlations tend to make it unfavorable for the vector $\mathbf{L}$ to lie in the horizontal plane. As the temperature is lowered and the antiferromagnetic vector of the gadolinium sublattice $\tilde{\mathbf{L}}$ induced by the f-d exchange increases, an anisotropic contribution of opposite sign will appear in the thermodynamic potential of the system and compete with the initial (easy-plane) one. Then at the corresponding temperature T_R the resultant anisotropy constant will change sign, and an "easy plane to easy axis" spin-reorientation transition will occur in the system (it is known[5] that this transition is not observed in the case of the nonmagnetic ions R=Y, La).

DISCUSSION OF THE RESULTS

Our proposed expression (7) for the magnetoelastic energy of the system allows an easy explanation of the experimentally observed behavior (Figs. 1 and 4) of the magnetostriction for the magnetic field directions $H\|c$ and $H\perp c$, both for the temperature region $T<10$ K and for $10\text{ K}<T<38$ K. Indeed, at a temperature $T\leqslant 10$ K, when the vector $\mathbf{L}$ is directed along the c axis and the field $H\|c$, at a certain value of the field H_{cr} a spin-reorientation transition occurs, and the vector $\mathbf{L}$ lies in the plane without changing its length. The lower the temperature, the larger the value of the threshold field. Starting from formula (7), one can conclude that at that point the magnetostriction has a jump, and $\lambda_C\sim(\gamma_1^2-\gamma_1^1)L^2$.

At the same field orientation $H\|c$ but for $T>10$ K the vector $\mathbf{L}$ lies in the easy plane, and the magnetostriction behaves in a monotonic manner (quadratically in the field; Fig. 1). For the field direction $H\perp c$ in the temperature region $T<10$ K the magnetic field H acting on the gadolinium subsystem disrupts the mechanism of the spin reorientation that is observed at temperature T_R and tips the vector $\mathbf{L}$ over into the basal plane, but perpendicular to the field (the in-plane anisotropy is extremely small), so that in this case the magnetostriction λ_C will exhibit a jump $\Delta\lambda_C\sim(\gamma_2^2-\gamma_2^1)L^2$.

At temperatures $T>10$ K the vector $\mathbf{L}$ lies in the plane, and in the general case there will be six types of domains in the system (in accordance with the three equivalent easy directions in the plane), so that the mean magnetostriction over the sample will be equal to zero. At low magnetic fields, when the vectors $\mathbf{L}$ of all the domains align counter to the field, the magnetostriction exhibits jumplike behavior $\Delta\lambda_a\sim\gamma_3L^2$. For the field direction $H\|c$ the magnetostriction behaves monotonically, in accordance with expression (7).

Analysis of the magnetoelectric contributions (6) permits a detailed interpretation of the behavior of the planar component of the electric polarization vector (Fig. 5). On the whole, the theory [expression (6) and Table I] permits the assertion that a quadratic magnetoelectric effect should be observed in our system. It is noteworthy here that the discussion of the magnetoelectric effect in the framework of the symmetry space group $R32$ with the invariant contributions (6) taken into account does not permit a satisfactory description of the behavior of the vertical component of the electric polarization vector, P_C. The similarity of its behavior with that of the magnetostriction λ_C argues, in particular, that for the magnetically ordered state the vector P_C should be an invariant (i.e., our system belongs to a polar class). In the absence of unambiguous analysis of the change of the crystal symmetry of the system at the point of the structural phase transition $T_C=156$ K, this remains an open question.

It follows from expression (6) that the symmetry of the system admits yet another magnetoelectric contribution $\sim\beta_2$ (of a relativistic nature), which is responsible for the spin-reorientation transition in an electric field. Indeed, for the state in which the antiferromagnetic vector lies in the basal plane (for the region $T>T_R$) the transverse component of the electric field applied in the basal plane induces the appearance of a component of the vector $\mathbf{L}$ directed along the c axis and, accordingly, in the temperature region $T<T_R$ this contribution brings about a reorientation of the antiferromagnetic vector from the easy axis to the easy plane under the influence of a transverse electric field.

Finally, the features of the symmetry of our system are such that, in principle, under certain conditions (in particular, in the presence of antiferromagnetic intralayer exchange) an antiferromagnetic phase transition could occur at the Néel point with the formation of a fundamentally noncollinear structure of the triangular type, described by a two-dimensional representation (by the basis vectors $\mathbf{B}_1$ and $\mathbf{B}_2$ mentioned previously). In this case it would not require very much effort to describe the spin-reorientation transition and so forth in the framework of the thermodynamic approach. However, the realization of an easy-plane triangular AFM structure in the temperature interval $10\text{ K}<T<38$ K would lead, for both the cases of weak and strong easy-plane anisotropy,[13] to the existence of yet another spin-reorientation phase transition in the high-temperature region at moderately high fields $H\perp c$ (completely achievable in our experiments). Since no such transformation was observed in principle in our studies, we shall assume, as in Ref. 8, that the features of our system are such that collinear AFM ordering is realized at the Néel point. We complete the discussion of the properties of the thermodynamic potential of the system (3) by calling attention to the presence of specific cross contributions in it that are capable of "admixing" exchange-noncollinear components to the fundamental collinear AFM mode both above and below the spin reorientation point. One can see that each of these noncollinear components corresponds to a different chirality (right or left "handedness").[14] This, in particular, attests that the magnetooptical properties of our system will be different on different sides of the spin reorientation point.

On the whole, the above-mentioned features of the behavior of the system $GdFe_3(BO_3)_4$ permit the assumption that it is a multiferroic compound.

In closing we thank M. N. Popova and A. N. Valil'ev for steady interest in our research, and K. I. Kamilov and A. V Kuvardin for making the thermal expansion measurements.

This study was supported by the Russian Foundation for Basic Research (#04-02-116592).

[*] E-mail: popov@plms.phys.msu.ru

[1)] After this article went to press, the preprint of an article entitled "Evidence for structure differentiation in the iron-helicoidal-chain in $GdFe_3(BO_3)_4$," by S. A. Klimin, D. Fausti, A. Meetsma, L. N. Besmaternykh, P. H. M. van Loosdrecht, and T. T. M. Palstra (to be published in Acta Cryst. B), came out, which contained a detailed description of the change of the crystal system at the point T_c; however, taking that change into account would not alter the basic conclusions found in our paper.

---

[1] D. A. Keszler, Curr. Opin. Solid State Mater. Sci. **1**, 204 (1996).
[2] M. H. Bartl, K. Gatterer, E. Cavalli, A. Speghini, and M. Bettinelli, Spectrochim. Acta, Part A **57**, 1981 (2001).
[3] A. M. Kalashnikova, V. V. Pavlov, R. V. Pisarev, L. M. Bezmaternykh, M. Bayer, and Th. Rasing, JETP Lett. **80**, 293 (2004).
[4] A. G. Gavriliuk, S. A. Kharlamova, I. S. Lyubutin, I. A. Troyan, S. G. Ovchinnikov, A. M. Potseluĭko, M. I. Eremets, and R. Boehler, JETP Lett. **80**, 426 (2004).
[5] J. A. Campa, C. Cascales, E. Gutierrez-Puebla, M. A. Monge, I. Rasines, and C. Ruiz-Valero, Chem. Mater. **9**, 237 (1997).
[6] Y. Hinatsu, Y. Doi, K. Ito, M. Wakeshima, and A. Alemi, J. Solid State Chem. **172**, 438 (2003).
[7] A. D. Balaev, L. N. Bezmaternykh, I. A. Gudim, V. L. Temerov, S. G. Ovchinnikov, and S. A. Kharlamova, J. Magn. Magn. Mater. **258–259**, 532 (2003).
[8] R. Z. Levitin, E. A. Popova, R. M. Chtsherbov, A. N. Vasiliev, M. A. Popova, E. P. Chukalina, S. A. Klimin, P. H. M. van Loosdrecht, D. Fausti, and L. N. Bezmaternykh, JETP Lett. **79**, 423 (2004).
[9] A. I. Pankrats, G. A. Petrakovskiĭ, L. N. Bezmaternykh, and O. A. Bayukov, Zh. Éksp. Teor. Fiz., **126**, 887 (2004) [JETP **99**, 766 (2004)].
[10] Yu. F. Popov, A. M. Kadomtseva, D. V. Belov, G. P. Vorob'ev, and A. K. Zvezdin, JETP Lett. **69**, 330 (1999).
[11] A. N. Vasil'ev, private communication.
[12] K. P. Belov, A. K. Zvezdin, A. M. Kadomtseva, and R. Z. Levitin, *Orientational Transitions in Rare-Earth Magnets* [in Russian], Nauka, Moscow (1979).
[13] M. F. Collins and O. A. Petrenko, Can. J. Phys. **75**, 605 (1997).
[14] E. A. Turov, A. V. Kolchanov, V. V. Men'shenin, I. F. Mirsaev, and V. V. Nikolaev, *Symmetry and the Physical Properties of Antiferromagnets* [in Russian], Fizmatlit, Moscow (2001).

Translated by Steve Torstveit

LOW TEMPERATURE PHYSICS VOLUME 31, NUMBERS 8–9 AUGUST–SEPTEMBER 2005

Incommensurate magnetism in the coupled spin tetrahedra system $Cu_2Te_2O_5Cl_2$

O. Zaharko,* H. M. Ronnow, A. Daoud-Aladine, S. Streule, F. Juranyi, and J. Mesot

Laboratory for Neutron Scattering, ETHZ & PSI, CH-5232 Villigen PSI, Switzerland

H. Berger

Institute de Physique de la Matière Complexe, EPFL, CH-1015 Lausanne, Switzerland

P. J. Brown

Institute Laue-Langevin, 156X, F-38042 Grenoble Cedex, France

(Submitted January 25, 2005)
Fiz. Nizk. Temp. **31**, 1068–1072 (August–September 2005)

Neutron scattering studies on powder and single crystals have provided new evidence for unconventional magnetism in $Cu_2Te_2O_5Cl_2$. The compound is built from tetrahedral clusters of $S=1/2$ Cu^{2+} spins located on a tetragonal lattice. Magnetic ordering, emerging at $T_N=18.2$ K, leads to a very complex multi-domain, most likely degenerate, ground state, which is characterized by an incommensurate (ICM) wave vector $\mathbf{k}\sim[0.15,0.42,1/2]$. The Cu^{2+} ions carry a magnetic moment of $0.67(1)\mu_B/Cu^{2+}$ at 1.5 K and form a four-helix spin arrangement with two canted pairs within the tetrahedra. A domain redistribution is observed when a magnetic field is applied in the tetragonal plane ($H_c\approx0.5$ T), but not for $H\|c$ up to 4 T. The excitation spectrum is characterized by two well-defined modes, one completely dispersionless at 6 meV, the other strongly dispersing to a gap of 2 meV. The reason for such complex ground state and spin excitations may be geometrical frustration of the Cu^{2+} spins within the tetrahedra, intra- and inter-tetrahedral couplings having similar strengths and strong Dzyaloshinski–Moriya anisotropy. Candidates for the dominant intra- and inter-tetrahedral interactions are proposed. © *2005 American Institute of Physics.* [DOI: 10.1063/1.2008143]

INTRODUCTION

Reduced dimensionality, geometrical frustration and low spin values lead to quantum fluctuations often resulting in interesting new ground states and spin dynamics.[1] The most famous examples are based on triangular units (triangular and kagomé lattices[2]) in two dimensions (2D) and tetrahedral clusters (FCC and pyrochlore lattices[3]) in 3D. The nature of the ground state in such systems is a subject of current strong interest, especially for the extreme quantum mechanical case $S=1/2$.

The copper tellurate $Cu_2Te_2O_5X_2$ (X=Cl, Br, space group P-4; Ref. 4) belong to a new family of such compounds. Their structure can be viewed as a stacking of layers of $Cu_4O_8Cl_4$ clusters along c. The four Cu^{2+} ions within such a cluster, Cu1 (x,y,z), Cu2 $(1-x,1-y,z)$, Cu3 $(y,1-x,-z)$, and Cu4 $(1-y,x,-z)$, form an irregular tetrahedron with two longer (Cu1–Cu2, Cu3–Cu4) and four shorter edges. The tetrahedra have a 2D square arrangement within the ab layers.

The $Cu_2Te_2O_5Cl_2$ system attracted much attention as the first magnetic susceptibility data fitted well a model of isolated tetrahedra.[4] The observed broad maximum between 20–30 K and a rapid drop at lower temperatures indicated a strength of the intra-tetrahedral coupling $J\sim38.5$ K. Raman spectroscopy, however, indicated a substantial inter-tetrahedral coupling along the c axis[5,6] and the data analysis have been performed[7] in terms of a dimerized model with the two pairs of Cu^{2+} spins: Cu1–Cu2 and Cu3–Cu4. Further magnetic susceptibility and specific heat measurements[5] indicated an onset of antiferromagnetic (AF) order at $T_N=18.2$ K, thus confirming the importance of inter-tetrahedral couplings. Recent neutron diffraction studies[8] revealed the details of the magnetic order: it is incommensurate and very complex.

In spite of considerable progress in experimental studies, the relevant intra- and inter-tetrahedral magnetic interactions in $Cu_2Te_2O_5Cl_2$ remain a puzzle due to the rather complex 3D exchange topology (Fig. 1). The intra-tetrahedral spin interactions are mediated via the superexchange paths Cu–O–Cu and can be described by J_1 and J_2 exchange constants. It was suggested[9] according to the Goodenough rules, that the J_2 interaction should be weakly antiferromagnetic if not ferromagnetic, while J_1 is antiferromagnetic and rather weak.[9] From the band structure calculations[10] it is expected that within the ab layers the J_a and J_d inter-tetrahedral couplings are substantial (see Fig. 1) and mediated by the halogen p orbitals. Between the adjacent layers the tetrahedra interact through the super-superexchange paths Cu–O...O–Cu and the corresponding inter-tetrahedral couplings are as well important.

The nature of the magnetic ordering transition is also still unclear. A strong spin-lattice coupling near T_N has been suggested from magnetic susceptibility and thermal conductivity studies.[11] However, the infrared spectroscopy study,[12] as well as high-resolution neutron diffraction study[8] gave no evidence of any lattice distortion.

We present neutron diffraction and inelastic scattering

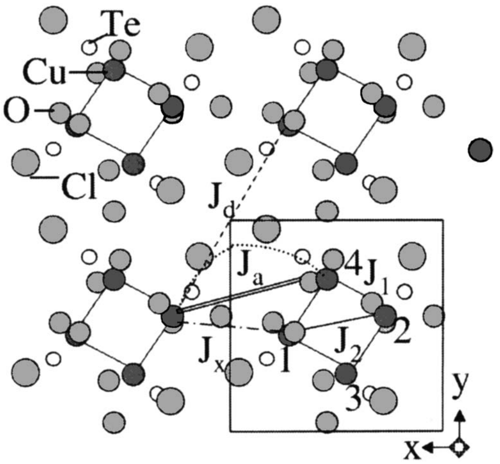

FIG. 1. The xy projection of the $Cu_2Te_2O_5Cl_2$ crystal structure ($z = -1/2$—$1/2$) with the J_1, J_2 and possible intertetrahedral exchange paths.[10] The double-line segment is normal to the incommensurate component of the wave vector $\mathbf{k}'$.[8]

results, which supply new information on the magnetic ground state, spin-orbit coupling and spin dynamics. We hope this will provide a better starting point for theoretical modeling.[13–17]

EXPERIMENTAL

High-purity powder and single crystals of $Cu_2Te_2O_5Cl_2$ were prepared by the halogen vapor transport technique, using $TeCl_4$ and Cl_2 as transport agents. Neutron powder diffraction (NPD) patterns were collected in the temperature range 1.5–30 K on the DMC instrument, with a neutron wavelength of $\lambda = 4.2$ Å and on the high-resolution HRPT instrument ($\lambda = 1.889$ Å) at SINQ, Villigen, Switzerland. The neutron single crystal diffraction (NSCD) experiments on two crystals of dimensions $2.5\times3\times5$ mm and $2\times3.5\times6$ mm were carried out using the diffractometers TriCS at SINQ ($\lambda = 1.18$ Å) and D15 ($\lambda = 1.17$ Å) at the high-flux ILL reactor, France. The NSCD with applied magnetic field were performed on a larger 1 cm^3 crystal on TriCS ($\lambda = 1.18$ and 2.4 Å) for three field directions $H \| a$, b, and c.

The inelastic neutron scattering experiment was carried out on 15 g powder on neutron time-of-flight spectrometer FOCUS ($\lambda = 2.8$ and 4 Å) at SINQ and on a large 1.5 cm^3 crystal on the IN8 thermal neutron three-axis spectrometer at ILL. IN8 was configured with doubly focusing monochromator and analyzer with a 5 cm graphite filter in k_f and fixed final neutron energy of 14.7 meV.

RESULTS

Diffraction

Below $T_N = 18$ K tiny magnetic peaks appeared (Fig. 2) in DMC neutron diffraction patterns of $Cu_2Te_2O_5Cl_2$, as already reported in Ref. 8. Moreover, the onset of magnetic order at T_N can be followed from the structural peaks in the HRPT data. The lattice constant $a(b)$ significantly decreases with temperature above T_N and changes very little below T_N (Fig. 2, inset). This implies that the spin-lattice coupling is substantial, but no changes of the crystal structure could be determined from the neutron patterns.

To determine correctly the magnetic ground state it is very important to elucidate the magnetic symmetry. The [001] projection of neutron diffraction pattern of a typical $Cu_2Te_2O_5Cl_2$ single crystal is presented in Fig. 3. Up to 16 magnetic satellites of the (0,0,0) reflection have been observed. The reflection set denoted by black circles arises from four arms of the star of the incommensurate (ICM) wave vector $\mathbf{k} \sim [0.150, 0.422, 1/2]$. The reflections denoted by dotted circles correspond to the star of another wave vector $\mathbf{k}' \sim [-0.150, 0.422, 1/2]$. The $\mathbf{k}$ and $\mathbf{k}'$ vectors are not related by the symmetry elements of the group P-4, and could belong to growth crystallographic twins. Since for several crystals studied the $\mathbf{k}'$ reflections are absent, we conclude that the $\mathbf{k}$ and $\mathbf{k}'$ sets are independent. Interestingly, the intensity ratio between the two first magnetic reflections for the $\mathbf{k}$ and $\mathbf{k}'$ sets is different, implying that the magnetic structures associated with these two stars are different.

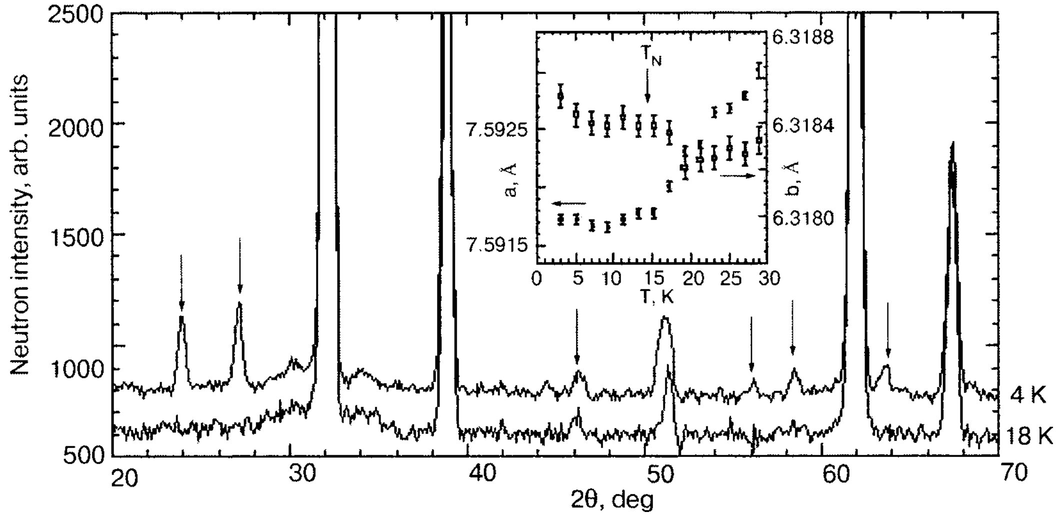

FIG. 2. The 18 and 4 K DMC NPD patterns of $Cu_2Te_2O_5Cl_2$ ($\lambda = 4.2$ Å), arrows point to magnetic reflections. Inset: temperature evolution of the lattice constants from HRPT NPD data ($\lambda = 1.889$ Å).

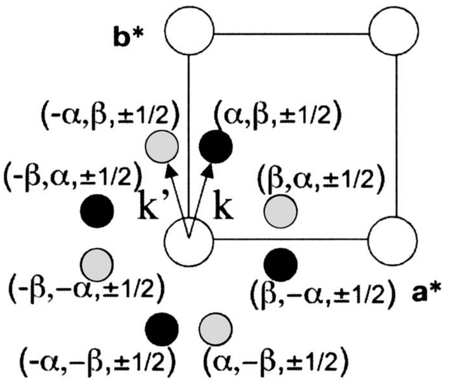

FIG. 3. The [001] projection of the reciprocal space of a $Cu_2Te_2O_5Cl_2$ single crystal. The black circles correspond to the **k** magnetic reflections and the dotted circles—to the **k**′ set; $\alpha=0.15$, $\beta=0.422$.

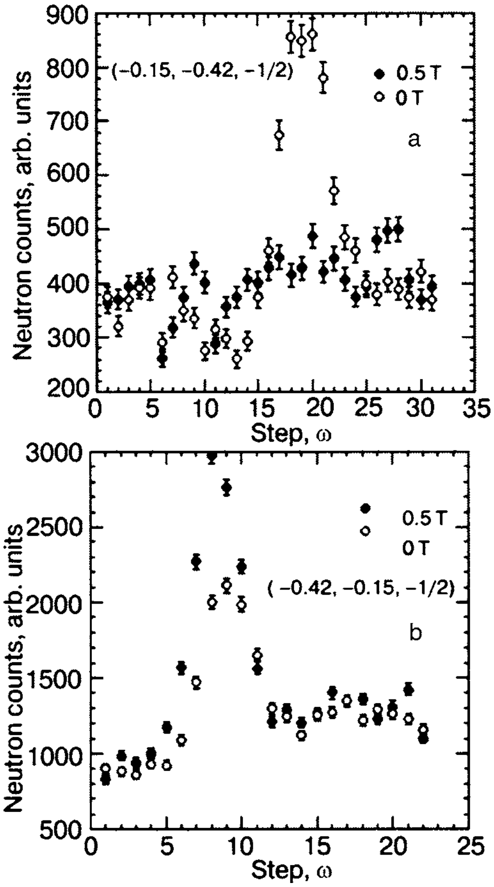

FIG. 4. The TriCS ω scans of the $(-0.15,-0.42,-1/2)$ (a) and $(0.42,-0.15,1/2)$ (b) magnetic reflections ($\lambda=2.4$ Å) at $H=0$ T and $H=0.5$ T along a.

We further tried to clarify if the magnetic structure is single-k or multi-k. In the case of a single-k magnetic structure the $\mathbf{k}(\mathbf{k}')$ set contains contributions of four configuration domains. The configuration domains must all have the same structure but possibly different populations. Each of them could have two 180 deg domains and two chiral domains. In the case of multi-k structure, the four arms of the star build one magnetic structure.

It is possible to distinguish the single-k or multi-k cases by studying the variation of magnetic intensities as a function of an applied magnetic field H. We performed such study for fields along a, b, and c crystal directions. For H along c the intensities of the magnetic reflections hkl with $l>0$ increase and for $l<0$ they decrease, but all reflections persist up to 4 T. This implies a change of the spin arrangement with respect to the zero-field magnetic structure, but without domain redistribution and/or meta-magnetic transition. For $H\|a$ a transition occurs at $H_c\sim0.5$ T: the intensities of the $(\pm\alpha,\pm\beta,\pm l/2)$ reflections vanish, while the magnetic reflections of the type $(\pm\beta,\pm\alpha,\pm l/2)$ change their intensities smoothly (Fig. 4). Flipping the field to $-a$ results in the same behavior. Switching off the field restores partly the vanished peaks. A similar picture is observed for $H\|b$, but now the $(\pm\beta,\pm\alpha,\pm l/2)$ reflections vanish at ~0.5 T. Our results imply that 0.5 T applied in the tetragonal plane is enough to depopulate the domains with the propagation vector nearly normal (90±10 deg) to the field direction. This supports the idea that the magnetic structure is a single-k and not a multi-k structure.

The model for the $\mathbf{k}'$ magnetic structure has been recently elaborated in Ref. 8. The only symmetry constraint is imposed by the commensurate component of the wave vector. It implies that the ab layers of tetrahedra alternating along c carry oppositely oriented spins. The magnetic moments of the four Cu^{2+} ions in the unit cell can be independent and a generalized helix characterizing the spin arrangement of each of them in the crystal is expressed as

$$S_j=\mathbf{A}\cos(\mathbf{k}\cdot\mathbf{r}_j+\psi)+\mathbf{B}\sin(\mathbf{k}\cdot\mathbf{r}_j+\psi).$$

The spin components are modulated by the wave vector **k**, and $\mathbf{r}_j$ is the radius vector to the origin of the jth unit cell. **A** and **B** are orthogonal vectors, which define the magnitude and direction of the axes of the helix, while ψ defines its phase. For the most general case 27 independent parameters should be considered. Since the available number of experimental observations does not allow to refine with confidence all of them, we imposed physically sound constraints: identical moment value for all four independent Cu^{2+} ions and a circular envelope of the helices. This lowered the number of independent parameters to 12.

Very good fits were obtained for a model (Fig. 5) in which the four Cu^{2+} moments in each tetrahedron form two

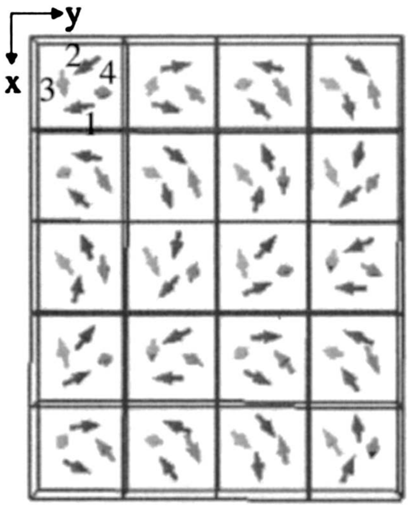

FIG. 5. The xy projection of the $Cu_2Te_2O_5Cl_2$ magnetic structure with the spin tetrahedra at the $z=0$ layer.

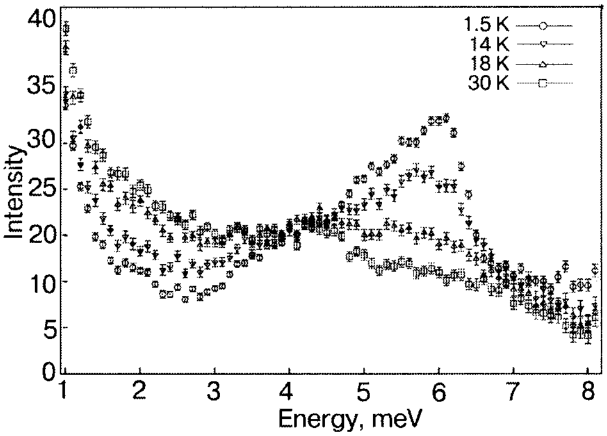

FIG. 6. Inelastic powder neutron scattering of $Cu_2Te_2O_5Cl_2$ integrated between 0.8 $Å^{-1}$ and 3.3 $Å^{-1}$ for four temperatures between 2 and 30 K. With incident energy $E_i=10.4$ meV inelastic focusing was adjusted to provide optimal resolution at 5 meV of 0.45 meV (full-width-half-maximum).

canted pairs: Cu1–Cu2 and Cu3–Cu4. The two spins of the pair share a common (**A**, **B**) plane, but the associated helices have different phases ψ. The difference between the phases defines the canting angle between spins of the pair α. The canting angle for the first pair is $\alpha_{12}=38(6)$ deg and for the second pair $\alpha_{34}=111(14)$ deg. The amplitude of the magnetic moment carried by each Cu^{2+} ion is $0.67(1)\mu_B$ at 1.5 K. It is interesting that the vector sum of the spins of one pair is the same for all tetrahedra in the crystal ($m_{12}=1.27(6)\mu_B$, $m_{34}=0.76(14)\mu_B$), while the local magnetic moment of the tetrahedra is not zero and changes from one unit cell to another. For an isotropic exchange the spin state of the tetrahedra would be zero, so our model might suggest that the two intra-tetrahedral couplings J_1 and J_2 are different and that the J_2 interaction is stronger.

Such a particular magnetic ground state might be a consequence of one dominant interaction or result from contributions of several inter-tetrahedral couplings of similar strengths. We tried to attribute the observed reciprocal wave vector $\mathbf{k}'=(-0.15,0.42,1/2)$ to some specific exchange inter-tetrahedral path in the structure and found a simple correlation not to $\mathbf{k}'$, but to the vector $(-0.15,-0.58,0)$. As this vector is related by a lattice translation to the vector $(-0.15,0.42,0)$, the two vectors mean a different choice of unit cell of the same magnetic structure. The ICM component is orthogonal to a specific set of planes containing the Cu^{2+} ions. One of these planes, presented by a double-line segment in Fig. 1, passes through the Cu2–Cu4 ions of the adjacent tetrahedra. This corresponds to the J_a coupling, which according to Ref. 10 is substantial and is mediated by the halogen orbitals. Based on these considerations we suggest that J_a is the dominant inter-tetrahedral coupling.

INELASTIC SCATTERING

Several inelastic neutron scattering studies have been performed to investigate the excitation spectrum of the $Cu_2Te_2O_5Cl_2$ system. Spectra from powder revealed in the ordered phase below T_N a spherically averaged density of states extending to a maximum at 6 meV, above which no significant scattering was detected up to 15 meV (Fig. 6). Raising the temperature above T_N, spectral weight shifted downwards to a broad quasi-elastic peak.

For single crystal neutron spectroscopy a single crystal was aligned with (3,1,0) and (0,0,1) in the horizontal scattering plane, such that (0.42,0.15,1/2) and the equivalent magnetic Bragg peaks were accessible given the wide (~5 deg) vertical resolution. Scans performed along the $Q=(h,h/3,3/2)$, (0.45,0.15,1), and (0,0,1) directions revealed two well defined excitation modes. One mode is completely dispersionless at 6.0 meV and shows no variation in intensity as a function of Q. The other mode displays strong dispersion along both accessible directions from a maximum energy close to the flat mode down to a minimum energy gap of 2.1 meV at the same positions in Q as the ICM magnetic Bragg peaks.

While more detailed modeling of the excitation spectrum is under way, several important conclusions can be read directly off the figure. If the system would be a collection of very weakly coupled tetramers, one would expect a series of essentially dispersionless modes. The strong dispersion observed in our measurements imply strong inter-tetrahedral coupling both within the ab plane and along the c axis. Secondly, a classical ordered magnetic structure with continuous symmetry of the order parameter should have gapless spin waves emerging from the magnetic Bragg peaks. The rather large energy gap must involve strong anisotropy terms in the Hamiltonian, whose origin remains to be determined.

SUMMARY

The presented results of neutron diffraction and inelastic neutron scattering evidence new details of the magnetic ordering in the $Cu_2Te_2O_5Cl_2$ compound. The idea of a single-k magnetic structure is strongly supported by the observed magnetic domains redistribution in an applied magnetic field. The presence of two different $\mathbf{k}$ and $\mathbf{k}'$ structures suggests that a number of ground states with equal or close energies might exist. The discovered relation between the incommensurate component of the wave vector and the inter-tetrahedral coupling J_a invites a theoretical revision of the $Cu_2Te_2O_5X_2$ system. The peculiar features of the spin excitation spectrum deserve further study.

The work was performed at SINQ, Paul Scherrer Institute, Villigen, Switzerland, at ILL reactor, Grenoble, France. We thank Prof. F. Mila, Dr. M. Prester, and Prof. A. Furrer for fruitful discussions and Swiss NCCR research pool MANEP of the Swiss NSF for financial support.

[*] E-mail: oksana.zaharko@pci.ch

---

[1] *Quantum Magnetism*, Vol. 645 of Lecture Notes in Physics, Springer-Verlag, Berlin, Heidelberg (2004).
[2] F. Mila, Eur. J. Phys. **21**, 499 (2000).
[3] A. P. Ramirez, "Geometrical frustration," in *Handbook of Magnetic Materials*, Vol. 13, Elsevier Science (2001).
[4] M. Johnsson, K. W. Tornroos, F. Mila, and P. Millet, Chem. Mater. **12**, 2853 (2000).
[5] P. Lemmens, K.-Y. Choi, E. E. Kaul, C. Geibel, K. Becker, W. Brenig, R. Valenti, C. Gross, M. Johnsson, P. Millet, and F. Mila, Phys. Rev. Lett. **87**, 227201 (2001).
[6] C. Gross, P. Lemmens, M. Vojta, R. Valenti, K.-Y. Choi, H. Kageyama, Z.

Hiroi, N. M. Mushnikov, T. Goto, M. Johnsson, and P. Millet, Phys. Rev. B **67**, 174405 (2003).
[7] J. Jensen, P. Lemmens, and C. Gross, Europhys. Lett. **64**, 689 (2003).
[8] O. Zaharko, A. Daoud-Aladine, S. Streule, J. Mesot, P.-J. Brown, and H. Berger, Phys. Rev. Lett. **93**, 217206 (2004).
[9] M. H. Whangbo, H. J. Koo, and D. Dai, J. Solid State Chem. **176**, 417 (2003).
[10] R. Valenti, T. Saha-Dasgupta, C. Gros, and H. Rosner, Phys. Rev. B **67**, 245110 (2003).
[11] M. Prester, A. Smontara, I. Živković, A. Bilušić, D. Drobac, H. Berger, and F. Bussy, Phys. Rev. B **69**, 180401(R) (2004).
[12] A. Perucchi, L. Deiorgi, H. Berger, and P. Millet, Eur. Phys. J. B **38**, 65 (2004).
[13] W. Brenig and K. W. Becker, Phys. Rev. B **64**, 214413 (2001).
[14] W. Brenig, Phys. Rev. B **67**, 64402 (2003).
[15] K. Totsuka and H.-J. Mikeska, Phys. Rev. B **66**, 54435 (2002).
[16] V. N. Kotov, M. E. Zhitomirsky, M. Elhajal, and F. Mila, Phys. Rev. B **70**, 214401 (2004).
[17] V. N. Kotov, M. E. Zhitomirsky, M. Elhajal, and F. Mila, J. Phys.: Condens. Matter **16**, S905 (2004).

This article was published in English in the original Russian journal. Reproduced here with stylistic changes by AIP.

LOW TEMPERATURE PHYSICS VOLUME 31, NUMBERS 8–9 AUGUST–SEPTEMBER 2005

Antiferromagnet-ferromagnet phase transition in lightly doped manganites

I. O. Troyanchuk* and V. A. Khomchenko

Institute of Solid State and Semiconductor Physics, NAS, 17 P. Brovka St., Minsk 220072, Belarus

V. V. Eremenko and V. A. Sirenko†

B. Verkin Institute for Low Temperature Physics and Engineering of the National Academy of Sciences of Ukraine, 47 Lenin Ave., Kharkov 61103, Ukraine

H. Szymczak

Institute of Physics, PAS, 32/46 Lotnikow Str., Warsaw 02-668, Poland

(Submitted February 18, 2005)
Fiz. Nizk. Temp. **31**, 1073–1080 (August–September 2005)

Magnetic and structural phase diagrams of the $La_{0.88}MnO_x$, $La_{1-x}Sr_x(Mn_{1-x/2}Nb_{x/2})O_3$, $Nd_{1-x}Ca_xMnO_3$, and $Bi_{1-x}Ca_xMnO_3$ series, constructed on the basis of x-ray, neutron powder diffraction, Young's modulus, magnetization and resistivity measurements, are presented. It is shown that the main factor controlling the antiferromagnet-ferromagnet phase transition in the manganites is a type of an orbital state. The results are discussed in the framework of structurally driven magnetic phase separation model. © *2005 American Institute of Physics.* [DOI: 10.1063/1.2008144]

I. INTRODUCTION

Mixed-valence manganites with a perovskite structure are the model objects for the physics of strongly correlated electronic systems. The interest in the study of manganites is due to a variety of phase states and transitions and intrinsic correlation of the crystal structure, magnetic, and transport properties. The nature of the interplay between the crystal structure, magnetic, and transport properties of manganites is still a matter of discussion in spite of numerous investigations. Several models have been proposed to explain a magnetic state evolution under hole doping as well as a metal-insulator transition at the Curie point. In the double-exchange model of Zener, simultaneous ferromagnetic and metallic transitions have been qualitatively explained by the fact that electrons tend to move between Mn^{3+} and Mn^{4+} ions having the same spin orientation, therefore electron delocalization favors the ferromagnetic order.[1] More recently Millis *et al.* pointed out that double exchange alone cannot account for many of the experimental results.[2] They showed that a Jahn-Teller-type electron-phonon coupling should play an important role in explanation of the colossal magnetoresistance effect. Another mechanism of antiferromagnet-ferromagnet phase transitions in manganites was proposed by Nagaev.[3] He assumed that the intermediate phase can be described as a inhomogeneous magnetic state driven by an electronic phase segregation. In this scenario the ferromagnetic regions contain an excess of holes and are metallic. Goodenough *et al.* argued that the magnetic properties of manganites were determined by the type of orbital state.[4] According to the rules for 180° superexchange, if the electronic configuration correlates with vibrational modes, $Mn^{3+}—O^{2-}—Mn^{3+}$ interactions are antiferromagnetic in case of the static Jahn-Teller effect and ferromagnetic when the Jahn-Teller effect is dynamic. Thus, antiferromagnet-ferromagnet phase transitions can occur going through a mixed state of phases with different orbital dynamics.

The recent magnetic phase diagrams of the $La_{1-x}Sr_xMnO_3$ and $La_{1-x}Ca_xMnO_3$ systems were constructed assuming a homogeneous canted magnetic state in a low doping range.[5,6] On the other hand, there are numerous experimental data which indicate the existence of phase separation in manganites. The results of nuclear magnetic resonance,[7,11] neutron diffraction,[11,12] muon spin relaxation,[13] x-ray absorption,[14] scanning tunneling spectroscopy,[15] and electron microscopy[16] experiments give evidence of magnetic and structural inhomogeneities, but the driving force of magnetic phase separation in manganites is still not fully clear. In order to contribute to the solution of this problem we have investigated the features of the antiferromagnet-ferromagnet phase transition in low-doped $La_{0.88}MnO_x$, $La_{1-x}Sr_x(Mn_{1-x/2}Nb_{x/2})O_3$, $Nd_{1-x}Ca_xMnO_3$, and $Bi_{1-x}Ca_xMnO_3$ manganites.

II. RESULTS AND DISCUSSION

A. $La_{0.88}MnO_x$ system

Tentative magnetic phase diagram of the $La_{0.88}MnO_x$ $\times(2.82 \leqslant x \leqslant 2.96)$ manganites is shown in Fig. 1. The most strongly reduced sample $La_{0.88}MnO_{2.82}$ is an antiferromagnet with a Néel temperature of 140 K. Its properties are found to be similar to the properties of stoichiometric $LaMnO_3$. Both compounds have very close unit cell parameters, the same magnetization value, and close temperatures of both magnetic ($T_N \sim 140$ K) and orbital orderings ($T_{OO} \sim 750$ K). The existence of orbital ordering in the A-type antiferromagnetic structure of $La_{0.88}MnO_{2.82}$ is corroborated by neutron diffraction measurements.[17] With increasing oxygen content up to the $x=2.85$ sample, the magnetic and orbital ordering temperatures lower while the magnetization increases

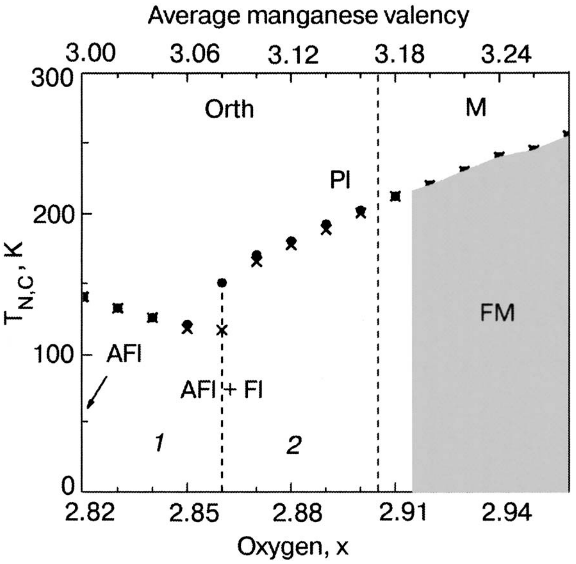

FIG. 1. Magnetic phase diagram of the $La_{0.88}MnO_x$ ($2.82 \leqslant x \leqslant 2.96$) system. Orth—orthorhombic crystal structure, M—monoclinic crystal structure; PI, AFI, FI, and FM—paramagnetic insulating, antiferromagnetic insulating, ferromagnetic insulating, and ferromagnetic metallic states, respectively. Areas 1 and 2 correspond to the concentration regions where an antiferromagnetic or ferromagnetic phase predominates, respectively.

slightly. Results of the neutron diffraction measurements carried out for the $x = 2.84$ sample confirm the appearance of a ferromagnetic component. A further increase of the oxygen concentration leads to a significant enhancement of the ferromagnetic contribution. The transition temperature to the paramagnetic state begins to increase and the transition becomes broader. Neutron diffraction data obtained for the $x = 2.87$ sample indicate that ferromagnetic coupling becomes predominant. No long-range antiferromagnetic order has been observed for this compound. At the same time, the refined magnetic moment is lower than that expected for the full spin arrangement. Besides, the relatively large magnetic anisotropy at low temperature assumes the presence of an anisotropic magnetic coupling which differs from the isotropic ferromagnetic one. This can be attributed to existence of either short-range antiferromagnetic clusters or a spin-glass phase. No pronounced thermomagnetic irreversibility indicating the anisotropic magnetic interactions is observed starting from the $x = 2.92$ sample. The values of magnetization estimated for the monoclinic compounds are close to those expected for full spin alignment. The ground state of all the orthorhombic compounds $2.82 \leqslant x \leqslant 2.90$ is insulating. It should be noted that the appearance of metallic conductivity does not coincide with the transition to monoclinic phase. Simultaneous first-order magnetic transition and metal-insulator transition at T_C are observed for $x \geqslant 2.92$ compounds.

A strong correlation between the magnetic and structural properties of $La_{0.88}MnO_x$ ($2.82 \leqslant x \leqslant 2.96$) manganites is observed. The hypothetical structural phase diagram of $La_{0.88}MnO_x$ ($2.82 \leqslant x \leqslant 2.96$) constructed using x-ray, neutron diffraction, Young's modulus, resistivity, and DTA data is shown in Fig. 2. For $La_{0.88}MnO_{2.82}$, the sharp anomalies of the Young's modulus and resistivity are associated with the removal of cooperative orbital ordering; it is observed at approximately 650 K. The DTA measurements revealed the release of latent heat in the range 650–730 K. Neutron diffraction data indicate the coexistence of orbitally ordered O^I and orbitally disordered O phases at $T = 700$ K. Another thermal anomaly connected with the transition to the monoclinic phase is observed in the temperature range $915 \leqslant T \leqslant 960$ K. With the increase of the oxygen content to $x = 2.83$, the temperatures of both orbital order-disorder and orthorhombic-monoclinic phase transitions decrease significantly. The range of coexistence of O^I and O phases becomes broader, while the width of the anomaly associated with the temperature-induced orthorhombic-monoclinic transition remains practically constant. Starting from the $x = 2.84$ sample, the differential thermal analysis does not show any significant heat effect, which could be interpreted as a transition to a pure orbitally disordered state; however, the anomaly related to the transition from an orthorhombic to a monoclinic phase remains well pronounced. Neutron diffraction data coupled with Young's modulus measurements indicate the existence of predominantly static Jahn-Teller distortions at room temperature and two-phase character of the crystal structure above $T \sim 470$ K. Inhomogeneous structural states are observed up to 650 K. Above this temperature the monoclinic phase is stabilized. A further increase of the oxygen concentration leads to the broadening and gradual disappearance of the anomaly which relates to the transition to the orbitally ordered state. The neutron diffraction study performed for the $La_{0.88}MnO_{2.87}$ compound indicates that the value of the MnO_6 octahedron distortion increases with decreasing temperature to 200 K. However, even in the case of $T = 200$ K, where the worst agreement factors for one-phase structural model have been observed, the introduction of the second orthorhombic phase was unsuccessful. Apparently, even at 200 K, the orbitally ordered clusters are still too small and separate to distinguish the O^I phase in the diffraction experiment. The temperature of orthorhombic-monoclinic phase transition gradually decreases as the oxygen content increases and starting from the $x = 2.91$ sample, the monoclinic phase is stabilized (Fig. 2). It is necessary to mention that the x-ray and neutron diffraction experiments can reveal a two-phase structural state rather in the case of macroscopic structural phase separation. In the cases of local structural inhomogeneities or nanometer scale structural clusters, these experiments give only an average picture of a structural state.[18] Thus, the correlation between the orbital state and magnetic properties of the $La_{0.88}MnO_x$ manganites is prominent. The static Jahn-Teller distortions are responsible for the *A*-type antiferromagnetic structure, while dynamic orbital correlations lead to ferromagnetism.

It is worth noting that there are two alternative models of orbital state corresponding to ferromagnetic ordering in manganites: 3D dynamic $d_{3z^2-r^2}$ orbital correlations and staggered ordering of $d_{3z^2-r^2}$ and $d_{x^2-y^2}$ orbitals. Neutron diffraction studies have shown that $LaMnO_3$ undergoes a structural transition from O^I-orthorhombic to O-orthorhombic phase at $T_{JT} = 750$ K.[19] The MnO_6 octahedron in the O-orthorhombic phase becomes nearly regular, i.e., the orbital ordering disappears.[19] However, x-ray absorption near the edge structure and the extended x-ray absorption fine structure at the Mn*K*-edge measurements have re-

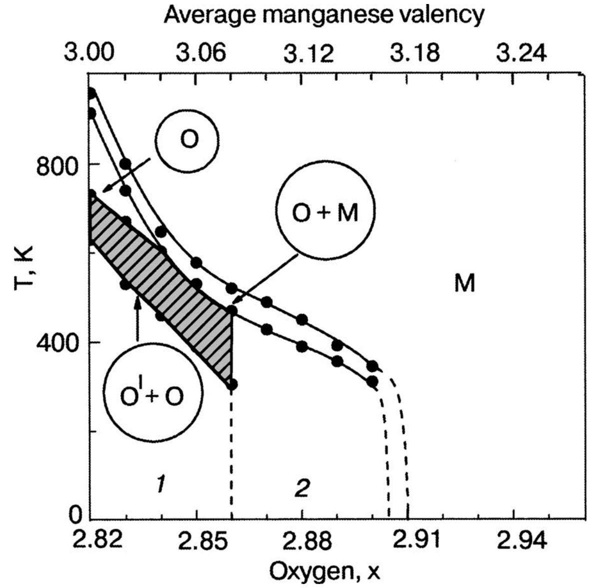

FIG. 2. Crystal structure phase diagram of the $La_{0.88}MnO_x$ ($2.82 \leq x \leq 2.96$) system. O^I, O, and M are orbitally ordered orthorhombic, orbitally disordered orthorhombic, and monoclinic phases, respectively. Areas 1 and 2 correspond to the concentration regions where the static Jahn-Teller distortions or dynamic orbital correlations predominate, respectively.

vealed that the MnO_6 octahedrons in $LaMnO_3$ remain tetragonally distorted at $T > T_{JT}$.[20] The empty Mn^{3+} electronic d states were shown to be unaltered through the Jahn-Teller transition. The lowest energy for the e_g electron corresponds to the three possible distortions giving to three degenerate vibronic states, $d_{x^2-r^2}$, $d_{y^2-r^2}$, and $d_{z^2-r^2}$, being the electronic orbitals of the vibronic state. The thermally excited electron jumps between these states above T_{JT} and is localized in an ordered state below T_{JT}. The orbital ordering proposed for $LaMnO_3$ arises then from the ordering of the local Jahn–Teller distortions. The high temperature (O-orthorhombic) phase can be described as a dynamical locally distorted phase with the strong antiferrodistortive first-neighbor coupling.[20]

A similar situation seems to be observed for Mn^{4+}-doped manganites. The atomic pair-density function of $La_{1-x}Sr_xMnO_3$ manganites ($0 \leq x \leq 0.4$), obtained by pulsed neutron diffraction, indicates the existence of tetragonally distorted MnO_6 octahedrons even in the rhombohedral metallic phase, when the crystallographic structure shows no JT distortions.[21] This is possible only in the case of the dynamic orbital correlations described above. One can assume that when one puts non-Jahn–Teller Mn^{4+} ions in the background of the Mn^{3+} ions, the e_g orbitals of all the Mn^{3+} ions surrounding the localized hole (Mn^{4+}) tend to be directed towards it, forming an orbital polaron.[22] Due to the strong antiferrodistortive Mn^{3+} first-neighbor coupling,[20] dynamic correlations of the $d_{3z^2-r^2}$ orbitals should arise.

According to the rules for 180° superexchange the dynamic orbital correlations lead to ferromagnetic interaction between the Mn^{3+} ions.[4] Hence, one can expect that ferromagnetism in manganites can arise even in the absence of Mn^{4+} ions, if only the JT effect is dynamic. For instance, Mn substitution with non-Jahn-Teller diamagnetic Nb^{5+}, Al^{3+}, Sc^{3+}, etc, ions should result in the appearance of ferromagnetic order. Below we show that this assumption is correct.

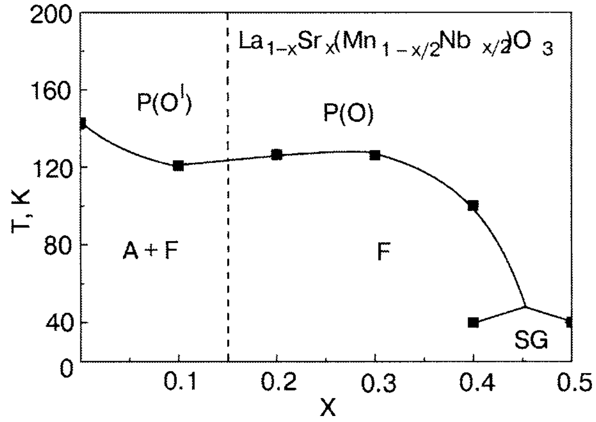

FIG. 3. Magnetic phase diagram for $La_{1-x}Sr_x(Mn_{1-x/2}Nb_{x/2})O_3$ series (A is antiferromagnet, F is ferromagnet, P is paramagnet, SG is spin glass; O^I and O are orbitally ordered and orbitally disordered phases, respectively).

The second possibility lies in description of the orbital state as a hybridization of the $d_{3z^2-r^2}$ and $d_{x^2-y^2}$ orbitals as $\cos(\theta/2)|3z^2-r^2\rangle \pm \sin(\theta/2)|x^2-y^2\rangle$. Such an orbital ordering was recently proposed experimentally and theoretically in the ferromagnetic insulating phase of $La_{0.88}Sr_{0.12}MnO_3$ and $Pr_{0.75}Ca_{0.25}MnO_3$.[23–25] The difficulties in determination of priority of the present models are conditioned by the fact that staggered ordering of $d_{3z^2-r^2}$ and $d_{x^2-y^2}$ orbitals can exhibit itself in experiments in the same way as 3D dynamic $d_{3z^2-r^2}$ orbital correlations.

B. $La_{1-x}Sr_x(Mn_{1-x/2}Nb_{x/2})O_3$ system

A hypothetical magnetic phase diagram of $La_{1-x}Sr_x(Mn_{1-x/2}Nb_{x/2})O_3$ is shown in Fig. 3. The parent $LaMnO_3$ compound shows the spontaneous magnetization value at 5 K corresponding to magnetic moment of $0.07\mu_B$ per Mn^{3+} ion. The Néel point, where spontaneous magnetization develops, is 143 K. According to Ref. 26 the spontaneous magnetization has a relativistic nature. Substitution of Mn with Nb leads to an enhancement of the spontaneous magnetization whereas the temperature of transition into paramagnetic state slightly decreases. In accordance with the magnetization data the $La_{0.8}Sr_{0.2}(Mn_{0.9}Nb_{0.1})O_3$ and $La_{0.7}Sr_{0.3}(Mn_{0.85}Nb_{0.15})O_3$ samples are ferromagnets with the magnetic moment per chemical formula around $2.3\mu_B$ and $2.6\mu_B$, respectively. Neutron diffraction study has revealed the magnetic moment of Mn^{3+} in the parent $LaMnO_3$ antiferromagnetic compound to be close to $3.5\mu_B$,[27] whereas Nb^{5+} is a diamagnetic ion, and hence the expected moment should be close to $3\mu_B$ per formula unit, in rather good agreement with the observed value. The Nb doped sample ($x=0.3$) has a well-defined Curie point: 123 K. Both Curie point and spontaneous magnetization start gradually to decrease when the Nb content exceeds 15% of the total number of sites in the manganese sublattice. The magnetic state changes cardinally as the concentration of niobium reaches 25%. We have observed the magnetic susceptibility of the $x=0.5$ sample dramatically decreases. ZFC magnetization shows a peak at 30 K. Below this temperature FC magnetization practically does not change. Taking into account the

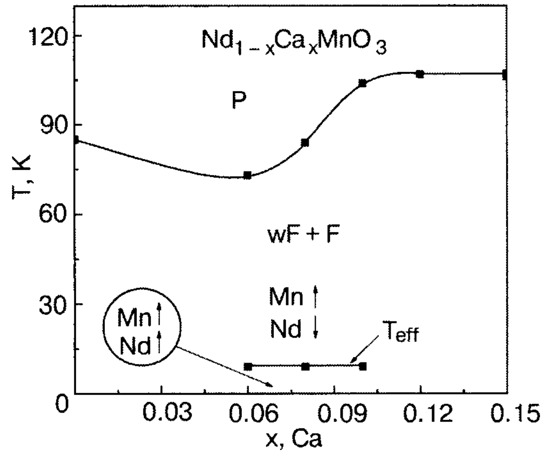

FIG. 4. Magnetic phase diagram of the $Nd_{1-x}Ca_xMnO_3$ low-doped manganites: wF is weak ferromagnet, F is ferromagnet, P is paramagnet, T_{eff} is the effective temperature of the reorientational phase transition.

character of $M(H)$ dependence we have concluded that the sample $x=0.5$ can be considered as spin glass with $T_f=30$ K. We can explain the collapse of long range ferromagnetic ordering by a diamagnetic dilution of the Mn sublattice. According to resistivity versus temperature measurements $La_{1-x}Sr_x(Mn_{1-x/2}Nb_{x/2})O_3$ samples are semiconductors. Below the Curie point a large value of the magnetoresistance is observed.

The results presented here deal with the facts that the Nb-doped $La_{1-x}Sr_x(Mn^{3+}_{1-x/2}Nb^{5+}_{x/2})O_3$ samples enriched with Mn^{3+} ions are ferromagnetic and show a large magnetoresistance. It is worth noting that the possibility of the existence of ferromagnetic ordering in the manganites, despite the absence of Mn^{3+} ions, reject the double exchange and the electronic phase separation concepts. The result obtained indicates an important role of ferromagnetic superexchange via oxygen scenario of magnetic interactions in manganites. According to the superexchange mechanism the $Mn^{3+}-O-Mn^{3+}$ and $Mn^{3+}-O-Mn^{4+}$ 180° magnetic interactions are strongly ferromagnetic for the orbitally disordered state whereas the $Mn^{4+}-O-Mn^{4+}$ ones are strongly antiferromagnetic.[4] The Curie point associated with $Mn^{3+}-O-Mn^{3+}$ positive superexchange may be close to room temperature for manganites with perovskite structure because our samples contain diamagnetic Nb^{5+} ions, which should strongly decrease the Curie point. The stoichiometric compound $LaMn^{3+}O_3$ also shows ferromagnetic interactions between Mn^{3+} ions when cooperative Jahn-Teller distortions have vanished at $T=750$ K. The orbital ordering changes the character of superexchange magnetic interactions, which in the orbitally ordered state become anisotropic.[4,28]

C. $Nd_{1-x}Ca_xMnO_3$ system

The hypothetical magnetic phase diagram of the $Nd_{1-x}Ca_xMnO_3$ system at low Ca doping level is presented in Fig. 4. Neutron diffraction shows that the samples with $x<0.08$ consist mainly of antiferromagnetic phase while at $x\geqslant 0.08$ the ferromagnetic component dominates. Under hole doping the temperature of the transition into paramagnetic state at first decreases and then around $x=0.1$ increases. We have observed two magnetic phase transitions in the range $0.06\leqslant x\leqslant 0.1$ as temperature decreases.

The $Nd_{1-x}Ca_xMnO_3$ solid solutions contain two types of magnetically active sublattices: neodymium and manganese ones. At first we discuss the Nd contribution into magnetic properties. The f-f exchange interaction in rare-earth sublattice is as a rule rather weak in comparison with d-d interaction between manganese ions. One can expect that neodymium magnetic moments should order as a result of f-d exchange interactions between neodymium and manganese sublattices. The study of magnetic properties of $Nd_{1-x}Ca_xMnO_3$ samples confirm this viewpoint. According to neutron diffraction data the magnetic moments of neodymium ions start to be ordered slightly below T_N. The magnetic moment of the Nd ion is about $1.2\mu_B$ at 2 K and is directed opposite to weak ferromagnetic vector in $NdMnO_3$, while in the sample $x=0.12$ the orientation of the Nd and Mn magnetic moments is the same. In the range $0.06\leqslant x\leqslant 0.10$ metamagnetic behavior was observed in large magnetic fields (triple hysteresis loops with a negative remanent magnetization).

According to our hypothesis, samples in the range $0.06\leqslant x\leqslant 0.10$ consist of antiferromagnetic (weak ferromagnetic) and ferromagnetic phases which are exchange coupled at the boundary. The neodymium sublattice in both weak ferromagnetic and ferromagnetic phases orders nearby the Néel point (Curie point). However, the orientation of neodymium magnetic moments in these two phases is different: f-d exchange is positive for the ferromagnetic phase, whereas it is negative in weak ferromagnetic phase. The ferromagnetic phase strongly affects magnetic properties of weak ferromagnetic phase due to exchange coupling at the boundary. This interaction may induce a reorientational transition from antiparallel orientation of neodymium moments and weak ferromagnetics vector to parallel one. We believe that nearby certain temperature the ground state of the Nd^{3+} ions becomes degenerate because opposite contributions from exchange coupled ferromagnetic and weak ferromagnetic phases at Nd site become equal. According to theoretical consideration this state should be unstable thus leading to magnetic structure transformation.[29] A neutron diffraction study carried out for the $x=0.08$ sample is in agreement with this interpretation of the low-temperature phase transition.

On the basis of magnetization data we propose an H-T magnetic phase diagram of the $Nd_{0.92}Ca_{0.08}MnO_{2.98}$ compound (Fig. 5). Depending on the prehistory in the wide range of magnetic field the phases with parallel or antiparallel orientation of neodymium and manganese sublattices in weak ferromagnetic phase can be realized. One can see that the value of magnetic field required for the change of relative orientation of the Nd and Mn magnetic moments in the weak ferromagnetic phase increases as temperature rises. The width of a field range in which the hysteresis is observed practically does not depend on a temperature. This type of magnetic phase diagram is in agreement with crossover of energy sub-levels of Nd ions.

D. $Bi_{1-x}Ca_xMnO_3$ system

Figure 6 presents a magnetic phase diagram of the

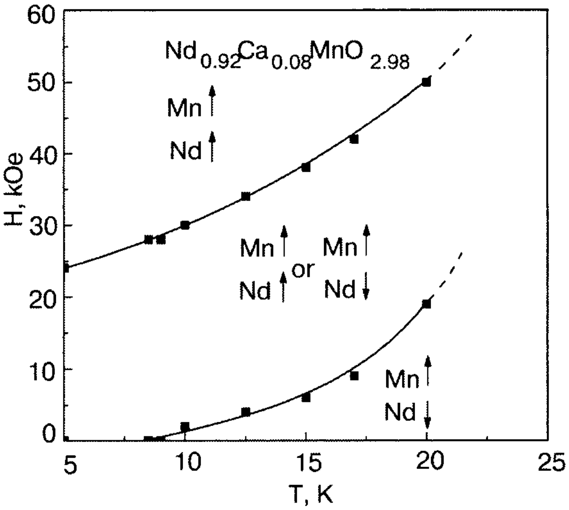

FIG. 5. The H-T magnetic phase diagram for the $Nd_{0.92}Ca_{0.08}MnO_{2.98}$ compound.

$Bi_{1-x}Ca_xMnO_3$ manganites. As the calcium content in the $Bi_{1-x}Ca_xMnO_3$ system increases, the latter passes through three different magnetic states, namely, ferromagnetic ($x \leqslant 0.1$), spin-glass ($0.15 \leqslant x \leqslant 0.25$), and antiferromagnetic ($x > 0.25$). In the case of antiferromagnetic compositions, the magnetic-ordering and structural-transformation temperatures vary only weakly within the concentration interval from $x = 0.25$ to 0.6. The ferromagnetic ordering in $BiMnO_3$ is most likely due to cooperative ordering of the $d_{x^2-y^2}$ orbitals.[30,31] With orbital ordering of this type, according to the Goodenough–Kanamori rules, ferromagnetic ordering becomes more energetically favorable than antiferromagnetic ordering. We may recall that rare-earth manganites exhibit orbital ordering of the d_{z^2} type, which stabilizes the A-type antiferromagnetic structure.[4] Orbital disorder in $BiMnO_3$ sets in, apparently, at a fairly high temperature, near 760 K. Replacement of bismuth ions by calcium results in the formation of quadrivalent manganese ions, which should be accompanied by destruction of orbital ordering due to the appearance of non-Jahn-Teller Mn^{4+} ions in the lattice. However, the orbitally disordered phase in manganites should be ferromagnetic,[4,28] whereas we observed a state of the spin-glass type. A direct transition from the antiferromagnetic to the spin-glass phase without passing through the ferromagnetic state was observed to occur in the rare-earth manganites $Sm_{1-x}Ba_xMnO_3$ and $Y_{1-x}Ca_xMnO_3$ ($x \sim 0.12$).[32,33] It should be pointed out that at approximately this concentration of rare-earth ions, the ferromagnetic-spin glass transition takes place in $Bi_{1-x}Ca_xMnO_3$.

There is more than one opinion on the nature of exchange interactions in manganites. The antiferromagnetic state certainly forms through oxygen-mediated superexchange interactions of the type Mn–O–Mn. Most researchers believe that the ferromagnetic state in manganites is created through double exchange, i.e., via direct carrier transfer between various lattice sites. In order for such an exchange mechanism to operate, manganese ions in different valence states must be present and the electrical conductivity must be high. The presence of manganese ions of different valencies is not a sufficient condition for high electrical conductivity; indeed, the $3d$ orbitals of manganese and the $2p$ orbitals of oxygen should also overlap strongly. It is believed that this parameter is controlled by the Mn–O–Mn bond angle.[4,30] The larger the lanthanide ion, the larger should be the Mn–O–Mn angle, the wider the $3d$ band, and, accordingly, the higher the magnetic ordering temperature and the electrical conductivity. It was observed that the magnetic state of the manganites also depends on the difference between the ionic radii of the rare-earth and the lanthanide ions. A large difference between the radii lowers, as a rule, the magnetic ordering temperature as a result of competition between various exchange interactions characterized by a large difference in the Mn–O–Mn angles. This is why the spin-glass state sets in in the $Sm_{1-x}Ba_xMnO_3$ system, wherein the average radius of the Sm and Ba ions is far larger than that between the Y and Ca cations in the $Y_{1-x}Ca_xMnO_3$ system.[32,33] However, in all rare earth manganites, the Mn^{3+}–O–Mn^{4+} exchange coupling in the orbitally disordered phase is apparently ferromagnetic. The Mn–O–Mn angles in bismuthbased manganites are fairly large, which is supported by structural studies[31] and the quite high Curie temperature of $BiMnO_3$. Hence, in the case of an orbitally disordered phase, one can expect the ferromagnetic part of exchange interactions to be dominant, which is at odds with experiment. Therefore, we believe that, in contrast to the rare-earth manganites, no orbitally disordered phase forms in the $BiMnO_3$ system in the concentration interval $0.1 \leqslant x \leqslant 0.3$. The spin-glass state forms in the $Bi_{1-x}Ca_xMnO_3$ system most likely as a result of competition between ferromagnetic interactions in $BiMnO_3$-type clusters and antiferromagnetic coupling in clusters in which the Mn^{3+} orbitals are frozen in random orientations. As the Ca^{2+} concentration increases, a new type of antiferromagnetic clusters, apparently due to charge ordering, appears. The existence in $Bi_{0.75}Ca_{0.25}MnO_3$ of large clusters, charge-ordered in a similar way to those in $Bi_{0.5}Ca_{0.5}MnO_3$, is suggested in studies of its elastic properties. Despite the presence of the spin-glass-type ground state, there is a certain fraction of states characterized by short-range order of the type of a charge-ordered phase, which is indicated by the fact that the Young modulus minima for the $x = 0.25$ and 0.35 compositions are close in temperature. We believe that the extremely high stability of the orbitally and charge-ordered states in bismuth-based manganites derives

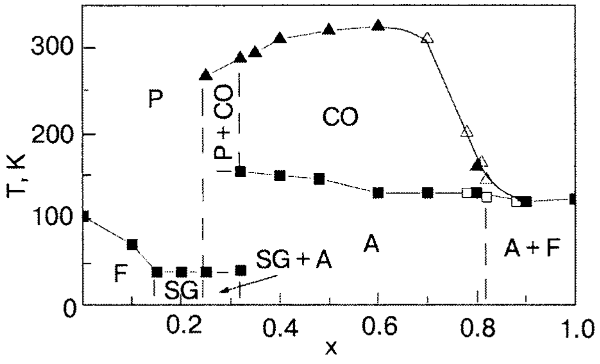

FIG. 6. Magnetic phase diagram of the $Bi_{1-x}Ca_xMnO_3$ manganites: A is antiferromagnet, F is ferromagnet, P is paramagnet, SG is spin glass, CO is charge-ordered state.

from the strongly anisotropic character of the Bi–O covalent bonding.

CONCLUSIONS

The magnetic and structural phase diagrams of $La_{0.88}MnO_x$, $La_{1-x}Sr_x(Mn_{1-x/2}Nb_{x/2})O_3$, $Nd_{1-x}Ca_xMnO_3$, and $Bi_{1-x}Ca_xMnO_3$ manganites have been proposed. It has been shown that the magnetic properties of the samples under study are determined by the type of their orbital state. The dynamic correlations of $d_{3z^2-r^2}$ orbitals favor ferromagnetic ordering in the manganites, while A-type antiferromagnetic structure is typical for the static Jahn-Teller distortions. It has been argued that concentrational transition from an antiferromagnetic to a ferromagnetic state occurs via the formation of inhomogeneous state due to structural phase separation mechanism.

This work was partly supported by Belarus and Ukrainian Fund for Basic Research (Grant F04MS-004 and Grant 10.01/001 F05K–012) Polish-Ukrainian Academies research project (No.4-2003), and by MES of Ukraine (Grant M/257-2004).

*E-mail: troyan@ifttp.bas-net.by
†E-mail: sirenko@ilt.kharkov.ua

---

[1] C. Zener, Phys. Rev. **82**, 403 (1951).
[2] A. J. Millis, B. I. Shraiman, and R. Müller, Phys. Rev. Lett. **77**, 175 (1996).
[3] E. L. Nagaev, Phys. Rep. **346**, 387 (2001).
[4] J. B. Goodenough, A. Wold, R. J. Arnott, and N. Menyuk, Phys. Rev. **124**, 373 (1961).
[5] G.-L. Liu, J.-S. Zhou, and J. B. Goodenough, Phys. Rev. B **64**, 144414 (2001).
[6] G. Biotteau, M. Hennion, F. Moussa, J. Rodríguez-Carvajal, L. Pinsard, A. Revcolevschi, Y. M. Mukovskii, and D. Shulyatev, Phys. Rev. B **64**, 104421 (2001).
[7] G. Allodi, R. De Renzi, and G. Guidi, Phys. Rev. B **57**, 1024 (1998).
[8] G. Papavassiliou, M. Fardis, M. Belesi, T. G. Maris, G. Kallias, M. Pissas, D. Niarchos, C. Dimitropoulos, and J. Dolinsek, Phys. Rev. Lett. **84**, 761 (2000).
[9] G. Papavassiliou, M. Belesi, M. Fardis, and C. Dimitropoulos, Phys. Rev. Lett. **87**, 177204 (2001).
[10] M. M. Savosta, V. I. Kamenev, V. A. Borodin, P. Novak, M. Marysco, J. Hejtmanek, K. Dorr, and M. Sahata, Phys. Rev. B **67**, 094403 (2003).
[11] P. A. Algarabel, J. M. De Teresa, J. Blasco, M. R. Ibarra, Cz. Kapusta, M. Sikora, D. Zajac, P. C. Riedi, and C. Ritter, Phys. Rev. B **67**, 134402 (2003).
[12] M. Hennion, F. Moussa, G. Biotteau, J. Rodriguez-Carvajal, L. Pinsard, and A. Revcolevschi, Phys. Rev. Lett. **81**, 1957 (1998).
[13] R. H. Heffner, L. P. Le, M. F. Hundley, J. J. Neumeier, G. M. Luke, K. Kojima, B. Nachumi, Y. J. Uemura, D. E. MacLaughlin, and S.-W. Cheong, Phys. Rev. Lett. **77**, 1869 (1996).
[14] C. H. Booth, F. Bridges, G. H. Kwei, J. M. Lawrence, A. L. Cornelius, and J. J. Neumeier, Phys. Rev. Lett. **80**, 853 (1998).
[15] M. Fath, S. Freisem, A. A. Menovsky, Y. Tomioka, J. Aarts, and J. A. Mydosh, Science **285**, 1540 (1999).
[16] M. Uehara, S. Mori, C. H. Chen, and S.-W. Cheong, Nature (London) **399**, 560 (1999).
[17] B. C. Hauback, H. Fjellvag, and N. Sakai, J. Solid State Chem. **124**, 43 (1996).
[18] T. Shibata, B. Bunker, J. F. Mitchel, and P. Schiffer, Phys. Rev. Lett. **88**, 207205 (2002).
[19] J. Rodriguez-Carvajal, M. Hennion, F. Moussa, A. H. Moudden, L. Pinsard, and A. Revcolevschi, Phys. Rev. B **57**, R3189 (1998).
[20] M. C. Sanchez, G. Subias, J. García, and J. Blasco, Phys. Rev. Lett. **90**, 045503 (2003).
[21] D. Louca, T. Egami, E. L. Brosha, H. Roder, and A. R. Bishop, Phys. Rev. B **56**, R8475 (1997).
[22] T. Mizokawa, D. I. Khomskii, and G. A. Sawatzky, Phys. Rev. B **63**, 024403 (2001).
[23] Y. Endoh, K. Hirota, S. Ishihara, S. Okamoto, Y. Murakami, A. Nishizawa, T. Fukuda, H. Kimura, H. Nojiri, K. Kaneko, and S. Maekawa, Phys. Rev. Lett. **82**, 4328 (1999).
[24] S. Okamoto, S. Ishihara, and S. Maekawa, Phys. Rev. B **61**, 14647 (2000).
[25] R. Kajimoto, H. Mochizuki, and H. Yoshizawa, Physica B **329–333**, 738 (2003).
[26] R. L. Rasera and G. L. Catchen, Phys. Rev. B **58**, 3218 (1998).
[27] E. O. Wollan and W. C. Koehler, Phys. Rev. **100**, 545 (1955).
[28] J. B. Goodenough, J.-S. Zhou, F. Rivadulla, and E. Winkler, J. Solid State Chem. **175**, 116 (2003).
[29] A. K. Zvezdin, V. M. Matveev, A. A. Mukhin, and A. I. Popov, *Rare-Earth Ions in Magnetically Ordered Crystsals* [in Russian], Nauka, Moscow (1985).
[30] I. O. Troyanchuk, N. V. Kasper, O. S. Mantytskaya, and S. P. Pastushonok, Zh. Éksp. Teor. Fiz., **105**, 239 (1994) [JETP **78**, 212 (1994)].
[31] T. Atou, H. Chiba, K. Ohoyama, Y. Yamaguchi, and Y. Syono, J. Solid State Chem. **145**, 639 (1999).
[32] I. O. Troyanchuk, D. D. Khalyavin, S. V. Truhanov, and H. Szymczak, J. Phys.: Condens. Matter **11**, 8707 (1999).
[33] R. Mathieu, P. Nordblad, D. N. H. Nam, N. X. Phuc, and N. V. Khiem, Phys. Rev. B **63**, 174405 (2001).

This article was published in English in the original Russian journal. Reproduced here with stylistic changes by AIP.

LOW TEMPERATURE PHYSICS VOLUME 31, NUMBERS 8–9 AUGUST–SEPTEMBER 2005

Odd magnetic dichroism of linearly polarized light in the antiferromagnet MnF_2

N. F. Kharchenko* and O. V. Miloslavskaya

B. Verkin Institute for Low Temperature Physics and Engineering, National Academy of Sciences of Ukraine, pr. Lenina 47, Kharkov 61103, Ukraine

A. A. Milner

Weizmann Institute of Science, Rehovot 76100, Israel

(Submitted July 11, 2005)
Fiz. Nizk. Temp. **31**, 1081–1088 (August–September 2005)

The two-sublattice tetragonal antiferromagnetic crystal manganese fluoride is found to exhibit dichroism induced by a magnetic field $H \| C_4 \| Z$ for linearly polarized light propagating along the tetragonal axis of the crystal also. The observed effect is odd with respect to the sign of the z projection of the field and the operation of reversing the directions of the sublattice magnetic moments of the antiferromagnet. The effect can be used for optical visualization of 180-degree (time-reversed) antiferromagnetic domains in MnF_2. *© 2005 American Institute of Physics.* [DOI: 10.1063/1.2008145]

INTRODUCTION

Manganese fluoride is a well-known model case of a purely spin two-sublattice tetragonal antiferromagnet (AFM). It has long served as a test object for checking theoretical ideas about the magnetic and elastic[1–3] properties of AFM crystals and their optical properties that result from the interaction of photons with the magnetic subsystem of the AFM and are manifested in the transparency region[4,5] and in the absorption[6–12] and scattering[12–14] of light.

Since the resultant orbital moment of the five $3d$ electrons of divalent manganese in MnF_2 is equal to zero and the spin of the Mn^{2+} ion is maximum, all of the electric-dipole transitions within the $3d^5$ configuration are doubly forbidden—by parity and by spin. The lowest-energy allowed electric-dipole transitions are of the type $^6S(3d^5) - {}^6P(3d^4 4p)$, and the charge-transfer transitions with the participation of the fluorine ions lie in the vacuum ultraviolet.[15] The zero value of the orbital moment in the ground state of the ion and the remoteness of the allowed electric-dipole optical transitions make for an extremely small value of the Faraday magnetooptic effect. Even in the visible range the contribution to the magnetic resonance transition effect is predominant over the electric-dipole contribution.[5]

For intra-configuration d-d transitions the spin selection rules are softened by the spin-orbit coupling. The parity forbiddenness is lifted in the presence of local static and dynamic breaking of inversion, in particular, for the simultaneous excitation of an exciton and magnon or of an exciton and odd phonon. In the exciton-magnon excitations the forbiddenness of the electric-dipole transition mechanism is lifted with respect to both parity and spin. Because of these mechanisms the absorption spectra of MnF_2 throughout the visible region exhibit weak excitonic magnetic-dipole transitions and their stronger electric-dipole satellites: exciton-magnon and exciton-phonon.[6–12] We note that the first observation of an exciton-magnon satellite in the absorption spectrum of an antiferromagnet was made on the MnF_2 crystal.[6]

Manganese fluoride is attracting attention not only in connection with opportunities for basic research.[16,17] In recent years there has been intensive study of the features of the magnetic hysteresis properties of magnetic heterostructures characterized by exchange-shifted magnetic hysteresis loops and containing ferromagnetic (FM) nanolayers or nanodots deposited on a crystalline slab or single-crystal film of an AFM. Research is being done on the mechanisms of exchange interaction between neighboring layers and the mechanisms giving rise to uniaxial magnetic anisotropy in the FM layer. Manganese fluoride, in particular, is used for the AFM base of these structures.[17] The presence of 180-degree (time-reversed) AFM domains in the AFM layer substantially alters their unidirectional magnetic properties. Therefore, in the creation of FM/AFM structures with specified hysteresis properties and also for creating structures with provisions for switching those properties, it is very desirable to have the possibility of visual monitoring and purposeful manipulation using 180-degree AFM domains.

The magnetic symmetry of AFM transition-metal fluorides allows effects which are sensitive to opposite orientations of the AFM vector. Because the anti-inversion operation $\bar{1}'$ is not among the symmetry elements of these crystals, the forbiddenness is lifted from unconventional magnetooptic effects—birefringence linear in the magnetic field or the linear magnetooptic effect (LMOE), and quadratic-in-magnetic-field rotation (QMR) of the plane of polarization of light. The LMOE and QMR have been observed[19] in the isostructural crystals CoF_2 and FeF_2. With the help of those effects, the 180-degree, or collinear antiferromagnetic domains have been visualized by an optical method;[20] previously those domains had been observed in these same crystals by a topographic method utilizing polarized neutron diffraction.[21]

In manganese fluoride neither the LMOE nor the QMR have been observed. The present study is devoted to the detection of the LMOE in the MnF_2 crystal. In the transparency region the expected effect is too small to be measured by the standard method. However, it was expected that the LMOE might manifest itself in the regions of the optical transitions, in effects which are odd in the field: magnetic linear birefringence and magnetic linear dichroism (MLD). The detection of LMOE could make it possible in principle to make optical observations of the collinear AFM domains in MnF_2, where they have been visualized previously only by methods of neutron topography. A test for the effects in question could be the presence of properties characteristic of the LMOE—oddness with respect to reversal of the field direction and oddness with respect to switching of the antiferromagnetic states (AFM^+ and $AFM^- = I' \cdot AFM^+$), connected to each other by the time inversion operation I'. The effect can be manifested most clearly in the longitudinal experimental geometry, $H \| k \| C_4$ (k is the wave vector), for which in the absence of magnetic field there is neither linear birefringence nor linear dichroism.

The inevitability that LMOE will be manifested in the MnF_2 crystal in the longitudinal experimental geometry can be seen from the following considerations. The magnetic point group of the AFM crystal, $4'/mmm'$, differs from the point group of the paramagnetic crystal, $4/mmm' \cdot I'$, by the circumstance that its tetragonal axis is an axis of symmetry only in combination with the time inversion operation. Since the symmetry group of the magnetic field does not contain the operation $4'$, in a magnetic field $H \| C_4$ the tetragonal crystal must, according to the Curie-Neumann symmetry principle, lower its symmetry to rhombic $mm'm'$ and become optically biaxial. The appearance of LMOE is due to the lifting of the energy quasi-degeneracy of the magnetic sublattices by the magnetic field. The unit cell of MnF_2 contains two magnetic ions, $Mn^{2+}(1)$ and $Mn^{2+}(2)$. The fluorine ions surrounding the manganese ions form distorted octahedra with symmetry $mmm(D_{2h})$. The octahedra for the $Mn^{2+}(1)$ sites are slightly elongated along the [110] axis, and those for the $Mn^{2+}(2)$ sites are elongated along $[1\bar{1}0]$. It can be assumed that the $Mn^{2+}(1)$ and $Mn^{2+}(2)$ sites form two interpenetrating optically biaxial subsystems possessing birefringence in the direction of the crystallographic axis C_4. Since the subsystems are rotated with respect to each other around C_4 by an angle of $\pi/2$, their birefringent properties in the direction of that axis are completely compensated. At temperatures below the Néel temperature T_N the spin moments of the magnetic ions lie along the tetragonal axis C_4 antiparallel to each other. In a magnetic field $H \| C_4$ the subsystems with spins directed along the field and the subsystems with spins directed counter to the field are no longer equivalent, and the compensation of the birefringent properties is broken. The dichroism and birefringence arising in magnetic field should be odd with respect to reversal of the magnetic field direction and at low fields should be proportional to the field strength, and their signs should be different for the antiferromagnetic states AFM^+ and AFM^- of the crystal. Together with the expected MLD, in the longitudinal geometry of the experiment there is also the usual magnetic circular dichroism (MCD), which was observed in Refs. 9 and 10. The presence of the two types of dichroism is equivalent to elliptical dichroism, which can always be represented as a superposition of circular and linear dichroisms. MLD, unlike MCD, is odd with respect to reversal of the directions of the magnetic moments of the sublattices.

LMOE is described by an axial c-tensor q_{ija} which is symmetric with respect to permutation of the first two indices and has components that change sign under the time inversion operation. The components of the tensor are identically zero in all antiferromagnets whose magnetic space group contains the antitranslation $\tau \cdot I'$ or anti-inversion $\bar{I}'$. The tensor q_{ija} has the same symmetry as the tensor describing the piezomagnetic effect. The matrices of the tensor for all magnetic crystals described by Shubnikov groups are given in Ref. 18. For a crystal with symmetry $4'/mmm'$ the tensor q_{ija} has only three nonzero components, $q_{yzx} = q_{xzy}$ and q_{xyz}. For $H \| C_4$ the LMOE is described by increments to the components of the dielectric tensor, $\Delta\varepsilon_{xy} = \Delta\varepsilon_{yx} = q_{xyz}H$. The field-induced dichroism for linearly polarized light is determined by the imaginary part of the tensor q_{xyz}.

In this paper we report the observation of magnetic field-induced dichroism of linearly polarized light in the region of three groups of absorption bands of the MnF_2 crystal, denoted in the literature as the A, C, and D groups. These groups are formed by the intra-configuration electronic transitions from the ground state ${}^6A_{1g}({}^6S_{5/2})$ of the Mn^{2+} ion to excited states split by the crystalline field and the spin-orbit coupling:

${}^6A_{1g}({}^6S_{5/2}) - {}^4T_{1g}({}^4G)$—the A group (in the 18480 cm^{-1} region)

${}^6A_{1g}({}^6S_{5/2}) - {}^4A_{1g}$, ${}^4E_g({}^4G)$—C group (in the 25300 cm^{-1} region)

${}^6A_{1g}({}^6S_{5/2}) - {}^4T_{2g}({}^4D)$—the D group (in the 28050 cm^{-1} region).

EXPERIMENT AND DISCUSSION

The manganese fluoride single crystals from which the samples were prepared were grown at the P. L. Kapitza Institute of Physics Problems. The samples were in the form of parallelepipeds with a base of around 2×2 mm and thickness 1.63 mm (for the spectral measurements in the A group of bands) and 0.19 mm (for measurements in the region of the C and D groups). With a double monochromator a spectral resolution in the MLD spectra of 2 cm^{-1} or better was obtained. The measurements were made by a modulation method with the use of a Jobin Yvon piezooptic modulator. The modulation frequency of the polarization of the light beam was 18 kHz. There was a provision for rotating the modulator around the optical axis of the apparatus so that the azimuths of the polarization axes of the light beam at the extremal phases of the modulation could be aligned parallel to specified orthogonal directions in the crystal. The samples were mounted in a capsule that was placed in a cold finger located in the evacuated cavity of a superconducting solenoid. The temperature of the sample was varied from 6 to 100 K by means of a heater mounted on the cold finger, and the measurements were made with a semiconductor thermometer glued to the capsule containing the sample.

The angle between the C_4 axis of the crystal and the direction of the light beam and also the angle between the C_4 axis and the axis of the solenoid were monitored visually by observation of the conoscopic figures. The axis of the light beam made an angle of less than 1° with the tetragonal axis of the sample. The cone angle of the irised light beam was not more than 1°. The optic axis of the crystal (the C_4 axis) was deviated from the magnetic-field direction by an angle close to 2°. The plane formed by the C_4 axis and the $\mathbf{H}$ vector was close to the (110) plane.

The presence of transverse magnetic-field components H_x and H_y gave the hope that, owing to the longitudinal magnetization $M_z = C_{zxy}H_xH_y$ induced by them, which is sensitive to the orientation of the antiferromagnetic vector, a uniform antiferromagnetic state will form in the sample[22] when it is cooled in a magnetic field H_x, H_y, H_z to temperatures below T_N. The discovery of the LMOE has made it possible to monitor a measure of the uniformity of the antiferromagnetic sample. As subsequent experiments showed, antiferromagnetic states close to the single-domain AFM$^+$ and AFM$^-$ states actually do form in the sample. The sample was heated to a temperature of around 100 K, i.e., above the Néel temperature $T_N = 67$ K, and then a magnetic field was applied ($H_x \approx 1.5$ kOe, $H_y \approx 1.6$ kOe, $H_z = +50$ kOe or $H_z = -50$ kOe), and the sample was cooled in that field to a temperature of 6 K.

The spectral measurements of the dichroism $\Delta D(\lambda) = (I_1 - I_2)/(I_1 + I_2)$ were carried out at a temperature of 6 K (here I_1 and I_2 are the intensities on emergence from the sample, of the light beams which on incidence had been polarized along the crystallographic directions [110] and $[1\bar{1}0]$, respectively). In measurements of the circular dichroism, I_1 and I_2 correspond to right and left circular polarization of the incident beams. The spectral resolution in the measurements was close to 2 cm^{-1}, and the error of determination of the absolute values of the photon energies was around 5 cm^{-1}. The values given here for the energies of the optical transitions and the oscillator strengths are the standard values taken from Ref. 8.

The values of the MCD and MLD are proportional to the splitting of the absorption bands in the magnetic field. The splitting of the exciton absorption band differs little from that of the absorption band at the intra-ion electronic transition, which is equal to

$$\Delta E_{\mathrm{ex}} = 2\mu_B H(g_0 S_0 - g_{\mathrm{ex}} S_{\mathrm{ex}}) = 2\mu_B H[S_0(g_0 - g_{\mathrm{ex}}) + g_{\mathrm{ex}}].$$

Here g_0, S_0 and $g_{\mathrm{ex}}, S_{\mathrm{ex}} = S_0 - 1$ are the g factors and spins of the ground and excited states, and μ_B is the Bohr magneton. The splitting of the exciton-magnon band,

$$\Delta E_{\mathrm{ex}-m} = 2\mu_B H(g_0 S_0 - g_{\mathrm{ex}} S_{\mathrm{ex}}) - 2\mu_B g_0 H$$
$$= 2\mu_B H(g_0 - g_{\mathrm{ex}}) S_{\mathrm{ex}}$$

is much smaller, since the g factors of the ground and excited states of the Mn^{2+} ion are close in value. Splitting of the exciton-magnon bands was not observed in the spectroscopic experiments.[7,8] It was determined from the value of the MCD in the band.[9,10] The value of the dichroism is proportional not only to the splitting but also to the intensity of the band, and the magnetic dichroisms of the exciton and exciton-magnon bands can therefore be close. In the experiments the MCD of the exciton band in the C group was approximately 3 times larger than the MCD of the exciton-magnon satellites.[10] In the A group the MCD of the exciton-magnon band was larger than the MCD of the exciton band, while the values of the dichroism differed less.[9] In our experiments the qualitative relationship between the values of the MCD in the exciton and exciton-magnon bands of these groups was the same, although the quantitative difference for the bands in the C group was smaller. The spectra of the MLD measured in this study reflected the structure of the groups of bands, but the relationship between the contributions of the exciton and exciton-magnon transitions was different.

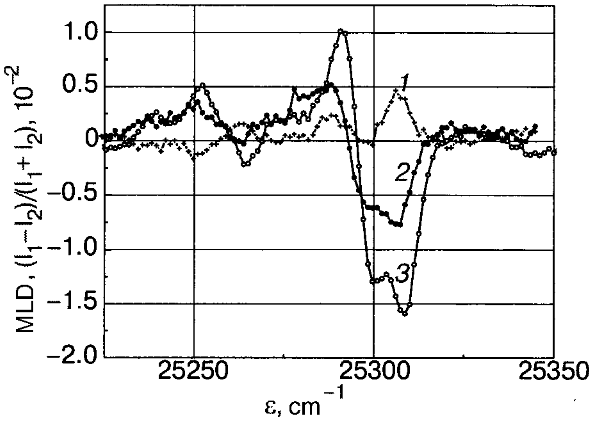

FIG. 1. Spectra of magnetic linear dichroism of MnF_2 in the region of the optical transition $^6A_{1g}(^6S_{5/2}) - {^4E_g}$, $^4A_{1g}(^4G)$ (the C group of bands), obtained at a field strength $H_z = +61$ kOe for different states of the sample. Curves *1* and *2* were obtained for different parts of a sample that had not been subjected to thermomagnetic treatment and contained collinear AFM domains. Curve *3* was obtained after a single-domain state AFM$^+$ had been created in the sample.

Figure 1 shows the results of a measurement of the MLD in the C group in different states of the sample. Curves *1* and *2* were obtained in a field $H_z = +61$ kOe with light passing through different parts of the sample, which had not been subjected to thermomagnetic treatment and was separated into AFM$^+$ and AFM$^-$ domains. It is seen that in one part (curve *1*) the MLD is close to zero; light passes through domains of both AFM states, and the path of the light in the AFM$^-$ domain is slightly longer than the path in the AFM$^+$ domain. In the other part (curve *2*) the AFM$^+$ domain is predominant. Curve *3* was obtained at the same field but with the sample prepared in a uniform AFM$^+$ state beforehand.

Figure 2 gives the spectra of the MLD of this same group, obtained in a single-domain sample in magnetic fields of different strength. One notices that in the absence of field the linear dichroism actually vanishes in the region of some absorption bands but remains well noticeable in the region of other bands. The cause of this behavior of the linear dichroism can be linked to different sensitivity of the optical transitions to the deviation from the ideal sample orientation $C_4 \| k \| H$ and to the presence of macroscopic strains in the sample. The variation of the value of the dichroism at the extrema of the spectrum with increasing field is close to linear.

Figure 3 shows the spectra of the MLD in the region of all three absorption groups. Prior to the measurements a suitable thermomagnetic treatment of the samples was carried out to prepare a uniform AFM state in them. The spectra of the MLD and the absorption spectrum of the MnF_2 crystal in the region of the A group of bands, formed by the so-called σ_1 and σ_2 magnon satellites of the electronic magnetic di-

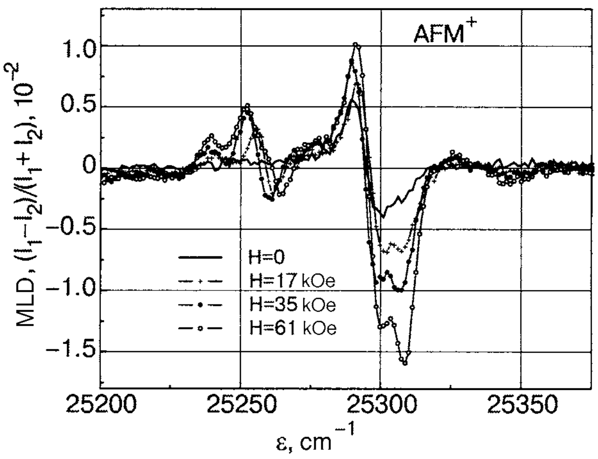

FIG. 2. Spectra of magnetic linear dichroism of $\mathrm{MnF_2}$ in the region of the *C* group of bands, measured for different values of the magnetic field strength. The sample was found in the $\mathrm{AFM^+}$ state.

pole transitions $^6A_{1g}(^6S_{5/2})-{}^4T_{1g}(^4G)$ are presented in Fig. 3a. The electronic transitions (not seen in the α spectrum) occur upon the absorption of photons with energies of $18418\ \mathrm{cm^{-1}}$ and $18435\ \mathrm{cm^{-1}}$ and have close values of the oscillator strength (3.4×10^{-11} and 3.0×10^{-11}). Electrons from the almost unsplit ground state $^6A_{1g}(t_{2g}^3e_g^2)$ of the manganese ion make a transition to the orbital components B_2 and B_3 of the excited state $^4T_{1g}(^4G)$, which is split by the spin-orbit coupling and the orthorhombic crystalline field. The electronic configuration of the excited states is close to $t_{2g}^4e_g^1$. The arrows indicate the positions of the maxima of the bands of their electric-dipole satellites (18476 and $18484\ \mathrm{cm^{-1}}$). These absorption bands (the oscillator strengths are 1×10^{-9} and 1.4×10^{-9}) are due to the simultaneous excitation of an exciton and a magnon, which propagate through different sublattices in opposite directions along the crystallographic axes [001] and [111]. Here the absorption of light is excited primarily by excitons and magnons with the maximal momenta, which correspond to the points *Z* and *A* in the Brillouin zone.

The induced linear dichroism in this group reaches its largest value (2.5×10^{-2} at a field strength $H_z=50$ kOe) in the vicinity of the first exciton-magnon transition. The sign of the field-induced dichroism changes when the direction of the magnetic field is reversed while the direction of the antiferromagnetic vector remains the same. This property is demonstrated in Fig. 3a. A sign change of the MLD also occurs when the antiferromagnetic state is changed from $\mathrm{AFM^+}$ to $\mathrm{AFM^-}$. The switching of the AFM states occurred, as expected, after the sample was heated to a temperature above the Néel point and then cooled in magnetic field. The prepared AFM state of the sample persisted as metastable in the oppositely directed field up to a strength of 61 kOe (the maximum field strength in the experiment) if the sample temperature was low enough ($T=6$ K). This is attested by the fact that the MLD spectra recorded for the $\mathrm{AFM^+}$ and $\mathrm{AFM^-}$ states at the same magnetic field are almost completely identical (up to the sign); see Fig. 3b. However, if the sample temperature was high enough (25–30 K), then in the geometry we used, a partial switching of the AFM state occurred as the field was increased—domains of the other, magnetically reversed (time-reversed) AFM state formed, and the value of the magnetic dichroism decreased.

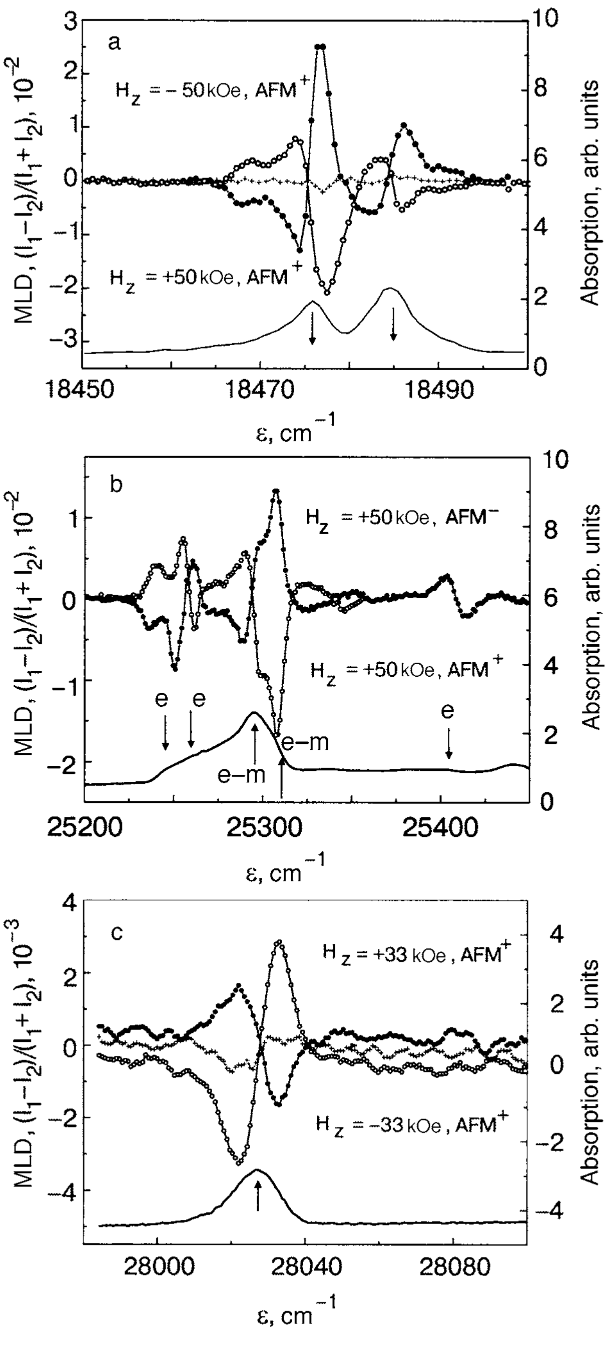

FIG. 3. Spectra of magnetic linear dichroism induced by a longitudinal magnetic field $H\|C_4:k$ in the $\mathrm{MnF_2}$ crystal in the region of the optical transitions $^6A_{1g}(^6S_{5/2})-{}^4T_{1g}(^4G)$ (the *A* group of bands) (a); $^6A_{1g}(^6S_{5/2})-{}^4E_g$, $^4A_{1g}(^4G)$ (the *C* group of bands) (b); $^6A_{1g}(^6S_{5/2})-{}^4T_{2g}(^4D)$ (the *D* group of bands) (c). The absorption spectrum is shown in the lower part of each panel. Prior to the measurements a uniform AFM state was created in the samples. The curves with data points in the form crosses were obtained at $H=0$.

Figure 3b shows the MLD spectra and the absorption spectrum of the *C* group of bands, formed by the transitions $^6A_{1g}(^6S_{5/2})-{}^4E_g$, $^4A_{1g}(^4G)$. The electronic configuration of the excited electronic states is close to $t_{2g}^3e_g^2$. The energies of two electronic (excitonic) magnetic-dipole transitions, M_1 and M_2 (25245 and $25260\ \mathrm{cm^{-1}}$), with oscillator strengths 0.5×10^{-8} and 0.9×10^{-8}, and their satellites (25295 and $25311\ \mathrm{cm^{-1}}$), with oscillator strengths 0.3×10^{-7} and 0.9

$\times 10^{-7}$, are indicated, along with the transition M_3 at $25404\,\mathrm{cm}^{-1}$, which apparently is also purely electronic (see Refs. 8 and 10). According to Ref. 8, the excited electronic states M_1 and M_2 are orbital components of the ^4E_g state, split by the z component of the orthorhombic crystalline field, while the M_3 state comes out of ^4A_g (Ref. 10). The field-induced dichroism is clearly seen not only in the region of strong electric-dipole exciton-magnon satellites but also in the region of weak magnetic-dipole transitions having a large g factor. We note that these transitions are much less visible in the α absorption spectrum than in the dichroism spectra. The largest value of the MLD is reached at an energy of $25310\,\mathrm{cm}^{-1}$ in the region of the second exciton-magnon band, where it is close to 1.7×10^{-2} in a magnetic field $H = 50$ kOe.

The spectral dependence of the MLD in the region of the D group of bands is shown in Fig. 3c. This part of the spectrum of the MnF_2 crystal is formed by optical transitions between the states $^6A_{1g}(^6S_{5/2})$ and $^4T_{2g}(^4D)$. The fraction of the $t_{2g}^3e_g^2$ configuration in the configurations of the excited states of the ion is appreciable, close to 0.83. The absorption band with maximum near $28026\,\mathrm{cm}^{-1}$ is attributed to an exciton-magnon transition.[8] The oscillator strength of this transition in the σ spectrum is 0.17×10^{-7}. Odd MLD was recorded in the region of this band. The figure shows the MLD spectra obtained for the AFM state of the sample in magnetic fields of opposite directions. The curves demonstrate the change of sign of the MLD for the same AFM state when the direction of the magnetic field is reversed. The maximum value of the dichroism, scaled to 50 kOe, in this band is close to 3.5×10^{-3}. We note that the amplitude of the anomalies on the curves are noticeably different. The difference is most likely due not to a partial switching of the AFM$^+$ state and the formation of AFM$^-$ domains but rather to the circumstance that in the higher energy region of the spectrum, the more-stringent tolerances on the deviations of the light beam from the tetragonal axis and on the allowable macroscopic stress in the sample are exceeded. A similar but less pronounced asymmetry is also observed in the spectra of the C group.

The stated properties of the MLD, viz., oddness with respect to a reversal of the field direction and with respect to switching of the AFM states, attest to the fact that the observed dichroism is indeed a manifestation of a linear magnetooptic effect.

The values of the MLD in all groups of absorption bands is of the same order as the usual magnetic circular dichroism. Figure 4 shows the MCD spectra which we obtained in the region of the A, C, and D groups of bands. The form of the MCD spectra in the region of the A and C groups is close to the form of the MCD spectra measured previously in Ref. 9 (A group) and 10 (C group), but the differences in the details are significant. The dispersion curves of the MLD and MCD are close for the A and D groups but noticeably different for the C group. In the A group both the MLD and MCD spectra, in addition to the features corresponding to exciton-magnon transitions, have a feature at $18465-18470\,\mathrm{cm}^{-1}$, which is the position of the magnetic-dipole excitonic transition that was predicted and observed in Ref. 6. Near $18456-18457\,\mathrm{cm}^{-1}$ a feature which was also observed in Ref. 9 is seen in the MCD spectrum (but not in the MLD).

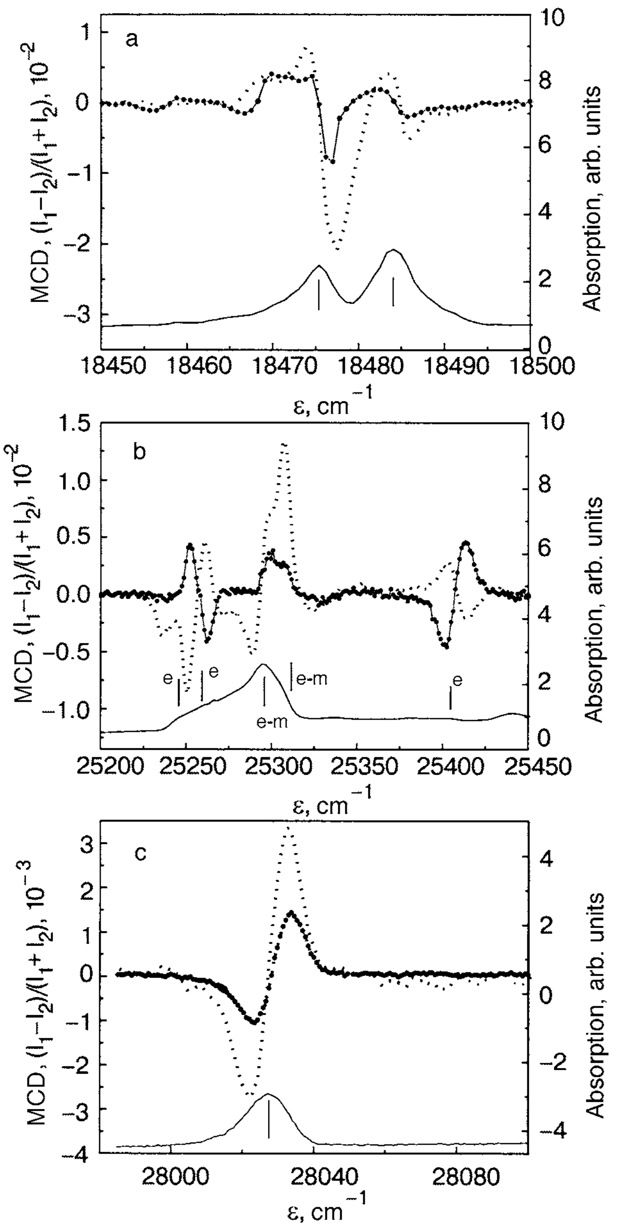

FIG. 4. Spectrum of magnetic circular dichroism (MCD) induced by a longitudinal magnetic field in the region of the optical transitions. The curves with filled dots are the MCD, the dotted curves are the MLD: $^6A_{1g}(^6S_{5/2}) - {}^4T_{1g}(^4G)$ (A group), $H = 50$ kOe (a); $^6A_{1g}(^6S_{5/2}) - {}^4E_g$, $^4A_{1g}(^4G)$ (C group), $H = 50$ kOe (b); $^6A_{1g}(^6S_{5/2}) - {}^4T_{2g}(^4D)$ (D group), $H = 33$ kOe (c). The absorption spectrum is shown in the lower part of each panel.

In the exciton-magnon bands the MLD is noticeably larger than the MCD, and therefore the values of the g factors for the exciton-magnon satellites and for magnons, which were determined on the basis of the values of the MCD of the corresponding absorption bands,[9,10] must be corrected with the MLD taken into account. In our opinion, the question of spontaneous magnetic circular (and linear) dichroism, which is discussed in Refs. 9 and 11, requires additional careful experimental study.

CONCLUSION

In the antiferromagnetic manganese fluoride crystal a longitudinal magnetic linear dichroism is observed in the exciton and exciton-magnon absorption bands: a magnetic field induces a different absorption of linearly polarized light propagating along the magnetic field vector parallel to the tetragonal axis of the crystal. It is found that the magnetic linear dichroism is odd with respect to reversal of the magnetic field direction and to switching of the antiferromagnetic state, i.e., to a reversal of the directions of the magnetic moments of the sublattices of the antiferromagnetic crystal. The largest MLD, close to 0.5×10^{-3} kOe^{-1}, was observed in the region of the first exciton-magnon satellite in the *A* group of bands of the absorption spectrum. The value of the effect is sufficient for visual observation of AFM domains in the MnF_2 crystal with the use of modern techniques for optical visualization of low-contrast objects and the methods of high-resolution spectroscopy.

It is clear that the MLD and MCD spectra complement each other and can be useful for determining the wave functions of the excited states and for revealing subtle differences in the behavior of excitons and magnons in magnetic field.

[*]E-mail: kharchenko@ilt.kharkov.ua

---

[1] R. A. Erickson, Phys. Rev. **90**, 779 (1953); A. S. Borovik-Romanov and H. Grimmer, "Magnetic properties," in *Physical Properties of Crystals*, Vol. D of Internatonal Tables for Crystallography, A. Authier (ed.), Published for the International Union of Crystallography by Kluwer Academic Publishers, Dordrecht-Boston-London (2003), p. 105.

[2] Jimia Zhao, Andrea V. Bragas, David J. Lockwood, and Roberto Merlin, ArXiv cond-mat/0311329 (2003).

[3] Y. Shapira, S. Foner, and A. Misetich, Phys. Rev. Lett. **23**, 98 (1969); R. L. Melcher, Phys. Rev. **2**, 733 (1970); K. L. Dudko, V. V. Eremenko, and L. M. Semenenko, Fiz. Nizk. Temp. **1**, 68 (1975) [Sov. J. Low Temp. Phys. **1**, 33 (1975)].

[4] A. S. Borovik-Romanov, N. M. Kreĭnes, A. A. Pankov, and M. A. Talalaev, Zh. Éksp. Teor. Fiz. **64**, 782 (1974) [*sic*]. I. R. Jahn and H. Dachs, Phys. Status Solidi B **57**, 681 (1973).

[5] N. F. Kharchenko and V. V. Eremenko, Fiz. Tverd. Tela (Leningrad), **9**, 1655 (1967) [Sov. Phys. Solid State **9**, 1302 (1967)].

[6] R. L. Greene, D. D. Sell, W. M. Yen, A. L. Schawlow, and R. M. White, Phys. Rev. Lett. **15**, 656 (1965).

[7] V. V. Eremenko and Yu. A. Popkov, Phys. Status Solidi **12**, 627 (1965); Philip G. Russell, Donald S. McClure, and J. W. Stout, Phys. Rev. Lett. **16**, 176 (1966); D. D. Sell, R. L. Greene, and Robert M. White, Phys. Rev. **158**, 489 (1967); D. D. Sell, J. Appl. Phys. **39**, 1030 (1968); T. Tsuboi and P. Ahmet, Phys. Rev. B **45**, 468 (1992).

[8] R. S. Meltzer and L. L. Lohr, J. Chem. Phys. **49**, 541 (1968); R. S. Meltzer, M. Lowe, and D. S. McClure, Phys. Rev. **180**, 561 (1969).

[9] Y. H. Wong, F. L. Scarpace, C. D. Pfeifer, and W. M. Yen, Phys. Rev. B **9**, 3086 (1974); P. W. Seltzer, W. C. Egbert, D. L. Huber, and W. M. Yen, *ibid.* **12**, 961 (1975).

[10] R. W. Schwartz, J. A. Spencer, W. C. Yeakel, P. N. Schatz, and W. G. Maisch, J. Chem. Phys. **60**, 2598 (1974).

[11] D. J. Lockwood, R. M. White, and W. M. Yen, Phys. Rev. B **69**, 174413 (2004).

[12] V. V. Eremenko, *Introduction to the Optical Spectroscopy of Magnets* [in Russian], Naukova Dumka, Kiev (1975).

[13] P. A. Fleury, S. P. S. Porto, and R. Loudon, Phys. Rev. Lett. **18**, 658 (1967); D. J. Lockwood and M. Cottam, Phys. Rev. B **35**, 1973 (1987).

[14] M. G. Cottam and D. J. Lockwood, *Light Scattering in Magnetic Solids*, Wiley, New York, (1986).

[15] W. Parkinson and E. W. Willams, J. Chem. Phys. **18**, 534 (1950).

[16] H. Mariette, F. Kany, and J. M. Hartman, Appl. Surf. Sci. **123/124**, 710 (1998); N. S. Sokolov, Y. Takeda, A. G. Banschikov, J. Harada, K. Inaba, H. Ofuchi, M. Tabuchi, and N. L. Yakovlev, *ibid.* **162/163**, 469 (2000).

[17] J. Nogues and I. K. Schuller, J. Magn. Magn. Mater. **192**, 203 (1999), Zhi-Pan Li, O. Petracic, J. Eisenmenger, and I. K. Schuller, ArXiv cond-matter/0501158 (2005).

[18] V. V. Eremenko, N. F. Kharchenko, Yu. G. Litvinenko, and V. M. Naumenko, Magneto-Optics and Spectroscopy of Antiferromagnets, Springer-Verlag, New York (1992); N. F. Kharchenko, Ferroelectrics **162**, 173 (1994).

[19] N. F. Kharchenko, V. V. Eremenko, and L. I. Belyi, JETP Lett. **28**, 325 (1979); N. F. Kharchenko, A. V. Bibik, and V. V. Eremenko, JETP Lett. **42**, 553 (1985).

[20] N. F. Kharchenko, V. V. Eremenko, and L. I. Belyi, JETP Lett. **29**, 392 (1979); V. V. Eremenko, N. F. Kharchenko, and L. I. Belyi, J. Appl. Phys. **50**, 7751 (1979).

[21] M. Schlenker and J. Baruchel, J. Appl. Phys. **49**, 1996 (1978); M. Schlenker, J. Baruchel, and B. Barbara, J. Magn. Magn. Mater. **15–18** (1980).

[22] A. V. Bibik, N. F. Kharchenko, and S. V. Petrov, Fiz. Nizk. Temp. **15**, 1280 (1989) [Sov. J. Low Temp. Phys. **15**, 707 (1989)].

Translated by Steve Torstveit

PERSONALIA

Viktor Grigor'evich Bar'yakhtar (on his 75th birthday)

[DOI: 10.1063/1.2044810]

On August 9, 2005 the prominent theoretical physicist Viktor Grigor'evich Bar'yakhtar, Member of the National Academy of Sciences of Ukraine, turned 75. In the course of over forty years he has published a paper that has been seminal in various fields of theoretical physics, carried on an enormous amount of scientific organizational activity within the NAS Ukraine system, served on government and international committees and scientific councils and on the editorial boards of journals, and taught at the Universities of Kharkov, Donetsk, and Kiev. He is the Director of the Institute of Magnetism of the NAS Ukraine, which was founded by him.

Bar'yakhtar obtained ground-breaking results in the theory of magnetism and phase transitions. In particular, he constructed a theory of magnetoacoustic resonance, a theory of the intermediate state near a first-order phase transition in magnetic field, a phenomenological description of relaxation processes in magnets, and a theory of the superconducting transition under pressures altering the topology of the Fermi surface. His scholarly activity is reflected in numerous articles, conference proceedings, and monographs. He has created an active and successful school of theoretical physicists.

Bar'yakhtar has been awarded the Order of Merit of Ukraine in Science and several State and Academy of Sciences prizes, orders, and medals.

Viktor Grigor'evich possesses great magnetism owing to the wealth of his scientific ideas and his sterling personal qualities. We heartily congratulate him on his birthday and wish him many more years of good health, creative activity, and charisma.

Editorial Board of *Low Temperature Physics*

Radii Nikolaevich Gurzhi (on his 75th birthday)

[DOI: 10.1063/1.2044811]

August 11, 2005 is the 75th birthday of the prominent theoretical physicist and Laureate of the State Prize of Ukraine, Radii Nikolaevich Gurzhi. The quantum kinetic equation for electrons, obtained by Gurzhi when a graduate student, became the basis for his well-known results in metal optics which extended the concepts of Landau's theory of the Fermi liquid into the region of relatively high frequencies.

Gurzhi's most important scientific ideas were announced during his work at the Ukrainian Physico-Technical Institute (from 1958). In his first paper, published in 1963, a system of quasiparticles in a solid was treated as a Poisueille fluid whose behavior is described by the equations of hydrodynamics. The term "Gurzhi effect" has long been used in the literature for manifestations of hydrodynamic phenomena in electrical conduction. Another unexpected effect predicted by Gurzhi and observed experimentally is the role of anharmonicities of arbitrarily high order in the thermal conductivity of ferromagnetic insulators. Gurzhi and his students have studied a wide range of problems in solid-state kinetics under conditions such that normal collision processes of quasiparticles dominate or compete with processes leading to momentum relaxation. The numerous results obtained on that topic have been presented in monographs and text books and have found wide experimental confirmation. Since his arrival in 1974 at the Institute for Low Temperature Physics and Engineering of the National Academy of Sciences of Ukraine, his ideas have been applied to new solid-state objects—nanostructures of reduced dimensionality. He has shown that lowering the dimensionality of the space radically alters the character of electron-electron scattering in conductors.

His colleagues and students who are celebrating this birthday value his special combination of scholarly and human qualities: his ability to frame unexpectedly simple questions in complex problems, and his informal, intelligent, and human style of personal contact irrespective of station. We esteem and love our dear Radii Nikolaevich and wish him long years of fruitful scientific activity.

Editorial Board of *Low Temperature Physics*

ERRATA

Erratum: Evgenii Stanislavovich Borovik on the ninetieth anniversary of his birth [Low Temperature Physics 31, 183 (2005)]

V. V. Eremenko and V. S. Borovikov

Due to a translation error, on page 183, in the third paragraph of the text, the title of the Candidate's Dissertation has been corrected. The correct title should read *The Heat Conductivity of Liquids ...*

1063-777X/2005/31(8–9)/1/$26.00